UNIVERSITÀ
DI PAVIA

**Dipartimento di Biologia e Biotecnologie "L. Spallanzani"**

# Diabetes - brain axis: association between metabolic biomarkers and recognition memory in two experimental preclinical models

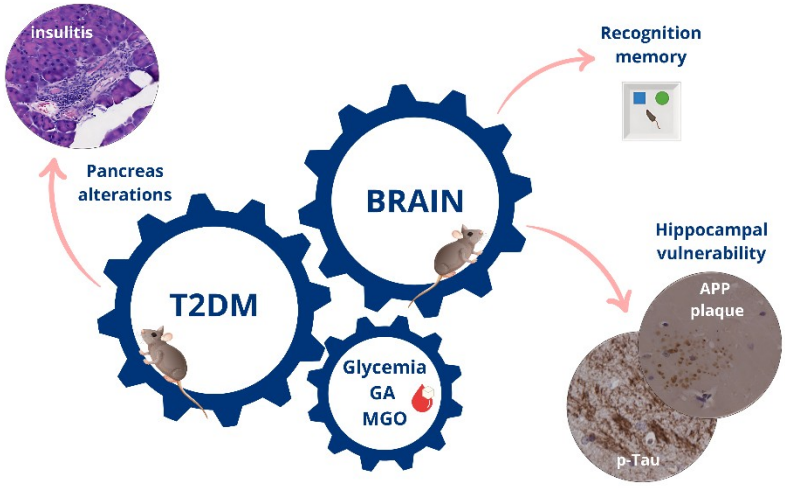


**Maria Teresa Venuti**

Dottorato di Ricerca in
Genetica, Biologia Molecolare e Cellulare
Ciclo XXXVIII – A.A. 2022-2025

## Summary

## 1. Abstract

Type 2 diabetes mellitus (T2DM) is the most common form of diabetes and one of the fastest-growing metabolic disorders worldwide. Beyond its systemic complications, T2DM increases the risk of cognitive impairment and dementia, particularly Alzheimer's disease (AD). This convergence has led to the concept of AD as "type 3 diabetes," driven by hyperglycemia, insulin resistance, oxidative stress, and the accumulation of advanced glycation end-products (AGEs). Despite this evidence, glycated hemoglobin (HbA1c) remains the gold-standard biomarker for glycemic control, although it reflects only long-term glycemia and is unreliable in several comorbidities. Glycated albumin (GA) and methylglyoxal (MGO) have emerged as promising alternatives: GA captures short-term glycemic variability, while MGO is a highly reactive dicarbonyl driving AGE formation. Their translational value in monitoring diabetes-related cognitive decline, however, has not been systematically investigated.

My Ph.D. project investigated the link between diabetes and cognitive impairment, with a specific focus on recognition memory and hippocampal pathology, and assessed the potential of GA and MGO as biomarkers of T2DM progression. A critical challenge was the choice of appropriate animal models. Animal models of diabetes lack standardized protocols and often yield inconsistent outcomes. Low-dose streptozotocin (STZ) can be interpreted as inducing either type 1–like or aspects of T2DM, and few longitudinal studies clarify its natural history. Similarly, HFD/STZ protocols vary widely between laboratories regarding STZ dosage, number of injections, and duration of high-fat feeding, limiting reproducibility and translational clarity.

To address this, two experimental models were developed. The first model (STZ model) was based on low-dose streptozotocin (STZ) administration in adult mice. This model was examined under two different conditions: one group of animals followed a normal diet (ND), while another group was exposed to a detrimental high-sugar (HS) diet. The HS diet was applied to evaluate whether excessive sugar intake could induce or exacerbate the diabetic condition. The second preclinical model (HFD/STZ model) combined a high-fat diet (HFD) with low-dose STZ treatment. In addition, HFD alone was studied to assess the specific contribution of diet-induced metabolic

changes. These models were followed longitudinally from adulthood to senescence, allowing integrated evaluation of systemic metabolism, biomarkers, behavior, and hippocampal injury.
As expected, in control mice glycemia and GA were not affected by advancing age, whereas MGO declined progressively, suggesting serum MGO may decrease as intracellular sequestration and AGE formation increase when detoxification capacity becomes less efficient. A long exposure to 10%HS supplementation modestly increased GA, but did not alter the other metabolic parameters (fasting glycemia and MGO) in both control and diabetic mice. Instead, HFD feeding produced progressive hyperglycemia and insulin resistance, confirming its role as a driver of metabolic dysfunction.

The STZ model induced a severe diabetic phenotype characterized by hyperglycemia, elevated GA, insulitis, and pancreatic islet disorganization, along with impaired recognition memory and hippocampal injury, with tau hyperphosphorylation and β-amyloid accumulation. Unexpectedly, most diabetic animals in this model exhibited partial spontaneous remission. This recovery was accompanied by partial restoration of pancreatic islet architecture, improved recognition memory, and attenuation of hippocampal injury, suggesting intrinsic plasticity at both the pancreatic and brain levels.

In contrast, the HFD/STZ model induced a persistent diabetic phenotype with sustained hyperglycemia, insulin resistance, elevated GA and MGO, pancreatic insulitis, impaired recognition memory, and severe hippocampal pathology, including tau hyperphosphorylation and β-amyloid accumulation.

Taken together, these findings demonstrate that GA and MGO provide complementary insights into diabetes progression and its neurological consequences. While HbA1c remains the conventional marker of long-term glycemic control, GA better reflects short-term fluctuations, and MGO captures the burden of dicarbonyl stress and AGE formation. The integration of these biomarkers with behavioral and neuropathological outcomes reinforces their translational potential for monitoring diabetes-related cognitive decline. Furthermore, the comparison of preclinical models revealed substantial differences: the STZ model displayed a tendency toward partial remission and functional recovery, whereas the HFD/STZ model produced a persistent and severe diabetic phenotype with sustained cognitive and hippocampal deficits.

In conclusion, this Ph.D. project highlights the importance of selecting appropriate experimental models to investigate the complex interplay between diabetes and brain pathology. It provides evidence that GA and MGO represent promising biomarkers of systemic metabolic dysregulation that are consistently associated with diabetes-related cognitive impairment and hippocampal alterations. The observation of spontaneous recovery in the STZ model suggests intrinsic plasticity at both pancreatic and neuronal levels. In contrast, the persistence of pathology in the HFD/STZ model underscores the detrimental impact of diet-induced metabolic alterations. Overall, these findings support the value of GA and MGO for monitoring diabetes-associated cognitive decline and point to new avenues for interventions aimed at preserving brain health in T2DM.

## 2. Abbreviations

AD: Alzheimer's Disease

AGEs: Advanced Glycation End-products

APOE: apolipoprotein E

APP: amyloid precursor protein

Aβ: β-amyloid

BACE-1: β-site amyloid precursor protein cleaving enzyme 1

BBB: Blood-Brain Barrier

CDK5: cyclin-dependent kinase 5

CI: Cognitive Impairment

CNS: Central Nervous System

COX-2: cyclooxygenase-2

CRP: C-reactive protein

DI: Discrimination Index

DM: Diabetes Mellitus

eNOS: endothelial nitric oxide synthase

ERS: Endoplasmic Reticulum Stress

FAD: familial AD

FI: Frailty Index

FPG: Fasting Plasma Glucose

G3P: Glyceraldehyde-3-phosphate

GA: Glycated Albumin

GIP: Glucose-dependent Insulinotropic Polypeptide

GLO: Glyoxalase

GLP-1: Glucagon-Like Peptide 1

GLUT: Glucose transporter

Grb2: Growth factor receptor-bound protein 2

GSH: Glutathione

GSK-3β: glycogen synthase kinase-3β

HbA1c: Glycated hemoglobin

HFD: High Fat Diet

HOMA-IR: Homeostatic Model Assessment of Insulin Resistance

IAPP: Amylin

IDE: Insulin-Degrading Enzyme

IDF: International Diabetes Federation

IFG: Impaired Fasting Glucose

IGF: Insulin-like Growth Factor

IGFRs: IGF receptors

IGT: Impaired Glucose Tolerance

IL: Interleukin

IR: Insulin Resistance

IRS: Insulin Receptor Substrates

IRs: Insulin Receptors

JNK: c-Jun N-terminal kinase

LTD: Long-Term Depression

LTP: Long-Term Potentiation

MAPK: mitogen-activated protein kinase

MCI: Mild Cognitive Impairment

MGO: Methylglyoxal

mTORC1: mammalian Target of rapamycin complex 1

NAFLD: Non-Alcoholic Fatty Liver Disease

NF-kB: Nuclear factor kappa-light-chain-enhancer of activated B cells

NFTs: Neurofibrillary tangles

NO: Nitric Oxide

NOR: Novel Object Recognition

NOS: Nitric Oxide Synthases

NOX: NADPH Oxidases

OGTT: Oral Glucose Tolerance Test

OL: Object Location

PCOS: Polycystic Ovary Syndrome

PHFs: Paired Helical Filaments

PP: Pancreatic Polypeptide

PP2A: protein phosphatase 2A

RAGE: Receptor of Advanced Glycation End-products

RMS: Rabson–Mendenhall syndrome

RNS: Reactive Nitrogen Species

ROS: Reactive Oxygen Species

sAPPα: soluble amyloid precursor protein alfa

sAPPβ: soluble amyloid precursor protein beta

SNPs: Single-nucleotide polymorphisms

STZ: Streptozotocin

T1DM: Type 1 Diabetes Mellitus

T2DM: Type 2 Diabetes Mellitus

T3DM: Type 3 Diabetes Mellitus

TAIRS: Type A IR syndrome

TBIRS: Type B IR syndrome

TNF: Tumor Necrosis Factor

WHO: World Health Organization

XO: Xanthine Oxidases

# 3. Introduction

## 3.1. Diabetes Mellitus: epidemiology and classification

Diabetes mellitus (DM) is a metabolic disorder characterized by chronic hyperglycemia resulting from insulin deficiency. Insulin is a hormone secreted by pancreatic β-cells, which, under pathological conditions, may either fail to be produced or, even if produced, may be insufficient or ineffectively utilized by the target cells of the organism (Nowotny et al., 2015).
DM currently represents a global public health issue. According to the International Diabetes Federation (IDF), in 2024 approximately 589 million individuals worldwide will be affected by DM. Both the IDF and the World Health Organization (WHO) further estimate that the prevalence of this condition will rise to 853 million cases by 2050 (International Diabetes Federation, 2025).
Beyond the characteristics of hyperglycemia, additional alterations are frequently observed in DM, including insulin resistance, compensatory hyperinsulinemia, and impaired insulin secretion. Moreover, DM is not limited to the two well-known forms but comprises up to nine distinct types, with the intermediate state of prediabetes also clinically recognized. Prediabetes is defined as a condition in which blood glucose levels are above the physiological range but not yet high enough to meet the diagnostic threshold for diabetes, typically between 110 and 125 mg/dL (5.7–6.4 mmol/L). This state is associated with impaired fasting glucose (IFG) and/or impaired glucose tolerance (IGT). Patients with prediabetes often present with abdominal or visceral obesity, dyslipidemia characterized by elevated triglycerides and/or reduced HDL cholesterol, and hypertension (American Diabetes Association, 2021).

Diabetes can be classified into two main forms: type 1 diabetes mellitus (T1DM) and type 2 diabetes mellitus (T2DM). Both forms are associated with chronic hyperglycemia caused by impaired carbohydrate, lipid, and protein metabolism (Hamzé et al., 2022).

### 3.1.1. Type 1 diabetes

T1DM is a multifactorial autoimmune disease in which genetic susceptibility, most strongly conferred by polymorphisms in the major histocompatibility complex (MHC), particularly human leukocyte antigen (HLA) class II alleles,

interacts with environmental triggers such as viral infections, dietary factors, and gut microbiota to initiate immune-mediated β-cell destruction (Tosur et al., 2025). These genetic and environmental interactions lead to the production of autoantibodies that trigger an autoimmune response against pancreatic β-cells. The disease manifests clinically when approximately 80% of these cells are destroyed, thereby suppressing insulin production. Typically, onset occurs during childhood or adolescence, and from the moment of diagnosis, patients require lifelong exogenous insulin therapy to manage their glycemia and prevent severe complications (Santiago et al., 2023).

The absence of insulin disrupts the functional and metabolic profile of organs involved in the fasting-feeding cycle. Consequently, glucagon activity predominates, driving the metabolic response of these organs under fasting conditions. In particular, the liver activates gluconeogenesis, leading to protein catabolism for the production of amino acids (mainly glutamine and alanine). Thus, despite glucose intake from the diet, the liver continues to release additional glucose into circulation. Insulin also promotes fatty acid storage in adipose tissue; in its absence, fatty acids are released from adipose depots and utilized, for example, by the liver to fuel gluconeogenesis or to produce ketone bodies. Dietary fatty acids, not being stored efficiently in adipose tissue, tend to accumulate in the bloodstream. In uncontrolled diabetic patients, ketone body levels increase significantly, representing the most critical risk factor. Ketone bodies are acidic molecules that, when present in excess, saturate the bicarbonate buffering system, leading to metabolic acidosis. In severe cases, this condition may progress to diabetic coma (Guthrie & Guthrie, 2004).

The clinical picture of T1DM reflects these underlying mechanisms: severe hyperglycemia, episodes of hypoglycemia linked to exogenous insulin administration, and a marked tendency toward ketoacidosis are common. From an endocrine perspective, patients generally present with preserved or increased peripheral insulin sensitivity (particularly at early stages), mostly elevated glucagon or normal levels of glucagon and reduced secretion of pancreatic polypeptide (PP), reduced or normal secretion of glucose-dependent insulinotropic polypeptide (GIP), and preserved glucagon-like peptide-1 (GLP1) (Guglielmi et al., 2017). A distinct variant, idiopathic T1DM, is characterized by insulinopenia and recurrent ketoacidosis in the absence of β-cell autoimmunity. Unlike the classical autoimmune form, this

variant shows no association with HLA polymorphisms, and its etiology remains unclear. It is not a monogenic form of diabetes (such as MODY), since it does not follow a defined pattern of genetic inheritance (American Diabetes Association, 2021).

### 3.1.2. Type 2 diabetes

T2DM, which accounts for approximately 90% of DM cases, is characterized by insulin resistance combined with a relative insulin deficiency, which can progress to severe deficiency with the onset of beta-cell failure. Clinically, T2DM is diagnosed when repeated fasting plasma glucose levels reach or exceed 126 mg/dL, and is confirmed by a 2-hour plasma glucose during a 75 g oral glucose tolerance test (OGTT) is ≥ 200 mg/dL, or when HbA1c is ≥ 6.5% (Villegas-Valverde et al., 2018).

The onset of T2DM is strongly influenced by lifestyle and dietary habits. Sedentary behavior, excess adiposity, and hypercaloric diets rich in refined carbohydrates and saturated fats represent the major risk factors, as they promote chronic hyperinsulinemia, low-grade inflammation, and lipid accumulation in insulin-sensitive tissues, progressively impairing insulin signaling and glucose homeostasis (Guthrie & Guthrie, 2004; Santiago et al., 2023).

The pathogenesis reflects a combination of insulin resistance, impaired peripheral glucose disposal, eventually leading to islet dysfunction and reduced insulin secretion. Thus, the pathology arises not from a lack of insulin production but from the inability of target tissues to respond to insulin signaling. Indeed, patients with T2DM can produce insulin, but their target cells become insensitive or nearly refractory to its action, giving rise to an insulin resistance condition (Khin et al., 2023; Figure 1).

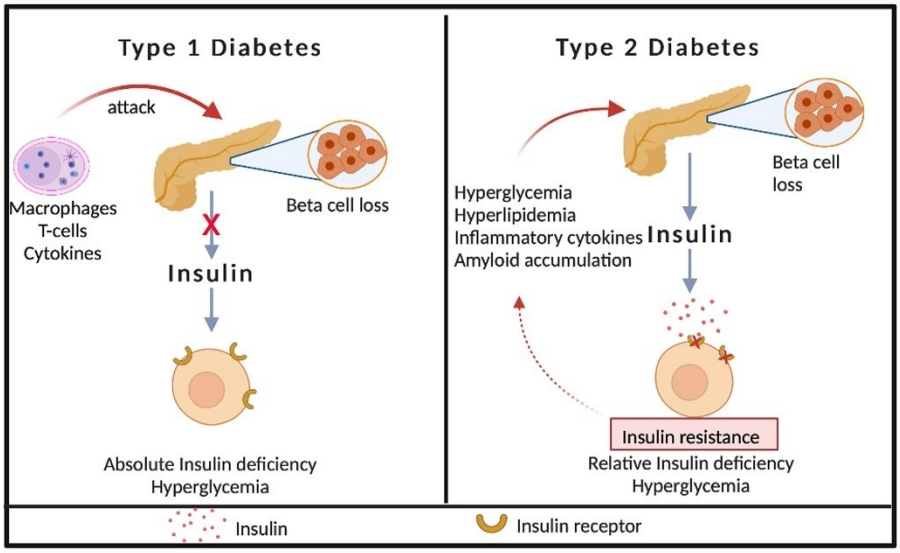


***Figure 1.*** *Different pathogenesis of T1DM and T2DM. T1DM results from immune-mediated destruction of pancreatic β-cells, causing absolute insulin deficiency and hyperglycemia. T2DM is characterized by β-cell dysfunction due to glucotoxicity, lipotoxicity, cytokines, amyloid deposits, and insulin resistance and/or hyperglycemia, leading to relative insulin deficiency in the context of peripheral insulin resistance (Khin et al., 2023).*

Consequently, T2DM is managed primarily with pharmacological agents that improve insulin sensitivity, reduce hepatic glucose production, or stimulate insulin secretion. For example, metformin reduces hepatic gluconeogenesis, thiazolidinediones improve insulin sensitivity in adipose tissue and muscle, and sulfonylureas stimulate pancreatic insulin secretion. However, due to the limitations of traditional therapies, including incomplete glycemic control and adverse effects, new classes of drugs have been developed. These include SGLT2 inhibitors, which lower blood glucose by reducing renal glucose reabsorption, and GLP-1 receptor agonists, which enhance insulin secretion, suppress glucagon, and reduce appetite. These agents are used not only to improve glycemic control but also to promote weight loss and provide cardiovascular and renal protection (Gieroba et al., 2025).

The metabolic profile of T2DM patients differs from that of T1DM patients. Although the organism experiences feeding-fasting fluctuations, it does not adequately respond to them. Initially, the pancreas compensates by increasing insulin secretion, leading to compensatory hyperinsulinemia, which characterizes metabolic syndrome (Syndrome X) (Guthrie & Guthrie, 2004).

Unlike in T1DM, residual endogenous insulin secretion in T2DM usually prevents excessive lipolysis and ketone body formation, reducing the risk of diabetic ketoacidosis. However, inappropriately elevated glucagon secretion despite hyperglycemia, together with hepatic insulin resistance, contributes to excessive hepatic glucose production, which is a major driver of fasting hyperglycemia (Barroso et al., 2024; Chung et al., 2015; DeFronzo, 2015). In T2DM, glucose uptake by adipose tissue and muscle is impaired, causing hyperglycemia. Insulin normally inhibits lipolysis and promotes lipid storage by stimulating lipoprotein lipase and suppressing hormone-sensitive lipase. In T2DM, insulin fails to suppress lipolysis, leading to excess release of free fatty acids (FFAs) from adipocytes. These FFAs are taken up by the liver, re-esterified into triglycerides, and secreted as VLDL, resulting in hypertriglyceridemia and atherogenic dyslipidemia (elevated TG, decreased HDL). Inflamed, hypertrophic adipose tissue loses capacity to efficiently store lipids, further exacerbating circulating TG and FFA levels (Adiels et al., 2008; Boden, 2011). In addition to these metabolic defects, inflammation, ectopic lipid deposition, endoplasmic reticulum stress (ERS), and oxidative stress further impair insulin sensitivity and β-cell function, contributing to disease onset and progression as well as to target organ damage. Nevertheless, the most significant complications associated with T2DM derive from chronic hyperglycemia, which may lead to non-enzymatic protein glycation and subsequent functional alterations in vital organs such as the lens and kidneys. Over the years, hyperglycemia has also been identified as a major contributing factor to severe cardiovascular complications (accounting for 50% of mortality in these patients) and to nervous system damage (Nowotny et al., 2015).

Additionally, there is a strong comorbidity with obesity: approximately 80% of T2DM patients are obese, although the majority of obese individuals are not diabetic (Guthrie & Guthrie, 2004).

### 3.2. The systemic complications of T2DM

As previously described, T2DM is a chronic multisystem disease in which long-standing hyperglycemia and insulin resistance translate into organ-specific complications that largely determine prognosis and quality of life. The main clinical features of T2DM will be described in this section.

### 3.2.1. Hyperglycemia

Hyperglycemia represents the central clinical manifestation of T2DM and constitutes the main driver of both acute and chronic complications.

In the fasting state, hyperglycemia arises from an inappropriately low insulin-to-glucagon ratio, which drives hepatic glucose overproduction. After meals, hyperglycemia stems from insufficient insulin availability or action, limiting glucose uptake in insulin-sensitive tissues. Postprandial excursions are further shaped by meal size and composition, carbohydrate content, and the dynamics of insulin release and glucagon suppression (Simon & Wittmann, 2019; Yari et al., 2020).

Sustained hyperglycemia has profound systemic effects. Higher glycemic levels are positively correlated with cardiovascular risk, and chronic exposure predisposes to acute metabolic decompensation, including diabetic ketoacidosis and hyperosmolar hyperglycemic state. In the long term, persistent hyperglycemia promotes the non-enzymatic glycation of proteins and lipids, leading to the accumulation of advanced glycation end-products (AGEs). These molecules interact with their receptor (RAGE), activate pro-inflammatory and oxidative pathways, and alter protein structure and function. Such processes underlie microvascular complications (retinopathy, nephropathy, neuropathy) and macrovascular disease (coronary artery disease, stroke, peripheral artery disease), which together account for the majority of morbidity and mortality in T2DM (Nowotny et al., 2015; Pliszka & Szablewski, 2024).

At the cellular level, excessive glucose enhances the production of reactive oxygen species (ROS), damages DNA and lipids, and disrupts mitochondrial function. This oxidative stress perpetuates inflammation, worsens insulin resistance, and accelerates β-cell dysfunction, creating a self-reinforcing cycle of metabolic deterioration (Nowotny et al., 2015).

Hyperglycemia also contributes to oncogenesis. The Warburg effect illustrates the reliance of tumor cells on glycolysis; abundant circulating glucose supports biosynthetic pathways and energy production, thereby favoring tumor growth and metastatic progression (Rahman et al., 2021; Wang et al., 2020).

In the nervous system, chronic hyperglycemia and AGE accumulation induce endothelial dysfunction, compromise the blood–brain barrier (BBB), and promote neuronal damage. These processes contribute to cognitive decline

and neurodegenerative changes, thus expanding the clinical burden of T2DM beyond its classical vascular complications (Simon & Wittmann, 2019; Yari et al., 2020).

Altogether, hyperglycemia is not only a diagnostic hallmark of T2DM but also a pathogenic force, linking metabolic dysregulation to acute crises, chronic vascular complications, oncogenesis, and neurological decline.

### 3.2.2. Insulin Resistance and hyperinsulinemia

Insulin resistance (IR) denotes a reduced responsiveness of insulin-target tissues to normal hormone concentrations, such that a higher-than-usual insulin level is required to achieve metabolic control. In other words, some cells or organs fail to respond adequately to physiological insulin, necessitating higher levels to maintain homeostasis. Clinically, IR encompasses rare, severe syndromes, including Donohue syndrome, Rabson–Mendenhall syndrome (RMS), type A IR syndrome (TAIRS), type B IR syndrome (TBIRS), type C IR/HAIR-AN, lipodystrophies, and other forms of severe IR (Lee et al., 2022; Szablewski, 2024).

In T2DM, sustained hyperglycemia often reflects diminished cellular insulin efficacy and reduced peripheral glucose utilization; to maintain euglycemia, β-cells increase insulin secretion, producing hyperinsulinemia. This adaptive drive involves β-cell hyperplasia and hypersecretion, but chronic overproduction ultimately impairs β-cell function, contributing to the onset and progression of T2DM. Hyperinsulinemia is therefore not only a marker of IR but also a pathogenic factor in its own right. Persistently high insulin alters cellular signaling, promotes lipogenesis, sympathetic overactivation, sodium retention, and endothelial dysfunction, and may contribute to hypertension, dyslipidemia, and atherosclerosis. Because of these maladaptive effects, some authors have introduced the concept of “insulin toxicity”, emphasizing that elevated insulin levels, independent of glycemia, are harmful to tissues and metabolic homeostasis (Cerf, 2013; Kolb et al., 2020).

Mechanistically, IR is multifactorial, arising from low-grade inflammation, disordered glucose handling with hyperglycemia and AGE formation, elevated free fatty acids and triglycerides, oxidative stress, mitochondrial dysfunction, endoplasmic reticulum stress, and reactive nitrogen species (RNS) (Fazakerley et al., 2018; Ma et al., 2018; Pinto-Junior et al., 2018).

Oxidative stress, in particular, increases highly reactive species that damage proteins, lipids, and nucleic acids (Dilworth et al., 2021).
Clinically, IR and hyperinsulinemia are closely associated with or contribute to non-alcoholic fatty liver disease (NAFLD), polycystic ovary syndrome (PCOS), Alzheimer's disease (AD), and cardiovascular and cerebrovascular disease (Li et al., 2021; Marušić et al., 2021; Sędzikowska & Szablewski, 2021).
Moreover, insulin can promote tumor development: epidemiological links connect IR/hyperinsulinemia to breast, colorectal, prostate, pancreatic, adrenocortical, endometrial, and other cancers (Szablewski, 2024).

Taken together, insulin resistance and compensatory hyperinsulinemia represent not only hallmarks of T2DM but also active drivers of metabolic deterioration. Their detrimental effects are largely mediated through enhanced oxidative stress and chronic low-grade inflammation, which will be further addressed in the following section.

### 3.2.3. Oxidative stress and Inflammation

Oxygen, essential for aerobic metabolism, can also give rise to highly reactive radicals. In its ground state, it bears two unpaired electrons and, upon excitation, can form singlet oxygen and other reactive derivatives collectively termed ROS. Primary enzymatic sources of ROS include NADPH oxidases (NOX) and xanthine oxidase (XO). In parallel, metabolites produced via nitric oxide synthases (NOS) are grouped as RNS. Endogenously, ROS and RNS originate from mitochondrial as well as non-mitochondrial enzymes. Within mitochondria, they arise during oxidative phosphorylation within the respiratory chain (notably complexes I and II) and via flavin-dependent enzymes in the matrix. RNS often result from the reaction of NOS-derived nitric oxide (NO) with existing ROS (Valko et al., 2007).
At physiological levels, ROS and RNS regulate stress responses, survival, and immune signaling. When their production exceeds antioxidant defenses (enzymatic: SOD, catalase; non-enzymatic: glutathione, ascorbate), oxidative stress develops. In diabetes, this imbalance is not incidental but a predictable consequence of the metabolic milieu, and it closely parallels the onset of complications (An et al., 2023).
In T2DM, hyperglycemia and insulin resistance both boost ROS production and weaken antioxidant capacity. Excess glucose increases electron leakage

from the mitochondrial respiratory chain. In the vasculature, ROS are also generated by NOX, XO, and uncoupled eNOS, reducing nitric oxide bioavailability and impairing endothelial function. Hyperglycemia further amplifies oxidative stress via four pathways: polyol flux, PKC activation, hexosamine flux, and AGE formation. Among these, AGE/RAGE signaling is especially relevant, as it activates NF-κB/MAPK cascades and NOX, linking glycation to inflammation and redox imbalance. Persistent oxidative stress impairs β-cell function, worsens insulin resistance, and promotes vascular damage, driving retinopathy, nephropathy, neuropathy, and cardiovascular disease (Caturano et al., 2023).

Oxidative cues and AGEs also act as danger signals. They activate pattern-recognition systems such as RAGE and selected TLRs, which trigger NF-κB–dependent transcription and cytokine release. Mitochondrial ROS, together with redox-sensitive adaptors, prime and activate the NLRP3 inflammasome. This promotes IL-1β/IL-18 maturation and links metabolic stress to β-cell dysfunction and vascular inflammation. Thus, ROS both initiates and results from inflammatory signaling, creating a cycle that sustains low-grade inflammation. This pro-inflammatory state is amplified in insulin-resistant adipose tissue. Visceral fat becomes immunologically active, with macrophage infiltration, pro-inflammatory polarization, and altered adipokine secretion. These changes increase circulating TNF-α, IL-6, and acute-phase reactants such as CRP. These mediators interfere with insulin signaling (via JNK and NF-κB), propagate endothelial dysfunction, and perpetuate systemic inflammation, thereby connecting overnutrition and inactivity to the vascular complications of T2DM (Tsalamandris et al., 2019).

The result is a tightly interlocked network in which hyperglycemia-driven redox stress and immune activation potentiate one another, constituting the mechanistic substrate for micro- and macrovascular damage and offering a plausible bridge to central nervous system vulnerability that will be explored in the following sections.

### 3.2.4. Cognitive impairment in T2DM

Cognitive impairment (CI) has emerged as a significant complication of T2DM, with multiple longitudinal and cross-sectional studies demonstrating that patients with T2DM are at substantially increased risk of both mild

cognitive impairment (MCI) and dementia (Biessels & Despa, 2018; Gudala et al., 2013; Jeong et al., 2025; Liao et al., 2025).

Over the last three decades, age-standardized rates of diabetes have shown a striking upward trend, with prevalence rising by approximately 90% globally. In 2021, diabetes affected more than half a billion people, and demographic projections suggest that the number of cases will more than double, reaching approximately 1.3 billion within the next 30 years (Ong et al., 2023).

This demographic expansion implies that T2DM-related cognitive complications will become an increasingly important public health concern.

The mechanisms linking T2DM to cognitive decline are multifactorial. Chronic hyperglycemia, insulin resistance, vascular dysfunction, oxidative stress, advanced glycation end products, and neuroinflammation act synergistically to drive neuronal injury. These processes converge on hallmark features of T2DM-related cognitive decline, including synaptic dysfunction, neuronal loss, white matter abnormalities, hippocampal atrophy, and impaired brain connectivity. Together, these changes compromise memory, executive function, and processing speed (Verdile et al., 2015).

Beyond clinical and imaging features, peripheral biomarkers have also been explored. Candidates include phosphorylated tau, glycogen synthase kinase-3β, inflammatory cytokines (IL-6, TNF-α), and advanced glycation end products, though findings remain inconsistent and require further validation (Aderinto et al., 2023; Liao et al., 2025).

Taken together, these insights highlight the multifactorial nature of cognitive decline in T2DM and emphasize the need for sensitive, standardized, and cost-effective diagnostic approaches to enable earlier identification and intervention.

### 3.3. Type 3 diabetes

Type 3 diabetes (T3DM) has been defined as a metabolic syndrome characterized by brain insulin resistance and consequent disruption of insulin signaling. This condition impairs cerebral glucose metabolism, promotes oxidative stress and neuroinflammation, and fosters neurodegeneration, particularly AD (Nguyen, Ta, Nguyen, Nguyen, & Van Giau, 2020).

The term “type 3 diabetes” was first proposed in 2005 by Suzanne de la Monte and colleagues. Examining post-mortem brain tissue from patients with AD,

they observed not only deficits in cerebral glucose metabolism but also insulin resistance, insulin-like growth factor (IGF) resistance, and abnormalities in signal-transduction pathways. Notably, AD brains showed up to 80% fewer insulin receptors compared with non-AD controls, as well as a significant reduction in IGF receptors. These changes were accompanied by relative deficiencies in insulin and IGF in the brain and cerebrospinal fluid, attributable to altered local expression. Based on these findings, AD was proposed to share features of T1DM (insulin deficiency) and T2DM (insulin resistance), warranting the designation "type 3 diabetes" (de la Monte et al., 2018).

### 3.3.1. Alzheimer's Disease

The term dementia refers to a neurodegenerative process that leads to the loss of primary intellectual functions, impairment of both short- and long-term memory, and consequent disability in occupational and interpersonal domains. Dementia is predominantly a late-onset disorder that, given the progressive increase in average life expectancy, affects a growing number of patients, with significant economic and social repercussions for society. Among the different types of dementia, AD represents the most common form of primary, irreversible neurodegeneration. AD is characterized by neuronal loss, cognitive deficits (primarily affecting memory), and neuroinflammation (Shieh et al., 2020).

Currently, AD affects approximately 56 million people worldwide, and its prevalence is expected to double by 2050 (Cummings et al., 2022).

Two main forms of AD have been described: sporadic (late-onset), which is the most common, and genetic (early-onset), which is associated with hereditary mutations (Bekris et al., 2010).

The sporadic form usually manifests after the age of 65, with incidence increasing exponentially with age, reaching a prevalence exceeding 1 in 3 after 85 years. Average life expectancy from the time of diagnosis is approximately 10 years (Wang et al., 2017).

The neuropathological hallmarks of AD, shared by both the familial and sporadic forms, include:

- Senile (neuritic) plaques, consisting of extracellular deposits of β-amyloid (Aβ);

- Neuronal degeneration, caused by the intracellular accumulation of hyperphosphorylated tau protein aggregates ("tangles");
- Cerebral amyloid angiopathy, resulting from β-amyloid accumulation around cerebral blood vessels;
- Neuronal death, occurring in the late stages of the disease (Carranza-naval et al., 2021).

The defining features of AD are the extracellular deposition of Aβ plaques and the intracellular aggregation of neurofibrillary tangles (NFTs), predominantly localized in the hippocampus and cerebral cortex, where they exert neurotoxic effects. However, the presence of these aggregates is not always correlated with the onset of the characteristic clinical symptoms observed in the advanced stages of the disease. Indeed, deposition of Aβ and NFTs may begin as early as the third decade of life as part of brain aging, with prevalence increasing with advancing age. This highlights the significant impact of lifestyle factors on neurodegeneration and the timing of AD onset (Shieh et al., 2020).

Neuroinflammation plays a pivotal role in AD pathogenesis, as demonstrated by alterations in the morphology and distribution of microglia and astrocytes observed in the brains of AD patients (Di Benedetto et al., 2022).

In addition, dysbiosis has emerged as a significant factor, with recent evidence indicating that the gut microbiota contributes to the physiological regulation of brain function (Dhami et al., 2023).
Alterations in gut microbial populations have been shown to influence normal brain function via the gut-brain axis. The bidirectional communication between the central nervous system (CNS) and the gastrointestinal tract is now recognized as a key element in the pathogenesis of several neuropsychiatric and neurodegenerative disorders, including AD. Conversely, AD itself can induce changes in gut microbiota composition (Carranza-naval et al., 2021).

The pathogenesis of AD is primarily linked to alterations in β-amyloid metabolism, particularly the highly neurotoxic Aβ42 peptide, which begins to form oligomers. These oligomers aggregate and damage synapses, promoting a proinflammatory state through the activation of microglia and astrocytes. The resulting inflammatory response further exacerbates the pathology by

disrupting ionic and oxidative homeostasis. In parallel, aberrant oligomerization and hyperphosphorylation of tau, a microtubule-stabilizing axonal protein, contribute to neuronal dysfunction and cell death, ultimately leading to the clinical manifestations of AD. Aβ is derived from amyloid precursor protein (APP), a transmembrane protein encoded by the APP gene on chromosome 21 and ubiquitously expressed in the CNS. APP is involved in synaptogenesis, long-term potentiation (LTP), and regulation of neuronal plasticity, and has also been implicated in axonal repair following injury. APP can undergo cleavage through two alternative pathways: a non-amyloidogenic pathway, in which α-secretase generates a soluble fragment (sAPPα); and an amyloidogenic pathway, in which β-secretase (BACE-1) and γ-secretase cleave APP at multiple sites, producing Aβ peptides of varying lengths, primarily Aβ40 and Aβ42 (Figure 2; Li & Hölscher, 2007; Stanciu et al., 2020).

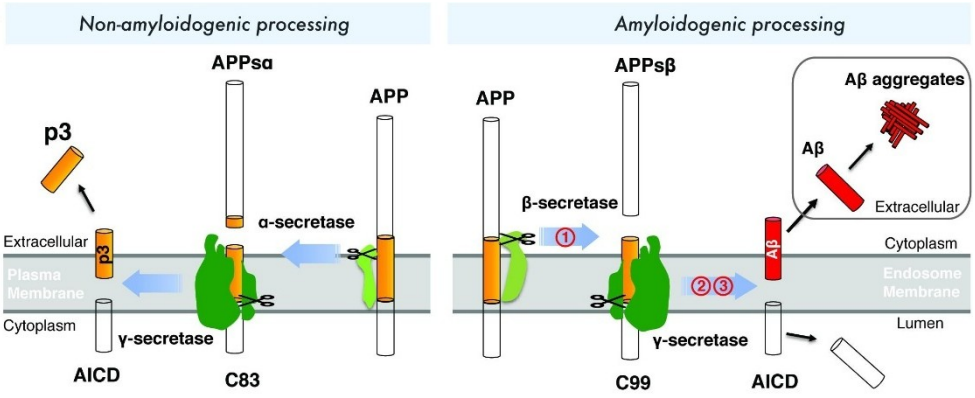


***Figure 2.*** *APP processing with normal and amyloidogenic pathway (Zhao et al., 2020).*

Physiologically, Aβ contributes to synaptic plasticity and neuronal survival, but an imbalance between its production and clearance leads to accumulation and toxicity (Baglietto-Vargas et al., 2016).

Insulin has been shown to stimulate α-secretase activity, thereby counteracting the pathological processes leading to Aβ formation. In AD, however, β-secretase activity predominates, generating sAPPβ, which is further processed by γ-secretase to produce insoluble Aβ monomers. Extracellular Aβ aggregates to form oligomers and plaques, which impair energy metabolism, inhibit LTP, and promote long-term depression (LTD) in murine models (Rajmohan & Reddy, 2017).

Pathological APP processing can also result from mutations in genes implicated in familial AD (FAD). These include APP itself (rare mutations), presenilin 1 (chromosome 14; the most common mutation site in FAD), and presenilin 2 (chromosome 1; rare mutations). Additionally, genetic susceptibility to AD is strongly associated with polymorphisms in the apolipoprotein E (APOE) gene on chromosome 19, which encodes the APOE glycoprotein. APOE is mainly expressed in the liver and in non-neuronal brain cells, where it functions as a lipoprotein and cholesterol carrier. Single-nucleotide polymorphisms (SNPs) produce isoforms that differentially affect AD risk, with APOE4 being the strongest genetic risk factor (Di Battista et al., 2016).

Tau protein, encoded by the MAPT gene on chromosome 17, exists in six isoforms generated by alternative splicing, distinguished by three (3R) or four (4R) microtubule-binding repeats. Under physiological conditions, tau localizes mainly to axons, where it stabilizes microtubules and regulates axonal transport and synaptic function. Phosphorylation of tau is dynamic and allows fine control of cytoskeletal remodeling. Notably, tau protein contains more than 85 phosphorylation sites regulated by over 20 kinases, including GSK-3, CDK5, MAPK, and PKA (Kimura et al., 2014).
Tau undergoes aberrant hyperphosphorylation, which reduces its affinity for microtubules, disrupts cytoskeletal integrity, and impairs axonal transport and synaptic development. Hyperphosphorylated tau aggregates spontaneously into paired helical filaments (PHFs), which accumulate as NFTs (Figure 3). Significantly, the density and distribution of NFTs correlate more strongly with cognitive decline than amyloid plaque burden, underscoring their pathogenic significance (Basheer et al., 2023).

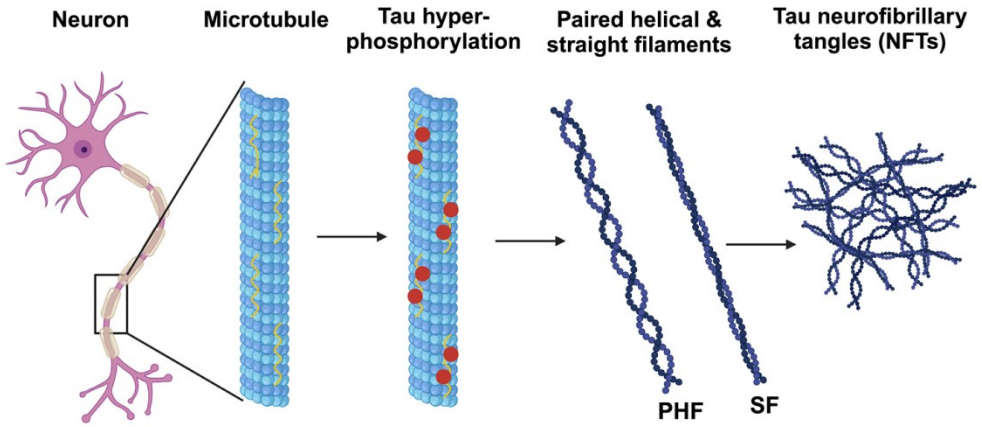


***Figure 3.*** *Tau pathogenesis (Chandran & Binninger, 2023).*

These cytoskeletal abnormalities, combined with neuronal depletion, induce a state of neuroinflammation (Heneka et al., 2015).
Emerging evidence suggests that tau oligomers, rather than mature tangles, are the most neurotoxic species. These soluble aggregates interfere with synaptic signaling, promote oxidative stress, and can spread trans-synaptically in a "prion-like" manner, propagating pathology across anatomically connected brain regions (Boyarko & Hook, 2021).
Given that tau phosphorylation is modulated by GSK-3, insulin signaling is believed to play a crucial role in this molecular mechanism (Hamzé et al., 2022).

Taken together, the dual accumulation of Aβ and pathological tau, compounded by neuroinflammation, establishes the core neuropathological features of AD. Growing evidence indicates that these processes are tightly modulated by insulin signaling, suggesting that brain insulin resistance is not merely a comorbidity but a central driver of neurodegeneration.

### 3.3.2. The role of insulin in the Brain

Insulin is a peptide hormone composed of two polypeptide chains totaling 51 amino acids, with a molecular weight of 5,808 Daltons. It is synthesized by β-cells within the pancreatic islets of Langerhans (Rulifson et al., 2002).
Peripheral insulin can cross the BBB, as evidenced by its increased concentration in neuronal cells, microvessels, and immature neuronal cells (Banks, 2004).

Recent studies have suggested the possibility of endogenous insulin production within the CNS, since mRNAs and preproinsulin-I have been detected in axons, synapses, and dendrites of rat brains, as well as in postmortem human brain tissue. However, the cerebral origin of insulin remains controversial, and it is still debated whether the locally produced amount is physiologically relevant (Duarte et al., 2012; Hamzé et al., 2022).
Insulin plays an essential role in glucose metabolic homeostasis not only peripherally but also within the CNS, where it influences learning and memory by modulating synaptic plasticity, synaptic density, synaptic transmission, and neurogenesis (Ott et al., 2012).
IGFs are proteins structurally related to insulin that bind to specific IGF receptors (IGFRs) but can also interact with insulin receptors (IRs). IGFs exist in two isoforms, IGF-1 and IGF-2, both of which play critical roles in metabolism, growth, and cellular proliferation in both peripheral tissues and neurons. In particular, IGF-1 acts as a key trophic factor for neurogenesis, myelination, synaptogenesis, neuroprotection, and regeneration following injury (Hamzé et al., 2022).

Insulin exerts its effects by binding to insulin receptors (IRs), which are widely expressed in peripheral tissues but also distributed throughout the CNS, notably in the cerebral cortex, hippocampus, hypothalamus, and amygdala (Wei et al., 2021). IRs belong to the family of receptor tyrosine kinases, and upon insulin binding, they undergo autophosphorylation at the tyrosine residues of the β-subunit. This triggers the recruitment and phosphorylation of multiple substrates, which in turn initiate downstream signaling cascades (Folch et al., 2018).
Among the activated substrates, the insulin receptor substrates (IRS), classified into six subtypes, are of particular importance. IRS-1 and IRS-2 specifically mediate phosphorylation cascades leading to the activation of the phosphoinositide 3-kinase (PI3K)–protein kinase B (Akt) pathway, which plays a crucial role in the CNS. The PI3K/Akt pathway regulates (Figure 4):

- the translocation of glucose transporter 4 (GLUT4) to the cell membrane, essential for maintaining glucose homeostasis in the brain (Mergenthaler et al., 2013);
- the activation of glycogen synthase kinase-3β (GSK-3β), which is involved in glucose metabolism, apoptosis, regulation of transcription

factors, and production of neurotrophic factors, thereby supporting neuronal development and survival (Ding et al., 2000);

- the activation of mammalian target of rapamycin complex 1 (mTORC1), which regulates growth and metabolic activities in both peripheral and neuronal cells (Jung et al., 2010);
- the recruitment of growth factor receptor-bound protein 2 (Grb2), which activates the SOS/RAS signaling cascade and subsequently the kinases ERK1 and ERK2, thereby regulating gene expression and cellular growth (Aviello et al., 2010);
- the release of pro-survival (Bcl-2) and pro-apoptotic (BAD) factors, which are involved in the regulation of cell survival (Saito et al., 2012).

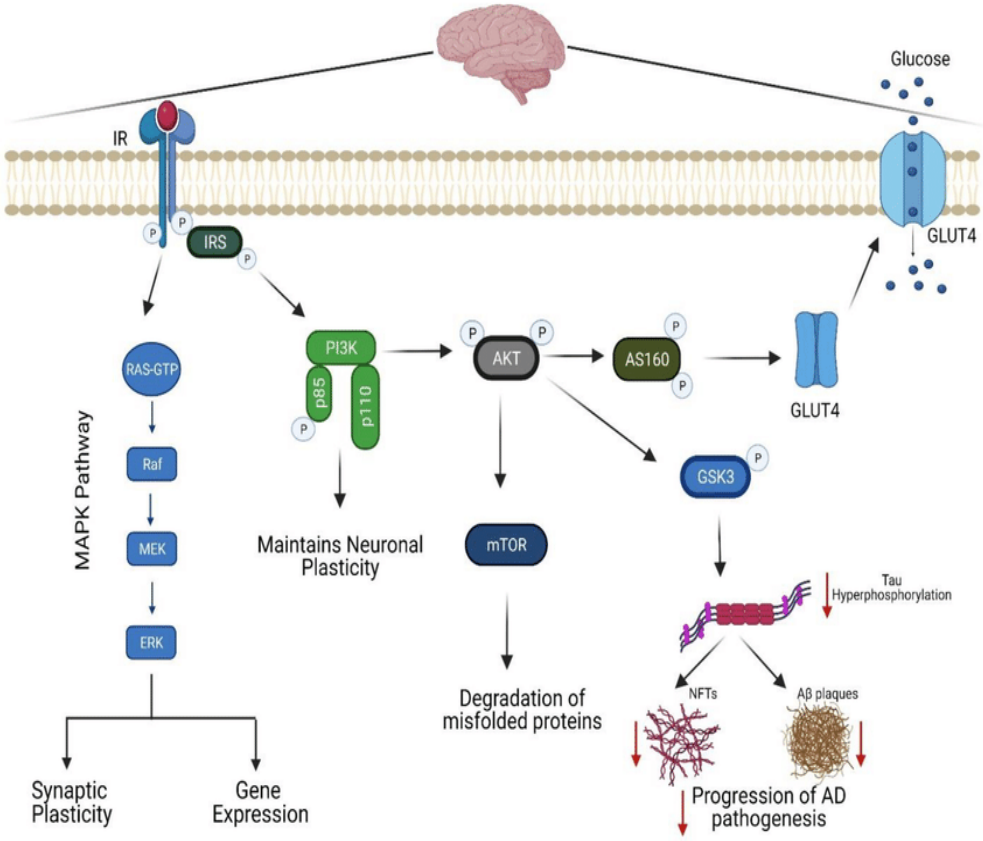


***Figure 4.*** *Insulin signaling cascade following activation of insulin receptors in the brain (Yadav & Dey, 2022).*

## 3.4. Pathophysiological mechanisms linking T2DM to T3DM

Epidemiological investigations have established that T2DM represents a significant risk factor for AD. Several population-based studies have demonstrated that elderly individuals with T2DM have an increased risk of developing AD, with estimates indicating approximately a 50% higher risk in individuals above 60 years of age (Chatterjee & Mudher, 2018; Huang et al., 2014; Mittal & Katare, 2016; Yu et al., 2020).
Longitudinal analyses support these findings: both Leibson et al. and Huang et al. reported that patients with adult-onset diabetes exhibit a significantly higher incidence of dementia when compared to age-matched non-diabetic cohorts (Huang et al., 2014; Leibson et al., 1997).
Overall, these data suggest that the presence of T2DM confers at least a twofold increase in the risk of AD (Barbagallo, 2014).

The underlying pathophysiological basis of this association is complex and involves multiple converging mechanisms. Among these, alterations in glucose metabolism, hyperinsulinemia, and insulin resistance have emerged as pivotal processes that bridge peripheral metabolic dysfunction and neurodegeneration (Chatterjee & Mudher, 2018).

The following subsections will examine in detail the principal mechanisms linking T2DM to AD, focusing on (i) hyperglycemia and hyperinsulinemia, and (ii) the role of insulin resistance, with particular emphasis on its impact on tau hyperphosphorylation, oxidative stress, and neuroinflammation through AGEs.

### 3.4.1. Hyperglycemia and hyperinsulinemia in AD

Hyperglycemia and hyperinsulinemia, two interconnected metabolic disturbances typical of T2DM, are increasingly recognized as factors that contribute to the onset and progression of AD. Epidemiological studies indicate that individuals with elevated blood glucose levels have an increased risk of dementia, and chronic hyperglycemia has been associated with a rapid progression from mild cognitive impairment to AD (Crane et al., 2013; Harris et al., 2012).
In animal models, chronic exposure to high-sugar or high-fructose diets induces cognitive decline, memory deficits, synaptic dysfunction, tau

hyperphosphorylation, and Aβ accumulation, thereby replicating features of AD pathology (Hwang et al., 2014; Jin et al., 2018; Moreira, 2013).
The brain's strict dependence on glucose as its primary energy source makes it particularly vulnerable to fluctuations in glycemic control (Al-Sayyar et al., 2023; Mergenthaler et al., 2013).
Persistent hyperglycemia promotes oxidative stress, mitochondrial dysfunction, and depletion of endogenous antioxidant systems, leading to activation of redox-sensitive pathways and neuronal damage (Chavda et al., 2024; Nday et al., 2018).
Moreover, abnormal glucose handling triggers non-enzymatic glycation processes and AGEs formation, while chronic hyperglycemia disrupts endothelial function and compromises BBB integrity, thereby reducing Aβ clearance and facilitating the entry of peripheral pro-inflammatory mediators into the CNS (Alkhalifa et al., 2023; Ponce-Lopez, 2025).
Hyperinsulinemia, which develops as a compensatory response to peripheral insulin resistance, exacerbates amyloid pathology in the periphery. However, despite elevated peripheral insulin levels, brain hyperinsulinemia is unlikely because insulin transport across the BBB is saturable. As a result, insulin levels in the brain are often reduced in T2DM, contributing to impaired central insulin signaling. This is supported by PET-FDG studies showing reduced cerebral glucose uptake in AD patients, indicating dysfunction in brain insulin signaling (Kellar & Craft, 2020; Ponce-Lopez, 2025). Both insulin and Aβ are substrates of the insulin-degrading enzyme (IDE), which is down-regulated in AD brains. Reduced IDE activity impairs Aβ degradation, contributing to its accumulation even in the presence of systemic hyperinsulinemia (Fazio et al., 2024; Kimura, 2016; Ott et al., 2012).
Models lacking IDE show significantly reduced Aβ clearance, greater plaque deposition, and metabolic features similar to T2DM. Additionally, evidence indicates that insulin influences APP trafficking and promotes extracellular Aβ release via MAPK-dependent pathways (Gasparini et al., 2001).
These processes demonstrate how hyperinsulinemia, beyond reflecting systemic metabolic dysregulation, directly contributes to the molecular cascade underlying AD.

Taken together, hyperglycemia and hyperinsulinemia create a metabolic environment that enhances oxidative stress, reduces Aβ clearance, and promotes its extracellular accumulation. While these alterations significantly

contribute to AD pathology, insulin resistance within the brain represents the pivotal mechanism that integrates metabolic stress with tau pathology, oxidative stress, and neuroinflammation, as discussed in the next section.

### 3.4.2. The role of insulin resistance in AD

Insulin resistance within the brain is increasingly recognized as the pivotal mechanism linking T2DM to AD. Beyond its systemic metabolic effects, impaired insulin signaling in neurons and glial cells disrupts key pathways involved in glucose utilization, synaptic plasticity, and memory consolidation (Arnold et al., 2018).

At the molecular level, IR does not act in isolation but triggers a cascade of deleterious events that converge on the core hallmarks of AD. By impairing intracellular signaling, brain IR promotes both amyloid and tau pathology, while simultaneously exacerbating oxidative stress and neuroinflammation.

The following subsections will discuss these processes in detail, focusing on (i) the relationship between IR and Aβ/tau metabolism, (ii) the contribution of IR to oxidative stress, and (iii) the interplay between IR and neuroinflammatory responses.

#### 3.4.2.1. IR and amyloid/tau pathology

In physiological conditions, insulin and IGF-1 contribute to Aβ clearance and prevent tau hyperphosphorylation, thereby exerting neuroprotective effects. In a state of insulin resistance, however, these protective mechanisms are disrupted, leading to reduced PI3K/Akt activation, disinhibition of GSK3β, and decreased IDE activity. As a result, Aβ degradation is impaired, tau phosphorylation increases, and the accumulation of amyloid plaques and neurofibrillary tangles is promoted (Benedict & Grillo, 2018; Cole & Frautschy, 2007; Li et al., 2015; Zhao & Townsend, 2009).

Moreover, insulin resistance shifts APP processing from the non-amyloidogenic α-secretase pathway toward β- and γ-secretase cleavage, thereby increasing Aβ generation (Folch et al., 2018; Rajmohan & Reddy, 2017).

Significantly, Aβ oligomers can further exacerbate neuronal insulin resistance by activating the TNF-α/JNK pathway and mitochondrial oxidative stress (Chen & Yan, 2007; Kaminsky, 2015; Reddy & Beal, 2008).

Beyond metabolic impairment, Aβ oligomers also interfere with synaptic function, reducing Akt activation, impairing GLUT4 translocation, and blocking hippocampal LTP, thereby directly linking insulin resistance to learning and memory deficits (Grillo et al., 2009; McNay & Pearson-Leary, 2020; Zhao et al., 2008).
Comparable processes occur in T2DM, where they contribute to peripheral insulin resistance, β-cell apoptosis, and increased oxidative stress (Kaneto et al., 2007; Shieh et al., 2020; Yung & Giacca, 2020).
This evidence supports a bidirectional relationship between Aβ and insulin resistance, creating a vicious circle that sustains metabolic and neurodegenerative dysfunction (Hamzé et al., 2022).
APP expression is not confined to the CNS but is also present in liver, skeletal muscle, adipose tissue, and pancreas. In T2DM, amyloid deposits resembling amyloid plaques have been identified in pancreatic islets. Moreover, amylin (IAPP), which shares cytotoxic properties with Aβ, has been co-localized with Aβ in the brain, suggesting a contribution to AD progression (Neth & Craft, 2017).

Tau pathology represents another critical outcome of insulin resistance. Usually, tau phosphorylation is dynamically regulated to maintain microtubule stability and axonal transport (Benedict & Grillo, 2018; Mandelkow et al., 2004; Sayas & Ávila, 2021).
Insulin and IGF-1 inhibit GSK3 activity, preventing aberrant tau phosphorylation and NFT formation (Cole & Frautschy, 2007; Gabbouj et al., 2019; Mullins et al., 2017).
In addition to GSK3β activation, downregulation of protein phosphatase 2A (PP2A), a major tau phosphatase, has been reported in T2DM, further exacerbating tau pathology (Qu et al., 2011).
In insulin-resistant states, reduced Akt activation results in GSK3 disinhibition and tau hyperphosphorylation, particularly in the cerebral cortex (Infante-Garcia et al., 2016; Ramos-Rodriguez et al., 2013).
Notably, tau is also expressed in pancreatic β-cells, where it regulates insulin trafficking and secretion. Increased hyperphosphorylated tau has been observed in pancreatic islets of T2DM patients, indicating a shared molecular mechanism between metabolic and neurodegenerative disorders (Maj et al., 2016; Miklossy et al., 2010).

Together, these findings show that insulin resistance promotes both Aβ accumulation and tau hyperphosphorylation, while toxic protein aggregates in turn exacerbate insulin signaling deficits. This self-reinforcing cycle offers a compelling mechanistic basis for defining AD as “type 3 diabetes.”

### 3.4.2.2. IR and oxidative stress

Oxidative stress is a major downstream consequence of insulin resistance in the brain. Under normal conditions, insulin signaling through the PI3K/Akt pathway supports mitochondrial homeostasis and regulates antioxidant defenses. In states of insulin resistance, however, impaired Akt activation leads to mitochondrial dysfunction, reduced ATP production, and excessive ROS production (Figure 5; Federico et al., 2012; Moreira et al., 2007; Shukla et al., 2011).

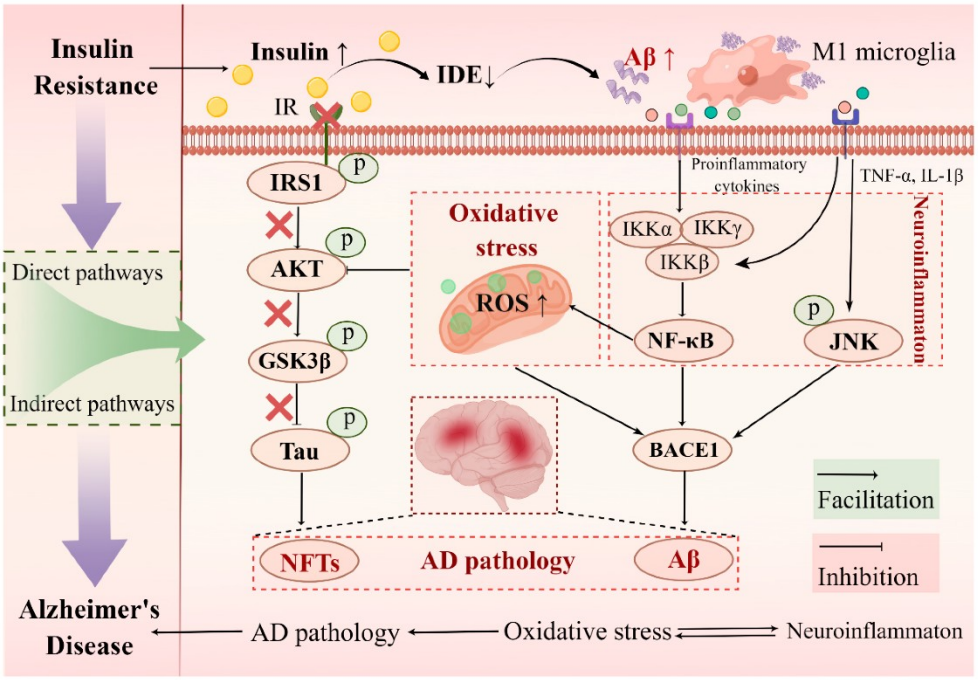


***Figure 5.*** *Insulin resistance promotes mitochondrial dysfunction and oxidative stress, leading to β-amyloid accumulation, tau hyperphosphorylation, and neurodegeneration in AD (Liu et al., 2022).*

The brain is particularly vulnerable, as peripheral metabolic stress can increase BBB permeability and facilitate the entry of reactive species into the CNS (Maciejczyk et al., 2019).
Excessive ROS not only damages DNA, lipids, and proteins but also activates redox-sensitive signaling cascades. In particular, c-Jun N-terminal kinase (JNK) and NF-κB pathways exacerbate insulin resistance and promote the release of pro-inflammatory cytokines, creating a self-reinforcing loop between oxidative stress and neuroinflammation (Kaneto et al., 2007; Morgan & Liu, 2011; Yung & Giacca, 2020).
Additionally, AGE/RAGE signaling contributes to ROS overproduction, linking oxidative stress to chronic inflammation and vascular dysfunction in diabetes (Singh et al., 2001; Yamagishi et al., 2012).
Mitochondria are a central target of oxidative injury. Studies in AD and diabetic models demonstrate that Aβ accumulates within mitochondria, impairs respiratory chain complexes, and increases ROS production, further aggravating oxidative stress and neuronal dysfunction (Akhter et al., 2017; Kaminsky, 2015; Reddy & Beal, 2008).

Together, these data indicate that oxidative stress is not merely a byproduct of insulin resistance, but an active contributor to the vicious cycle that links metabolic dysfunction with neurodegeneration in AD

#### 3.4.2.3. IR and neuroinflammation

Neuroinflammation is a hallmark of both T2DM and AD and is increasingly recognized as a key mediator linking metabolic dysfunction to neurodegeneration. Post-mortem studies of AD brains demonstrate elevated levels of pro-inflammatory cytokines such as IL-1β and IL-6, in association with amyloid plaques and neurofibrillary tangles (Blum-Degena et al., 1995).
In T2DM, low-grade chronic inflammation driven by adipose tissue dysfunction and immune cell infiltration promotes systemic release of cytokines and adipokines that can cross the BBB, thereby initiating central inflammatory responses (Banks, 2005; Kubaszek et al., 2003; Lumeng et al., 2007; Ouchi et al., 2011).
Microglia and astrocytes are central mediators of this process. Their activation leads to the secretion of TNF-α, IL-1β, and IL-6, the upregulation of cyclooxygenase-2 (COX-2), and enhanced lipid peroxidation, which together

exacerbate oxidative stress and synaptic dysfunction (Carrero et al., 2012; Mehlhorn et al., 2000).
Elevated Aβ levels can further amplify these responses by stimulating microglial activation and increasing TNF-α release, ultimately impairing synaptic plasticity and cognitive performance (Sims-Robinson et al., 2010).
At the molecular level, the AGE–RAGE–NF-κB axis represents a central pathway. AGEs, which accumulate in both diabetes and AD, activate their receptor RAGE on neurons, glia, and endothelial cells, promoting NF-κB–dependent transcription of inflammatory mediators (Patel & Santani, 2009; Singh et al., 2001; Yamagishi et al., 2012).
Notably, RAGE also binds Aβ oligomers and facilitates their transport across the BBB, thereby enhancing cytokine release and vascular permeability (Cai et al., 2016; Deane et al., 2003).

Overall, neuroinflammation functions both as a driver and a consequence of insulin resistance, establishing a self-perpetuating cycle in which cytokine release, NF-κB activation, and RAGE signaling converge to sustain neuronal injury. This inflammatory loop links peripheral metabolic disturbances with central neurodegenerative processes.

### 3.4.3. Interconnected pathogenic loops linking T2DM to T3DM

The relationship between T2DM and AD is not explained by a single pathway but rather by the convergence of multiple interdependent mechanisms. Chronic hyperglycemia promotes the formation of AGEs and the activation of the AGE–RAGE axis, which sustains oxidative stress, vascular dysfunction, and inflammatory signaling. In parallel, systemic hyperinsulinemia and peripheral insulin resistance affect the brain, leading to impaired PI3K/Akt signaling, tau hyperphosphorylation, and a shift in APP processing toward amyloidogenic cleavage. These alterations are further amplified by mitochondrial dysfunction and ROS overproduction, which compromise neuronal survival and synaptic integrity.
At the same time, glial activation and cytokine release establish a state of chronic neuroinflammation that feeds back on insulin signaling pathways and exacerbates oxidative stress. Vascular dysfunction and BBB impairment contribute to this vicious cycle by reducing Aβ clearance and enhancing brain exposure to circulating inflammatory mediators. Importantly, both Aβ and

hyperphosphorylated tau reinforce insulin resistance, creating a bidirectional relationship between protein aggregation and metabolic dysfunction.

Taken together, these mechanisms form a self-perpetuating network in which systemic metabolic alterations characteristic of T2DM converge with neuropathological processes typical of AD. Insulin resistance emerges as the central hub of this integrated loop, providing a rationale for why AD has been conceptualized as T3DM.

These limitations underscore the complexity of T2DM-AD interactions. While converging evidence supports insulin resistance and its downstream pathways as central mechanisms, the multifactorial nature of the disease, the heterogeneity of clinical outcomes, and the limited specificity of available biomarkers highlight the need for integrative and longitudinal approaches to fully elucidate this relationship.

### 3.5. Current biomarkers and their limitation

The diagnosis and monitoring of T2DM are traditionally based on metabolic biomarkers. According to the WHO, the diagnostic criteria include fasting plasma glucose (FPG) (≥ 126 mg/dL), at two-hour plasma glucose during an oral glucose tolerance test (OGTT) (≥ 200 mg/dL), random glycemia in the presence of classic symptoms (≥ 200 mg/dL), and glycated hemoglobin (HbA1c ≥ 6.5%) (World Health Organization, 2018).

While widely adopted, these biomarkers have important limitations: both FPG and OGTT are subject to intraindividual variability and may be influenced by acute factors such as stress or medication use, whereas HbA1c, despite reflecting average glycemia over the previous three months, fails to capture daily fluctuations and hypoglycemic episodes and is affected by hematologic conditions, ethnicity, and renal impairment (Cerf, 2013; World Health Organization, 2018).

Beyond these parameters, T2DM is associated with systemic alterations in lipid, protein, hematological, and cytokine profiles, all of which highlight the chronic inflammatory and prothrombotic milieu underlying the disease. In particular, protein modifications induced by sustained hyperglycemia, such as the non-enzymatic glycation of serum proteins, are increasingly acknowledge as key mediators of diabetic complications (Le et al., 2025).

Among these, glycated albumin (GA) has emerged as a reliable short-term glycemic marker, while methylglyoxal (MGO), a highly reactive dicarbonyl compound, is a critical precursor of advanced glycation end products.

Both biomarkers, discussed in the following sections, provide mechanistic insights into the molecular cascade linking hyperglycemia to vascular and neuronal damage, and could complement traditional diagnostic tools in the clinical management of T2DM.

### 3.5.1. Glycated albumin

Albumin is the most abundant plasma protein in humans, accounting for 50-60% of circulating protein mass. Owing to its tertiary structure, albumin binds reversibly to a wide range of small molecules, including metal ions and drugs, thereby influencing their pharmacokinetics. Its relatively long half-life makes albumin particularly prone to biochemical modifications through both enzymatic and non-enzymatic mechanisms. Under conditions of oxidative stress and hyperglycemia, albumin undergoes non-enzymatic glycation, producing GA via the Maillard reaction, in which glucose binds to the N-terminal or to lysine/arginine residues of the protein (Fanali et al., 2012; Raghav & Ahmad, 2014).
GA levels increase proportionally to glycemic burden and oxidative stress, leading to structural modifications such as local unfolding, exposure of hydrophobic pockets, and increased molecular weight. These changes are not merely biochemical: high GA levels contribute to cellular and tissue injury, playing a pathogenic role in the development of diabetic complications, including retinopathy, nephropathy, neuropathy, and cardiovascular disease (Freitas et al., 2017; Raghav & Ahmad, 2014; Wu et al., 2016). Importantly, increased protein glycation has also been detected in the cerebrospinal fluid of AD patients, further supporting the mechanistic link between T2DM and neurodegeneration (Ayoub et al., 2025).

Clinically, GA reflects average glycemia over a period of about 2-3 weeks, thereby representing an intermediate-term marker between fasting glucose and HbA1c (Figure 6). Unlike HbA1c, GA is unaffected by erythrocyte lifespan and is thus more accurate in conditions such as anemia, hemoglobinopathies, and chronic kidney disease. It is also sensitive to rapid glycemic changes, making it useful for assessing short-term therapeutic efficacy. Compared to

HbA1c, GA can be measured through enzymatic assays without fasting requirements, from both serum and plasma, with reduced costs and faster turnaround times (Freitas et al., 2017; Zendjabil, 2020).

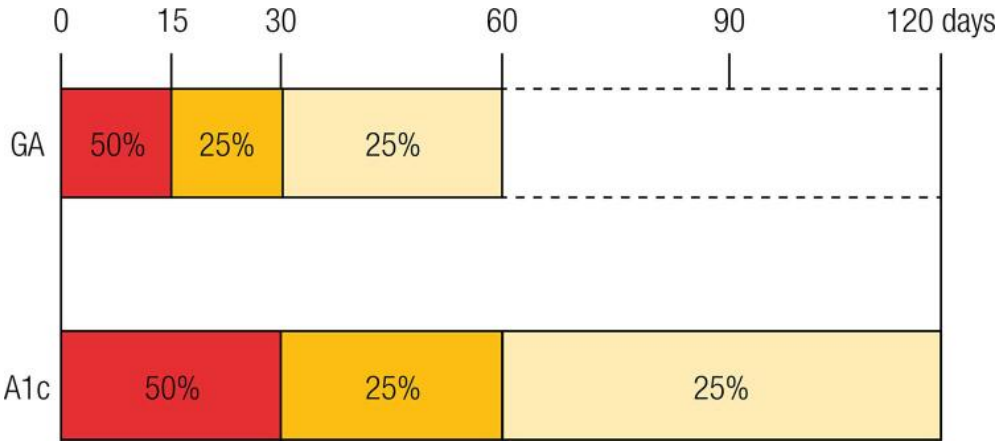


***Figure 6.*** *Glycation rates of GA and HbA1c. GA are formed over approximately eight weeks, with the first two weeks accounting for about half of their total production. In contrast, HbA1c requires around four months to reach full formation, although the first month contributes to about half of the overall production (Freitas et al., 2017).*

Nevertheless, GA has certain limitations. Its levels are influenced by sex and age, being generally higher in women and in adults compared to children. Moreover, the rate of false positives and negatives remains significant, limiting its use as a stand-alone diagnostic tool. For these reasons, GA is increasingly considered a complementary biomarker to traditional measures such as HbA1c rather than a full substitute (Giglio et al., 2020; Zendjabil, 2020).

### 3.5.2. Methylglyoxal

MGO is a highly reactive dicarbonyl compound produced predominantly as a byproduct of glycolysis, from intermediates such as glyceraldehyde-3-phosphate (G3P), fructose, and aminoacetone (Lee et al., 2009; Liu et al., 2011).

Under conditions of insulin resistance and hyperglycemia, MGO production is enhanced not only via carbohydrate metabolism but also through lipid

catabolism (acetone, acetoacetate) and amino acid degradation (tyrosine, serine, threonine, glycine), as summarized in Figure 7 (Ahmed et al., 2005; Kim et al., 2012).

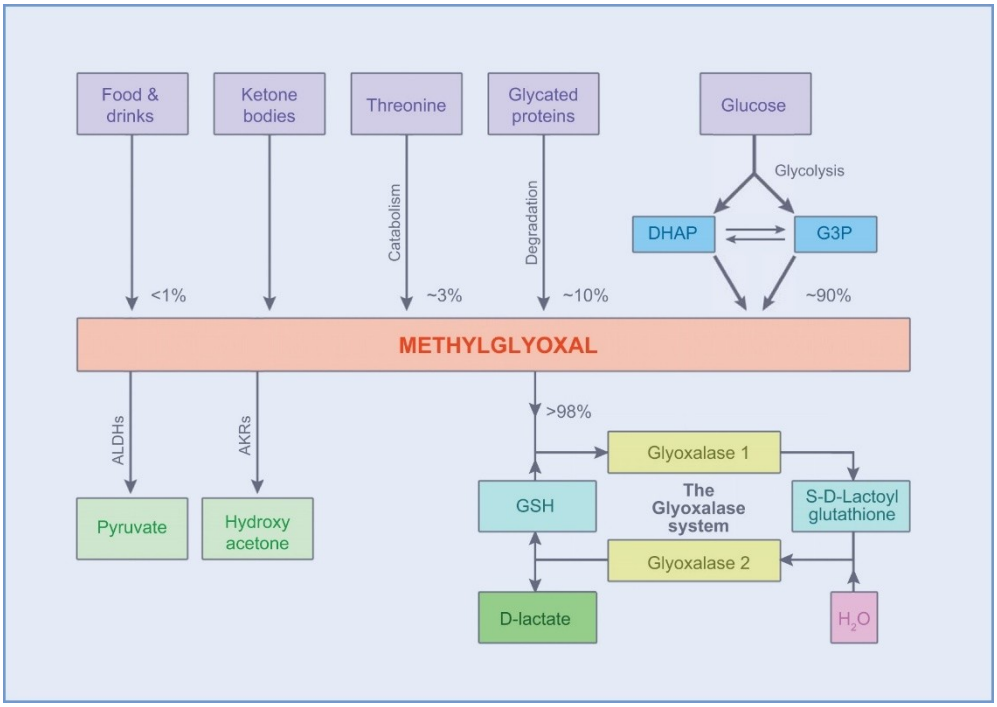


***Figure 7.*** *Formation and detoxification of methylglyoxal (MGO). MGO is mainly produced from triosephosphate degradation, with minor contributions from threonine, acetoacetate, and glycated proteins. Dietary intake is negligible (<1%). Detoxification occurs predominantly via the glyoxalase system (C. G. Schalkwijk & Stehouwer, 2020).*

Exogenous sources can further increase MGO load. Dietary excess of glucose and fructose stimulates its formation together with ROS, while foods exposed to dry-heat cooking methods such as grilling, frying, or roasting are particularly enriched in MGO. Notably, dairy products and beverages, including coffee and whisky, rank among the richest dietary sources of MGO measured in commercial foods (Shamsaldeen et al., 2016; Tan et al., 2008).
Physiologically, plasma MGO concentrations in healthy individuals range between 60 and 500 nM, while intracellular levels are maintained between 1 and 5 nM. In diabetic patients, however, plasma concentrations can reach up

to 500 μM, with significant accumulation also detected in the pancreas, skeletal muscle, and adipose tissue (C. G. Schalkwijk & Stehouwer, 2020).
This elevation is associated with decreased glutathione (GSH) availability and reduced expression of glucose transporters such as GLUT2 in pancreatic β-cells and GLUT4 in adipocytes. To counteract MGO toxicity, mammalian cells rely on the glyoxalase (GLO) system, a cytosolic enzymatic pathway that converts MGO into D-lactate. Measurement of urinary D-lactate has been proposed as an indirect index of MGO metabolism (Negre-Salvayre et al., 2009; Rabbani et al., 2016; Sutkowska et al., 2023).
Beyond being a major precursor of AGEs through reactions with arginine, lysine, and cysteine residues of proteins, MGO can also modify lipids and DNA, and exerts direct pathogenic effects. In particular, it interferes with insulin receptor signaling by modifying IRS-1, leading to disruption of downstream pathways in muscle, endothelial, and pancreatic β-cells (Dornadula et al., 2015; Schalkwijk et al., 2008).
This mechanism provides a direct molecular link between MGO accumulation, insulin resistance, and diabetic complications.
Clinically, elevated plasma MGO levels have been associated with multiple diabetes-related complications, including chronic kidney disease, macroangiopathy, and cognitive impairment (Shamsaldeen et al., 2016; Ogawa et al., 2010).
While monitoring MGO concentrations could represent a useful tool for evaluating systemic and neurological risk, its application as a clinical biomarker is currently limited by variability in assay methodologies, instability within biological samples, and the unresolved issue of whether MGO functions primarily as a biomarker or as an active driver of pathology.

Taken together, both glycated albumin and methylglyoxal illustrate how short-term glycemic markers and glycation precursors can provide mechanistic insights beyond conventional indices of glucose control. However, their translational application is still limited, and their relationship with functional outcomes such as physical and cognitive performance is still under investigation. This highlights the need to integrate biomarker studies with multidimensional concepts such as frailty and cognitive frailty, which capture the systemic vulnerability induced by diabetes and its impact on brain health.

### 3.6. Frailty and cognitive frailty

Frailty is a multidimensional clinical syndrome characterized by reduced physiological reserve and increased vulnerability to stressors, predisposing individuals to adverse outcomes such as disability, hospitalization, and mortality (Robertson et al., 2013).

Unlike chronological age, frailty reflects multisystem dysregulation across musculoskeletal, immune, and nervous systems, thus explaining why not all elderly individuals become frail (Figure 8; Bandeen-Roche et al., 2006; Fried et al., 2001; Piggott & Tuddenham, 2020).

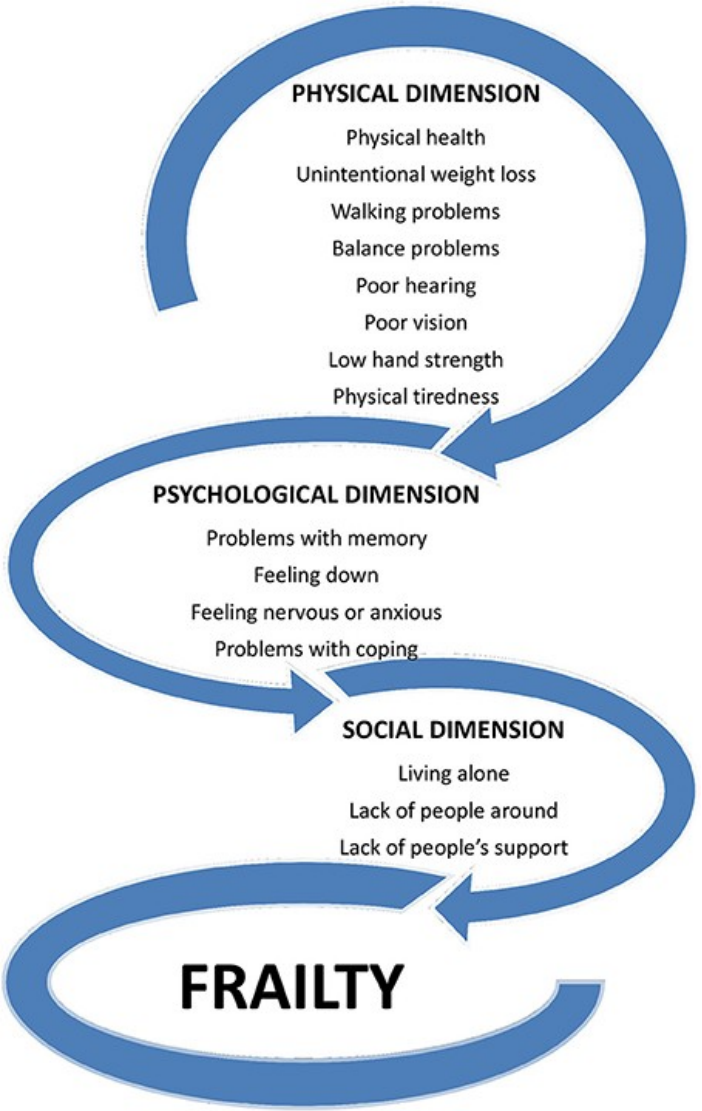


***Figure 8.*** *Multidimensionality of frailty (Sacha et al., 2017).*

Two main models are commonly used to define and measure frailty: the phenotype model proposed by Fried, defined by the presence of at least three clinical indicators (slow walking speed, weakness, unintentional weight loss, fatigue, reduced physical activity), and the deficit accumulation model, in which the Frailty Index (FI) quantifies the proportion of health deficits present in an individual (Palliyaguru et al., 2019; Parks et al., 2012; Rockwood et al., 2017).
More recently, the concept of cognitive frailty has been introduced to describe the coexistence of physical frailty and cognitive impairment in the absence of dementia or other neurodegenerative disorders (Aguilar-Navarro et al., 2025; Kelaiditi et al., 2013; Lu et al., 2022).
This condition highlights the interaction between systemic metabolic vulnerability and early cognitive decline. One proposed mechanism is the brain-muscle loop theory, whereby the central nervous system regulates muscle function, and skeletal muscle secretes myokines that contribute to neuronal physiology and synaptic plasticity (Kostka et al., 2024; Pedersen, 2019).

This bidirectional relationship offers a biological basis for the observed overlap between frailty, insulin resistance, and cognitive impairment in T2DM.

### 3.6.1. Recognition memory as a cognitive marker

Memory is not a unitary faculty but a multicomponent system supported by distinct brain circuits. A fundamental distinction exists between declarative (explicit) memory, mediated by the hippocampus and parahippocampal cortices, and non-declarative (implicit) memory, which includes skills, habits, priming, and conditioning and relies on structures such as the striatum, amygdala, cerebellum, and neocortex (Squire & Dede, 2015).
Within declarative memory, episodic memory enables conscious recall of personal experiences and is characterized by three processes: encoding, consolidation, and retrieval (Matthews, 2015).
A central aspect of episodic memory is recognition memory, the ability to discriminate familiar from novel stimuli, which is a core feature of both human and animal cognition (Bevandić et al., 2024; Bird, 2017; Boyle & Brown, 2025).

Two major theoretical models have been proposed to explain recognition memory. The single-process model views it as a continuum of familiarity strength, where "knowing" (familiarity) and "remembering" (contextual recollection) differ only quantitatively. In contrast, the dual-process model posits that recognition memory is supported by two distinct and qualitatively different mechanisms: familiarity judgments mediated by the perirhinal cortex, and recollection of contextual associations mediated by the hippocampus (Brown & Aggleton, 2001).

Evidence from experimental studies, including work from our laboratory, supports the dual-process model. For example, extracts of Hericium erinaceus enhanced the "knowledge" component (tested by novel object recognition and emergence tasks) without affecting the "remember" component (tested by object location and Y-maze tasks), suggesting a dissociation between these processes (Rossi et al., 2018).

Recognition memory is particularly vulnerable to aging. Elderly individuals exhibit deficits in recall and familiarity tasks compared to younger adults, with the knowledge component being more strongly affected, as confirmed by recent meta-analyses (Graves et al., 2017; Rhodes et al., 2019).

This sensitivity to aging underscores its relevance as an early cognitive marker. Importantly, recognition memory is one of the first domains impaired in MCI and AD, conditions where hippocampal dysfunction plays a central role (Michailidis et al., 2022; Nguyen, & Giau, 2020; Rao et al., 2022).

In the context of T2DM, hyperglycemia, oxidative stress, and insulin resistance further compromise hippocampal function, accelerating recognition memory decline. Preclinical studies support this link: diabetic rodents display consistent impairments in tasks such as novel object recognition (NOR) and spatial paradigms, including object location and Y-maze, thereby mirroring key aspects of human cognitive vulnerability (Aderinto et al., 2023; Kassab et al., 2019; Patel et al., 2016; Vilela et al., 2023).

Altogether, recognition memory emerges as a sensitive and translational cognitive marker that bridges aging, diabetes, and neurodegeneration. Its dual-process architecture and dependence on hippocampal and parahippocampal circuits make it an informative endpoint for experimental studies aimed at disentangling the interplay between metabolic dysfunction and cognitive decline.

## 3.7. Preclinical mouse models as tools to investigate diabetes and cognitive decline

The limitations of traditional metabolic markers, the emerging role of glycated proteins, and the concept of frailty highlight the multifactorial nature of diabetes-related cognitive decline. Recognition memory, in particular, emerges as a sensitive and translational cognitive endpoint that mirrors hippocampal vulnerability and provides a valuable bridge between preclinical and clinical research. To experimentally dissect the mechanistic links between metabolism, cognition, and neuropathology, animal models are indispensable tools. Their controlled setting allows the integration of metabolic, behavioral, and neuropathological assessments, thereby providing a comprehensive framework to investigate how T2DM contributes to neurodegeneration. T2DM is a heterogeneous disorder characterized primarily by insulin resistance. While some subtypes can be traced to single-gene mutations, in most patients the onset, progression, and long-term complications arise from the interaction between genetic and environmental factors. Therefore, animal models of T2DM should capture complexity and heterogeneity. Particularly valuable are models that combine hyperglycemia with obesity, dyslipidemia, and hypertension, as these replicate the multifactorial profile of human T2DM (Rees & Alcolado, 2005).

Murine models include both genetic and induced approaches. Among genetic models, ob/ob and db/db mice, harboring mutations in the leptin gene or its receptor, exhibit hyperglycemia, obesity, and insulin resistance. By contrast, NSY mice develop diabetes without obesity, thus providing a lean diabetic phenotype (Lee & Cox, 2010).

However, to model diabetes-associated cognitive decline, induced models based on streptozotocin (STZ) and high-fat diet (HFD) exposure are commonly employed.

### 3.7.1. Streptozotocin protocols

STZ is a nitrosourea compound, isolated from *Streptomyces achromogenes* in 1959, that selectively targets pancreatic β-cells.
Because of its structural similarity to glucose, STZ is taken up by GLUT2 transporters, which are highly expressed in β-cells. After cellular uptake, its methylnitrosourea moiety induces DNA alkylation and fragmentation, leading

to oxidative stress, β-cell necrosis, and progressive insulin deficiency (Figure 9; Al-awar et al., 2016).

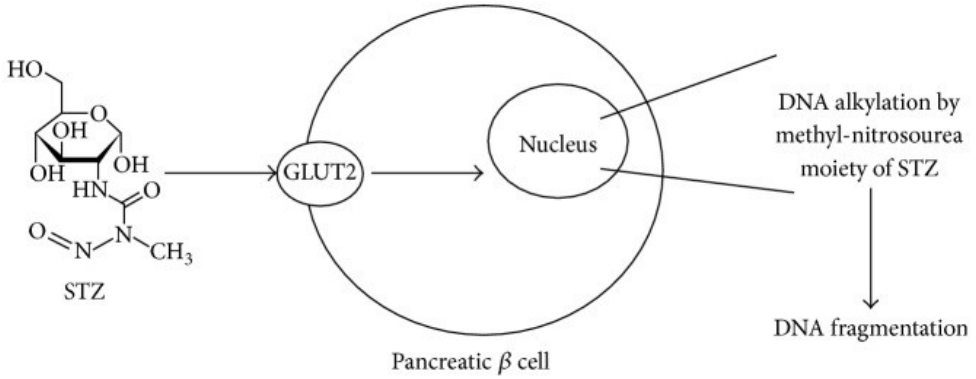


***Figure 9.*** *The action of STZ on β cells of the pancreas (Al-awar et al., 2016).*

STZ has a short half-life, as it is rapidly metabolized in the liver and excreted via the kidneys. In addition to experimental research, it is also used clinically as a chemotherapeutic agent for pancreatic islet cell tumors. The response to a diabetogenic dose of STZ in rodents occurs in three phases: (i) transient hyperglycemia shortly after injection, (ii) transient hypoglycemia, due to insulin release from damaged β-cells, and (iii) sustained hyperglycemia with hypoinsulinemia, polyuria, and glycosuria (Al-awar et al., 2016).

Its diabetogenic effect is dose-dependent: high doses (100-200 mg/kg) cause almost complete β-cell ablation, leading to severe insulin deficiency and hyperglycemia, while low doses (30-60 mg/kg) induce partial β-cell loss, resulting in a milder diabetic phenotype (Bauer et al., 2023; Sims-Robinson et al., 2010).

A single high dose of STZ has therefore been reported to induce a pathology more similar to T1DM. Conversely, the use of multiple low doses of STZ has been described to induce either T1DM (Bauer et al., 2023; Furman, 2021; Wu & Huan, 2008) or T2DM (Cassano et al., 2020; Lai et al., 2024).

To refine the model and reduce β-cell toxicity, STZ has often been administered in combination with nicotinamide. This approach produces a stable, moderate hyperglycemia associated with partial β-cell dysfunction (approximately 60% loss of function), but it typically produces insulin dependence rather than insulin resistance (Furman, 2021; Ghasemi & Jeddi, 2023). Thus, the actual diabetic phenotype resulting from low-dose STZ administration remains controversial.

Although the STZ model reproduces important metabolic and neurological alterations, it lacks several key features of human T2DM, such as obesity and progressive insulin resistance, which limit its translational applicability. Furthermore, sensitivity to STZ varies by strain, sex, and age, and inappropriate dosing can cause high mortality, further complicating reproducibility across studies. For these reasons, STZ is frequently combined with dietary manipulations to generate models that more closely align with human T2DM.

### 3.7.2. The combination of a High-fat diet and STZ

Diet-induced obesity is another strategy to model T2DM. Rodents exposed to an HFD progressively develop obesity, insulin resistance, and dyslipidemia (Stott & Marino, 2020).

Importantly, HFD-fed mice also exhibit behavioral alterations, including anxiety-like traits and cognitive impairment (Henn et al., 2022).

The combination of HFD with low-dose STZ has emerged as a particularly effective strategy to replicate the complex metabolic and neurological features of human T2DM. In this model, HFD induces insulin resistance, while STZ triggers partial β-cell dysfunction, resulting in a phenotype characterized by obesity, hyperglycemia, and impaired insulin secretion. This dual-hit paradigm closely mimics the pathophysiology of late-stage T2DM and provides a robust platform for investigating diabetes-associated complications, including cognitive decline (Marino et al., 2023; Rees & Alcolado, 2005).

Overall, the HFD/STZ model is considered the most effective for replicating the metabolic and cognitive features of human T2DM, but variability in diet composition, dosing schedules, and animal strains complicates reproducibility. In addition, long-term maintenance requires continued dietary exposure, which may increase costs and introduce confounding nutritional effects.

## 4. Aims of the research

Diabetes mellitus (DM) is a major global health challenge with rising prevalence worldwide. Among the different forms of DM, this project specifically focuses on type 2 diabetes mellitus (T2DM), which accounts for more than 90% of cases and represents the fastest-growing metabolic disorder globally. T2DM is strongly associated with aging, sedentary lifestyle, and obesity, factors that also increase the risk of cognitive impairment and dementia, particularly Alzheimer's disease (AD) (Patel et al., 2016; Wium-Andersen et al., 2020). The underlying mechanisms include hyperglycemia, insulin resistance, oxidative stress, and the accumulation of advanced glycation end-products (AGEs), all of which accelerate neuronal dysfunction and brain aging (Nowotny et al., 2015). This convergence has led to the concept of AD as "type 3 diabetes" (Kciuk et al., 2024; Michailidis et al., 2022). Despite this growing awareness, in clinical practice, HbA1c remains the gold-standard biomarker for glycemic control. However, it reflects only long-term glycemia and is unreliable in several comorbid conditions (Freitas et al., 2017). Glycated albumin (GA) and methylglyoxal (MGO) have emerged as promising alternatives: GA reflects short-term variability (Piuri et al., 2020), while MGO is a reactive dicarbonyl compound that drives AGE formation and neuronal injury (Shamsaldeen et al., 2016; Schalkwijk & Stehouwer, 2020). Both GA and MGO have therefore been proposed as valuable tools for improving the prevention, monitoring, and risk stratification of diabetes and its complications, including cognitive decline.

Within this translational perspective, and supported by the INVITALIA Brevetto+ program on patented analytes for innovative diagnostics, the present doctoral project set out to investigate how diabetes promotes cognitive impairment, with a specific focus on recognition memory, and to evaluate the translational value of GA and MGO as biomarkers of disease progression.
A critical aspect of the study was the selection of an appropriate animal model. We excluded genetic models, as they do not allow longitudinal monitoring of the transition from the physiological to the pathological state. For this reason, chemically induced paradigms were considered, although they present several specific limitations. As previously discussed in the Introduction section, STZ-based models are highly heterogeneous: their outcome depends on multiple variables, including the age at induction, the total dose administered, and the

injection protocol (single high-dose vs multiple low-dose protocols), as well as factors such as strain, sex, or diet. Consequently, the type of diabetes reproduced by STZ is not always clearly defined, and the translational validity of these models remains debated. Moreover, to our knowledge, no previous studies employing STZ-based protocols have described either the long-term effects of STZ administration or the independent impact of HFD alone, leaving a critical gap in understanding disease progression over time.

Given these considerations, this project implemented two complementary models: (i) a low-dose streptozotocin (STZ) protocol; and (ii) a combined high-fat diet (HFD) and STZ model, complemented by the study of HFD alone. In addition, a detrimental high-sugar (HS) diet in drinking water was applied to only STZ-treated mice to test whether excessive sugar intake could further aggravate the diabetic condition.

These models were followed longitudinally from adulthood to senescence, enabling the evaluation of GA and MGO in relation to conventional measures (glycemia) and the investigation of central outcomes, including recognition memory and Alzheimer-like neuropathology.

The underlying hypothesis was that diabetes accelerates memory decline and hippocampal dysfunction through peripheral metabolic dysfunction, and that GA and MGO could serve as more sensitive biomarkers than HbA1c to capture these processes. Accordingly, the project was structured around five interconnected goals:

- to validate and compare complementary murine models of T2DM;
- to assess the translational reliability of GA and MGO in reflecting short-term metabolic alterations and disease progression;
- to evaluate whether a high-sugar diet further exacerbates the diabetic phenotype;
- to investigate how these metabolic alterations translate into cognitive impairment, with a specific focus on recognition memory;
- to evaluate the diabetes-induced damage to pancreatic and hippocampal tissues.

Overall, this work aimed to provide a comprehensive framework for understanding how diabetes and diet shape the trajectory of brain aging, while establishing GA and MGO as clinically relevant biomarkers for the early detection and personalized monitoring of diabetes-related cognitive decline.

# 5. Materials and methods

## 5.1. Experimental design and animal models

All the animals used in this work were wild-type pathogen-free male mice (strain C57BL/6J), purchased from Charles River company (Calco, Italy). The mice were acclimated to their environmental condition for almost one week before starting experiments conducted in the Animal Care Facility at the University of Pavia. The mice were housed in single plastic cages at 21 ± 2 °C, with humidity at 50 ± 10%, with an automatically controlled 12-hour light/dark cycle. Water and food were provided ad libitum. All experimental procedures were carried out following the guidelines of the institutional welfare committee and were approved by the Ethics Committee of the University of Pavia (Ministry of Health, License number 220/2022-PR), in compliance with the European Council Directive 2010/63/EU on the protection of animals used for scientific purposes.

All mice were initially fed a standard diet (normal diet, ND), consisting of 4RF21 pellets supplied by Mucedola Srl. The ND comprised 42.63% kcal of carbohydrates, 18.50% kcal of protein, and 3% kcal of fats.

In Model 1, only half of the animals were given 10% sucrose-enriched drinking water ad libitum (high-sugar group, HS) as their sole fluid source.

In Model 2, all animals were shifted to a high-fat diet (HFD) following a two-week acclimation period on the ND. HFD pellets were obtained from the Laboratory of Dr. Piccioni Srl (Gessate, MI, Italy) and consisted of 20% kcal from carbohydrates, 15% kcal from protein, and 59% kcal from fat.

### 5.1.1. Model 1: STZ model

The first experimental model involved thirty-five 9-month-old wild-type male mice. The study employed a longitudinal design, comprising five experimental time points (Figure 10), which began at 9 months of age (T0) and continued until the animals reached 19 months of age.
At the baseline time point (T0), all mice were maintained on a normal diet (ND), and assessments were conducted for fasting blood glucose, glycated albumin (GA), and methylglyoxal (MGO), along with spontaneous behavioral evaluations.
At T1 (13 months of age), the animals were randomly assigned to two groups:

- a control group (CTRL, n=17) that received daily intraperitoneal injections of physiological saline (0.9% NaCl) for five consecutive days.
- a diabetic group (DM, n=18) that received 5 intraperitoneal injections of 50 mg/kg streptozotocin (STZ) to induce diabetes (details provided in the subsequent section).

At T2 (one-month post-injection), fasting glycemia, GA, and MGO levels were assessed in all animals to confirm diabetes induction. From T2 onward, half of the animals in each group were given 10% sucrose-enriched drinking water ad libitum (high-sugar group, HS) as their only fluid source. Consequently, four experimental groups were defined:

- CTRL maintained on ND (CTRL-ND)
- CTRL receiving HS water (CTRL-HS)
- DM maintained on ND (DM-ND)
- DM receiving HS water (DM-HS)

Metabolic and behavioral evaluations were repeated at T3 (16 months) and T4 (19 months), including measurements of fasting glycemia, GA, MGO, and behavioral performance. At T4, all animals were euthanized, and tissues were collected for further analyses.

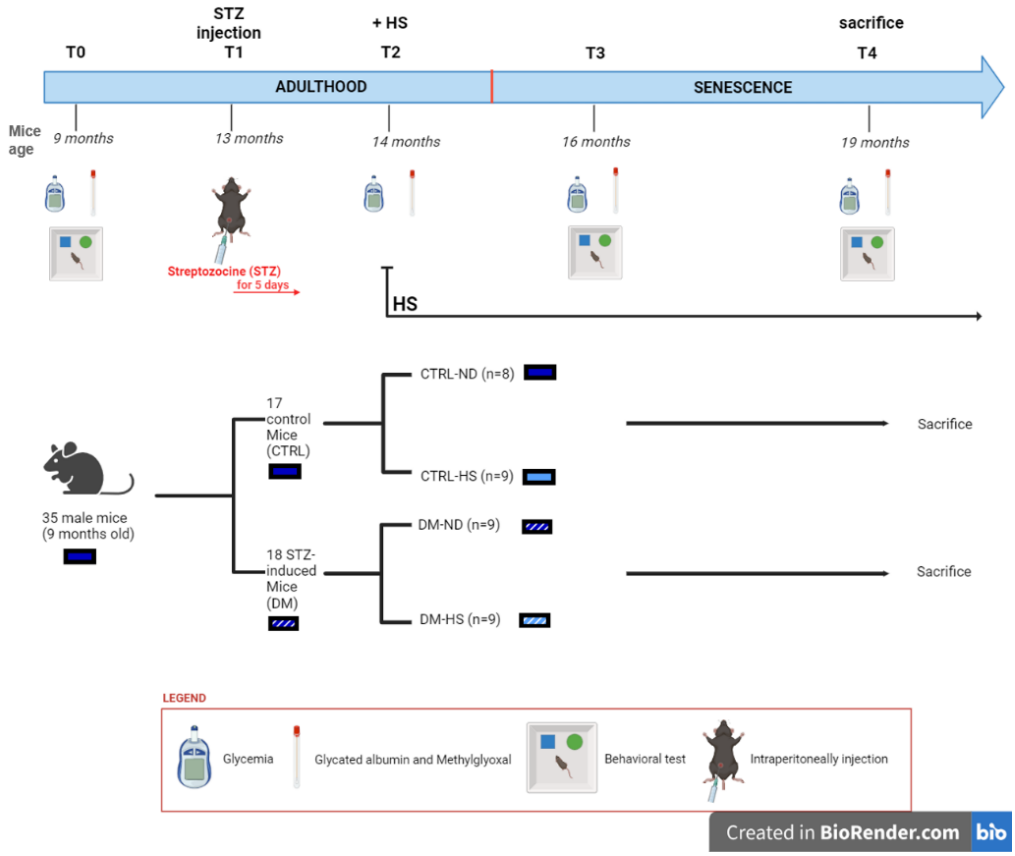


***Figure 10.*** *Experimental plan of STZ model.*

### 5.1.2. Model 2: HFD/STZ model

In this second experimental model, fourteen male wild-type mice were used, starting at 10 months of age. The study design consisted of five time points (Figure 11), spanning from 10 months (T0) to 16 months of age (T5).

At baseline (T0), all mice were transitioned from a normal diet to an HFD diet. Fasting blood glucose levels were measured, along with an oral glucose tolerance test (OGTT).

At T1 (one month after HFD initiation), fasting glycemia, GA, and MGO levels were measured, and spontaneous behavioral tests were performed.

At T2 (two weeks before STZ treatment), fasting glycemia, GA, MGO, and behavioral performance were reassessed.

At T3 (14 months of age), mice were randomly assigned to two groups:

- HFD group (n = 7), which continued on the HFD and received i.p. injections of physiological saline (0.9% NaCl) for five consecutive days.
- HFD/STZ group (n = 7), which remained on the HFD and received 5 i.p. injections of 50 mg/kg STZ to induce diabetes (detailed protocol provided in the following section).

At T4 (one month after injections), fasting glycemia was measured to verify the diabetic state.
At the final timepoint (T5, 16 months of age), fasting glycemia, GA, and MGO were measured again. OGTT and spontaneous behavioral tests were also conducted. Subsequently, all animals were sacrificed, and blood and organs were collected for further analysis, as described in the Materials and Methods section.
Throughout the study, body weight, food intake, and water consumption were monitored at regular intervals.

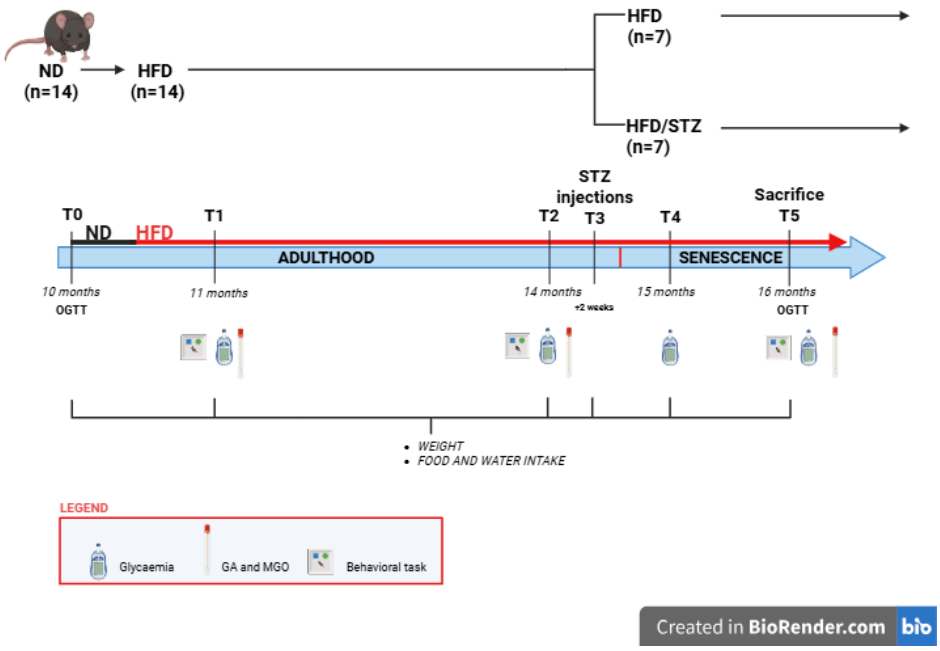


***Figure 11**. Experimental plan of HFD/STZ model.*

## 5.2. Glycemic index of ND and HS diets

At T0, the test to measure the glycemic index of ND and HS diets was performed, following the standard procedure used for GI testing in humans (Campbell et al., 2018). The protocol used for humans is designed to evaluate how 50 g of available carbohydrates (defined as total carbohydrate minus dietary fiber content) affect glycemia over time, according to the International Standard Organization (ISO 26642) (International Standards Organization. We assumed that the amount of CHO to test in each mouse is proportional to its weight. Specifically, we consider that 50 g of CHO are tested in 50 kg of human weight. Similarly, we administered 30 mg of CHO for every 30 g of body weight in each mouse. We performed the testing of the different diets in 3 subsequent days, using a glucose bolus as the standard reference glycemic index value of 100.

Therefore, each mouse was fed a portion of pure glucose solution, ND, or HS diets on a petri dish, with the serving size calculated to provide 30 mg of available carbohydrate during a 15-minute food intake period. Blood glucose levels were measured using a glucometer at 30, 60, 90, 120, 150, and 180 minutes after ingestion. Using the mathematical and statistical analysis software ORIGIN, the glycemic response curve was constructed, and the incremental area under the curve (AUC) of glucose, ND, and HS for each mouse was calculated. The glycemic index was then calculated as follows:

$$IG = \frac{AUCd}{AUCg} \cdot 100$$

Where: AUCd is the area under the curve of the diet test; AUCg is the area under the curve of the glucose test.

## 5.3. Diabetes induction: the Low-Dose STZ induction protocol

Diabetes was induced in mice according to protocols established by the Animal Models of Diabetic Complications Consortium (AMDCC) (Furman, 2021; K. K. Wu & Huan, 2008). A 50 mg/kg of STZ dose, dissolved in 100 mM citrate buffer, was administered via intraperitoneal injection for five consecutive days. Control animals received an equivalent volume of physiological saline (0.9% NaCl). One month after the final injection, fasting blood glucose levels were measured via tail vein sampling after a 4-hour fast.

In the STZ model, fasting blood glucose levels exceeding 300 mg/dL up to 600 mg/dl (16.7 mmol/L to 33.3 mmol/L) are considered as a classification criterion for diabetes (Furman, 2021; Graham et al., 2011). In the mouse model 2, the T2DM was induced by combining a high-fat diet (HFD) with STZ administration, as previously described. In this case, mice were considered diabetic if fasting glucose levels exceeded 250 mg/dL, according to established diagnostic criteria for this model (Chen et al., 2024; Furman, 2021; Peng et al., 2021).

## 5.4. Metabolic parameters

### 5.4.1. Weight, food, and water intake evaluation

Throughout the experimental period, body weight, food consumption, and water intake were routinely monitored in all experimental groups. Specifically, food intake was assessed only in the HFD/STZ model, while body weight and water intake were measured in both models. Body weight was measured using a calibrated digital scale with a precision of ±0.01 g. In both mouse models, body weight measurements were performed at the same time of day to minimize variability due to circadian fluctuations. Food intake was assessed by calculating the difference between the amount of food provided and the residual food remaining in each cage after 24 hours. Similarly, water intake was determined by measuring the volume of drinking water consumed over 24 hours, using graduated water bottles. These parameters were used to evaluate the impact of different dietary regimens and diabetes induction on body weight dynamics and metabolic behavior over time.

### 5.4.2. Measurement of fasting glucose, GA, and MGO

Mice were fasted for 12–16 hours before the measurement of fasting blood glucose, GA, and MGO levels. Blood samples were collected from the tail vein. For blood glucose measurement, a small drop of blood was applied to a test strip and analyzed using a OneTouch Verio Reflect® glucometer (Lifescan Italy Srl).

For the assessment of serum GA and MGO levels, approximately 200 µL of blood was collected using synthetic swabs (Copan 552C, purchased from

Diagnostic International Distribution S.p.A.), which ensure efficient sample collection and release, and subsequently analysed by GekLab laboratory using specific ELISA kits. Serum GA concentrations were determined using a Mouse Glycated Albumin ELISA Kit (LLD: 11.3 pmol/mL; Abbexa Ltd., Cambridge Science Park, Cambridge, U.K.), while MGO levels were measured using the OxiSelect™ Methylglyoxal Competitive ELISA Kit (lower detection limit: 0 µg/mL; Cell Biolabs, San Diego, CA, USA). This assay quantitates protein adducts of methylglyoxal-derived hydroimidazolone (MG-H1) (Nowotny et al., 2015).

### 5.4.3. The OGTT test

Oral glucose tolerance tests (OGTT) were performed at time points T0 and T5 in the HFD/STZ mouse model. Mice were fasted overnight before receiving an oral gavage of glucose solution (Glucosio Sclavo Diagnostics; 75 g/150 mL) at a dose of 1 g/kg body weight, following established protocols (Ayala et al., 2010; Nagy & Einwallner, 2018). Blood glucose levels were measured at baseline (0 minutes, fasting glycemia) and 30-minute intervals for up to 3 hours post-glucose administration. Glucose response curves and the corresponding area under the curve (AUC) were calculated for each animal using ORIGIN 6.0 software. Mean values and SEM for both glucose curves and AUCs were subsequently derived.

### 5.4.4. Insulin determination and HOMA-IR

At T5 in the HFD/STZ model, all mice were fasted for 12 hours before blood collection. Blood samples were obtained and centrifuged at 1500 RCF for 10 minutes to separate the serum. Serum insulin levels were quantified using a Mouse/Rat Insulin ELISA Kit (EMR0002, FineTest; Labclinics, Barcelona, Spain). Insulin resistance was evaluated using the homeostasis model assessment of insulin resistance (HOMA-IR), calculated according to the following formula:

$$HOMA - IR = \frac{fasting\ plasma\ glucose\left(\frac{mmol}{L}\right) X\ fasting\ plasma\ insulin\left(\frac{\mu IU}{mL}\right)}{22.5}$$

## 5.5. Behavioral test

Spontaneous behavioral tests were conducted without the use of external rewards or punishments to assess recognition memory and novelty-seeking behavior in mice. Animal activity was monitored and quantified using the SMART Video Tracking System (Biological Instruments, Besozzo, Varese, Italy) with a sampling rate of 40 ms per point, coupled with a Sony color CCD camera (PAL format).
In the STZ model, mice underwent a single behavioral test, the Novel Object Recognition (NOR) test, at specific time points (T0, T3, and T4). In the HFD/STZ model, at designated time points (T1, T2, and T5), animals underwent three behavioral tests: NOR, Object Location (OL), and Y-Maze. Specific cognitive parameters were selected and analyzed for each test, as described below. Between trials, the testing arena was thoroughly cleaned with 70% ethanol to remove olfactory traces from previous subjects.

### 5.5.1. Novel object recognition (NOR) test

The Novel Object Recognition (NOR) test evaluates exploratory behavior towards novelty and recognition memory (knowledge component) in rodents. The test, which lasts three days, is characterized by three main phases: habituation (or open arena), familiarization, and testing. During the first phase of habituation, which is carried out in the first two days, the mice were placed one at a time inside a white arena with no objects inside. Each mouse was left free to explore the empty arena for 15 minutes to familiarize themselves with the environment in which the test would later take place. Following this, the mice were removed from the arena and repositioned in their respective cages. On the third day, during the familiarization phase, the mice were positioned, always one at a time, within the same arena in which two identical objects were placed. The animals were left free to explore the two objects for 5 minutes, after which they were transferred back to their cages for 10 minutes (retention phase). During this time-lapse, the arena and the objects were cleaned with 70% ethanol, and one of the two objects was replaced with another object with a different shape, size, and color. Next, during the test phase, the mice were returned to the same arena and were left free to explore

the familiar object and the new object for 5 minutes, after which they were returned to their respective cages (Figure 12).

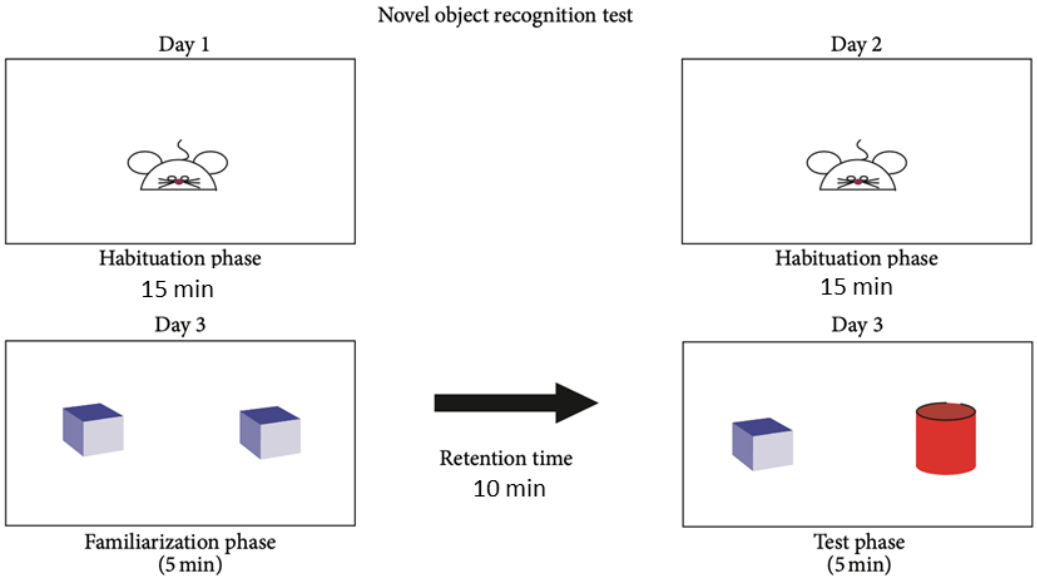


***Figure 12**. Experimental set-up and procedure for NOR task (Brandalise et al., 2017).*

In this test, we evaluated two cognitive parameters: (i) the number of approaches and (ii) the total duration of the approaches for both the familiar object and the new object. The approaches were defined as when the distance between the mice's snout and the object is equal to or less than 2 cm.
To assess the mice capability to discriminate between the familiar and the novel object, we calculated the mean novelty discrimination index (DI) using the formula:

$$DI = \frac{(n - f)}{(n + f)}$$

where n is the number or duration of approaches to the new object and f is the number or time of approaches to the familiar one. The DI value can range from -1 to 1, where -1 indicates complete preference towards the familiar object, 0 indicates no preference, and 1 indicates complete preference for the new object.

### 5.5.2. Object location (OL) test

The Object Location (OL) is a spontaneous behavioral test that allows to investigate the "remember" component of the recognition memory in rodents (Rossi et al., 2018). This test consists of the same phases as the NOR task: two days of habituation (15 minutes per day) and the familiarization, retention, and test phase on the third day. The test procedure is identical to the NOR up to the test phase. After 5 minutes of the familiarization phase, the mouse was removed from the arena and placed inside its cage for 10 minutes. During this period, the arena and objects were cleaned with 70% ethanol, and one of the two was moved to a different location in the arena. In the subsequent test phase, the animals were repositioned in the same arena and were left free to explore the familiar object and the repositioned object for 5 minutes (Figure 13).

In the OL test, we investigated the exact parameters of the NOR test: (i) the number of approaches and (ii) the duration of the approaches for both the familiar object and the repositioned one.

To assess the discrimination between the familiar object and the repositioned one, the discrimination index (DI) was calculated in the same way as it was done for the NOR task.

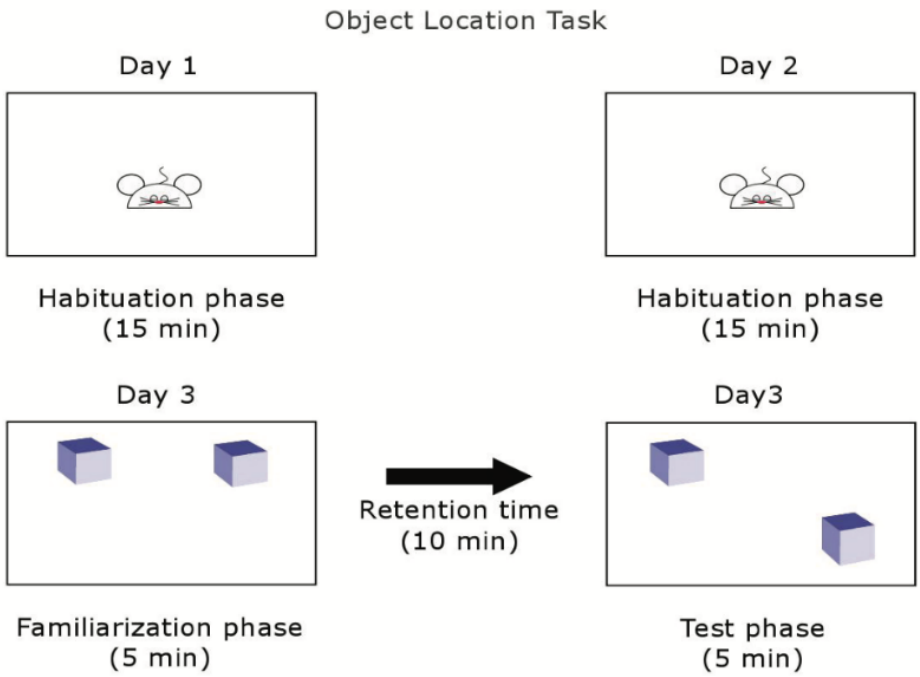


***Figure 13.*** *Experimental set-up and procedure for NOR task (Rossi et al., 2018).*

### 5.5.3. Y-maze test

The Y maze test is usually used to study the "remember" component of the recognition memory and spatial working memory. This test is carried out in a Y-shaped labyrinth consisting of three symmetrical solid gray plastic arms (40 cm long, 12 cm high, 8 cm wide) positioned at an angle of 120 ° to each other. Each session began with placing the mouse in the center of the maze. The mouse is left free to explore the three arms for 8 minutes (Figure 14). In this test, an "arm entry" was defined as all 4 of the animal's limbs entering an arm of the maze. A "triad" or "triplet" was defined as a set of 3 arm entries in which each consecutive entry was into a different arm of the maze. If the arms of the Y maze are designated A, B, and C, an entry will proceed as ABC, ACB, BAC, BCA, CAB, or CBA. On the contrary, a failure was defined as repeated entry into the same arm (AAA, ABA, ACA, AAB, AAC, BBB, BAB, BCB, BBC, CCC, CBC, CAC, CCB, or CCA). The number of arm entries and the number of triads were measured.
In particular, the percentage of triplet alternation was considered as a cognitive parameter, calculated by using the following formula:

$$\frac{\text{Number of triplets}}{\text{Number of total entries - 2}} \times 100$$

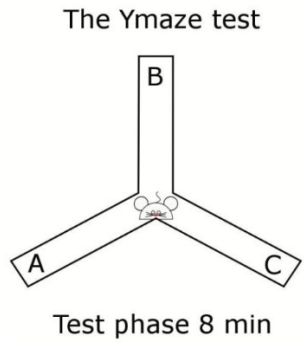


***Figure 14**. Experimental set-up and procedure for Y maze task (Rossi et al., 2018).*

## 5.6. Frailty index calculation

We used a variant of Parks's procedure to measure the frailty index (FI) during aging (Parks et al., 2012). Park's FI procedure is as follows. Mean reference values for each parameter used to construct the FI are obtained at T0. For each mouse and at different experimental times, the values of these parameters are compared with the mean reference values. The values that are 1 standard deviation (SD) above or below the mean reference value are given a FI value of 0.25; the values that are different of 2 SD are scored as 0.5; the values that are different of 3 SD are 0.75; the values that are more than 3 SD above the mean reference receive the maximal frailty value of 1. Parameters that are different from the mean reference values by less than 1 SD receive a score of 0. These values are averaged to obtain an FI for each animal so that a mouse with no deficits has a FI score of 0 and an animal with all possible maximal deficiencies has a FI score of 1 (Parks et al., 2012).

Whereas Parks's method for creating the FI used a graded scale, we developed a method to derive more accurate values during aging. The mean reference value and the SD for each studied parameter were calculated at T0 (11 months). The values obtained from each mouse at different experimental times were compared to the mean value at T0 using the following formula:

$$FI = \frac{Value - Mean\ at\ T0}{SD\ at\ T0} * \pm 0.25$$

This procedure was used for creating Cognitive FI.

Furthermore, for the HFD/STZ model, this procedure was applied to derive specific FI reflecting the "knowledge" (assessed via the NOR test) and "remember" (assessed via the OL and Y-maze tests) components of recognition memory. Finally, to obtain a global cognitive FI of recognition memory, the FI from the two components were subsequently averaged.

## 5.7. Histological analysis

All mice were decapitated at 19 (for the STZ model) or 16 (for the HFD/STZ model) months after anesthetization with isofluorane (Aldrich, Milwaukee, WI, USA). The head/body of the pancreas and brain were immediately excised, washed in 0.9% NaCl, and fixed by immersion for 7 h in 4% paraformaldehyde in 0.1 M phosphate (pH 7.4). The tissues were then dehydrated through a graded series of ethanol and finally embedded in Paraplast X-TRA (Sigma Aldrich, Milan, Italy). Using a manual rotatory microtome, 6 µm-thick pancreatic and 8 µm-thick brain coronal sections were cut serially and collected on silane-coated slides.

At the time of use, the sections included in Paraplast X-tra were then deparaffinized for 20 minutes in xylene (Carlo Erba, Cornaredo, Italy), subsequently rehydrated by using a descending alcoholic scale protocol that includes five steps of 5 minutes each, as follows: xylene 50%/absolute ethanol 50%, absolute ethanol, ethanol 95%, ethanol 80%, and finally ethanol 70%. Next, the sections were rinsed in phosphate-buffered saline (PBS). The sections were then used for Hematoxylin and Eosin (H&E) staining and brightfield immunohistochemistry evaluations.

### 5.7.1. Hematoxylin/eosin staining

The deparaffinized and rehydrated sections of pancreas and hippocampus tissues were immersed in hematoxylin for 10 minutes and then washed with running water for about 2 minutes. Next, the sections were washed twice in distilled water (H20d) and immersed in eosin for 2 minutes. After two washes in H20d, the slices were dehydrated following an ascending alcoholic scale protocol consisting of five steps: 80% ethanol (fast), 95% ethanol, absolute ethanol, xylene 50%/absolute ethanol 50%, and xylene (3 minutes each).

Finally, the slides were mounted with Eukitt (Kindler gmbH) for the bright-field microscope analysis.

Given the complex architecture and functional specialization of both the pancreas and central nervous system (CNS), H&E staining provided a clear overview of tissue organization and delineated region-specific histological characteristics (Li et al., 2022; Longnecker, 2021; Roda et al., 2019). Brightfield microscopy at low magnification enables clear identification of distinct areas within the pancreas and hippocampus. Whereas the coronal plane and subregional anatomy of the hippocampus were readily visualized, the coronal orientation of the pancreas was only confirmed based on the presence of rounded pancreatic ducts lined with cuboidal epithelium and the distribution of the islets of Langerhans.

Sections were observed by Leica DM6B WF microscope (Leica Microsystems, Buccinasco, MI, Italy). The images were acquired with a Leica dfc 7000 t CCD camera (Leica microsystems, Buccinasco, MI, Italy) and stored on a PC running the Leica Application Suite X (LAS X) software (Version 5.1.0). The whole hippocampus was reconstructed using the LAS X Navigator imaging system, including the merge function.

#### 5.7.1.1. Insulitis scoring

H&E-stained pancreatic tissue sections were then observed for the assessment of lymphocytic infiltrates in the Langerhans pancreatic islets. To determine the presence and severity of insulitis, a minimum of 30 islets for each experimental group were evaluated. All evaluations were conducted under double-blinded conditions. The degree of insulitis was graded according to the following: normal islet, score 0; perivascular/periductal infiltration, score 1; peri-insulitis, score 2; mild insulitis (< 25% of the islet infiltrated), score 3; and severe insulitis (more than 25% of the islet infiltrated), score 4 (Pavlovic et al., 2018; Pejnovic et al., 2013).

#### 5.7.1.2. Hippocampal injury evaluation

For histopathological evaluation, four sections per mouse were examined. The most representative figures of the hippocampus were selected and are shown, with a focus on the Dentate Gyrus (DG) and *Cornu Ammonis* (CA) regions. Concerning the quantitative evaluation, the following measurements were

performed: (i) whole thickness of DG layer; (ii) pyramidal cell layer thickness of CA subdivisions; (ii) cell density (number of cells/area in mm2) in the same areas was measured.

### 5.7.2. Immunohistochemistry

After deparaffination in xylene (Carlo Erba, Cornaredo, Italy), the sections were rehydrated in a series of decreasing ethanol concentrations and rinsed in phosphate-buffered saline (PBS, Sigma-Aldrich, Milan, Italy). The hippocampal slides were incubated at RT for 7 min in a blocking buffer for the suppression of the endogenous peroxidases (3% H2O2 in 10%methanol in PBS), then for 20 min in foetal calf serum to block non-specific antigen binding sites. Immunohistochemistry was performed using commercial antibodies on mice and human hippocampal sections, to localize the presence and distribution of two specific markers involved in Alzheimer pathology: (i) Anti-Beta (β)-Amyloid (AβPP), and (ii) Anti-phospho-Tau (Ser235) (details and dilutions are reported in Table 1). The sections were incubated at 4°C overnight in a dark chamber. Subsequently, the slides were incubated with biotinylated secondary antibodies (Vector Laboratories, Burlingame, CA, USA) for 30 minutes and horseradish peroxidase conjugated avidin-biotin complex (Vector Laboratories, Burlingame, CA, USA) for 30 minutes at RT. Then, 0.05% 3,3-diaminobenzidine tetrahydrochloride (DAB; Sigma Aldrich, Milan, Italy) with 0.01% H2O2 in Tris–HCl buffer (0.05 M, pH 8) was used as a chromogen, followed by nuclear counterstaining with Haematoxylin. Then, sections were dehydrated in ethanol, cleared in xylene (Carlo Erba Reagents, Cornaredo, Italy), and finally mounted in Eukitt (Kindler, Freiburg, Germany). For control staining, the primary antibody was omitted in some sections, which were incubated with phosphate-buffered saline only. No immunoreactivity was observed in this condition.

| | Antigen | Species, Manifacturers | Dilution |
|---|---|---|---|
| **Primary antibodies** | Anti-**Beta (β)-Amyloid** | Mouse monoclonal IgG1, clone 22C11, Chemicon (MAB348, Sigma-Aldrich, St. Louis, MO, USA) | 1:100 |
| | Anti-**phospho-Tau** (Ser235) | Mouse monoclonal IgG1k, clone RN235, Sigma-Aldrich (MABN2275, Sigma-Aldrich, St. Louis, MO, USA) | 1:500 |
| **Secondary antibodies** | Biotinylated horse anti-mouse IgG | Horse, Cat# PK-6102, Vector Laboratories (Burlingame, CA, USA) | 1:200 |

***Table 1**. Primary and secondary antibodies used for immunohistochemical reactions.*

### 5.7.3. Quantitative analysis

For the quantitative assessment of the two markers, the immunopositivity was analyzed in four hippocampal subregions: the molecular layer of CA1 (ML-CA1), the pyramidal layer of CA1 (P-CA1), the pyramidal layer of CA3 (P-CA3), and the molecular layer of the dentate gyrus (ML-DG).

Sections were observed by Leica DM6B WF microscope (Leica Microsystems, Buccinasco, MI, Italy). The images were acquired with a Leica dfc 7000 t CCD camera (Leica microsystems, Buccinasco, MI, Italy) and stored on a PC running the Leica Application Suite X (LAS X) software (Version 5.1.0). Furthermore, three sections per animal were analyzed using ImageJ (ImageJ 1.46p, NIH, Bethesda, MA, USA), and for each animal the mean and standard error of the mean (SEM) were calculated.

*p-Tau analysis*

After image acquisition, bright-field images were inverted so that immunopositive areas appeared lighter than the background or non-stained neurons. Background intensity and hematoxylin staining were subtracted. The density of pixels in immunopositive areas was measured and expressed as optical density (OD). For each section, OD measurements were performed in 10 rectangular regions of interest (ROIs 40x40) for molecular layers (Figure 15A) and 10 circular (ROIs 30x30) for pyramidal layers (Figure 15B). The background OD from each section was subtracted from the measured values. The dimensions of the ROIs and the magnification were kept constant across all analyses.

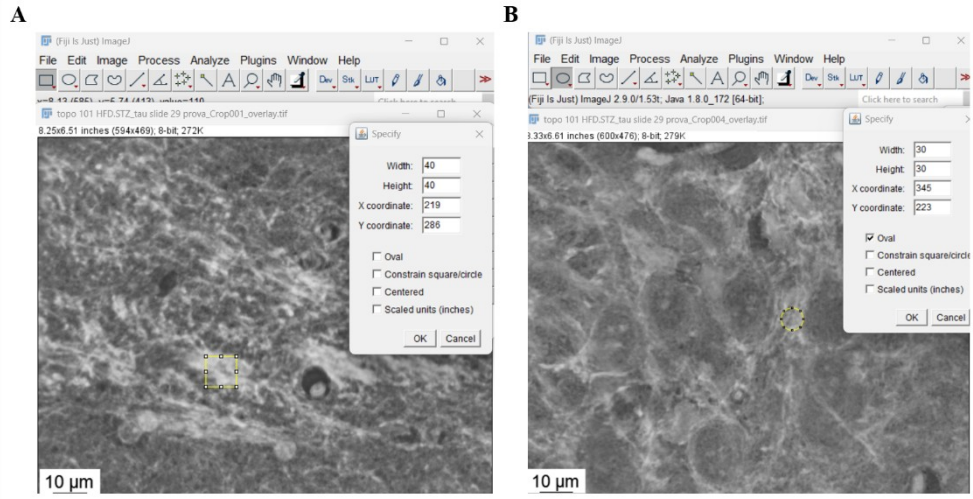


***Figure 15.*** *ImageJ toolbar with "Rectangular selection" (A) and "Oval selection" (B) with ROIs specification.*

*APP analysis*

For each section, the area of plaque and the number of APP spots were measured using the “polygon selection” (Figure 16A) and “multi-point” (Figure 16B) tools, respectively. Subsequently, these data were considered to calculate the APP plaque density applying the following formula:

$$\frac{number\ of\ single\ APP\ spots}{area\ plaque}$$

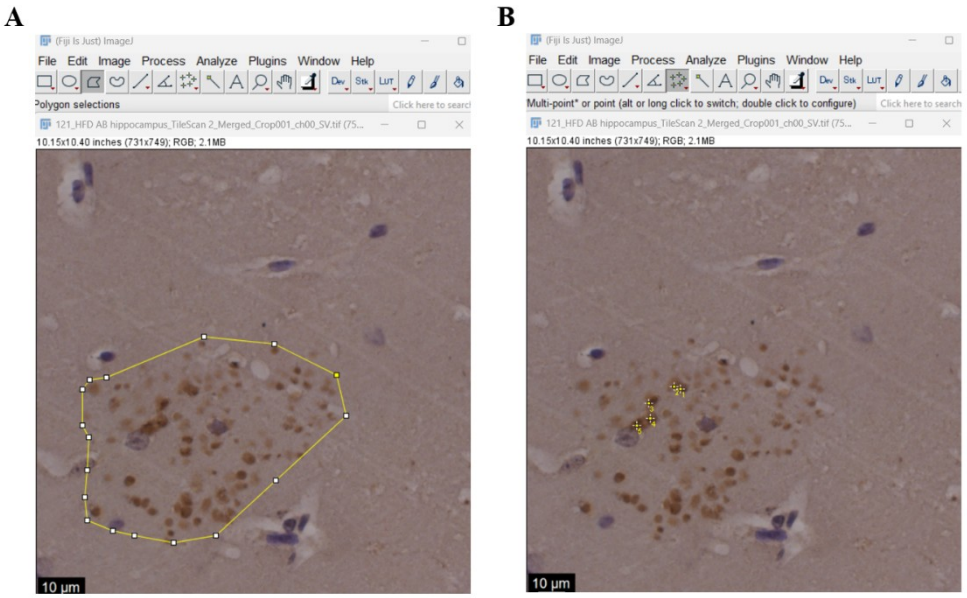


***Figure 16.*** *ImageJ toolbar with "polygon selection" (A) and "multi-point" (B) with ROIs specification.*

## 5.8. Statistical analysis

The values obtained were expressed in terms of mean ± standard error of the mean (SEM, Standard Error of the Mean). The statistical analysis of Kaplan-Meier graphs was performed using a Log-Rank (Mantel-Cox) test. To evaluate the statistical differences among the experimental groups in fasting glycemia, GA, MGO, weight, food and water intake, Global DI, Global FI, and quantitative analysis of hippocampus tissue, the unpaired t-test and the ANOVA One-Way test followed by the Bonferroni post-hoc test, were performed. Microsoft Excel and Prism 5 (GraphPad Software, San Diego, CA, USA) were used for statistical analysis. Statistical significance was assigned as follows: $P < 0.05$ (*), $P < 0.01$ (**), $P < 0.001$ (***).

# 6. Results

My Ph.D. project aimed to investigate the metabolic, cognitive, and hippocampal consequences of diabetes and diet-induced metabolic alterations in mice. To this end, two longitudinal and complementary experimental models were developed. The first model, hereafter referred to as STZ, was based on low-dose streptozotocin (STZ) administration in adult mice. This model was examined under two different conditions: one group of animals followed a normal diet (ND), while another group was exposed to a detrimental high-sugar (HS) diet. The HS diet was applied to evaluate whether excessive sugar intake could induce or exacerbate the diabetic condition.
The second preclinical model, hereafter referred to as HFD/STZ, combined a high-fat diet (HFD) with low-dose STZ treatment. In addition, HFD alone was studied to assess the specific contribution of diet-induced metabolic changes.

Data obtained from the STZ model have been published in Frontiers in Physiology (Venuti et al., 2025), and a second paper describing the results of the HFD/STZ model is currently in preparation.

## 6.1. Metabolic biomarkers in non-diabetic mice

To evaluate the systemic impact of dietary interventions and diabetes induction, metabolic parameters were assessed in the control groups of each model. Fasting glycemia, glycated albumin (GA), and methylglyoxal (MGO) were measured in control animals fed a normal diet (CTRL-ND), provided by the animal facility, or a high-sugar diet (CTRL-HS), as well as in mice exposed to a high-fat diet (HFD). Furthermore, in the HFD-fed mice, the OGTT was performed to evaluate the presence of glucose intolerance.

### 6.1.1. Glycemia, glycated albumin, and methylglyoxal in mice fed a normal and high-sugar diet

Monitoring peripheral metabolic markers is essential to characterize the systemic effects of dietary interventions and to evaluate their potential contribution to diabetes-related alterations. In this study, fasting glycemia, GA, and MGO were assessed longitudinally in mice fed either an ND or an HS diet.
As expected, in CTRL-ND mice, fasting glycemia at T2 (14 months of age; 104.45 ± 2.94 mg/dL, n = 8) was not significantly different from baseline

levels at T0 (98.44 ± 2.83 mg/dL, n = 35). The same levels of fasting glycemia were also maintained at T3 (16 months of age; 94.50 ± 5.15 mg/dL, n = 8) and T4 (19 months of age; 97.29 ± 8.58 mg/dL, n = 8), with no statistical difference across timepoints (Figure 17A).
Similarly, no significant changes in GA were detected at any monitored timepoint: T0 (29.13 ± 1.81 pmol/mL, n = 35), T2 (35.05 ± 1.65 pmol/mL, n = 8), T3 (14.77 ± 0.81 pmol/mL, n = 8), and T4 (26.66 ± 2.62 pmol/mL, n = 8; Figure 17B).
However, MGO concentrations at T2 (2.04 ± 0.22 μg/mL, n = 8) were comparable to those at T0 (2.72 ± 0.21 μg/mL, n = 35), but significantly declined with age. Specifically, values decreased from T0 (2.72 ± 0.21 μg/mL, n=35) to subsequent timepoints (T2: 2.04 ± 0.22 μg/mL; T3: 1.26 ± 0.27 μg/mL, p = 0.017; T4: 1.22 ± 0.15 μg/mL, p = 0.023; Figure 17C).
In summary, while fasting glycemia and GA remained stable between 9 and 19 months of age in ND-fed mice, as expected, MGO showed a significant age-related reduction.

After 5 months of ND (T2), a group of mice (n = 9) was switched to an HS diet, and were monitored for 2 months (T3) and 5 months (T4).
At T3, fasting glycemia in CTRL-HS mice (98.78 ± 5.76 mg/dL, n = 9) was statistically indistinguishable from that in CTRL-ND mice, a trend maintained at T4 (CTRL-HS: 86.78 ± 5.06 mg/dL; Figure 17A). Thus, prolonged intake of 10% HS over five months did not alter fasting glucose levels when compared to mice fed a normal diet. Moreover, glycemia remained stable across the entire experimental period in both CTRL-ND and CTRL-HS groups.
Furthermore, at T3, the GA level in CTRL-HS mice (27.76 ± 8.0 pmol/mL, n = 9) was comparable to that in CTRL-ND animals. However, at T4, GA in CTRL-HS mice (78.08 ± 15.08 pmol/mL, n = 9) was significantly elevated relative to CTRL-ND mice ($p < 0.001$; Figure 17B). This suggests a detrimental impact of prolonged HS intake on the glycation process.
Regarding MGO, a similar age-related decline in its levels, as seen in ND-fed mice, was also detected in CTRL-HS mice (T3: 1.18 ± 0.24 μg/mL, p = 0.005; T4: 0.64 ± 0.14 μg/mL, T4 vs T3: $p < 0.001$). Importantly, MGO levels were comparable between CTRL-ND and CTRL-HS groups at corresponding timepoints.

Overall, these findings indicate that a 10% HS diet does not adversely affect glycemia, GA, or MGO levels up to T3. However, an extended HS diet for five months led to a marked increase in GA at T4, without affecting glucose levels, suggesting that GA is a more sensitive indicator of long-term 10% HS exposure. Additionally, we suggest that the senescence process could cause the decline in MGO, which was independent of diet regimen.

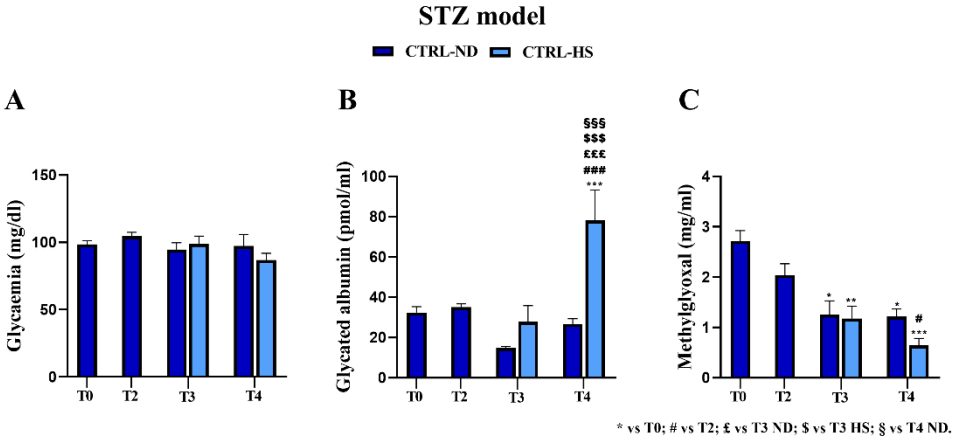


***Figure 17.*** *Comparison between normal (ND) and high sugar (HS) diet in control mice (CTRL) at different experimental timepoints. Fasting glycemia (A), Glycated albumin (B), and Methylglyoxal (C) levels were measured at T0 and T2 in CTRL mice, at T3 and T4 in CTRL-ND and CTRL-HS animals. Statistical significance (One-Way ANOVA followed by Bonferroni post-hoc test): * vs T0, # vs T2, £ vs T3 ND, $ vs T3 HS, § vs T4 ND. For all symbols reported p < 0.05 (*, #, £, $, §); p < 0.01 (**, ##, ££, $$, §§); p < 0.001 (***, ###, £££, $$$, §§§).*

### 6.1.2. Glycemia, glycated albumin, methylglyoxal, and oral glucose tolerance test in mice fed with high-fat diet

Following the same approach previously described, fasting glycemia was measured at designated time points throughout the study to evaluate the metabolic effects of HFD alone. Before HFD at T0 (10 months of age), mice fed an ND exhibited euglycemia (94.16 ± 2.11 mg/dl, n = 14). After one month (T1: 162.08 ± 5.28 mg/dl, n = 14), four months (T2: 154.87 ± 10.32 mg/dl, n = 14), and six months (T5: 143.29 ± 12.97 mg/dl, n = 7) of HFD, fasting glycemia values were significantly elevated compared to T0 (T1 and T2: $p < 0.0001$; T5: $p = 0.00011$). In the HFD group, no statistically significant

differences were detected among the different experimental timepoints (Figure 18A).
These findings indicate that HFD alone induces a rapid, stable elevation in fasting glycemia, reaching a 72.13% increase after one month. This hyperglycemic state persists throughout the six-month monitoring period.

As with fasting glycemia, GA levels were monitored before HFD (T0: 29.15 ± 2.11 pmol/mL, n = 14), and after one (T1: 14.91 ± 7.58 pmol/mL, n = 14), four (T2: 52.17 ± 6.34 pmol/mL, n = 14), and six months (T5: 24.92 ± 2.23 pmol/mL, n = 7) of HFD. Specifically, after four months of HFD, GA levels significantly increased compared to T0 ($p = 0.002$) and T1 ($p = 0.001$), but decreased significantly at T5 ($p = 0.016$; Figure 18B). While glycemia exhibited a rapid response after only one month of diet switch, GA levels showed a delayed response, with a significant increase emerging after four months of HFD exposure. Thereafter, GA concentrations declined, suggesting a dynamic metabolic adaptation to a prolonged HFD regimen.

MGO levels in HFD mice showed a significant reduction at T1 (1.31 ± 0.05 µg/mL, n = 14) compared to T0 ND (2.27 ± 0.30 µg/mL, n = 14; $p = 0.011$). Furthermore, MGO levels further decreased at both T2 (0.27 ± 0.07 µg/mL, n = 14) and T5 (0.22 ± 0.07 µg/mL, n = 7), relative to T1 (1.31 ± 0.05 µg/mL, n = 14; $p < 0.0001$ for T2 and $p = 0.0001$ for T5; Figure 18C). This progressive reduction over time mirrored the trend previously observed in ND and HS mice of the first model, confirming the hypothesis of an age-related decline in fasting MGO levels.

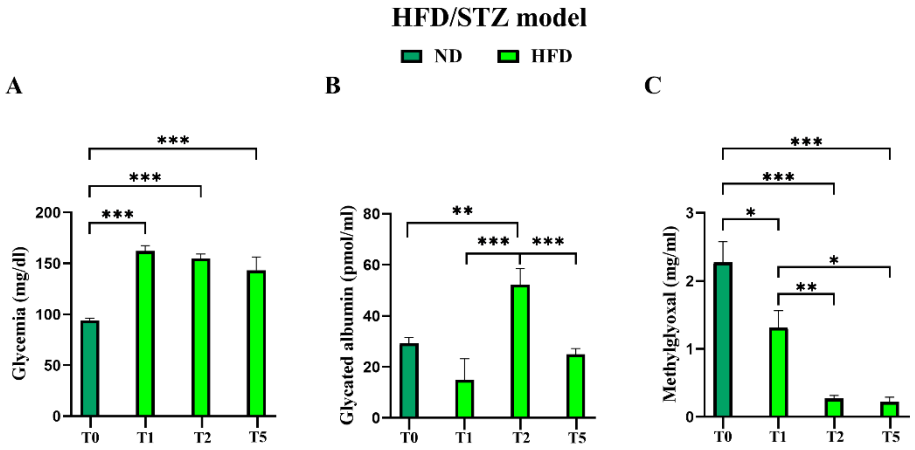


***Figure 18.*** *HFD effect on fasting glycemia, GA and MGO. (A) Fasting glycemia, (B) Glycated albumin, and (C) Methylglyoxal at T0 in ND mice (dark green) and at T1, T2, T4, and T5 in HFD mice (green). Values are reported as mean ± SEM. Statistical significance (one-way ANOVA followed by Bonferroni post-hoc test): $p < 0.05$ (*); $p < 0.01$ (**); $p < 0.001$ (***).*

Given the hyperglycemia in HFD mice, the OGTT was conducted to evaluate the presence of glucose intolerance. Specifically, this test was performed at T0 in CTRL mice (n = 14) and at T5 in HFD mice (n = 3). For each animal, the glucose response curve and the corresponding area under the curve (AUC) were calculated (Figure 19A and B, respectively).

In CTRL mice, the glucose peak (4.44 ± 0.27 mmol/L) occurred 30 minutes after glucose administration and gradually declined thereafter, indicating normal glucose homeostasis. In contrast, the HFD group displayed a higher glucose peak (6.99 ± 1.19 mmol/L), followed by a more rapid decline compared to CTRL mice (Figure 19A). Nevertheless, the AUC in CTRL mice at T0 was 556.74 ± 31.99 mmol/L × min, while the AUC in HFD mice at T5 was slightly elevated (582.61 ± 45.86 mmol/L × min), without reaching statistical significance (Figure 19B). These results demonstrated normal glucose tolerance.

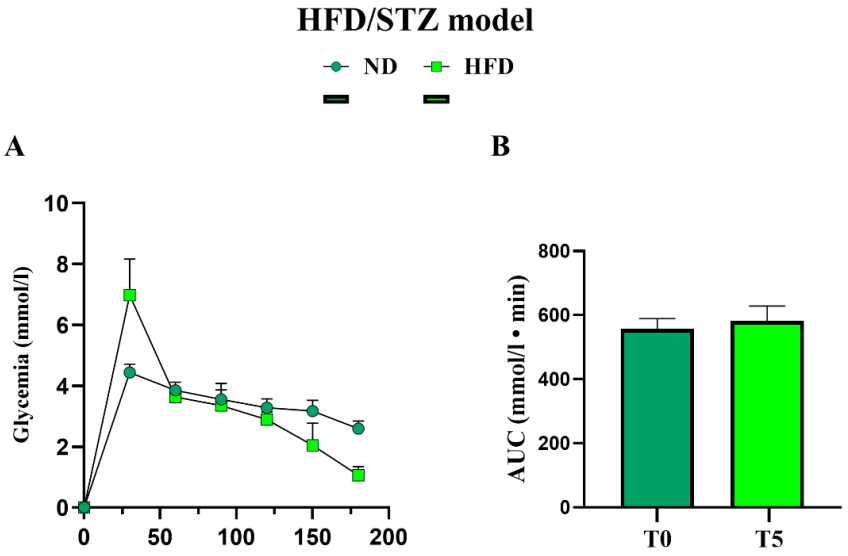


***Figure 19.*** *HFD effect on OGTT test. (A) Mean of response glucose curves and (B) Mean of Area under the curve (AUC) of OGTT at T0 in CTRL mice (dark green) and at T5 in HFD (green). Data are presented as mean ± SEM. Statistical significance (One-Way ANOVA followed by Bonferroni post-hoc test): $p < 0.05$ (*); $p < 0.01$ (**); $p < 0.001$ (***).*

## 6.2. Diabetes induction on the two experimental models

After establishing the longitudinal profiles of metabolic parameters in ND, HS, and HFD-fed mice, these parameters were investigated in diabetic conditions. In both experimental models, diabetes was induced in adult mice using the same low-dose STZ protocol, as described in section 5.3 of Materials and Methods. This approach enabled direct comparison between STZ alone and the combined HFD/STZ condition. In both models, metabolic alterations were monitored by fasting glycemia, GA, and MGO. Furthermore, in the HFD/STZ model, additional assessments included OGTT, plasma insulin levels, and the Homeostatic Model Assessment of Insulin Resistance (HOMA-IR) to evaluate insulin resistance.

### 6.2.1. Metabolic parameters of diabetic mice in STZ model

In this first model, diabetes was established at T1, corresponding to 13 months of age (DM-ND, n = 18). One month following STZ administration (T2), all treated mice exhibited a significant and pronounced increase in fasting

glycemia (mean: 421.5 ± 21.63 mg/dL, n = 18; Figure 20A) compared to pre-induction levels at T0 (98.44 ± 2.83 mg/dL, $p < 0.001$). Notably, each mouse exceeded 300 mg/dL for three consecutive days, fulfilling diagnostic criteria for diabetes in STZ-treated rodents (Furman, 2021; Graham et al., 2011; Liu et al., 2020). In accordance with the Animal Models of Diabetic Complications Consortium (AMDCC), these animals were classified as diabetic (DM). Overall, fasting glycemia at T2 represented a 412.7% increase relative to T0.

Concomitantly, GA levels were markedly elevated at T2 (113.37 ± 26.39 pmol/mL, n = 18) compared to baseline (29.13 ± 1.81 pmol/mL, n = 35; $p = 0.0062$; Figure 20B), reflecting a 389.6% increase. In contrast, MGO levels in the DM group at T2 (3.12 ± 0.66 µg/mL, n = 35) remained comparable to T0 values (2.72 ± 0.21 µg/mL, n = 18). Thus, one month post-STZ treatment, both glycemia and GA were significantly elevated, whereas MGO remained unchanged.

At T3 (two months post-induction), both DM-HS and DM-ND mice demonstrated a tendency toward decreased fasting glycemia (DM-HS: 342.78 ± 61.41 mg/dL, n = 9; DM-ND: 332.22 ± 46.40 mg/dL, n = 9), though still significantly above T0 levels ($p < 0.001$). Glycemia further declined at T4 (five months post-induction) in both DM-HS (152.60 ± 33.25 mg/dL) and DM-ND (217.33 ± 54.54 mg/dL) mice. These values, although reduced compared to T2, were no longer significantly different from baseline T0 levels. No significant differences in glycemia were observed between DM-HS and DM-ND groups at either T3 or T4. Collectively, these results suggest a partial spontaneous recovery of glycemic control over time following STZ induction, and importantly, indicate that high-sugar (HS) water intake did not exacerbate glycemia at any measured time point.

GA levels, after peaking at T2, remained elevated but did not differ significantly at subsequent time points (T3 and T4) in either group (T3: DM-HS 93.04 ± 58.61 pmol/mL; DM-ND 93.62 ± 36.61 pmol/mL; T4: DM-HS 97.16 ± 29.27 pmol/mL; DM-ND 71.22 ± 21.45 pmol/mL; Figure 20B). Notably, GA values remained 3-4 times higher than baseline, confirming its utility as a robust biomarker of diabetes in STZ-treated animals. Unlike glycemia, GA did not decline at T4, suggesting sustained non-enzymatic glycation despite partial normalization of glucose levels.

As observed in control mice, MGO levels in DM animals showed a non-significant downward trend over time. However, at T3, MGO was significantly elevated in DM-HS mice (3.57 ± 0.48 µg/mL, n = 9) relative to DM-ND mice (2.03 ± 0.21 µg/mL, n = 9; p = 0.01). At T4, following continued HS intake, MGO levels in DM-HS mice significantly declined (0.64 ± 0.18 µg/mL) compared to T3 (1.32 ± 0.10 µg/mL; p = 0.0009; Figure 20C).

Since HS intake did not affect glycemia at any experimental time point, either in control or diabetic mice, animals were pooled at T3 and T4 within the respective CTRL and DM groups to assess longitudinal effects of metabolic parameters (Figure 21). Animals that did not survive to T4 were excluded (CTRL: n = 16; DM: n = 14).

In CTRL mice, fasting glycemia remained stable over time: T0 (97.5 ± 4.05 mg/dL), T2 (103.31 ± 3.02 mg/dL), T3 (97.75 ± 3.91 mg/dL), and T4 (91.37 ± 4.73 mg/dL; Figure 21A). In contrast, DM mice exhibited a marked glycemic increase at T2 (419.87 ± 32.38 mg/dL) compared to T0 (103.64 ± 7.69 mg/dL; $p < 0.001$) and to CTRL mice at T2 ($p < 0.001$). Although glycemia decreased significantly in DM mice at T3 (296.57 ± 32.61 mg/dL) and T4 (194.21 ± 37.04 mg/dL), values remained elevated relative to CTRL mice ($p < 0.001$), though no longer significantly different from T0.

Regarding GA, CTRL mice showed a significant increase at T4 (59.46 ± 12.89 pmol/mL) compared to T0 (29.37 ± 2.33 pmol/mL; p = 0.007). GA levels decreased significantly at T3 (17.76 ± 1.35 pmol/mL; $p < 0.001$ vs. T0, p = 0.03 vs. T2; Figure 21C), with the T4 increase primarily attributable to the HS diet. In DM mice, GA levels significantly increased at T2 (76.59 ± 20.87 pmol/mL vs. T0: 33.29 ± 5.47 pmol/mL; p = 0.02), and also differed from CTRL at the same time point (p = 0.0064). GA levels subsequently declined at T3 (75.82 ± 25.08 pmol/mL) and T4 (63.07 ± 12.76 pmol/mL), but the differences were not statistically significant. However, at T3, a significant difference persisted between DM and CTRL groups (p = 0.043).

For MGO, CTRL mice showed significant reductions at T3 (0.98 ± 0.21 µg/mL) and T4 (0.84 ± 0.17 µg/mL) compared to T0 (2.27 ± 0.30 µg/mL; p = 0.009 and p = 0.03, respectively; Figure 21E). Similarly, DM mice exhibited a significant decrease in MGO at T4 (1.07 ± 0.12 µg/mL) compared to T0 (2.77 ± 0.40 µg/mL; p = 0.01; Figure 21F). No significant difference in MGO was detected between CTRL and DM groups at T2, although at T3, MGO was

significantly higher in DM mice (2.58 ± 0.41 µg/mL) relative to CTRL (p = 0.0003). At T4, MGO levels were comparable between groups. Notably, the increase observed at T3 in DM mice was primarily attributable to the HS regimen.

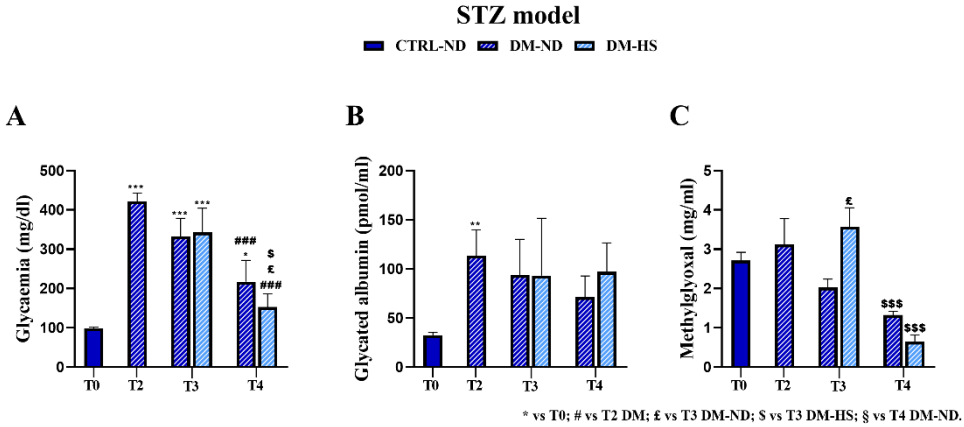


***Figure 20.*** *Comparison between control mice fed with normal diet (CTRL-ND) and diabetic mice fed with both normal diet (DM-ND) and high sugar diet (DM-HS) at different experimental timepoints. Fasting glycemia (A), Glycated albumin (B), and Methylglyoxal (C) levels were measured at T2 in DM mice (n=18), and at T3 and T4 in DM-ND and DM-HS animals. All data were compared to each other and compared to the value measured at T0 (n=35). The value is reported as mean ± Standard Error of the Mean (SEM). Statistical significance: (One-Way ANOVA followed by Bonferroni post-hoc test): * vs T0, # vs T2 DM, £ vs T3 DM-ND, $ vs T3 DM-HS, § vs T4 DM-ND. For all symbols reported p < 0.05 (*, #, £, $, §); p < 0.01 (**, ##, ££, $$, §§); p < 0.001 (***, ###, £££, $$$, §§§).*

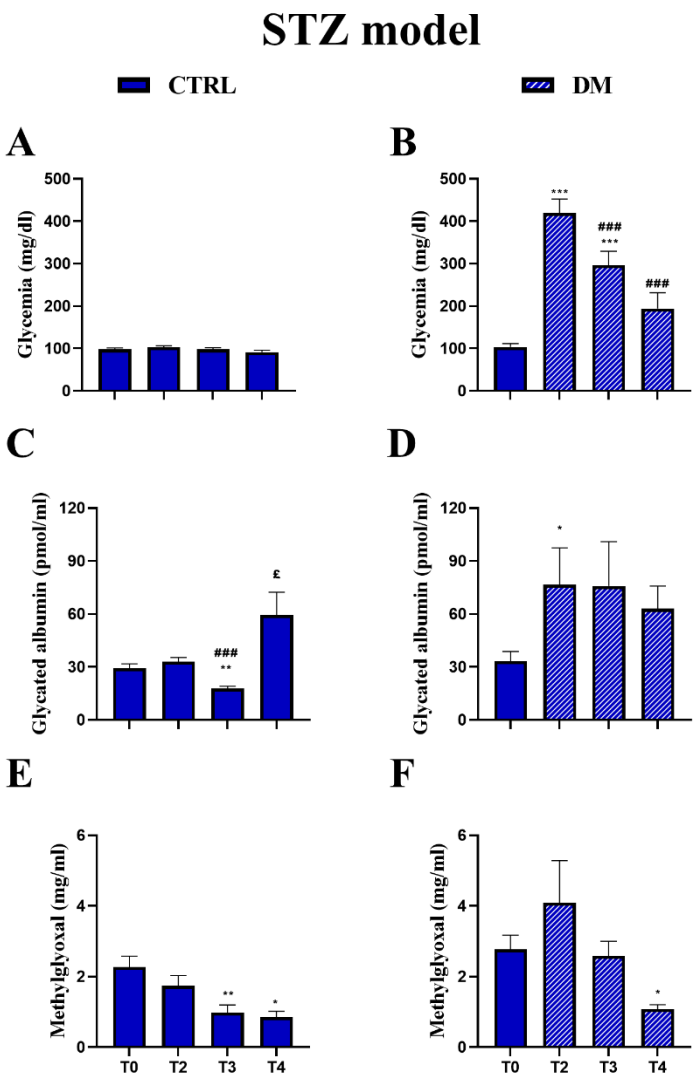


***Figure 21**. Comparison at all experimental times in control (CTRL) and diabetic (DM) mice. Fasting glycemia in CTRL (A) and DM (B), Glycated albumin in CTRL (C) and DM (D), and Methylglyoxal in CTRL (E) and DM (F) levels were assessed at T2, T3, and T4. The values are reported as mean ± Standard Error of the Mean (SEM). Statistical significance (Repeated Measures ANOVA followed by Bonferroni post-hoc test): * vs T0, # vs T2, £ vs T3. For all symbols reported $p < 0.05$ (*, #, £); $p < 0.01$ (**, ##, ££); $p < 0.001$ (***, ###, £££).*

### 6.2.2. Glycemic recovery in diabetic mice of STZ model: relationship with GA and MGO

Since some animals partially recovered from STZ-induced hyperglycemia, we stratified diabetic mice into persistent and recovered groups. This subdivision provided insight into the relationship between glycemic normalization and long-term behavior of GA and MGO.

To further explore and clarify the relationship between glycemia, glycated albumin (GA), and methylglyoxal (MGO), values obtained from diabetic mice (DM-ND and DM-HS combined) are presented in Figure 22. The analysis revealed a wide variability in both GA and MGO levels.

Based on individual glycemic values at T3 and using a threshold of 300 mg/dL, diabetic mice were stratified into two subgroups. The DM-REC group included animals that had recovered to normoglycemia (mean glycemia: 215.90 ± 15.82 mg/dL, n = 10), while the DM group comprised mice with persistent hyperglycemia above the threshold (mean glycemia: 489.50 ± 35.81 mg/dL, n = 8; T3 DM, Figure 22A). The difference in glycemia between these two groups at T3 was statistically significant ($p < 0.001$).

Interestingly, by T4, only two mice retained glycemia values above the 300 mg/dL threshold (481 ± 108 mg/dL, n = 2), whereas the remaining mice showed a significant reduction in glycemia (146.42 ± 16.16 mg/dL, n = 12; T4 DM-REC; $p < 0.001$, Figure 22A).

To assess whether glycemia at T3 correlated with GA or MGO levels, the two subgroups were further analyzed in Figures 22B and 22C. No statistically significant differences were observed for GA between the groups: T3 DM (161.79 ± 69.46 pmol/mL), T3 DM-REC (93.96 ± 40.47 pmol/mL), T4 DM (148.67 ± 88.54 pmol/mL), and T4 DM-REC (69.12 ± 14.01 pmol/mL; Figure 22B). While GA tended to decrease in DM-REC animals at both T3 and T4 compared to their hyperglycemic counterparts, the variability in data prevented statistical significance.

Conversely, MGO levels partially mirrored the glycemic profile. A significant reduction in MGO was observed in DM-REC animals at T4 (1.03 ± 0.14 µg/mL) compared to T3 DM mice (2.49 ± 0.34 µg/mL; $p = 0.046$) and T3 DM-REC mice (2.98 ± 0.54 µg/mL; $p = 0.002$; Figure 22C), suggesting a stronger correlation between MGO and glycemic improvement than with GA.

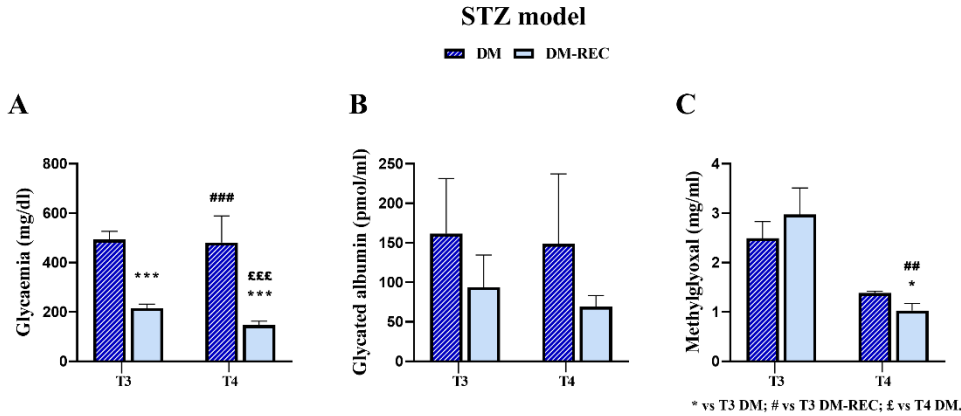


***Figure 22.*** *Comparison between diabetic mice (DM) and diabetic-recovery (DM-REC) animals at chosen experimental timepoints. Mice divided into two subgroups: DM, with fasting glycemia values higher than 300 mg/dl, and DM-REC, with fasting glycemia values lower than 300 mg/dl. (A) fasting glycemic values, (B) fasting GA values and (C) MGO values. Graphs showing the mean value line and the Standard Error of the Mean (SEM) error bars. Statistical significance (Unpaired T-test): * vs T3 DM, # vs T3 DM-REC, £ vs T4 DM. For all symbols reported p < 0.05 (*, #, £); p < 0.01 (**, ##, ££); p < 0.001 (***, ###, £££).*

### 6.2.3. Metabolic parameters of diabetic mice in HFD/STZ model

In this second model, diabetes was established at T3, corresponding to 14 months of age. After one month after STZ injection, the fasting blood glucose levels were significantly elevated (T4: 365.43 ± 14.36 mg/dl, n = 5) compared to HFD mice at the corresponding time points ($p = 1.5 \times 10^{-10}$, Figure 23A). Based on established diagnostic criteria for hyperglycemia in mice (≥250 mg/dl; Chen et al., 2024; Furman, 2021), all STZ-treated animals met the threshold for classification as diabetic.

Furthermore, at T5 (two months after STZ-injections), the fasting glycemia maintained the elevated value (T5: 356.86 ± 15.94 mg/dl, n = 5), and showed a statistically significant difference compared to HFD mice at the same time ($p = 5.4 \times 10^{-10}$).

Moreover, HFD/STZ mice at T5 exhibited a significantly elevated GA level (44.65 ± 8.35 pmol/mL, n = 5), comparable to the GA value in HFD mice at T2 but significantly higher than in HFD mice at T5 (p = 0.024, Figure 23B). Additionally, MGO levels in HFD/STZ mice at T5 (0.72 ± 0.20 µg/mL, n =

5) were significantly increased compared to both T2 and T5 values in HFD-only mice (p = 0.006, Figure 23C).

These findings indicate that STZ administration in HFD-fed mice not only exacerbates hyperglycemia but also counteracts the metabolic adaptations observed under HFD alone, as reflected by elevated GA and MGO levels.

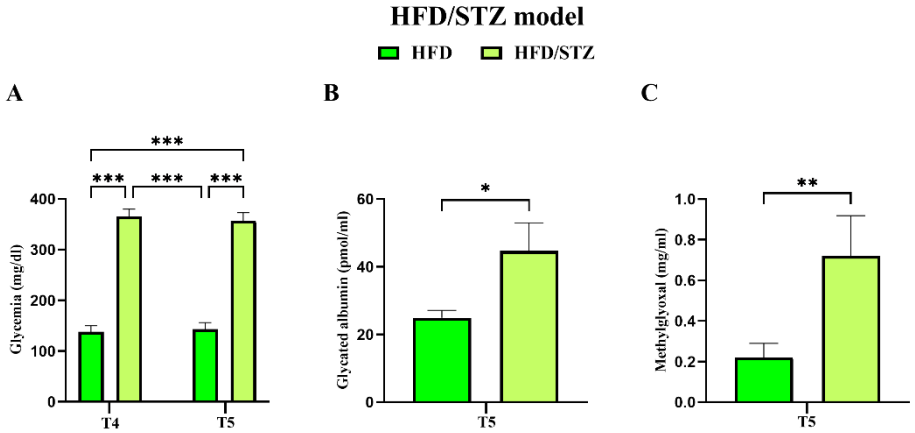


***Figure 23**. Fasting glycemia, GA and MGO in HFD (green) and HFD/STZ (light green) mice. (A) Fasting glycemia at T4 and T5; (B) Glycated albumin, and (C) Methylglyoxal levels at T5. Data are presented as mean ± SEM. Statistical significance (One-Way ANOVA followed by Bonferroni post-hoc test): p < 0.05 (*); p < 0.01 (**); p < 0.001 (***).*

To evaluate insulin resistance in HFD/STZ mice, the OGTT, plasma insulin, and HOMA-IR were performed at T5 and compared to HFD mice at the same time point.

The OGTT was conducted in HFD/STZ mice (n = 3), as described in section 5.4.3 of the Materials and Methods.
These mice exhibited a markedly elevated glucose peak (11.21 ± 0.69 mmol/L), which remained persistently high for over three hours post-glucose administration, indicative of profound glucose intolerance (Figure 24A). Consistently, the AUC in the HFD/STZ group was significantly increased (1702.60 ± 136.29 mmol/L × min) compared to both the CTRL group at T0 ($p = 1.9 \times 10^{-11}$) and the HFD group at T5 ($p = 8 \times 10^{-9}$; Figure 24B).

Furthermore, at T5, plasma insulin levels were measured in both HFD and HFD/STZ mice. Insulin concentrations were comparable between groups,

with no statistically significant difference observed (HFD: 12.10 ± 2.15 ng/mL, n = 7; HFD/STZ: 9.39 ± 1.10 ng/mL, n = 5; Figure 24C). However, the HOMA-IR index was significantly elevated in the HFD/STZ group (214.85 ± 26.49, n = 7) compared to the HFD group (106.34 ± 21.04, n = 7; p = 0.008; Figure 24D), indicating a marked increase in insulin resistance following STZ administration.

Collectively, these data demonstrate that the combination of HFD and STZ leads to pronounced glucose intolerance and insulin resistance, consistent with the development of a severe diabetic phenotype (Abdul-Ghani et al., 2006; Tomlinson et al., 2008).

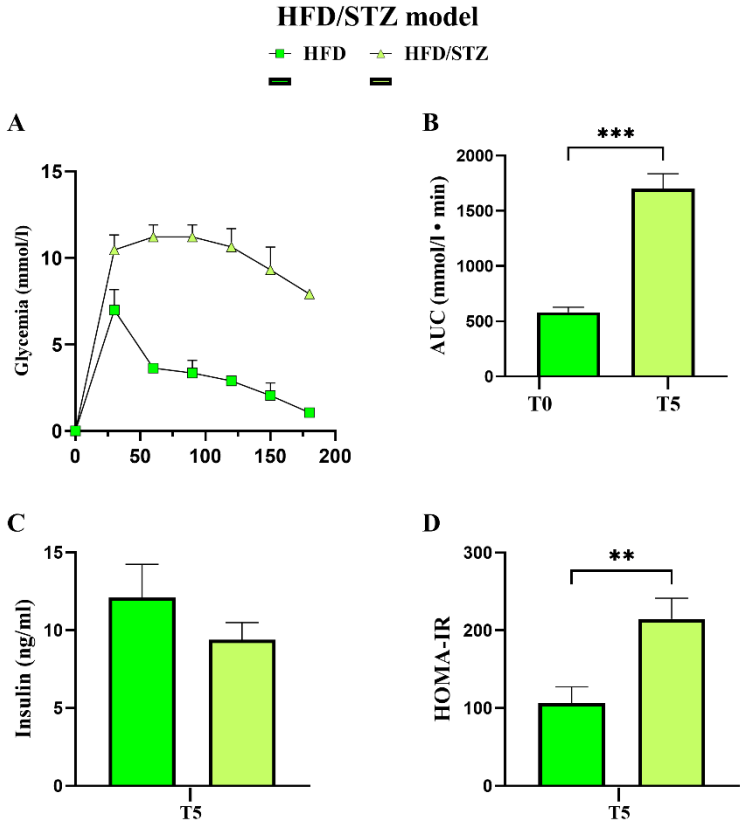


***Figure 24.*** *Insulin resistance induced by the HFD/STZ combination. (A) Mean of response glucose curves and (B) Mean of Area under the curve (AUC) of OGTT at T5 in both HFD (green) and HFD/STZ mice (light green). (C) Insulin concentrations at T5; (D) HOMA-IR index at T5. Data are presented as mean ± SEM. Statistical significance (One-Way ANOVA followed by Bonferroni post-hoc test): $p < 0.05$ (*); $p < 0.01$ (**); $p < 0.001$ (***).*

## 6.3. STZ induction effect on body weight, water intake, and survival probability in the two experimental models

In addition to glycemic and biochemical parameters, body weight, food, and water intake were longitudinally monitored in both experimental models to characterize further the metabolic profile associated with diabetes induction.

In the STZ model, control mice on a normal diet (CTRL-ND) showed a progressive age-related weight gain, from 30.9 ± 0.3 g at T0 to 36.1 ± 2.1 g at T4 (*p-value* < 0.001 vs. T0). By contrast, DM-ND exhibited significant weight loss, reaching 30.0 ± 1.1 g at T4 (*p-value* = 0.0086 vs. CTRL-ND). HS diet further promoted weight gain in controls (39.1 ± 1.5 g at T4), while DM-HS mice did not display marked weight loss (Figure 25). Water intake was approximately doubled in diabetic groups compared with controls (∼9 mL/day vs. 4 mL/day). Regarding food intake, any changes were observed (data not shown).

In the HFD/STZ model, HFD-only mice displayed progressive weight gain, whereas HFD/STZ mice showed a significant reduction, from 35.7 ± 0.9 g at T4 to 32.8 ± 0.5 g at T5 ($p < 0.001$; Figure 26). Food intake remained comparable between groups (~3 g/day). In contrast, water consumption was markedly elevated in diabetic mice, reaching 19.7 ± 0.8 mL/day at T5 versus HFD controls ($p < 0.001$), with an increase of ~27% between T4 and T5, indicating progressive polydipsia (data not shown).

Taken together, these findings show that diabetes induction was consistently associated with reduced body weight and increased water consumption in both models. In contrast, dietary sucrose attenuated weight loss in the STZ paradigm, and HFD/STZ mice displayed pronounced polydipsia despite unchanged food intake.

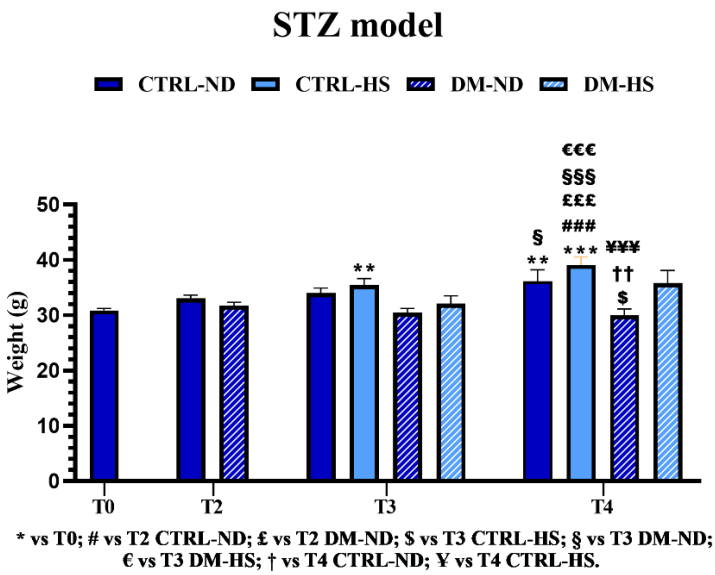


***Figure 25***. *Weight was measured at T0 in controls (CTRL), at T2 in CTRL and diabetic (DM) mice, and at T3 in CTRL and DM mice, both in normal (ND) and high sugar (HS) diet conditions. Values are presented as mean ± SEM. Statistical significance for data presented in (Two-Way ANOVA followed by Bonferroni post-hoc test): * vs T0, # vs T2 CTRL-ND, £ vs T2 DM-ND, $ vs T3 CTRL-HS, § vs T3 DM-ND, € vs T3 DM-HS, † vs T4 CTRL-ND, ¥ vs T4 CTRL-HS. For all symbols reported p < 0.05 (*, #, £, $, §, €, †, ¥); p < 0.01 (**, ##, ££, $$, §§, €€, ††, ¥ ¥); p < 0.001 (***, ###, £££, $$$, §§§, €€€, †††, ¥ ¥ ¥).*

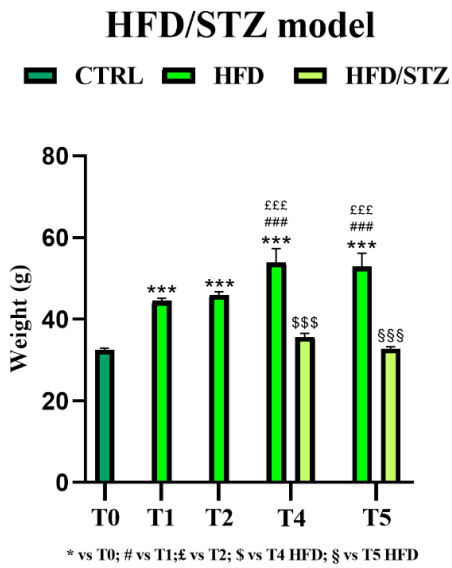


***Figure 26.*** *Weight was measured at T0 in CTRL (dark green), at T1, T2 in HFD (green), and at T4 and T5 in HFD and HFD/STZ (light green) mice. Values are presented as mean ± SEM. Statistical significance for data presented in (Two-Way ANOVA followed by Bonferroni post-hoc test): * vs T0, # vs T1, £ vs T2, $ vs T4 HFD, § vs T5 HFD. For all symbols reported p < 0.05 (*, #, £, $, §); p < 0.01 (**, ##, ££, $$, §§); p < 0.001 (***, ###, £££, $$$, §§§).*

Survival probability was monitored to evaluate the impact of diabetes induction and metabolic alterations on lifespan. Kaplan–Meier curves were generated for both models, allowing comparisons between diabetic and control groups as well as between single and combined metabolic insults.

In the STZ model, Kaplan-Meier survival analysis (Figure 27A) revealed a statistically significant difference among the survival curves of CTRL-ND, CTRL-HS, DM-ND, and DM-HS groups ($p = 0.0241$), indicating that both STZ-induced diabetes and HS water intake significantly influenced survival outcomes.

Notably, a direct comparison between CTRL-ND and DM-ND groups revealed no significant difference in survival probability, suggesting that diabetes alone did not compromise lifespan up to senescence (19 months of age). Similarly, HS consumption alone did not affect survival in CTRL mice (CTRL-ND vs. CTRL-HS). In contrast, a significant difference was found between DM-ND and DM-HS groups ($p = 0.0275$), indicating that HS intake

negatively affected survival in diabetic animals. A significant difference was also identified between CTRL-HS and DM-HS groups ($p = 0.0275$), demonstrating that diabetes reduced survival in the presence of HS consumption. Thus, the combination of diabetes and HS intake was detrimental, leading to reduced survival probability in DM-HS animals compared to all other groups. By 18 months of age, survival probability in DM-HS mice dropped to 55.55%.

To further investigate the link between survival and glycemic control, we analyzed the relationship between Kaplan-Meier survival probability and fasting glycemia at T3. A statistically significant difference in survival curves was observed between DM-ND and DM-HS mice ($p = 0.0295$, Figure 27B), indicating an influence of glycemic status on mortality in diabetic animals.

Specifically, only DM mice exhibited fasting glycemia levels between 500–600 mg/dL ($n = 5$). All DM-HS animals in this range ($n = 3$) died, while all DM-ND mice ($n = 2/2$) survived, highlighting a deleterious effect of HS intake under extreme hyperglycemic conditions. These findings suggest that although elevated glycemia contributes to mortality risk, it is not sufficient on its own to explain the outcome in diabetic mice fully.

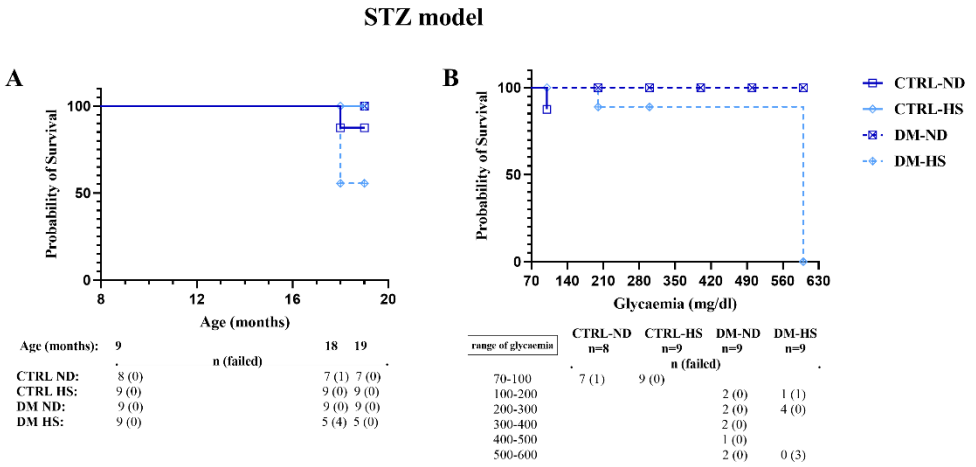


***Figure 27.*** *Kaplan-Meier survival analysis. Panel (A): Kaplan-Meier survival analysis showing survival curves of CTRL and DM mice, fed with either ND or HS diet. It should be noted that the DM-ND and CTRL-HS symbols are overlapped. In the lower part of panel B, the whole number of mice (n) and the number of dead mice (in brackets), at different ages, are reported. Panel (B): Kaplan-Meier analysis presenting survival curves of DM mice, fed with either ND or HS diet, relative to the glycemia value assessed at 18 months of age (T3). In the lower part of panel C, the number of alive mice (n) and the number of dead mice (in brackets) are listed. Statistics for Kaplan-Meier analysis was obtained with a Log (Mantel-Cox) rank test.*

In the HFD/STZ model, Kaplan–Meier survival analysis (Figure 28) revealed no significant differences between the HFD and HFD/STZ groups, indicating that STZ treatment did not affect overall survival probability, despite the death of two out of seven mice at T4.

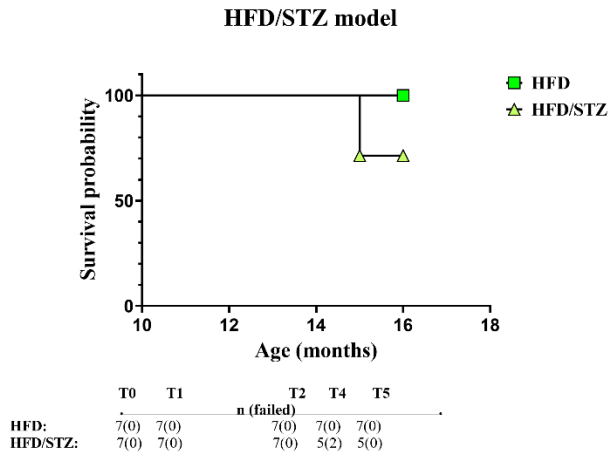


***Figure 28.*** *survival probability. (A): Kaplan-Meier survival curves. Statistical significance for Kaplan-Meier analysis was obtained with a Log (Mantel-Cox) rank test.*

## 6.4. Histopathological analysis of the pancreas islets: insulitis score in the two models

For both experimental models, histopathological analysis of pancreatic islets was performed to assess diabetes-induced alterations. Coronal pancreatic sections were collected from CTRL, DM, and DM-REC mice of the first model at 19 months of age (T4), and from HFD and HFD/STZ mice of the second model at 16 months of age (T5). The tissues were then processed for histological evaluation using hematoxylin and eosin (H&E) staining to assess diabetes-induced alterations in pancreatic morphology (for details, see 5.7.1 section of material and methods). A semiquantitative scoring system, as described by Pavlovic et al. (2018), was applied under conventional brightfield microscopy to estimate the extent of tissue damage, using a scale ranging from 0 (undetectable) to 4 (severe). Specifically, the lesion scores were defined as follows: score 0, normal islets; score 1, perivascular/periductal infiltration; score 2, peri-insulitis; score 3, mild insulitis (< 25% of the islet infiltrated); score 4, severe insulitis (more than 25% of the islet infiltrated).

In the first model, the histological evaluation of CTRL mice revealed a well-preserved pancreatic cytoarchitecture, with the majority of islets (82.82%) categorized as normal (score 0). In contrast, DM mice exhibited a marked reduction in normal islets, with only 6.94% scoring 0. Interestingly, DM-REC

animals showed a partial recovery of islet morphology, with 58.53% of islets appearing normal (Figure 29A-B).
DM mice displayed substantial levels of islet inflammation, with mild insulitis (score 3) observed in 22.22% and severe insulitis (score 4) in 30.56% of islets. In DM-REC mice, these values dropped considerably, with mild and severe insulitis recorded at 2.68% and 4.52%, respectively, indicating reduced immune infiltration.
Perivascular and periductal infiltration (score 1) was present in 13.37% of islets in CTRL mice but increased to 26.96% in DM mice, before decreasing to 20.41% in the DM-REC group. Meanwhile, peri-insulitis (score 2) occurred at similar frequencies in both DM and DM-REC animals (13.89% and 13.87%, respectively), but remained lower in CTRL mice (2.51%).

These results demonstrate that STZ treatment induced a persistent inflammatory response in the pancreatic islets of DM mice, characterized by high-grade insulitis. However, a partial restoration of normal islet structure was evident in DM-REC animals, indicating some recovery of pancreatic integrity over time (Figure 29A-B).

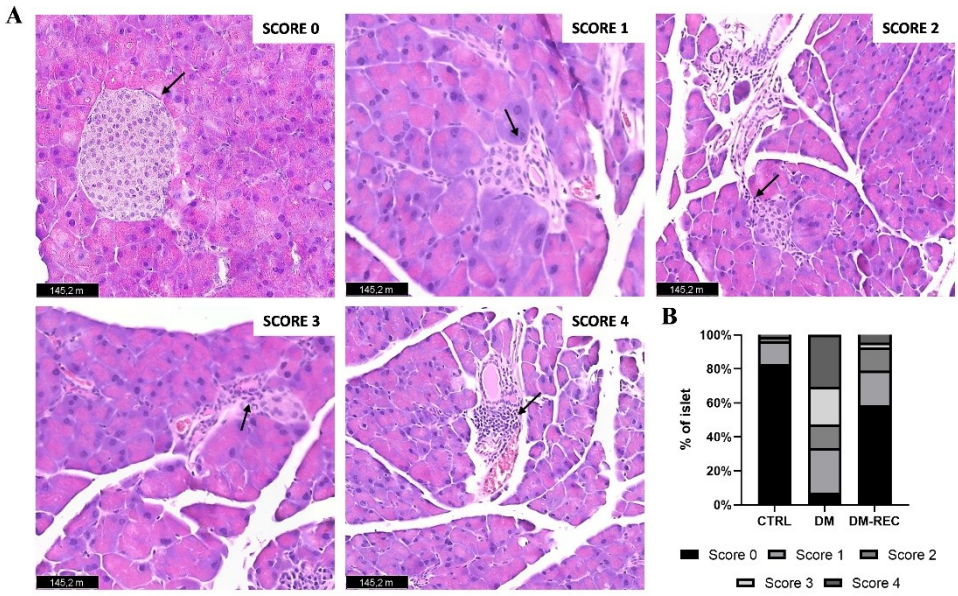


***Figure 29.*** *Pancreas islet insulitis in CTRL, DM, and DM-REC at T4. Histological characterization by H&E staining. (A) Representative micrographs showing the pancreas from different groups. Black arrows for each micrograph indicated the alteration observed for each score. Light microscopy magnification: 40x. Scale bars 145.2 m. (B) Insulitis was reduced in DM-REC mice compared to DM animals. Semiquantitative scale ranging from undetectable (0) to severe (4) tissue damage. In particular, degree of lesions was recorded and graded as follows: 0, normal islet; 1, perivascular/periductal infiltration; 2, peri-insulitis; 3, mild insulitis (< 25% of the islet infiltrated); 4, severe insulitis (more than 25% of the islet infiltrated).*

In the second model, the islet morphology was largely preserved in HFD mice, with 56.98% of the islets scored as 0, indicating normal architecture. In contrast, the HFD/STZ group exhibited a marked decrease in intact islets, with only 1.78% classified as score 0, pointing to significant structural disruption (Figure 30A-B).

Perivascular/periductal infiltration (score 1) was more commonly observed in the HFD group (24.42%) than in the HFD/STZ group (17.86%). Conversely, the prevalence of peri-insulitis (score 2) was higher in HFD/STZ mice (23.21%) compared to HFD mice (6.98%). Similarly, mild insulitis (score 3) was more frequently detected in HFD/STZ mice (39.28%) than in HFD mice (8.14%). The occurrence of severe insulitis (score 4) was also elevated in the

HFD/STZ group (17.86%) relative to the HFD group (3.49%) (Figure 30A-B).

These findings clearly demonstrate that the combination of a high-fat diet and STZ treatment induces substantially greater pancreatic islet damage compared to HFD alone, as reflected by the increased frequency of higher insulitis scores in the HFD/STZ group.

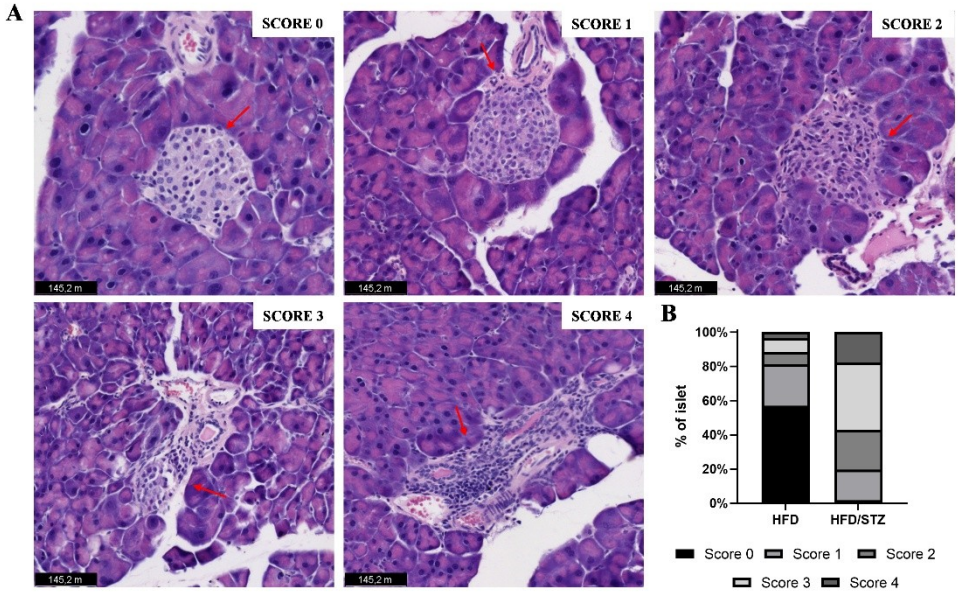


***Figure 30**. Pancreatic islet insulitis in HFD and HFD/STZ mice at T5. Histological characterization by H&E staining. (A) Representative micrographs showing pancreas architecture from different groups. Red arrows highlight characteristic features associated with each score. Light microscopy magnification: 40x. Scale bars 145.2 µm. (B) Semi-quantitative scale ranging from undetectable (0) to severe (4) tissue damage. In particular, the degree of lesions was recorded and graded as follows: 0, normal islet; 1, perivascular/periductal infiltration; 2, peri-insulitis; 3, mild insulitis (< 25% of the islet infiltrated); 4, severe insulitis (more than 25% of the islet infiltrated).*

## 6.5. Cognitive decline and frailty

The link between metabolic dysfunction and cognitive aging was explored by evaluating recognition memory and frailty in both models.

Cognitive performance was initially evaluated in the STZ model using the Novel Object Recognition (NOR) test, with a specific focus on the "knowledge" component of recognition memory. In the subsequent HFD/STZ model, the assessment was extended to also explore the "remember" component through the Object Location (OL) and Y-maze tasks. Furthermore, the Discrimination Index (DI) was calculated based on both the time and the number of approaches for the NOR and OL tasks. In the Y-maze, the percentage of spontaneous alternations in triplets was assessed. In both models, a frailty index (FI) was calculated to provide an integrated measure of systemic and behavioral vulnerability (for details, see sections 5.5 and 5.6 of the Materials and Methods).

### 6.5.1. STZ model: knowledge component of recognition memory and frailty index

In the STZ model, the NOR test was performed at T0, T3, and T4, following the same longitudinal experimental design and time points used for metabolic markers, to enable an association between cognitive and systemic parameters.

As previously observed in metabolic parameters, the analysis of behavioral outcomes revealed no significant differences between mice maintained on ND or HS diets in either the CTRL or DM groups (data not shown). Consequently, dietary conditions were excluded as variables, and subsequent analyses focused solely on comparisons between CTRL and DM mice. Furthermore, based on the variation in fasting glycemia observed at T3, DM mice were stratified into two subgroups: DM, with fasting glycemia > 300 mg/dl, and DM-REC, with fasting glycemia < 300 mg/dl (Figure 22A).

In CTRL mice, a physiological age-related decline in recognition memory was detected, consistent with prior findings (Ratto et al., 2019). Specifically, the global FI in CTRL mice increased progressively from 0.00 ± 0.04 at T0 (n=35) to 0.21 ± 0.11 at T3 (n=12) and further to 0.64 ± 0.13 at T4 (n=12) (Figure 31B).

Three months after STZ treatment (T3), DM mice exhibited a significant reduction in recognition memory, as reflected by both a decline in the DI and an increase in the frailty index (Figure 31A-B). The global FI of DM mice at T3, was 0.54 ± 0.09 (n = 8), significantly higher than that of CTRL mice at the same time point ($p$ = 0.04) (Figure 31B). By contrast, DM-REC mice at

T3 exhibited a restored global FI (0.21 ± 0.15, n = 10), comparable to that of CTRL mice, suggesting a recovery of cognitive function in correlation with normalized glycemia.

At T4, most STZ-induced mice showed glycemic recovery, qualifying them as DM-REC, and their recognition memory performance aligned with that of age-matched CTRL animals (Figure 31B). This recovery was also evidenced by improvements in both the DI and the global FI derived from the NOR test (0.53 ± 0.09, n = 12) (Figure 31A-B), indicating a partial reversal of the cognitive impairments caused by STZ.

However, a subset of DM mice (n = 3) continued to show severely impaired locomotor activity. These animals interacted with the novel and familiar objects only 1-2 times over 5 minutes, with each interaction lasting under 3 seconds. As a result, their low activity levels at T4 precluded the calculation of a valid frailty index.

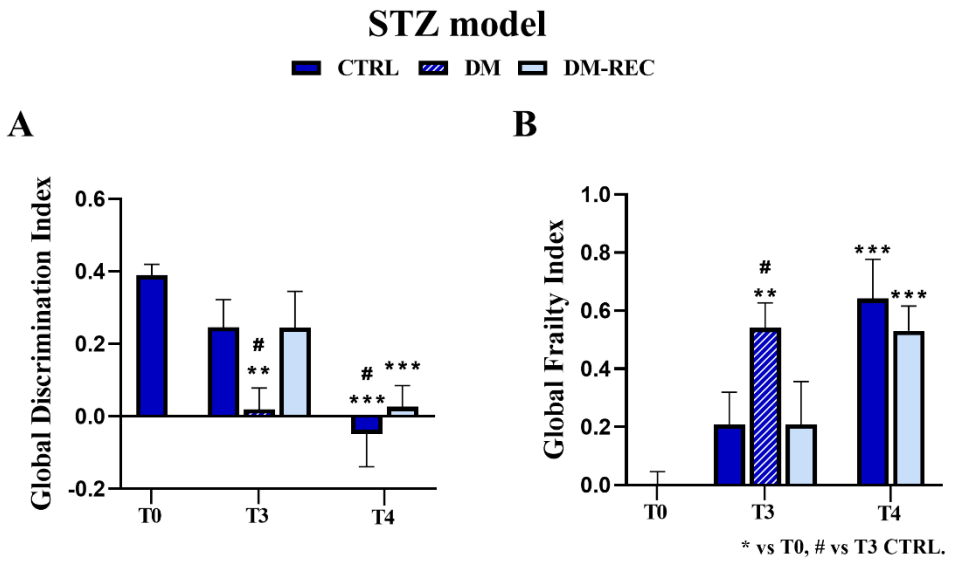


***Figure 31.*** *Novel Object Recognition test (NOR) data. Panels (A) and (B): Global Discrimination Index (DI) and Global Frailty Index (FI), respectively. Values are presented as mean ± Standard Error of the Mean (SEM). Statistical significance (One-Way ANOVA followed by Bonferroni post-hoc test): * vs T0, # vs T3 CTRL, £ vs T3 DM, $ vs T3 DM-REC, § vs T4 CTRL. For all symbols reported p < 0.05 (*, #, £, $, §); p < 0.01 (**, ##, ££, $$, §§); p < 0.001 (***, ###, £££, $$$, §§§).*

### 6.5.2. HFD/STZ model: knowledge and remember component of recognition memory and frailty index

In the HFD/STZ model, the NOR, OL, and Y-maze tasks were performed at T1, T2, and T5 to align recognition performance with metabolic parameter changes.

In HFD mice, the discrimination index (DI) for both the number of approaches (Figure 32A) and the time spent exploring objects (Figure 32B) in the novel object recognition (NOR) test remained unchanged at T2 (0.22 ± 0.07 and 0.45 ± 0.09, n = 14, respectively) compared to T1 (0.25 ± 0.03 and 0.45 ± 0.04, n = 14). However, after six months of HFD (T5), a significant reduction in the DI for the number of approaches was observed (0.12 ± 0.04, n = 7) compared to T1 ($p = 0.037$), indicating emerging cognitive impairment. No significant change in the DI for exploration time was detected at T5 (0.28 ± 0.08, n = 7). The global DI of the NOR test (Figure 32C), combining both metrics, revealed a significant cognitive decline at T5 (0.17 ± 0.06, n = 7) compared to T1 (0.34 ± 0.03, n = 14; $p = 0.016$). This decline was evident only after prolonged HFD exposure, as no significant differences were detected between T1 and T2 (0.33 ± 0.08, n = 14).
In the HFD/STZ group, recognition memory deficits were more pronounced. At T5, both the DI for number of approaches (−0.09 ± 0.08, n = 5) and exploration time (0.00 ± 0.09, n = 5) significantly declined compared to T1 ($p = 0.0017$ and $p = 0.0027$, respectively), T2 ($p = 0.013$ and $p = 0.0068$), and also compared to HFD mice at T5 ($p = 0.038$ and $p = 0.032$). The global DI in HFD/STZ mice at T5 (−0.04 ± 0.07, n = 5) was significantly reduced relative to T1 ($p = 0.001$), T2 ($p = 0.004$), and HFD mice at the same time point ($p = 0.038$).

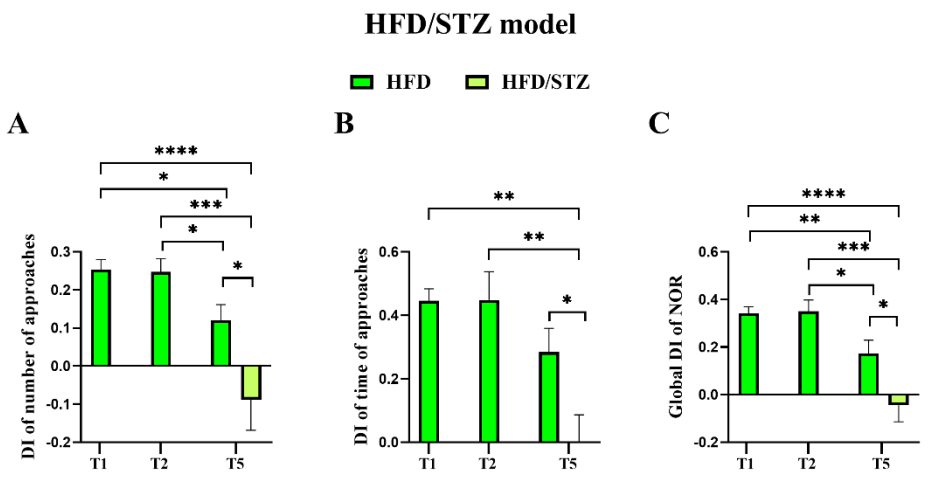


***Figure 32***. *Novel Object Recognition test (NOR) data. Discrimination Index (DI) of the number of approaches (A) and time of approaches (B); Global DI of NOR test (C) in HFD (blue) and HFD/STZ (light blue) mice. Data are presented as mean ± SEM. Statistical significance (One-Way ANOVA followed by Bonferroni post-hoc test): $p < 0.05$ (*); $p < 0.01$ (**); $p < 0.001$ (***).*

In HFD mice, the discrimination index (DI) for both the number of approaches (Figure 33A) and the time spent exploring objects (Figure 33B) in the object location (OL) test did not significantly change at T2 (0.17 ± 0.05 and 0.09 ± 0.06, n = 14, respectively) or T5 (0.16 ± 0.04 and 0.10 ± 0.04, n = 7) compared to T1 (0.16 ± 0.02 and 0.20 ± 0.03, n = 14). Similarly, the global DI of the OL test (Figure 33C) showed no significant effect of HFD after one (T1, 0.17 ± 0.02, n = 14), four (T2, 0.13 ± 0.05, n = 14), and six months (T5, 0.13 ± 0.04, n = 7) of diet.

Figure 33D shows the percentage of alternation triplets obtained from the Y-maze test. In HFD mice, the percentage of alternation remained stable at T2 (58.50 ± 1.13%, n = 14) and T5 (62.18 ± 3.68%, n = 7) compared to T1 (59.30 ± 1.26%, n = 14).

In contrast, HFD/STZ mice displayed a significant decrease in the DI for both the number (Figure 33A) and time of approaches (Figure 33B) in the OL test at T5 (−0.07 ± 0.05 and −0.14 ± 0.06, n = 5, respectively) compared to T1 ($p = 0.022$ and $p = 0.00043$) and T2 ($p = 0.0021$ and $p = 0.048$). These values were also significantly lower than those of HFD mice at T5 ($p = 0.014$ and $p = 0.016$).

Accordingly, the global DI of the OL test (Figure 33C) revealed a significant cognitive decline in HFD/STZ mice at T5 (−0.10 ± 0.06, n = 5) compared to T1 (p = 0.0065), T2 (p = 0.0065), and HFD mice at T5 (p = 0.023).
Similarly, in the Y-maze test, HFD/STZ mice showed a significant reduction in the percentage of alternation at T5 (50.53 ± 2.96%, n = 5) compared to T1 (p = 0.017), T2 (p = 0.0061), and HFD mice at the same time point (p = 0.045, Figure 33D).

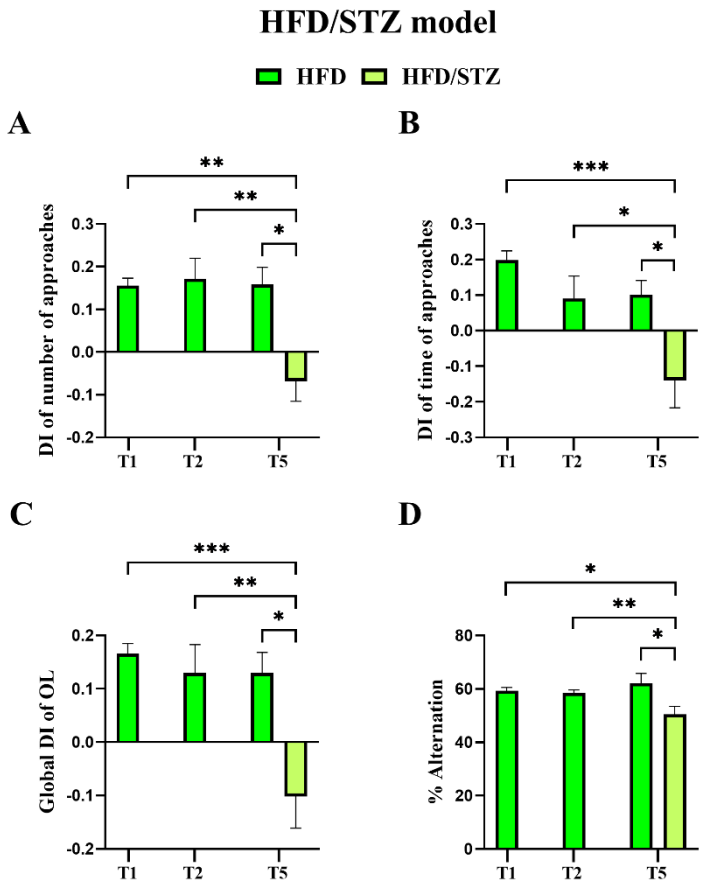


***Figure 33.*** *Object Location (OL) and Y-maze tests data. Discrimination Index (DI) of number of approaches (A) and time of approaches (B); Global DI of OL test (C); % of alternation triplet in Y-maze test (D) in HFD (blue) and HFD/STZ (light blue) mice. Data are presented as mean ± SEM. Statistical significance (One-Way ANOVA followed by Bonferroni post-hoc test): p < 0.05 (*); p < 0.01 (**); p < 0.001 (***).*

For all selected parameters and behavioral tests, we calculated the FI (see Materials and Methods). Specifically, a global FI for the "knowledge" component was derived from the NOR test (Figure 34A), while a global FI for the "remember" component was obtained by combining the results from the OL and Y-maze tests (Figure 34B). These two global FI values were then combined to generate the overall global FI of Recognition Memory (Figure 34C).

In HFD mice, the global FI of knowledge was not affected after four months of treatment (T2, 0.01 ± 0.12, n = 14) compared to baseline (T1, 0.00 ± 0.04, n = 14). However, after six months (T5, 0.22 ± 0.10, n = 7), a significant increase was observed compared to T1 ($p = 0.037$, Figure 34A). Regarding the "remember" component, no significant changes were detected at one (T1, 0.00 ± 0.03), four (T2, 0.06 ± 0.06), or six months (T5, 0.06 ± 0.07) following the start of HFD (Figure 34B).

Consequently, the global FI of recognition memory was stable after four months of HFD (T2, 0.04 ± 0.06, n = 14 vs. T1, 0.00 ± 0.02, n = 14), but showed a significant increase at six months (T5, 0.14 ± 0.05, n = 7) compared to T1 ($p = 0.02$, Figure 34C).

In contrast, HFD/STZ mice exhibited a marked and statistically significant increase in the global FI of knowledge at T5 (0.58 ± 0.10, n = 5) compared to both T1 ($p = 0.0012$) and T2 ($p = 0.0049$), as well as to HFD mice at T5 ($p = 0.038$, Figure 34A). Similarly, for the "remember" component, HFD/STZ mice showed a significant increase at T5 (0.50 ± 0.07, n = 5) relative to T1 ($p = 4.4 \times 10^{-6}$), T2 ($p = 0.00019$), and HFD mice at the same timepoint ($p = 0.0011$, Figure 34B). Finally, the global FI of recognition memory in HFD/STZ mice was significantly elevated at T5 (0.54 ± 0.05, n = 5) compared to T1 ($p = 2.42 \times 10^{-8}$), T2 ($p = 1.29 \times 10^{-6}$), and T5 in HFD mice ($p = 0.0024$, Figure 34C).

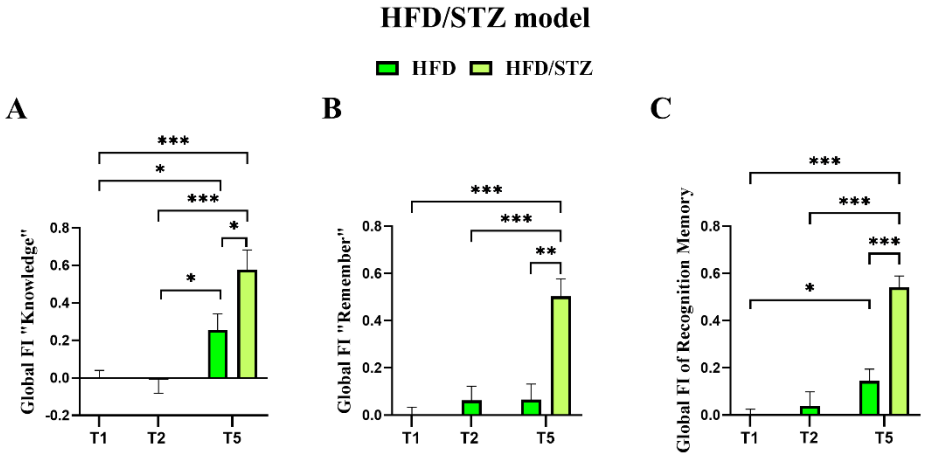


***Figure 34.*** *The HFD/STZ combination induced a decline in recognition memory. Global Frailty Index (FI) of «Knowledge» (A), and «Remember» components (B); Global FI of Recognition memory (C) in HFD (blue) and HFD/STZ (light blue) mice. Data are presented as mean ± SEM Statistical significance (One-Way ANOVA followed by Bonferroni post-hoc test): $p < 0.05$ (*); $p < 0.01$ (**); $p < 0.001$ (***).*

## 6.6. Neurodegenerative signatures in the Hippocampus

To investigate if diabetes and metabolic alterations were associated with central nervous system alterations, hippocampal structure and pathology were analyzed in both models. Morphological assessments were performed to detect age- and diabetes-related changes in hippocampal subregions. At the same time, immunohistochemistry for phosphorylated Tau (p-Tau) and β-amyloid (Aβ) was carried out to evaluate molecular markers of Alzheimer-like neurodegeneration.

### 6.6.1. Morphological changes in the hippocampal architecture

Hippocampal cytoarchitecture was analyzed in both models to determine whether diabetes induction affected structural integrity. Specific subregions were examined for age- and diabetes-related changes in neuronal organization and tissue morphology. Coronal brain sections were collected from CTRL, DM, and DM-REC mice of the first model at 19 months of age (T4), and from HFD and HFD/STZ mice of the second model at 16 months of age (T5). The tissues were then processed for histological evaluation using H&E staining. The analysis focused on the dentate gyrus (DG) and the Ammon's horn,

including the CA1-CA2-CA3 subdivisions (for details, see 5.7.1 section of material and methods).

#### 6.6.1.1. STZ model

Hippocampal morphology was examined in CTRL, DM, and DM-REC mice at T4, and the representative H&E-stained micrographs are shown in Figure 35A.

The overall gross morphology of the hippocampus appeared preserved across all experimental groups. The Ammon's horn maintained its typical organization into four areas, CA1, CA2, CA3, and CA4, the latter embedded within the V-shaped DG region. High-magnification images of the DG in CTRL, DM, and DM-REC mice revealed the presence of the three well-defined layers: the molecular layer (ML), granule cell layer (GL), and pleomorphic layer (PL). In the CA regions, the characteristic trilaminar structure was observed, consisting of the outer polymorphic layer (Stratum oriens, SO), the middle pyramidal cell layer (Stratum pyramidale, SP), and the inner molecular layer (Stratum radiatum, SR).

Quantitative analysis revealed region-specific alterations, assessed in terms of both layer thickness and cell density, with significant changes confined to the CA1 and CA3 subregions (Figure 35), while the DG and CA2 areas remained unaffected (data not shown).

Specifically, a significant reduction in the thickness of both CA1 ($p < 0.001$) and CA3 ($p = 0.0113$) was detected in DM mice compared to CTRL animals. In contrast, DM-REC mice displayed a significant increase in thickness in both CA1 ($p < 0.001$) and CA3 ($p = 0.0053$) compared to DM mice (Figure 35B-C).

Furthermore, quantification of neuronal cell density in the CA1 and CA3 areas showed a marked decrease in DM mice relative to CTRL animals ($p < 0.001$ and $p = 0.0011$, respectively). Conversely, DM-REC mice exhibited a significant increase in cell density compared to DM mice in both CA1 ($p = 0.0003$) and CA3 ($p = 0.007$) regions (Figure 35D).

These findings collectively suggest that STZ-induced diabetes induces structural hippocampal impairments, particularly within the CA1 and CA3 subregions, which can be partially reversed upon glycemic recovery.

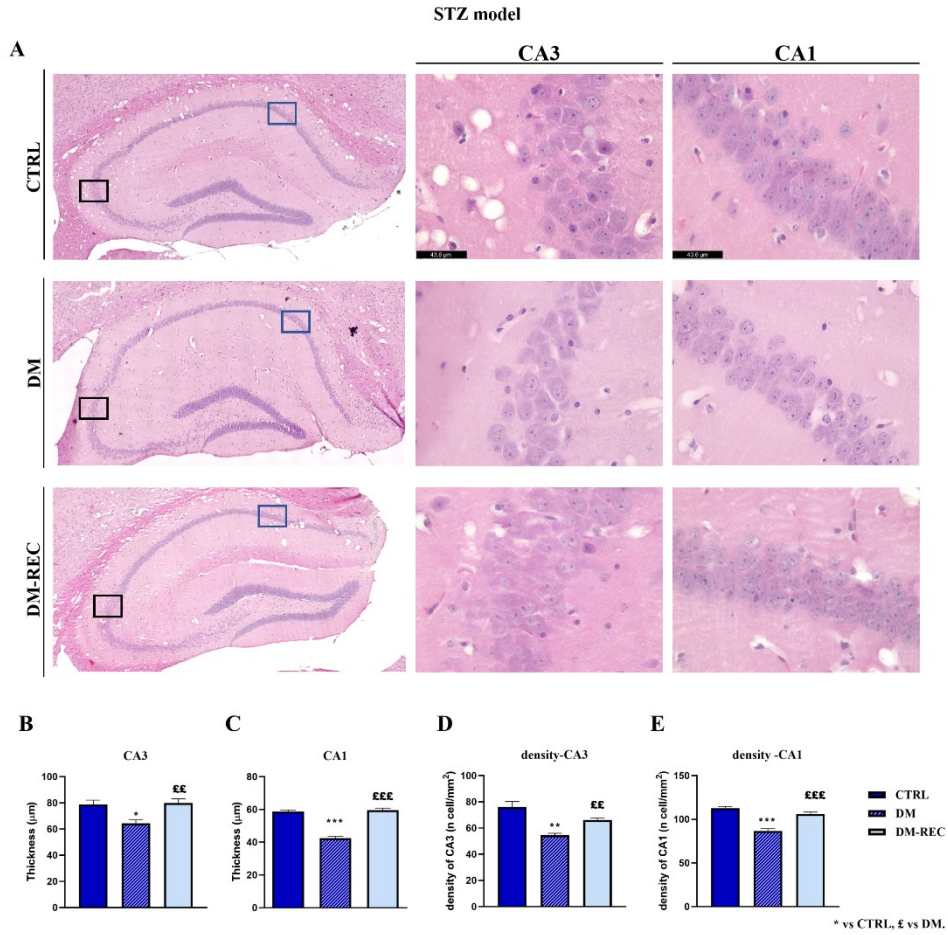


***Figure 35.*** *Histological characterization of hippocampus by H&E staining. Panel (A): Representative brain sections showing the hippocampal cytoarchitecture. Left column: the whole hippocampus images were obtained with LASX Navigator. Black and blue squares indicate the ROI region for CA3 and CA1, respectively. Center and right column: high-magnification micrographs of CA3 and CA1, respectively, from CTRL, DM and DM-REC mice. Light microscopy magnification: 40x. Scale bars 43.6 µm. Panel (B-E): Histograms showing the thickness of CA3 (B) and CA1 (C) and the cell density measured in CA3 (D) and CA1 (E) in CTRL, DM and DM-REC mice. Values are presented as mean ± Standard Error of the Mean (SEM). Statistical significance (One-Way ANOVA followed by Bonferroni post-hoc test): * vs CTRL, £ vs DM. For all symbols reported $p < 0.05$ (*, £); $p < 0.01$ (**, ££); $p < 0.001$ (***, £££).*

#### 6.6.1.2. HFD/STZ model

Hippocampal morphology was examined in HFD and HFD/STZ mice at T5, and the representative micrographs are shown in Figure 36A. Although the overall hippocampal architecture appeared preserved in both groups, specific alterations were evident in the CA1, CA2, and CA3 regions, while the DG areas remained unaffected (data not shown).

High-magnification images revealed the characteristic three-layer organization of the hippocampus (SO, SP, and SR). Quantitative analysis showed significant thinning of these layers in the CA1, CA2, and CA3 subregions of HFD/STZ mice compared to HFD controls ($p = 1 \times 10^{-14}$ for all, Figures 36B-D). Moreover, cell density was markedly reduced in the CA1 ($p = 4 \times 10^{-4}$), CA2 ($p = 9.1 \times 10^{-3}$), and CA3 ($p = 3.7 \times 10^{-2}$) areas of HFD/STZ mice relative to HFD mice (Figures 36E-G).

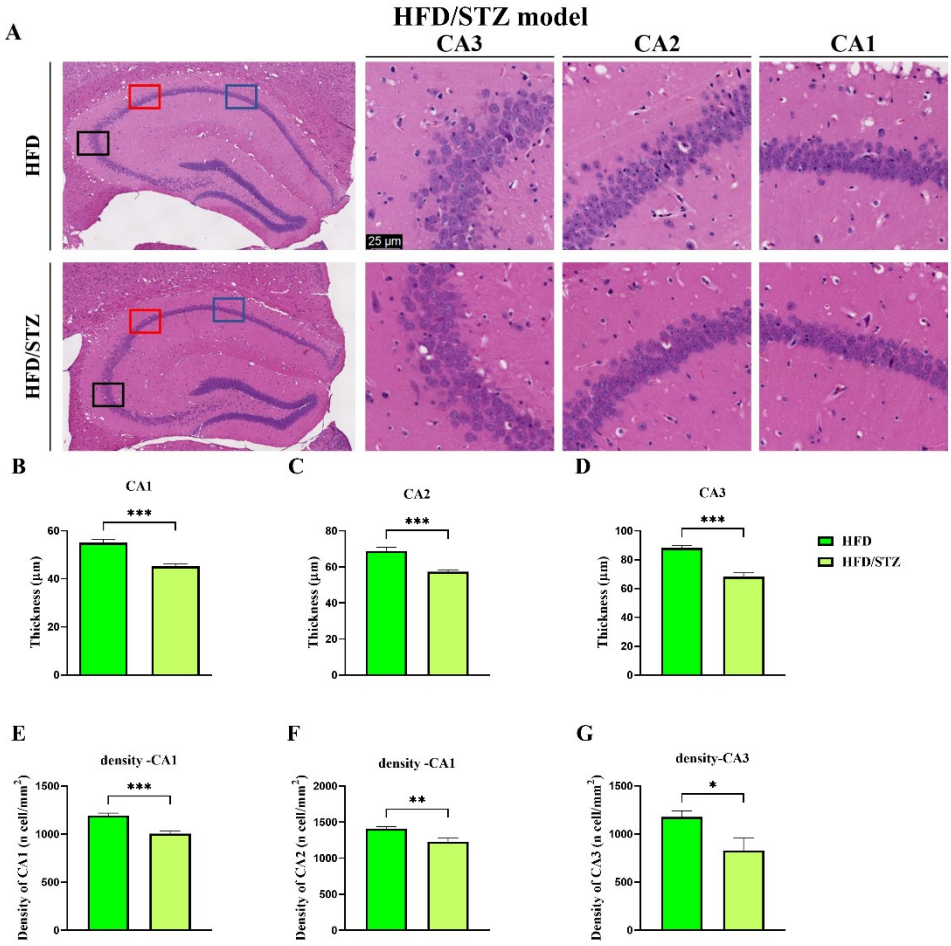


***Figure 36.*** *Histological characterization of the hippocampus by H&E staining. Representative brain sections showing the hippocampal cytoarchitecture (A): Left column: the whole hippocampus images were obtained with LASX Navigator. Black, red, and blue squares indicate the ROI region for CA3, CA2, and CA1, respectively. Center and right column: high-magnification micrographs of CA3, CA2, and CA1, respectively, from HFD and HFD/STZ mice. Light microscopy magnification: 40x. Scale bars 25 µm. Histograms showing the thickness of CA3 (B), CA2 (C), and CA1 (D) and the cell density measured in CA3 (E), CA2 (F), and CA1 (G) in HFD (blue) and HFD/STZ (light blue) mice. Values are presented as mean ± Standard Error of the Mean (SEM). Statistical significance (One-Way ANOVA followed by Bonferroni post-hoc test): $p < 0.05$ (*); $p < 0.01$ (**); $p < 0.001$ (***).*

### 6.6.2. Molecular pathology: p-Tau and β-Amyloid immunohistochemistry

Immunohistochemical analyses were performed to evaluate whether diabetes and metabolic alterations were associated with Alzheimer-like molecular hallmarks in the hippocampus. Coronal brain sections were collected from CTRL, DM, and DM-REC mice of the first model at 19 months of age (T4), and from HFD and HFD/STZ mice of the second model at 16 months of age (T5). The tissues were then processed for p-Tau and Aβ antibodies. These markers were selected as indicators of tauopathy and amyloid deposition, providing complementary insights into the neurodegenerative burden across experimental groups. In particular, in the two experimental models, immunopositivity for both markers was analyzed in four hippocampal subregions: the molecular layer of CA1 (ML-CA1), the pyramidal layer of CA1 (P-CA1), the pyramidal layer of CA3 (P-CA3), and the molecular layer of the dentate gyrus (ML-DG). Specifically, p-Tau immunoreactivity was quantified as optical density (OD) within the immunopositivity regions. In contrast, APP plaque density (number of APP spots/area plaque) was evaluated for β-amyloid (see sections 5.7.2 and 5.7.3 of Materials and Methods for details).

#### 6.6.2.1. STZ model

In STZ model, the analysis focused on comparing CTRL, DM, and DM-REC groups to determine whether diabetes induction or subsequent glycemic recovery influenced hippocampal p-Tau accumulation and Aβ deposition. Representative images for p-tau and Aβ markers are shown in Figure 37A and Figure 38A.

Specifically, in the ML-CA1 region (Figure 37B), DM mice exhibited a significant increase in p-Tau OD (44.30 ± 5.33), compared to CTRL mice (17.65 ± 1.37; $p = 0.006$), and also compared to DM-REC mice (15.25 ± 0.07; $p = 0.006$). Similar patterns were observed in P-CA1 and P-CA3 (Figure 37C-D), where p-Tau levels were significantly elevated in DM (P-CA1: 25.65 ± 3.73, P-CA3: 39.86 ± 8.01) compared to CTRL (P-CA1: 11.54 ± 1.69, $p = 0.04$; P-CA3: 14.27 ± 5.76, $p = 0.04$) and DM-REC (P-CA1: 9.01 ± 1.84, $p = 0.03$; P-CA3: 21.51 ± 2.87, $p = 0.03$). In the ML-DG region (Figure 37E), a significant increase in p-Tau was also detected in DM mice (19.34 ± 0.50)

compared to CTRL (6.96 ± 1.90, p = 0.03) and also to DM-REC mice (6.61 ± 3.00, p = 0.03). Notably, no significant differences were observed between DM-REC and CTRL mice in the mean p-tau OD of DM-REC compared to CTRL mice.

Regarding β-amyloid, no APP plaques were observed in CTRL mice in any hippocampal subregion. In contrast, APP plaques were detected in DM and DM-REC mice. Analysis of plaque density revealed statistically significant differences between DM and DM-REC mice in ML-CA1 (5.76 ± 1.85 vs 2.09 ± 0.26, respectively; p = 0.03; Figure 38B), P-CA1 (6.06 ± 1.79 vs 2.91 ± 0.28; p-value = 0.04; Figure 38C), and ML-DG (3.25 ± 1.49 vs 0.73 ± 0.73; p = 0.04; Figure 38D) regions, with DM mice showing higher densities. Notably, no APP plaques were observed in the P-CA3 region in any of the groups.

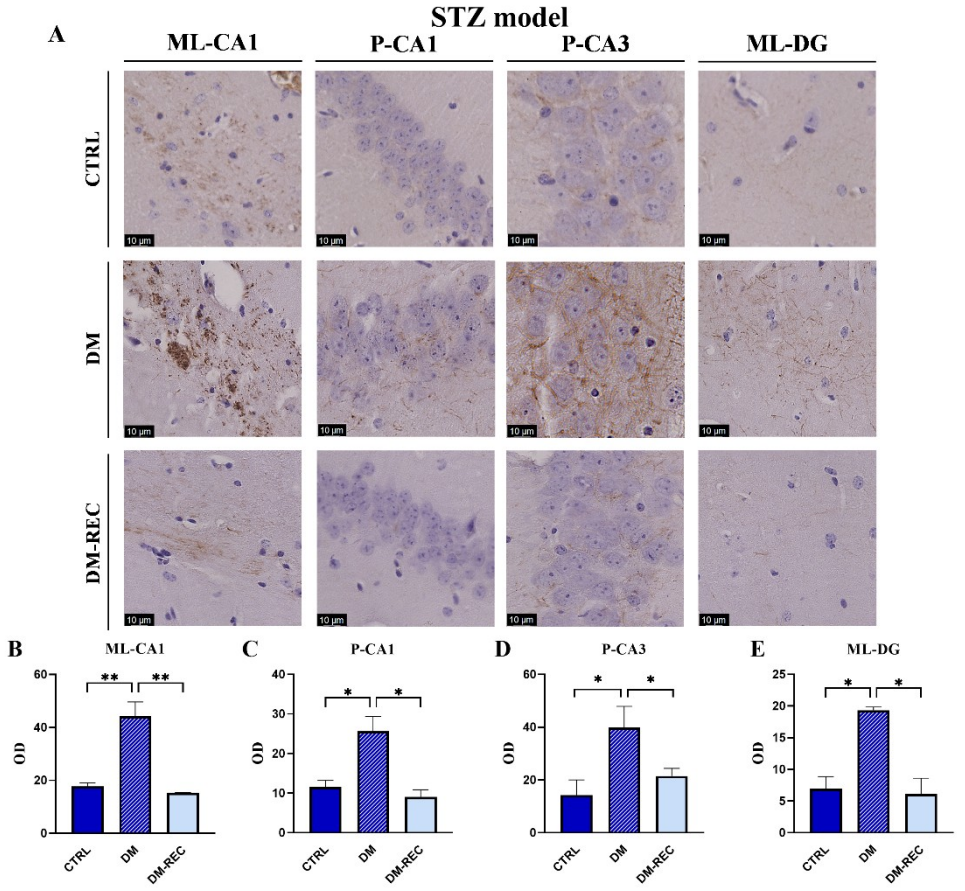


***Figure 37.*** *Immunohistochemical reactions for hyperphosphorylated Tau (p-Tau) (Ser235). Panel (A): Representative images of Molecular layer of CA1 (ML-CA1), Pyramidal layer of CA1 (P-CA1), Pyramidal layer of CA3 (P-CA3), and Molecular layer of Dent gyrus (ML-DG) from CTRL (upper row), DM (Central row), and DM-REC (down row) mice. Scale bars 10 µm. Panel (B-E): Histograms showing the Optical density (OD) of p-Tau signals in ML-CA1 (B), P-CA1 (C), P-CA3 (D), ML-DG © in CTRL (blue), DM (blue with white lines), and DM-REC (light blue) mice. Values are presented as mean ± Standard Error of the Mean (SEM). Statistical significance (One-Way ANOVA followed by Bonferroni post-hoc test): $p < 0.05$ (*); $p < 0.01$ (**); $p < 0.001$ (***).*

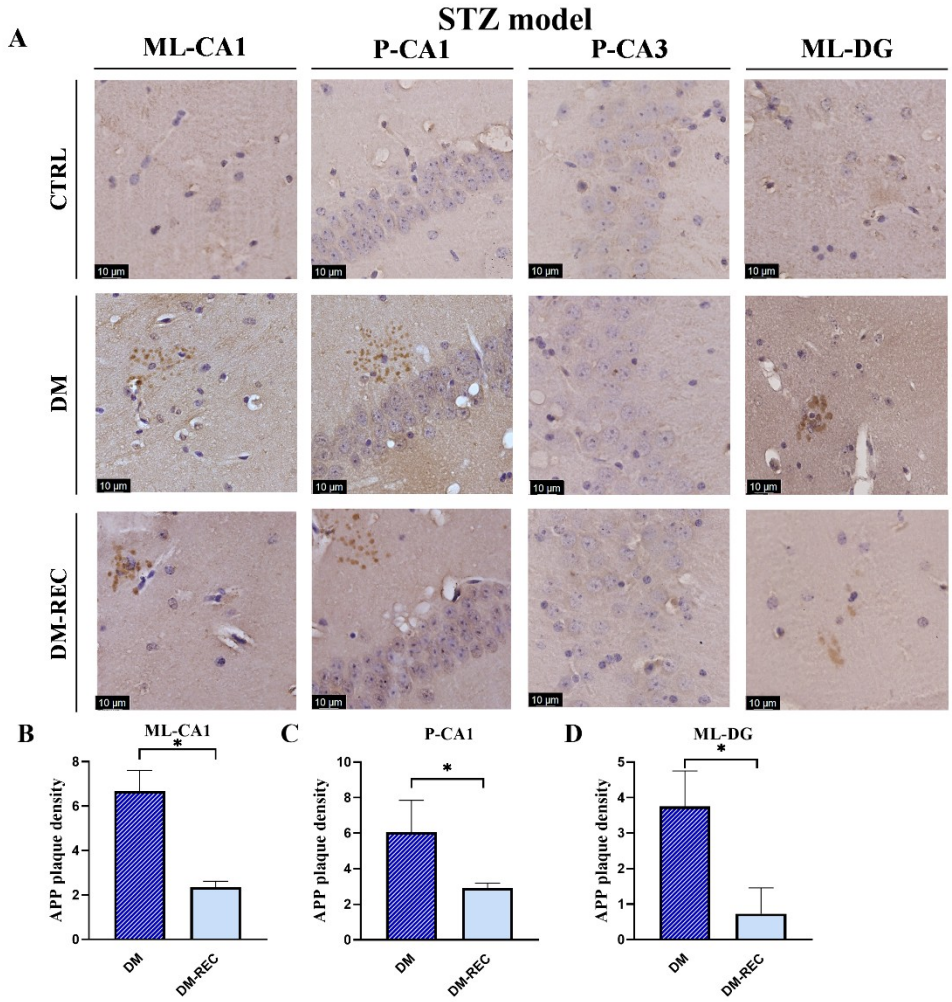


***Figure 38.*** *Immunohistochemical reactions for Anti-Beta (β) Amyloid. Panel (A): Representative images of Molecular layer of CA1 (ML-CA1), Pyramidal layer of CA1 (P-CA1), Pyramidal layer of CA3 (P-CA3), and Molecular layer of Dent gyrus (ML-DG) from CTRL (upper row), DM (Central row), and DM-REC (down row) mice. Scale bars 10 µm. Panel (B-E): Histograms showing the APP plaque density (number of APP spots/area plaque) in ML-CA1 (B), P-CA1 (C), ML-DG (D) in DM (blue with white lines), and DM-REC (light blue) mice. Values are presented as mean ± Standard Error of the Mean (SEM). Statistical significance (One-Way ANOVA followed by Bonferroni post-hoc test): $p < 0.05$ (*); $p < 0.01$ (**); $p < 0.001$ (***).*

#### 6.6.2.2. HFD/STZ model

In the HFD/STZ model, comparisons with HFD controls were carried out to evaluate whether the combination of insulin resistance and β-cell damage enhanced Alzheimer-like pathology in the hippocampus. Representative images for p-tau and Aβ markers are shown in Figure 39A and Figure 40A.

For p-Tau, HFD/STZ mice showed a significant increase in OD in the ML-CA1 region (58.73 ± 6.53; Figure 39B) compared to HFD mice (23.17 ± 4.05; $p = 0.003$). Elevated p-Tau levels were also observed in P-CA1 and P-CA3 (Figure 39C-D), with HFD/STZ mice displaying a significantly elevated (P-CA1: 31.33 ± 6.50, P-CA3: 57.19 ± 2.54) compared to HFD (P-CA1: 12.21 ± 2.27, $p = 0.03$; P-CA3: 31.94 ± 3.22, $p = 0.04$). In the ML-DG region (Figure 39E), p-Tau was significantly increased in HFD/STZ mice (37.98 ± 7.91) compared to HFD (8.89 ± 0.44, $p = 0.01$).

Regarding β-amyloid, APP deposits were detected in both groups. However, no deposits were observed in the ML-DG region in HFD group, but only in HFD/STZ mice (4.08 ± 2.11). Quantitative analysis of deposit density revealed significant increases in HFD/STZ mice compared to HFD in ML-CA1 (4.63 ± 0.14 vs 2.28 ± 0.93, respectively; $p = 0.03$; Figure 40B), and in P-CA1 (5.68 ± 0.41 vs 3.08 ± 0.39; $p = 0.005$; Figure 40C) regions, with HFD/STZ mice showing the highest densities. Notably, no statistical difference was observed in the P-CA3 region (Figure 40D) between HFD and HFD/STZ mice (4.42 ± 0.03 vs 3.65 ± 0.57).

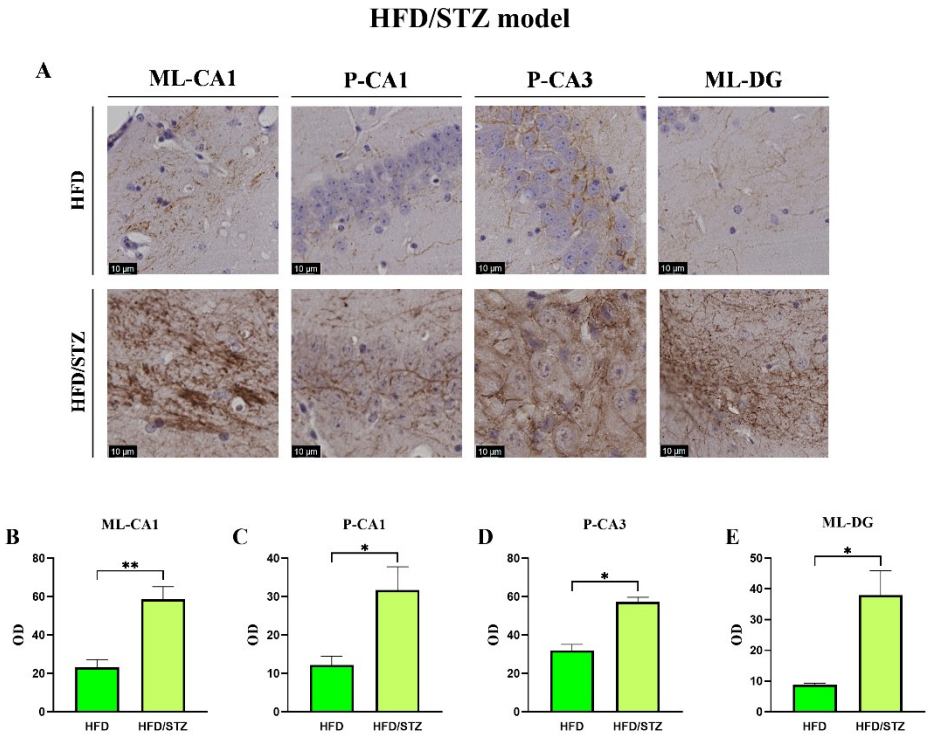


***Figure 39.*** *Immunohistochemical reactions for hyperphosphorylated Tau (p-Tau) (Ser235). Panel (A): Representative images of Molecular layer of CA1 (ML-CA1), Pyramidal layer of CA1 (P-CA1), Pyramidal layer of CA3 (P-CA3), and Molecular layer of Dent gyrus (ML-DG) from HFD (upper row), and HFD/STZ (Central row) mice. Scale bars 10 µm. Panel (B-E): Histograms showing the Optical density (OD) of p-Tau signals in ML-CA1 (B), P-CA1 (C), P-CA3 (D), ML-DG (E) in HFD (green), and HFD/STZ (light green) mice. Values are presented as mean ± Standard Error of the Mean (SEM). Statistical significance (One-Way ANOVA followed by Bonferroni post-hoc test): $p < 0.05$ (*); $p < 0.01$ (**); $p < 0.001$ (***).*

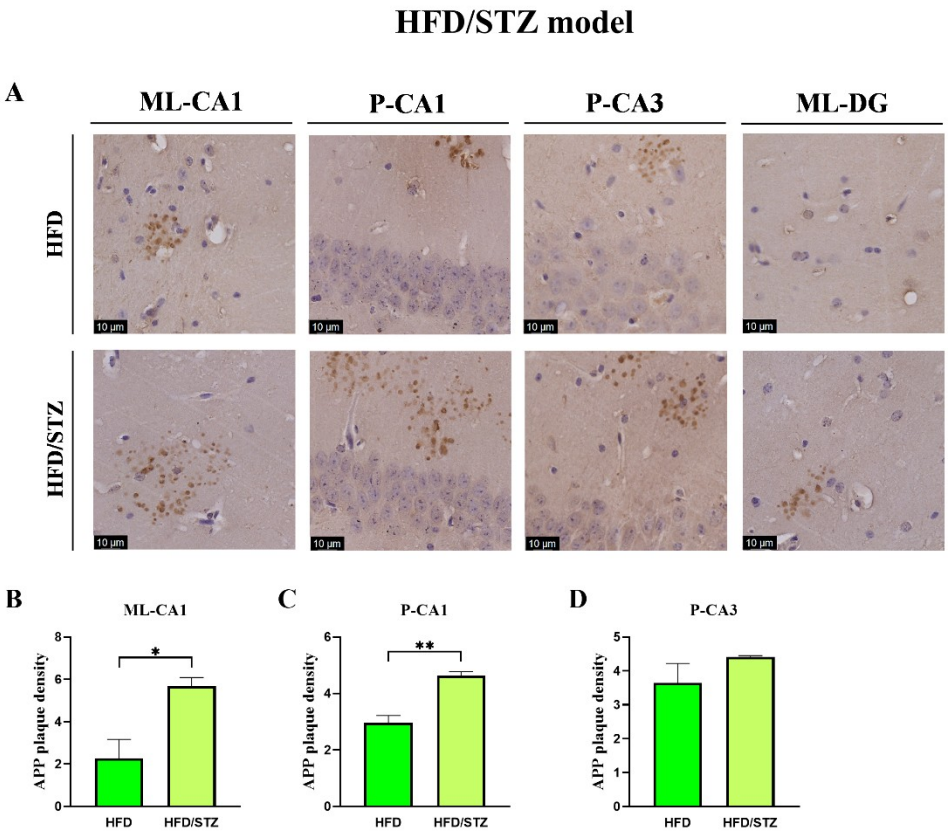


***Figure 40.*** *Immunohistochemical reactions for Anti-Beta (β) Amyloid. Panel (A): Representative images of Molecular layer of CA1 (ML-CA1), Pyramidal layer of CA1 (P-CA1), Pyramidal layer of CA3 (P-CA3), and Molecular layer of Dent gyrus (ML-DG) from HFD (upper row), and HFD/STZ (Central row) mice. Scale bars 10 µm. Panel (B-E): Histograms showing the APP plaque density (number of APP spots/area plaque) in ML-CA1 (B), P-CA1 (C), and P-CA3 (D) in HFD (green), and HFD/STZ (light green) mice. Values are presented as mean ± Standard Error of the Mean (SEM). Statistical significance (One-Way ANOVA followed by Bonferroni post-hoc test): $p < 0.05$ (*); $p < 0.01$ (**); $p < 0.001$ (***).*

# 7. Discussion

Type 2 diabetes mellitus (T2DM) is increasingly recognized not only as a systemic metabolic disorder but also as a driver of accelerated brain aging and dementia risk. Epidemiological and experimental evidence consistently support the concept of "type 3 diabetes," whereby peripheral metabolic dysfunction converges on central mechanisms of neurodegeneration (Kciuk et al., 2024; Michailidis et al., 2022; Patel et al., 2016; Wium-Andersen et al., 2020).

Among the multiple pathways implicated, chronic hyperglycemia and advanced glycation processes are particularly relevant, as they promote vascular damage, oxidative stress, and neuroinflammation, ultimately leading to hippocampal vulnerability and Alzheimer-like pathology. Identifying biomarkers that capture these mechanisms is therefore critical to improve both experimental modeling and clinical monitoring.

Conventional measures such as HbA1c provide an integrated view of long-term glycemic control. However, they are limited in sensitivity to short-term fluctuations and do not capture the contribution of dicarbonyl stress. For this reason, glycated albumin (GA) and methylglyoxal (MGO) were selected as candidate biomarkers. GA reflects glycemic variability over shorter time scales, while MGO is a highly reactive dicarbonyl compound directly implicated in the formation of advanced glycation end-products (AGEs) and in cellular toxicity (Ayoub et al., 2025; Oliveira et al., 2024).

Their evaluation in experimental diabetes models provided an opportunity to test whether they may serve as more responsive and mechanistically relevant indicators of glycemic variability and dicarbonyl stress, as well as their association with recognition memory and hippocampal injury.

To address these questions, two murine models of T2DM were established and followed longitudinally from adulthood to senescence, allowing the parallel monitoring of systemic metabolism, GA, and MGO dynamics, frailty indices, and recognition memory. Furthermore, hippocampus and pancreas morphology were studied at the experimental endpoint.

The discussion that follows is organized around four main themes: (i) the diabetic condition induced in the two animal models; (ii) the validity as glycation markers of GA and MGO as short-term indicators of diabetic condition; (iii) the impact of dietary on fasting glycemia, MGO and GA values and the association with recognition memory performances; and (iv) the

association between diabetic condition, cognitive decline, and p-tau and APP/amyloid as Alzheimer-like neuropathology. Together, these considerations aim to situate the findings of this thesis within the broader context of diabetes research and neurodegeneration, while highlighting both the strengths and the limitations of the adopted approaches.
A general limitation of experimental diabetes research is that no single animal model can fully reproduce the multifactorial nature of the human disease. T2DM arises from the interaction of insulin resistance, β-cell dysfunction, dietary factors, and aging, and each model reflects only part of this complexity. For this reason, complementary approaches are needed to capture both the systemic and the neurological consequences of the disease (Rees & Alcolado, 2005).

The study was designed around two complementary paradigms to capture different trajectories of diabetes: (i) a low-dose streptozotocin (STZ) protocol, which induces partial β-cell dysfunction; and (ii) a combined high-fat diet (HFD) and STZ model, complemented by the study of HFD alone, to reproduce the multifactorial interaction between insulin resistance and β-cell loss. In addition, a detrimental high-sugar (HS) diet in drinking water was applied to only STZ-treated mice to test whether excessive sugar intake could further aggravate the diabetic condition. These models were followed longitudinally from adulthood to senescence, enabling the evaluation of GA and MGO in relation to conventional measures (glycemia) and the investigation of central outcomes, including recognition memory decline and p-Tau and APP/amyloid as Alzheimer-like neuropathology.

To separate the effects of diabetes from those of aging or diet, several control conditions were included. Non-diabetic controls (CTRL) of the STZ model provided a reference for age-related changes in systemic parameters such as glycemia, GA, and MGO. This was important to determine whether alterations observed in diabetic animals could be attributed to the disease itself or simply to advancing age.
In addition, high-sugar (HS) supplementation was tested in non-diabetic controls to assess whether dietary sugar intake alone is sufficient to perturb metabolic homeostasis in adult animals. Similarly, a group maintained on high-fat diet (HFD) without STZ allowed the evaluation of diet-induced metabolic parameters alteration and insulin resistance in the absence of

chemical β-cell injury. Together, these comparisons made it possible to separate the contribution of aging, dietary factors, and diabetes induction to metabolic parameters.

In the CTRL group of the STZ model, fasting glycemia remained within the physiological range throughout the observation period, confirming that aging alone did not drive the onset of hyperglycemia.
Similarly, GA values were stable across time, indicating that age by itself does not significantly affect short-term glycation under normoglycemic conditions. In contrast, MGO levels showed a progressive decline with age. This pattern is consistent with the notion that serum MGO may decrease as intracellular sequestration and AGE formation increase when detoxification capacity becomes less efficient (Dhar & Desai, 2012; Kold-Christensen & Johannsen, 2020). Thus, aging was associated with subtle biochemical shifts, but not with overt disruption of glucose homeostasis.

Supplementation with HS did not induce diabetes in adult non-diabetic mice. Fasting glucose values remained in the normal range, confirming previous reports that adult rodents show relative resistance to sugar-induced hyperglycemia (Coirini et al., 2022). Interestingly, GA values increased only after prolonged exposure, suggesting that cumulative dietary sugar may modulate short-term glycation processes even in the absence of overt hyperglycemia. MGO levels, however, were unaffected, reinforcing the idea that dicarbonyl stress requires an underlying diabetic condition to become manifest. These findings indicate that while excessive sugar intake may exacerbate existing metabolic alterations, it is not sufficient to induce diabetes in otherwise healthy adult animals.

The prolonged HFD exposure resulted in a progressive elevation of fasting glycemia, accompanied by increased body mass. These effects cannot be attributed to aging, as shown by comparison with our previous dataset in the first model, where control animals maintained stable fasting glucose (~90–100 mg/dL) and showed only modest weight gain at later ages (~36 g at 19 months). Thus, the observed alterations can be ascribed specifically to dietary intervention. Despite the absence of internal age-matched controls in this study, the insulin concentrations and HOMA-IR indices of HFD-fed mice align with values reported for insulin-resistant models in the literature (Heyward et al., 2012; Meng et al., 2010). Collectively, these findings indicate

that HFD feeding alone is sufficient to induce early insulin resistance, with severity modulated by both starting age and intervention length.
However, GA levels increased after four months of exposure, confirming chronic glycemic stress, but they surprisingly declined again with continued diet, implying possible metabolic adaptation to sustained nutritional overload. Furthermore, comparing these values with those of age-matched CTRL of the STZ model, it is evident that the rise in GA is diet-driven, while its subsequent decline reflects long-term compensatory responses.
Regarding MGO levels, they decreased with age regardless of diet, reflecting the same pattern observed in the CTRL group of the first model.

Taken together, these results indicate that aging alone does not significantly affect glycemia or GA, though it is associated with a decline in circulating MGO. HS supplementation in CTRL animals produced only a late and modest increase in GA, without altering glucose or MGO. HFD diet, in contrast, induced clear metabolic alterations, including hyperglycemia, insulin resistance, and alterations in GA, thereby establishing it as a predisposing condition for diabetes.
These findings provide the baseline for interpreting the diabetic phenotypes observed in the STZ and HFD/STZ models, and for assessing the added value of GA and MGO as early markers of diabetes.

In the STZ model, diabetes was induced at 13 months of age, corresponding to late adulthood in mice (~43 human years; Dutta & Sengupta, 2016). One month after induction, all diabetic mice displayed severely elevated fasting glucose, averaging approximately fourfold higher than controls, confirming the robustness of the initial phenotype. However, the longitudinal follow-up revealed an unexpected trajectory: rather than remaining stable, the diabetic phenotype showed progressive spontaneous remission in a large proportion of animals. By 16 months of age (3 months after STZ injections), approximately 55% of animals showed partial remission, and by 19 months of age (6 months after STZ injections), nearly 90% had normalized glycemia.
To our knowledge, such recovery has not been previously reported, likely because most studies adopt cross-sectional designs and terminate experiments within weeks after induction. This novel observation suggests that STZ-induced diabetes in adult mice is not invariably irreversible but instead exhibits a transient course characterized by early severity and later plasticity.

While this reduces its translational validity as a model of chronic T2DM, it provides a unique window to study endogenous mechanisms of recovery. Candidate processes may include β-cell replication via IRS2/PI3K/Akt signaling, neogenesis from progenitor cells, α-to-β cell trans-differentiation, and immunomodulatory pathways that may promote regeneration (Dor et al., 2004; Ji et al., 2022; Shahedi et al., 2024; Yin et al., 2006).

Pancreatic histology reinforced this interpretation. STZ-treated animals displayed insulitis and islet disorganization, but those in the recovery subgroup (DM-REC) showed partial restoration of islet structure, suggesting regenerative processes at work. This correlation between glycemic recovery and histological improvement underscores the importance of a longitudinal design to capture the dynamic evolution of diabetes.

The addition of a high-sugar supplement (DM-HS) did not exacerbate hyperglycemia compared to diabetic animals on normal diet. This aligns with previous reports that adult mice are relatively resistant to dietary sugar challenges (Coirini et al., 2022). However, survival outcomes revealed an important interaction: DM-HS animals had markedly reduced lifespan, with only ~55% surviving to 18 months. Strikingly, none of the animals with extreme glycemia (>500 mg/dL) survived, indicating that dietary sugar compounds increase mortality risk in severe diabetes even without consistently worsening glycemia. This observation has translational implications, as it mirrors epidemiological data linking high sugar intake to increased mortality in diabetic patients (Ma et al., 2023; Yang et al., 2014).

GA levels in STZ-induced diabetic animals increased early, within one month of induction, and remained elevated until T4, even in mice that had normalized glycemia. This persistence suggests that GA reflects ongoing glycation and dicarbonyl stress beyond overt hyperglycemia, reinforcing its potential as a more sensitive biomarker than fasting glucose for detecting alterations in glucose and dicarbonyl metabolism.

Importantly, no significant differences were observed between DM-ND and DM-HS animals, indicating that the diabetic state itself outweighed the contribution of dietary sugar to GA variability.

MGO levels in diabetic animals followed a distinct trajectory. In contrast to the age-related decline observed in controls, MGO concentrations increased after 3 months of STZ induction in DM-HS mice, counteracting the normal age-dependent reduction, before declining again after another 3 months

alongside glycemic recovery. This profile indicates that MGO may act as a transient marker of glycation activity, particularly when dietary challenges compound diabetes. Its normalization in recovered animals suggests that MGO accumulation is closely tied to ongoing hyperglycemia rather than residual systemic alterations.

Overall, the STZ model revealed an acute and severe diabetic state that, contrary to prevailing assumptions, was transient and partially reversible. This limits its construct validity for modeling chronic human diabetes. However, it provides a unique opportunity to investigate endogenous recovery processes and to evaluate GA and MGO as biomarkers of ongoing metabolic changes beyond overt hyperglycemia.

In the second model, diabetes was induced at 14.5 months of age (~48 human years; Dutta & Sengupta, 2016) by combining high-fat diet (HFD) feeding with low-dose STZ administration, the same chemical protocol used for the first model. This dual-hit approach aimed to reproduce the interaction between insulin resistance and β-cell dysfunction that characterizes human disease trajectories.

The combined HFD/STZ protocol generated a more severe and persistent diabetic phenotype. Fasting glycemia after one month of STZ injections, all animals exhibited diabetic fasting glucose levels (exceeded 250 mg/dL), confirming the effectiveness of the induction. At 16 months of age, corresponding to 2 months after STZ induction, hyperglycemia remained stable, and no signs of recovery were observed, in clear contrast with the partial remission seen in the STZ-only model. Beyond this window, the longitudinal course of HFD/STZ mice remains unknown, which represents a limitation of the model. However, the primary objective of this paradigm was to establish a stable diabetic phenotype suitable for the study of metabolic and cognitive alterations. To avoid the confound of potential recovery, analysis was therefore restricted to the 16-month time point. Within this timeframe, the HFD/STZ model provided a consistent phenotype without signs of recovery.

A defining feature of this model was the combination of persistent hyperglycemia with clear evidence of insulin resistance. Insulin levels and HOMA-IR indices were markedly elevated in HFD/STZ mice, confirming that the metabolic dysfunction was not limited to β-cell loss but also involved

impaired insulin sensitivity. This dual pathology strongly parallels the human condition, where insulin resistance and β-cell dysfunction jointly drive disease progression. It also distinguishes the HFD/STZ paradigm from the STZ-only model, which lacks significant insulin resistance.

GA and MGO profiles further corroborated the severity of the phenotype. GA remained persistently elevated, reflecting sustained short-term glycemic instability, while MGO concentrations were high despite the age-related decline seen in controls and HFD mice. This divergence highlights ongoing dicarbonyl stress and advanced glycation, processes known to mediate complications of diabetes, including vascular damage and neurodegeneration (C. G. Schalkwijk & Stehouwer, 2020).

Pancreatic histology confirmed extensive islet disruption and severe insulitis, with higher grades (3-4) predominating. These lesions exceeded those observed in HFD-fed animals, underscoring the synergistic contribution of insulin resistance and STZ-induced β-cell toxicity to irreversible pancreatic failure.

Survival outcomes also diverged between models. HFD/STZ mice exhibited persistently reduced survival, reflecting the relentless progression of their metabolic impairment. This supports the view that chronic insulin resistance combined with β-cell dysfunction leads to irreversible systemic frailty and higher mortality.

Taken together, the HFD/STZ paradigm provided a translationally relevant model of diabetes, faithfully reproducing the chronic and progressive nature of the human disease within the monitored window, with persistent hyperglycemia, elevated GA and MGO, severe β-cell damage, and reduced survival. Although stability was confirmed only up to 16 months of age, this model fulfilled its purpose of providing a robust platform for investigating long-term systemic and neurological complications of diabetes.

The association between diabetes and cognitive impairment has been consistently demonstrated in both clinical and experimental studies. Patients with T2DM show a higher risk of developing dementia, particularly Alzheimer's disease, and often present with early deficits in memory, attention, and executive function (Michailidis et al., 2022; Patel et al., 2016; Wium-Andersen et al., 2020). Animal studies have provided converging

evidence that hyperglycemia, insulin resistance, and advanced glycation accelerate brain aging and predispose to neurodegenerative changes (Ayoub et al., 2025; Oliveira et al., 2024). Within this framework, recognition memory represents a particularly sensitive marker, as it relies on hippocampal and cortical networks that are highly vulnerable to metabolic and neurodegenerative stress (Bird, 2017; Rao et al., 2022; Vilela et al., 2023).
Recognition memory is not a unitary construct but comprises at least two partially dissociable components: knowledge (familiarity with a previously encountered stimulus) and remember (the recollection of contextual details). This distinction has been increasingly recognized in both human and animal studies, with evidence that the two processes rely on overlapping but distinct neural substrates (Brown & Aggleton, 2001). Assessing both components is therefore essential to capture the full spectrum of diabetes-related memory dysfunction.

In the STZ model, the knowledge component of recognition memory was analyzed using the novel object recognition (NOR) task, whereas in the HFD/STZ model, the assessment was extended to include both knowledge and remember components.

High-sugar supplementation was not assessed at the cognitive or neuropathological level, as it did not produce measurable alterations in metabolic parameters or in recognition memory performance, either in controls or in diabetic animals. For this reason, the following analyses focus exclusively on control, HFD-alone, STZ-alone (DM), and HFD/STZ groups.

In CTRL mice of the STZ model, recognition memory gradually declined with age, consistent with physiological cognitive aging (Ratto et al., 2019).
In HFD-fed animals, recognition memory was only subtly impaired. When compared with the age-matched controls of the first model, no meaningful differences emerged, indicating that diet alone did not accelerate decline. Furthermore, when considered within the broader trajectory of age-related changes previously characterized in our laboratory (Roda et al., 2023), both the knowledge and remember components in HFD animals aligned with normal aging patterns. Together, these findings suggest that a prolonged high-fat diet contributes modestly to cognitive decline, largely through age-related mechanisms and metabolic alterations rather than overt diabetes.

In the first model, after 3 months from STZ induction, diabetic animals displayed severe cognitive impairment, with the global frailty index more than doubling relative to age-matched controls, indicating that diabetes accelerated the cognitive decline. Notably, animals in the recovery subgroup regained NOR performance comparable to controls, demonstrating that restoration of glycemic control can reverse familiarity-based memory deficits. This finding highlights the plasticity of recognition memory circuits and supports the hypothesis that early metabolic interventions may preserve or restore cognitive function (Kleinridders et al., 2015).
By 16 months of age, cognitive testing was affected by two major limitations: increased frailty and reduced locomotor activity, which constrained exploratory behavior, and the very small number of animals that remained diabetic (only 2 mice, as ~90% had undergone recovery). These factors preclude firm conclusions about recognition memory at the latest time point. Nevertheless, DM-REC animals maintained cognitive performance comparable to controls, indicating that cognitive recovery remained stable over time despite these experimental condition's constraints.

In the second model, HFD/STZ mice displayed an elevated cognitive frailty index, comparable to values previously reported in STZ-only mice at the same age. The combined treatment accelerated cognitive decline, with persistent and generalized deficits affecting both the knowledge and remember components of recognition memory. Compared to HFD-fed mice, these impairments were markedly more severe, underscoring the role of insulin resistance and β-cell dysfunction in exacerbating cognitive deterioration. Taken together, these findings support an association between hyperglycemia, insulin resistance, and glycation and recognition memory impairment, consistent with clinical and experimental evidence linking metabolic syndrome to accelerated neurocognitive aging and increased dementia risk (Hamzé et al., 2022; Shieh et al., 2020; Yu et al., 2025).

The hippocampus was selected as the primary region for histopathological analysis because of its central role in recognition memory and its well-established vulnerability to metabolic dysfunction and neurodegeneration. Clinical and experimental studies consistently show that hippocampal atrophy, neuronal loss, and synaptic alterations are among the earliest brain changes associated with both diabetes and Alzheimer's disease (Jash et al.,

2020; Kciuk et al., 2024; Michailidis et al., 2022). Moreover, hyperglycemia, insulin resistance, and glycation stress converge on pathways that promote tau hyperphosphorylation and amyloid accumulation, processes that particularly affect hippocampal circuits (Ayoub et al., 2025; Oliveira et al., 2024).

In control animals, hippocampal architecture was preserved, with no histological evidence of structural alterations in the analyzed regions.

HFD-only animals were analyzed histologically, but interpretation was limited by the lack of age-matched controls for direct comparison. Within this constraint, the changes observed were modest relative to diabetic groups. This is in line with previous reports showing that chronic HFD exposure can induce moderate hippocampal alterations, including reduced neurogenesis and synaptic dysfunction, though typically less severe than those associated with overt diabetes (González Olmo et al., 2023; Zhuang et al., 2022).

In the diabetic mice of the STZ model, clear neurodegenerative changes were detected in CA1 and CA3 subfields, where pyramidal layers appeared thinner and neuronal density was reduced. Immunohistochemical analyses further revealed increased tau phosphorylation and APP/amyloid deposition in diabetic mice. Although histological evaluations were performed later than the cognitive assessments, the presence of these alterations is consistent with the hypothesis that systemic metabolic alteration contributes to hippocampal vulnerability and may underlie the memory impairment observed at earlier stages (Biessels & Despa, 2018; Jash et al., 2020; Michailidis et al., 2022). Remarkably, in the recovery subgroup (DM-REC), both structural and molecular alterations were attenuated: neuronal density partially recovered, and p-Tau and APP/amyloid immunoreactivity decreased. This suggests that hippocampal circuits retain a degree of plasticity and that normalization of glucose metabolism can mitigate AD-related pathology, in line with evidence that early interventions may slow or reverse neurodegenerative changes (Kleinridders et al., 2015).

In the second model, neuropathological alterations were more widespread, with HFD/STZ mice showing structural damage across CA1, CA2, and CA3. Although the overall hippocampal morphology remained recognizable, quantitative analysis revealed clear reductions in pyramidal layer thickness and neuronal density, pointing to a loss of cytoarchitectural integrity in

memory-related subregions. These structural deficits were accompanied by sustained tau phosphorylation and amyloid accumulation, molecular hallmarks of Alzheimer-like pathology. Together, these changes align with recent evidence linking metabolic alterations to hippocampal vulnerability and are consistent with the notion that the combined burden of insulin resistance and β-cell failure exacerbates hippocampal damage and accelerates neurodegenerative cascades (De Felice & Ferreira, 2014; Peng et al., 2021; Vilela et al., 2023).

Taken together, these findings highlight the complex interplay between hyperglycemia, insulin resistance, glycation, and hippocampal alterations, underscoring the value of complementary experimental models in disentangling the systemic and neurological dimensions of diabetes.

## 8. Conclusions and Future Perspectives

This doctoral project demonstrates that diabetes profoundly affects not only systemic metabolism but also brain health, accelerating cognitive decline and promoting p-Tau and APP/amyloid accumulation. By adopting a longitudinal design across two complementary murine models, it was possible to dissect both the reversible and the chronic trajectories of diabetes and to link systemic alterations with cognitive and neuropathological outcomes.

A major contribution of this work is the introduction of glycated albumin (GA) and methylglyoxal (MGO) as biomarkers in experimental models of type 2 diabetes. Both markers proved sensitive to short-term fluctuations and to the persistent glycation process, often beyond what was captured by conventional glycemia. Their consistent association with metabolic and hippocampal alterations highlights their potential value in translational research and clinical applications.

The two models adopted offered complementary insights. The STZ-only paradigm revealed an unexpected capacity for spontaneous recovery, reducing its translational validity as a model of chronic diabetes but providing a unique opportunity to explore endogenous mechanisms of β-cell and hippocampal plasticity. In contrast, the HFD/STZ model reproduced a more stable diabetic phenotype, combining insulin resistance and β-cell loss, and better reflecting the chronic progression of human disease. Together, these approaches underscore the need to integrate multiple models to capture the multifactorial nature of diabetes and its neurological complications.

At the same time, several limitations should be acknowledged. Sample sizes were modest, particularly in the HFD/STZ cohort, and only male animals were included across both models, precluding the assessment of sex-specific responses. The follow-up was restricted to a defined time window, limiting conclusions about longer-term trajectories, especially in the HFD/STZ model. Moreover, mechanistic analyses of inflammation, oxidative stress, and insulin signaling were beyond the scope of this study, leaving open questions about the molecular mediators of recovery and decline.

Future studies should therefore expand to larger and sex-balanced cohorts, adopt longer longitudinal designs, and integrate multi-omics approaches to unravel the pathways linking hyperglycemia, insulin resistance, dicarbonyl

stress, and neurodegeneration. Interventional studies, testing dietary modulation, antidiabetic drugs, or neuroprotective strategies, will be essential to establish the predictive and therapeutic value of GA and MGO. Finally, translational efforts connecting animal and clinical cohorts will be crucial to validate these biomarkers and to explore their role in stratifying cognitive risk in diabetic populations.

In summary, this work provides new insights into how diabetes may accelerate brain aging, emphasizes the complementary strengths and limitations of experimental models, and suggests GA and MGO as promising biomarkers associated with metabolic and cognitive alterations. These findings set the stage for future research aimed at developing personalized strategies to monitor and mitigate diabetes-related neurodegeneration.
Ultimately, bridging preclinical models with clinical translation will be essential to integrate metabolic and cognitive aspects of diabetes management.

## 9. References

A. Shamsaldeen, Y., S. Mackenzie, L., A. Lione, L., & D. Benham, C. (2016). Methylglyoxal, A Metabolite Increased in Diabetes is Associated with Insulin Resistance, Vascular Dysfunction and Neuropathies. *Current Drug Metabolism*, *17*(4), 359–367. https://doi.org/10.2174/1389200217666151222155216

Abdul-Ghani, M. A., Tripathy, D., & DeFronzo, R. A. (2006). Contributions of β-Cell Dysfunction and Insulin Resistance to the Pathogenesis of Impaired Glucose Tolerance and Impaired Fasting Glucose. *Diabetes Care*, *29*(5), 1130–1139. https://doi.org/10.2337/dc05-2179

Aderinto, N., Olatunji, G., Abdulbasit, M., Ashinze, P., Faturoti, O., Ajagbe, A., Ukoaka, B., & Aboderin, G. (2023). The impact of diabetes in cognitive impairment: A review of current evidence and prospects for future investigations. *Medicine*, *102*(43), e35557. https://doi.org/10.1097/MD.0000000000035557

Adiels, M., Olofsson, S.-O., Taskinen, M.-R., & Borén, J. (2008). Overproduction of Very Low–Density Lipoproteins Is the Hallmark of the Dyslipidemia in the Metabolic Syndrome. *Arteriosclerosis, Thrombosis, and Vascular Biology*, *28*(7), 1225–1236. https://doi.org/10.1161/ATVBAHA.107.160192

Aguilar-Navarro, S. G., Mimenza-Alvarado, A. J., Yeverino-Castro, S. G., Caicedo-Correa, S. M., & Cano-Gutiérrez, C. (2025). Cognitive Frailty and Aging: Clinical Characteristics, Pathophysiological Mechanisms, and Potential Prevention Strategies. *Archives of Medical Research*, *56*(1), 103106. https://doi.org/10.1016/j.arcmed.2024.103106

Ahmed, N., Mirshekar-Syahkal, B., Kennish, L., Karachalias, N., Babaei-Jadidi, R., & Thornalley, P. J. (2005). Assay of advanced glycation endproducts in selected beverages and food by liquid chromatography with tandem mass spectrometric detection. *Molecular Nutrition & Food Research*, *49*(7), 691–699. https://doi.org/10.1002/mnfr.200500008

Akhter, F., Chen, D., Yan, S. F., & Yan, S. S. (2017). *Mitochondrial Perturbation in Alzheimer's Disease and Diabetes* (pp. 341–361). https://doi.org/10.1016/bs.pmbts.2016.12.019

Al-awar, A., Kupai, K., Veszelka, M., Szűcs, G., Attieh, Z., Murlasits, Z., Török, S., Pósa, A., & Varga, C. (2016). Experimental Diabetes Mellitus in Different Animal Models. *Journal of Diabetes Research*, *2016*, 1–12. https://doi.org/10.1155/2016/9051426

Al-Sayyar, A., Hammad, M. M., Williams, M. R., Al-Onaizi, M., Abubaker, J., & Alzaid, F. (2023). Neurotransmitters in Type 2 Diabetes and the Control of Systemic and Central Energy Balance. *Metabolites*, *13*(3), 384. https://doi.org/10.3390/metabo13030384

Alkhalifa, A. E., Al-Ghraiybah, N. F., Odum, J., Shunnarah, J. G., Austin, N., & Kaddoumi, A. (2023). Blood–Brain Barrier Breakdown in Alzheimer's Disease: Mechanisms and Targeted Strategies. *International Journal of Molecular Sciences*, *24*(22), 16288. https://doi.org/10.3390/ijms242216288

American Diabetes Association. (2021). 2. Classification and Diagnosis of Diabetes: Standards of Medical Care in Diabetes—2021. In *Diabetes Care* (Vol. 44, Issue Supplement_1). https://doi.org/10.2337/dc21-S002

An, Y., Xu, B., Wan, S., Ma, X., Long, Y., Xu, Y., & Jiang, Z. (2023). The role of oxidative stress in diabetes mellitus-induced vascular endothelial dysfunction. *Cardiovascular Diabetology*, *22*(1), 237. https://doi.org/10.1186/s12933-023-01965-7

Aviello, G., Rowland, I., Gill, C. I., Acquaviva, A. M., Capasso, F., McCann, M., Capasso, R., Izzo, A. A., & Borrelli, F. (2010). Anti-proliferative effect of rhein, an anthraquinone isolated from Cassia species, on Caco-2 human adenocarcinoma cells. *Journal of Cellular and Molecular Medicine*, *14*(7), 2006–2014. https://doi.org/10.1111/j.1582-4934.2009.00815.x

Ayala, J. E., Samuel, V. T., Morton, G. J., Obici, S., Croniger, C. M., Shulman, G. I., Wasserman, D. H., & McGuinness, O. P. (2010). Standard operating procedures for describing and performing metabolic tests of glucose homeostasis in mice. *DMM Disease Models and Mechanisms*, *3*(9–10), 525–534. https://doi.org/10.1242/dmm.006239

Ayoub, S., Arabi, M., Al-Najjar, Y., Laswi, I., Outeiro, T. F., & Chaari, A. (2025). Glycation in Alzheimer's Disease and Type 2 Diabetes: The Prospect of Dual Drug Approaches for Therapeutic Interventions. *Molecular Neurobiology*. https://doi.org/10.1007/s12035-025-05051-9

Baglietto-Vargas, D., Shi, J., Yaeger, D. M., Ager, R., & LaFerla, F. M. (2016). Diabetes and Alzheimer's disease crosstalk. *Neuroscience & Biobehavioral Reviews*, *64*, 272–287. https://doi.org/10.1016/j.neubiorev.2016.03.005

Bandeen-Roche, K., Xue, Q.-L., Ferrucci, L., Walston, J., Guralnik, J. M., Chaves, P., Zeger, S. L., & Fried, L. P. (2006). Phenotype of Frailty:

Characterization in the Women's Health and Aging Studies. *The Journals of Gerontology Series A: Biological Sciences and Medical Sciences*, *61*(3), 262–266. https://doi.org/10.1093/gerona/61.3.262

Banks, W. (2005). Blood-Brain Barrier Transport of Cytokines: A Mechanism for Neuropathology. *Current Pharmaceutical Design*, *11*(8), 973–984. https://doi.org/10.2174/1381612053381684

Banks, W. A. (2004). The source of cerebral insulin. *European Journal of Pharmacology*, *490*(1–3), 5–12. https://doi.org/10.1016/j.ejphar.2004.02.040

Barbagallo, M. (2014). Type 2 diabetes mellitus and Alzheimer's disease. *World Journal of Diabetes*, *5*(6), 889. https://doi.org/10.4239/wjd.v5.i6.889

Barroso, E., Jurado-Aguilar, J., Wahli, W., Palomer, X., & Vázquez-Carrera, M. (2024). Increased hepatic gluconeogenesis and type 2 diabetes mellitus. *Trends in Endocrinology & Metabolism*, *35*(12), 1062–1077. https://doi.org/10.1016/j.tem.2024.05.006

Basheer, N., Smolek, T., Hassan, I., Liu, F., Iqbal, K., Zilka, N., & Novak, P. (2023). Does modulation of tau hyperphosphorylation represent a reasonable therapeutic strategy for Alzheimer's disease? From preclinical studies to the clinical trials. *Molecular Psychiatry*, *28*(6), 2197–2214. https://doi.org/10.1038/s41380-023-02113-z

Bauer, B. M., Bhattacharya, S., Bloom-Saldana, E., Irimia-Dominguez, J. M., & Fueger, P. T. (2023). Dose-dependent progression of multiple low-dose streptozotocin-induced diabetes in mice. *Physiological Genomics*, *55*(9), 381–391. https://doi.org/10.1152/physiolgenomics.00032.2023

Bekris, L. M., Yu, C.-E., Bird, T. D., & Tsuang, D. W. (2010). Review Article: Genetics of Alzheimer Disease. *Journal of Geriatric Psychiatry and Neurology*, *23*(4), 213–227. https://doi.org/10.1177/0891988710383571

Benedict, C., & Grillo, C. A. (2018). Insulin Resistance as a Therapeutic Target in the Treatment of Alzheimer's Disease: A State-of-the-Art Review. *Frontiers in Neuroscience*, *12*. https://doi.org/10.3389/fnins.2018.00215

Bevandić, J., Chareyron, L. J., Bachevalier, J., Cacucci, F., Genzel, L., Newcombe, N. S., Vargha-Khadem, F., & Ólafsdóttir, H. F. (2024). Episodic memory development: Bridging animal and human research. *Neuron*, *112*(7), 1060–1080.

https://doi.org/10.1016/j.neuron.2024.01.020

Biessels, G. J., & Despa, F. (2018). Cognitive decline and dementia in diabetes mellitus: mechanisms and clinical implications. *Nature Reviews Endocrinology*, *14*(10), 591–604. https://doi.org/10.1038/s41574-018-0048-7

Bird, C. M. (2017). The role of the hippocampus in recognition memory. *Cortex*, *93*, 155–165. https://doi.org/10.1016/j.cortex.2017.05.016

Blum-Degena, D., Müller, T., Kuhn, W., Gerlach, M., Przuntek, H., & Riederer, P. (1995). Interleukin-1β and interleukin-6 are elevated in the cerebrospinal fluid of Alzheimer's and de novo Parkinson's disease patients. *Neuroscience Letters*, *202*(1–2), 17–20. https://doi.org/10.1016/0304-3940(95)12192-7

Boden, G. (2011). Obesity, insulin resistance and free fatty acids. *Current Opinion in Endocrinology, Diabetes & Obesity*, *18*(2), 139–143. https://doi.org/10.1097/MED.0b013e3283444b09

Boyarko, B., & Hook, V. (2021). Human Tau Isoforms and Proteolysis for Production of Toxic Tau Fragments in Neurodegeneration. *Frontiers in Neuroscience*, *15*. https://doi.org/10.3389/fnins.2021.702788

Boyle, A., & Brown, S. A. B. (2025). Episodic Memory in Animals. *Philosophy Compass*, *20*(5). https://doi.org/10.1111/phc3.70037

Brandalise, F., Cesaroni, V., Gregori, A., Repetti, M., Romano, C., Orrù, G., Botta, L., Girometta, C., Guglielminetti, M. L., Savino, E., & Rossi, P. (2017). Dietary Supplementation of Hericium erinaceus Increases Mossy Fiber-CA3 Hippocampal Neurotransmission and Recognition Memory in Wild-Type Mice. *Evidence-Based Complementary and Alternative Medicine*, *2017*. https://doi.org/10.1155/2017/3864340

Brown, M. W., & Aggleton, J. P. (2001). Recognition memory: What are the roles of the perirhinal cortex and hippocampus? *Nature Reviews Neuroscience*, *2*(1), 51–61. https://doi.org/10.1038/35049064

Cai, Z., Liu, N., Wang, C., Qin, B., Zhou, Y., Xiao, M., Chang, L., Yan, L.-J., & Zhao, B. (2016). Role of RAGE in Alzheimer's Disease. *Cellular and Molecular Neurobiology*, *36*(4), 483–495. https://doi.org/10.1007/s10571-015-0233-3

Campbell, G., Belobrajdic, D., & Bell-Anderson, K. (2018). Determining the Glycaemic Index of Standard and High-Sugar Rodent Diets in C57BL/6 Mice. *Nutrients*, *10*(7), 856. https://doi.org/10.3390/nu10070856

Carranza-naval, M. J., Vargas-soria, M., Hierro-bujalance, C., Baena-nieto, G., Garcia-alloza, M., Infante-garcia, C., & Del Marco, A. (2021). Alzheimer's disease and diabetes: Role of diet, microbiota and inflammation in preclinical models. *Biomolecules*, *11*(2), 1–25. https://doi.org/10.3390/biom11020262

Carrero, I., Gonzalo, M. R., Martin, B., Sanz-Anquela, J. M., Arévalo-Serrano, J., & Gonzalo-Ruiz, A. (2012). Oligomers of beta-amyloid protein (Aβ1-42) induce the activation of cyclooxygenase-2 in astrocytes via an interaction with interleukin-1beta, tumour necrosis factor-alpha, and a nuclear factor kappa-B mechanism in the rat brain. *Experimental Neurology*, *236*(2), 215–227. https://doi.org/10.1016/j.expneurol.2012.05.004

Cassano, V., Leo, A., Tallarico, M., Nesci, V., Cimellaro, A., Fiorentino, T. V., Citraro, R., Hribal, M. L., De Sarro, G., Perticone, F., Sesti, G., Russo, E., & Sciacqua, A. (2020). Metabolic and Cognitive Effects of Ranolazine in Type 2 Diabetes Mellitus: Data from an in vivo Model. *Nutrients*, *12*(2), 382. https://doi.org/10.3390/nu12020382

Caturano, A., D'Angelo, M., Mormone, A., Russo, V., Mollica, M. P., Salvatore, T., Galiero, R., Rinaldi, L., Vetrano, E., Marfella, R., Monda, M., Giordano, A., & Sasso, F. C. (2023). Oxidative Stress in Type 2 Diabetes: Impacts from Pathogenesis to Lifestyle Modifications. *Current Issues in Molecular Biology*, *45*(8), 6651–6666. https://doi.org/10.3390/cimb45080420

Cerf, M. E. (2013). Beta Cell Dysfunction and Insulin Resistance. *Frontiers in Endocrinology*, *4*. https://doi.org/10.3389/fendo.2013.00037

Chandran, S., & Binninger, D. (2023). Role of Oxidative Stress, Methionine Oxidation and Methionine Sulfoxide Reductases (MSR) in Alzheimer's Disease. *Antioxidants*, *13*(1), 21. https://doi.org/10.3390/antiox13010021

Chatterjee, S., & Mudher, A. (2018). Alzheimer's Disease and Type 2 Diabetes: A Critical Assessment of the Shared Pathological Traits. *Frontiers in Neuroscience*, *12*. https://doi.org/10.3389/fnins.2018.00383

Chavda, V., Yadav, D., Patel, S., & Song, M. (2024). Effects of a Diabetic Microenvironment on Neurodegeneration: Special Focus on Neurological Cells. *Brain Sciences*, *14*(3), 284. https://doi.org/10.3390/brainsci14030284

Chen, J. X., & Yan, S. Du. (2007). Amyloid-β-Induced Mitochondrial

Dysfunction. *Journal of Alzheimer's Disease*, *12*(2), 177–184. https://doi.org/10.3233/JAD-2007-12208

Chen, M., Pan, P., Zhang, H., Li, R., Ren, D., & Jiang, B. (2024). Latilactobacillus sakei QC9 alleviates hyperglycaemia in high-fat diet and streptozotocin-induced type 2 diabetes mellitus mice via the microbiota–gut–liver axis. *Food & Function*, *15*(15), 8008–8029. https://doi.org/10.1039/D4FO02316A

Chung, S. T., Hsia, D. S., Chacko, S. K., Rodriguez, L. M., & Haymond, M. W. (2015). Increased gluconeogenesis in youth with newly diagnosed type 2 diabetes. *Diabetologia*, *58*(3), 596–603. https://doi.org/10.1007/s00125-014-3455-x

Coirini, H., Rey, M., Gonzalez Deniselle, M. C., & Kruse, M. S. (2022). Long-Term Memory Function Impairments following Sucrose Exposure in Juvenile versus Adult Rats. *Biomedicines*, *10*(11), 2723. https://doi.org/10.3390/biomedicines10112723

Cole, G. M., & Frautschy, S. A. (2007). The role of insulin and neurotrophic factor signaling in brain aging and Alzheimer's Disease. *Experimental Gerontology*, *42*(1–2), 10–21. https://doi.org/10.1016/j.exger.2006.08.009

Crane, P. K., Walker, R., Hubbard, R. A., Li, G., Nathan, D. M., Zheng, H., Haneuse, S., Craft, S., Montine, T. J., Kahn, S. E., McCormick, W., McCurry, S. M., Bowen, J. D., & Larson, E. B. (2013). Glucose Levels and Risk of Dementia. *New England Journal of Medicine*, *369*(6), 540–548. https://doi.org/10.1056/NEJMoa1215740

Cummings, J., Lee, G., Nahed, P., Kambar, M. E. Z. N., Zhong, K., Fonseca, J., & Taghva, K. (2022). Alzheimer's disease drug development pipeline: 2022. *Alzheimer's & Dementia: Translational Research & Clinical Interventions*, *8*(1). https://doi.org/10.1002/trc2.12295

De Felice, F. G., & Ferreira, S. T. (2014). Inflammation, Defective Insulin Signaling, and Mitochondrial Dysfunction as Common Molecular Denominators Connecting Type 2 Diabetes to Alzheimer Disease. *Diabetes*, *63*(7), 2262–2272. https://doi.org/10.2337/db13-1954

de la Monte, S. M., Tong, M., & Wands, J. R. (2018). The 20-Year Voyage Aboard the Journal of Alzheimer's Disease: Docking at 'Type 3 Diabetes', Environmental/Exposure Factors, Pathogenic Mechanisms, and Potential Treatments. *Journal of Alzheimer's Disease*, *62*(3), 1381–1390. https://doi.org/10.3233/JAD-170829

Deane, R., Du Yan, S., Submamaryan, R. K., LaRue, B., Jovanovic, S., Hogg, E., Welch, D., Manness, L., Lin, C., Yu, J., Zhu, H., Ghiso, J., Frangione, B., Stern, A., Schmidt, A. M., Armstrong, D. L., Arnold, B., Liliensiek, B., Nawroth, P., … Zlokovic, B. (2003). RAGE mediates amyloid-β peptide transport across the blood-brain barrier and accumulation in brain. *Nature Medicine*, *9*(7), 907–913. https://doi.org/10.1038/nm890

DeFronzo, R. A. (2015). Pathogenesis of type 2 diabetes mellitus. In *International Textbook of Diabetes Mellitus* (pp. 371–400). Wiley. https://doi.org/10.1002/9781118387658.ch25

Dhami, M., Raj, K., & Singh, S. (2023). Relevance of gut microbiota to Alzheimer's Disease (AD): Potential effects of probiotic in management of AD. *Aging and Health Research*, *3*(1), 100128. https://doi.org/10.1016/j.ahr.2023.100128

Dhar, I., & Desai, K. (2012). Aging: Drugs to Eliminate Methylglyoxal, a Reactive Glucose Metabolite, and Advanced Glycation Endproducts. In *Pharmacology*. InTech. https://doi.org/10.5772/34337

Di Benedetto, G., Burgaletto, C., Bellanca, C. M., Munafò, A., Bernardini, R., & Cantarella, G. (2022). Role of Microglia and Astrocytes in Alzheimer's Disease: From Neuroinflammation to Ca2+ Homeostasis Dysregulation. *Cells*, *11*(17), 2728. https://doi.org/10.3390/cells11172728

Dilworth, L., Facey, A., & Omoruyi, F. (2021). Diabetes Mellitus and Its Metabolic Complications: The Role of Adipose Tissues. *International Journal of Molecular Sciences*, *22*(14), 7644. https://doi.org/10.3390/ijms22147644

Ding, V. W., Chen, R.-H., & McCormick, F. (2000). Differential Regulation of Glycogen Synthase Kinase 3β by Insulin and Wnt Signaling. *Journal of Biological Chemistry*, *275*(42), 32475–32481. https://doi.org/10.1074/jbc.M005342200

Dor, Y., Brown, J., Martinez, O. I., & Melton, D. A. (2004). Adult pancreatic β-cells are formed by self-duplication rather than stem-cell differentiation. *Nature*, *429*(6987), 41–46. https://doi.org/10.1038/nature02520

Dornadula, S., Elango, B., Balashanmugam, P., Palanisamy, R., & Kunka Mohanram, R. (2015). Pathophysiological Insights of Methylglyoxal Induced Type-2 Diabetes. *Chemical Research in Toxicology*, *28*(9), 1666–1674. https://doi.org/10.1021/acs.chemrestox.5b00171

Duarte, A. I., Moreira, P. I., & Oliveira, C. R. (2012). Insulin in Central Nervous System: More than Just a Peripheral Hormone. *Journal of Aging Research*, *2012*, 1–21. https://doi.org/10.1155/2012/384017

Fanali, G., di Masi, A., Trezza, V., Marino, M., Fasano, M., & Ascenzi, P. (2012). Human serum albumin: From bench to bedside. *Molecular Aspects of Medicine*, *33*(3), 209–290. https://doi.org/10.1016/j.mam.2011.12.002

Fazakerley, D. J., Minard, A. Y., Krycer, J. R., Thomas, K. C., Stöckli, J., Harney, D. J., Burchfield, J. G., Maghzal, G. J., Caldwell, S. T., Hartley, R. C., Stocker, R., Murphy, M. P., & James, D. E. (2018). Mitochondrial oxidative stress causes insulin resistance without disrupting oxidative phosphorylation. *Journal of Biological Chemistry*, *293*(19), 7315–7328. https://doi.org/10.1074/jbc.RA117.001254

Federico, A., Cardaioli, E., Da Pozzo, P., Formichi, P., Gallus, G. N., & Radi, E. (2012). Mitochondria, oxidative stress and neurodegeneration. *Journal of the Neurological Sciences*, *322*(1–2), 254–262. https://doi.org/10.1016/j.jns.2012.05.030

Folch, J., Ettcheto, M., Busquets, O., Sánchez-López, E., Castro-Torres, R., Verdaguer, E., Manzine, P., Poor, S., García, M., Olloquequi, J., Beas-Zarate, C., Auladell, C., & Camins, A. (2018). The Implication of the Brain Insulin Receptor in Late Onset Alzheimer's Disease Dementia. *Pharmaceuticals*, *11*(1), 11. https://doi.org/10.3390/ph11010011

Freitas, P. A. C., Ehlert, L. R., & Camargo, J. L. (2017). Glycated albumin: a potential biomarker in diabetes. *Archives of Endocrinology and Metabolism*, *61*(3), 296–304. https://doi.org/10.1590/2359-3997000000272

Fried, L. P., Tangen, C. M., Walston, J., Newman, A. B., Hirsch, C., Gottdiener, J., Seeman, T., Tracy, R., Kop, W. J., Burke, G., & McBurnie, M. A. (2001). Frailty in Older Adults: Evidence for a Phenotype. *The Journals of Gerontology Series A: Biological Sciences and Medical Sciences*, *56*(3), M146–M157. https://doi.org/10.1093/gerona/56.3.M146

Furman, B. L. (2021). Streptozotocin-Induced Diabetic Models in Mice and Rats. *Current Protocols*, *1*(4). https://doi.org/10.1002/cpz1.78

Gabbouj, S., Ryhänen, S., Marttinen, M., Wittrahm, R., Takalo, M., Kemppainen, S., Martiskainen, H., Tanila, H., Haapasalo, A., Hiltunen, M., & Natunen, T. (2019). Altered Insulin Signaling in Alzheimer's

Disease Brain – Special Emphasis on PI3K-Akt Pathway. *Frontiers in Neuroscience*, *13*. https://doi.org/10.3389/fnins.2019.00629

Ghasemi, A., & Jeddi, S. (2023). Streptozotocin As a Tool for Induction of Rat Models of Diabetes: a Practical Guide. *EXCLI Journal*, *22*, 274–294. https://doi.org/10.17179/excli2022-5720

Gieroba, B., Kryska, A., & Sroka-Bartnicka, A. (2025). Type 2 diabetes mellitus – conventional therapies and future perspectives in innovative treatment. *Biochemistry and Biophysics Reports*, *42*, 102037. https://doi.org/10.1016/j.bbrep.2025.102037

Giglio, R. V., Lo Sasso, B., Agnello, L., Bivona, G., Maniscalco, R., Ligi, D., Mannello, F., & Ciaccio, M. (2020). Recent Updates and Advances in the Use of Glycated Albumin for the Diagnosis and Monitoring of Diabetes and Renal, Cerebro- and Cardio-Metabolic Diseases. *Journal of Clinical Medicine*, *9*(11), 3634. https://doi.org/10.3390/jcm9113634

González Olmo, B. M., Bettes, M. N., DeMarsh, J. W., Zhao, F., Askwith, C., & Barrientos, R. M. (2023). Short-term high-fat diet consumption impairs synaptic plasticity in the aged hippocampus via IL-1 signaling. *Npj Science of Food*, *7*(1), 35. https://doi.org/10.1038/s41538-023-00211-4

Graham, M. L., Janecek, J. L., Kittredge, J. A., Hering, B. J., & Schuurman, H.-J. (2011). The streptozotocin-induced diabetic nude mouse model: differences between animals from different sources. *Comparative Medicine*, *61*(4), 356–360. http://www.ncbi.nlm.nih.gov/pubmed/22330251

Graves, L. V, Moreno, C. C., Seewald, M., Holden, H. M., Van Etten, E. J., Uttarwar, V., McDonald, C. R., Delano-Wood, L., Bondi, M. W., Woods, S. P., Delis, D. C., & Gilbert, P. E. (2017). Effects of Age and Gender on Recall and Recognition Discriminability. *Archives of Clinical Neuropsychology*, *32*(8), 972–979. https://doi.org/10.1093/arclin/acx024

Grillo, C. A., Piroli, G. G., Hendry, R. M., & Reagan, L. P. (2009). Insulin-stimulated translocation of GLUT4 to the plasma membrane in rat hippocampus is PI3-kinase dependent. *Brain Research*, *1296*, 35–45. https://doi.org/10.1016/j.brainres.2009.08.005

Gudala, K., Bansal, D., Schifano, F., & Bhansali, A. (2013). Diabetes mellitus and risk of dementia: A meta-analysis of prospective observational studies. *Journal of Diabetes Investigation*, *4*(6), 640–650. https://doi.org/10.1111/jdi.12087

Guglielmi, C., Del Toro, R., Lauria, A., Maurizi, A. R., Fallucca, S., Cappelli, A., Angeletti, S., Lachin, J. M., & Pozzilli, P. (2017). Effect of GLP-1 and GIP on C-peptide secretion after glucagon or mixed meal tests: Significance in assessing B-cell function in diabetes. *Diabetes/Metabolism Research and Reviews*, *33*(6). https://doi.org/10.1002/dmrr.2899

Guthrie, R. A., & Guthrie, D. W. (2004). Pathophysiology of Diabetes Mellitus. *Critical Care Nursing Quarterly*, *27*(2), 113–125. https://doi.org/10.1097/00002727-200404000-00003

Hamzé, R., Delangre, E., Tolu, S., Moreau, M., Janel, N., Bailbé, D., & Movassat, J. (2022). Type 2 Diabetes Mellitus and Alzheimer's Disease: Shared Molecular Mechanisms and Potential Common Therapeutic Targets. *International Journal of Molecular Sciences*, *23*(23). https://doi.org/10.3390/ijms232315287

Harris, J. J., Jolivet, R., & Attwell, D. (2012). Synaptic Energy Use and Supply. *Neuron*, *75*(5), 762–777. https://doi.org/10.1016/j.neuron.2012.08.019

Heneka, M. T., Carson, M. J., Khoury, J. El, Landreth, G. E., Brosseron, F., Feinstein, D. L., Jacobs, A. H., Wyss-Coray, T., Vitorica, J., Ransohoff, R. M., Herrup, K., Frautschy, S. A., Finsen, B., Brown, G. C., Verkhratsky, A., Yamanaka, K., Koistinaho, J., Latz, E., Halle, A., … Kummer, M. P. (2015). Neuroinflammation in Alzheimer's disease. *The Lancet Neurology*, *14*(4), 388–405. https://doi.org/10.1016/S1474-4422(15)70016-5

Henn, R. E., Elzinga, S. E., Glass, E., Parent, R., Guo, K., Allouch, A. M., Mendelson, F. E., Hayes, J., Webber-Davis, I., Murphy, G. G., Hur, J., & Feldman, E. L. (2022). Obesity-induced neuroinflammation and cognitive impairment in young adult versus middle-aged mice. *Immunity & Ageing*, *19*(1), 67. https://doi.org/10.1186/s12979-022-00323-7

Heyward, F. D., Walton, R. G., Carle, M. S., Coleman, M. A., Garvey, W. T., & Sweatt, J. D. (2012). Adult mice maintained on a high-fat diet exhibit object location memory deficits and reduced hippocampal SIRT1 gene expression. *Neurobiology of Learning and Memory*, *98*(1), 25–32. https://doi.org/10.1016/j.nlm.2012.04.005

Huang, C.-C., Chung, C.-M., Leu, H.-B., Lin, L.-Y., Chiu, C.-C., Hsu, C.-Y., Chiang, C.-H., Huang, P.-H., Chen, T.-J., Lin, S.-J., Chen, J.-W., & Chan, W.-L. (2014). Diabetes Mellitus and the Risk of Alzheimer's Disease: A Nationwide Population-Based Study. *PLoS ONE*, *9*(1),

e87095. https://doi.org/10.1371/journal.pone.0087095

Hwang, I. K., Choi, J. H., Nam, S. M., Park, O. K., Yoo, D. Y., Kim, W., Yi, S. S., Won, M.-H., Seong, J. K., & Yoon, Y. S. (2014). Activation of microglia and induction of pro-inflammatory cytokines in the hippocampus of type 2 diabetic rats. *Neurological Research*, *36*(9), 824–832. https://doi.org/10.1179/1743132814Y.0000000330

Infante-Garcia, C., Ramos-Rodriguez, J. J., Galindo-Gonzalez, L., & Garcia-Alloza, M. (2016). Long-term central pathology and cognitive impairment are exacerbated in a mixed model of Alzheimer's disease and type 2 diabetes. *Psychoneuroendocrinology*, *65*, 15–25. https://doi.org/10.1016/j.psyneuen.2015.12.001

International Diabetes Federation. (2025). *IDF Diabetes Atlas* (11th ed.). International Diabetes Federation. https://diabetesatlas.org/

Jash, K., Gondaliya, P., Kirave, P., Kulkarni, B., Sunkaria, A., & Kalia, K. (2020). Cognitive dysfunction: A growing link between diabetes and Alzheimer's disease. *Drug Development Research*, *81*(2), 144–164. https://doi.org/10.1002/ddr.21579

Jeong, S., Lin, L., Leone, A.-P., & Hsu, Y.-H. (2025). Type 2 diabetes and late-onset Alzheimer's disease and related dementia: A longitudinal cohort study integrating polygenic risk score. *Journal of Alzheimer's Disease*, *105*(1), 107–119. https://doi.org/10.1177/13872877251326107

Ji, Z., Lu, M., Xie, H., Yuan, H., & Chen, Q. (2022). β cell regeneration and novel strategies for treatment of diabetes (Review). *Biomedical Reports*, *17*(3), 72. https://doi.org/10.3892/br.2022.1555

Jin, L., Lin, L., Li, G.-Y., Liu, S., Luo, D.-J., Feng, Q., Sun, D.-S., Wang, W., Liu, J.-J., Wang, Q., Ke, D., Yang, X.-F., & Liu, G.-P. (2018). Monosodium glutamate exposure during the neonatal period leads to cognitive deficits in adult Sprague-Dawley rats. *Neuroscience Letters*, *682*, 39–44. https://doi.org/10.1016/j.neulet.2018.06.008

Jung, C. H., Ro, S.-H., Cao, J., Otto, N. M., & Kim, D.-H. (2010). mTOR regulation of autophagy. *FEBS Letters*, *584*(7), 1287–1295. https://doi.org/10.1016/j.febslet.2010.01.017

Kaminsky, Y. G. (2015). Critical analysis of Alzheimer rsquo s amyloid-beta nbsp toxicity to mitochondria. *Frontiers in Bioscience*, *20*(1), 4304. https://doi.org/10.2741/4304

Kaneto, H., Matsuoka, T., Katakami, N., Kawamori, D., Miyatsuka, T.,

Yoshiuchi, K., Yasuda, T., Sakamoto, K., Yamasaki, Y., & Matsuhisa, M. (2007). Oxidative Stress and the JNK Pathway are Involved in the Development of Type 1 and Type 2 Diabetes. *Current Molecular Medicine*, *7*(7), 674–686. https://doi.org/10.2174/156652407782564408

Kassab, S., Begley, P., Church, S. J., Rotariu, S. M., Chevalier-Riffard, C., Dowsey, A. W., Phillips, A. M., Zeef, L. A. H., Grayson, B., Neill, J. C., Cooper, G. J. S., Unwin, R. D., & Gardiner, N. J. (2019). Cognitive dysfunction in diabetic rats is prevented by pyridoxamine treatment. A multidisciplinary investigation. *Molecular Metabolism*, *28*, 107–119. https://doi.org/10.1016/j.molmet.2019.08.003

Kciuk, M., Kruczkowska, W., Gałęziewska, J., Wanke, K., Kałuzińska-Kołat, Ż., Aleksandrowicz, M., & Kontek, R. (2024). Alzheimer's Disease as Type 3 Diabetes: Understanding the Link and Implications. *International Journal of Molecular Sciences*, *25*(22), 11955. https://doi.org/10.3390/ijms252211955

Kelaiditi, E., Cesari, M., Canevelli, M., Abellan van Kan, G., Ousset, P.-J., Gillette-Guyonnet, S., Ritz, P., Duveau, F., Soto, M. E., Provencher, V., Nourhashemi, F., Salva, A., Robert, P., Andrieu, S., Rolland, Y., Touchon, J., Fitten, J. L., & Vellas, B. (2013). Cognitive frailty: Rational and definition from an (I.A.N.A./I.A.G.G.) International Consensus Group. *The Journal of Nutrition, Health & Aging*, *17*(9), 726–734. https://doi.org/10.1007/s12603-013-0367-2

Kellar, D., & Craft, S. (2020). Brain insulin resistance in Alzheimer's disease and related disorders: mechanisms and therapeutic approaches. *The Lancet Neurology*, *19*(9), 758–766. https://doi.org/10.1016/S1474-4422(20)30231-3

Khin, P. P., Lee, J. H., & Jun, H.-S. (2023). Pancreatic Beta-cell Dysfunction in Type 2 Diabetes. *European Journal of Inflammation*, *21*. https://doi.org/10.1177/1721727X231154152

Kim, J., Kim, O. S., Kim, C.-S., Sohn, E., Jo, K., & Kim, J. S. (2012). Accumulation of argpyrimidine, a methylglyoxal-derived advanced glycation end product, increases apoptosis of lens epithelial cells both in vitro and in vivo. *Experimental & Molecular Medicine*, *44*(2), 167. https://doi.org/10.3858/emm.2012.44.2.012

Kimura, T., Ishiguro, K., & Hisanaga, S. (2014). Physiological and pathological phosphorylation of tau by Cdk5. *Frontiers in Molecular Neuroscience*, *7*. https://doi.org/10.3389/fnmol.2014.00065

Kleinridders, A., Cai, W., Cappellucci, L., Ghazarian, A., Collins, W. R., Vienberg, S. G., Pothos, E. N., & Kahn, C. R. (2015). Insulin resistance in brain alters dopamine turnover and causes behavioral disorders. *Proceedings of the National Academy of Sciences*, *112*(11), 3463–3468. https://doi.org/10.1073/pnas.1500877112

Kolb, H., Kempf, K., Röhling, M., & Martin, S. (2020). Insulin: too much of a good thing is bad. *BMC Medicine*, *18*(1), 224. https://doi.org/10.1186/s12916-020-01688-6

Kold-Christensen, R., & Johannsen, M. (2020). Methylglyoxal Metabolism and Aging-Related Disease: Moving from Correlation toward Causation. *Trends in Endocrinology & Metabolism*, *31*(2), 81–92. https://doi.org/10.1016/j.tem.2019.10.003

Kostka, M., Morys, J., Małecki, A., & Nowacka-Chmielewska, M. (2024). Muscle–brain crosstalk mediated by exercise-induced myokines - insights from experimental studies. *Frontiers in Physiology*, *15*. https://doi.org/10.3389/fphys.2024.1488375

Kubaszek, A., Pihlajamäki, J., Komarovski, V., Lindi, V., Lindström, J., Eriksson, J., Valle, T. T., Hämäläinen, H., Ilanne-Parikka, P., Keinänen-Kiukaanniemi, S., Tuomilehto, J., Uusitupa, M., & Laakso, M. (2003). Promoter Polymorphisms of the TNF-α (G-308A) and IL-6 (C-174G) Genes Predict the Conversion From Impaired Glucose Tolerance to Type 2 Diabetes. *Diabetes*, *52*(7), 1872–1876. https://doi.org/10.2337/diabetes.52.7.1872

Lai, P., Zhang, L., Qiu, Y., Ren, J., Sun, X., Zhang, T., Wang, L., Cheng, S., Liu, S., Zhuang, H., Lu, D., Zhang, S., Liang, H., & Chen, S. (2024). Heat stress reduces brown adipose tissue activity by exacerbating mitochondrial damage in type 2 diabetic mice. *Journal of Thermal Biology*, *119*, 103799. https://doi.org/10.1016/j.jtherbio.2024.103799

Le, T. N., Bright, R., Truong, V. K., Li, J., Juneja, R., & Vasilev, K. (2025). Key biomarkers in type 2 diabetes patients: A systematic review. *Diabetes, Obesity and Metabolism*, *27*(1), 7–22. https://doi.org/10.1111/dom.15991

Lee, A. W. S., & Cox, R. D. (2010). Use of mouse models in studying type 2 diabetes mellitus. *Expert Reviews in Molecular Medicine*, *12*, e40. https://doi.org/10.1017/S1462399410001729

Lee, O., Bruce, W. R., Dong, Q., Bruce, J., Mehta, R., & O'Brien, P. J. (2009). Fructose and carbonyl metabolites as endogenous toxins. *Chemico-*

*Biological Interactions*, *178*(1–3), 332–339. https://doi.org/10.1016/j.cbi.2008.10.011

Lee, S.-H., Park, S.-Y., & Choi, C. S. (2022). Insulin Resistance: From Mechanisms to Therapeutic Strategies. *Diabetes & Metabolism Journal*, *46*(1), 15–37. https://doi.org/10.4093/dmj.2021.0280

Leibson, C. L., Rocca, W. A., Hanson, V. A., Cha, R., Kokmen, E., O'Brien, P. C., & Palumbo, P. J. (1997). Risk of Dementia among Persons with Diabetes Mellitus: A Population-based Cohort Study. *American Journal of Epidemiology*, *145*(4), 301–308. https://doi.org/10.1093/oxfordjournals.aje.a009106

Li, L., & Hölscher, C. (2007). Common pathological processes in Alzheimer disease and type 2 diabetes: A review. *Brain Research Reviews*, *56*(2), 384–402. https://doi.org/10.1016/j.brainresrev.2007.09.001

Li, T., Cao, H., & Ke, D. (2021). Type 2 Diabetes Mellitus Easily Develops into Alzheimer's Disease via Hyperglycemia and Insulin Resistance. *Current Medical Science*, *41*(6), 1165–1171. https://doi.org/10.1007/s11596-021-2467-2

Li, X., Leng, S., & Song, D. (2015). Link between type 2 diabetes and Alzheimer’s disease: from epidemiology to mechanism and treatment. *Clinical Interventions in Aging*, 549. https://doi.org/10.2147/CIA.S74042

Li, Z., Muench, G., Wenhart, C., Goebel, S., & Reimann, A. (2022). Definition of a sectioning plane and place for a section containing hoped-for regions using a spare counterpart specimen. *Scientific Reports*, *12*(1), 13342. https://doi.org/10.1038/s41598-022-17380-z

Liao, X., Zhang, Y., Xu, J., Yin, J., Li, S., Dong, K., Shi, X., Xu, W., Ma, D., Chen, X., Yu, X., & Yang, Y. (2025). A Narrative Review on Cognitive Impairment in Type 2 Diabetes: Global Trends and Diagnostic Approaches. *Biomedicines*, *13*(2), 473. https://doi.org/10.3390/biomedicines13020473

Liu, J., Wang, R., Desai, K., & Wu, L. (2011). Upregulation of aldolase B and overproduction of methylglyoxal in vascular tissues from rats with metabolic syndrome. *Cardiovascular Research*, *92*(3), 494–503. https://doi.org/10.1093/cvr/cvr239

Liu, Q., Wang, Z., Cao, J., Dong, Y., & Chen, Y. (2022). The Role of Insulin Signaling in Hippocampal-Related Diseases: A Focus on Alzheimer's

Disease. *International Journal of Molecular Sciences*, *23*(22), 14417. https://doi.org/10.3390/ijms232214417

Liu, Y., Zhang, D., Yuan, J., Song, L., Zhang, C., Lin, Q., Li, M., Sheng, Z., Ma, Z., Lv, F., Gao, G., & Dong, J. (2020). Hyperbaric Oxygen Ameliorates Insulin Sensitivity by Increasing GLUT4 Expression in Skeletal Muscle and Stimulating UCP1 in Brown Adipose Tissue in T2DM Mice. *Frontiers in Endocrinology*, *11*. https://doi.org/10.3389/fendo.2020.00032

Longnecker, D. S. (2021). Anatomy and Histology of the Pancreas. *Pancreapedia*, *1*, 1–24. https://doi.org/10.3998/panc.2021.01

Lu, S., Xu, Q., Yu, J., Yang, Y., Wang, Z., Zhang, B., Wang, S., Chen, X., Zhang, Y., Zhu, X., & Hong, K. (2022). Prevalence and possible factors of cognitive frailty in the elderly with hypertension and diabetes. *Frontiers in Cardiovascular Medicine*, *9*. https://doi.org/10.3389/fcvm.2022.1054208

Lumeng, C. N., Bodzin, J. L., & Saltiel, A. R. (2007). Obesity induces a phenotypic switch in adipose tissue macrophage polarization. *Journal of Clinical Investigation*, *117*(1), 175–184. https://doi.org/10.1172/JCI29881

M. Di Battista, A., M. Heinsinger, N., & William Rebeck, G. (2016). Alzheimer's Disease Genetic Risk Factor APOE-ε4 Also Affects Normal Brain Function. *Current Alzheimer Research*, *13*(11), 1200–1207. https://doi.org/10.2174/1567205013666160401115127

Ma, L., Hu, Y., Alperet, D. J., Liu, G., Malik, V., Manson, J. E., Rimm, E. B., Hu, F. B., & Sun, Q. (2023). Beverage consumption and mortality among adults with type 2 diabetes: prospective cohort study. *BMJ*, e073406. https://doi.org/10.1136/bmj-2022-073406

Ma, Q., Li, Y., Wang, M., Tang, Z., Wang, T., Liu, C., Wang, C., & Zhao, B. (2018). Progress in Metabonomics of Type 2 Diabetes Mellitus. *Molecules*, *23*(7), 1834. https://doi.org/10.3390/molecules23071834

Maciejczyk, M., Żebrowska, E., & Chabowski, A. (2019). Insulin resistance and oxidative stress in the brain: What's new? *International Journal of Molecular Sciences*, *20*(4). https://doi.org/10.3390/ijms20040874

Maj, M., Hoermann, G., Rasul, S., Base, W., Wagner, L., & Attems, J. (2016). The Microtubule-Associated Protein Tau and Its Relevance for Pancreatic Beta Cells. *Journal of Diabetes Research*, *2016*, 1–12.

https://doi.org/10.1155/2016/1964634

Mandelkow, E.-M., Thies, E., Trinczek, B., Biernat, J., & Mandelkow, E. (2004). MARK/PAR1 kinase is a regulator of microtubule-dependent transport in axons. *Journal of Cell Biology*, *167*(1), 99–110. https://doi.org/10.1083/jcb.200401085

Marino, F., Salerno, N., Scalise, M., Salerno, L., Torella, A., Molinaro, C., Chiefalo, A., Filardo, A., Siracusa, C., Panuccio, G., Ferravante, C., Giurato, G., Rizzo, F., Torella, M., Donniacuo, M., De Angelis, A., Viglietto, G., Urbanek, K., Weisz, A., … Cianflone, E. (2023). Streptozotocin-Induced Type 1 and 2 Diabetes Mellitus Mouse Models Show Different Functional, Cellular and Molecular Patterns of Diabetic Cardiomyopathy. *International Journal of Molecular Sciences*, *24*(2), 1132. https://doi.org/10.3390/ijms24021132

Marušić, M., Paić, M., Knobloch, M., & Liberati Pršo, A.-M. (2021). NAFLD, Insulin Resistance, and Diabetes Mellitus Type 2. *Canadian Journal of Gastroenterology and Hepatology*, *2021*, 1–9. https://doi.org/10.1155/2021/6613827

Matthews, B. R. (2015). Memory Dysfunction. *Continuum*, *21*(3), 613–626. https://doi.org/10.1212/01.CON.0000466656.59413.29

McNay, E. C., & Pearson-Leary, J. (2020). GluT4: A central player in hippocampal memory and brain insulin resistance. *Experimental Neurology*, *323*, 113076. https://doi.org/10.1016/j.expneurol.2019.113076

Mehlhorn, G., Hollborn, M., & Schliebs, R. (2000). Induction of cytokines in glial cells surrounding cortical β-amyloid plaques in transgenic Tg2576 mice with Alzheimer pathology. *International Journal of Developmental Neuroscience*, *18*(4–5), 423–431. https://doi.org/10.1016/S0736-5748(00)00012-5

Meng, R., Zhu, D.-L., Bi, Y., Yang, D.-H., & Wang, Y.-P. (2010). Apocynin Improves Insulin Resistance through Suppressing Inflammation in High-Fat Diet-Induced Obese Mice. *Mediators of Inflammation*, *2010*, 1–9. https://doi.org/10.1155/2010/858735

Mergenthaler, P., Lindauer, U., Dienel, G. A., & Meisel, A. (2013). Sugar for the brain: the role of glucose in physiological and pathological brain function. *Trends in Neurosciences*, *36*(10), 587–597. https://doi.org/10.1016/j.tins.2013.07.001

Michailidis, M., Moraitou, D., Tata, D. A., Kalinderi, K., Papamitsou, T., & Papaliagkas, V. (2022). Alzheimer's Disease as Type 3 Diabetes: Common Pathophysiological Mechanisms between Alzheimer's Disease and Type 2 Diabetes. *International Journal of Molecular Sciences*, *23*(5). https://doi.org/10.3390/ijms23052687

Miklossy, J., Qing, H., Radenovic, A., Kis, A., Vileno, B., Làszló, F., Miller, L., Martins, R. N., Waeber, G., Mooser, V., Bosman, F., Khalili, K., Darbinian, N., & McGeer, P. L. (2010). Beta amyloid and hyperphosphorylated tau deposits in the pancreas in type 2 diabetes. *Neurobiology of Aging*, *31*(9), 1503–1515. https://doi.org/10.1016/j.neurobiolaging.2008.08.019

Mittal, K., & Katare, D. P. (2016). Shared links between type 2 diabetes mellitus and Alzheimer's disease: A review. *Diabetes & Metabolic Syndrome: Clinical Research & Reviews*, *10*(2), S144–S149. https://doi.org/10.1016/j.dsx.2016.01.021

Moreira, P. I. (2013). High-sugar diets, type 2 diabetes and Alzheimer's disease. *Current Opinion in Clinical Nutrition and Metabolic Care*, *16*(4), 440–445. https://doi.org/10.1097/MCO.0b013e328361c7d1

Moreira, P. I., Santos, M. S., Seiça, R., & Oliveira, C. R. (2007). Brain mitochondrial dysfunction as a link between Alzheimer's disease and diabetes. *Journal of the Neurological Sciences*, *257*(1–2), 206–214. https://doi.org/10.1016/j.jns.2007.01.017

Morgan, M. J., & Liu, Z. (2011). Crosstalk of reactive oxygen species and NF-κB signaling. *Cell Research*, *21*(1), 103–115. https://doi.org/10.1038/cr.2010.178

Mullins, R. J., Diehl, T. C., Chia, C. W., & Kapogiannis, D. (2017). Insulin Resistance as a Link between Amyloid-Beta and Tau Pathologies in Alzheimer's Disease. *Frontiers in Aging Neuroscience*, *9*. https://doi.org/10.3389/fnagi.2017.00118

Nagy, C., & Einwallner, E. (2018). Study of In Vivo Glucose Metabolism in High-fat Diet-fed Mice Using Oral Glucose Tolerance Test (OGTT) and Insulin Tolerance Test (ITT). *Journal of Visualized Experiments*, *131*. https://doi.org/10.3791/56672

Nday, C. M., Eleftheriadou, D., & Jackson, G. (2018). Shared pathological pathways of Alzheimer's disease with specific comorbidities: current perspectives and interventions. *Journal of Neurochemistry*, *144*(4), 360–389. https://doi.org/10.1111/jnc.14256

Negre-Salvayre, A., Salvayre, R., Augé, N., Pamplona, R., & Portero-Otín, M. (2009). Hyperglycemia and Glycation in Diabetic Complications. *Antioxidants & Redox Signaling*, *11*(12), 3071–3109. https://doi.org/10.1089/ars.2009.2484

Neth, B. J., & Craft, S. (2017). Insulin Resistance and Alzheimer's Disease: Bioenergetic Linkages. *Frontiers in Aging Neuroscience*, *9*. https://doi.org/10.3389/fnagi.2017.00345

Nguyen, T. T., Ta, Q. T. H., Nguyen, T. K. O., Nguyen, T. T. D., & Giau, V. Van. (2020). Type 3 diabetes and its role implications in alzheimer's disease. *International Journal of Molecular Sciences*, *21*(9), 1–16. https://doi.org/10.3390/ijms21093165

Nguyen, T. T., Ta, Q. T. H., Nguyen, T. K. O., Nguyen, T. T. D., & Van Giau, V. (2020). Type 3 Diabetes and Its Role Implications in Alzheimer's Disease. *International Journal of Molecular Sciences*, *21*(9), 3165. https://doi.org/10.3390/ijms21093165

Nowotny, K., Jung, T., Höhn, A., Weber, D., & Grune, T. (2015). Advanced glycation end products and oxidative stress in type 2 diabetes mellitus. *Biomolecules*, *5*(1), 194–222. https://doi.org/10.3390/biom5010194

Ogawa, S., Nakayama, K., Nakayama, M., Mori, T., Matsushima, M., Okamura, M., Senda, M., Nako, K., Miyata, T., & Ito, S. (2010). Methylglyoxal Is a Predictor in Type 2 Diabetic Patients of Intima-Media Thickening and Elevation of Blood Pressure. *Hypertension*, *56*(3), 471–476. https://doi.org/10.1161/HYPERTENSIONAHA.110.156786

Oliveira, A. L., de Oliveira, M. G., Mónica, F. Z., & Antunes, E. (2024). Methylglyoxal and Advanced Glycation End Products (AGEs): Targets for the Prevention and Treatment of Diabetes-Associated Bladder Dysfunction? *Biomedicines*, *12*(5), 939. https://doi.org/10.3390/biomedicines12050939

Ong, K. L., Stafford, L. K., McLaughlin, S. A., Boyko, E. J., Vollset, S. E., Smith, A. E., Dalton, B. E., Duprey, J., Cruz, J. A., Hagins, H., Lindstedt, P. A., Aali, A., Abate, Y. H., Abate, M. D., Abbasian, M., Abbasi-Kangevari, Z., Abbasi-Kangevari, M., Abd ElHafeez, S., Abd-Rabu, R., … Vos, T. (2023). Global, regional, and national burden of diabetes from 1990 to 2021, with projections of prevalence to 2050: a systematic analysis for the Global Burden of Disease Study 2021. *The Lancet*, *402*(10397), 203–234. https://doi.org/10.1016/S0140-6736(23)01301-6

Ott, V., Benedict, C., Schultes, B., Born, J., & Hallschmid, M. (2012).

Intranasal administration of insulin to the brain impacts cognitive function and peripheral metabolism. *Diabetes, Obesity and Metabolism*, *14*(3), 214–221. https://doi.org/10.1111/j.1463-1326.2011.01490.x

Ouchi, N., Parker, J. L., Lugus, J. J., & Walsh, K. (2011). Adipokines in inflammation and metabolic disease. *Nature Reviews Immunology*, *11*(2), 85–97. https://doi.org/10.1038/nri2921

Palliyaguru, D. L., Moats, J. M., Di Germanio, C., Bernier, M., & de Cabo, R. (2019). Frailty index as a biomarker of lifespan and healthspan: Focus on pharmacological interventions. *Mechanisms of Ageing and Development*, *180*, 42–48. https://doi.org/10.1016/j.mad.2019.03.005

Parks, R. J., Fares, E., MacDonald, J. K., Ernst, M. C., Sinal, C. J., Rockwood, K., & Howlett, S. E. (2012). A Procedure for Creating a Frailty Index Based on Deficit Accumulation in Aging Mice. *The Journals of Gerontology: Series A*, *67A*(3), 217–227. https://doi.org/10.1093/gerona/glr193

Patel, S. S., Gupta, S., & Udayabanu, M. (2016). Urtica dioica modulates hippocampal insulin signaling and recognition memory deficit in streptozotocin induced diabetic mice. *Metabolic Brain Disease*, *31*(3), 601–611. https://doi.org/10.1007/s11011-016-9791-4

Patel, S., & Santani, D. (2009). Role of NF-κB in the pathogenesis of diabetes and its associated complications. *Pharmacological Reports*, *61*(4), 595–603. https://doi.org/10.1016/S1734-1140(09)70111-2

Pavlovic, S., Petrovic, I., Jovicic, N., Ljujic, B., Miletic Kovacevic, M., Arsenijevic, N., & Lukic, M. L. (2018). IL-33 Prevents MLD-STZ Induction of Diabetes and Attenuate Insulitis in Prediabetic NOD Mice. *Frontiers in Immunology*, *9*. https://doi.org/10.3389/fimmu.2018.02646

Pedersen, B. K. (2019). Physical activity and muscle–brain crosstalk. *Nature Reviews Endocrinology*, *15*(7), 383–392. https://doi.org/10.1038/s41574-019-0174-x

Pejnovic, N. N., Pantic, J. M., Jovanovic, I. P., Radosavljevic, G. D., Milovanovic, M. Z., Nikolic, I. G., Zdravkovic, N. S., Djukic, A. L., Arsenijevic, N. N., & Lukic, M. L. (2013). Galectin-3 Deficiency Accelerates High-Fat Diet–Induced Obesity and Amplifies Inflammation in Adipose Tissue and Pancreatic Islets. *Diabetes*, *62*(6), 1932–1944. https://doi.org/10.2337/db12-0222

Peng, L., Fang, X., Xu, F., Liu, S., Qian, Y., Gong, X., Zhao, X., Ma, Z., Xia,

T., & Gu, X. (2021). Amelioration of Hippocampal Insulin Resistance Reduces Tau Hyperphosphorylation and Cognitive Decline Induced by Isoflurane in Mice. *Frontiers in Aging Neuroscience*, *13*. https://doi.org/10.3389/fnagi.2021.686506

Piggott, D. A., & Tuddenham, S. (2020). The gut microbiome and frailty. *Translational Research*, *221*, 23–43. https://doi.org/10.1016/j.trsl.2020.03.012

Pinto-Junior, D. C., Silva, K. S., Michalani, M. L., Yonamine, C. Y., Esteves, J. V., Fabre, N. T., Thieme, K., Catanozi, S., Okamoto, M. M., Seraphim, P. M., Corrêa-Giannella, M. L., Passarelli, M., & Machado, U. F. (2018). Advanced glycation end products-induced insulin resistance involves repression of skeletal muscle GLUT4 expression. *Scientific Reports*, *8*(1), 8109. https://doi.org/10.1038/s41598-018-26482-6

Piuri, G., Basello, K., Rossi, G., Soldavini, C. M., Duiella, S., Privitera, G., Spadafranca, A., Costanzi, A., Tognon, E., Cappelletti, M., Corsetto, P. A., Rizzo, A. M., Speciani, A. F., & Ferrazzi, E. (2020). Methylglyoxal, Glycated Albumin, PAF, and TNF-α: Possible Inflammatory and Metabolic Biomarkers for Management of Gestational Diabetes. *Nutrients*, *12*(2), 479. https://doi.org/10.3390/nu12020479

Pliszka, M., & Szablewski, L. (2024). Associations between Diabetes Mellitus and Selected Cancers. *International Journal of Molecular Sciences*, *25*(13), 7476. https://doi.org/10.3390/ijms25137476

Ponce-Lopez, T. (2025). Peripheral Inflammation and Insulin Resistance: Their Impact on Blood–Brain Barrier Integrity and Glia Activation in Alzheimer's Disease. *International Journal of Molecular Sciences*, *26*(9), 4209. https://doi.org/10.3390/ijms26094209

Qu, Z., Jiao, Z., Sun, X., Zhao, Y., Ren, J., & Xu, G. (2011). Effects of streptozotocin-induced diabetes on tau phosphorylation in the rat brain. *Brain Research*, *1383*, 300–306. https://doi.org/10.1016/j.brainres.2011.01.084

Rabbani, N., Xue, M., & Thornalley, P. J. (2016). Methylglyoxal-induced dicarbonyl stress in aging and disease: first steps towards glyoxalase 1-based treatments. *Clinical Science*, *130*(19), 1677–1696. https://doi.org/10.1042/CS20160025

Raghav, A., & Ahmad, J. (2014). Glycated serum albumin: A potential disease marker and an intermediate index of diabetes control. *Diabetes & Metabolic Syndrome: Clinical Research & Reviews*, *8*(4), 245–251.

https://doi.org/10.1016/j.dsx.2014.09.017

Rahman, M. S., Hossain, K. S., Das, S., Kundu, S., Adegoke, E. O., Rahman, M. A., Hannan, M. A., Uddin, M. J., & Pang, M.-G. (2021). Role of Insulin in Health and Disease: An Update. *International Journal of Molecular Sciences*, *22*(12), 6403. https://doi.org/10.3390/ijms22126403

Rajmohan, R., & Reddy, P. H. (2017). Amyloid-Beta and Phosphorylated Tau Accumulations Cause Abnormalities at Synapses of Alzheimer's disease Neurons. *Journal of Alzheimer's Disease*, *57*(4), 975–999. https://doi.org/10.3233/JAD-160612

Ramos-Rodriguez, J. J., Ortiz, O., Jimenez-Palomares, M., Kay, K. R., Berrocoso, E., Murillo-Carretero, M. I., Perdomo, G., Spires-Jones, T., Cozar-Castellano, I., Lechuga-Sancho, A. M., & Garcia-Alloza, M. (2013). Differential central pathology and cognitive impairment in pre-diabetic and diabetic mice. *Psychoneuroendocrinology*, *38*(11), 2462–2475. https://doi.org/10.1016/j.psyneuen.2013.05.010

Rao, Y. L., Ganaraja, B., Murlimanju, B. V., Joy, T., Krishnamurthy, A., & Agrawal, A. (2022). Hippocampus and its involvement in Alzheimer's disease: a review. *3 Biotech*, *12*(2), 55. https://doi.org/10.1007/s13205-022-03123-4

Ratto, D., Corana, F., Mannucci, B., Priori, E. C., Cobelli, F., Roda, E., Ferrari, B., Occhinegro, A., Di Iorio, C., De Luca, F., Cesaroni, V., Girometta, C., Bottone, M. G., Savino, E., Kawagishi, H., & Rossi, P. (2019). Hericium erinaceus improves recognition memory and induces hippocampal and cerebellar neurogenesis in frail mice during aging. *Nutrients*, *11*(4). https://doi.org/10.3390/nu11040715

Reddy, P. H., & Beal, M. F. (2008). Amyloid beta, mitochondrial dysfunction and synaptic damage: implications for cognitive decline in aging and Alzheimer's disease. *Trends in Molecular Medicine*, *14*(2), 45–53. https://doi.org/10.1016/j.molmed.2007.12.002

Rees, D. A., & Alcolado, J. C. (2005). Animal models of diabetes mellitus. *Diabetic Medicine*, *22*(4), 359–370. https://doi.org/10.1111/j.1464-5491.2005.01499.x

Rhodes, S., Greene, N. R., & Naveh-Benjamin, M. (2019). Age-related differences in recall and recognition: a meta-analysis. *Psychonomic Bulletin & Review*, *26*(5), 1529–1547. https://doi.org/10.3758/s13423-019-01649-y

Robertson, D. A., Savva, G. M., & Kenny, R. A. (2013). Frailty and cognitive impairment—A review of the evidence and causal mechanisms. *Ageing Research Reviews*, *12*(4), 840–851. https://doi.org/10.1016/j.arr.2013.06.004

Rockwood, K., Blodgett, J. M., Theou, O., Sun, M. H., Feridooni, H. A., Mitnitski, A., Rose, R. A., Godin, J., Gregson, E., & Howlett, S. E. (2017). A Frailty Index Based On Deficit Accumulation Quantifies Mortality Risk in Humans and in Mice. *Scientific Reports*, *7*(1), 43068. https://doi.org/10.1038/srep43068

Roda, E, Bottone, M., Biggiogera, M., Milanesi, G., & Coccini, T. (2019). Pulmonary and hepatic effects after low dose exposure to nanosilver: Early and long-lasting histological and ultrastructural alterations in rat. *Toxicology Reports*, *6*, 1047–1060. https://doi.org/10.1016/j.toxrep.2019.09.008

Roda, Elisa, De Luca, F., Ratto, D., Priori, E. C., Savino, E., Bottone, M. G., & Rossi, P. (2023). Cognitive Healthy Aging in Mice: Boosting Memory by an Ergothioneine-Rich Hericium erinaceus Primordium Extract. *Biology*, *12*(2), 196. https://doi.org/10.3390/biology12020196

Rossi, P., Cesaroni, V., Brandalise, F., Occhinegro, A., Ratto, D., Perrucci, F., Lanaia, V., Girometta, C., Orrù, G., & Savino, E. (2018). Dietary Supplementation of Lion's Mane Medicinal Mushroom, Hericium erinaceus (Agaricomycetes), and Spatial Memory in Wild-Type Mice. *International Journal of Medicinal Mushrooms*, *20*(5), 485–494. https://doi.org/10.1615/IntJMedMushrooms.2018026241

Rulifson, E. J., Kim, S. K., & Nusse, R. (2002). Ablation of Insulin-Producing Neurons in Flies: Growth and Diabetic Phenotypes. *Science*, *296*(5570), 1118–1120. https://doi.org/10.1126/science.1070058

Sacha, J., Sacha, M., Soboń, J., Borysiuk, Z., & Feusette, P. (2017). Is It Time to Begin a Public Campaign Concerning Frailty and Pre-frailty? A Review Article. *Frontiers in Physiology*, *8*. https://doi.org/10.3389/fphys.2017.00484

Saito, Y., Tanaka, Y., Aita, Y., Ishii, K., Ikeda, T., Isobe, K., Kawakami, Y., Shimano, H., Hara, H., & Takekoshi, K. (2012). Sunitinib induces apoptosis in pheochromocytoma tumor cells by inhibiting VEGFR2/Akt/mTOR/S6K1 pathways through modulation of Bcl-2 and BAD. *American Journal of Physiology-Endocrinology and Metabolism*, *302*(6), E615–E625. https://doi.org/10.1152/ajpendo.00035.2011

Santiago, J. A., Karthikeyan, M., Lackey, M., Villavicencio, D., & Potashkin, J. A. (2023). Diabetes: a tipping point in neurodegenerative diseases. *Trends in Molecular Medicine*, *29*(12), 1029–1044. https://doi.org/10.1016/j.molmed.2023.09.005

Sayas, C. L., & Ávila, J. (2021). GSK-3 and Tau: A Key Duet in Alzheimer's Disease. *Cells*, *10*(4), 721. https://doi.org/10.3390/cells10040721

Schalkwijk, C., Brouwers, O., & Stehouwer, C. (2008). Modulation of Insulin Action by Advanced Glycation Endproducts: A New Player in the Field. *Hormone and Metabolic Research*, *40*(09), 614–619. https://doi.org/10.1055/s-0028-1082085

Schalkwijk, C. G., & Stehouwer, C. D. A. (2020). Methylglyoxal, a Highly Reactive Dicarbonyl Compound, in Diabetes, Its Vascular Complications, and Other Age-Related Diseases. *Physiological Reviews*, *100*(1), 407–461. https://doi.org/10.1152/physrev.00001.2019

Sędzikowska, A., & Szablewski, L. (2021). Insulin and insulin resistance in alzheimer's disease. *International Journal of Molecular Sciences*, *22*(18). https://doi.org/10.3390/ijms22189987

Shahedi, F., Munggela Foma, A., Mahmoudi-Aznaveh, A., Mazlomi, M. A., Azizi, Z., & Khorramizadeh, M. R. (2024). Differentiation of Pancreatic Beta Cells: Dual Acting of Inflammatory Factors. *Current Stem Cell Research & Therapy*, *19*(6), 832–839. https://doi.org/10.2174/1574888X18666230504093649

Shieh, J. C. C., Huang, P. T., & Lin, Y. F. (2020). Alzheimer's Disease and Diabetes: Insulin Signaling as the Bridge Linking Two Pathologies. *Molecular Neurobiology*, *57*(4), 1966–1977. https://doi.org/10.1007/s12035-019-01858-5

Shukla, V., Mishra, S. K., & Pant, H. C. (2011). Oxidative Stress in Neurodegeneration. *Advances in Pharmacological Sciences*, *2011*, 1–13. https://doi.org/10.1155/2011/572634

Simon, K., & Wittmann, I. (2019). Can blood glucose value really be referred to as a metabolic parameter? *Reviews in Endocrine and Metabolic Disorders*, *20*(2), 151–160. https://doi.org/10.1007/s11154-019-09504-0

Sims-Robinson, C., Kim, B., Rosko, A., & Feldman, E. L. (2010). How does diabetes accelerate Alzheimer disease pathology? *Nature Reviews Neurology*, *6*(10), 551–559. https://doi.org/10.1038/nrneurol.2010.130

Singh, R., Barden, A., Mori, T., & Beilin, L. (2001). Advanced glycation end-

products: a review. *Diabetologia*, *44*(2), 129–146. https://doi.org/10.1007/s001250051591

Squire, L. R., & Dede, A. J. O. (2015). Conscious and Unconscious Memory Systems. *Cold Spring Harbor Perspectives in Biology*, *7*(3), a021667. https://doi.org/10.1101/cshperspect.a021667

Stanciu, G. D., Bild, V., Ababei, D. C., Rusu, R. N., Cobzaru, A., Paduraru, L., & Bulea, D. (2020). Link between Diabetes and Alzheimer's Disease Due to the Shared Amyloid Aggregation and Deposition Involving Both Neurodegenerative Changes and Neurovascular Damages. *Journal of Clinical Medicine*, *9*(6), 1713. https://doi.org/10.3390/jcm9061713

Stott, N. L., & Marino, J. S. (2020). High Fat Rodent Models of Type 2 Diabetes: From Rodent to Human. *Nutrients*, *12*(12), 3650. https://doi.org/10.3390/nu12123650

Sutkowska, E., Fecka, I., Marciniak, D., Bednarska, K., Sutkowska, M., & Hap, K. (2023). Analysis of Methylglyoxal Concentration in a Group of Patients with Newly Diagnosed Prediabetes. *Biomedicines*, *11*(11), 2968. https://doi.org/10.3390/biomedicines11112968

Szablewski, L. (2024). Insulin Resistance: The Increased Risk of Cancers. *Current Oncology*, *31*(2), 998–1027. https://doi.org/10.3390/curroncol31020075

Tan, D., Wang, Y., Lo, C., Sang, S., & Ho, C. (2008). Methylglyoxal: Its Presence in Beverages and Potential Scavengers. *Annals of the New York Academy of Sciences*, *1126*(1), 72–75. https://doi.org/10.1196/annals.1433.027

Tomlinson, J. W., Finney, J., Gay, C., Hughes, B. A., Hughes, S. V., & Stewart, P. M. (2008). Impaired Glucose Tolerance and Insulin Resistance Are Associated With Increased Adipose 11β-Hydroxysteroid Dehydrogenase Type 1 Expression and Elevated Hepatic 5α-Reductase Activity. *Diabetes*, *57*(10), 2652–2660. https://doi.org/10.2337/db08-0495

Tosur, M., Onengut-Gumuscu, S., & Redondo, M. J. (2025). Type 1 Diabetes Genetic Risk Scores: History, Application and Future Directions. *Current Diabetes Reports*, *25*(1), 22. https://doi.org/10.1007/s11892-025-01575-5

Tsalamandris, S., Antonopoulos, A. S., Oikonomou, E., Papamikroulis, G.-A., Vogiatzi, G., Papaioannou, S., Deftereos, S., & Tousoulis, D. (2019). The

Role of Inflammation in Diabetes: Current Concepts and Future Perspectives. *European Cardiology Review*, *14*(1), 50–59. https://doi.org/10.15420/ecr.2018.33.1

Valko, M., Leibfritz, D., Moncol, J., Cronin, M. T. D., Mazur, M., & Telser, J. (2007). Free radicals and antioxidants in normal physiological functions and human disease. *The International Journal of Biochemistry & Cell Biology*, *39*(1), 44–84. https://doi.org/10.1016/j.biocel.2006.07.001

Venuti, M. T., Roda, E., Brandalise, F., Sarkar, M., Cappelletti, M., Speciani, A. F., Soffientini, I., Priori, E. C., Giammello, F., Ratto, D., Locatelli, C. A., & Rossi, P. (2025). A pathophysiological intersection between metabolic biomarkers and memory: a longitudinal study in the STZ-induced diabetic mouse model. *Frontiers in Physiology*, *16*. https://doi.org/10.3389/fphys.2025.1455434

Verdile, G., Keane, K. N., Cruzat, V. F., Medic, S., Sabale, M., Rowles, J., Wijesekara, N., Martins, R. N., Fraser, P. E., & Newsholme, P. (2015). Inflammation and Oxidative Stress: The Molecular Connectivity between Insulin Resistance, Obesity, and Alzheimer's Disease. *Mediators of Inflammation*, *2015*(1). https://doi.org/10.1155/2015/105828

Vilela, W. R., Bellozi, P. M. Q., Picolo, V. L., Cavadas, B. N., Marques, K. V. S., Pereira, L. T. G., Guirao, A. R. de Y., Amato, A. A., Magalhães, K. G., Mortari, M. R., Medei, E. H., Goulart, J. T., & de Bem, A. F. (2023). Early-life metabolic dysfunction impairs cognition and mitochondrial function in mice. *The Journal of Nutritional Biochemistry*, *117*, 109352. https://doi.org/10.1016/j.jnutbio.2023.109352

Villegas-Valverde, C., Kokuina, E., & Breff-Fonseca, M. (2018). Strengthening National Health Priorities for Diabetes Prevention and Management. *MEDICC Review*, *20*(4), 5. https://doi.org/10.37757/MR2018.V20.N4.2

Wang, J., Gu, B. J., Masters, C. L., & Wang, Y. J. (2017). A systemic view of Alzheimer disease - Insights from amyloid-β metabolism beyond the brain. *Nature Reviews Neurology*, *13*(10), 612–623. https://doi.org/10.1038/nrneurol.2017.111

Wang, M., Yang, Y., & Liao, Z. (2020). Diabetes and cancer: Epidemiological and biological links. *World Journal of Diabetes*, *11*(6), 227–238. https://doi.org/10.4239/wjd.v11.i6.227

Wei, Z., Koya, J., & Reznik, S. E. (2021). Insulin Resistance Exacerbates Alzheimer Disease via Multiple Mechanisms. *Frontiers in Neuroscience*, *15*(July), 1–10. https://doi.org/10.3389/fnins.2021.687157

Wium-Andersen, I. K., Rungby, J., Jørgensen, M. B., Sandbæk, A., Osler, M., & Wium-Andersen, M. K. (2020). Risk of dementia and cognitive dysfunction in individuals with diabetes or elevated blood glucose. *Epidemiology and Psychiatric Sciences*, *29*, e43. https://doi.org/10.1017/S2045796019000374

World Health Organization. (2018). *Diabetes*.

Wu, K. K., & Huan, Y. (2008). Streptozotocin-Induced Diabetic Models in Mice and Rats. *Current Protocols in Pharmacology*, *40*(1). https://doi.org/10.1002/0471141755.ph0547s40

Wu, W.-C., Ma, W.-Y., Wei, J.-N., Yu, T.-Y., Lin, M.-S., Shih, S.-R., Hua, C.-H., Liao, Y.-J., Chuang, L.-M., & Li, H.-Y. (2016). Serum Glycated Albumin to Guide the Diagnosis of Diabetes Mellitus. *PLOS ONE*, *11*(1), e0146780. https://doi.org/10.1371/journal.pone.0146780

Yadav, Y., & Dey, C. S. (2022). Ser/Thr phosphatases: One of the key regulators of insulin signaling. *Reviews in Endocrine and Metabolic Disorders*, *23*(5), 905–917. https://doi.org/10.1007/s11154-022-09727-8

Yamagishi, S., Maeda, S., Matsui, T., Ueda, S., Fukami, K., & Okuda, S. (2012). Role of advanced glycation end products (AGEs) and oxidative stress in vascular complications in diabetes. *Biochimica et Biophysica Acta (BBA) - General Subjects*, *1820*(5), 663–671. https://doi.org/10.1016/j.bbagen.2011.03.014

Yang, Q., Zhang, Z., Gregg, E. W., Flanders, W. D., Merritt, R., & Hu, F. B. (2014). Added Sugar Intake and Cardiovascular Diseases Mortality Among US Adults. *JAMA Internal Medicine*, *174*(4), 516. https://doi.org/10.1001/jamainternmed.2013.13563

Yari, Z., Behrouz, V., Zand, H., & Pourvali, K. (2020). New Insight into Diabetes Management: From Glycemic Index to Dietary Insulin Index. *Current Diabetes Reviews*, *16*(4), 293–300. https://doi.org/10.2174/1573399815666190614122626

Yin, D., Tao, J., Lee, D. D., Shen, J., Hara, M., Lopez, J., Kuznetsov, A., Philipson, L. H., & Chong, A. S. (2006). Recovery of Islet β-Cell Function in Streptozotocin- Induced Diabetic Mice. *Diabetes*, *55*(12), 3256–3263. https://doi.org/10.2337/db05-1275

Yu, J. H., Han, K., Park, S., Cho, H., Lee, D. Y., Kim, J.-W., Seo, J. A., Kim, S. G., Baik, S. H., Park, Y. G., Choi, K. M., Kim, S. M., & Kim, N. H. (2020). Incidence and Risk Factors for Dementia in Type 2 Diabetes Mellitus: A Nationwide Population-Based Study in Korea. *Diabetes & Metabolism Journal*, *44*(1), 113. https://doi.org/10.4093/dmj.2018.0216

Yu, X., He, H., Wen, J., Xu, X., Ruan, Z., Hu, R., Wang, F., & Ju, H. (2025). Diabetes-related cognitive impairment: Mechanisms, symptoms, and treatments. *Open Medicine*, *20*(1). https://doi.org/10.1515/med-2024-1091

Yung, J. H. M., & Giacca, A. (2020). Role of c-Jun N-terminal Kinase (JNK) in Obesity and Type 2 Diabetes. *Cells*, *9*(3), 706. https://doi.org/10.3390/cells9030706

Zendjabil, M. (2020). Glycated albumin. *Clinica Chimica Acta*, *502*, 240–244. https://doi.org/10.1016/j.cca.2019.11.007

Zhao, J., Liu, X., Xia, W., Zhang, Y., & Wang, C. (2020). Targeting Amyloidogenic Processing of APP in Alzheimer's Disease. *Frontiers in Molecular Neuroscience*, *13*. https://doi.org/10.3389/fnmol.2020.00137

Zhao, W.-Q., & Townsend, M. (2009). Insulin resistance and amyloidogenesis as common molecular foundation for type 2 diabetes and Alzheimer's disease. *Biochimica et Biophysica Acta (BBA) - Molecular Basis of Disease*, *1792*(5), 482–496. https://doi.org/10.1016/j.bbadis.2008.10.014

Zhao, W., De Felice, F. G., Fernandez, S., Chen, H., Lambert, M. P., Quon, M. J., Krafft, G. A., & Klein, W. L. (2008). Amyloid beta oligomers induce impairment of neuronal insulin receptors. *The FASEB Journal*, *22*(1), 246–260. https://doi.org/10.1096/fj.06-7703com

Zhuang, H., Yao, X., Li, H., Li, Q., Yang, C., Wang, C., Xu, D., Xiao, Y., Gao, Y., Gao, J., Bi, M., Liu, R., Teng, G., & Liu, L. (2022). Long-term high-fat diet consumption by mice throughout adulthood induces neurobehavioral alterations and hippocampal neuronal remodeling accompanied by augmented microglial lipid accumulation. *Brain, Behavior, and Immunity*, *100*, 155–171. https://doi.org/10.1016/j.bbi.2021.11.018

## 10. Acknowledgments

I would like to express my heartfelt gratitude to all those who have contributed to the development and completion of this work.

First and foremost, I am deeply thankful to my supervisors, Prof. Paola Rossi and Prof. Maria Grazia Bottone, for welcoming me into their laboratories and for their constant support of my research activities. I am especially grateful to Prof. Rossi for her invaluable guidance, corrections, and suggestions, and for supporting my academic training from the very beginning.

I would also like to thank GEK Lab S.r.l. and SMA Center S.r.l. in Milan, and in particular to Dr. Attilio Speciani, Dr. Mattia Cappelletti, and Dr. Michela Speciani, for their collaboration, their warm welcome, and for giving me the opportunity to enrich my training within their professional environment.

A very special thanks goes to Prof. Elisa Roda and Dr. Federico Brandalise for their support, both on a scientific and personal level.

I would also like to thank my fellow PhD colleagues, with whom I shared this entire journey, together with laughter, challenges, and moments of relief. I am equally thankful to my laboratory colleagues, with whom I shared meals, crossword puzzles, and countless laughs, as well as difficult times. Thank you for supporting me and for putting up with me. I will miss you all, darlings.

I am deeply grateful to all my friends, the ones I met in Pavia and those who have been with me throughout my life. Your presence and encouragement have made this journey lighter and more joyful.

Finally, I would like to express my deepest gratitude to my family for always being there to help and support me, even from far away. A special acknowledgement goes to my beloved grandmother, who taught me to be determined, resilient, and always to stay positive.

Last but not least, I would like to thank my boyfriend Peppe and my dog Pepe, for always being by my side and facing this long journey together with me. Thank you for supporting every decision I have made and for always being there. I could not have done this without you.

# 11. List of original manuscripts



## AUTOMATIC COMPUTATION OF THE GLYCEMIC INDEX: DATA DRIVEN ANALYSIS OF THE GLUCOSE STANDARD

FABIO CREDALI †, MARIA TERESA VENUTI †, DANIELE BOFFI, AND PAOLA ROSSI

ABSTRACT. The Glycemic Index (GI) is a tool for classifying carbohydrates based on their impact on postprandial glycemia, useful for diabetes prevention and management. This study applies a mathematical model for a data driven simulation of the glycemic response following glucose ingestion. The analysis reveals a direct correlation between glucose response profiles and parameters describing glucose absorption, enabling the classification of subjects into three groups based on the timing of their glycemic peak. Our results offer potential applications for both glycemic index simulation and advancing biological studies on diabetes.

**Keywords:** glycemic index, data driven analysis, glucose-insulin system, ODEs.

**2020 Mathematics Subject Classification:** 92B05, 92C30, 92C42.

### 1. INTRODUCTION

Diabetes is a major global health concern, with 589 million adults (20-79 years) affected and 3.4 million deaths reported in 2024 by the International Diabetes Federation (IDF). The total number of people living with diabetes is predicted to rise to 853 million by 2050 [4]. The 90% of these cases are type 2 diabetes (T2DM), making it the predominant form of the disease worldwide [2, 3].

T2DM is characterized by peripheral insulin resistance and progressive pancreatic $\beta-$cell dysfunction, resulting in chronic hyperglycemia. Due to its insidious and often asymptomatic onset, T2DM is frequently diagnosed at a late stage, increasing the likelihood of complications at the time of diagnosis [22, 26]. The etiology of T2DM is multifactorial, involving a combination of genetic predisposition and environmental factors. Major risk factors include excess body weight, advancing age, certain ethnic backgrounds, and a family history of diabetes. Effective management relies on comprehensive lifestyle modification, emphasizing a balanced diet, regular physical activity, weight management, and smoking cessation. When lifestyle changes alone are insufficient to maintain glycemic control, pharmacological intervention is introduced, with metformin serving as the standard first-line therapy [4].

Lifestyle interventions are effective in preventing or delaying T2DM progression [41, 27, 35]. Scientific consensus highlights the impact of dietary choices on T2DM risk, with high glycemic index/load (GI/GL) diets potentially contributing to disease onset, though causality remains uncertain. The concept of GI was introduced in 1981 to classify carbohydrates based on their effect on postprandial glycemia [25]. It represents the blood glucose response of a 50-gram carbohydrate portion of food, expressed as a percentage of the same amount of carbohydrate from a reference food (usually pure glucose). The GI ranks the glycemic potential of carbohydrates in different food. Various factors influence GI, including carbohydrate type, starch properties, food processing,

† These authors contributed equally to this work.

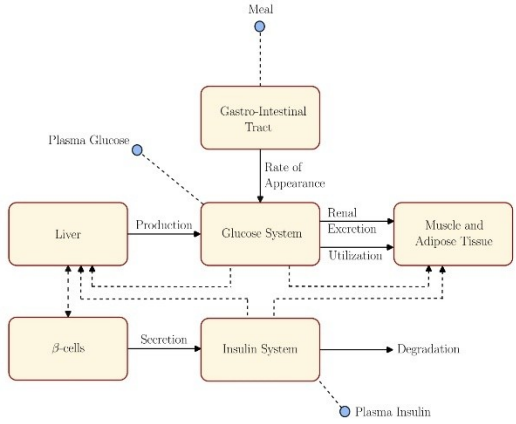


FIGURE 1. Representation of the Dalla Man–Rizza–Cobelli model with six compartments (yellow boxes) and their relations.

estimation. The results and the related discussion are then collected in Section 4. Finally, in Section 5, we draw some conclusions and mention future advancements.

## 2. Model of the glucose–insulin system

We consider the Dalla Man–Rizza–Cobelli model of the glucose-insulin system introduced in [19]. The biological system is described by several ordinary differential equations grouped into six compartments, representing the process of digestion. Such compartments are the gastrointestinal tract, the liver, the glucose absorption system, the muscle and adipose tissues, the pancreas ($\beta-$cells), and the insulin kinetics. A schematic representation of the compartments, together with their interplay, is shown in Figure 1. We now recall all the governing equations and the meaning of all involved variables and biological parameters.

### 2.1. **Glucose subsystem.**

The glucose subsystem consists of two equations describing the evolution of glucose masses in plasma and rapidly equilibrating tissues $G_p$ (mg/kg) and in slowly

equilibrating tissues $G_{\mathrm{t}}$ (mg/kg)

$$(1)\quad \begin{cases} \dot{G}_{\mathrm{p}}(t) = EGP(t) + Ra(t) - U_{\mathrm{ii}}(t) - E(t) - k_1 \cdot G_{\mathrm{p}}(t) + k_2 \cdot G_{\mathrm{t}}(t) & G_{\mathrm{p}}(0) = G_{\mathrm{p}b} \\ \dot{G}_{\mathrm{t}}(t) = -U_{\mathrm{id}}(t) + k_1 \cdot G_{\mathrm{p}}(t) - k_2 \cdot G_{\mathrm{t}}(t) & G_{\mathrm{t}}(0) = G_{\mathrm{t}b} \\ G(t) = \dfrac{G_{\mathrm{p}}}{V_G}. \end{cases}$$

The plasma glucose concentration $G$ (mg/dL) is obtained dividing $G_{\mathrm{p}}$ by the distribution volume of glucose $V_G$ (dL/kg). In the first equation, $EGP$ (mg/kg/min) is the endogenous glucose production, $Ra$ (mg/kg/min) denotes the rate of appearance of glucose in plasma, and $E$ (mg/kg/min) the renal excretion. The letter $U$ (mg/kg/min) stands for the glucose utilization which is classified into insulin independent $U_{\mathrm{ii}}$ and insulin dependent $U_{\mathrm{id}}$ (see Section 2.5). Finally, $k_1$ and $k_2$ ($\mathrm{min}^{-1}$) are two rate parameters, while the initial conditions are the basal values $G_{\mathrm{p}b}$, $G_{\mathrm{t}b}$ of $G_{\mathrm{p}}$ and $G_{\mathrm{t}}$, respectively.

2.2. **Insulin subsystem.** The insulin subsystem is governed by two equations describing the relation between the insulin mass in plasma $I_p$ (pmol/kg) and in the liver $I_\ell$ (pmol/kg). The equations read

$$(2)\quad \begin{cases} \dot{I}_\ell(t) = -(m_1 + m_3(t)) \cdot I_\ell(t) + m_2 \cdot I_p(t) + S(t) & I_\ell(0) = I_{\ell b} \\ \dot{I}_p(t) = -(m_1 + m_4) \cdot I_p(t) + m_1 \cdot I_\ell(t) & I_p(0) = I_{pb} \\ I(t) = \dfrac{I_p}{V_I}. \end{cases}$$

The variable $S$ (pmol/kg/min) represents the insulin secretion, which is further described in Section 2.6. The insulin concentration in plasma $I$ (pmol/L) is obtained by dividing $I_p$ by the distribution volume of insulin $V_I$ ($\mathrm{kg}^{-1}$). The coefficients $m_1$, $m_2$, $m_4$ ($\mathrm{min}^{-1}$) are fixed rate parameters. On the other hand, the coefficient $m_3$ is expressed as a function of the hepatic insulin extraction $HE$, we have

$$(3)\qquad HE(t) = -m_5 \cdot S(t) + m_6, \qquad m_3(t) = \frac{HE(t) \cdot m_1}{1 - HE(t)},$$

where, $m_5$ and $m_6$ ($\mathrm{min}^{-1}$) are constant rate parameters too. More information regarding $HE$ and its relation with $m_3$ at basal level can be found in [19, Sect. III-B]. The initial conditions $I_{\ell b}$ and $I_{pb}$ are the basal values of $I_\ell$ and $I_p$, respectively.

2.3. **Endogenous Glucose Production.** The Endogenous Glucose Production (EGP) is expressed in terms of glucose in plasma $G_{\mathrm{p}}$, portal insulin $I_{\mathrm{po}}$ (pmol/kg) and delayed insulin signal $I_{\mathrm{d}}$ (pmol/L), as

$$(4)\quad \begin{aligned} &EGP(t) = k_{\mathrm{p}1} - k_{\mathrm{p}2} \cdot G_{\mathrm{p}}(t) - k_{\mathrm{p}3} \cdot I_{\mathrm{d}} - k_{\mathrm{p}4} \cdot I_{\mathrm{po}} \\ &EGP(0) = EGP_b. \end{aligned}$$

More precisely, $I_{\mathrm{po}}$ is the amount of insulin in the portal vein and its associated equation will be described in Section 2.6. On the other hand, $I_{\mathrm{d}}$ is governed by the following pair of equations

$$\begin{cases} \dot{I}_1(t) = -k_i \cdot (I_1(t) - I(t)) & I_1(0) = I_b \\ \dot{I}_{\mathrm{d}}(t) = -k_i \cdot (I_{\mathrm{d}}(t) - I_1(t)) & I_{\mathrm{d}}(0) = I_b, \end{cases}$$

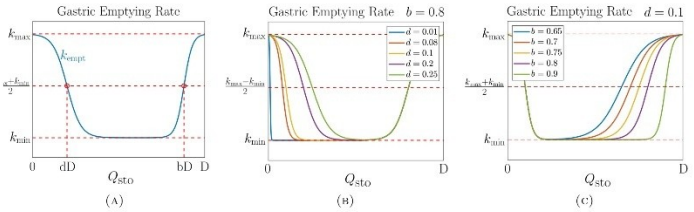


FIGURE 2. (A) Profile of gastric emptying rate $k_{\mathrm{empt}}$ for fixed values of $d$ and $b$. (B) Profile of $k_{\mathrm{empt}}$ in variation of $d$ with $b = 0.8$. (C) Profile of $k_{\mathrm{empt}}$ in variation of $b$ with $d = 0.1$.

where $I_1$ is an auxiliary variable. Regarding the involved parameters, $k_{\mathrm{p1}}$ (mg/kg/min) is the extrapolated $EGP$ at zero glucose and insulin, indeed at basal state the following relation holds

$$k_{\mathrm{p1}} = EGP_b + k_{\mathrm{p2}} \cdot G_{\mathrm{p}b} + k_{\mathrm{p3}} \cdot I_b + k_{\mathrm{p4}} \cdot I_{\mathrm{po},b} \tag{5}$$

Furthermore, $k_{\mathrm{p2}}$ ($\mathrm{min}^{-1}$) is the liver glucose effectiveness, $k_{\mathrm{p3}}$ (mg/kg/min per pmol/l) and $k_{\mathrm{p4}}$ (mg/kg/\min/(pmol/kg)) govern the amplitude of the insulin action on the liver. Finally, $k_i$ ($\mathrm{min}^{-1}$) takes into account the delay between insulin signal and insulin action. $EGP$ denotes the glucose production carried out by the liver, thus only nonnegative values are admissible and a constraint is added to the model [36].

2.4. **Gastrointestinal tract.** This set of equations describes the transit of glucose in stomach and intestine, as well as its absorption. The total amount of glucose is denoted by $Q_{\mathrm{sto}}$ (mg), that is the sum of glucose in solid phase $Q_{\mathrm{sto}}^{(1)}$ and triturated phase $Q_{\mathrm{sto}}^{(2)}$. The glucose mass in the intestine is denoted by $Q_{\mathrm{gut}}$ (mg). We have the following equations

$$\begin{cases} \dot{Q}_{\mathrm{sto}}^{(1)}(t) = -k_{\mathrm{gri}} \cdot Q_{\mathrm{sto}}^{(1)}(t) + D \cdot \delta(t) & Q_{\mathrm{sto}}^{(1)}(0) = 0 \\ \dot{Q}_{\mathrm{sto}}^{(2)}(t) = -k_{\mathrm{empt}}(Q_{\mathrm{sto}}) \cdot Q_{\mathrm{sto}}^{(2)}(t) + k_{\mathrm{gri}} \cdot Q_{\mathrm{sto}}^{(1)}(t) & Q_{\mathrm{sto}}^{(2)}(0) = 0 \\ \dot{Q}_{\mathrm{gut}}(t) = -k_{\mathrm{abs}} \cdot Q_{\mathrm{gut}}(t) + k_{\mathrm{empt}}(Q_{\mathrm{sto}}) \cdot Q_{\mathrm{sto}}^{(2)}(t) & Q_{\mathrm{gut}}(0) = 0 \\ Q_{\mathrm{sto}}(t) = Q_{\mathrm{sto}}^{(1)} + Q_{\mathrm{sto}}^{(2)} \\ Ra(t) = \dfrac{f \cdot k_{\mathrm{abs}} \cdot Q_{\mathrm{gut}}(t)}{BW}. \end{cases}$$

The letter $D$ (mg) denotes the quantity of ingested glucose, while $\delta$ (dimensionless) is an impulse function (with Gaussian profile, for instance). Again, $Ra$ is the glucose rate of appearance in plasma, depending on the body weight $BW$ (kg) and on the fraction of intestinal absorption actually appearing in plasma. As initial conditions, the quantities of glucose in stomach and intestine are both assumed to be null. Finally, $k_{\mathrm{abs}}$ ($\mathrm{min}^{-1}$) is the rate of intestinal absorption, $k_{\mathrm{gri}}$ ($\mathrm{min}^{-1}$) the rate of grinding and $k_{\mathrm{empt}}(Q_{\mathrm{sto}})$ the rate of gastric emptying [16, 19].

We point out that $k_{\text{empt}}$ depends on the quantity $Q_{\text{sto}}$ as prescribed by the following relation

$$k_{\text{empt}}(Q_{\text{sto}}) = k_{\min} + \left(\frac{k_{\max} - k_{\min}}{2}\right)(\tanh(a(Q_{\text{sto}} - bD)) - \tanh(c(Q_{\text{sto}} - dD)) + 2). \tag{6}$$

The profile of such function is shown in Figure 2. More precisely, $k_{\text{empt}} = k_{\max}$ when the stomach contains the amount $D$ of ingested glucose. Then it decreases to its minimum $k_{\min}$ during the digestion process and returns back to $k_{\max}$ when the stomach is empty. The parameter $b$ is the percentage of glucose dose for which $k_{\text{empt}}$ decreases at the average $(k_{\max} + k_{\min})/2$, as well as $d$ is the percentage of dose for which $k_{\text{cmpt}}$ is back to $(k_{\max} + k_{\min})/2$. Notice that $bD$ corresponds to the inflection point in the decreasing phase, while $dD$ corresponds to the inflection point in the recovery phase.

The decay and recovery rates $a$ and $c$, respectively, depend on $b$, $d$ and $D$. Indeed, at the time of ingestion, $k_{\text{empt}}$ decreases with rate

$$a = \frac{5}{2D(1-b)},$$

whereas the recovery rate at the end of the digestion process is

$$c = \frac{5}{2dD}.$$

We remark that if $b$ is in a large percentage, then the decay rate $a$ is also large: this implies a slow digestion since $k_{\text{cmpt}}$ rapidly reaches its minimum. A similar reasoning applies to $d$. If $d$ is small, then the rate $c$ is large, implying a fast recovery phase from $k_{\min}$ back to $k_{\max}$.

2.5. **Glucose utilization.** As we already mentioned before, the total glucose utilization $U$ is the sum of two contributions [19, Sect. III-C-3]: the insulin independent and the insulin dependent utilization, denoted by $U_{\text{ii}}$ and $U_{\text{id}}$, respectively. More precisely, $U_{\text{ii}}$ represents the glucose uptake of the nervous system, which is thus assumed to be constant, i.e. $U_{\text{ii}} = F_{\text{cns}}$. On the other hand, $U_{\text{id}}$ depends on the glucose in tissues $G_{\text{t}}$ as described by the Michaelis–Menten law

$$U_{\text{id}}(t) = \frac{V_m(X(t)) \cdot G_{\text{t}}(t)}{K_m(X(t)) + G_{\text{t}}(t)}, \tag{7}$$

where $V_m(x) = V_{m0} + x \cdot V_{mx}$ and $K_m(x) = K_{m0}$ are linear functions of the insulin in the interstitial fluid $X$ (pmol/L) governed by

$$\dot{X}(t) = -p_{2U} \cdot X(t) + p_{2U} \cdot \big(I(t) - I_b\big). \tag{8}$$

The coefficient $p_{2U}$ ($\text{min}^{-1}$) is the rate of insulin action on the peripheral glucose utilization, $I_b$ denotes the basal level of insulin concentration.

2.6. **Insulin secretion.** The secretion of insulin by the pancreas is described by a set of four equations. We first observe that the insulin secretion is obtained by multiplying the portal insulin $I_{\text{po}}$ by the transfer rate $\gamma$ ($\text{min}^{-1}$) between portal vein and liver, i.e.

$$S(t) = \gamma \cdot I_{\text{po}}(t). \tag{9}$$

The portal insulin solves the following equation

$$\dot{I}_{\text{po}} = -\gamma \cdot I_{\text{po}} + S_{\text{po}}(t), \qquad I_{\text{po}}(0) = I_{\text{po},b} \tag{10}$$

where

$$
\begin{aligned}
S_{\mathrm{po}}(t) &= \begin{cases} Y(t) + K \cdot \dot{G}(t) + S_b & \text{if } \dot{G} > 0 \\ Y(t) + S_b & \text{if } \dot{G} \leq 0, \end{cases} \\
\dot{Y}(t) &= \begin{cases} -\alpha \cdot [Y(t) - \beta \cdot (G(t) - h)] & \text{if } \beta \cdot (G(t) - h) \geq -S_b \\ -\alpha \cdot Y(t) - \alpha \cdot S_b & \text{if } \beta \cdot (G(t) - h) < -S_b \end{cases} \qquad Y(0) = 0,
\end{aligned} \tag{11}
$$

and $K$ (pmol/kg per mg/dL) is the pancreatic responsivity to the glucose rate of change, $\alpha$ ($\mathrm{min}^{-1}$) denotes the delay between the glucose signal and the secretion of insulin by the pancreas, $\beta$ (pmol/kg/min per mg/dL) is the pancreatic responsivity to glucose. Finally, the constant $h$ (mg/dL) is the threshold of glucose above which the $\beta-$cells begin the production of new insulin. Usually, $h = G_b$. The symbol $S_b$ denotes the basal level of insulin secretion.

2.7. **Glucose renal excretion.** The kidneys release glucose in plasma when its quantity decreases under a certain threshold $k_{e_2}$ (mg/kg). This phenomenon is represented with a linear relation, where $k_{e_1}$ ($\mathrm{min}^{-1}$) is the glomerular filtration rate,

$$
E(t) = \begin{cases} k_{e_1}(G_{\mathrm{p}}(t) - k_{e_2}) & \text{if } G_{\mathrm{p}}(t) > k_{e_2} \\ 0 & \text{if } G_{\mathrm{p}}(t) \leq k_{e_2}. \end{cases} \tag{12}
$$

## 3. Parameters estimation

In this section we describe the procedure we adopt to estimate part of the parameters involved in the system of ODEs. The estimation is performed by means of a constrained optimization algorithm on a dataset of sampled glucose curves.

Our attention is focused on the rate of appearance parameters, which describe the glucose kinetics in the gastrointestinal tract (see Section 2.4) as well as $k_{\mathrm{empt}}$, and the endogenous glucose production parameters, appearing in the definition of $EGP$, see (4). Such parameters have a direct effect on the blood glucose concentration $G$ since they describe the absorption of glucose and its endogenous production. In Table 1 we report the list of parameters we aim to estimate together with their lower and upper bounds, which have been extrapolated from previous studies (see e.g. [16, 19]). We also report the parameters' initial value. All the other physical constants are fixed and listed in Table 2 [19, Tab. 1]. If a parameter is not reported in Table 1 and Table 2, then it is computed from some the other quantities. Regarding $EGP$, we estimate its basal value $EGP_b$ and then we compute $k_{\mathrm{p1}}$ by applying the relation in (5).

We denote by $(t_i, \mathsf{G}_i)$ the *in vivo* sample points of a certain glucose concentration curve, measured at the time instant $t_i$ (min), for $i = 1, \ldots, N$, with $t_1 = 0$ corresponding to the basal state. Moreover $\boldsymbol{\vartheta} = (k_{\mathrm{min}}, k_{\mathrm{max}}, k_{\mathrm{abs}}, k_{\mathrm{gri}}, b, d, EGP_b, k_{\mathrm{p2}}, k_{\mathrm{p3}}, k_{\mathrm{p4}}, k_i)$ denotes the vector of parameters we are going to estimate and $G(t; \boldsymbol{\vartheta})$ (mg/dl) is the associated glucose concentration curve resulting from the mathematical model.

In order to obtain the instance of $\boldsymbol{\vartheta}$ providing a good fitting of the sample $(t_i, \mathsf{G}_i)$, we minimize the following loss function, where $EGP(t; \boldsymbol{\vartheta})$ denotes the curve of $EGP$ obtained from the mathematical model at the point $(t, \boldsymbol{\vartheta})$,

$$
\mathcal{L}(\boldsymbol{\vartheta}) = \frac{1}{N} \sum_{i=1}^{N} [\mathsf{G}_i - G(t_i; \boldsymbol{\vartheta})]^2 + \chi \mathbb{I}_{\{z<0\}}(\min\{EGP(t; \boldsymbol{\vartheta})\}). \tag{13}
$$

| **Parameters ($\vartheta$)** | **Lower bound** | **Upper bound** | **Initial value ($\vartheta_0$)** |
|---|---|---|---|
| *Rate of Appearance parameters* | | | |
| $k_{\min}$ | 1e-04 | 0.025 | 0.015 |
| $k_{\max}$ | 0.035 | 0.1 | 0.0558 |
| $k_{\text{abs}}$ | 0.01 | 0.3 | 0.057 |
| $k_{\text{gri}}$ | 1e-05 | 0.1 | 0.049 |
| $b$ | 0.65 | 0.995 | 0.85 |
| $d$ | 1e-07 | 0.01 | 0.00018 |
| *Endogenous Glucose Production parameters* | | | |
| $EGP_b$ | 1.5 | 2.5 | 2 |
| $k_{\text{p2}}$ | 1e-3 | 0.01 | 0.0021 |
| $k_{\text{p3}}$ | 1e-05 | 0.02 | 0.009 |
| $k_{\text{p4}}$ | 1e-04 | 0.1 | 0.0618 |
| $k_i$ | 1e-05 | 1e-03 | 0.0079 |

TABLE 1. Lower/upper bounds and initial value for parameters estimation.

| **Parameter name** | **Value** | **Parameter** | **Value** |
|---|---|---|---|
| $V_G$ | 1.88 | $F_{\text{cns}}$ | 1 |
| $k_1$ | 0.065 | $V_{m0}$ | 2.50 |
| $k_2$ | 0.079 | $V_{mx}$ | 0.047 |
| $V_I$ | 0.05 | $K_{m0}$ | 225.59 |
| $m_1$ | 0.190 | $p_{2U}$ | 0.0331 |
| $m_2$ | 0.484 | $K$ | 2.30 |
| $m_4$ | 0.194 | $\alpha$ | 0.050 |
| $m_5$ | 0.0304 | $\beta$ | 0.11 |
| $m_6$ | 0.6471 | $\gamma$ | 0.5 |
| $HE_b$ | 0.6 | $k_{e_1}$ | 1e-04 |
| $f$ | 0.90 | $k_{e_2}$ | 339 |

TABLE 2. List of fixed parameters. During our simulation, we also fix the quantity of ingested glucose $D = 50000$ mg and the body weight $BW = 78$ kg.

More precisely, the first term is the mean squared error of the simulated glucose concentration at the sample points $t_i$ $(i = 1, \ldots, N)$, while the second term forces $EGP$ to be nonnegative by penalizing the error indicator by a constant $\chi = 10^6$. Indeed, $\mathbb{I}_{\{z<0\}}$ is the characteristic function defined as

$$\mathbb{I}_{\{z<0\}}(x) = \begin{cases} 1 & \text{if } x < 0 \\ 0 & \text{otherwise.} \end{cases} \tag{14}$$

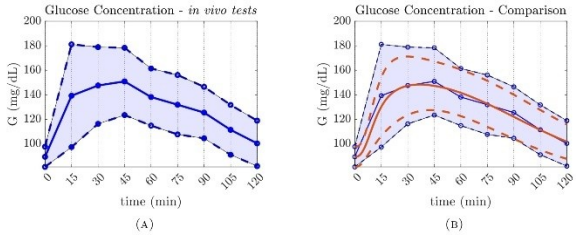


FIGURE 3. Comparison between *in vivo* and estimated glucose concentration curves over the 35 considered subjects. (A) Mean and deviation of the *in vivo* glucose curves of our database. (B) Comparison between mean and deviation of *in vivo* curves (blue lines) and estimated curves (orange lines).

The minimization process is carried out by means of the constrained optimization function `fmincon` provided by MATLAB, which implements the interior point algorithm discussed in [10, 46, 33]. The process is initialized by setting $\boldsymbol{\vartheta} = \boldsymbol{\vartheta}_0$ with the values reported in Table 1 and terminates when $\mathcal{L}(\boldsymbol{\vartheta}) < \mathsf{tol}$ or $\boldsymbol{\vartheta}$ varies less than a prescribed tolerance tol. In particular, we fix tol =1e-10. As additional stopping criteria we adopt the maximum number of iterations and the maximum number of evaluations of $\mathcal{L}$, which must be smaller than 500 times the size of $\boldsymbol{\vartheta}$ (i.e. 5500 iterations). At each iteration of `fmincon`, the ODE system is solved on a time grid with step $\Delta t = 0.05$.

## 4. RESULTS

4.1. **Our dataset.** The database consists of 35 glycemic response curves obtained by 35 healthy subjects (range of age: 20-40) provided by the Laboratory of Neurobiology and Integrated Physiology (University of Pavia, Italy).

Each volunteer received precise behavioral instructions to avoid distorting the test results. In particular, they were advised not to consume alcohol in the previous 12 hours, smoke cigarettes, or participate in strenuous physical exercise in the previous days. Each subject received 50 g of glucose orally (Glucose Sclavo, diagnostic 75 g/150 ml) after fasting for at least 12 hours, according to the procedure defined by the International Organization for Standardization [1]. Blood glucose was monitored using the Lifescan One Touch UltraEasy© system, which uses a glucose oxidase biosensor as a dosing method [9, 48]. Specifically, blood glucose was measured before glucose ingestion (corresponding to basal or fasting glycemia) and then every 15 minutes after ingestion up to 2 hours later.

4.2. **Estimated curves.** The model simulation allows for the description of the physiological events that occur in the postprandial state following the ingestion of glucose solution by the healthy subjects in the database. As previously described, 35 healthy subjects consumed a solution containing 50 g of glucose within 15 minutes, after which glucose concentration levels were measured every 15 minutes for 2 hours. Figure 3 shows a comparison between the data measured in vivo

| **Parameter name** | **Mean ± SD** |
|---|---|
| *Rate of Appearance parameters* | |
| $k_{\min}$ | 0.0086 ± 0.0102 |
| $k_{\max}$ | 0.0831 ± 0.0246 |
| $k_{\text{abs}}$ | 0.2266 ± 0.0943 |
| $k_{\text{gri}}$ | 0.0785 ± 0.0262 |
| $b$ | 0.7391 ± 0.0976 |
| $d$ | 0.0050 ± 8.1557e-06 |
| *Endogenous Glucose Production parameters* | |
| $EGP_b$ | 1.8871 ± 0.4055 |
| $k_{\text{p2}}$ | 0.0044 ± 0.0040 |
| $k_{\text{p3}}$ | 0.0143 ± 0.0072 |
| $k_{\text{p4}}$ | 0.0251 ± 0.0376 |
| $k_i$ | 6.7815e-04 ± 4.1366e-04 |

TABLE 3. Mean value and standard deviation for each parameter estimated on our dataset.

and the estimates obtained using the model. The model accurately estimates the glucose curves measured in vivo. Moreover, Table 3 reports the average value and the standard deviation of each estimated parameter.

The dynamic interaction between glucose absorption, endogenous production, insulin secretion, and glucose utilization during the postprandial state is plotted in Figure 4. More precisely, plasma insulin concentration (Figure 4b) exhibits a pattern similar to that of glucose (Figure 4a), with a delayed peak compared to glucose. This delay is due to the time required for insulin to reach the plasma circulation after being released by pancreatic $\beta-$cells in response to the rise in glucose levels. Notably, insulin secretion (Figure 4e) shows an early and large peak that precedes the plasma one and then progressively reduces as glucose concentration decreases. Similarly, endogenous glucose production (Figure 4c) undergoes a rapid reduction during the initial minutes, driven by the effect of insulin, followed by a gradual recovery, as the trends of glucose and insulin in the bloodstream.

The profile of glucose utilization (Figure 4f) is similar to that of insulin, with a progressive increase up to a plateau. The variability reflects the differences between individuals in insulin sensitivity and cellular glucose metabolism. The rate of glucose appearance $Ra$ (Figure 4d) decreases after an initial peak: this behavior is consistent with the rapid absorption of glucose from the intestine, which immediately follows a meal. This trend reflects the systemic clearance of glucose from the plasma.

The shaded regions, common across all panels, represent the standard deviation (SD) emphasizing the model's ability to capture not only the mean physiological processes but also the inter-individual variability. These findings validate the model's capacity to accurately simulate the key physiological processes involved in glucose metabolism, with particular emphasis on the temporal dynamics and individual variability of the responses.

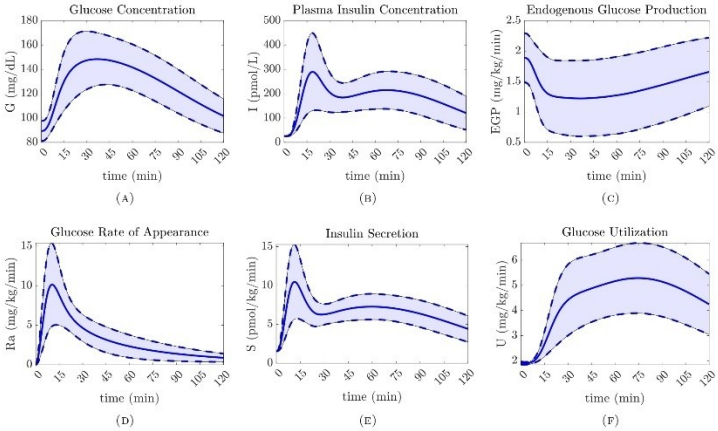


FIGURE 4. Quantities of (A) glucose concentration, (B) plasma insulin concentration, (C) endogenous glucose production, (D) glucose rate of appearance, (E) insulin secretion, and (F) glucose utilization. The solid line represents the mean of 35 subjects, and the shaded area represents the SD.

4.3. **Three behaviors.** In this section, we describe the individual glucose tolerance of the subjects, along with its relation with the dynamics of the entire system.

More precisely, we identified three distinct behaviors as represented in Figure 5 for three reference subjects. From Figure 5a, we observe that such classification might depend on the time of glycemic peak. In fact, the glycemic peak of Subject 33 (blue line) occurred within 30 minutes after ingestion, indicating rapid glucose absorption, as also shown by the associated $Ra$ and $U$ curves (see Figures 5d and 5f, respectively). However, looking at Subject 21 (red line), the glycemic peak occurred between 30 and 50 minutes after ingestion. This behavior indicats a moderate glycemic response, as seen in the appearance rate and the glucose utilization plots (see Figures 5d and 5f, respectively). Subject 6 (yellow line) showed a completely different behavior, as the glycemic peak was more delayed, occurring 60 minutes after ingestion. The related glucose rate of appearance (Figure 5d) exhibited a gradual and slow glucose uptake correlated with a low ability to utilize ingested glucose, see Figure 5f.

As represented in Figures 5b and 5e, the glucose dynamics affected the insulin response. Subject 33 had a high pancreatic response, resulting in a significant increase in insulin concentration to compensate for the immediate glucose peak. The immediate action of insulin led to a decrease in endogenous glucose production (Figure 5c). Subject 21 showed regular and moderate insulin

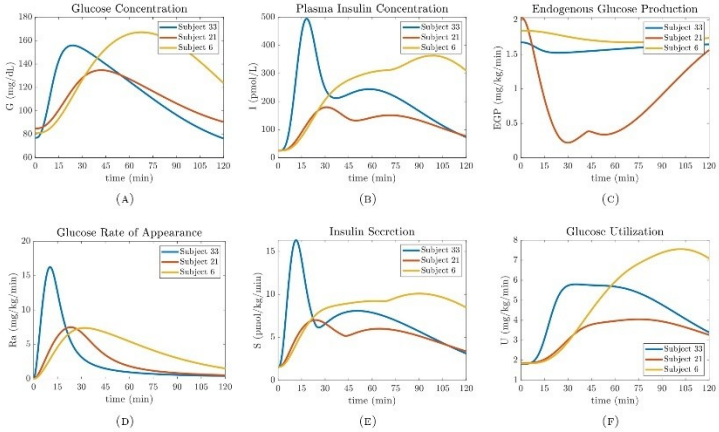


FIGURE 5. Quantities of (A) glucose concentration, (B) plasma insulin concentration, (C) endogenous glucose production, (D) glucose rate of appearance, (E) insulin secretion, and (F) glucose utilization of subjects 33 (blue line), 21 (red line), 6 (yellow line).

secretion, which is correlated with a gradual suppression of gluconeogenesis. Due to its delayed glucose peak, Subject 6 exhibited a slow and progressive increase of insulin secretion and action, resulting in a remarkable contribution in reducing the endogenous glucose production.

The three subjects displayed different metabolic reactions, reflecting the biological variability of glycemic regulation.

4.3.1. *Analysis of rate of appearance parameters.* Following the previous discussion, we analyze the correlation between the three behaviors and the estimated rate of appearance parameters. To this end, we subdivide the database into three groups based on the time of the glucose peak. Group 1 corresponds to the subject with an early peak (30 minutes after glucose ingestion); Group 2 corresponds to a medium peak (between 30 and 50 minutes after ingestion); and Group 3 corresponds to a late peak (after 50 minutes). The analysis aims at exploring the relationship between peak time and two key kinetic parameters: the absorption rate constant ($k_{\text{abs}}$) and the grinding rate constant ($k_{\text{gri}}$) (see Table 4, and Figures 6 and 7). We have six outliers, which will be subsequently analyzed in detail.

In particular, the subjects of Group 1 shows the largest absorption rate ($k_{\text{abs}} = 0.2917 \pm 0.0062$ $\text{min}^{-1}$) and the largest grinding rate ($k_{\text{gri}} = 0.0939 \pm 0.0033$ $\text{min}^{-1}$), indicating a rapid metabolic

| | # Subjects | Peak Time | $k_{\text{abs}}$ | $k_{\text{gri}}$ |
|---|---|---|---|---|
| Group 1 | 16 | $24.8938 \pm 0.9295$ | $0.2917 \pm 0.0062$ | $0.0939 \pm 0.0033$ |
| Group 2 | 8 | $38.1625 \pm 2.1192$ | $0.1291 \pm 0.0164$ | $0.0695 \pm 0.0073$ |
| Group 3 | 5 | $66.8800 \pm 4.9753$ | $0.0861 \pm 0.0136$ | $0.0436 \pm 0.0086$ |

TABLE 4. Mean values and standard deviation of peak time, $k_{\text{abs}}$, and $k_{\text{gri}}$ for subjects divided into three groups based on the time of the glycemic peak: Group 1 (peak time $< 30$ min), Group 2 (peak time between $30 - 50$ min), and Group 3 (peak time $> 50$ min).

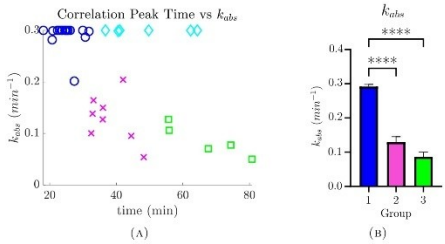


FIGURE 6. Correlation plots between time of glycemic peak and $k_{\text{abs}}$ (rate of absorption). (A) Scatter plot of $k_{\text{abs}}$ for Group 1 (blue circles), Group 2 (magenta crosses), Group 3 (green squares), and six outliers (cyan diamond). (B) Statistical comparison of $k_{\text{abs}}$ among the 3 groups. Statistical significance (One–Way ANOVA followed by Bonferroni *post-hoc* test): $p < 0.05$ (*); $p < 0.01$ (**); $p < 0.001$ (***); $p < 0.0001$ (****).

response. For subjects in Group 2, the absorption rate is markedly lower than in Group 1 ($k_{\text{abs}} = 0.1291 \pm 0.0164$ min$^{-1}$), and their grinding rate is also reduced ($k_{\text{gri}} = 0.0695 \pm 0.0073$ min$^{-1}$), suggesting slower glucose uptake and metabolic processing. Instead, subjects in Group 3 exhibit the lowest values for both kinetic parameters ($k_{\text{abs}} = 0.0861 \pm 0.0136$ min$^{-1}$, $k_{\text{gri}} = 0.0436 \pm 0.0086$ min$^{-1}$), indicating a significantly slower absorption and grinding process compared to the other groups. These findings suggest a clear inverse relationship between the time of glycemic peak and the kinetic parameters governing glucose absorption and processing. Individuals who exhibited an earlier glycemic peak tend to have higher metabolic efficiency, characterized by faster glucose absorption (larger $k_{\text{abs}}$) and increased glucose processing (larger $k_{\text{gri}}$). However, individuals with delayed glycemic peaks show a markedly slower metabolic response, indicating physiological variations in glucose handling that may be essential to evaluate metabolic health and disease risk. Furthermore, the correlations between $k_{\text{abs}}$, $k_{\text{gri}}$, and the glycemic peak time (see Figure 8) confirm an inverse relationship between peak time and metabolic efficiency, highlighting glucose absorption and processing variability.

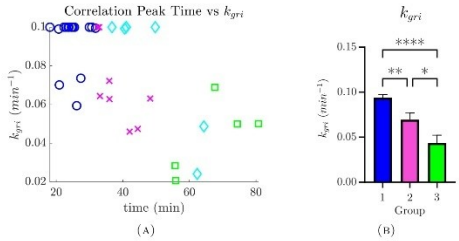


FIGURE 7. Correlation plots between time of glycemic peak and $k_{\text{gri}}$ (rate of grinding). (A) Scatter plot of $k_{\text{gri}}$ for Group 1 (blue circles), Group 2 (magenta crosses), Group 3 (green squares), and six outliers (cyan diamond). (B) Statistical comparison of $k_{\text{gri}}$ among the 3 groups. Statistical significance (One Way ANOVA followed by Bonferroni *post-hoc* test): $p < 0.05$ (*); $p < 0.01$ (**); $p < 0.001$ (***); $p < 0.0001$ (****).

We analyzed also other rate of appearance parameters (see Figure 9). $k_{\text{max}}$, $k_{\text{min}}$, $d$, and $b$ describe different aspects of the gastric emptying process, capturing its variability and dynamics across subjects. More precisely, $k_{\text{max}}$ and $k_{\text{min}}$ represent the maximum and minimum rate of gastric emptying, respectively, and reflect normal biological variability. The parameter $b$, which represents the percentage amount of glucose remaining in the stomach when the emptying rate has decreased to halfway between $k_{\text{max}}$ and $k_{\text{min}}$ (see (6) and Figure 2), appears to be correlated with both the timing and maximum value of glucose concentration..

When $b$ assumes a large value, the emptying rate $k_{\text{empt}}$ decreases faster to $k_{\text{min}}$, meaning that the emptying process is slow. This implies that the glucose assimilation is prolonged over time. On the other hand, a small value of $b$, results in a slower decrease of $k_{\text{empt}}$ to $k_{\text{min}}$ so that the emptying process and glucose assimilation are faster. These observations are evident for subjects belonging to Group 1. Indeed, the subjects with $G \leq 155$ mg/dL show a statistically larger $b$ compared to subjects with $G > 155$ mg/dL, see Figure 10. Regarding Group 2 and Group 3, no clear classification could be identified in dependence on gastric emptying.

The parameter $d$, characterizing the recovery of $k_{\text{empt}}$ to $k_{\text{max}}$, remains constant across the group of subjects, indicating a stable parameter in the gastric emptying process.

In any case, the correlation between $b$ and the maximum of glucose concentration observed in Group 1 further supports the idea that gastric emptying dynamics plays a crucial role in shaping postprandial glycemic responses.

As mentioned before, by looking at Figure 6, we can identify six outliers (cyan diamonds) since their rate $k_{\text{abs}}$ suggests a classification into Group 1, but the glycemic peak is realized after 30 min from glucose ingestion. Therefore, their data were excluded from the grouped statistical analyses for further investigation. The glucose response of such subjects is reported in Figure 11, where a red cross denotes the maximum of $G$, i.e. $\overline{G} = \max_{t\in[0,120]} G(t)$.

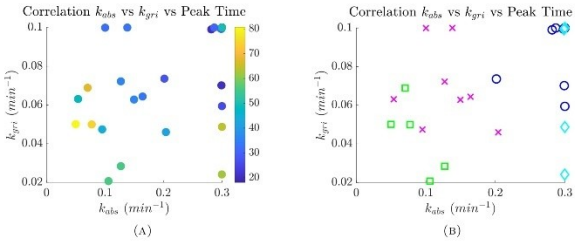


FIGURE 8. Correlation plots between $k_{\text{abs}}$, $k_{\text{gri}}$ and the time of glycemic peak. (A) Scatter plot of $k_{\text{abs}}$ and $k_{\text{gri}}$, where the color scale represents the peak time (min). (B) Scatter plot of $k_{\text{abs}}$ and $k_{\text{gri}}$ for Group 1 (blue circles), Group 2 (magenta crosses), Group 3 (green squares), and six outliers (cyan diamond).

We present an automatic procedure to obtain more information from the outliers' responses and understand if they could be classified in one of the identified groups. We distinguish the concept of mathematical peak (that is $\overline{G}$) and biological peak $G^{bio}$ was distinguished. By biological peak we mean the value of $G$ which could be considered as the maximum of the glycemic response with respect to the behavior of the glucose-insulin system. For the subjects already classified into the three groups, $G^{bio} = \overline{G}$.

The biological peak of the outliers can be estimated as $G^{bio} = \overline{G} - \mathsf{tol}_G$, where $\mathsf{tol}_G$ is a tolerance and was set to $\mathsf{tol}_G = 2.6$ mG/dL in the tests. If $G^{bio}$ is close to $\overline{G}$, then the two quantities basically coincide. On the other hand, if $G^{bio}$ is far away from $\overline{G}$, it means that the glucose response reaches $G^{bio}$ and then shows a very slow increase to $\overline{G}$. In this case, we can consider as peak time the instant $t^{bio}$ associated with $G^{bio}$, instead of $\overline{t} = \text{argmax}_{t\in[0,120]} G(t)$.

We represent $G^{bio}$ by a red circle in Figure 11. It is evident that the glucose response of Subjects 12, 25 and 26 reached a plateau so that the biological peak time $t^{bio}$ allows classification of those subjects as part of Group 1. On the other hand, $t^{bio} \approx \overline{t}$ for Subjects 16, 27 and 41 so that their status as outliers remains unchanged: their biological parameters were similar to those of Group 1, but $\overline{t} > 30$ min so that a clear classification is not possible.

After adding Subjects 12, 25 and 26 to Group 1, we recomputed the related statistics; the results are reported in Table 5. Moreover, Figure 12 collects the updated correlation plots between the Peak Time and $k_{\text{abs}}$, $k_{\text{gri}}$ and $b$ respectively, while in Figure 13 the associated histograms are reported. Specifically, $k_{\text{abs}}$ is statistically highest in Group 1 compared to Group 2 and Group 3. Similarly, $k_{\text{gri}}$ was significantly higher in Group 1 than in the other groups. We observe distrinct kinetic behaviors within Group 1, which was further divided based on the value of $G^{bio}$, with all comparisons showing statistical significance.

We emphasize once again that the rate of appearance parameters are an effective tool to analyze glucose responses and identify different metabolic reactions.

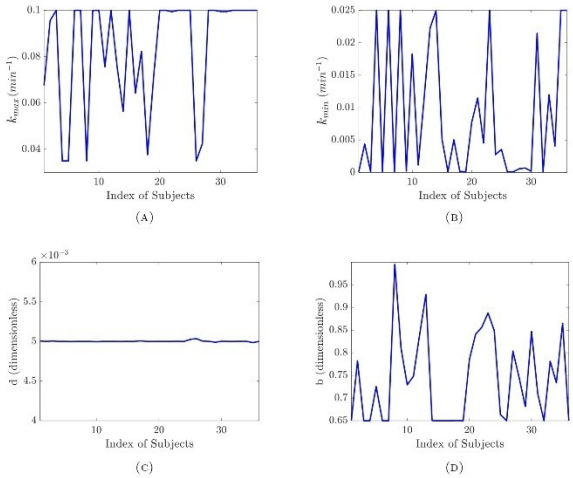


FIGURE 9. Gastric emptying parameters with respect to the index of subjects. (A) $k_{\max}$, (B) $k_{\min}$, (C) $d$, (D) $b$.

| | # Subjects | Peak Time | $k_{\text{abs}}$ | $k_{\text{gri}}$ |
|---|---|---|---|---|
| Group 1 | 19 | $24.2026 \pm 0.9315$ | $0.2929 \pm 0.0052$ | $0.0948 \pm 0.0028$ |
| *Detail:* | # Subjects | $G^{bio}$ | $b$ | |
| $G^{bio} \leq 155$ | 10 | $139.9808 \pm 2.1676$ | $0.8038 \pm 0.0149$ | |
| $G^{bio} > 155$ | 9 | $176.8198 \pm 3.9325$ | $0.6767 \pm 0.0109$ | |

TABLE 5. Mean values and standard deviation of Peak Time, $k_{\text{abs}}$, and $k_{\text{gri}}$ for Group 1 (after classification of outlier Subjects). In detail, mean values and standard deviation of $G^{bio}$ and $b$ for the sub-groups having $G^{bio} \leq 155$ and $G^{bio} > 155$. For the subjects we classified at the beginning, $G^{bio} = \overline{G}$.

## 5. CONCLUSION

The standard procedure for computing the Glycemic Index of food is not immediate and easy to perform due to the several requirements listed by the International Standard Organization (ISO):

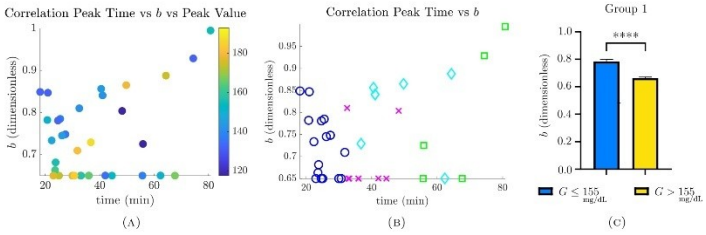


FIGURE 10. Correlation plots between the time of glycemic peak, $b$ and the glycemic peak value. (A) Scatter plot of Peak Time, $b$, and Peak Value, where the color scale represents the peak value ($mg/dl$). (B) Scatter plot of Peak Time and $b$ for Group 1 (blue circles), Group 2 (magenta crosses), Group 3 (green squares), and six outliers (cyan diamond). (C) Comparing the parameter $b$ Group 1 for subjects with glucose values $G \leq 155$ mg/dL (blue) and $G > 155$ mg/dL (yellow). Statistical significance (One–Way ANOVA followed by Bonferroni *post-hoc* test): $p < 0.05$ (*); $p < 0.01$ (**); $p < 0.001$ (***); $p < 0.0001$ (****).

the procedure consists in testing a group of at least ten people, which should adhere to a set of behavioral guidelines, even during the days before the test.

Our final goal is the design of an automatic procedure for computing GI without the need for human testing, and this paper represents a first step in that direction. The idea is to exploit a mathematical model [19] to estimate the glucose response, given the composition of the ingested food.

In this work, we focused on the ingestion of pure glucose, whose blood response is the standard reference for computing GI of food. More precisely, we exploited a datasets of *in vivo* measurements to estimate the parameters governing the mathematical model. We observed that the glucose responses provided by the model are well-approximating the laboratory results. In addition, we noticed that the correlation between a subset of parameters (i.e. the rate of appearance parameters describing glucose absorption) and the glucose curves allows us to classify subjects into three groups depending on the time they reach the glycemic peak. This feature may also be employed for further analysis regarding glycaemia and/or disease prevention.

We plan to extend the results of this preliminary work to larger datasets. Moreover, we will also study the correlation between the parameters governing the mathematical model and the ingestion of composite food, which may contain fat, proteins and fibers beyond glucose/carbohydrates.

## 6. ACKNOWLEDGMENTS

D. Boffi and F. Credali are members of the GNCS/INdAM research group. This research was funded by the University of Pavia, Fondi Ricerca Giovani (FRG 2024), Department of Biology and Biotechnology "L. Spallanzani", University of Pavia.

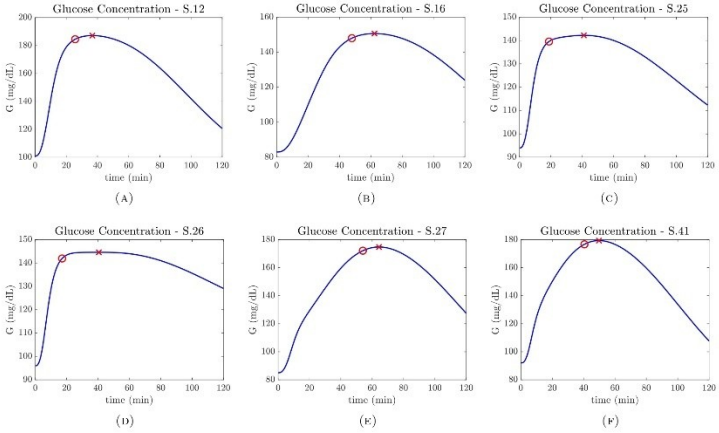


FIGURE 11. Glycemic response for the subjects classified as outliers. The red cross indicates the mathematical peak $(\overline{t}, \overline{G})$, whereas the red circle represents the biological glucose peak $(t^{bio}, G^{bio})$. For Subjects (A) 12, (C) 25, (D) 26 the biological peak corresponds to the beginning of the plateau.

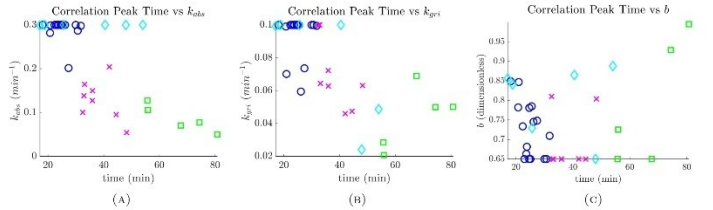


FIGURE 12. Correlation plots of (A) $k_{\text{abs}}$, (B) $k_{\text{gri}}$ and (C) $b$ with respect to the time of glycemic peak for Group 1 (blue circles), Group 2 (magenta crosses), Group 3 (green squares). Notice that three of six outliers (cyan diamonds) are now classified as part of Group 1.

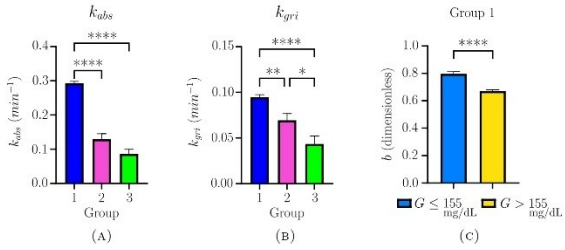


FIGURE 13. Histograms of (A) $k_{\text{abs}}$, (B) $k_{\text{gri}}$ for Group 1 (blue), Group 2 (magenta), Group 3 (green), and (C) $b$ of Group 1 for subjects with glucose values $G \leq 155$ mg/dL (blue) and $G > 155$ mg/dL (yellow). Statistical significance (One Way ANOVA followed by Bonferroni *post-hoc* test): $p < 0.05$ (*); $p < 0.01$ (**); $p < 0.001$ (***); $p < 0.0001$ (****).

## REFERENCES


[1] ISO 26642:2010 (E): Food products - Determination of the glycaemic index (GI) and recommendation for food classification. *International Standard Organization*, 2010, reviewed and confirmed in 2016.

[2] GBD Compare Data Visualization, 2024. *Institute for Health Metrics and Evaluation (IHME)*, WA: IHME, University of Washington, https://www.healthdata.org/data-tools-practices/interactive-visuals/gbd-compare, accessed on April 8, 2025.

[3] GBD Foresight Visualization, 2024. *Institute for Health Metrics and Evaluation (IHME)*, WA: IHME, University of Washington, https://vizhub.healthdata.org/gbd-foresight/, accessed on April 8, 2025.

[4] IDF Diabetes Atlas, 11th edition, 2025. *International Diabetes Federation*, https://diabetesatlas.org/, accessed on April 8, 2025.

[5] A. W. Barclay, L. S. Augustin, F. Brighenti, E. Delport, C. J. Henry, J. L. Sievenpiper, K. Usic, Y. Yuexin, A. Zurbau, and T. M. Wolever. Dietary glycaemic index labelling: A global perspective. *Nutrients*, 13(9):3244, 2021.

[6] R. N. Bergman, Y. Z. Ider, C. R. Bowden, and C. Cobelli. Quantitative estimation of insulin sensitivity. *American Journal of Physiology-Endocrinology And Metabolism*, 236(6):E667, 1979.

[7] J. Brand-Miller and A. E. Buyken. The relationship between glycemic index and health. *Nutrients*, 12(2):536, 2020.

[8] E. Breda, M. K. Cavaghan, G. Toffolo, K. S. Polonsky, and C. Cobelli. Oral glucose tolerance test minimal model indexes of $\beta$-cell function and insulin sensitivity. *Diabetes*, 50(1):150 158, 2001.

[9] F. Brouns, I. Bjorck, K. N. Frayn, A. L. Gibbs, V. Lang, G. Slama, and T. M. S. Wolever. Glycaemic index methodology. *Nutrition Research Reviews*, 18(1):145 171, jun 2005.

[10] R. H. Byrd, M. E. Hribar, and J. Nocedal. An interior point algorithm for large-scale nonlinear programming. *SIAM Journal on Optimization*, 9(4):877 900, 1999.

[11] M. Campioni, G. Toffolo, R. Basu, R. A. Rizza, and C. Cobelli. Minimal model assessment of hepatic insulin extraction during an oral test from standard insulin kinetic parameters. *American Journal of Physiology-Endocrinology and Metabolism*, 297(4):E941–E948, 2009.

[12] C. Cobelli and C. Dalla Man. Minimal and maximal models to quantitate glucose metabolism: tools to measure, to simulate and to run in silico clinical trials. *Journal of diabetes science and technology*, 16(5):1270–1298, 2022.

[13] C. Cobelli, C. Dalla Man, G. Toffolo, R. Basu, A. Vella, and R. Rizza. The oral minimal model method. *Diabetes*, 63(4):1203–1213, 2014.

[14] C. Cobelli, G. Federspil, G. Pacini, A. Salvan, and C. Scandellari. An integrated mathematical model of the dynamics of blood glucose and its hormonal control. *Mathematical Biosciences*, 58(1):27–60, 1982.

[15] C. Cobelli and A. Mari. Validation of mathematical models of complex endocrine-metabolic systems. a case study on a model of glucose regulation. *Medical and Biological Engineering and Computing*, 21:390–399, 1983.

[16] C. Dalla Man, M. Camilleri, and C. Cobelli. A system model of oral glucose absorption: validation on gold standard data. *IEEE Transactions on Biomedical Engineering*, 53(12):2472–2478, 2006.

[17] C. Dalla Man, A. Caumo, and C. Cobelli. The oral glucose minimal model: estimation of insulin sensitivity from a meal test. *IEEE Transactions on Biomedical Engineering*, 49(5):419–429, 2002.

[18] C. Dalla Man, D. M. Raimondo, R. A. Rizza, and C. Cobelli. GIM, simulation software of meal glucose-insulin model. 2007.

[19] C. Dalla Man, R. A. Rizza, and C. Cobelli. Meal simulation model of the glucose-insulin system. *IEEE Transactions on biomedical engineering*, 54(10):1740–1749, 2007.

[20] C. Dalla Man, G. Toffolo, R. Basu, R. A. Rizza, and C. Cobelli. A model of glucose production during a meal. In *2006 International Conference of the IEEE Engineering in Medicine and Biology Society*, pages 5647–5650. IEEE, 2006.

[21] A. De Gaetano, S. Panunzi, A. Matone, A. Samson, J. Vrbikova, B. Bendlova, and G. Pacini. Routine OGTT: a robust model including incretin effect for precise identification of insulin sensitivity and secretion in a single individual. *PLoS One*, 8(8):e70875, 2013.

[22] E. W. Gregg, Y. Li, J. Wang, N. Rios Burrows, M. K. Ali, D. Rolka, D. E. Williams, and L. Geiss. Changes in diabetes-related complications in the United States, 1990–2010. *New England Journal of Medicine*, 370(16):1514–1523, 2014.

[23] R. Hovorka, V. Canonico, L. J. Chassin, U. Haueter, M. Massi-Benedetti, M. O. Federici, T. R. Pieber, H. C. Schaller, L. Schaupp, and T. Vering. Nonlinear model predictive control of glucose concentration in subjects with type 1 diabetes. *Physiological measurement*, 25(4):905, 2004.

[24] P. G. Jacobs, P. Herrero, A. Facchinetti, J. Vehi, B. Kovatchev, M. D. Breton, A. Cinar, K. S. Nikita, F. J. Doyle, J. Bondia, et al. Artificial intelligence and machine learning for improving glycemic control in diabetes: Best practices, pitfalls, and opportunities. *IEEE reviews in biomedical engineering*, 17:19–41, 2023.

[25] D. J. Jenkins, T. Wolever, R. H. Taylor, H. Barker, H. Fielden, J. M. Baldwin, A. C. Bowling, H. C. Newman, A. L. Jenkins, and D. V. Goff. Glycemic index of foods: a physiological basis for carbohydrate exchange. *The American journal of clinical nutrition*, 34(3):362–366, 1981.

[26] D. R. King P, Peacock I. The UK prospective diabetes study (UKPDS): clinical and therapeutic implications for type 2 diabetes. *Br J Clin Pharmacol.*, 1999.

[27] E. Kondrad, A. Westling, E. Burke, and S. Weldon. Metformin vs. lifestyle changes for prevention of type 2 diabetes mellitus. *American family physician*, 107(4):422–423, 2023.

[28] G. Livesey, R. Taylor, H. F. Livesey, A. E. Buyken, D. J. Jenkins, L. S. Augustin, J. L. Sievenpiper, A. W. Barclay, S. Liu, and T. M. Wolever. Dietary glycemic index and load and the risk of type 2 diabetes: a systematic review and updated meta-analyses of prospective cohort studies. *Nutrients*, 11(6):1280, 2019.

[29] A. Lovegrove, C. Edwards, I. De Noni, H. Patel, S. El, T. Grassby, C. Zielke, M. Ulmius, L. Nilsson, and P. Butterworth. Role of polysaccharides in food, digestion, and health. *Critical reviews in food science and nutrition*, 57(2):237–253, 2017.

[30] D. Malkova, R. Evans, K. Frayn, S. Humphreys, P. Jones, and A. Hardman. Prior exercise and postprandial substrate extraction across the human leg. *American Journal of Physiology-Endocrinology and Metabolism*, 279(5):E1020–E1028, 2000.

[31] K. Marsh, A. Barclay, S. Colagiuri, and J. Brand-Miller. Glycemic index and glycemic load of carbohydrates in the diabetes diet. *Current diabetes reports*, 11:120–127, 2011.

[32] T. Moxon, O. Gouseti, and S. Bakalis. In silico modelling of mass transfer & absorption in the human gut. *Journal of Food engineering*, 176:110–120, 2016.

[33] J. Nocedal, F. Öztoprak, and R. A. Waltz. An interior point method for nonlinear programming with infeasibility detection capabilities. *Optimization Methods and Software*, 29(4):837–854, 2014.

[34] F. Piccinini, C. Dalla Man, A. Vella, and C. Cobelli. A model for the estimation of hepatic insulin extraction after a meal. *IEEE Transactions on Biomedical Engineering*, 63(9):1925–1932, 2015.

[35] A. Ramachandran, C. Snehalatha, S. Mary, B. Mukesh, A. Bhaskar, V. Vijay, and I. D. P. P. (IDPP). The Indian Diabetes Prevention Programme shows that lifestyle modification and metformin prevent type 2 diabetes in Asian Indian subjects with impaired glucose tolerance (IDPP-1). *Diabetologia*, 49:289–297, 2006.

[36] R. A. Rizza, G. Toffolo, and C. Cobelli. Accurate measurement of postprandial glucose turnover: why is it difficult and how can it be done (relatively) simply? *Diabetes*, 65(5):1133–1145, 2016.
[37] M. D. Robertson, R. A. Henderson, G. E. Vist, and R. D. E. Rumsey. Extended effects of evening meal carbohydrate-to-fat ratio on fasting and postprandial substrate metabolism. *The American journal of clinical nutrition*, 75(3):505–510, 2002.
[38] W. R. Russell, A. Baka, I. Björck, N. Delzenne, D. Gao, H. R. Griffiths, E. Hadjilucas, K. Juvonen, S. Lahtinen, and M. Lansink. Impact of diet composition on blood glucose regulation. *Critical reviews in food science and nutrition*, 56(4):541–590, 2016.
[39] O. D. Sánchez, E. Ruiz-Velázquez, A. Y. Alanís, G. Quiroz, and L. Torres-Treviño. Parameter estimation of a meal glucose–insulin model for t1dm patients from therapy historical data. *IET systems biology*, 13(1):8–15, 2019.
[40] S. Q. Siler, R. A. Neese, M. P. Christiansen, and M. K. Hellerstein. The inhibition of gluconeogenesis following alcohol in humans. *American Journal of Physiology-Endocrinology and Metabolism*, 275(5):E897–E907, 1998.
[41] M. Uusitupa, T. A. Khan, E. Viguiliouk, H. Kahleova, A. A. Rivellese, K. Hermansen, A. Pfeiffer, A. Thanopoulou, J. Salas-Salvadó, and U. Schwab. Prevention of type 2 diabetes by lifestyle changes: a systematic review and meta-analysis. *Nutrients*, 11(11):2611, 2019.
[42] M. Viceconti, C. Cobelli, T. Haddad, A. Himes, B. Kovatchev, and M. Palmer. In silico assessment of biomedical products: the conundrum of rare but not so rare events in two case studies. *Proceedings of the Institution of Mechanical Engineers, Part H: Journal of Engineering in Medicine*, 231(5):455–466, 2017.
[43] P. Vicini, A. Caumo, and C. Cobelli. Glucose effectiveness and insulin sensitivity from the minimal models: consequences of undermodeling assessed by Monte Carlo simulation. *IEEE transactions on biomedical engineering*, 46(2):130–137, 1999.
[44] R. Visentin, E. Campos-Náñez, M. Schiavon, D. Lv, M. Vettoretti, M. Breton, B. P. Kovatchev, C. Dalla Man, and C. Cobelli. The UVA/Padova type 1 diabetes simulator goes from single meal to single day. *Journal of diabetes science and technology*, 12(2):273–281, 2018.
[45] R. Visentin, M. Schiavon, R. Basu, A. Basu, C. Dalla Man, and C. Cobelli. Physiological models for artificial pancreas development. In *The Artificial Pancreas*, pages 123–152. Elsevier, 2019.
[46] R. A. Waltz, J. L. Morales, J. Nocedal, and D. Orban. An interior algorithm for nonlinear optimization that combines line search and trust region steps. *Mathematical programming*, 107(3):391–408, 2006.
[47] T. Wolever. Is glycaemic index (GI) a valid measure of carbohydrate quality? *European journal of clinical nutrition*, 67(5):522–531, 2013.
[48] T. M. S. Wolever, H. H. Vorster, I. Björck, J. Brand-Miller, F. Brighenti, J. I. Mann, D. D. Ramdath, Y. Granfeldt, S. Holt, T. L. Perry, C. Venter, and Xiaomei Wu. Determination of the glycaemic index of foods: interlaboratory study. *European Journal of Clinical Nutrition*, 57(3):475–482, mar 2003.

Computer, Electrical and Mathematical Sciences and Engineering division, King Abdullah University of Science and Technology, Thuwal 23955, Saudi Arabia
*Email address*: fabio.credali@kaust.edu.sa

Dipartimento di Biologia e Biotecnologie "Lazzaro Spallanzani", Università degli Studi di Pavia, via Ferrata 9, 27100, Pavia, Italy
*Email address*: mariateresa.venuti01@universitadipavia.it

Computer, Electrical and Mathematical Sciences and Engineering division, King Abdullah University of Science and Technology, Thuwal 23955, Saudi Arabia; Dipartimento di Matematica "F. Casorati", Università degli Studi di Pavia, via Ferrata 5, 27100, Pavia, Italy
*Email address*: daniele.boffi@kaust.edu.sa

Dipartimento di Biologia e Biotecnologie "Lazzaro Spallanzani", Università degli Studi di Pavia, via Ferrata 9, 27100, Pavia, Italy
*Email address*: paola.rossi@unipv.it

Biomedicine & Pharmacotherapy 188 (2025) 118204

Contents lists available at ScienceDirect

Biomedicine & Pharmacotherapy

journal homepage: www.elsevier.com/locate/biopha

# Hericium erinaceus extracts promote neuronal differentiation and excitability through nootropic metabolite activity

Federico Brandalise [a], Erica Cecilia Priori [b], Francesca Giammello [b,c], MariaTeresa Venuti [b], Daniela Ratto [b], Lorenzo Goppa [d,e], Carlo Alessandro Locatelli [f], Elena Savino [d], Elisa Roda [f], Paola Rossi [b,*]

[a] Department of Biomedical Sciences, Division of Neuroscience and Clinical Pharmacology, University of Cagliari, Cittadella Universitaria di Monserrato, Monserrato 09042, Italy
[b] Department of Biology and Biotechnology "L. Spallanzani", University of Pavia, Pavia 27100, Italy
[c] PhD Program in Genetics, Molecular and Cellular Biology, University of Pavia, Italy
[d] Department of Earth and Environmental Sciences (DSTA), University of Pavia, Pavia 27100, Italy
[e] PhD Program in Earth and Environmental Sciences, University of Pavia, Italy
[f] Laboratory of Clinical & Experimental Toxicology, Pavia Poison Centre, National Toxicology Information Centre, Toxicology Unit, Istituti Clinici Scientifici Maugeri IRCCS Pavia, Pavia 27100, Italy

ARTICLE INFO

*Keywords:*
Neuroblastoma
SH-SY5Y
*Hericium erinaceus*
Neuronal differentiation
Patch clamp
Voltage-gated sodium currents
Cell proliferation
Action potential
Erinacines
Hericenones
Voltage-Gated Sodium Channel

ABSTRACT

This study investigates the effects of a blend of *Hericium erinaceus* (lion's mane mushroom) extract on the differentiation of SH-SY5Y cells, a human neuroblastoma cell line, revealing potential therapeutic implications for neuroblastoma management. Treatment with this blend induced cells differentiation towards a neuron-like profile, as evidenced by enhanced neuronal excitability and upregulation of neuronal markers, such as βIII-tubulin and synaptotagmin. Additionally, the treatment significantly reduced PCNA, a key regulator of proliferation, alongside a decrease in stemness markers, indicating a shift toward a more mature and less proliferative phenotype. These findings demonstrate the ability of *Hericium erinaceus* to promote neuronal differentiation and inhibit proliferation in neuroblastoma cells, highlighting its therapeutic potential for managing neuroblastoma and potentially other neurological disorders. The results suggest that *Hericium erinaceus* may serve as a promising candidate for the development of novel neuroregenerative therapies.

## 1. Introduction

Neuroblastoma stands as one of the most aggressive pediatric cancers, posing a challenge in oncology due to its complex etiology and variable clinical manifestations[1]. Originating from neural crest progenitor cells, it primarily affects young children and displays a spectrum of behaviors, from spontaneous regression to aggressive metastasis[2]. Despite advances in surgery, chemotherapy, and radiotherapy, the prognosis for high-risk neuroblastoma remains poor (5-year relative survival rate ~50 %)[3], highlighting the urgent need for novel therapeutic strategies.

The SH-SY5Y cell line is widely used as a model in neuroblastoma research, offering a tractable system to study the disease's molecular mechanisms and therapeutic responses[4]. These cells retain several tumor-like features and can differentiate into neuronal-like cells upon exposure to various factors, reflecting neurogenesis processes [1–3].

Various protocols have been employed to induce differentiation in SH-SY5Y cells, encompassing a diverse range of inducers and methodologies. For instance, retinoic acid, a derivative of vitamin A, has been extensively utilized to drive neuronal differentiation in SH-SY5Y cells by activating retinoic acid receptors and downstream signaling pathways involved in neurogenesis [4]. Similarly,

*Abbreviations:* TPA 12-O, tetradecanoylphorbol-13-acetate; He, *Hericium erinaceus*; MTT assay 3, 4,5-dimethylthiazol-2-yl-2,5-diphenyltetrazolium bromide assay; Cm, Membrane capacitance; Rm, Membrane resistance; Vm, Resting membrane potential; TTX, Tetrodotoxin; VGSC, Voltage-gated sodium channel; I-V plots, Current-voltage plots; SNARE, Soluble N-ethylmaleimide-sensitive factor Attachment protein REceptor; PCNA, Proliferating Cell Nuclear Antigen.

* Corresponding author.
*E-mail address:* paola.rossi@unipv.it (P. Rossi).

https://doi.org/10.1016/j.biopha.2025.118204
Received 15 January 2025; Received in revised form 19 May 2025; Accepted 21 May 2025
Available online 24 May 2025

12-O-tetradecanoylphorbol-13-acetate (TPA), a potent protein kinase C activator, has been shown to induce neuronal differentiation in SH-SY5Y cells by modulating intracellular signaling cascades [5]. Additionally, brain-derived neurotrophic factor (BDNF), a neurotrophin crucial for neuronal survival and differentiation, has been employed to promote neuronal differentiation in SH-SY5Y cells, highlighting the diverse array of strategies available to researchers for studying neuronal differentiation in this cell model [6,7].

Recently, natural compounds have emerged as promising tools in neuroprotection and neuroregeneration[12-13]. Among these, *Hericium erinaceus* (H. erinaceus), also known as lion's mane mushroom, has attracted attention for its neurotrophic properties. Its extracts contain bioactive compounds such as erinacines and hericenones, which have been shown to stimulate BDNF and nerve growth factor (NGF) production[14-17], key regulators of neuronal survival, differentiation, and synaptic plasticity.

Recent publications, such as the studies conducted by Mori et al. and Brandalise et al. have significantly contributed to our understanding of the neuroregenerative properties inherent in H. erinaceus extract [8–10]. These investigations, along with others [11,12], have elucidated the extract's remarkable capacity to not only enhance neurogenesis but also to ameliorate cognitive decline in animal models of neurodegenerative diseases. Kawagishi et al. [13] uncovered compelling evidence about the extract's ability to stimulate neurogenesis, a process crucial for brain repair and cognitive function in human astrocytoma cells. Similarly, Rossi et al., 2018's study underscored the extract's potential in mitigating cognitive decline [11], thereby highlighting its promise as a therapeutic agent for neurodegenerative disorders.

Building on this background, we hypothesize that long-term exposure to H. erinaceus extract promotes neuronal differentiation in SH-SY5Y cells. Through extended treatment, we aim to evaluate its potential to reduce proliferative activity and support differentiation, offering a novel perspective on neuroblastoma intervention.

## 2. Materials and methods

### 2.1. Cells and treatments

#### 2.1.1. SH-SY5Y cells

SH-SY5Y cells, a human neuroblastoma cell line provided by ATCC (ATCC CRL- 2266) (Manassas, Virginia, US), were grown in a 1:1 mix of DMEM and Ham's F12 supplemented with 10 % FBS and 1 % penicillin/streptomycin at 37 °C and 5% $CO_2$. When reaching confluence, cells were divided and plated in a new fresh growth medium. Cell passaging was performed by centrifugation at 1900 rpm for 7 minutes before resuspension in the new fresh growth medium. Cells were always maintained at low passages (between 3 and 10). All cell culture reagents were purchased from Euroclone (Milan, Italy). Complete culture medium was supplemented with 50 μg/mL He1 + 50ug/mL He2. The treatment for H. erinaceus (He) condition was performed by plating and maintaining cells in He1 + He2 supplemented culture medium for > 200 hours, with a maximum of 288 hours. To ensure the maintenance of nutrients in the cell culture throughout the entire duration of the treatment, cells were plated at low confluence with 25 % more medium compared to standard growth conditions, and the essential parameters for cell cultivation (cell culture media volume and pH) were monitored daily.

#### 2.1.2. LUHMES cells

LUHMES cells (Lund Human Mesencephalic; originally derived from human female fetal mesencephalon; ATCC, VA, USA) were cultured and differentiated following established protocols [14,15]. Cells were maintained at 37 °C in a humidified incubator with 5 % $CO_2$. For proliferation, LUHMES cells were grown in Advanced DMEM/F-12 (Thermo Fisher Scientific, Waltham, MA, USA), supplemented with 2 mM L-glutamine (Thermo Fisher), 1 × N2 supplement (Thermo Fisher), and 40 ng/mL basic fibroblast growth factor (bFGF, PeproTech). Flasks or plates were pre-coated with poly-L-ornithine (50 μg/mL, Sigma-Aldrich) and fibronectin (1 μg/mL, Sigma-Aldrich). For differentiation, cells were plated at a density of 2–4 × $10^4$ cells/$cm^2$ in differentiation medium consisting of Advanced DMEM/F-12 supplemented with 1 × N2, 2 mM L-glutamine, 1 mM dibutyryl cyclic AMP (Sigma-Aldrich), 2 ng/mL glial cell line-derived neurotrophic factor (GDNF, PeproTech), and 1 μg/mL tetracycline (Sigma-Aldrich). Media was refreshed every other day. Differentiation was carried out for 10 days to allow maturation into post-mitotic dopaminergic-like neurons. For electrophysiological recordings, cells were plated on 12 mm glass coverslips pre-coated with poly-L-ornithine (10 μg/mL) and laminin (10 μg/mL, Sigma-Aldrich). After the 10-day differentiation period, LUHMES cells were treated with the He blend at the same concentration used for SH-SY5Y cells (50 μg/mL He1 + 50 μg/mL He2) and for an equivalent duration (>200 hours) to ensure experimental consistency across cell models

#### 2.1.3. Preparation of Mushroom Extracts

Two strains of He collected in Italy has been used in this work, He1 and He2. The mycelia of these strains were isolated in pure culture from sporophores collected in a Mediterranean environment from living oaks (Siena province, Tuscany, Italy). The strains were identified by molecular analysis and preserved in MicUNIPV, the Fungal Research Culture Collection at the University of Pavia (Italy) [16]. In particular, He1 mycelium and He2 cultivated sporophore were chosen. The procedures for extracting compounds from these strains have been thoroughly documented in several studies [24–26]. For the alcoholic extraction, 1 g of both lyophilized He1 mycelium (obtained from liquid culture containing 2 % Malt extract) and He2 sporophore cultivated at the Botanical Garden greenhouse (Pavia University, Italy) was blended with 10 mL of ethanol 70 % and 30 % water, left in the thermostat at 50 °C for 24 h. At the end, the material was transferred for centrifugation (4000 rpm for 3 min) and the supernatant was stored at −20 °C for HPLC analysis [17–19]. The metabolites were identified and measured through HPLC-UV-ESI/MS analyses, previously described [24–26]. This method allows for the precise identification and quantification of various metabolites present in the extract. Specific standards and carefully calibrated curves were utilized to ensure the accuracy and reliability of the measurements. Standard compounds of erinacines and hericenones were kindly provided by Prof. Hirokazu Kawagishi (Shizuoka University, Japan), as previously reported [18], while ergothioneine was kindly donated by Tetrahedron (Paris, France). The erinacine A content in He1 mycelium (150 μg/g) is consistent with those reported by Krzyczkowski et al. (2010) in enhanced submerged cultivation studies [18]. He2 sporophore contains high levels of hericenones C (1560 μg/g) and D (188 μg/g). Ergothioneine was present in both the He1 mycelium (0.58 mg/g) and in He2 sporophore (2.4 mg/g), giving a final ergothioneine concentration of 2.98 mg/g. These values align with the findings for certain strains reported by Lee et al. (2016) [19]. The erinacine A content in He1 mycelium (150 μg/g) is consistent with those reported by Krzyczkowski et al. (2010) [20]. He2 sporophore contains high levels of hericenones C (1560 μg/g) and D (188 μg/g). Ergothioneine was present in both the He1 mycelium (0.58 mg/g) and in He2 sporophore (2.4 mg/g), giving a final ergothioneine concentration of 2.98 mg/g. These values align with the findings for certain strains reported by Lee et al. (2016) [21].

#### 2.1.4. MTT assay

In order to select the appropriate, non-toxic He dose to be used in the following analyses, as a first experimental step, a range of He mixture concentration was evaluated through the MTT [3-(4,5-dimethylthiazol-2-yl)-2,5-diphenyltetrazolium bromide]. Briefly, SH-SY5Y cells were seeded in a 96-well plate at a density of 10,000 cells/well (0.2 mL medium per well) and incubated for 24 hours in a humidified atmosphere containing 5 % of $CO_2$. The following day, the culture medium was replaced with fresh medium added with He1 and He2 in combination in

a concentration ranging from 5 to 250 μg/mL. For the control condition, cells were incubated with the culture medium only. After 48 h-exposure, 20 μL of MTT solution (HelloBio, UK) was added to each well; this operation was performed in the dark, and the plates were subsequently incubated for 3 hours at 37°C. Cell viability was then assessed by measuring the samples' absorbance at 550 nm using the Multiplate reader BioTek ELx808 (Italy). As a background value, all experiments were conducted while assessing in parallel blank samples containing He1, He2 and MTT in culture medium (without cells) to exclude the occurrence of non-enzymatic reduction of MTT by He1 and He2. The optical density of the formazan formed in the control group cells was taken as 100 %. Cell viability % was calculated as follows:

$$\text{Cell viability\%} = \frac{(\text{Absorbance value of treated cells} - \text{Absorbance value of blank})}{(\text{Absorbance value of untreated cells} - \text{Absorbance value of blank})} \times 100.$$

*2.1.5. Patch-Clamp Experiments*

Electrical signals were recorded with an Axopatch 200-B amplifier (Molecular Devices, USA), [−3 dB; cutoff frequency (fc) = 1 kHz] and sampled with a Digidata-1440A interface. Electrophysiological recordings were performed in Whole-Cell configuration on SH-SY5Y cells. Cells were recorded in a bath solution containing (in mM): NaCl 130, KCl 4, Hepes 10, glucose 10, $CaCl_2$ 2, $MgSO_4$ 1, pH 7.4. Glass borosilicate pipettes were pulled using Flaming/Brown micropipette puller P-97 (Sutter Instrument Co., USA) to achieve a 4–7 MΩ resistance and were filled with (in mM): $K^+$- gluconate 126, NaCl 4, Hepes 5, glucose 15, $MgSO_4$ 1, BAPTA FREE 0,1, BAPTA $Ca^{2+}$ 0005, ATP 3. GTP 0,1 pH 7.2. The current recordings in voltage clamp configuration were performed with the following protocols: a series of voltage steps ranging from −60 mV to + 140 mV with an increment of 20 mV, and a series of voltage steps ranging from −120 mV to + 40 mV with an increment of 20 mV at a sampling rate of 20 kHz were delivered to the cells. The passive properties of the cell (including membrane resistance and capacitance) were measured by eliciting a hyperpolarizing step of −10 mV from the holding potential of −60 mV [22,23].

For the depolarizing protocols, the PN leak subtraction of the Clampex program (pClamp 10 software) was used to eliminate the effects of the leakage current on the whole-cell responses [24,25]. The following compounds were bath-perfused in the patch-clamp experiments: TTX 1 μM (Hello Bio), Nifedipine 10 μM (Hello Bio), to selectively block the VGSC-mediated current [26]. Current-clamp recordings: The resting membrane potential (RMP) was assessed after break in the cell. The holding potential was set according to a value ~-70 mV. The current clamp protocol consisted of a series of 5 pA steps of current injection, starting from a negative injection of −10 pA. Outward currents were measured in voltage clamp by applying subsequent voltage steps of + 20 mV from a holding potential of −60 mV, up to + 140 mV [27]. Steady outward currents were recorded as the average of the last 50 ms of the voltage step. Inactivating outward currents were calculated by subtracting the sustained outward current from peak outward currents [28]. Inward currents were calculated in voltage clamp as the negative peak recorded at 0 mV by applying subsequent voltage steps of + 20 mV from a holding potential of −120 mV, up to + 40 mV [29]. Electrophysiological analysis and statistics were performed using Clampfit 10.6 (Molecular Devices), OriginPro 9.1 and GraphPad Prism version 10.0.0 for Windows.

*2.1.6. Phase contrast microscopy*

SH-SY5Y cells were plated on 22 × 22 mm coverslip at a density of 10.000 cells per coverslip and observed under inverted phase contrast microscopy equipped with a 20 × objective (Olympus CKX41) after 24, 72, 144 and 200 hours exposure to He (50μl/mL + 50μl/mL) with the aim to evaluate the onset of potential changes/alteration of cell morphology. Digital micrographs were acquired with a camera (Olympus MagniFire digital camera), stored on a PC and processed with the Olympus CellˆF 3.1 software. The analysis of cell density was performed using ImageJ software 1.54 (NIH, USA). Specifically, four random images in each well were acquired at 40 × magnification for each replicate and then converted to binary images and analyzed with the "particle analysis tool". The cell density was calculated as number of cells/area and expressed in mm [2]. Data are presented as the mean ± SEM. The number and the length of neurite were analyzed by the semi-automated tracing ImageJ plugin NeuronJ. Using this plugin, neurites are manually traced, thanks to an algorithm that compares the pixel intensity on the neurite with its adjacent pixel neighborhoods, automatically updating the cursor to follow an estimated path of the neurite and increasing the accuracy and speed of tracing. After the neurites are traced, a text file is generated that contains measurements of the lengths of all the neurites [30].

*2.1.7. Hematoxylin and eosin and Nissl staining*

For the morphological evaluations, control and treated cells were grown on coverslips (22 mm×22 mm), fixed with 4 % formalin (20 min), and post-fixed with 70 % ethanol at −20°C for at least 24 h. The samples were rehydrated for 10 min in PBS 1X and then were incubated with hematoxylin and eosin or Nissl stainings. For Hematoxylin and eosin, the samples were incubated with hematoxylin for 10 minutes, washed with PBS 1x, and stained with eosin for 30 seconds. For Nissl, the slides were incubated with cresyl violet 0.1 % for 5 minutes. Lastly, for both staining, cells were washed in PBS 1X and mounted with a drop of Mowiol (Calbiochem-Inalco, Italy) for microscopy visualization.

*2.1.8. Clonogenic assay*

Cells were plated in a 6 well plate at a density of 300 cells/well in 2 mL of control and He supplemented growth medium. Cells were then incubated at 37 °C for a minimum of 10 days, to allow optimal growth of the colonies. After 11 days cells were fixed using ice-cold methanol and colonies were colored with Crystal Violet (CV) 0,1 % (PanReac AppliChem, Italy) to evaluate the number and area of colonies obtained in different conditions. Digital micrographs were acquired with a camera (Olympus MagniFire digital camera), stored on a PC and processed with the Olympus CellˆF software (version n. 3.1). The analysis of cell density was performed using ImageJ software 1.54 (NIH, USA). Specifically, four random images in each well were acquired at 20 × magnification for each replicate and then converted to binary images and analyzed with the "particle analysis tool". The cell area was expressed in mm [2]. Data are presented as the mean ± SEM.

*2.1.9. Immunofluorescence Reactions*

For the immunofluorescence quantifications, three independent experiments were performed for each experimental condition. After reactions, control and treated cells were grown on coverslips (22 mm×22 mm), fixed with 4 % formalin (20 min), and post-fixed with 70 % ethanol at −20°C for at least 24 h. The samples were rehydrated for 10 min in PBS and then incubated with 1 % Bovine Serum Albumin (BSA) to block nonspecific binding sites. Subsequently, the cells were immunolabeled using the mouse monoclonal anti-bIII tubulin (ValidAb, Hello Bio, UK), the mouse monoclonal anti-PCNA (Merck, Italy), the rabbit monoclonal antibody anti-CD133 (Cell Signaling Technology,

USA), the mouse polyclonal antibody anti-Nav (Neuromab, USA), the rabbit polyclonal antibody anti-Synaptotagmin-1,2 (Abcam, Cambridge, UK), diluted 1:200, 1:200, 1:200, 1:250, 1:200 in PBS (Merck, Italy) for 1 hour at RT in a dark, moist chamber. Then, the cells were washed with PBS and incubated for 45 min with goat anti-mouse IgG (H + L) highly cross-adsorbed secondary antibody, Alexa Fluor Plus 594 and goat anti-mouse IgG (H + L) highly cross-adsorbed secondary antibody, Alexa Fluor Plus 488 both diluted 1:200 in PBS (Thermo Fisher Scientific, Italy), and phalloidin conjugated with Alexa Fluor 488. DNA counterstaining was performed using 0.1 mg/mL Hoechst 33258 (Merck, Italy). Lastly, cells were mounted with a drop of Mowiol (Calbiochem-Inalco, Italy) for microscopy visualization.

#### 2.1.10. Immunocytochemical Evaluations

For the immunofluorescence quantifications, three independent experiments were performed for each experimental condition. After reactions, coverslips were examined using a Leica DM6B WF microscope (Leica microsystems, Italy), and images were captured with an ORCA-Flash4.0 V3 Digital CMOS camera C13440–20CU (Hamamatsu Photonics, Italy), and results were analyzed using the Leica Application Suite X (LAS X) software (Version 5.1.0). For each condition, 11 quadrants (about 50 cells) were evaluated for random analysis. Single-channel images were analyzed in grayscale, with the minimum value being 0 (black) and the maximum value being 255 (white). The mean fluorescence intensity was measured using ImageJ software 1.54 (NIH, USA) and expressed as the mean ± SEM.

To prevent potential discrepancies in results caused by slight procedural variations, all immunostaining reactions were simultaneously performed, and, as a control, some cells were incubated without primary antibodies, using only PBS; any immunoreactivity was observed under this condition. To assess the immunopositivity of cells for the examined markers, all experiments were conducted in parallel with bank samples incubated without primary antibodies. In detail, the mean fluorescence intensity of blank samples was subtracted from the mean fluorescence intensity of immunostained cells. Immunopositivity was established when the mean fluorescence intensity value of single cells exceeded that of the blank samples.

### 2.2. Statistical analysis

All data are expressed as the mean ± standard error of the mean (SEM) based on the experimental values obtained from three independent experiments conducted under identical conditions. Statistical significance was determined at three levels: $p < 0.05$ (*), $p < 0.01$ (**), and $p < 0.001$ (***). For comparisons between two groups, the Mann-Whitney *U* test or unpaired *t*-test was applied, depending on the distribution and variance of the data. For multiple group comparisons, one-way or two-way analysis of variance (ANOVA) was performed to evaluate the interaction effects of independent variables. When significant differences were identified, post hoc tests, including Bonferroni's test or Dunnett's test, were conducted to pinpoint specific group differences while controlling for multiple comparisons. The analyses were performed using Prism software (GraphPad, version X) and Origin 2021 (OriginLab), with all statistical methods validated for appropriate assumptions regarding data normality and variance. Prior to parametric testing, data distribution was assessed using the Shapiro-Wilk test, and homogeneity of variances was verified using Levene's test. Nonparametric tests were employed when data failed to meet these assumptions.

### 2.3. Development of a standardized Hericium erinaceus blend: harnessing synergistic bioactive properties

Before evaluating the effects of *Hericium erinaceus* (He) extracts on SH-SY5Y cells, assessed in terms of morphological, molecular and physiological changes, we firstly determined the optimal blend to be tested. Hence, after a comprehensive analysis of various strains of He from the Italian peninsula at our disposal, we selected two distinct extracts, namely He1 and He2, which we have previously characterized [19,20,28–30]. Based on these knowledge, we proposed a blend composed of He1 and He2, with the clear notion in mind that it can provide a wide array of nootropic bioactive metabolites, in high concentrations (for details, see Table 1).

**Table 1**
Concentration of selected nootropic bioactive metabolites in the blend (He1 + He2). Values are expressed as micrograms per gram of dried extract (μg/g).

| Bioactive Metabolites | Quantity (μg per gram of dried extract) |
|---|---|
| Erinacine A | 150 |
| Hericenones C | 1560 |
| Hericenones D | 188 |
| Ergothioneine | 2980 |

Among these compounds, Erinacine A is recognized for its neuroprotective properties [31–33], while Ergothioneine serves as a potent antioxidant [34–36]. Conversely, Hericenones C and D have demonstrated significant neurotrophic and anti-inflammatory effects [13]. Hence, based on He1 and He2 complementary bioactive profile, we selected sporophore extract and mycelium extract for He2 and He1, respectively. By blending these latter in a 1:1 ratio, we aim at harnessing a comprehensive spectrum of He nootropic metabolites, potentially offering synergistic benefits for neuronal health, leveraging the distinct but complementary properties of each extract. Such a blend may enhance cellular resilience against oxidative stress, promote neuronal growth, and mitigate inflammatory responses, thereby providing a multifaceted defense against neurodegenerative processes.

## 3. Results

### 3.1. Establishment of optimal concentration of Hericium erinaceus extracts

The SH-SY5Y cell line has emerged as a well-known model for neuronal differentiation [1], hence this in vitro model was chosen to test the effects/properties of the blend, made by mycelium of He1 and sporophore of He2. For convenience, the blend will be referred to as "He" from this point on in the manuscript. As the initial step in our experimental procedure, we identified the appropriate He concentration to be tested. Therefore, an MTT assay was performed to assess cell viability following 72 hours exposure to increasing concentrations of He (Fig. 1a). The combined exposure to 50 μg/mL He1 and 50 μg/mL He2 results in a viability reduction of 1.60 ± 4.22 % (n = 3) (Fig. 1a). Therefore, the blend containing 50 μg/mL of He1 and 50 μg/mL of He2 extracts was selected for the following experiments (see Methods).

### 3.2. Morphological changes and reduced proliferation in He-exposed SH-SY5Y cells

Based on previous studies revealing that He extracts are capable to influence cell morphology and proliferation rates, we initially focused on these aspects to understand He effects on SH-SY5Y cells. Specifically, we investigated the morphological changes of SH-SY5Y cells in response to He treatment. Literature data well documented that when SH-SY5Y cells are induced to differentiate using agents such as TPA, they adopt a more elongated, neurite-bearing phenotype resembling mature neurons [37]. Additionally, neurotrophic factors like BDNF have been shown to promote neuronal differentiation and reduce proliferation in SH-SY5Y cells by activating specific signaling pathways [38].

To characterize cellular morphology and to assess potential differentiation phenomena, hematoxylin and eosin (H&E) and Nissl staining were performed (Fig. 1b) after 200 hours of He 50ug/mL exposure. The staining revealed noticeable differences in cell morphology comparing control and He-treated cells. In fact, control cells appeared closely

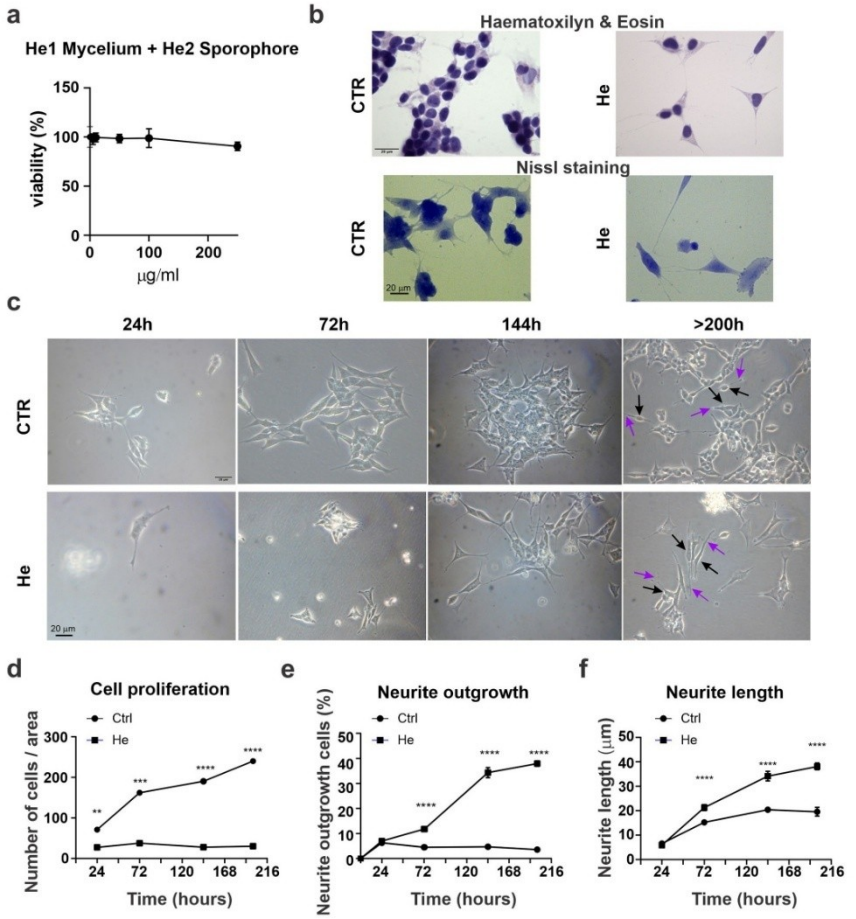


**Fig. 1.** Time-dependent reduction of cell proliferation and enhancement of neurite outgrowth in SH-SY5Y cells following He exposure, rich in nootropic bioactive metabolites. (a) Cell viability assessment: SH-SY5Y cells were treated with increasing concentrations (0, 5, 10, 50, 100, 250 µg/mL) of a blend combining He mycelium (He1) and sporophore (He2) extracts. Cell viability (% relative to untreated control) was measured. (b) Hematoxylin and eosin staining: micrographs displaying cellular morphology of SH-SY5Y cells under control (CTR) and He-treated conditions (He). Scale bar: 20 µm. (c) Representative phase-contrast images: morphological changes and neurite extension in SH-SY5Y cells under CTR conditions and after 24, 72, 144, and over 200 hours exposure to He. Black arrows point to the cell body of the cells while purple arrow indicate the location of some neurites (d) Quantification of cell proliferation: number of cells per area (148 µm2) at selected time points for both CTR and He-treated groups. (e) Neurite outgrowth analysis: percentage of cells exhibiting neurite outgrowth over time in CTR and He-treated groups. (f) Neurite length measurement: average neurite length at various time points, highlighting significant elongation in the He-treated group.

packed with less pronounced cytoplasmic extensions, whereas He-treated cells exhibited elongated cell bodies and extended neurites, suggestive of neuronal differentiation.

To have a better resolution of these morphological changes while simultaneously tracking the proliferation rate, we employed phase-contrast microscopy to observe neurite outgrowth, a hallmark of

neuronal differentiation, both in control and He-treated condition (Fig. 1c). This approach allowed us to monitor dynamic cellular processes and provided a more detailed comprehension of He-induced differentiation.

Cell proliferation analysis was conducted at different time points to determine the effect of He treatment on cells growth rate (Fig. 1c). Data revealed a significant decrease in cell proliferation comparing He-treated cells with the control group, already 24 hours after exposure, further exacerbated at prolonged exposure times (number of cells/area; 24 h: CTR 85.00 ± 2.88, n = 3; He 28.66 ± 0.88, n = 3; $p = 4.8 \times 10^{-5}$,

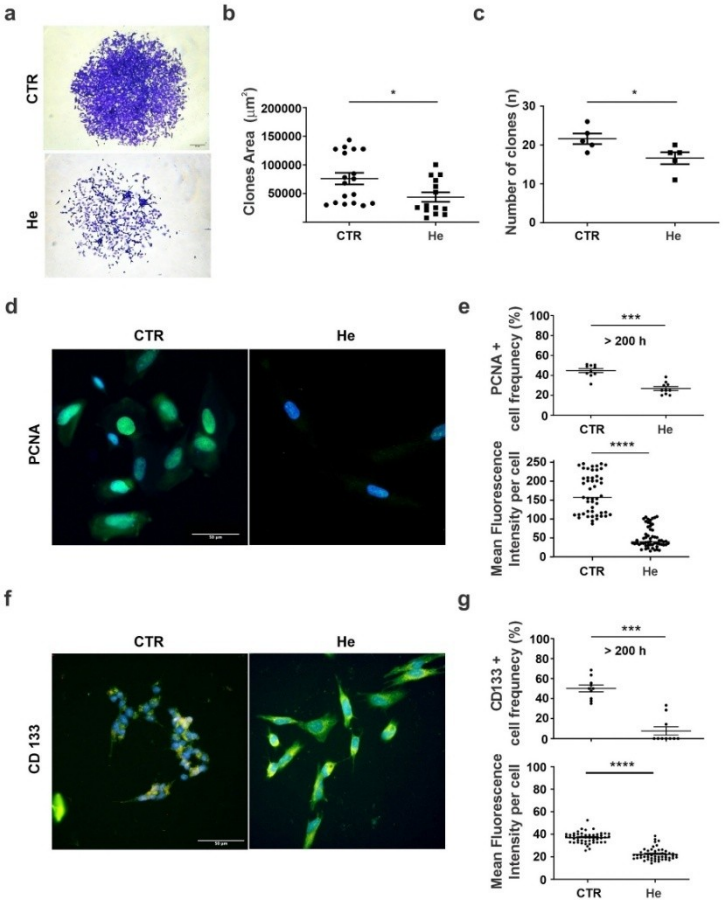


**Fig. 2.** Effects of He Treatment on Colony Forming, Proliferation and Stemness marker expression (a) Colony forming assay: representative micrographs of crystal violet-stained colonies showing noticeable morphological differences comparing control (CTR) and He-treated SH-SY5Y cells. (b) Quantitative analysis of colony area. (c) Quantitative analysis of the number of colonies. (d) Representative immunofluorescence images of PCNA staining in SH-SY5Y cells under control conditions (CTR) and after > 200 hours exposure to He. PCNA immunolabelling: green fluorescence; DNA (stained with Hoechst 33258): blue fluorescence. Scale bar: 50 µm. (e) Quantitative analysis of PCNA: immunopositive cell frequency (%) and mean fluorescence intensity per cell in control and He-treated groups. (f) Representative immunofluorescence images of CD133 staining in SH-SY5Y cells in control conditions (CTR) and after > 200 hours He exposure. CD133 immunolabelling: green fluorescence; DNA (stained with Hoechst 33258): blue fluorescence. Scale bar: 50 µm. (g) Quantitative analysis of CD133: immunopositive cell frequency (%) and mean fluorescence intensity per cell in control and He-treated groups.

unpaired *t*-test; 72 h: CTR 170.00 ± 4.16, n = 3; He 39.66 ± 2.03, n = 3; p = 9.5 × $10^{-6}$, unpaired *t*-test; 144 h: CTR 190.16 ± 0.84, n = 3; He 27.94 ± 2.22, n = 3; p = 2.75 × $10^{-6}$, unpaired *t*-test; >200 h: CTR 240.0 ± 3.96, n = 3; He 30.26 ± 1.59, n = 3; p = 1.02 × $10^{-6}$, unpaired *t*-test, Fig. 1d). Morphological analysis indicated a significant increase in neurite outgrowth over time in He-treated cells compared to control group starting from 72 hours (% of cell with neurite; 24 h: CTR 4.716 ± 0.16, n = 3; He 6.99 ± 0.22, n = 3; p = 0.001, unpaired *t*-test; 72 h: CTR 4.51 ± 0.201, n = 3; He 11.75 ± 0.41, n = 3; p = 9.1 × $10^{-8}$, unpaired *t*-test; 144 h: CTR 4.67 ± 0.15, n = 3; He 34.32 ± 2.02, n = 3; p = 1.26 × $10^{-4}$, unpaired *t*-test; >200 h: CTR 3.57 ± 0.19, n = 3; He 37.94 ± 1.04, n = 3; p = 5.36 × $10^{-7}$, unpaired *t*-test; Fig. 1e). Consistently, the measurement of neurite length revealed a significant increase in He-treated cells compared to control starting at 72 hours (CTR: ~15.00 ± 1.50 μm; He: ~25.00 ± 1.80 μm), at 144 hours (CTR: ~19.00 ± 1.70 μm; He: ~38.00 ± 1.60 μm), and at 200 hours (CTR: 19.55 ± 1.79 μm, n = 48; He: 38.08 ± 1.48 μm, n = 48; p < 0.0001, ANOVA followed by Šidák's multiple comparisons test, Fig. 1f).

### 3.3. He Treatment reduces clonogenic capability, proliferation and stemness marker expression

In the previous chapter, we demonstrated that the proliferation rate of SH-SY5Y cells is decreased in the presence of He, accompanied by elongated neurites. These characteristics are typically associated with reduced stemness and enhanced differentiation. To investigate the effects of He on SH-SY5Y cell proliferation and differentiation, we performed colony formation assays parallelly assessing key proliferation and stemness markers. The colony forming assays revealed a significant reduction both in colony area and colony number in He-treated cells compared to the control group (Fig. 2a). Quantitative analysis showed that the colony area was significantly reduced in the He-treated cells (CTR: 76,089 ± 10,106 $μm^2$, n = 18; He: 43,797 ± 8265 $μm^2$, n = 14; p = 0.0242, unpaired *t*-test; Fig. 2b). Similarly, the number of colonies formed by He-treated cells was markedly diminished compared to control group (CTR: 21.60 ± 1.36, n = 5; He: 16.60 ± 1.53, n = 5; p = 0.0409, unpaired *t*-test; Fig. 2c). These findings suggest that He treatment reduces the clonogenic capability of SH-SY5Y cells, indicating a potential shift towards a more differentiated state.

To further evaluate this shift, we analyzed the expression of PCNA (Proliferating Cell Nuclear Antigen) and CD133, as typical markers associated with proliferation and stemness, respectively. Immunofluorescence staining revealed a notable reduction in PCNA expression in He-treated cells compared to controls (Fig. 2d). Quantitative evaluation indicated a significant decrease both in the frequency of PCNA-immunopositive cells (CTR: 67.85 ± 4.19 %, n = 6; He: 27.48 ± 4.19 %, n = 6; p = 0.0002, unpaired *t*-test, Fig. 2e top) as well as in the mean fluorescence intensity per cell (CTR: 95.46 ± 11.38, n = 6; He: 40.91 ± 11.38, n = 6; p = 0.0007, unpaired *t*-test; Fig. 2e bottom). These results indicate that He exposure significantly suppresses cell proliferation. Additionally, the assessment of CD133 expression showed a significant reduction in He-treated cells compared to controls (Fig. 2f). The frequency of the CD133-immunoreactive cells substantially decreased in the He-treated group (CTR: 71.00 ± 3.08 %, n = 6; He: 35.50 ± 3.08 %, n = 6; p = 0.0002, unpaired *t*-test, Fig. 2g top). Likewise, the mean fluorescence intensity per cell was significantly lower in He-treated group (CTR: 36.94 ± 0.67, n = 50; He: 22.15 ± 0.75, n = 50; p < 0.0001, unpaired *t*-test; Fig. 2g bottom). This reduction in CD133 expression further supports the idea that He treatment promotes differentiation towards a more mature neuronal phenotype.

Collectively, these results indicate that He treatment significantly suppresses proliferation and promotes differentiation in SH-SY5Y cells. The reduced colony formation, paralleled by the decreased PCNA and CD133 expression, corroborate the hypothesis that He is capable to induce a shift towards a differentiated neuronal state.

### 3.4. Passive properties analysis of SH-SY5Y cells after prolonged exposure to he

Previous studies have shown that He have an impact neuronal cells and oligodendrocytes, by modulating their morphology and functional properties [8,28,39,40]. Specifically, He has been reported to induce changes in cell morphology, such as neurite outgrowth and myelin production. Given these reported effects, we hypothesized that the morphological changes induced by He could also impact their passive electrophysiological properties. Changes in cell morphology, such as neurite elongation, are known to influence parameters like input resistance, membrane time constant, and capacitance, which are crucial for cellular excitability and signalin. To investigate this, we sought to measure the electriophysiological passive membrane properties of our *in vitro* model. Specifically, using patch-clamp recordings, we examined the cells passive properties such as Membrane Capacitance (Cm) and Membrane Resistance (Rm) to assess any alterations induced by He treatment, comparing the control group with the one receiving a prolonged exposure (> 200 hours) to He (Fig. 3a). While the fast component of the membrane time constant ($τ_{fast}$) was unchanged in the two conditions (CTR: 0.19 ± 0.03 ms, n = 16; He: 0.18 ± 0.03 ms, n = 14; p = 0.59, Mann-Whitney Test, Fig. 3b left) the slow component of the membrane time constant ($τ_{slow}$) was significantly slower in He group compared to the control one (CTR: 0.60 ± 0.09 ms, n = 17; He: 14.92 ± 0.16 ms, n = 14; p = 0.018, Mann-Whitney Test, Fig. 3b right).

Likewise, a significant increment in Cm was detected in He -treated SH-SY5Y cells (CTR: 10.91 ± 1.31 pF, n = 17; He: 14.92 ± 1.34 pF, n = 19; p = 0.04, Mann-Whitney Test, Fig. 3c left). Instead, no differences were observed between the control and He group for the Rm (CTR: 1.02 ± 0.11 GΩ, n = 16; He: 1.00 ± 0.10 GΩ, n = 18; p = 0.81, Mann-Whitney Test, Fig. 3c center) and the resting membrane potential (Vm) (CTR: −35.63 ± 2.32 mV, n = 16; He: −32.53 ± 2.24 mV, n = 17; p = 0.30, Mann-Whitney Test, Fig. 3c right). Overall, these findings indicate that He treatment modulates the slow component of the membrane time constant and the membrane capacitance, consistently with the observed increase in neurite outgrowth and so cellular surface of the distal compartment. These electrophysiological changes likely reflect underlying mechanisms of neuronal differentiation and functional maturation following prolonged exposure to He.

### 3.5. He treatment induces electrophysiological changes in inward and outward currents of SH-SY5Y cells

Inward currents play a crucial role in neuronal differentiation and maturation, with their expression and magnitude influencing the developmental state of neurons [41–44]. To investigate the effects of He treatment on these currents, we examined the kinetic properties of inward currents in SH-SY5Y cells (Fig. 4a). Our analysis revealed notable differences between control and He-treated cells. Although the time to peak was similar between the two groups (CTR: 46.14 ± 1.1 ms, n = 13; He: 43.25 ± 0.95 ms, n = 15; p = 0.065, Mann-Whitney Test; Fig. 4b), He-treated cells exhibited significantly shorter half-width (CTR: 3.34 ± 0.48 ms, n = 14; He: 2.13 ± 0.35 ms, n = 15; p = 0.0064, Mann-Whitney Test; Fig. 4b), rise time 10–90 % (CTR: 1.97 ± 0.48 ms, n = 15; He: 0.86 ± 0.09 ms, n = 14; p = 0.0073, Mann-Whitney Test; Fig. 4b), and decay time (CTR: 6.81 ± 1.56 ms, n = 13; He: 3.12 ± 0.33 ms, n = 15; p = 0.0307, Mann-Whitney Test; Fig. 4b). These findings suggest that He treatment positively modulates the kinetic of inward currents, consistent with an increase in Nav-mediated currents, which are typically characterized by faster activation and inactivation compared to Cav-mediated currents. To further elucidate the mechanisms underlying these changes, we compared the current-voltage (I-V) relationships of inward currents between control and He-treated cells. The I-V plots revealed that the peak current amplitude occurred at similar holding potentials for both groups (~0 mV). This observation remained consistent regardless of whether we analyzed absolute peak

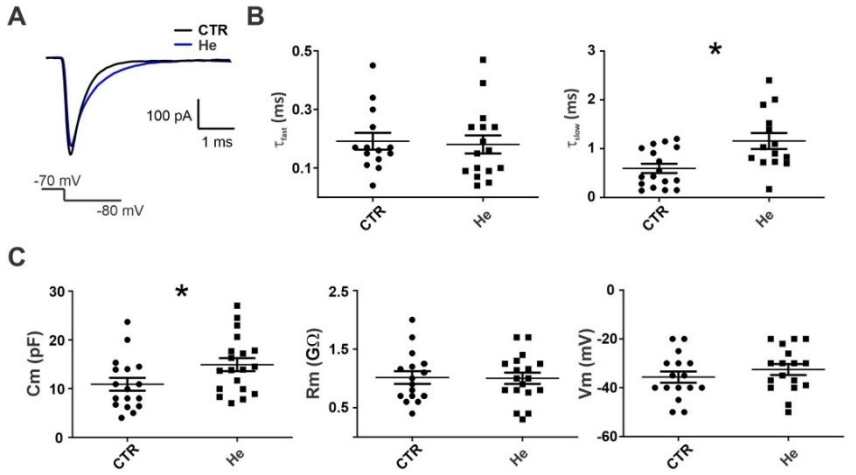


**Fig. 3.** Passive properties analysis of the SH-SY5Y cells reveals higher membrane capacitance and unchanged membrane resistance and resting membrane potential after > 200 hours of He compared to the control condition (CTR). (a) Representative averaged traces from control (black) and > 200 hours of He exposure (blue), showing the response to a hyperpolarizing voltage step from −80 mV to −70 mV. (b) Pool data for all of the recorded cells for Membrane Time Constant Fast and Slow (τ fast, τ slow), and (c) membrane capacitance (Cm), membrane resistance(Rm) and resting membrane potential (Vm).

amplitudes or normalized the values to the maximum current (Fig. 4c,d). These results indicate that the He-induced upregulation of inward currents is primarily due to an increase in channel density rather than a shift in activation properties.

Outward currents are also critical for neuronal differentiation and the development of action potentials. To assess the impact of He treatment on outward potassium currents, we analyzed steady-state outward currents in SH-SY5Y cells subjected to incremental depolarizing steps from a holding potential of −60 mV. This protocol was specifically designed to minimize contamination from inward current components. We observed a significant reduction in the outward steady-state current in the He-treated group compared to controls. The control group exhibited a peak outward current amplitude of 887.3 ± 380.4 pA (n = 12), whereas He-treated cells showed a markedly lower amplitude (381.8 ± 248.2 pA; n = 14; p = 0.0003, Mann-Whitney Test, Fig. 4f). Additionally, analysis of the distribution of cells with steady-state and inactivating outward currents revealed a significant shift in He-treated cells. Specifically, 42.9 % of He-treated cells exhibited inactivating outward currents, whereas no such expression was detected in control cells (Fig. 4g). These findings suggest that He treatment alters potassium channel expression or function, which may contribute to the observed changes in the electrophysiological profile of SH-SY5Y cells.

Together, these results demonstrate that He treatment induces substantial changes in both inward and outward currents, influencing the kinetic properties of Nav and Cav channels, as well as the amplitude and type of potassium currents. These electrophysiological changes likely reflect underlying mechanisms of neuronal differentiation and functional maturation following prolonged exposure to He extract.

### 3.6. Long-term exposure to he increases Na+ TTX-sensitive currents

We investigated the effects of long-time He treatment on the functional development of voltage-dependent currents in SH-SY5Y cells. SH-SY5Y cells displayed a variety of inward and outward currents under both control (CTR) and He-treated conditions. Incremental depolarizing voltage-clamp steps were applied to analyze inward currents. He-treated cells showed a significant increase in inward current amplitude compared to controls (CTR: −342.8 ± 34.98 pA, n = 12; He: −737 ± 122.1 pA, n = 13; p = 0.004, Mann-Whitney test, Fig. 5a, b). To assess the contribution of voltage-gated sodium channels (Nav) to these inward currents, we applied tetrodotoxin (TTX, 1 μM), a selective Nav blocker. TTX significantly reduced inward currents in both groups (CTR baseline: −392.80 ± 79.45 pA; CTR TTX: −238.60 ± 40.95 pA; p = 0.0098, paired *t*-test; He baseline: −640.20 ± 214.10 pA; He TTX: −4.00 ± 4.00 pA; p = 0.0418, paired *t*-test, Fig. 5a, c). The percentage reduction of TTX-sensitive current was significantly greater in He-treated cells (CTR: 38.6 ± 3.5 %, n = 5; He: 99.00 ± 1 %, n = 5; p = 0.0079, Mann-Whitney test, Fig. 5c). To investigate the temporal dynamics of inward current modulation, we performed a time-course analysis over a 216-hour period (Fig. 5d). At baseline (0 h), the mean inward current peak amplitude was –317.5 ± 54.5 pA in control cells (n = 4) and –188.8 ± 25.2 pA in He-treated cells (n = 4). While the current amplitude remained relatively stable in the control group, reaching –380.0 ± 58.3 pA at 216 hours (n = 5), He-treated cells exhibited a progressive and marked increase in inward current amplitude, reaching –621.4 ± 119.5 pA at 216 hours (n = 7). This difference between groups was statistically significant (p = 0.0025, Mann–Whitney test). To explore the residual TTX-insensitive current, we applied nifedipine (5 μM), a blocker of L-type calcium channels (Cav). Nifedipine significantly reduced inward current in control cells (CTR baseline: −282.6 ± 71.16 pA; CTR nifedipine: −84.40 ± 23.28 pA; p = 0.0357, paired *t*-test, Fig. 5e, f), but had no significant effect in He-treated cells (He baseline: −322.4 ± 91.44 pA; He nifedipine: −296.2 ± 76.48 pA; p = 0.2007, paired *t*-test, Fig. 5e, f). The percentage reduction was significantly higher in control cells (CTR: 66.34 ± 7.8 %, n = 5; He: 5.92 ± 2.73 %, n = 5; p = 0.0159, Mann-Whitney test, Fig. 5f). These results indicate that He treatment

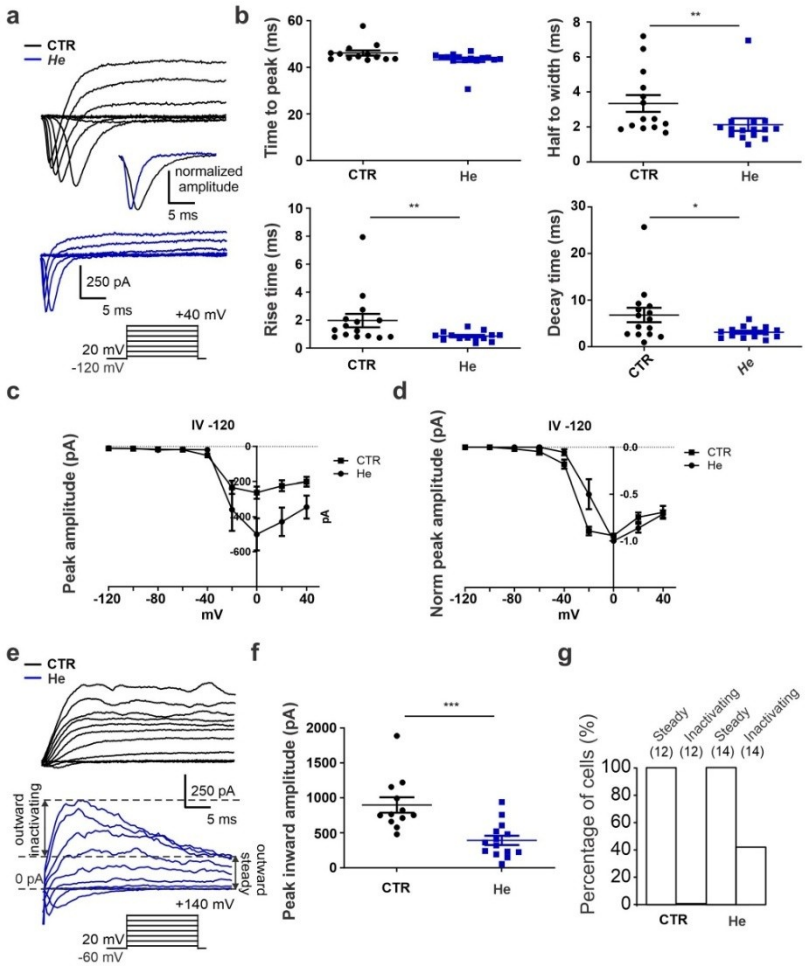


**Fig. 4. Differential Impact of He on Inward and Outward Conductances Density.** a) Example traces of inward and outward currents repertoire from control (black) and He treated cells (blue) in response to depolarizing voltage steps from −120 mV to + 40 mV. Inset: Schematic of the voltage protocol and amplitude normalization of the inward current from a representative example of a record derived from the control and He condition. (b) Quantification of kinetic properties of inward currents in control and treated groups: time to peak (top left), half-width (top right), rise time (bottom left), and decay time (bottom right). (c) Average I-V plot showing peak inward current amplitude as a function of voltage for control and Hericium treated cells. d) Normalized peak inward current amplitude for control and treated cells, normalized to the maximum amplitude for each group. (e) Example traces from control (black) and He treated cells (blue) for progressively depolarized voltage steps from −60 mV to + 140 mV, showing the inactivating and steady-state outward currents. (f) Pooled data showing peak outward current amplitude for control and treated cells. (g) Percentage of cells displaying steady-state and inactivating outward current profiles for both control and He-treated groups.

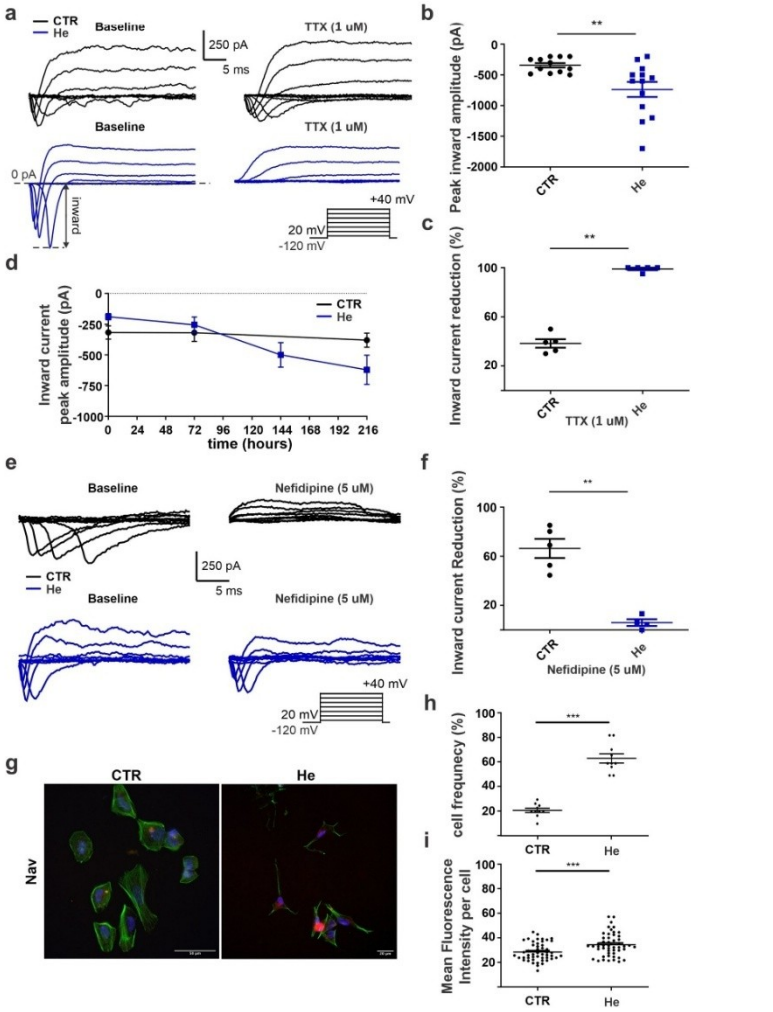


**Fig. 5.** Electrophysiological and Immunofluorescence Analyses of SH-SY5Y Cells After He Treatment. (a) Representative traces of inward current recordings from SH-SY5Y cells in control (black) and after > 200 hours of He treatment (blue), showing responses to depolarizing voltage steps from −120 mV to + 40 mV at baseline and after TTX (1 μM) application. (b) Summary plot of peak inward current amplitudes for control and He-treated groups. (c) Percentage reduction in inward current amplitude following TTX application for control and He-treated cells. (d) Time-course analysis of peak inward current amplitude in control and He-treated cells over 216 hours (e) Representative traces of inward currents in control (black) and He-treated cells (blue) before and after Nifedipine (5 μM) application. (f) Percentage reduction in inward current amplitude following Nifedipine application for control and He-treated cells.

leads to a dominance of TTX-sensitive currents (Nav) and a reduction in Cav activity. Immunofluorescence analysis showed that He-treated cells had higher Nav channel expression compared to controls (Fig. 5g). Quantitative analysis revealed a significant increase in the frequency of Nav-positive cells (CTR: 25.00 ± 4.8 %, n = 8; He: 67.50 ± 3.5 %, n = 8; $p < 0.001$, unpaired *t*-test, Fig. 5h). Additionally, the mean fluorescence intensity per cell was significantly higher in He-treated cells (CTR: 28.49 ± 1.051, n = 49; He: 34.39 ± 1.321, n = 50; $p < 0.001$, unpaired *t*-test, Fig. 5i).

These findings demonstrate that long-term exposure to He enhances the expression and function of Nav channels in SH-SY5Y cells, while reducing the contribution of Cav channels. This shift in ion channel activity may underlie the electrophysiological changes associated with He-induced neuronal differentiation.

### *3.7. Enhanced neuronal excitability and marker expression following he treatment*

Nav channels are primarily expressed in excitable cells and play a critical role in initiating action potentials (APs). Given the observed increase in Nav channel expression, we hypothesized that He treatment might enhance cell excitability, resulting in a more pronounced action potential profile. This hypothesis aligns with existing literature suggesting that differentiated SH-SY5Y cells exhibit increased action potential firing. To assess this, current-clamp experiments were conducted on SH-SY5Y cells both under control and He-treated conditions. Depolarizing current steps of increasing amplitude were injected into the recorded cells, and changes in membrane potential along with AP frequency were recorded (Fig. 6a). The analysis revealed that a higher proportion of He-treated cells displayed single APs compared to control cells, where a notable subset failed to produce APs in response to current injection (CTR single AP: 60.8 %, n = 14/23; CTR no AP: 34.9 %, n = 8/23; He single AP: 78 %, n = 14/18; He no AP: 0 %, n = 0/18; Fig. 6b). Moreover, a significant fraction of He-treated cells exhibited repetitive AP firing (CTR repeated AP: 4.3 %, n = 1/23; He repeated AP: 22 %, n = 4/18; Fig. 6b), resembling neuronal activity patterns.

The latency to the first AP against the injected current, showed results between the two groups (Fig. 6c) and the AP frequency plotted against the injected current indicated that He-treated cells achieved a maximum firing frequency of 24.8 ± 9.7 Hz (n = 3, Fig. 6d), resembling to some cortical [45], hippocampal excitatory cells [46] and amygdala neuron [22]. Analysis of AP characteristics demonstrated a significant increase in AP amplitude in He-treated cells (CTR: 33.18 ± 5.59 mV, n = 8; He: 52.86 ± 4.63 mV, n = 7; $p = 0.03$, Mann-Whitney test, Fig. 6e). Additionally, AP duration was significantly shorter in He-treated cells (CTR: 38.44 ± 11.41 ms, n = 8; He: 23.95 ± 11.65 ms, n = 9; $p = 0.0254$, Mann-Whitney test, Fig. 6f), and the AP threshold was more depolarized (CTR: −53.13 ± 1.67 mV, n = 8; He: −45.56 ± 2.69 mV, n = 9; $p = 0.046$, Mann-Whitney test, Fig. 6g).

These findings suggest that He treatment enhances the excitability of SH-SY5Y cells, likely due to increased functional expression of Nav channels, thereby enhancing AP characteristics and differentiation toward a neuronal-like phenotype.

To corroborate the differentiation induced by He treatment, we evaluated the expression of neuronal markers, specifically βIII-tubulin and synaptotagmin, which are indicative of neuronal differentiation and synaptic vesicle release, respectively (Fig. 6h,k). Immunofluorescence evaluation, assessed both in terms of immunopositive cell frequency and optical density (OD), revealed that βIII-tubulin immunoreactivity was significantly higher in He group (βIII-tubulin: CTR: 40.5 % ± 5.8, n = 10/23; He: 72.2 % ± 4.5, n = 13/18; $p < 0.001$, unpaired *t*-test, Fig. 6h,i) which also showed a significantly higher βIII-tubulin expression, as indicated by OD (>200 hours CTR: 34.66 ± 3.69 A.U., n = 37; >200 hours He: 72.26 ± 6.81 A.U., n = 37; $p = 0.00039$, unpaired *t*-test, Fig. 6h,j). Similarly, synaptotagmin-immunopositive cells frequency was significantly higher in the He group (synaptotagmin: CTR: 10 % ± 3.5, n = 1/10; He: 65 % ± 6.8, n = 6/10; $p < 0.0001$, unpaired *t*-test, Fig. 6k,l). Synaptotagmin expression, associated with the SNARE complex and neurotransmitter release, was also significantly elevated in He-treated cells (>200 hours CTR: 29.87 ± 1.28 A.U., n = 10; He: 67.50 ± 10.86 A.U., n = 10; $p < 0.0001$, unpaired *t*-test, Fig. 6k,m). These results support the hypothesis that prolonged He exposure promotes SH-SY5Y cell differentiation toward a neuronal-like state, paralleled by reduced proliferative capacity. To assess whether the differentiation effects observed with the He blend could be attributed to a single compound, we exposed SH-SY5Y cells to Ergothioneine (ERGO) alone for > 200 hours at the same concentration present in the blend (2.98 mg/g). While no significant changes were detected in action potential (AP) properties such as amplitude, duration, or threshold, a higher proportion of cells were able to elicit a single AP compared to the control group (Supplementary Fig. 1). The absence of more robust electrophysiological changes and repetitive firing, however, indicates that ERGO alone is insufficient to reproduce the full neuronal phenotype. Consequently, these findings support the conclusion that the complete He metabolite spectrum, with its nootropic properties, is required to achieve the full extent of neuronal differentiation and functional maturation previously described. To strengthen the physiological relevance of our findings and address concerns about appropriate controls, we additionally tested the effect of the He extract on LUHMES cells differentiated into dopaminergic-like neurons. In this model, He treatment did not significantly alter resting membrane potential, rheobase, or spontaneous firing frequency, suggesting the extract does not interfere with the basal electrophysiological properties of healthy neuronal cells (Supplementary Fig. 2).

## 4. Discussion

In the present study, we demonstrate that treatment with He extract for approximately 200 hours induces a pronounced shift towards a neuron-like phenotype in SH-SY5Y cells, a well-established human neuroblastoma cell line commonly utilized as an in vitro model for studying neurodevelopmental processes and evaluating potential therapeutic interventions. This neurogenic effect is characterized by enhanced voltage-gated sodium current and expression of neuronal markers such as βIII-tubulin and reduction in markers linked to cell proliferation such as PCNA, corroborating the differentiation process.

Medicinal mushrooms have been increasingly recognized for their potential anticancer properties, as highlighted in several recent reviews [47–49]. These fungi, particularly those used in traditional Chinese medicine, contain a plethora of bioactive compounds such as polysaccharides, lectins, and triterpenoids, which exhibit a variety of anti-tumor activities [50].

Another significant aspect of He's anticancer activity is its ability to inhibit angiogenesis [51]. By blocking angiogenesis, He effectively starves the tumor, preventing its growth and spread. Studies have identified that the erinacines [52] and hericenones in He can inhibit angiogenesis, highlighting their potential in anti-tumor strategies.

Moreover, He has been found to possess immunomodulatory properties, enhancing the body's immune response against cancer cells [53]. Polysaccharides from this mushroom stimulate the activity of macrophages, natural killer cells, and lymphocytes, which are crucial for detecting and destroying malignant cells. This immunostimulatory effect not only aids in direct tumor suppression but also enhances the effectiveness of other cancer treatments [54].

Clinical studies and animal models further support the anticancer potential of He. For instance, in models of colon cancer, extracts from He has been shown to reduce tumor size and inhibit metastasis [55]. Additionally, in vitro studies on human gastric cancer cells have demonstrated that He extracts can suppress cell proliferation and induce apoptosis [56].

He has garnered attention for its remarkable pro-neuronal properties, underpinned by its rich composition of bioactive compounds [33,

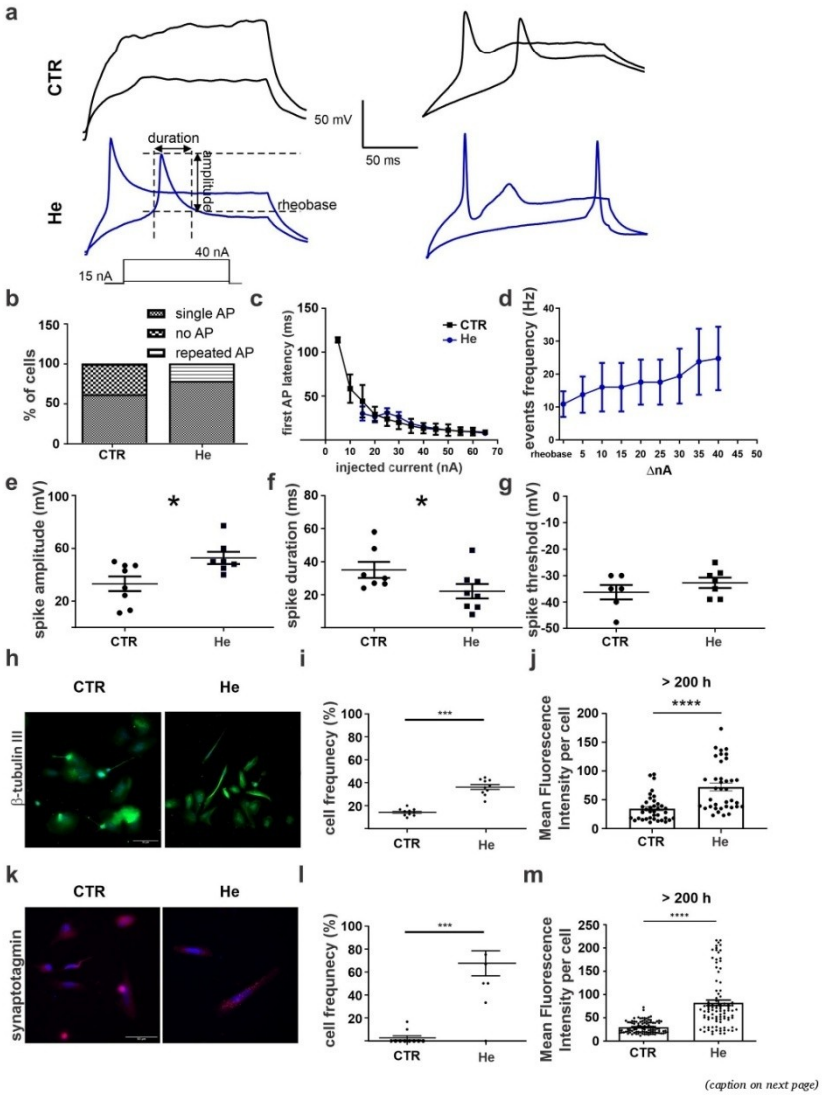


(caption on next page)

**Fig. 6.** SH-SY5Y cells treated with He exhibit increased excitability and expression of neuronal markers compared to the control group. a) Representative action potential (AP) traces recorded in current clamp mode from SH-SY5Y cells in the control group (black, CTR) and the He-treated group (blue, He) in response to the same current injection (15–40 nA). Parameters measured include AP amplitude, duration, threshold, and rheobase. (b) Percentage of cells responding to the current injection protocol with no AP, single AP, or repeated firing of APs in both conditions (CTR vs. He). (c) Comparison of the latency to the first AP as a function of injected current between CTR and He-treated cells. (d) Frequency of events (Hz) in He-treated cells as a function of incremental current steps (ΔnA). (e) Quantification of AP amplitude (mV) showing significant differences between CTR and He groups. (f) Quantification of AP duration (ms), revealing a significant reduction in He-treated cells compared to CTR. (g) Comparison of AP threshold (mV) between CTR and He cells. (h) Representative micrographs showing immunofluorescence labelling for βIII-tubulin in CTR and He-treated cells. (i) βIII-tubulin-immunopositive cell frequency (%) in both groups, demonstrating a significant increase in He-treated cells. (j) βIII-tubulin mean fluorescence intensity per cell, revealing a marked upregulation in He group after > 200 hours exposure. k) Representative micrographs depicting immunofluorescence labelling for synaptotagmin in CTR and He-treated cells. (l) Synaptotagmin-immunopositive cell frequency (%) showing significantly higher levels in He group. (m) Synaptotagmin mean fluorescence intensity per cell in CTR and He groups after > 200 hours exposure, indicating a significant increase in the expression of synaptic marker after He treatment.

57]. These compounds, including polysaccharides and hericenones, have been extensively studied for their ability to promote neuronal survival, neurite outgrowth, and synaptic plasticity [58,59]. Brandalise et al. demonstrated the pro-neuronal potential of He extract in a study where treatment with the extract led to enhanced synaptic pruning in hippocampal rat organotypic slice cultures [28]. Similarly, Mori et al. conducted a clinical trial in elderly individuals with mild cognitive impairment, showing significant improvements in cognitive function following supplementation with He extract [60]. These findings underscore the promising role of in promoting neurogenesis and neuronal function, offering potential therapeutic perspective for neurological disorders.

Our study adds relevant insights to the growing body of publications supporting the differentiation-inducing effects of He extract. Mori et al. provided insights into the underlying mechanisms, demonstrating the nerve growth factor (NGF)-inducing activity of He in human astrocytoma cells [8]. NGF plays a crucial role in promoting neuronal differentiation and survival, making it a key mediator of He-induced differentiation. The bioactive compounds in He, particularly erinacines and hericenones, are most likely responsible for mimicking NGF activity or enhancing NGF production, as evidenced by studies demonstrating their ability to stimulate NGF synthesis in astrocytes and promote neuronal differentiation [8,13,33]. In cancer biology, inducing differentiation is a recognized strategy to impede cancer progression, as differentiated cancer cells typically exhibit reduced proliferative rates and increased susceptibility to therapeutic interventions. The differentiation-inducing potential of He extract offers a promising avenue for combating neuroblastoma and other neurodevelopmental disorders.

While various differentiation protocols already exist, such as those utilizing retinoic acid and TPA, their clinical translation is hindered by several limitations. Retinoic acid, for example, is known to exhibit teratogenic effects and has poor blood-brain barrier permeability, limiting its therapeutic utility in neurological disorders. TPA, on the other hand, is associated with cytotoxicity and inflammation, posing safety concerns for long-term use. In contrast, He extract is well-tolerated and capable of crossing the blood-brain barrier, making it an attractive candidate for therapeutic interventions. Furthermore, its differentiation-inducing effects offer a safer and more efficacious alternative to existing protocols, potentially overcoming the translational barriers associated with conventional agents. Voltage-gated ion channels play a pivotal role in neuronal differentiation and maturation, with their expression and activity dynamically regulated during development.

Voltage-gated calcium channels (VGCCs) are crucial for mediating calcium influx, which drives processes such as neurotransmitter release, gene expression, and neurite outgrowth. However, their expression tends to decrease as neurons mature, reflecting a shift in ion channel functionality during differentiation. For instance, high-voltage-activated calcium currents decrease during cerebellar granule cell development in situ [43,44], while inwardly rectifying potassium currents and VGSC expression patterns emerge distinctively during differentiation [43]. These changes underscore the critical shift from voltage gated calcium channel towards voltage dependent sodium channel supporting the functional maturation of neurons.

In the context of He treatment, our findings suggest that He modulates this ion channel remodeling process. Specifically, He treatment leads to a significant upregulation of VGSC-mediated inward currents, accompanied by a reduction in VGCC activity. This shift may reflect an advanced differentiation and maturation state induced by He, aligning with its observed ability to promote neuronal marker expression and suppress proliferation.

The observed effects of He extract on neurite outgrowth and inward current amplitude upregulation suggest a multifaceted mechanism of action. The rapid onset of these effects, evident within 24 hours of application, implies the involvement of fast-acting signaling pathways, such as possibly the NGF-TrkA pathway. NGF, a key neurotrophic factor, plays a pivotal role in promoting neurite outgrowth and synaptic plasticity, suggesting its potential involvement in mediating He-induced differentiation [13,33,58]. Additionally, the progressive enhancement of these effects over 200 hours suggests a more profound influence, potentially involving modulation of gene expression. This prolonged effect may entail the activation of transcription factors and epigenetic modifiers, leading to sustained changes in neuronal phenotype and function. Further elucidation of these mechanisms is essential for understanding the therapeutic potential of He extract and its implications for neuroblastoma management. In conclusion, our study demonstrates that He extract promotes neuronal differentiation and reduces proliferation in SH-SY5Y neuroblastoma cells. The observed shift toward a neuron-like phenotype, characterized by increased expression of neuronal markers and enhanced voltage-gated sodium currents highlights the extract's potential as a differentiation-inducing agent. Given the known blood–brain barrier permeability of HE extract [61] and its pronounced *in vitro* effects on neuronal differentiation, further *in vivo* studies are currently being planned to evaluate its efficacy in neuroblastoma models. These investigations will also explore potential synergistic effects with existing therapies and assess the safety profile of prolonged exposure.

## Author contributions

FG, ECP, FB, performed the experiments. FG, ECP, FB, CL, PR analyzed the data, participated in language editing and manuscript revision. FG, ECP, FB, MV, DR, LG contributed to the *in vitro* experiments. PR, FB, ER, ES conceived and designed the study. ER, PR and FB provided the conception and design of the study, PR, ES, ER, FB participated in the drafting and revision and supervised the study. All authors contributed to the article and approved the submitted version.

## CRediT authorship contribution statement

**Daniela Ratto:** Writing – review & editing, Supervision, Methodology. **MariaTeresa Venuti:** Software, Methodology, Data curation. **Carlo Alessandro Locatelli:** Validation, Conceptualization. **Lorenzo Goppa:** Visualization, Investigation. **Elisa Roda:** Resources, Methodology, Data curation. **Elena Savino:** Writing – review & editing,

Validation, Supervision. **Paola Rossi:** Writing – review & editing, Writing – original draft, Visualization, Validation, Supervision, Funding acquisition, Formal analysis, Data curation, Conceptualization. **Erica Cecilia Priori:** Writing – original draft, Investigation, Formal analysis. **Federico Brandalise:** Writing – review & editing, Writing – original draft, Investigation, Formal analysis, Data curation, Conceptualization. **Francesca Giammello:** Writing – original draft, Investigation, Formal analysis.


## Funding

This research was funded by (i) the University of Pavia, Fondi Ricerca Giovani (FRG 2020), Department of Biology and Biotechnology "L. Spallanzani", University of Pavia and (ii) the Italian Ministry of Education, University and Research (MIUR): Department of Excellence Program (2018–2022), Department of Biology and Biotechnology "L. Spallanzani", University of Pavia.


## Declaration of Competing Interest

The authors declare that they have no known competing financial interests or personal relationships that could have appeared to influence the work reported in this paper.


## Acknowledgements

The graphical abstract was created using resources provided by BioRender.com. We gratefully acknowledge Prof. Hirokazu Kawagishi (Shizuoka University, Japan) for generously providing the erinacine and hericenone standard compounds, and Tetrahedron (Paris, France) for kindly donating the ergothioneine standard used in this study.


## Appendix A. Supporting information

Supplementary data associated with this article can be found in the online version at doi:10.1016/j.biopha.2025.118204.

## Data availability

Data will be made available on request.

## References


[1] M.M. Shipley, C.A. Mangold, M.L. Szpara, Differentiation of the SH-SY5Y human neuroblastoma cell line, J. Vis. Exp. (2016) 53193.

[2] L. Agholme, T. Lindstrom, K. Kågedal, J. Marcusson, M. Hallbeck, An in vitro model for neuroscience: differentiation of sh-sy5y cells into cells with morphological and biochemical characteristics of mature neurons, JAD 20 (2010) 1069–1082.

[3] A. D'Aloia, V. Pastori, S. Blasa, G. Campioni, F. Peri, E. Sacco, et al., A new advanced cellular model of functional cholinergic-like neurons developed by reprogramming the human SH-SY5Y neuroblastoma cell line, Cell Death Discov. 10 (2024) 24.

[4] J.A. Korecka, R.E. Van Kesteren, E. Blaas, S.O. Spitzer, J.H. Kamstra, A.B. Smit, et al., Phenotypic characterization of retinoic acid differentiated SH-SY5Y cells by transcriptional profiling, PLoS ONE 8 (2013) e63862.

[5] T. Coccini, S. Vecchio, M. Crevani, U. De Simone, Cytotoxic effects of 3,4-Catechol-PV (One Major MDPV Metabolite) on human dopaminergic SH-SY5Y cells, Neurotox. Res. 35 (2019) 49–62.

[6] B.J. Goldie, M.M. Barnett, M.J. Cairns, BDNF and the maturation of posttranscriptional regulatory networks in human SH-SY5Y neuroblast differentiation, Front. Cell. Neurosci. 8 (2014) 325.

[7] L. Hromadkova, D. Bezdekova, J. Pala, S. Schedin-Weiss, L.O. Tjernberg, C. Hoschl, et al., Brain-derived neurotrophic factor (BDNF) promotes molecular polarization and differentiation of immature neuroblastoma cells into definitive neurons, Biochim Biophys. Acta Mol. Cell Res. 1867 (2020) 118737.

[8] K. Mori, Y. Obara, M. Hirota, Y. Azumi, S. Kinugasa, S. Inatomi, et al., Nerve growth factor-inducing activity of hericium erinaceus in 1321n1 human astrocytoma cells, Biol. Pharm. Bull. 31 (2008) 1727–1732.

[9] K. Mori, Y. Obara, T. Moriya, S. Inatomi, N. Nakahata, Effects of Hericium erinaceus on amyloid β(25-35) peptide-induced learning and memory deficits in mice, Biomed. Res. 32 (2011) 67–72.

[10] F. Brandalise, V. Cesaroni, A. Gregori, M. Repetti, C. Romano, G. Orrù, et al., Dietary Supplementation of *Hericium erinaceus* increases mossy fiber-CA3 hippocampal neurotransmission and recognition memory in wild-type mice, Evid. Based Complement. Altern. Med. 2017 (2017) e3864340.

[11] P. Rossi, V. Cesaroni, F. Brandalise, A. Occhinegro, D. Ratto, F. Perrucci, et al., Dietary supplementation of lion's mane medicinal mushroom, hericium erinaceus (Agaricomycetes), and spatial memory in wild-type mice, Int. J. Med. Mushrooms 20 (2018) 485–494.

[12] F. Brandalise, E. Roda, D. Ratto, L. Goppa, M.L. Gargano, F. Cirlincione, et al., Hericium erinaceus in neurodegenerative diseases: from bench to bedside and beyond, how far from the shoreline? J. Fungi 9 (2023) 551.

[13] H. Kawagishi, A. Shimada, S. Hosokawa, H. Mori, H. Sakamoto, Y. Ishiguro, et al., Erinacines E, F, and G, stimulators of nerve growth factor (NGF)-synthesis, from the mycelia of *Hericium erinaceum*, Tetrahedron Lett. 37 (1996) 7399–7402.

[14] A. Neuhof, Y. Tina, A. Reska, B.H. Falkenburger, S. Gründer, Large acid-evoked currents, mediated by ASIC1a, accompany differentiation in human dopaminergic neurons, Front Cell Neurosci. 15 (2021) 668008.

[15] D. Scholz, D. Pöltl, A. Genewsky, M. Weng, T. Waldmann, S. Schildknecht, et al., Rapid, complete and large-scale generation of post-mitotic neurons from the human LUHMES cell line, J. Neurochem. 119 (2011) 957–971.

[16] V. Cesaroni, M. Brusoni, C.M. Cusaro, C. Girometta, C. Perini, A.M. Picco, et al., Phylogenetic Comparison between Italian and Worldwide Hericium Species (Agaricomycetes), Int J. Med Mushrooms 21 (2019) 943–954.

[17] E. Roda, E.C. Priori, D. Ratto, F. De Luca, C. Di Iorio, P. Angelone, et al., Neuroprotective Metabolites of Hericium erinaceus promote neuro-healthy aging, Int. J. Mol. Sci. 22 (2021) 6379.

[18] F. Corana, V. Cesaroni, B. Mannucci, R.M. Baiguera, A.M. Picco, E. Savino, et al., Array of metabolites in itallian hericium erinaceus mycelium, primordium, and sporophore, Molecules 24 (2019) 3511.

[19] D. Ratto, F. Corana, B. Mannucci, E.C. Priori, F. Cobelli, E. Roda, et al., Hericium erinaceus improves recognition memory and induces hippocampal and cerebellar neurogenesis in frail mice during aging, Nutrients 11 (2019) 715.

[20] W. Krzyczkowski, E. Malinowska, F. Herold, Erinacine A biosynthesis in submerged cultivation of Hericium erinaceum: quantification and improved cultivation, Eng. Life Sci. 10 (2010) 446–457.

[21] D.G. Lee, H.-W. Kang, C.-G. Park, Y.-S. Ahn, Y. Shin, Isolation and identification of phytochemicals and biological activities of *Hericium erinaceus* and their contents in *Hericium* strains using HPLC/UV analysis, J. Ethnopharmacol. 184 (2016) 219–225.

[22] O. Mirante, F. Brandalise, J. Bohacek, I.M. Mansuy, Distinct molecular components for thalamic- and cortical-dependent plasticity in the lateral amygdala, Front Mol. Neurosci. 7 (2014), https://doi.org/10.3389/fnmol.2014.00062.

[23] F. Brandalise, U. Gerber, P. Rossi, Golgi cell-mediated activation of postsynaptic GABAB receptors induces disinhibition of the golgi cell-granule cell synapse in rat cerebellum, PLOS ONE 7 (2012) e43417.

[24] F. Brandalise, B.E. Kalmbach, E.P. Cook, D.H. Brager, Impaired dendritic spike generation in the Fragile X prefrontal cortex is due to loss of dendritic sodium channels, J. Physiol. 601 (2023) 831–845.

[25] D. Ratto, B. Ferrari, E. Roda, F. Brandalise, S. Siciliani, F. De Luca, et al., Squaring the circle: a new study of inward and outward-rectifying potassium currents in U251 GBM cells, Cell Mol. Neurobiol. 40 (2020) 813–828.

[26] F. Giammello, C. Biella, E.C. Priori, M.A.D.S. Filippo, R. Leone, F. D'Ambrosio, et al., Modulating voltage-gated sodium channels to enhance differentiation and sensitize glioblastoma cells to chemotherapy, Cell Commun. Signal 22 (2024) 434.

[27] F. Brandalise, M. Ramieri, E. Pastorelli, E.C. Priori, D. Ratto, M.T. Venuti, et al., Role of Na+ /Ca2+ exchanger (NCX) in glioblastoma cell migration (In Vitro), IJMS 24 (2023) 12673.

[28] F. Brandalise, V. Cesaroni, A. Gregori, M. Repetti, C. Romano, G. Orrù, et al., Dietary supplementation of hericium erinaceus increases mossy fiber-CA3 hippocampal neurotransmission and recognition memory in wild-type mice, Evid. Based Complement Altern. Med 2017 (2017) 3864340.

[29] D. Ratto, B. Ferrari, E. Roda, F. Brandalise, S. Siciliani, F. De Luca, et al., Squaring the circle: a new study of inward and outward-rectifying potassium currents in U251 GBM cells, Cell Mol. Neurobiol. 40 (2020) 813–828.

[30] J. Popko, A. Fernandes, L.M. Lanier, Automated analysis of neuronj tracing data, Cytom. Part A: J. Int. Soc. Anal. Cytol. 75 (2009) 371.

[31] M. Cernelič Bizjak, Z. Jenko Pražnikar, S. Kenig, M. Hladnik, D. Bandelj, A. Gregori, et al., Effect of erinacine A-enriched Hericium erinaceus supplementation on cognition: a randomized, double-blind, placebo-controlled pilot study, J. Funct. Foods 115 (2024) 106120.

[32] A.G. Contato, C.A. Conte-Junior, Lion's mane mushroom (Hericium erinaceus): a neuroprotective fungus with antioxidant, anti-inflammatory, and antimicrobial potential—a narrative review, Nutrients 17 (2025) 1307.

[33] I. Szucko-Kociuba, A. Trzeciak-Ryczek, P. Kupnicka, D. Chlubek, Neurotrophic and Neuroprotective Effects of Hericium erinaceus, Int J. Mol. Sci. 24 (2023) 15960.

[34] Y. Qiu, G. Lin, W. Liu, F. Zhang, R.J. Linhardt, X. Wang, et al., Bioactive compounds in *Hericium erinaceus* and their biological properties: a review, Food Sci. Hum. Wellness 13 (2024) 1825–1844.

[35] O.I. Aruoma, J.P.E. Spencer, N. Mahmood, Protection against oxidative damage and cell death by the natural antioxidant ergothioneine, Food Chem. Toxicol. 37 (1999) 1043–1053.

[36] I.K. Cheah, B. Halliwell, Ergothioneine; antioxidant potential, physiological function and role in disease, Biochim. Et. Biophys. Acta BBA Mol. Basis Dis. 1822 (2012) 784–793.

[37] H. Teppola, J.-R. Sarkanen, T.O. Jalonen, M.-L. Linne, Morphological differentiation towards neuronal phenotype of sh-sy5y neuroblastoma cells by estradiol, retinoic acid and cholesterol, Neurochem. Res. 41 (2016) 731–747.
[38] L. Hromadkova, D. Bezdekova, J. Pala, S. Schedin-Weiss, L.O. Tjernberg, C. Hoschl, et al., Brain-derived neurotrophic factor (BDNF) promotes molecular polarization and differentiation of immature neuroblastoma cells into definitive neurons, Biochim. Et. Biophys. Acta BBA Mol. Cell Res. 1867 (2020) 118737.
[39] R. Martínez-Mármol, Y. Chai, J.N. Conroy, Z. Khan, S.-M. Hong, S.B. Kim, et al., Hericerin derivatives activates a pan-neurotrophic pathway in central hippocampal neurons converging to ERK1/2 signaling enhancing spatial memory, J. Neurochem. 165 (2023) 791–808.
[40] H.-T. Huang, C.-H. Ho, H.-Y. Sung, L.-Y. Lee, W.-P. Chen, Y.-W. Chen, et al., Hericium erinaceus mycelium and its small bioactive compounds promote oligodendrocyte maturation with an increase in myelin basic protein, Sci. Rep. 11 (2021) 6551.
[41] S. Mirzadeghi, E. Shahbazi, K. Hemmesi, S. Nemati, H. Baharvand, J. Mirnajafi-Zadeh, et al., Development of membrane ion channels during neural differentiation from human embryonic stem cells, Biochem. Biophys. Res. Commun. 491 (2017) 166–172.
[42] M. Song, O. Mohamad, D. Chen, S.P. Yu, Coordinated development of voltage-gated $Na^+$ and $K^+$ currents regulates functional maturation of forebrain neurons derived from human induced pluripotent stem cells, Stem Cells Dev. 22 (2013) 1551–1563.
[43] P. Rossi, E. D'Angelo, J. Magistretti, M. Toselli, V. Taglietti, Age-dependent expression of high-voltage activated calcium currents during cerebellar granule cell development in situ, Pflug. Arch. 429 (1994) 107–116.
[44] F. Brandalise, R. Lujan, R. Leone, F. Lodola, V. Cesaroni, C. Romano, et al., Distinct expression patterns of inwardly rectifying potassium currents in developing cerebellar granule cells of the hemispheres and the vermis, Eur. J. Neurosci. 43 (2016) 1460–1473.
[45] T.A. Zolnik, A. Bronec, A. Ross, M. Staab, R.N.S. Sachdev, Z. Molnár, et al., Layer 6b controls brain state via apical dendrites and the higher-order thalamocortical system, Neuron 112 (2024) 805–820.e4.
[46] S. Soldado-Magraner, F. Brandalise, S. Honnuraiah, M. Pfeiffer, M. Moulinier, U. Gerber, et al., Conditioning by subthreshold synaptic input changes the intrinsic firing pattern of CA3 hippocampal neurons, J. Neurophysiol. 123 (2020) 90–106.
[47] S.K. Panda, G. Sahoo, S.S. Swain, W. Luyten, Anticancer activities of mushrooms: a neglected source for drug discovery, Pharmaceuticals 15 (2022) 176.
[48] P. Ray, S. Kundu, D. Paul, Exploring the therapeutic properties of chinese mushrooms with a focus on their anti-cancer effects: a systemic review, Pharmacol. Res. Mod. Chin. Med. 11 (2024) 100433.
[49] H.-J. Park, Current uses of mushrooms in cancer treatment and their anticancer mechanisms, Int. J. Mol. Sci. 23 (2022) 10502.
[50] P. Nowakowski, R. Markiewicz-Żukowska, J. Bielecka, K. Mielcarek, M. Grabia, K. Socha, Treasures from the forest: Evaluation of mushroom extracts as anti-cancer agents, Biomed. Pharmacother. 143 (2021) 112106.
[51] S.P. Kim, M.Y. Kang, J.H. Kim, S.H. Nam, M. Friedman, Composition and mechanism of antitumor effects of Hericium erinaceus mushroom extracts in tumor-bearing mice, J. Agric. Food Chem. 59 (2011) 9861–9869.
[52] P. Prasher, M. Sharma, A.K. Sharma, J. Sharifi-Rad, D. Calina, C. Hano, et al., Key oncologic pathways inhibited by Erinacine A: a perspective for its development as an anticancer molecule, Biomed. Pharmacother. 160 (2023) 114332.
[53] X. Sheng, J. Yan, Y. Meng, Y. Kang, Z. Han, G. Tai, et al., Immunomodulatory effects of Hericium erinaceus derived polysaccharides are mediated by intestinal immunology, Food Funct. 8 (2017) 1020–1027.
[54] K. Sheng, J. Yang, Y. Xu, X. Kong, J. Wang, Y. Wang, Alleviation effects of grape seed proanthocyanidin extract on inflammation and oxidative stress in a D-galactose-induced aging mouse model by modulating the gut microbiota, Food Funct. 13 (2022) 1348–1359.
[55] S.P. Kim, S.H. Nam, M. Friedman, Hericium erinaceus (Lion's Mane) mushroom extracts inhibit metastasis of cancer cells to the lung in CT-26 colon cancer-tansplanted mice, J. Agric. Food Chem. 61 (2013) 4898–4904.
[56] G. Li, K. Yu, F. Li, K. Xu, J. Li, S. He, et al., Anticancer potential of Hericium erinaceus extracts against human gastrointestinal cancers, J. Ethnopharmacol. 153 (2014) 521–530.
[57] G. Venturella, V. Ferraro, F. Cirlincione, M.L. Gargano, Medicinal mushrooms: bioactive compounds, use, and clinical trials, Int. J. Mol. Sci. 22 (2021) 634.
[58] C.-C. Zhang, X. Yin, C.-Y. Cao, J. Wei, Q. Zhang, J.-M. Gao, Chemical constituents from Hericium erinaceus and their ability to stimulate NGF-mediated neurite outgrowth on PC12 cells, Bioorg. Med Chem. Lett. 25 (2015) 5078–5082.
[59] J. Raman, H. Lakshmanan, P.A. John, C. Zhijian, V. Periasamy, P. David, et al., Neurite outgrowth stimulatory effects of myco synthesized AuNPs from Hericium erinaceus (Bull.: Fr.) Pers. on pheochromocytoma (PC-12) cells, Int. J. Nanomed. 10 (2015) 5853.
[60] K. Mori, S. Inatomi, K. Ouchi, Y. Azumi, T. Tuchida, Improving effects of the mushroom Yamabushitake (Hericium erinaceus) on mild cognitive impairment: a double-blind placebo-controlled clinical trial, Phytother. Res 23 (2009) 367–372.
[61] B.-J. Ma, J.-W. Shen, H.-Y. Yu, Y. Ruan, T.-T. Wu, X. Zhao, Hericenones and erinacines: stimulators of nerve growth factor (NGF) biosynthesis in Hericium erinaceus, Mycology (2010), https://doi.org/10.1080/21501201003735556.

Journal of Fungi

MDPI

*Article*

# Improving the Proteome-Mining of *Schizophyllum commune* to Enhance Medicinal Mushroom Applications

**Anthea Desiderio [1], Lorenzo Goppa [1], Carlo Santambrogio [2], Stefania Brocca [2], Simone Buratti [1], Carolina Elena Girometta [1], Meghma Sarkar [3], Maria Teresa Venuti [3], Elena Savino [1], Paola Rossi [3,*] and Emanuele Ferrari [4,*]**

[1] Department of Earth and Environmental Sciences (DSTA), University of Pavia, 27100 Pavia, Italy; anthea.desiderio01@universitadipavia.it (A.D.); lorenzo.goppa01@universitadipavia.it (L.G.); simone.buratti@unipv.it (S.B.); carolinaelena.girometta@unipv.it (C.E.G.); elena.savino@unipv.it (E.S.)
[2] Department of Biotechnology and Biosciences, University of Milano-Bicocca, 20126 Milan, Italy; carlo.santambrogio@unimib.it (C.S.); stefania.brocca@unimib.it (S.B.)
[3] Department of Biology and Biotechnology "L. Spallanzani", University of Pavia, 27100 Pavia, Italy; meghma.sarkar01@universitadipavia.it (M.S.); mariateresa.venuti01@universitadipavia.it (M.T.V.)
[4] Molecular Ecology Group (MEG), Water Research Institute (CNR-IRSA), National Research Council of Italy, 28922 Verbania, Italy
* Correspondence: paola.rossi@unipv.it (P.R.); emanuele.ferrari@cnr.it (E.F.)

**Abstract:** This study presents the first comprehensive proteomic profile of an Italian strain of *Schizophyllum commune*, a highly heterogeneous white-rot fungal species with significant potential for industrial, nutraceutical, cosmeceutical, and clinical applications. Three protein extraction methods and their impact on yield and resulting protein composition have been compared. Results revealed that the combination of Tris–Cl and urea increases the total protein yield and the variety of enzymatic species related to pivotal pathways. Notably, over 2000 proteins were identified, including enzymes involved in the growth and development of mycelium, trehalose biosynthesis, and different types of carbohydrate-active enzymes (CAZymes). These enzymes are crucial for nutraceutical and agro-industrial applications of *S. commune*. The multiple-step proteomic approach used could be a model for investigating other fungal species.

**Keywords:** protein isolation; proteomics; extraction method; medicinal mushroom; mycelium



Academic Editor: Yanbin Yin

Received: 23 December 2024
Revised: 21 January 2025
Accepted: 3 February 2025
Published: 5 February 2025

**Citation:** Desiderio, A.; Goppa, L.; Santambrogio, C.; Brocca, S.; Buratti, S.; Girometta, C.E.; Sarkar, M.; Venuti, M.T.; Savino, E.; Rossi, P.; et al. Improving the Proteome-Mining of *Schizophyllum commune* to Enhance Medicinal Mushroom Applications. *J. Fungi* **2025**, *11*, 120. https://doi.org/10.3390/jof11020120



## 1. Introduction

Medicinal mushrooms (MMs) have been used for centuries for their therapeutic and nutritional benefits, thanks to their bioactive compounds like polysaccharides, terpenoids, and proteins [1,2]. Known for their immunomodulatory, anticancer, antiviral, and anti-inflammatory properties, they are a key research focus [3]. Among the MMs, *Schizophyllum commune* Fr. is a widespread saprotrophic basidiomycete found on broadleaf trees. It has diverse biological effects, including anti-inflammatory, antimicrobial, antioxidant, and anticancer properties [4]. A hallmark molecule of this mushroom is the schizophyllan (SPG), a β-(1→3)/(1→6)-glucan extracellular polysaccharide [5]. Schizophyllan is valued for its immunomodulatory, antitumor, and potential wound-healing properties, acting as a biological response modifier [6] and exhibiting antioxidant effects [7]. *S. commune* produces bioactive compounds, including polyphenols, which have antioxidant and anti-inflammatory effects by neutralizing free radicals and reducing oxidative stress [8].

As a lignicolous fungus, *S. commune* plays a vital role in nutrient cycling by decomposing lignocellulosic materials through a variety of hydrolytic enzymes, including

cellulases, endoglucanases, β-glucosidases, and hemicellulases such as xylanases [9,10]. The wood-degrading ability of *S. commune* could be crucial for industrial applications such as bioremediation and biofuel production [11,12]. Oxidoreductases, including laccases and various peroxidases, are responsible for their roles in lignin degradation, dye decolorization, and synthesis of valuable aromatic compounds [13]. Under laboratory conditions, *S. commune* easily grows on various media, forming fluffy-white mycelia. It is used as a model organism in functional genomics [14] and for applications in mycomaterials [15]. Despite these potential applications, the protein profile of *S. commune* remains partially unknown.

A critical part preceding fungal proteome analysis is the extraction process. Efficient protein extraction methods are essential for mushrooms due to their complex tissue structure and robust cell walls composed of chitin, glucans, and proteins. Common approaches include mechanical disruption, such as grinding tissues in liquid nitrogen or using bead-beating techniques to break the cell walls and release intracellular contents. Chemical treatments with detergents (e.g., SDS, Triton X-100), chaotropic agents (e.g., urea, thiourea), and various solvents (e.g., ethanol, methanol, acetone) are often employed to solubilize proteins. Additionally, protease inhibitors are used to minimize protein degradation during the extraction process. These techniques, tailored to the unique properties of mushrooms, provide the foundation for robust proteomic analyses. While efficient protein extraction is critical due to the complexity and robustness of mushroom tissues, the indiscriminate use of a full range of chemical and mechanical approaches should be avoided. Instead, extraction methods should be tailored to the specific objective, avoiding unnecessary steps and minimizing the use of solvents and reagents. This approach aims to combine both simplicity and efficacy in the extraction process [16].

Currently, integrating data from proteomics, transcriptomics, and metabolomics provides insights into enzyme families, regulatory networks, and specific molecular pathways. Recent advances in proteomics have enabled the detailed analysis of fungal metabolism, supported by complete genomes and extensive genomic data. Early research primarily focused on human pathogens, especially filamentous ascomycetes, in which specific proteins play key roles in host recognition and virulence [17,18]. Proteomics studies on MMs began around the 2000s, mainly on *Ganoderma lucidum* (Fr.) P. Karst., driven by a growing interest in their biological properties and potential biotechnological use [19]. Proteomics has also been successfully applied to cultivable fungi and wood decayers such as the model species *Phanerochaete chrysosporium* Burds. The focus of these studies was to understand the enzyme patterns involved in the degradation of lignocellulose and persistent organic pollutants [20,21]. This highlights the potential of proteomics to reveal insights beyond transcriptomics, particularly under varying growth conditions that significantly influence enzymatic networks like those involved in lignocellulose degradation [22,23]. Proteomics is essential for characterizing protein expression under specific conditions, aiding in the selection of fungal strains with desirable biotechnological traits. However, proteomic profiles are highly sensitive to experimental variables, including culture conditions and protein extraction methods [24,25].

A few studies on the *S. commune* protein profile, under peculiar environmental conditions, have focused on specific aspects such as secreted proteins related to wood degradation [26] and protein expression profiles in response to the mycoparasite *Trichoderma viride* Pers. [27], and various metabolic pathways for metal tolerance [28]. *Leucaena leucocephala* wood (LLW) was used as a substrate for *S. commune* ISTL04 to produce extracellular proteins and schizophyllan under submerged fermentation [26]. Proteome analysis involved SDS-PAGE separation and nano LC-MS/MS profiling, identifying 79 extracellular proteins classified by their biological roles. Maximum production was observed on day 18, yielding 8.53 mg $mL^{-1}$ of sugar, 391 mg $L^{-1}$ of extracellular protein, and 4.2 g $L^{-1}$ (0.21 g $g^{-1}$ LLW)

of exopolysaccharide (EPS). EPS, identified as schizophyllan, was characterized using FTIR and GC-MS. Another study investigated protein profile changes in *S. commune* when paired with the biocontrol fungus *Trichoderma viride* for 48 h [27]. Using two-dimensional (2D) protein gel electrophoresis and matrix-assisted laser desorption/ionization time-of-flight mass spectrometry, they revealed significant proteomic changes. *S. commune* showed a 61% increase in proteins related to transcription and translation, along with a 17% rise in proteins for cell walls and hyphal biogenesis, while metabolism-related proteins decreased by 64%. Meanwhile, *T. viride* exhibited mycoparasitic behavior, with elevated levels of proteins linked to proteolysis and carbohydrate metabolism. These findings highlight the *S. commune* upregulation of mechanisms to counteract *T. viride* mycoparasitic activity, particularly cell wall lysis and antibiosis. This study provides insights into natural resistance mechanisms and has implications for the design of improved biocontrol strategies. Finally, the investigation of inositol phosphate signaling in *S. commune* highlighted its role in growth, sexual reproduction, and metabolic adaptation [28]. Overexpression of the corresponding gene revealed its involvement in cell wall integrity, intracellular trafficking, and significant impacts on mushroom formation and metabolism, as evidenced by proteomic analyses. Altered inositol signaling also enhances metal tolerance (e.g., to cadmium, cesium, and zinc), with metal exposure reducing intracellular calcium levels and influencing kinase and phosphatase expression within the inositol cycle.

These examples of research demonstrate considerable diversity, especially in the method of extracting and identifying proteomic profiles. In this study, the proteomic profile of *S. commune* mycelium was investigated to identify functional metabolic pathways with potential applications in agro-waste recycling, industrial production, and human or animal health. The culture medium (malt extract) and extraction procedures were chosen to minimize the loss of proteins possibly involved in crucial biological pathways. We suggest that the multiple-step proteomic approach described, integrating different databases, could be used as a model for investigating other fungal species.

## 2. Materials and Methods

### *2.1. Fungal Strain Isolation, Identification, and Conservation*

The basidiome of *S. commune* was collected from *Populus alba L.* in Bereguardo (Pavia, Italy) and isolated in pure culture in Petri dishes containing 2% *w*/*v* Malt Extract Agar (MEA). The strain was identified by macro- and micro-morphological characteristics followed by molecular analysis. Total genomic DNA from lyophilized mycelium was extracted using the Nucleospin Plant II kit (Macherey-Nagel, Düren, Germany). The primer pair ITS1-ITS4 was used to amplify the Internal Transcribed Spacer (ITS) region by Polymerase Chain Reaction (PCR) as reported in the method [29]. The fungal strain in pure culture is cataloged as MicUNIPV_S.c.1 in the Fungal Research Culture Collection (MicUNIPV) of the Mycology Laboratory at the Department of Earth and Environmental Sciences (DSTA) (University of Pavia, Italy). The strain is maintained both at 4 °C in MEA and −80 °C in a water-glycerol solution for long-term conservation [30].

### *2.2. Mycelium Growth*

*S. commune* mycelium was grown in MEA Petri dishes for 15 days at 25 °C in the dark. From the fully colonized plate, 10 portions of colonized medium (surface about 0.25 $cm^2$ each) were sterilely withdrawn and inoculated into flasks (capacity of 1 L) containing 400 mL of 2% *w*/*v* ME. Before inoculation, flasks were sterilized by autoclave (121 °C, 20 min) and sealed with raw cotton to facilitate gaseous exchange. Incubation was carried out in dark and static conditions at 25 °C. After 15 days, mycelium was washed with sterile deionized water, lyophilized for 24 h at −50 °C and 1 mbar and finally stored at −20 °C.

### 2.3. Protein Extraction Procedures

The extraction procedures were developed based on a previous study [31], combining mechanical disruption using a bead mill with extraction of both soluble and insoluble protein fractions using different buffers. Lyophilized mycelium was frozen in liquid nitrogen for 60 s and then finely grounded using a pestle and mortar. The resulting powder was subjected to three distinct extraction methods (A1, A2 and B).

Method A1: 100 mg of fungal powder was suspended in 1 mL of 10 mM Tris–Cl buffer pH 8 and homogenized with 100 mg of glass beads (diameter mechanical ~500 µm), using a FastPrep-24 (MP Biomedicals, Irvine, CA, USA for 4 cycles of 30 s at 6.5 m/s speed). The sample was then centrifuged (15 min, 14,000× *g*, room temperature) to separate the soluble and insoluble fractions. The soluble fraction was named sample A1.

Method A2: The insoluble fraction obtained with Method A1 was washed twice with acetone, resuspended in a solubilization buffer (8 M urea in 10 mM Tris–Cl buffer, pH 8) and incubated at room temperature for 24 h before brief centrifugation was applied to remove particulate matter and glass beads. This fraction was named sample A2.

Method B: 100 mg of the fungal powder was suspended in 1 mL of 10% (*v*/*v*) trichloroacetic acid (TCA) for protein precipitation. The sample was homogenized as previously described (FastPrep-24—MP Biomedicals, Irvine, CA, USA—4 cycles of 30 s at 6.5 m/s speed, in the presence of glass beads) and centrifuged (15 min, 14,000× *g*, room temperature). The resulting pellet was washed twice with acetone, resuspended in a solubilization buffer (8 M urea in 10 mM Tris–Cl buffer, pH 8) and incubated at room temperature for 24 h. After incubation, the sample was briefly centrifuged to remove particulate matter and glass beads.

Briefly, the use of three distinct extraction methods resulted in the generation of three types of samples: A1 (soluble fraction from Method A1), A2 (insoluble fraction from Method A1), and B (pellet from Method B). The protein content of each sample was quantified by absorbance spectroscopy employing a Bradford assay (with absorbance calibrated against a bovine serum albumin standard). Protein composition was assessed by loading 10 µL of each sample on a 14% SDS-PAGE gel, run on a mini-gel apparatus (Bio-Rad, Berkeley, CA, USA), according to the Laemmli method [32].

### 2.4. LC-MS/MS Analysis

Samples A1, A2, and B were diluted to a final concentration of 10 mM Tris–Cl buffer (pH 8) and 4 M urea. The extracted proteins were reduced with 10 mM dithiothreitol, alkylated with 50 mM iodacetamide and digested with trypsin 16 h at 37 °C (with urea diluted to a final concentration of 2 M). The resulting peptides were desalted using Ziptip C-18 columns, lyophilized and suspended in 0.1% formic acid. The samples were then analyzed by LC/MS using an Orbitrap Fusion instrument (Thermo Fisher Scientific, Waltham, MA, USA) equipped with an HPLC system (EASY-1000). Peptides were separated on a 50 cm C-18 column (Thermo Fisher Scientific, Waltham, MA, USA) using a 120 min gradient (solvent A: 100% milliQ water, 0.1% formic acid; solvent B: 20% milliQ water, 80% acetonitrile, 0.1% formic acid). Detection was performed in the orbitrap analyzer, and fragmentation occurred in the ion trap analyzer using high-energy collision dissociation (HCD) with helium gas. Two technical replicates were performed for each sample.

### 2.5. Protein Identification, Functional and Statistical Analysis

Protein identification was performed with MaxQuant 2.0.3.0 [33] against the *S. commune* database downloaded from Uniprot in April 2023. All parameters were set at default values except for the following. Mass search tolerances were set to 10 ppm for MS and 0.6 Dalton for MS/MS. Carbamidomethylation of cysteines was set as a fixed modifica-

tion, while methionine oxidation was set as a variable modification. The possible missed cleavages for trypsin/P were set to 3. The false discovery rate was set to 1% at peptide and protein levels based on a target/decoy search. Unique and razor peptides were used by Peptide Spectrum Match (PSM) to quantify proteins. For each individual technical replicate, the extracted proteins, taking into account the average spectral count among the three replicates, were quantified.

The mass spectrometry proteomics data have been deposited to the ProteomeXchange Consortium via the PRIDE partner repository [34] with the dataset identifier PXD048036 and 10.6019/PXD048036.

Perseus was used for post-processing data and statistical analysis. The sample comparison of the enriched Cellular Component terms was performed with FunRich using the Uniprot Database [35]. DAVID was used for functional analysis and for statistical analysis of the enrichment of Gene Ontology terms, and a $p$-value < 0.01 was considered significant [36]. The enriched terms were then clustered according to semantic similarity using Revigo [37].

## 3. Results

### *3.1. Different Protein Content and Proteomic Identification in the Three Extracts*

The three samples resulting from the extraction procedures (A1, A2, and B) contained different total protein amounts according to Bradford assay and SDS-PAGE analysis (Figure S1). Specifically, sample A1 corresponds to soluble proteins extracted under native conditions using an aqueous buffer containing 10 mM Tris–Cl at pH 8, while sample A2 represents the insoluble proteins that were subsequently extracted with urea in the same buffer. Sample B, on the other hand, consists of proteins precipitated with trichloroacetic acid (TCA) and then solubilized in urea, representing a different extraction approach targeting both soluble and insoluble fractions.

Sample A1 contains about four times the total protein content (3.1 $\pm$ 0.1 mg/mL) compared to A2 (0.81 $\pm$ 0.08 mg/mL) and 10 times that of sample B (0.35 $\pm$ 0.05 mg/mL). Interestingly, the number of different proteins identified through the proteomic approach did not correlate with the total protein content measured by the Bradford assay. This means that, despite its higher protein content, sample A1 exhibits lower protein diversity compared to the other samples. Such a discrepancy is unlikely to stem from an artifact in the protein concentration measurement arising from the diverse detectability of specific proteins owing to their composition or size. The Bradford assay applied to complex protein mixtures is generally robust and less prone to significant biases of this nature.

As shown in the Venn diagram (Figure 1), a total of 2465 proteins were identified in the three samples (File S2). Around 30% of these proteins (713) were common in all three samples, confirming the presence of a protein core that was extracted independently from the extraction procedure (Figure 1).

Sample A1 yielded the lowest number of identified proteins (n = 1084). Of these, 297 proteins were only shared with sample A2, 27 with sample B, and 47 were unique to A1. Sample A2 had the highest number of identified proteins (n = 2105). Apart from those shared with A1, A2 also had a significant overlap with sample B (n = 583) and 512 proteins unique to it. Sample B yielded a number of n = 1609 identified proteins, of which 286 proteins are unique for this sample (Figure 1).

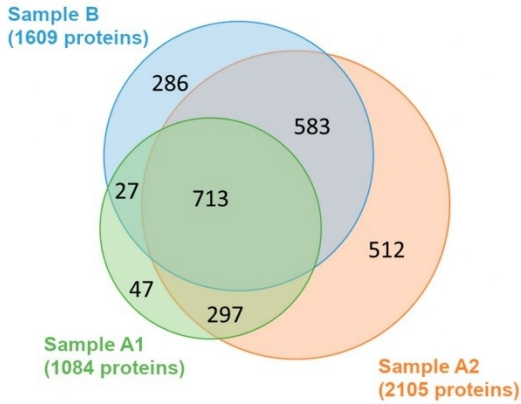


**Figure 1.** Venn's diagram shows the number of identified extracted proteins in samples A1, A2, and B. Around 30% of the proteins were identified in all samples (713 proteins), indicating a core of proteins easily extracted with all three methods. Sample A2 showed the highest number of unique proteins, which were not identified in the other samples (512 proteins).

### 3.2. *Cellular Compartmentalization of the Extracted Proteins: The Gene Ontology Cellular Component Analysis*

Enrichment analysis based on the Gene Ontology Cellular Component (GO-CC) terms was assessed to identify the cellular compartment of the proteins identified, comparing with the list of proteins in the *S. commune* reference proteome database. GO-CC terms were found for 906 out of the total 2465 proteins identified (about 37%). Considering each sample separately, the number of proteins to which a GO-CC term was assigned was 394 for sample A1 (~37%), 815 for sample A2 (~38%), and 562 for sample B (~35%).

In particular, in 12 cellular components, at least one extract showed a statistically significant enrichment compared to the whole proteome of *S. commune* (Table 1). Notably, cytoplasm and ribosomal proteins were enriched in all three samples, but a higher number of proteins were found in extract A2. The three methods clearly differ in extraction power, with sample A2 showing the highest enrichment of the 12 CC terms selected (Table 1). The analysis of GO-CC was focused on the differences among the three extracts (Table 1).

**Table 1.** GO-CC terms statistically enriched in at least one of the samples, A1, A2, and B, when compared to the whole proteome. For each sample, the total number of proteins for each GO-CC is reported in the first column. The *p*-values were calculated in DAVID using Fisher's Exact test. *p*-values < 0.01 are considered significant of an enrichment (indicated by the symbol *).

| | Sample A1 | | Sample A2 | | Sample B | |
|---|---|---|---|---|---|---|
| **Cellular Component** | **# Proteins** | ***p*-Value** | **# Proteins** | ***p*-Value** | **# Proteins** | ***p*-Value** |
| Cytoplasm | 71 | $8.39 \times 10^{-12}$ * | 139 | $4.03 \times 10^{-26}$ * | 99 | $2.53 \times 10^{-17}$ * |
| Ribonucleoprotein complex | 51 | $1.15 \times 10^{-18}$ * | 59 | $8.21 \times 10^{-10}$ * | 37 | $8.88 \times 10^{-4}$ * |
| Ribosome | 52 | $5.46 \times 10^{-24}$ * | 56 | $4.38 \times 10^{-12}$ * | 38 | $1.71 \times 10^{-6}$ * |
| Mitochondrial inner membrane | 12 | 1.00 | 31 | $6.23 \times 10^{-4}$ * | 11 | 1.00 |

**Table 1.** *Cont.*

| | Sample A1 | | Sample A2 | | Sample B | |
|---|---|---|---|---|---|---|
| **Cellular Component** | **# Proteins** | ***p*-Value** | **# Proteins** | ***p*-Value** | **# Proteins** | ***p*-Value** |
| Eukaryotic translation initiation factor 3 complex | 5 | 1.00 | 11 | $1.74 \times 10^{-5}$ * | 8 | $9.40 \times 10^{-3}$ * |
| Eukaryotic 48S preinitiation complex | 3 | 1.00 | 9 | $3.73 \times 10^{-4}$ * | 7 | 0.02 |
| Proteasome regulatory particle, base subcomplex | 8 | $4.06 \times 10^{-5}$ * | 9 | $3.73 \times 10^{-4}$ * | 7 | 0.02 |
| Eukaryotic 43S preinitiation complex | 3 | 1.00 | 9 | $3.73 \times 10^{-4}$ * | 7 | 0.02 |
| Chaperonin-containing T-complex | 0 | 1.00 | 8 | $1.73 \times 10^{-3}$ * | 8 | $8.69 \times 10^{-5}$ * |
| Proteasome core complex, alpha-subunit complex | 7 | $4.80 \times 10^{-5}$ * | 7 | $7.99 \times 10^{-3}$ * | 7 | $5.85 \times 10^{-4}$ * |
| Proteasome core complex, beta-subunit complex | 6 | $4.62 \times 10^{-4}$ * | 6 | 0.04 | 5 | 0.14 |
| Proteasome complex | 6 | $4.62 \times 10^{-4}$ * | 6 | 0.04 | 5 | 0.14 |

The percentage of annotated proteins for each GO-CC term is calculated on the ratio between the number of proteins annotated for that GO-CC term and the total number of annotated proteins in the sample (394 for sample A1, 815 for sample A2, and 562 for sample B, Figure 2).

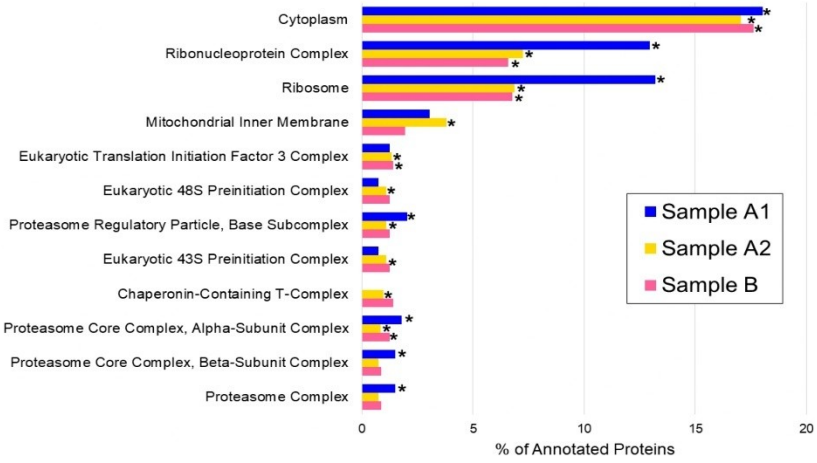


**Figure 2.** Percentage of annotated proteins for each GO-CC term. For each sample, the percentage has been calculated as the ratio between the number of proteins annotated for GO-CC terms and the total number of annotated proteins in the sample (394 for sample A1, 815 for sample A2, and 562 for sample B). The significant enrichment in the samples with respect to the whole proteome (as reported in Table 1) is indicated by the symbol * beside the bars ($p$-value < 0.01).

To identify in detail the differences in protein abundances as detected by CCs in all three samples, the Peptide Spectrum Matches (PSMs) were assessed. PSMs (or spectral count) allow the comparison of protein abundances without using any labeling in the preparation of samples and are based on the number of peptides identified for each protein group. When comparing sample A2 with sample A1, an increase in the abundance of membrane proteins, including mitochondrial, Golgi apparatus, and endoplasmic reticulum membranes, was observed (Table 2). In agreement with the biophysical and chemical characterization of membrane proteins, a huge number of proteins were insoluble in aqueous solutions and thus extracted by urea.

**Table 2.** Number of proteins, quantification (total PSMs), and fold change values (calculated with FUNRICH) for samples A2 and A1, divided per cellular component. The fold change value is the ratio of protein expression based on PSMs. When comparing samples A2 and A1, a fold change value greater than 1.0 indicates a protein overexpressed in A2. CC terms with at least six proteins identified and over 20 PSMs in sample A2 and with a fold value equal to or higher than 1.0 (relative to sample A1) are shown. The cellular components "Cytoplasm" and "Membrane" were assigned to proteins where no more specific cellular component was available.

| Cellular Component | # Identified Proteins | | Quantification (PSMs) | | Fold Change Value |
|---|---|---|---|---|---|
| | Sample A2 | Sample A1 | Sample A2 | Sample A1 | |
| Chaperonin-Containing T-Complex | 8 | 0 | 147.5 | 0 | 3280.7 |
| Microtubule | 9 | 3 | 75.5 | 2.4 | 7.0 |
| Arp2/3 Protein Complex | 6 | 3 | 21.9 | 1.3 | 3.7 |
| Eukaryotic 43S Preinitiation Complex | 9 | 3 | 72 | 4.3 | 3.7 |
| Eukaryotic 48S Preinitiation Complex | 9 | 3 | 72 | 4.3 | 3.7 |
| Eukaryotic Translation Initiation Factor 3 Complex | 11 | 5 | 84.1 | 5.3 | 3.5 |
| Golgi Membrane | 14 | 5 | 85.6 | 5.6 | 3.4 |
| Mitochondrial Inner Membrane | 31 | 12 | 129.2 | 14.1 | 2.0 |
| Plasma Membrane | 17 | 6 | 106.5 | 12.3 | 1.9 |
| Proteasome Regulatory Particle, Base Subcomplex | 9 | 8 | 120.7 | 15.7 | 1.7 |
| Cytosol | 10 | 3 | 42.1 | 7 | 1.3 |
| Endoplasmic Reticulum Membrane | 24 | 8 | 75.1 | 12.5 | 1.3 |
| Proteasome Complex | 6 | 6 | 42 | 7.3 | 1.2 |
| Nucleus | 81 | 38 | 392.6 | 70 | 1.2 |
| Spliceosomal Complex | 16 | 7 | 32.7 | 6 | 1.2 |
| Mitochondrion | 29 | 17 | 207.9 | 41.3 | 1.1 |
| Respirasome | 9 | 5 | 28.7 | 5.7 | 1.1 |
| Cytoplasm | 139 | 71 | 1051.5 | 210 | 1.1 |
| Membrane | 183 | 76 | 601.2 | 124 | 1.1 |

The same pattern was observed when comparing samples A2 and B (Table 3). The proteins associated with respirasome, ribosome, and various organelle membranes (Endoplasmic Reticulum, Golgi, and Mitochondria) showed the highest fold change values, meaning that the proteins from these compartments were more expressed in sample A2. Consequently, it appears that the method used for sample A2 is the most effective for isolating proteins from membranes among the different extraction methods under investigation.

**Table 3.** Number of proteins, quantification (total PSMs), and fold change values (calculated with FUNRICH) for samples A2 and B, divided per cellular component. The fold change value is the ratio of protein expression based on PSMs. When comparing samples A2 and B, a fold change value greater than 1.0 indicates a protein overexpressed in A2. CC terms with at least six proteins identified and over 20 PSMs in sample A2 and with a fold value equal to or higher than 1.0 (relative to sample B) are shown.

| Cellular Component | # Identified Proteins | | Quantification (PSMs) | | Fold Change Value |
|---|---|---|---|---|---|
| | Sample A2 | Sample B | Sample A2 | Sample B | |
| Respirasome | 9 | 3 | 28.7 | 5 | 3.0 |
| Endoplasmic Reticulum Membrane | 24 | 9 | 75.1 | 17.2 | 2.3 |
| Golgi Membrane | 14 | 9 | 85.6 | 20.7 | 2.2 |
| Ribosome | 56 | 38 | 449.7 | 108.9 | 2.2 |
| Ribonucleoprotein Complex | 59 | 37 | 438.8 | 109.6 | 2.1 |
| Mitochondrial Inner Membrane | 31 | 11 | 129.2 | 36.4 | 1.9 |
| Cellular Anatomical Entity | 7 | 5 | 53.4 | 16.2 | 1.7 |
| Mitochondrion | 29 | 20 | 207.9 | 63.2 | 1.7 |
| Spliceosomal Complex | 16 | 7 | 32.7 | 10 | 1.7 |
| Chaperonin-Containing T-Complex | 8 | 8 | 147.5 | 47.7 | 1.6 |
| Small Ribosomal Subunit | 7 | 6 | 78.8 | 25.7 | 1.6 |
| Cytoplasm | 139 | 99 | 1051.5 | 438.6 | 1.3 |
| Eukaryotic Translation Initiation Factor 3 Complex | 11 | 8 | 84.1 | 36.8 | 1.2 |
| Eukaryotic 43S Preinitiation Complex | 9 | 7 | 72 | 31.7 | 1.2 |
| Eukaryotic 48S Preinitiation Complex | 9 | 7 | 72 | 31.7 | 1.2 |
| Proteasome Regulatory Particle, Base Subcomplex | 9 | 7 | 120.7 | 53.7 | 1.2 |
| Membrane | 183 | 109 | 601.2 | 289.8 | 1.1 |
| Microtubule | 9 | 7 | 75.5 | 37 | 1.1 |
| Plasma Membrane | 17 | 15 | 106.5 | 53.4 | 1.1 |
| Endoplasmic Reticulum | 13 | 9 | 92 | 47 | 1.0 |

### *3.3. Functional Analysis and Characterization of the Extracted Proteins*

A functional analysis was performed to understand which metabolic pathways are present in the three extracts. Proteins identified in the three samples (2465 proteins) were pooled together and processed with DAVID https://david.ncifcrf.gov/ (accessed on 3 February 2025) [36]. Considering all samples, 47 Gene Ontology Biological Process terms were found to be enriched (File S3). Consequently, the software Revigo was employed to remove redundant GO terms, cluster them by similarity, and visualize data in a treemap. Enriched terms could be classified into 10 superclusters indicated by different colors (Figure 3). Each supercluster is composed of semantically and functionally related GO-BP terms or clusters of semantically similar GO-BP terms. These are represented by rectangles whose size is proportional to the fold enrichment in protein expression with respect to the whole proteome. Fold enrichment is the ratio quantifying how much more (or less) a specific category is represented in a protein subset compared to what would be expected by chance in the entire dataset. This metric highlights biological processes, molecular functions, or cellular components that are statistically overrepresented and thus relevant to the biological context of the analyzed subset, aiding in the interpretation of proteomics data.

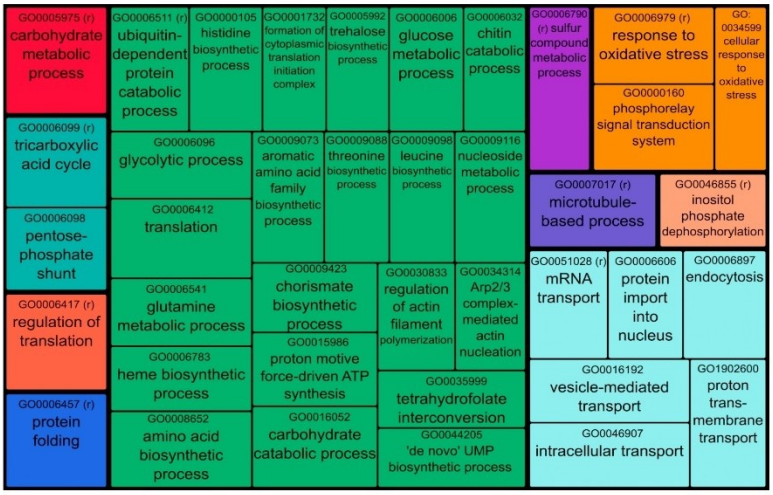


**Figure 3.** Treemap view clustered with REVIGO of GO Biological Process terms associated with fungal proteins. Each rectangle is a single GO term or a representative term of a cluster of semantically similar GO terms (indicated by r in brackets) with size related to the fold enrichment with respect to the whole proteome. The "superclusters" of related terms are visualized with different colors.

The treemap exhibits that the green supercluster is the one that comprises more GO-BP terms related to the biosynthesis and degradation of proteins and polysaccharides. It is important to note the presence of clusters of trehalose biosynthesis (GO:0005992) and carbohydrate catabolic processes (GO0016052) within the green supercluster. Trehalose production plays a vital role in fungal metabolism, supporting the growth and development of mycelium while also acting as a thermo-protector. Carbohydrate catabolic processes involve a range of enzymes responsible for the biosynthesis, modification, binding, and breakdown of carbohydrates, collectively known as carbohydrate-active enzymes (CAZymes or CAZy) [38]. Furthermore, considering the GO-BP terms, an enrichment of proteins involved in intra- and extracellular transport (light blue supercluster) and in response to oxidative stress (orange supercluster) were observed too.

The light sea green supercluster consists of two important metabolic processes: the pentose-phosphate shunt and the tricarboxylic acid cycle. It is important to emphasize the significance of these pathways, with a particular focus on the tricarboxylic acid cycle, which is linked to the growth and development of mycelium. The key enzymes involved in this metabolic pathway, isocitrate lyase and malate synthase, are part of the glyoxylate cycle enzyme. This cycle appears to be involved in the transition phase between vegetative growth and the development of the fruiting body [39,40]. Across the other superclusters, a wide range of activities were observed, including metabolic processes, protein folding, cell division, and gene control processes, protein folding, cell division, and gene control.

Among the biological processes enriched for *S. commune*, the attention was then focused on the metabolic pathways that are promising for industrial and health applications (Table 4). The most interesting molecular pathways considered were trehalose biosynthesis, response to oxidative stress, pentose-phosphate shunt, tricarboxylic acid cycle, CAZymes

and inositol phosphatase dephosphorylation. A quantitative comparison (based on PSMs) of the expression of enzymes related to these processes in the three samples was performed. In each metabolic pathway, specific enzymes known as "key enzymes" (indicated in bold and underlined) have been identified based on literature data. These enzymes are of significant scientific interest due to the crucial role they play in the pathway and their potential applications in various fields. Significantly higher amounts of most proteins, particularly key enzymes, were observed in sample A2 across all the metabolic pathways under investigation.

**Table 4.** The enzymes involved in the six molecular pathways investigated are listed in the table, and the difference in expression between the three samples is compared. For each enzyme, the UniProt Accession Number (first column) is indicated, the recommended name, EC number, and alternative name (second column), and the average PSMs for each sample (third, fourth, and fifth columns). The enzymes indicated with an asterisk in the A1 and B columns show a significant decrease with respect to A2 (*t*-test, *p*-values < 0.01 are considered significant). The molecular pathways in which the proteins of interest were identified are indicated in bold. Proteins that were detected at the highest concentration using the A2 extractive method are highlighted in both bold and underlined.

| Key Enzyme | Trehalose Biosynthesis | PSMs Sample A1 | PSMs Sample A2 | PSMs Sample B |
|---|---|---|---|---|
| **D8QC44** | Trehalose-6-phosphate synthase (EC 2.4.1.15) (UDP-glucose-glucosephosphate glucosyltransferase) | 0.0 * | 10.7 | 2.0 * |
| D8QIA1 | Trehalase (EC 3.2.1.28) (Alpha-trehalose glucohydrolase) | 0.0 | 2.3 | 0.0 |
| **Q2HZZ3** | Trehalose phosphorylase (EC 2.4.1.231) | 13.7 * | 42.0 | 23.0 * |
| | **Response to oxidative stress** | PSMs Sample A1 | PSMs Sample A2 | PSMs Sample B |
| **D8PT51** | Superoxide dismutase (EC 1.15.1.1) | 8.3 * | 20.0 | 3.0 * |
| D8Q7V6 | Superoxide dismutase (EC 1.15.1.1) | 1.7 * | 8.0 | 0.0 |
| S5VRV3 | Superoxide dismutase (EC 1.15.1.1) | 0.7 | 2.3 | 0.0 * |
| D8PMW1 | Catalase (EC 1.11.1.6) | 0.0 | 2.7 | 4.3 |
| **D8PTL6** | Catalase (EC 1.11.1.6) | 1.3 * | 23.0 | 4.0 * |
| D8QLS5 | Heme peroxidase | 0.0 | 1.3 | 0.0 |
| **D8QBR0** | Peroxidase (EC 1.11.1.-) | 1.0 * | 12.7 | 5.7 * |
| | **Pentose-phosphate Shunt** | PSMs Sample A1 | PSMs Sample A2 | PSMs Sample B |
| **D8PMS0** | 6-phosphogluconate dehydrogenase, decarboxylating (EC 1.1.1.44) | 15.7 * | 35.7 | 14.3 * |
| D8PP98 | Ribulose-phosphate 3-epimerase (EC 5.1.3.1) | 1.7 | 2.0 | 2.7 |
| D8PNV4 | Glucose-6-phosphate 1-dehydrogenase (EC 1.1.1.49) | 0.7 * | 15.7 | 1.7 * |
| D8PNV6 | Glucose-6-phosphate 1-dehydrogenase (EC 1.1.1.49) | 1.0 | 3.7 | 0.0 * |
| D8PN33 | 6-phosphogluconolactonase (6PGL) (EC 3.1.1.31) | 1.7 * | 5.0 | 0.0 * |
| **D8PXY7** | Transaldolase (EC 2.2.1.2) | 14.3 | 22.7 | 21.7 |
| **D8PWF8** | Transketolase (EC 2.2.1.1) | 5.7 * | 24.0 | 4.3 * |

**Table 4.** *Cont.*

| | Tricarboxylic acid cycle | PSMs Sample A1 | PSMs Sample A2 | PSMs Sample B |
|---|---|---|---|---|
| D8QDQ7 | Isocitrate dehydrogenase [NADP] (EC 1.1.1.42) | 1.7* | 5.3 | 0.0 * |
| **D8Q9D5** | Malate synthase (EC 2.3.3.9) | 9.7 * | 33.7 | 14.7 * |
| **D8Q486** | Oxalate oxidase | 3.3 * | 13.3 | 10.3 * |
| D8QFS7 | Malate dehydrogenase (EC 1.1.1.37) | 3.0 * | 15.3 | 21.7 * |
| D8QLH9 | Malate dehydrogenase (EC 1.1.1.37) | 3.0 * | 15.7 | 19.3 * |
| D8Q525 | Citrate synthase | 6.7 * | 22.7 | 2.0 * |
| D8PX28 | Citrate synthase | 0.0 * | 8.7 | 0.7 * |
| D8QEN1 | ATP citrate synthase (EC 2.3.3.8) (ATP-citrate (pro-S-)-lyase) (Citrate cleavage enzyme) | 0.7 * | 54.7 | 31.0 * |
| **D8PMP1** | Isocitrate lyase | 1.7 | 1.7 | 0.0 * |
| **D8Q077** | Isocitrate lyase | 8.7 * | 26.7 | 13.7 * |
| D8PZN4 | Trehalase (EC 3.2.1.28) (Alpha-trehalose glucohydrolase) | 6.7 * | 22.7 | 0.0 * |
| | **Carbohydrate-Active Enzymes (CAZymes)** | | | |
| | **Carbohydrate metabolic processes (GHs class)** | PSMs Sample A1 | PSMs Sample A2 | PSMs Sample B |
| D8PUK9 | Glycoside hydrolase family 31 protein/ beta-glucosidase | 2.7 * | 12.0 | 15.7 |
| D8PJY8 | Glycoside hydrolase family 125 protein | 0.3 | 4.7 | 6.7 |
| D8PK12 | Glycoside hydrolase family 43 protein | 0.0 | 0.0 | 1.0 |
| D8PL55 | Glycoside hydrolase family 43 and carbohydrate-binding module family 35 protein | 1.3 | 1.3 | 2.7 |
| D8PLY0 | Glycoside hydrolase family 76 protein | 0.0 | 0.3 | 0.7 |
| D8PMG3 | Glycoside hydrolase family 92 protein | 1.7 | 6.0 | 8.0 |
| D8PMG6 | Glycoside hydrolase family 92 protein | 0.3 | 3.0 | 4.7 |
| D8PMH4 | Glycoside hydrolase family 2 protein | 1.7 | 1.7 | 0.0 * |
| D8PPV4 | Glycoside hydrolase family 92 protein | 3.3 | 0.7 | 5.7 * |
| D8PS75 | Glycoside hydrolase family 18 protein | 1.0 * | 5.0 | 3.3 |
| D8PSJ0 | Glycoside hydrolase family 2 protein | 0.0 | 0.0 | 0.7 |
| D8PVQ7 | Glycoside hydrolase family 5 protein/ glucan 1,3-beta-glucosidase | 0.7 | 0.7 | 1.0 |
| D8PXL2 | Glycoside hydrolase family 5 protein/ glucan 1,3-beta-glucosidase | 0.3 | 0.0 | 0.0 |
| D8PXU7 | Glycoside hydrolase family 15 protein | 1.7 | 4.0 | 0.7 * |
| D8QJY6 | Glycoside hydrolase family 95 protein | 0.0 | 1.0 | 1.3 |
| D8PJV0 | Beta-glucosidase (EC 3.2.1.21) | 0.0 | 1.3 | 0.0 |
| **D8PS34** | 1,4-alpha-glucan-branching enzyme (EC 2.4.1.18) (Glycogen-branching enzyme) | 1.3 | 20.3 | 4.0 |
| D8PNW5 | Beta-glucosidase | 0.0 | 1.3 | 2.3 |
| D8PQP1 | glucan 1,3-beta-glucosidase | 0.7 * | 3.7 | 0.0 * |
| **D8PU51** | Beta-glucosidase | 5.3 | 10.0 | 22.0 * |
| **D8PUK9** | Beta-glucosidase | 2.7 * | 12.0 | 15.7 |
| **D8Q8Q6** | Beta-glucosidase | 0.0 | 2.0 | 0.0 |
| **D8Q3Q9** | Beta-galactosidase (EC 3.2.1.23) | 1.0 | 7.3 | 8.0 |

**Table 4.** *Cont.*

| | | | | |
|---|---|---|---|---|
| **D8PK76** | Beta-galactosidase (EC 3.2.1.23) | 2.0 | 5.7 | 7.7 |
| **D8PM67** | Beta-galactosidase (EC 3.2.1.23) | 0.0 | 0.3 | 0.3 |
| **D8Q3Q9** | Beta-galactosidase (EC 3.2.1.23) | 1.0 | 7.3 | 8.0 |
| **D8PQ92** | Alpha-galactosidase (EC 3.2.1.22) (Melibiase) | 3.3 * | 12.3 | 15.7 |
| **D8QGJ4** | Alpha-mannosidase (EC 3.2.1.24) | 16.7 | 32.0 | 7.3 * |
| | **Carbohydrate metabolic processes (GTs class)** | PSMs Sample A1 | PSMs Sample A2 | PSMs Sample B |
| D8Q7P4 | Glycosyltransferase family 32 protein | 0.0 | 1.0 | 0.0 |
| D8QHQ3 | Glycosyltransferase family 20 protein | 0.3 * | 10.7 | 0.0 * |
| **D8PXY7** | Transaldolase (EC 2.2.1.2) | 14.3 | 22.7 | 21.7 |
| | **Inositol phosphatase dephosphorylation** | PSMs Sample A1 | PSMs Sample A2 | PSMs Sample B |
| **D8PM90** | Inositol-1-monophosphatase (EC 3.1.3.25) | 2.0 | 1.7 | 3.0 |

As shown in the table, sample A2 appears to be the richest not only in the quantity of extracted proteins but also in the variety of enzymatic species related to pivotal pathways. In particular, some enzymes that are present in Table 4 will be described for their application in the discussion. This section may be divided by subheadings. It should provide a concise and precise description of the experimental results, their interpretation, and the experimental conclusions that can be drawn.

## 4. Discussion

This study represents the first proteomic analysis of an Italian strain of *S. commune*, a species that shows remarkable morpho-physiological and molecular variability. It is expected that traits specific to this population can be identified using proteomic analysis [41,42].

Mycelium grown in a nutrient-rich medium (ME 2% *w*/*v*) resulted in the identification of over 2000 proteins involved in different metabolic pathways.

In proteomic analyses, the extraction procedure is a crucial step in obtaining reliable and reproducible results since it significantly influences both the yield and diversity of the proteins obtained. In this study, to minimize protein loss, the mycelium of *S. commune* was first subjected to bead milling, a mechanical lysis method for protein extraction generally recognized as non-selective [43]. The following extraction was carried out under different conditions: (i) native conditions, separating the soluble fraction (sample A1) and the insoluble fraction extracted with urea (sample A2), or (ii) in the presence of TCA (sample B). Each sample differs not only in protein extraction yield but also in the diversity of the identified proteins.

In particular, sample A2, representing the insoluble fraction subsequently extracted with urea and Tris-Cl, showed the highest number of identified proteins (2105), with a significant number of unique proteins not found in the other samples. Sample A2 had the highest number of proteins, indicating that urea was a more effective agent for protein extraction.

Our results are consistent with those of other studies. Taunk et al. [44] showed that the combination of urea and Tris–Cl maximizes the yield of protein extraction in mammalian cells. Chi and Cho [45] showed that in soybean meal samples, the use of urea increased protein extraction efficiency by 90%.

Furthermore, TCA (used for sample B), traditionally used for protein isolation, resulted in an overall decrease in the protein yield. Even with the inclusion of appropriate detergents, TCA was found to be less effective for total protein extraction compared to other reagents [46,47].

It should be noted that the choice of extraction method affects not only the total yield but also the proteins that can be recovered. In particular, sample A2 showed enrichment of proteins from various cellular compartments, including the cytoplasm, membranes, and ribosomes, highlighting the importance of selecting the most effective method for isolating proteins from complex samples. Notably, no enzymatic treatments were used to digest the cell wall to keep the extraction process as simple and reproducible as possible.

Relatively few transcriptomic and proteomic analyses on *S. commune* have been performed so far [26–28,48]. In contrast to a previous study that evaluated the degradative activity of *S. commune* ISTL04 through the analysis of extracellular enzyme expression [26], our study focuses on characterizing the intracellular proteome of *S. commune* under standard growth conditions without external stimuli that could influence enzyme expression. Other proteomics studies focused on the relationship between *S. commune* and the antagonist *Trichoderma viride*, investigating their defense mechanisms [27] and on a single metabolic pathway, the inositol phosphate, and its impact on fungal metabolism [28]. In our work, the broad range of extracted proteins allows for the investigation of multiple metabolic pathways by using widely employed databases, such as Gene Ontology and Uniprot. Consequently, our experimental design is more easily replicable. Since the fungus is not induced to produce specific enzymes or activate specific metabolic pathways, the extracted proteins are more abundant in both total number and diversity.

Several proteins enriched in metabolic pathways under the growth conditions employed were examined in depth. First, attention was placed on the trehalose biosynthesis pathway [49] since this carbohydrate is known as a food stabilizer and protective agent against oxidative stress, holding substantial value in the industry [50,51]. In our samples of *S. commune*, the following key enzymes have been successfully identified: trehalose synthase (UniProt accession number D8QC44), trehalase (D8QIA1), and trehalose phosphorylase (Q2HZZ3) (see Table 4). It is worth noticing that only method A2 allowed for the extraction of these enzymes in sufficient quantities to enable their subsequent identification. This underscores the importance of using a reliable extraction procedure to avoid the loss of important biological information. Trehalose is known for its effectiveness as a food stabilizer and a protective agent against oxidative stress. It holds substantial value in the industry, with applications extending to the pharmaceutical and cosmetic sectors due to its thermal-protective properties [52,53]. The expression of enzymes involved in the trehalose biosynthesis pathway by *S. commune* shows potential for the development of the enzymatic synthesis of trehalose with significant cost savings and reduced production time compared to the expensive and complex chemical synthesis currently in use.

The present proteomic analysis also detected 2 out of 6 major classes in the family of CAZy family carbohydrate-active enzymes [54,55]: glycosyl hydrolases (GHs) and glycosyl transferases (GTs). On the other hand, polysaccharide lyases (PLs), carbohydrate esterases (CEs), carbohydrate-binding modules (CBMs) and auxiliary activities (AAs) did not exceed the detection limit. In mushrooms, CAZymes play vital roles in the development of fruiting bodies [56], in cell wall formation, and in nutrient uptake, as well as in the breakdown of lignocellulosic substrates [40]. Researching CAZymes can enhance our understanding of biological processes and improve fungal cultivation [51]. CAZymes are crucial for breaking down complex carbohydrates, aiding digestion, and promoting nutrient absorption in the human gut microbiota, where the human genome encodes only 17 such enzymes. Specifically, glycoside hydrolase (GH) and glycosyl transferase (T) enzymes are vital for a

healthy microbiome [57–59]. CAZymes also play a role in immune defense and reducing inflammation, with decreased expression linked to various diseases. Therefore, we aimed to investigate which CAZymes are expressed by *S. commune* under specific growth conditions.

Among the various GH enzymes, alpha-mannosidase (D8QGJ4) was found in higher amounts in the extract A2. This CAZyme has been identified as a potential target for tumor and cancer treatment [60] and is involved in the post-translational modification of secreted proteins [61]. Other GH enzymes significantly expressed in *S. commune* are 1,4-alpha-glucan (D8PS34) and trehalose phosphorylase (Q2HZZ3), both of which are implicated in the biosynthesis of Trehalose. Also, in this case, sample A2 showed a higher presence of these two enzymes, which play a crucial role in the food industries [62]. In *Hypsizygus marmoreus* (Peck) H.E. Bigelow, the expression of 1,4-alpha-glucan and trehalose phosphorylase was observed during the primordium phase of growth and not during the mycelia growth [63]. In contrast, the expression of these enzymes was high as early as the mycelial growth stage of the *S. commune* used in this study.

Finally, beta-glucosidase enzymes (D8PJV0, D8PU51, D8PUK9, D8Q8Q6) are relevant due to their hydrolytic action in degrading lignocellulosic components, thereby facilitating the growth and subsequent development of mushrooms [63,64]. Recently, β-glucosidase has gained attention in the industrial sector as a valuable enzyme for repurposing food waste [65]. Hence, it can be deduced that extract A2 contains the highest amount of all the CAZymes previously discussed.

Among the CAZy family, two enzymes belonging to the GTs class were identified: α-galactosidase (D8PQ92) and β-galactosidase (D8Q3Q9, D8PK76, D8PM67, and D8Q3Q9). Alpha-galactosidase can break down galactose residues found in oligosaccharides, such as raffinose-family oligosaccharides. Nowadays, it is used to reduce stachyose and raffinose in soybean flour for industrial applications in the food and feed industries [66]. However, these enzymes could be applied in agriculture, food production, and biomedicine [67,68].

Beta-galactosidases derived from fungi find innovative applications in the production of prebiotic compounds, recycling agro-industrial wastes and removing lactose from dairy products [69–72]. Based on promising preliminary results, mushroom-derived mixtures containing β-galactosidases may offer more economical solutions for bioethanol production from cheese whey [23].

Among the 10 superclusters presented in the treemap, significant enrichment was also observed in the pentose-phosphate shunt. This metabolic pathway is crucial for the biosynthesis of erythritol [73]. This molecule influences not only mycelial growth but also the formation of the fruiting body [74]. The main enzymes involved in this metabolic pathway are 6-phosphogluconate dehydrogenase-decarboxylating (Uniprot D8PMS0), transketolase (D8PWF8), and transaldolase (D8PXY7), [73,75]. All identified enzymes were significantly enriched in sample A2. Erythritol is becoming increasingly popular as a natural sweetener, used in low-calorie foods and beverages, and as an additive with artificial sweeteners. Research has focused on reducing production costs through fermentation optimization to meet the rising demand in various industries [73].

Sample A2 showed a higher amount of enzymes involved in the tricarboxylic acid cycle, another relevant pathway closely connected with oxaloacetate biosynthesis. The production of oxalic acid in wood decay fungi is essential during the vegetative phase to derive energy from glucose oxidation [38]. Moreover, the production of oxalic acid prevents the inhibition of ligninolytic enzymes caused by an increase in reactive oxygen species [76]. The main enzymes involved in this pathway are malate synthase (D8Q9D5), oxalate oxidase (D8Q486), and isocitrate lyase (D8Q077), which are expressed at significantly higher levels in sample A2 tan in samples A1 and B.

Finally, the biosynthesis of inositol-phosphate is one of the most complex metabolic pathways related to growth and metabolic adaptation, as well as upregulation during sexual development [77]. Inositol-1-monophosphatase (EC 3.1.3.25) was also identified in the mycelium of *S. commune*, but there were not many differences in its expression among the three extraction methods: A1, A2 and B.

Activation of these metabolic processes leads to the production of reactive oxygen species. The proteomic profile of *S. commune* clearly indicates the expression of various enzymes involved in detoxifying reactive species, such as superoxide dismutases, catalases, and peroxidases [78]. However, it should be noted that in wood-decay mushrooms, peroxidases, in turn, include both enzymes involved in detoxification and lignin degradation, the latter providing self-protection in the fungal organism [22]. In the present study, no lignin was added to the culture medium and peroxidase activity was, therefore, related to basic metabolic functions.

## 5. Conclusions

This study highlights the significance and innovation of utilizing enzymes extracted from a fungal species renowned for its dual roles in medicinal applications and myco-remediation. By conducting the research under standardized growth conditions, we achieved a "general" enzymatic characterization free from the influence of internal or external stressors, thereby capturing the intrinsic metabolic potential of this species. The extraction method A2 proved critical in maximizing the yield and diversity of isolated enzymes, facilitating the recovery of proteins from various cellular compartments, and ensuring a comprehensive proteomic profile. This approach enabled the identification of enzymes with high industrial and nutraceutical and myco-remediation relevance, including trehalose synthase and trehalase, critical for trehalose biosynthesis, a process that is currently complex and costly. These fungal-derived enzymes could streamline the study of trehalose biosynthetic pathways in specific fungal species.

Additionally, this study identified significant levels of peroxidases and catalases, enzymes well-known for their antioxidant properties. Further investigations are needed to determine their potential medical applications, especially in oxidative stress management. Notably, the presence of CAZy enzymes is of particular interest for the dietary use of *S. commune*, as they may positively influence gut flora and enhance intestinal health. With the growing demand for bioactive-enriched products, *S. commune* could be considered a valuable source of proteins and bioactive molecules for novel food production.

In conclusion, given this fungal species' high enzymatic potential under standard growth conditions and the demonstrated advantages of the A2 extraction method, future research could focus on optimizing the expression of industrially and nutraceutical-relevant enzymes. This research establishes a foundation for utilizing this fungal species as a sustainable source of bioactive enzymes with extensive applications in biotechnology, medicine, and environmental science.

**Supplementary Materials:** The following supporting information can be downloaded at https://www.mdpi.com/article/10.3390/jof11020120/s1, Figure S1. SDS-PAGE analysis of S. commune protein extracts obtained using three methods. Lane 1: Molecular weight marker (MWM); Lane 2: Soluble fraction extracted with Method A1 (Tris buffer, mechanical disruption); Lane 3: Insoluble fraction solubilized with Method A2 (urea-based buffer); Lane 4: Protein extract obtained with Method B (TCA precipitation and urea-based solubilization). Equal volumes of each sample were loaded. File S2. Protein list of all identified proteins in the three technical replicates (TR1, TR2, TR3) for the three samples (A1, A2, B). In the table for each protein these attributes are indicated: UniProt Accession, Protein Name, Gene Name, Peptide Spectrum Matches (PSMs) for each technical replicate, Average of PSMs for each sample. File S3. List of enriched Gene Ontology Biological

Process (GO-BP) terms considering all identified proteins. For each term in the table are reported: GO-BP term; number of identified proteins annotated in the sample; UniProt Accession of identified proteins; total number of annotated proteins in sample; number of *S. commune* proteins annotated; total number of *S. commune* annotated with GO term; fold enrichment.

**Author Contributions:** Conceptualization A.D., L.G., C.S., E.F., S.B. (Stefania Brocca) and E.S.; methodology, A.D., L.G., C.S., E.F. and S.B. (Stefania Brocca); software, C.S. and E.F.; validation, A.D., L.G., C.S., E.F., S.B. (Stefania Brocca) and E.S.; formal analysis, E.F.; investigation, A.D., L.G., S.B. (Simone Buratti), C.E.G., C.S., E.F., S.B. (Stefania Brocca), M.T.V., M.S. and E.S.; data curation, A.D., L.G., E.F., C.S. and S.B. (Stefania Brocca); writing—original draft preparation, A.D., L.G., S.B. (Simone Buratti), C.E.G., C.S., E.F., S.B. (Stefania Brocca), M.T.V., M.S., E.S. and P.R.; writing—review and editing, A.D., L.G., S.B. (Simone Buratti), C.E.G., C.S., E.F., S.B. (Stefania Brocca), M.T.V., M.S., E.S. and P.R.; visualization, A.D., L.G., S.B. (Simone Buratti), C.E.G., C.S., E.F., S.B. (Stefania Brocca), M.T.V., M.S., E.S. and P.R.; supervision, A.D., L.G., S.B. (Simone Buratti), C.E.G., C.S., E.F., S.B. (Stefania Brocca), M.T.V., M.S., E.S. and P.R.; funding acquisition, E.S. and P.R. All authors have read and agreed to the published version of the manuscript.

**Funding:** This study was supported by Fondazione Cariplo and Regione Lombardia, Grant No. 2018-1765, through the project entitled "MYCO-ADVANCED LEATHER MATERIALS (MATER)".

**Institutional Review Board Statement:** Not applicable.

**Informed Consent Statement:** Not applicable.

**Data Availability Statement:** All data generated or analyzed during this study are included in this manuscript and its Supplementary Materials. The mass spectrometry proteomics data have been deposited to the ProteomeXchange Consortium via the PRIDE partner repository with the dataset identifier PXD048036 and https://doi.org/10.6019/PXD048036 (accessed on 2 February 2025).

**Conflicts of Interest:** The authors declare no conflicts of interest.

## Abbreviations

The following abbreviations are used in this manuscript:

| | |
|---|---|
| BP | Biological process |
| CAZymes | Carbohydrate-active enzymes |
| CC | Cellular Component |
| GO | Gene Ontology |
| LC-MS/MS | Liquid Chromatography with tandem mass spectrometry |
| ME | Malt Extract |
| MEA | Malt Extract Agar |
| PSM | Peptide Spectrum Match |
| TCA | Trichloroacetic acid |

## References

1. Venturella, G.; Ferraro, V.; Cirlincione, F.; Gargano, M.L. Medicinal mushrooms: Bioactive compounds, use, and clinical trials. *Int. J. Mol. Sci.* **2021**, *22*, 634. [CrossRef] [PubMed]
2. Tee, P.Y.E.; Krishnan, T.; Cheong, X.T.; Maniam, S.A.; Looi, C.Y.; Ooi, Y.Y.; Chua, L.L.C.; Fung, S.Y.; Chia, A.Y.Y. A review on the cultivation, bioactive compounds, health-promoting factors and clinical trials of medicinal mushrooms *Taiwanofungus camphoratus*, *Inonotus obliquus* and *Tropicoporus linteus*. *Fungal Biol. Biotechnol.* **2024**, *11*, 7. [CrossRef] [PubMed]
3. Yu, C.; Dong, Q.; Chen, M.; Zhao, R.; Zha, L.; Zhao, Y.; Zhang, M.; Zhang, B.; Ma, A. The effect of mushroom dietary fiber on the gut microbiota and related health benefits: A review. *J. Fungi* **2023**, *9*, 1028. [CrossRef] [PubMed]
4. Abd Razak, D.L.; Abd Ghani, A.; Lazim, M.I.M.; Khulidin, K.A.; Shahidi, F.; Ismail, A. *Schizophyllum commune* (Fries) mushroom: A review on its nutritional components, antioxidative, and anti-inflammatory properties. *Curr. Opin. Food Sci.* **2024**, *56*, 101129. [CrossRef]
5. Zhang, Y.; Kong, H.; Fang, Y.; Nishinari, K.; Phillips, G.O. Schizophyllan: A review on its structure, properties, bioactivities and recent developments. *Bioact. Carbohydr. Diet. Fibre.* **2013**, *1*, 53–71. [CrossRef]

6. Zhong, K.; Tong, L.; Liu, L.; Zhou, X.; Liu, X.; Zhang, Q.; Zhou, S. Immunoregulatory and antitumor activity of schizophyllan under ultrasonic treatment. *Int. J. Biol. Macromol.* **2015**, *80*, 302–308. [CrossRef]
7. Gou, Z.; Peng, Z.; Wang, S.; Chen, L.; Ma, Z.; Kang, Y.; Kang, I.; Sun, L.; Wang, R.; Xu, H.; et al. Efficient production and skincare activity evaluation of schizophyllan, a β-glucan derived from *Schizophyllum commune* NTU-1. *Int. J. Biol. Macromol.* **2023**, *241*, 124504. [CrossRef]
8. Mišković, J.; Karaman, M.; Rašeta, M.; Krsmanović, N.; Berežni, S.; Jakovljević, D.; Piattoni, F.; Zambonelli, A.; Gargano, M.L.; Venturella, G. Comparison of two *Schizophyllum commune* strains in production of acetylcholinesterase inhibitors and antioxidants from submerged cultivation. *J. Fungi* **2021**, *7*, 115. [CrossRef] [PubMed]
9. Ahmad, N.; Aslam, S.; Hussain, N.; Bilal, M.; Iqbal, H.M. Transforming lignin biomass to value: Interplay between ligninolytic enzymes and lignocellulose depolymerization. *BioEnergy Res.* **2023**, *16*, 1246–1263. [CrossRef]
10. Kumar, A.; Bharti, A.K.; Bezie, Y. Schizophyllum commune: A fungal cell-factory for production of valuable metabolites and enzymes. *BioResources* **2022**, *17*, 5420–5436. [CrossRef]
11. Basso, V.; Schiavenin, C.; Mendonça, S.; de Siqueira, F.G.; Salvador, M.; Camassola, M. Chemical features and antioxidant profile by *Schizophyllum commune* produced on different agroindustrial wastes and byproducts of biodiesel production. *Food Chem.* **2020**, *329*, 127089. [CrossRef]
12. Asgher, M.; Wahab, A.; Bilal, M.; Iqbal, H.M.N. Lignocellulose degradation and production of lignin modifying enzymes by *Schizophyllum commune* IBL-06 in solid-state fermentation. *Biocatal. Agric. Biotechnol.* **2016**, *6*, 195–201. [CrossRef]
13. Tovar-Herrera, O.E.; Martha-Paz, A.M.; Pérez-Llano, Y.; Aranda, E.; Tacoronte-Morales, J.E.; Pedroso-Cabrera, M.T.; Arévalo-Niño, K.; Folch-Mallol, J.L.; Batista-García, R.A. *Schizophyllum commune*: An unexploited source for lignocellulose degrading enzymes. *MicrobiologyOpen* **2018**, *7*, e00637. [CrossRef] [PubMed]
14. Vonk, P.J. Functional Genomics in *Schizophyllum commune*. Ph.D. Thesis, Utrecht University, Utrecht, The Netherlands, 2022.
15. Appels, F.V.; Dijksterhuis, J.; Lukasiewicz, C.E.; Jansen, K.M.; Wösten, H.A.; Krijgsheld, P. Hydrophobin gene deletion and environmental growth conditions impact mechanical properties of mycelium by affecting the density of the material. *Sci. Rep.* **2018**, *8*, 4703. [CrossRef] [PubMed]
16. Shankar, A.; Sharma, K.K. Fungal Secondary Metabolites in Food and Pharmaceuticals in the Era of Multi-Omics. *Appl. Microbiol. Biotechnol.* **2022**, *106*, 3465–3488. [CrossRef]
17. Giddey, K.; Monod, M.; Barblan, J.; Potts, A.; Waridel, P.; Zaugg, C.; Quadroni, M. Comprehensive analysis of proteins secreted by *Trichophyton rubrum* and *Trichophyton violaceum* under in vitro conditions. *J. Proteome Res.* **2007**, *6*, 3081–3092. [CrossRef] [PubMed]
18. Leng, W.; Liu, T.; Li, R.; Yang, J.; Wie, C.; Zhang, W.; Jin, Q. Proteomic profile of dormant *Trichophyton rubrum* conidia. *BMC Genom.* **2008**, *9*, 303. [CrossRef] [PubMed]
19. Jakopovic, B.; Oršolić, N.; Kraljević Pavelić, S.; Jakopovich, I. Proteomic Research on the Therapeutic Properties of Medicinal Mushrooms. In *Mushrooms with Therapeutic Potentials: Recent Advances in Research and Development*; Springer Nature: Singapore, 2023; pp. 309–344.
20. Adav, S.S.; Chao, L.T.; Sze, S.K. Quantitative secretomic analysis of *Trichoderma reesei* strains reveals enzymatic composition for lignocellulosic biomass degradation. *Mol. Cell. Proteom.* **2012**, *11*, 1–15. [CrossRef] [PubMed]
21. Chen, Z.; Yin, H.; Peng, H.; Lu, G.; Liu, Z.; Dang, Z. Identification of novel pathways for biotransformation of tetrabromobisphenol A by *Phanerochaete chrysosporium*, combined with mechanism analysis at proteome level. *Sci. Total Environ.* **2019**, *659*, 1352–1361. [CrossRef] [PubMed]
22. Doria, E.; Altobelli, E.; Girometta, C.; Nielsen, E.; Zhang, T.; Savino, E. Evaluation of lignocellulolytic activities of ten fungal species able to degrade poplar wood. *Int. Biodeter. Biodegrad.* **2014**, *94*, 160–166. [CrossRef]
23. Zhu, N.; Liu, J.; Yang, J.; Lin, Y.; Yang, Y.; Ji, L.; Li, M.; Yuan, H. Comparative analysis of the secretomes of *Schizophyllum commune* and other wood-decay basidiomycetes during solid-state fermentation reveals its unique lignocellulose-degrading enzyme system. *Biotechnol. Biofuels* **2016**, *9*, 42. [CrossRef]
24. Li, G.; Jian, T.; Liu, X.; Lv, Q.; Zhang, G.; Ling, J. Application of metabolomics in fungal research. *Molecules* **2022**, *27*, 7365. [CrossRef]
25. Saw, N.M.M.T.; Suwanchaikasem, P.; Zuniga-Montanez, R.; Qiu, G.; Marzinelli, E.M.; Wuertz, S.; Williams, R.B. Influence of extraction solvent on nontargeted metabolomics analysis of enrichment reactor cultures performing enhanced biological phosphorus removal (EBPR). *Metabolites* **2021**, *11*, 269. [CrossRef] [PubMed]
26. Singh, M.K.; Kumar, M.; Thakur, I.S. Proteomic characterization and schizophyllan production by *Schizophyllum commune* ISTL04 cultured on *Leucaena leucocephala* wood under submerged fermentation. *Bioresour. Technol.* **2017**, *236*, 29–36. [CrossRef] [PubMed]
27. Ujor, V.C.; Peiris, D.G.; Monti, M.; Kang, A.S.; Clements, M.O.; Hedger, J.N. Quantitative proteomic analysis of the response of the wood-rot fungus, *Schizophyllum commune*, to the biocontrol fungus, *Trichoderma viride*. *Lett. Appl. Microbiol.* **2012**, *54*, 336–343. [CrossRef] [PubMed]
28. Murry, R.; Traxler, L.; Pötschner, J.; Krüger, T.; Kniemeyer, O.; Krause, K.; Kothe, E. Inositol signaling in the basidiomycete fungus *Schizophyllum commune*. *J. Fungi.* **2021**, *7*, 470. [CrossRef] [PubMed]

29. Girometta, C.E.; Bernicchia, A.; Baiguera, R.M.; Bracco, F.; Buratti, S.; Cartabia, M.; Picco, A.M.; Savino, E. An Italian Research Culture Collection of Wood Decay Fungi. *Diversity* **2020**, *12*, 58. [CrossRef]
30. Cartabia, M.; Girometta, C.E.; Baiguera, R.M.; Buratti, S.; Babbini, S.; Bernicchia, A.; Savino, E. Lignicolous fungi collected in northern Italy: Identification and morphological description of isolates. *Diversity* **2022**, *14*, 413. [CrossRef]
31. Ham, T.H.; Lee, Y.; Kwon, S.W.; Jang, M.J.; Park, Y.J.; Lee, J. Increasing Coverage of Proteome Identification of the Fruiting Body of *Agaricus bisporus* by Shotgun Proteomics. *Foods* **2020**, *9*, 632. [CrossRef] [PubMed]
32. Laemmli, U.K. Cleavage of structural proteins during the assembly of the head of bacteriophage T4. *Nature* **1970**, *227*, 680–685. [CrossRef] [PubMed]
33. Tyanova, S.; Temu, T.; Cox, J. The MaxQuant computational platform for mass spectrometry-based shotgun proteomics. *Nat. Protoc.* **2016**, *11*, 2301–2319. [CrossRef]
34. Perez-Riverol, Y.; Bai, J.; Bandla, C.; García-Seisdedos, D.; Hewapathirana, S.; Kamatchinathan, S.; Kundu, D.J.; Prakash, A.; Frericks-Zipper, A.; Eisenacher, M.; et al. The PRIDE database resources in 2022: A hub for mass spectrometry-based proteomics evidences. *Nucleic Acids Res.* **2022**, *50*, D543–D552. [CrossRef]
35. Pathan, M.; Keerthikumar, S.; Ang, C.S.; Gangoda, L.; Quek, C.Y.; Williamson, N.A.; Mouradov, D.; Sieber, O.M.; Simpson, R.J.; Salim, A.; et al. FunRich: An open access standalone functional enrichment and interaction network analysis tool. *Proteomics* **2015**, *15*, 2597–2601. [CrossRef] [PubMed]
36. Sherman, B.T.; Hao, M.; Qiu, J.; Jiao, X.; Baseler, M.W.; Lane, H.C.; Imamichi, T.; Chang, W. DAVID: A web server for functional enrichment analysis and functional annotation of gene lists (2021 update). *Nucleic Acids Res.* **2022**, *50*, W216–W221. [CrossRef]
37. Supek, F.; Bošnjak, M.; Škunca, N.; Šmuc, T. REVIGO Summarizes and Visualizes Long Lists of Gene Ontology Terms. *PLoS ONE* **2011**, *6*, e21800. [CrossRef]
38. Park, Y.J.; Jeong, Y.U.; Kong, W.S. Genome sequencing and carbohydrate-active enzyme (CAZyme) repertoire of the white rot fungus *Flammulina elastica*. *Int. J. Mol. Sci.* **2018**, *19*, 2379. [CrossRef]
39. Yoon, J.J.; Hattori, T.; Shimada, M. A metabolic role of the glyoxylate and tricarboxylic acid cycles for development of the copper-tolerant brown-rot fungus *Fomitopsis palustris*. *FEMS Microbiol. Lett.* **2002**, *217*, 9–14. [CrossRef] [PubMed]
40. Yoon, J.J.; Munir, E.; Miyasou, H.; Hattori, T.; Shimada, M.; Terashita, T. A possible role of the key enzymes of the glyoxylate and gluconeogenesis pathways for fruit-body formation of the wood-rotting basidiomycete *Flammulina velutipes*. *Mycoscience* **2002**, *43*, 327–332. [CrossRef]
41. Kües, U. From Two to Many: Multiple Mating Types in Basidiomycetes. *Fungal Biol. Rev.* **2015**, *29*, 126–166. [CrossRef]
42. Carreño-Ruiz, S.D.; Lázaro, A.a.Á.; García, S.C.; Hernández, R.G.; Chen, J.; Navarro, G.K.G.; Fajardo, L.V.G.; Pérez, N.D.C.J.; Cruz, M.T.D.L.; Blanco, J.C.; et al. New Record of *Schizophyllum* (Schizophyllaceae) from Mexico and the Confirmation of Its Edibility in the Humid Tropics. *Phytotaxa* **2019**, *413*, 137–148. [CrossRef]
43. Ahmed, T.; Suzauddula, M.; Akter, K.; Hossen, M.; Islam, M.N. Green Technology for Fungal Protein Extraction—A Review. *Separations* **2024**, *11*, 186. [CrossRef]
44. Taunk, K.; Paul, D.; Dabhi, R.; Venkatesh, C.; Jajula, S.; Naik, V.; Tamhankar, A.; Naiya, T.; Kumar Santra, M.; Rapole, S.A. Single step and rapid protein extraction protocol developed for cell lines and tissues: Compatible for gel based and gel free proteomic approaches. *Methods* **2023**, *220*, 29–37. [CrossRef] [PubMed]
45. Chi, C.H.; Cho, S.J. Extraction solvent's effect on protein profiles of processed soybean meal. *Food Biosci.* **2020**, *37*, 100734. [CrossRef]
46. Jaipal Reddy, P.; Anand Rao, A.; Malhotra, D.; Sharma, S.; Kumar, R.; Jain, R.; Gollapalli, K.; Pendharkar, N.; Rapole, S.; Srivastava, S. A simple protein extraction method for proteomic analysis of diverse biological specimens. *Curr. Proteom.* **2013**, *10*, 298–311. [CrossRef]
47. Santa, C.; Anjo, S.I.; Manadas, B. Protein precipitation of diluted samples in SDS-containing buffer with acetone leads to higher protein recovery and reproducibility in comparison with TCA/acetone approach. *Proteomics* **2016**, *16*, 1847–1851. [CrossRef] [PubMed]
48. Ohm, R.A.; de Jong, J.F.; Lugones, L.G.; Aerts, A.; Kothe, E.; Stajich, J.E.; de Vries, R.P.; Record, E.; Levasseur, A.; Baker, S.E.; et al. Genome sequence of the model mushroom *Schizophyllum commune*. *Nat. Biotechnol.* **2010**, *28*, 957–963. [CrossRef]
49. Ohtake, S.; Wang, Y.J. Trehalose: Current use and future applications. *J. Pharm. Sci.* **2011**, *100*, 2020–2053. [CrossRef] [PubMed]
50. Liu, X.; Wu, X.; Wei, G.; Qu, J.; Qiang, C.; Huang, C.; Zhang, J. Protective roles of trehalose in *Pleurotus pulmonarius* during heat stress response. *J. Integr. Agric.* **2019**, *18*, 428–437. [CrossRef]
51. Agarwal, N.; Singh, S.P. A novel trehalose synthase for the production of trehalose and trehalulose. *Microbiol Spectr.* **2021**, *9*, e0133321. [CrossRef]
52. Chen, A.; Tapia, H.; Goddard, J.M.; Gibney, P.A. Trehalose and its applications in the food industry. *Compr. Rev. Food Sci. Food Saf.* **2022**, *21*, 5004–5037. [CrossRef] [PubMed]
53. Drula, E.; Garron, M.L.; Dogan, S.; Lombard, V.; Henrissat, B.; Terrapon, N. The carbohydrate-active enzyme database: Functions and literature. *Nucleic Acids Res.* **2022**, *50*, D571–D577. [CrossRef] [PubMed]

54. Chettri, D.; Verma, A.K. Biological significance of carbohydrate active enzymes and searching their inhibitors for therapeutic applications. *Carbohydr. Res.* **2023**, *529*, 108853. [CrossRef] [PubMed]
55. Cantarel, B.L.; Lombard, V.; Henrissat, B. Complex carbohydrate utilization by the healthy human microbiome. *PLoS ONE*. **2012**, *7*, e28742. [CrossRef]
56. Tashkandi, M.; Baz, L. Function of CAZymes encoded by highly abundant genes in rhizosphere microbiome of *Moringa oleifera*. *Saudi J. Biol. Sci.* **2023**, *30*, 103578. [CrossRef]
57. Ye, S.; Shah, B.R.; Li, J.; Liang, H.; Zhan, F.; Geng, F.; Li, B. A critical review on interplay between dietary fibers and gut microbiota. *Trends Food Sci.* **2022**, *124*, 237–249. [CrossRef]
58. Koenig, J.E.; Spor, A.; Scalfone, N.; Fricker, A.D.; Stombaugh, J.; Knight, R.; Angenent, L.T.; Ley, R.E. Succession of microbial consortia in the developing infant gut microbiome. *Proc. Natl. Acad. Sci. USA* **2011**, *108* (Suppl. S1), 4578–4585. [CrossRef]
59. Onyango, S.O.; Juma, J.; De Paepe, K.; Van de Wiele, T. Oral and gut microbial carbohydrate-active enzymes landscape in health and disease. *Front. Microbiol.* **2021**, *12*, 653448. [CrossRef] [PubMed]
60. Amin, K.; Tranchimand, S.; Benvegnu, T.; Abdel-Razzak, Z.; Chamieh, H. Glycoside hydrolases and glycosyltransferases from hyperthermophilic archaea: Insights on their characteristics and applications in biotechnology. *Biomolecules* **2021**, *11*, 1557. [CrossRef]
61. Morosanova, M.A.; Fedorova, T.V.; Polyakova, A.S.; Morosanova, E.I. Agaricus bisporus crude extract: Characterization and analytical application. *Molecules* **2020**, *25*, 5996. [CrossRef] [PubMed]
62. Ban, X.; Dhoble, A.S.; Li, C.; Gu, Z.; Hong, Y.; Cheng, L.; Holler, T.P.; Kaustubh, B.; Li, Z. Bacterial 1, 4-α-glucan branching enzymes: Characteristics, preparation and commercial applications. *Crit. Rev. Biotechnol.* **2020**, *40*, 380–396. [CrossRef] [PubMed]
63. Yang, X.; Lin, R.; Xu, K.; Guo, L.; Yu, H. Comparative proteomic analysis within the developmental stages of the mushroom white *Hypsizygus marmoreus*. *J. Fungi* **2021**, *7*, 1064. [CrossRef] [PubMed]
64. Shankar, A.; Jain, K.K.; Kuhad, R.C.; Sharma, K.K. Comparison of lignocellulosic enzymes and CAZymes between ascomycetes (Trichoderma) and basidiomycetes (Ganoderma) species: A proteomic approach. *Z. Naturforsch. C* **2023**, *80*, 21–32. [CrossRef] [PubMed]
65. Roukas, T.; Kotzekidou, P. From food industry wastes to second generation bioethanol: A review. *Rev. Environ. Sci. Bio/Technol.* **2022**, *21*, 299–329. [CrossRef]
66. Geng, X.; Tian, G.; Zhao, Y.; Zhao, L.; Wang, H.; Ng, T.B. A Fungal α-Galactosidase from *Tricholoma matsutake* with broad substrate specificity and good hydrolytic activity on raffinose family oligosaccharides. *Molecules* **2015**, *20*, 13550–13562. [CrossRef]
67. Bhatia, S.; Singh, A.; Batra, N.; Singh, J. Microbial production and biotechnological applications of α-galactosidase. *Int. J. Biol. Macromol.* **2020**, *150*, 1294–1313. [CrossRef]
68. Bangoria, P.; Patel, A.; Shah, A.R. Characterization of a fungal α-galactosidase and its synergistic effect with β-mannanase for hydrolysis of galactomannan. *Carbohydr. Res.* **2023**, *531*, 108893. [CrossRef]
69. Saqib, S.; Akram, A.; Halim, S.A.; Tassaduq, R. Sources of β-galactosidase and its applications in food industry. *Biotech* **2017**, *7*, 79. [CrossRef]
70. Volford, B.; Varga, M.; Szekeres, A.; Kotogán, A.; Nagy, G.; Vágvölgyi, C.; Papp, T.; Takó, M. β-galactosidase-producing isolates in mucoromycota: Screening, enzyme production, and applications for functional oligosaccharide synthesis. *J. Fungi* **2021**, *7*, 229. [CrossRef]
71. Singh, R.V.; Sambyal, K. β-Galactosidase as an industrial enzyme: Production and potential. *Chem. Pap.* **2023**, *77*, 11–31. [CrossRef]
72. Lu, L.; Guo, L.; Wang, K.; Liu, Y.; Xiao, M. β-Galactosidases: A great tool for synthesizing galactose-containing carbohydrates. *Biotechnol. Adv.* **2020**, *39*, 107465. [CrossRef]
73. Ibrahim, O. Erythritol chemical structure, biosynthesis pathways, properties, applications, and production. *Int. J. Microbiol. Biotechnol.* **2021**, *6*, 59. [CrossRef]
74. Kuroda, K.; Hirakawa, S.; Suzuki, M.; Shinji, K.; Ogasa, K.; Uraji, T.; Amachi, T.; Ueda, M. Growth acceleration of plants and mushroom by erythritol. *Plant Biotechnol.* **2008**, *25*, 489–492. [CrossRef]
75. Diamantopoulou, P.; Papanikolaou, S. Biotechnological production of sugar-alcohols: Focus on *Yarrowia lipolytica* and edible/medicinal mushrooms. *Process Biochem.* **2023**, *124*, 113–131. [CrossRef]
76. Munir, E.; Yoon, J.J.; Tokimatsu, T.; Hattori, T.; Shimada, M. New role for glyoxylate cycle enzymes in wood-rotting basidiomycetes in relation to biosynthesis of oxalic acid. *J. Wood Sci.* **2001**, *47*, 368–373. [CrossRef]
77. Murry, R.; Kniemeyer, O.; Krause, K.; Saiardi, A.; Kothe, E. Crosstalk between Ras and inositol phosphate signaling revealed by lithium action on inositol monophosphatase in *Schizophyllum commune*. *Adv. Biol. Regul.* **2019**, *72*, 78–88. [CrossRef]
78. Xu, L.; Guo, L.; Yu, H. Label-free comparative proteomics analysis revealed heat stress responsive mechanism in *Hypsizygus marmoreus*. *Front. Microbiol.* **2021**, *11*, 541967. [CrossRef]

frontiers | Frontiers in Physiology

TYPE Original Research
PUBLISHED 12 March 2025
DOI 10.3389/fphys.2025.1455434



OPEN ACCESS

EDITED BY
John D. Imig,
University of Arkansas for Medical Sciences, United States

REVIEWED BY
Ali Çetin,
University of Health Sciences, Türkiye
Susana Cardoso,
University of Coimbra, Portugal

*CORRESPONDENCE
Paola Rossi,
paola.rossi@unipv.it

RECEIVED 26 June 2024
ACCEPTED 06 February 2025
PUBLISHED 12 March 2025

CITATION
Venuti MT, Roda E, Brandalise F, Sarkar M, Cappelletti M, Speciani AF, Soffientini I, Priori EC, Giammello F, Ratto D, Locatelli CA and Rossi P (2025) A pathophysiological intersection between metabolic biomarkers and memory: a longitudinal study in the STZ-induced diabetic mouse model.
*Front. Physiol.* 16:1455434.
doi: 10.3389/fphys.2025.1455434



# A pathophysiological intersection between metabolic biomarkers and memory: a longitudinal study in the STZ-induced diabetic mouse model

Maria Teresa Venuti[1], Elisa Roda[2], Federico Brandalise[3], Meghma Sarkar[1], Mattia Cappelletti[4], Attilio F. Speciani[4], Irene Soffientini[1], Erica Cecilia Priori[1], Francesca Giammello[1], Daniela Ratto[1], Carlo A. Locatelli[2] and Paola Rossi[1]*

[1]Department of Biology and Biotechnology "L. Spallanzani", University of Pavia, Pavia, Italy, [2]Laboratory of Clinical and Experimental Toxicology, Pavia Poison Centre, National Toxicology Information Centre, Toxicology Unit, Istituti Clinici Scientifici Maugeri IRCCS, Pavia, Italy, [3]Department of Biomedical Sciences, Div. Neuroscience and Clinical Pharmacology, University of Cagliari, Cagliari, Italy, [4]GEK Lab, Milano, Italy

Diabetes mellitus (DM) is a metabolic disorder characterized by high blood sugar levels due to insufficient insulin production or insulin resistance. Recently, metabolic biomarkers, such as glycated albumin (GA) and methylglyoxal (MGO), have been successfully employed for the management of diabetes and its complications. The main goal of this study was to investigate the relationship between metabolic parameters, related to diabetic conditions, and the recognition memory, a declarative episodic long-term memory, in a streptozotocin (STZ)-induced diabetes mouse model. The longitudinal experimental plan scheduled five experimental timepoints, starting from 9 months and lasting until 19 months of age, and included different evaluations: i) fasting serum glucose, GA, and MGO, ii) recognition memory performance; iii) histological examinations of pancreas and hippocampus. At 13 months of age, mice were randomly divided into two groups, and STZ (50 mg/kg i.p.) or vehicle was administered for 5 consecutive days. Mice were fed with a normal diet but, starting from 14 months, half of them were given water with a high sugar (HS) to explore the potential detrimental effects of HS intake to hyperglycemia. Our main outcomes are as follows: i) HS intake alone does not contribute to worsened diabetic condition/hyperglycemia; ii) GA emerges as a reliable biomarker for monitoring diabetic conditions, consistently increasing with hyperglycemia; iii) diabetic conditions correlate with a worsening of recognition memory; iv) diabetic mice display mild-to-severe insulitis and injured hippocampal cytoarchitecture, detectable in Ammon's horns regions CA1 and CA3; v) correlation among recovered normal fasting glycemic level and recognition

memory, partial regaining of physiological pancreatic morphology, and hippocampal cytoarchitecture.

KEYWORDS

diabetes, MGO, glycated albumin, recognition memory, hippocampus, pancreas, streptozotocin-induced

## 1 Introduction

Diabetes mellitus (DM) is a metabolic condition leading to chronic high blood sugar levels due to insufficient insulin production or ineffective effects of insulin on target cells. Two primary forms of diabetes have been characterized. Type 1 diabetes (T1DM) is typically diagnosed during childhood and is a multifactorial disease with a strong genetic component in which the pancreatic cells stop producing insulin. Type 2 diabetes (T2DM) is generally diagnosed in adulthood and is instead related to lifestyle factors. Both types result in long-term high blood sugar levels. T2DM is less severe, but it accounts for 90% of diabetes cases. It does not always require insulin for treatment and, therefore, is called an "insulin-independent" form of diabetes. The condition is primarily caused by long-term consumption of a high-calorie, high-sugar diet, which results in frequent and significant insulin spikes that eventually desensitize target cells, causing prolonged hyperglycemia (Guthrie and Guthrie, 2004; Nowotny et al., 2015).

One significant consequence of prolonged hyperglycemia is the increased formation of advanced glycation end products (AGEs), which activate AGE receptors (RAGE), leading to oxidative stress and increase in inflammation (Bierhaus et al., 2001; Soares et al., 2013; Meireles et al., 2015; Bettiga et al., 2019; Mori et al., 2024; Oliveira et al., 2024). This AGE–RAGE pathway is implicated in the development of diabetes-related complications such as cardiovascular disease, kidney damage, and neurodegenerative disorders (Giacco and Brownlee, 2010; Srikanth et al., 2011). DM is diagnosed and classified using blood biomarkers such as glucose and glycated hemoglobin (HbA1c), measured through various tests (Ramachandra Bhat et al., 2019). Monitoring these biomarkers is critical for preventing or managing the adverse physiological effects of diabetes (Yazdanpanah et al., 2017), and other emerging biomarkers like glycated albumin (GA) and methylglyoxal (MGO) are gaining attention (Kouzuma et al., 2002; Freitas et al., 2017; Piuri et al., 2020; Belinskaia et al., 2021).

GA is linked to organ damage, including kidney disease and atherosclerosis, and promotes insulin resistance through reactive oxygen species (ROS) generation (Wu et al., 2016; Paradela-Dobarro et al., 2019). It offers a viable alternative to HbA1c for assessing glycemic balance over shorter time periods, particularly when HbA1c cannot be measured (Freitas et al., 2017; Krhač and Lovrenčić, 2019). MGO, a reactive byproduct of glucose metabolism, serves as a precursor to AGEs and plays a pivotal role in the development of diabetic complications. Its accumulation contributes to vascular dysfunction, insulin signaling disruption, and chronic inflammation (Kong et al., 2020; Bhattacharya et al., 2023). High levels of MGO have been detected in diabetic patients (in plasma, pancreas, muscle, and adipose tissue) and correlated to a reduction in glucose and glutathione transporters. These disruptions impair vascular health and exacerbate diabetes-related complications such as chronic kidney disease and cognitive deficits (Ogawa et al., 2010; Li et al., 2012; Cai et al., 2014; A; Shamsaldeen et al., 2016; Gill et al., 2019; Ramachandra Bhat et al., 2019; Sutkowska et al., 2023). The role of AGEs in diabetes-induced cognitive decline is still unknown (Momeni et al., 2021).

Under physiological circumstances, MGO is detoxified by the glyoxalase system, which consists of glyoxalase I and II (Glo1 and Glo2), preventing excessive formation of AGE. The biochemical pathways through which MGO is linked to the development of diabetes, vascular complications of diabetes, and other age-related diseases have been described (Schalkwijk and Stehouwer, 2020).

Several epidemiological studies show that diabetes is the major risk factor for neurodegeneration: approximately 29% of people with T2DM experience cognitive decline and neurodegeneration. This association underscores the systemic nature of diabetes, which not only affects peripheral organs, but it also has profound effects on the central nervous system. Insufficient insulin uptake appears to be the main trigger for neurodegenerative mechanisms, particularly in the hippocampus, where insulin resistance induces cognitive decline associated with neurodegeneration (Shieh et al., 2020). It has been found that diabetes can speed up the progression from mild cognitive impairment (MCI) to severe dementia (Patel et al., 2016; Farajpour et al., 2017; Dove et al., 2021; Ding et al., 2024). Recognition memory, a declarative long-term episodic form of memory, is one of the most important features of human personality that is lost owing to MCI. A decline in recognition memory is observed in rodents with diabetes using various cognitive tasks, such as novel object recognition (NOR) or placement tests (Patel et al., 2016; Farajpour et al., 2017; Kassab et al., 2019; Presta et al., 2024). Cognitive decline is defined as a deterioration in cognitive functions, including difficulty with language and memory loss. Over time, cognitive decline can lead to disorders such as MCI or senile dementia. Specifically, one of the most studied diseases concerning glucose intake is Alzheimer's disease (AD), which some authors define also as type 3 diabetes, for its suggested metabolic component (Yazdanpanah et al., 2017; Nguyen et al., 2020; Michailidis et al., 2022). The hippocampus plays a central role in memory and learning, making it a critical area affected in both dementia and Alzheimer'sdisease(Raoetal.,2022). Hyperglycemiainducesoxidative stress, inflammation, and neuronal damage, particularly impacting the hippocampus, a key region for memory and learning. Insulin resistance in the brain further disrupts hippocampal-dependent memory processes, contributing to cognitive decline as observed in MCI, dementia, and Alzheimer's disease. Recognition memory deficits, commonly assessed through the novel object recognition (NOR) task, serve as a marker of early cognitive changes (Hu et al., 2019; Li et al., 2020; Barone et al., 2021; Aderinto et al., 2023).

High sucrose consumption has been shown to induce glucose intolerance, hyperinsulinemia, and hyperglycemia in different animal models (Oliveira et al., 2014; Flister et al., 2018; Melo et al.,

2019; Seshadri et al., 2019). Alterations in metabolic profiles (hypertriglyceridemia and hyperinsulinemia) as well as increased liver lipogenic gene expression, oxidative stress, and inflammatory markers were evinced in rats fed for less than 21 days with 10% sucrose in their drinking water (Castro et al., 2024). The metabolic disturbances caused by high sugar intake, such as hypertriglyceridemia and oxidative stress, are paralleled by neuroinflammation and cognitive decline, suggesting that diet plays a pivotal role in the interplay between diabetes and neurodegenerative diseases (Coirini et al., 2022). Diets rich in refined sugar not only contribute to obesity but also impair cognitive functions like memory and cognitive flexibility (Kalaria et al., 2008; Kanoski and Davidson, 2011; Cheke et al., 2016). In particular, the effect involved hippocampal recognition memory performance in rodents, particularly during the early stages of cognitive decline (Beilharz et al., 2016). Furthermore, consumption of 35% sucrose-sweetened water for 9 weeks can lead to pre-diabetes and glucose intolerance in mice (Burgeiro et al., 2017). In a transgenic mouse model of AD, sucrose intake has been shown to exacerbate insulin resistance and amyloidosis, both of which contribute to memory deficits (Cao et al., 2007; Orr et al., 2014).

The antibiotic streptozotocin (STZ) selectively destroys pancreatic β-cells, which induces diabetes, thus providing valuable insights into the pathophysiology of diabetes. In particular, a high-dose STZ protocol induces the complete destruction of pancreatic β-cells, reproducing T1DM. On the contrary, a low dose of STZ induces a gradual death of pancreatic β-cells, mimicking the pathogenesis of T2DM (Hahn et al., 2020; Furman, 2021; Bauer et al., 2023a). These models have allowed scientists to explore the molecular mechanisms underlying diabetes-related complications, especially the role of hyperglycemia in disease progression. The STZ-induced diabetes model was chosen to monitor the progression of DM over time, with the goal of identifying new biomarkers involved in the onset and diagnosis of the disease. A preclinical animal model of diabetes was developed, opening the question of a long-term induction of type II diabetes with multiple low doses of STZ.

This study focuses on several key points: the potential use of new biomarkers for T2DM, such as GA and MGO, and the relationship between those peripheric metabolic biomarkers and cognitive functions. Specifically, we explore how these biomarkers are linked to cognitive performance, including declarative memory, focusing on recognition memory, a long-term form of memory. Furthermore, the experimental model has allowed us to assess the recovery in time of both peripheric metabolic biomarkers and cognitive performance, thus obtaining a confirmation of their direct relationship.

# 2 Material and Methods

## 2.1 Animals

Thirty-five 9-month-old wild-type male mice (strain C57BL-6J) were maintained on a 12-h light/dark cycle in single cages in the Animal Care Facility at the University of Pavia. Water and food were provided *ad libitum*. All experiments were carried out according to the guidelines laid out by the institution's animal welfare committee, the Ethics Committee of Pavia University (Ministry of Health, License number 220/2022-PR), also in compliance with the European Council Directive 2010/63/EU on the care and use of laboratory animals.

TABLE 1 Nutritional composition of control diet pellets (ND). The energy value was 387.6 Kcal/100 g.

| Composition | g/100 g |
|---|---|
| Carbohydrate | 42.63 |
| Sugar | 3.68 |
| Protein | 18.50 |
| Fat | 3.00 |
| Fiber | 6.00 |

Mice were fed the animal facility's diet (normal diet or ND), which was a standard 4RF21 pellet supplied by Mucedola Srl. The pellet was prepared following the standard pelleting procedure, which involved using dry saturated steam, a drying phase, and subsequent cooling.

Table 1 shows the nutritional composition of the ND pellet.

## 2.2 *In vivo* longitudinal study

The investigational design scheduled five experimental timepoints (Figure 1), starting from 9 months (T0) and lasting until the mice reached 19 months of age. T0: at 9 months, all animals were fed the ND; fasting glycemia, glycated albumin (GA), and methylglyoxal (MGO) were measured, and spontaneous behavioral tests were performed. T1: 13-month-old mice were randomly divided into two groups: i) 17 control animals (CTRL) were intraperitoneally (i.p.) injected with physiological saline (0.9% sodium chloride) for 5 consecutive days, while ii) the other 18 mice (namely, DM) were i.p. injected with an STZ solution to induce diabetes (namely, STZ induction, see detailed protocols described in the following paragraph). One month after the injections (T2), fasting glycemia, GA, and MGO were assessed in all mice to verify the efficacy of STZ induction. Starting at T2, half of the mice belonging to each group, both CTRL and DM, were supplemented with 10% sucrose water *ad libitum* as their only source for drinking (high-sugar group or HS). Therefore, mice were divided into four groups: CTRL fed with ND (CTRL-ND), CTRL watered with HS(CTRL-HS), DMfedwith ND(DM-ND), and DMwateredwith HS (DM-HS). After 16 months (T3) and 19 months (T4), fasting glycemia, GA, and MGO were monitored, and spontaneous behavioral tests were performed. All animals were sacrificed at the last experimental timepoint (T4), and organs were collected as described (see section *Material and Methods* Section 2.6).

## 2.3 Diabetes induction

Diabetes was chemically induced by intraperitoneal injection of STZ for 5 consecutive days, according to Animals Models of Diabetic Complication Consortium (AMDCC) (Wu and Huan,

10.3389/fphys.2025.1455434

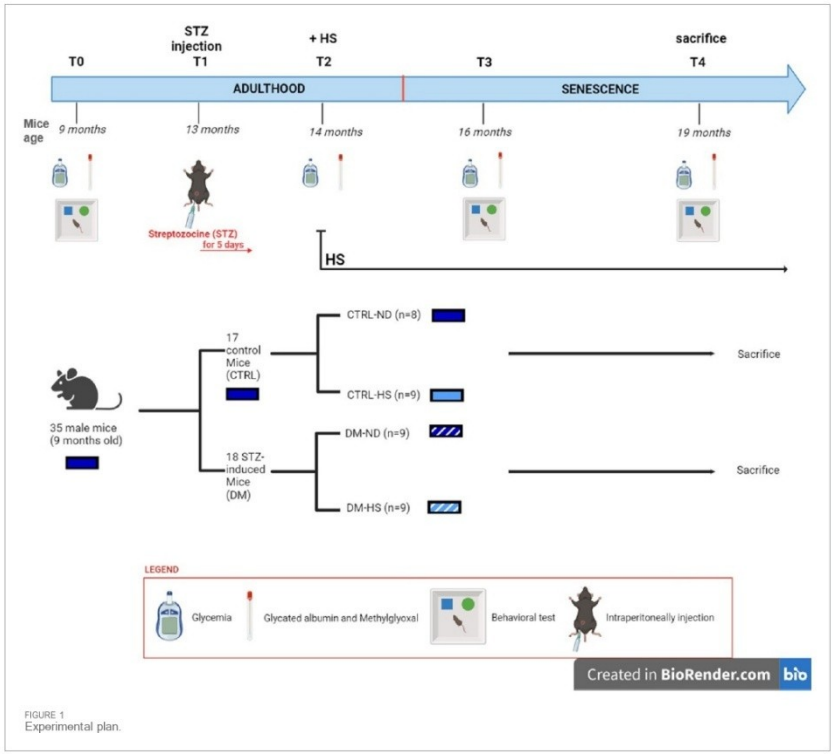


FIGURE 1
Experimental plan.

2008; Furman, 2021). Most papers reported diabetes induction performed at murine ages ranging from 8 to 12 weeks (3 months), equivalent to approximately 20 human years, which corresponds to the early/juvenile adulthood phase in humans (Holstad and Sandler, 1999; Nørgaard et al., 2020; Furman, 2021). Differently, in our current investigation, diabetes has been induced at 13 months of age (T1), approximately equivalent to 43 human years, corresponding to the late adulthood phase. We specifically selected this age, which corresponds to the late adulthood phase, to mimic the pathology of human type 2 diabetes and its distinctive onset, which typically develops in adulthood at the age of 45 years (Reed et al., 2021; Carrillo-Larco et al., 2024). It should also be taken into careful consideration that the choice of diabetes induction at 13 months of age allowed us to minimize the impact of synaptic plasticity phenomena associated with recognition memory during the juvenile phase.

In brief, to induce diabetes, a 50-mg/kg STZ dose, dissolved in 100 mM citrate buffer solution, was administered daily by i.p. injection to mice belonging to the DM group (namely, STZ mice), while control animals received physiological saline (0.9% NaCl). At T2, 1 month after the last treatment, blood glucose was measured by tail vein sampling, both in CTRL and STZ animals which have been fasted for 4 h. The STZ mouse was considered diabetic if the fasting blood glucose exceeds 300 mg/dL for three consecutive measurements. In the mouse model, fasting blood glucose level exceeding 300 mg/dL up to 600 mg/dL (16.7 mmol/L to 33.3 mmol/L) is considered a criterion for classification of diabetes (Graham et al., 2011; Furman, 2021).

## 2.4 Measurement of fasting glycemia, GA, and MGO

Mice were fasted for 12–16 h before fasting glycemia, GA, and MGO measurements. Blood was collected from the tail vein. Specifically, a drop of blood was taken to assess blood glucose,

run on a reactive strip, and then read using a OneTouch Verio Reflect® glucometer (Lifescan Italy Srl).

To assess fasting blood sample collection to measure serum GA and MGO, 200 µL of blood was collected using synthetic swabs and analyzed by the GEK Lab laboratory using a specific ELISA kit. In particular, the human GA concentrations in plasma samples were determined using a Mouse Glycated Albumin (GA) ELISA Kit (LLD 11.3 pmol/mL, Abbexa Ltd., Cambridge Science Park, Cambridge, U.K.), and the MGO was determined using the OxiSelect™ Methylglyoxal Competitive ELISA Kit (lower range of detection 0 µg/mL, Cell Biolabs, San Diego, CA, USA), which is an enzyme immunoassay developed for the detection/quantitation of protein adducts of methylglyoxal-derived hydroimidazolone (MG-H1) (Nowotny et al., 2015).

## 2.5 Behavioral test and cognitive frailty index

A spontaneous behavioral test was performed to assess murine recognition memory. In particular, mouse activity was quantified by a SMART video tracking system with a selected sampling time of 40 ms/point (2Biological Instruments, Besozzo, Varese, Italy) and a Sony CCD color video camera (PAL). At selected timepoints, i.e., T0, T3, and T4, all mice performed the novel object Recognition (NOR) task, which is a highly validated test for assessing recognition memory, to evaluate their ability to recognize a novel object in the environment, hence assessing the efficacy of their memory for the objects.

### 2.5.1 Novel object recognition (NOR) test

The novel object recognition task was carried out as previously described (Brandalise et al., 2017; Ratto et al., 2019; Roda et al., 2022); in particular, the procedure consisted of three primary phases: open arena, familiarization, and test. During the test phase, the number of approaches and the time of approaches to the familiar and the novel objects were measured as cognitive parameters. To evaluate the discrimination between novel and familiar objects, the mean novelty discrimination index (DI) was calculated by using the following formula (Silvers et al., 2007):

$$DI = (n - f)/(n + f)$$

where (n) is the average time or number of approaches to the novel object and (f) is the average time or number of approaches to the familiar object (Table 1). The DI ranged from −1 to 1, where −1 means a complete preference for the familiar object, 0 means no preference, and 1 means a complete preference for the novel object.

For each parameter, the corresponding locomotor frailty index (FI) was calculated by using the following formula (Parks et al., 2012):

$$FI = (Value - Mean\ Value\ at\ T0)/(SD\ at\ T0) * 0.25.$$

## 2.6 Morphological evaluation of the pancreas and hippocampus

At T4, all mice were deeply anesthetized before decapitation using isoflurane inhalation (Aldrich, Milwaukee, WI, USA). The head/body of the pancreas and the brain were immediately excised, washed in 0.9% NaCl, fixed by immersion for 7 and 48 h at room temperature in 4% paraformaldehyde in 0.1 M phosphate buffer (pH 7.4), and post-fixed in the same fixative medium at 4°C for 1.5 h. Then, tissues were kept in absolute ethanol for 1 h, followed by acetone, and finally embedded in Paraplast X-TRA (Sigma-Aldrich, Milan, Italy). Using a manual rotatory microtome, 6-µm-thick pancreatic and 8-µm-thick brain coronal sections were cut serially and collected on silane-coated slides.

### 2.6.1 Light microscopy: H&E

To reveal the pathophysiology and estimate potential structural pancreatic and hippocampus alterations, hematoxylin and eosin (H&E) staining was performed as previously described (Kádár et al., 2009; Lattouf et al., 2014; Roda et al., 2017; Luca et al., 2023).

In particular, since both the pancreas and CNS possess more complex specialized structures compared to other tissues, the H&E allows for an overview of tissue structures, anatomical order, and area-specific settings (Jordan et al., 2011; Zhang and Xiong, 2014; Roda et al., 2019; Longnecker, 2021; Li et al., 2022). Therefore, using the brightfield examination of H&E-stained samples at low magnification, pancreatic and hippocampal site identification was achieved, allowing the identification of precise brain sections and also distinguishing typical pancreatic microanatomy. In particular, concerning the pancreas, the coronal aspect was determined by examining the morphology of pancreatic ducts and islets of Langerhans. Specifically, in case of a spherical-shaped duct lined with the cuboidal epithelium, the coronal plane orientation was assumed.

Sections were observed using a Leica DM6B WF microscope (Leica Microsystems, Buccinasco, MI, Italy). The images were acquired using a Leica DFC 7000 t CCD camera (Leica Microsystems, Buccinasco, MI, Italy) and stored on a PC running the Leica Application Suite X (LAS X) software (version 5.1.0). The imaging system (LAS X Navigator) and the merge function were used to reconstruct the whole hippocampus.

#### 2.6.1.1 Insulitis scoring

H&E-stained pancreatic tissue sections were then observed for the assessment of lymphocytic infiltrates in the pancreatic islets of Langerhans. A minimum of 30 islets/group were scored for insulitis. Scoring was performed under double-blinded conditions. The degree of insulitis was graded according to the following criteria: normal islet, score 0; perivascular/periductal infiltration, score 1; peri-insulitis, score 2; mild insulitis (<25% of the islets infiltrated), score 3; and severe insulitis (more than 25% of the islets infiltrated), score 4 (Pejnovic et al., 2013; Pavlovic et al., 2018).

#### 2.6.1.2 Hippocampal injury evaluation

For histopathological evaluation, five slides (approximately 20 sections) per mouse were examined. The most representative figures of the hippocampus were selected and are shown. In particular, the dentate gyrus (DG) and Ammon's horn region were scrutinized. Concerning the quantitative evaluation, the following were measured: i) whole thickness of the DG layer; ii) pyramidal cell layer thickness of CA subdivisions; iii) cell density (number of cells/area in mm2).

10.3389/fphys.2025.1455434

### 2.7 Statistics

The values obtained were expressed in terms of the mean ± standard error of the mean (SEM, standard error of the mean). The statistical analysis of Kaplan–Meier graphs was obtained with a log-rank (Mantel–Cox) test. To evaluate the statistical differences between different experimental groups in fasting glycemia, GA, MGO, weight, global DI, global FI, and quantitative analysis of hippocampus tissue, the one-way ANOVA test was used, followed by the Bonferroni *post hoc* test. The repeated measures ANOVA test followed by the Bonferroni *post hoc* test was carried out for the comparison of glycemia, GA, and MGO in CTRL and DM experimental groups. Microsoft Excel and Prism 9 (GraphPad Software, San Diego, CA, USA) were used for statistical analysis. Statistical significance was determined by the following *p*-values: $P < 0.05$; $P < 0.01$; $P < 0.001$.

## 3 Results

### 3.1 Non-diabetic mice: the influence of time, aging, and high sugar water intake on metabolic parameters

Using a longitudinal approach, glycemia, glycated albumin, and methylglyoxal levels were monitored from adulthood (T0, 9 months) to senescence (T4, 19 months), as illustrated in the experimental design (Figure 1). At T1, mice were repeatedly injected with either NaCl 0.9% (CTRL, n = 17) or STZ (50 mg/kg), STZ to induce diabetic conditions (DM, n = 18) (for details, see Materials and Methods, 2.3). Starting from T2, animals were randomized into two experimental groups: half of the mice were given with high-sugar water (CTRL-HS mice, n = 9; DM-HS mice, n = 9), while the remaining mice were continued with the normal diet of the animal facility (CTRL-ND mice, n = 8; DM-ND, n = 9). The two regimens were maintained for 5 months and monitored at chosen timepoints i.e., T3 and T4, 2 and 5 months after i.p. injections, respectively.

In CTRL mice, 1 month after i.p. injections of the physiological solution (T2), the mean glycemic value (104.45 ± 2.94 mg/dL, n = 8) was statistically comparable to that measured at T0 (98.44 ± 2.83 mg/dL, n = 35; Figure 2A). In addition, regarding GA, any difference recorded at T2 (35.05 ± 1.65 pmol/mL, n = 8) was comparable to that in T0 (29.13 ± 1.81 pmol/mL, n = 35; Figure 2B). Finally, the MGO mean value at T2 (2.04 ± 0.22 μg/mL, n = 8) was comparable to that calculated at T0 (2.72 ± 0.21 μg/mL, n = 35; Figure 2C).

At T3, the mean glycemic value of the CTRL-HS group (98.78 ± 5.76 mg/dL, n = 9) was comparable to that assessed in the CTRL-ND group (94.50 ± 5.15 mg/dL, n = 8). These data were further confirmed at T4, when the mean glycemic value of the CTRL-HS group (86.78 ± 5.06 mg/dL, n = 9) was comparable to that measured in the CTRL-ND group (97.29 ± 8.58 mg/dL, n = 8; Figure 2A). Hence, it follows that 5-month lasting (T4) HS supplementation did not elicit differences in fasting glycemic values, which were comparable to those determined in mice fed with a normal

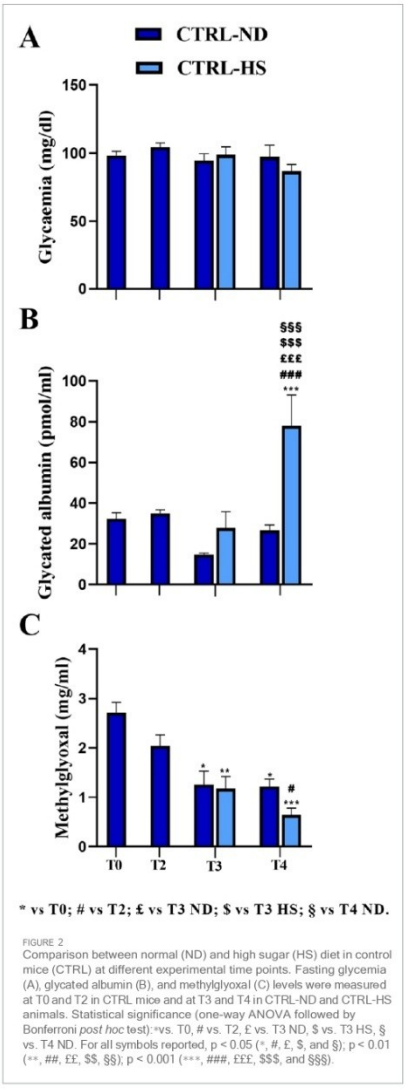


FIGURE 2
Comparison between normal (ND) and high sugar (HS) diet in control mice (CTRL) at different experimental time points. Fasting glycemia (A), glycated albumin (B), and methylglyoxal (C) levels were measured at T0 and T2 in CTRL mice and at T3 and T4 in CTRL-ND and CTRL-HS animals. Statistical significance (one-way ANOVA followed by Bonferroni *post hoc* test):*vs. T0, # vs. T2, £ vs. T3 ND, $ vs. T3 HS, § vs. T4 ND. For all symbols reported, $p < 0.05$ (*, #, £, $, and §); $p < 0.01$ (**, ##, ££, $$, §§); $p < 0.001$ (***, ###, £££, $$$, and §§§).

diet. Furthermore, from adulthood to senescence, any statistically significant difference in fasting glycemia was documented both in CTRL-ND and CTRL-HS groups.

Concerning the GA values, in CTRL-ND mice, any statistically significant difference was measured throughout the whole experimental duration, namely, from T0 to T4. At T3, the mean GA value in CTRL-HS animals (27.76 ± 8.0 pmol/mL, n = 9) was comparable to that calculated in CTRL-ND mice (14.77 ± 0.81 pmol/mL, n = 8). Notably, at T4, the mean GA value in CTRL-HS animals (78.08 ± 15.08 pmol/mL, n = 9) was statistically higher than that assessed in CTRL-ND mice at the same experimental timepoint (26.66 ± 2.62 pmol/mL, n = 8, $p$-value < 0.001; Figure 2B). Thus, the HS diet seemed to trigger a detrimental effect on GA values at T4 in the late senescence phase; notably, this mean value was statistically different from those measured at all the experimental timepoints in CTRL-ND mice (see Supplementary Table 1A).

Glycemic and GA mean values did not change during the lifespan, from adulthood to the senescence, as evidenced by comparing data gauged at all timepoints in CTRL mice fed with normal diet; differently, MGO significantly decreased during aging, as clearly detectable comparing mean values measured at T0 with those assessed at later timepoints (T0: 2.72 ± 0.21 μg/mL, n = 35; T2: 2.04 ± 0.22 μg/mL, n = 8; T3: 1.26 ± 0.27 μg/mL, n = 8, $p$-value = 0.017; T4: 1.22 ± 0.15 μg/mL, n = 8, $p$-value = 0.023; Figure 2C; Supplementary Table 1B). The same result was revealed in CTRL-HS mice (T3: 1.18 ± 0.24 μg/mL, n = 9, $p$-value = 0.005; T4: 0.64 ± 0.14 μg/mL, n = 9, $p$-value < 0.001, Figure 2C; Supplementary Table 1B). Interestingly, the mean MGO value measured in CTRL-ND mice was comparable to that determined in CTRL-HS animals.

Taken together, all the above reported data indicate that a 10% high sugar water intake alone did not exert detrimental effects on the three metabolic evaluated parameters until T3. Nonetheless, when prolonging intake of HS water for additional 3 months, the albumin glycation process increased significantly without any change in glycemic values, suggesting that the former is more sensitive to long-lasting HS intake. The decrease in MGO values during aging also persisted in animals belonging to the HS regimen group.

## 3.2 STZ-induced diabetes: the influence of time, aging, and high sugar water intake on metabolic parameters

STZ induction was performed at T1 giving five consecutive i.p. injections during 5 subsequent days (DM-ND, n = 18). One month after STZ induction (T2), all STZ-induced mice displayed a dramatic statistically significant increase in the glycemic fasting values (on the mean, DM 421.5 ± 21.63 mg/dL, n = 18; Figure 3A) compared to T0 (98.44 ± 2.83 mg/dL, $p$-value < 0.001). It should be noted that all mice had a glycemic value higher than 300 mg/dL for three consecutive fasting measures in succeeding days, in accordance to literature data reporting a similar threshold value for the STZ-induced diabetic animal model (Graham et al., 2011; Liu et al., 2020; Furman, 2021). Hence, it was possible to classify these animals as diabetic mice (DM) in accordance with the Animal Models of Diabetic Complications Consortium (AMDCC). Notably, 1 month from STZ induction, the fasting glycemic mean value was definitely higher (412.7%) than that measured before the induction protocol.

Remarkably, at T2, the GA mean value was further dramatically increased (113.37 ± 26.39 pmol/mL, n = 18) compared to that assessed at T0 (29.13 ± 1.81 pmol/mL, n = 35, $p$-value = 0.0062; Figure 3B), even reaching a 389.6% increase in DM mice.

Diversely, the MGO mean value measured at T2 in the DM group (3.12 ± 0.66 μg/mL, n = 35) was comparable to that calculated at T0 (2.72 ± 0.21 μg/mL, n = 18).

Therefore, 1 month after STZ induction, both glycemia and GA increased compared to T0, while the mean MGO value remained relatively constant.

Notably, at T3, 2 months after the HS diet both DM-HS (342.78 ± 61.41 mg/dL, n = 9) and DM-ND mice (332.22 ± 46.40 mg/dL, n = 9; Figure 3A) showed a decrease in glycemic mean values, even though the value still remained statistically greater than that measured at T0 ($p$-value < 0.001; see Supplementary Table 2A). The glycemic mean value was further diminished at T4, after 5 months of HS diet, in both DM-HS (152.60 ± 33.25 mg/dL) and DM-ND (217.33 ± 54.54 mg/dL) mice, when compared with those assessed at T2 (Figure 3A; Supplementary Table 2A); any statistical significance was measured when comparing measures obtained at T4 with the mean value calculated at T0. The mean glycemic values assessed at T3 and T4 were not statistically different when comparing DM-ND and DN-HS mice. In conclusion, the effect of STZ induction on the glycemic value of DM mice was partially reversed 3 months after repeated injections, and the high sugar water intake had no detrimental effect on glycemic values at all checked experimental timepoints.

After an initial increase at T2, the GA mean value did not further change in a statistically significant manner at subsequent timepoints, namely, T3 and T4, in DM-ND (93.62 ± 36.61 pmol/mL, n = 9) and DM-HS mice (93.04 ± 58.61 pmol/mL, n = 9) and in DM-ND (71.22 ± 21.45 pmol/mL, n = 9) and DM-HS animals (97.16 ± 29.27 pmol/mL, n = 9), respectively (Figure 3B). In particular, the GA mean value still remained 3–4 times higher than that measured before STZ induction. Therefore, GA serves as a good biomarker for DM mice, mirroring the fasting glycemic value until T3. At T4, contrary to fasting glycemic values, GA did not decrease.

As in control mice, a tendency to decrease with time was revealed in DM animals, whose MGO mean values diminished from adulthood to senescence, without reaching statistical significance. At T3, a significant increase in MGO was measured in DM-HS mice (3.57 ± 0.48 μg/mL, n = 9) compared to DM-ND (2.03 ± 0.21 μg/mL, n = 9, $p$-value = 0.01). At T4, following an additional 3 months of high sugar water intake, the MGO mean value significantly decreased in DM-HS mice (0.64 ± 0.18 μg/mL) compared to that measured in the same animals at the previous timepoints (T3) (1.32 ± 0.10 μg/mL, $p$-value = 0.0009; Figure 3C; Supplementary Table 2B).

As previously described, HS had no statistically significant effect on glycemic values both in CTRL and DM mice. Therefore, we pulled together the data regardless of the diet regimen at T3 and T4 to detect the differences within the two experimental groups CTRL and DM (Figure 4), analyzing the data by repeated measures ANOVA followed by the Bonferroni *post hoc* test from T0 to T4. For

10.3389/fphys.2025.1455434

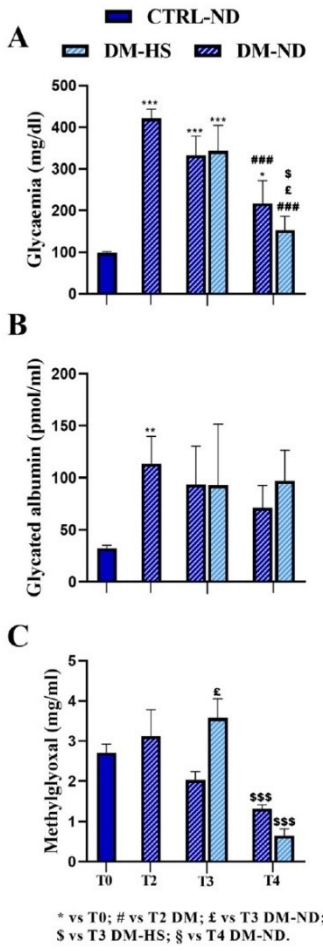


FIGURE 3
Comparison between normal (ND) and high sugar (HS) diet in control (CTRL) and diabetic mice (DM) at different experimental time points. Fasting glycemia (A), glycated albumin (B), and methylglyoxal (C) levels were measured at T2 in DM mice (n = 18) and at T3 and T4 in DM-ND and DM-HS animals. All data were compared to each other and compared to the value measured at T0 (n = 35). The value is reported as the mean ± standard error of the mean (SEM). Statistical significance: (one-way ANOVA followed by Bonferroni *post hoc* test): *vs. T0, # vs. T2 DM, £ vs. T3 DM-ND, $ vs. T3 DM-HS, § vs. T4 DM-ND. For all symbols reported, $p < 0.05$ (*, #, £, $, and §); $p < 0.01$ (**, ##, ££, $$, and §§); $p < 0.001$ (***, ###, £££, $$$, and §§§).

this reason, the dead animals at T4 were excluded from the analysis (CTRL: n = 16; DM: n = 14).

In the CTRL group, no significant variations were observed across T0 (97.5 ± 4.05 mg/dL, n = 16), T2 (103.31 ± 3.02 mg/dL, n = 16), T3 (97.75 ± 3.91 mg/dL, n = 16), and T4 (91.37 ± 4.73 mg/dL, n = 16), indicating stable fasting glycemia throughout the experimental period (Figure 4A). Conversely, the DM group exhibited a marked and statistically significant increase in glycemia at T2 (419.87 ± 32.38 mg/dL, n = 14) compared to T0 DM (103.64 ± 7.69 mg/dL, n = 14, *p-value* < 0.001; Figure 4B) and also compared to CTRL animals at the same timepoint (*p*-value < 0.001; Supplementary Table 3A; Supplementary Figure 2A). At T3, the mean glycemic value decreased in DM mice (296.57 ± 32.61 mg/dL, n = 14) compared to both T0 (*p-value* < 0.001) and T2 DM (*p*-value < 0.001), nonetheless differing from that assessed in CTRL mice at the same time point (*p*-value < 0.001; Supplementary Table 3A; Supplementary Figure 2A). Furthermore, at T4, the mean glycemic values in DM mice (194.21 ± 37.04 mg/dL, n = 14) further decreased compared to those at T2 (*p*-value < 0.001) and were also significantly different from those of CTRL mice at the same time point. In contrast, no statistically significant difference was assessed when compared to T0 (Supplementary Table 3A; Supplementary Figure 2A).

Regarding mean GA values, the CTRL group showed a significant increase at T4 (59.46 ± 12.89 pmol/mL) compared to T0 (29.37 ± 2.33 pmol/mL, *p-value* = 0.007). In contrast, no significant changes were detected at T2 (33.03 ± 2.36 pmol/mL), and a statistical decrease was observed at T3 (17.76 ± 1.35 pmol/mL) compared to both T0 and T2 (*p-value* < 0.001 and *p-value* = 0.03, respectively; Figure 4C). Remarkably, as described previously, the CTRL GA value was mainly affected by the HS regimen at T4. In the DM group, a significant increase in GA levels was observed at T2 (76.59 ± 20.87 pmol/mL) compared to T0 (33.29 ± 5.47 pmol/mL, *p-value* = 0.02) and CTRL mice at the same time point (*p*-value = 0.0064; Supplementary Table 3B; Supplementary Figure 2B). GA levels were subsequently decreased at T3 (75.82 ± 25.08 pmol/mL) and T4 (63.07 ± 12.76 pmol/mL) in DM mice, although statistical significance was not maintained across all time points (Figure 4D). However, a statistically significant difference was revealed between DM and CTRL mice at T3 (*p*-value = 0.043; Supplementary Table 3B; Supplementary Figure 2B).

Regarding the mean MGO value, the CTRL group showed a significant reduction at T3 (0.98 ± 0.21 μg/mL) and T4 (0.84 ± 0.17 μg/mL) compared to T0 (2.27 ± 0.30 μg/mL, *p-value* = 0.009 and *p-value* = 0.03, respectively), while no significant change was detected at T2 (1.73 ± 0.29 μg/mL; Figure 4E). Similarly, in the DM group, MGO levels significantly decreased at T4 (1.07 ± 0.12 μg/mL) compared to T0 (2.77 ± 0.40 μg/mL, *p-value* = 0.01; Figure 4F). Furthermore, no statistically significant increase was measured at T2 in DM mice (4.09 ± 1.18 μg/mL) compared to CTRL mice. However, at T3, a statistically significant increase was assessed in DM animals (2.58 ± 0.41 μg/mL) compared to CTRL mice (*p-value* = 0.0003; Supplementary Table 3C; Supplementary Figure 2C). At T4, the mean MGO value in DM mice was compared to that calculated in CTRL animals. It should be underlined that at T3, the mean MGO value was primarily affected by the HS regimen in DM mice, as previously reported.

10.3389/fphys.2025.1455434

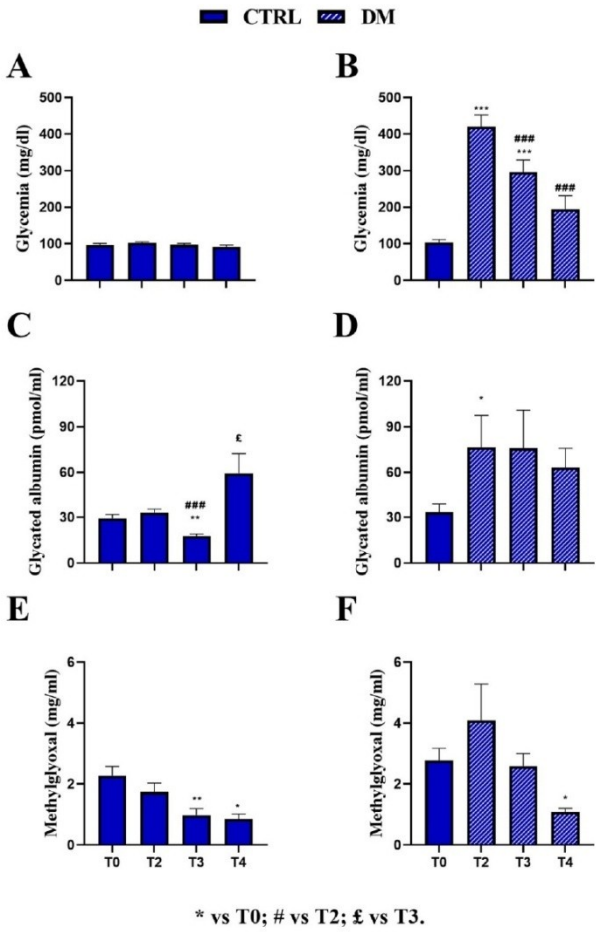


FIGURE 4
Comparison at all experimental times in control (CTRL) and diabetic (DM) mice. Fasting glycemia in CTRL (A) and DM (B), glycated albumin in CTRL (C) and DM (D), and methylglyoxal in CTRL (E) and DM (F) levels were assessed at T2, T3, and T4. The values are reported as the mean ± standard error of the mean (SEM). Statistical significance (repeated measures ANOVA followed by Bonferroni *post hoc* test):*vs. T0, # vs. T2, £ vs. T3. For all symbols reported, $p < 0.05$ (*, #, £); $p < 0.01$ (**, ##, and ££); $p < 0.001$ (***, ###, and £££).

10.3389/fphys.2025.1455434

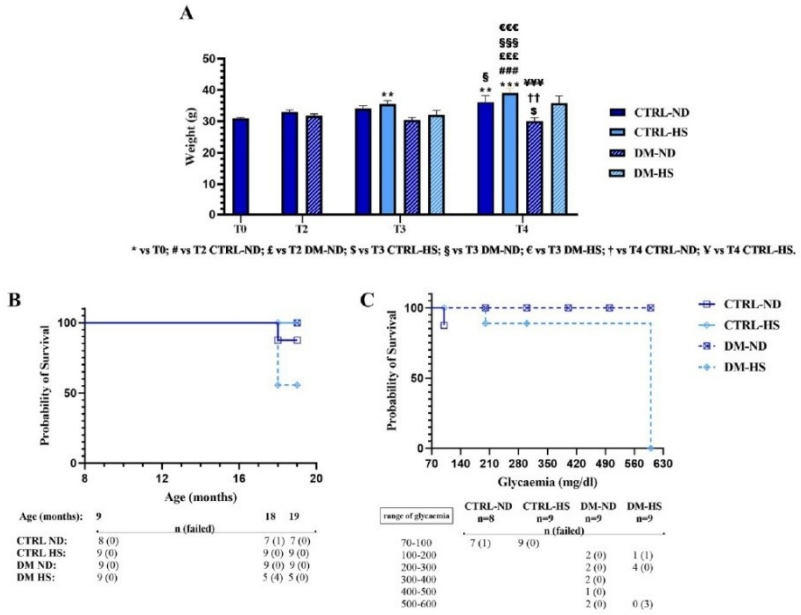


FIGURE 5
Weight monitoring and Kaplan-Meier survival analysis. Panel (A): weight measured at T0 in controls (CTRL), at T2 in CTRL and diabetic (DM) mice, and at T3 in CTRL and DM both in normal (ND) and high sugar (HS) diet conditions. Values are presented as mean ± SEM. Panel (B): Kaplan-Meier survival analysis showing survival curves of CTRL and DM mice, fed with either ND or HS diet. It should be noted that the DM-ND and CTRL-HS symbols are overlapped. In the lower part of panel B, the whole number of mice (n) and the number of dead mice (in brackets), at different ages, are reported. Panel (C): Kaplan-Meier analysis presenting survival curves of DM mice, fed with either ND or HS diet, relative to the glycemic value assessed at 18 months of age (T3). In the lower part of panel C, the number of alive mice (n) and the number of dead mice (in brackets) are listed. Statistical significance for data presented in Panel A (two-way ANOVA followed by Bonferroni *post hoc* test): *vs. T0, # vs. T2 CTRL-ND, £ vs. T2 DM-ND, $ vs. T3 CTRL-HS, § vs. T3 DM-ND, € vs. T3 DM-HS, †vs. T4 CTRL-ND, and ¥ vs. T4 CTRL-HS. For all symbols reported, $p < 0.05$ (*, #, £, $, §, €, †, and ¥); $p < 0.01$ (**, ##, ££, $$, §§, €€, ††, and ¥ ¥); $p < 0.001$ (***, ###, £££, $$$, §§§, €€€, †††, and ¥ ¥ ¥). Panel (B, C): statistics for Kaplan-Meier analysis was obtained with a log-rank (Mantel-Cox) test.

## 3.3 Diabetic condition influenced weight, drinking, and survival probability

The influence of diabetic conditions on body weight was investigated in all experimental groups at different timepoints (T0, T2, T3, and T4; Figure 5A).

At 9 months of age (T0), mice weighed 30.89 ± 0.33 g (n = 35). During aging, from adolescence to senescence, mice fed with the animal facility's ND displayed an increase in weight gain (T2: 33.6 ± 0.58 g, n = 17; T3: 34 ± 0.93 g, n = 8; and T4: 36.14 ± 2.10 g), and this increase was gaged statistically significant at T4 compared to T0 (*p-value* < 0.001). On the contrary, DM mice fed with the same ND lost weight during aging (T2: 31.72 ± 0.61 g, n = 18; T3: 30.44 ± 0.80 g, n = 9), and this decrease became statistically significant at T4 (30.00 ± 1.13 g, n = 9) when compared to CTRL-ND mice evaluated at the same experimental time point (*p-value* = 0.0086).

During aging, both at T3 and T4, the weight of CTRL mice fed with HS tended to increase more than that measured in CTRL-ND mice, but any statistical significance was determined (CTRL-HS: 35.44 ± 1.19 g and 39.11 ± 1.46 g at T3 and T4, respectively) (Figure 5A; Supplementary Table 4). During aging, any statistically significant weight change was assessed in DM mice fed with HS (T3: 32.11 ± 1.40 g, n = 9; T4: 35.80 ± 2.31 g n = 5), suggesting that HS water intake counterbalanced the weight loss seen in DM-ND mice.

The water intake of diabetic mice (about 9 mL/day) increased by two-fold compared to that of control mice (approximately 4 mL/day). The weight loss and the higher water intake

10.3389/fphys.2025.1455434

confirmed that this preclinical model had the same features of human diabetes (Liu et al., 2019).

The Kaplan–Meier survival analysis was performed in all experimental conditions during the mouse lifespan (Figure 7B) to monitor the survival probability (%). Comparing CTRL-ND, CTRL-HS, DM-ND, and DM-HS survival curves, a statistical significance was evidenced (*p-value* = 0.0241), indicating that both variables, i.e., HS water intake and diabetes induction, were crucial for survival probability.

It should be noted that the survival probability obtained by a direct comparison between CTRL-ND and DM-ND mice is similar, suggesting that diabetes alone was insufficient to influence the survival of animals up to the senescence phase (19 months of age). Furthermore, the survival probability obtained by a direct comparison between CTRL-ND and CTRL-HS mice indicated that HS alone did not alter the survival of control animals. Furthermore, a statistically significant difference between DM-ND and DM-HS mice was gaged (*p-value* = 0.0275), showing that HS affected the survival of diabetic animals. Additionally, a statistically significant difference was determined in survival rates while comparing CTRL-HS and DM-HS mice (*p-value* = 0.0275), indicating that diabetes modified the survival of animals treated with HS.

Therefore, we can conclude that the association between the diabetic condition and HS water intake affects animals' survival, with DM-HS mice displaying a lower survival likelihood compared to all other experimental groups. Specifically, at 18 months of age, the survival probability in the DM-HS group was 55.55%.

We investigated more in-depth the relationship between the Kaplan–Meier survival probability considering the fasting glycemic level at T3 and the mice's fate. Comparing DM-ND and DM-HS survival curves, a statistical significance was revealed, indicating that the fasting glycemic values influenced the survival of diabetic animals (*p-value* = 0.0295; Figure 5C).

In particular, only DM mice displayed a fasting glycemic value ranging between 500 and 600 mg/dL (n = 5). The survival probability measured for DM-HS mice (n = 0/3) was 0%, while settled on a percentage of 100% for DM-ND (n = 2/2), demonstrating the detrimental effect of HS in DM mice. Therefore, fasting glycemic values were not sufficient to illustrate the death of diabetic mice.

## 3.4 Reversal of STZ-induced diabetes

Furthermore, with the aim of deepening the comprehension and clarifying the relationship between glycemia, GA, and MGO, the values assessed in DM mice (as the sum of DM-ND and DM-HS) are shown in Figure 6. The analysis revealed the scattering of data in both GA and MGO values.

According to the individual glycemic value and considering a threshold value of 300 mg/dL at T3, DM mice were divided into two groups: the DM-REC group (DM mice recovering normal glycemia) consisted of animals with glycemic values lower than the threshold level (mean value: 215.90 ± 15.82 mg/dL, n = 10, T3 DM RECA), whereas the DM group consisted of diabetic mice with a glycemic value greater than the threshold level (489.50 ± 35.81 mg/dL, n = 8, T3 DM; Figure 6). Interestingly, at T3, the glycemic values in DM mice were significantly different compared to those measured in DM-REC mice (*p-value* < 0.001).

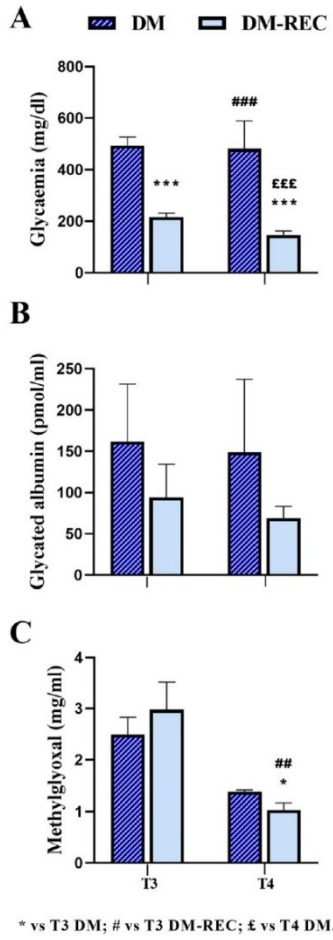


FIGURE 6
Comparison between diabetic mice (DM) and diabetic-recovery (DM-REC) animals at chosen experimental time points. Mice were divided into two subgroups: DM, with fasting glycemic values higher than 300 mg/dL, and DM-REC, with fasting glycemic values lower than 300 mg/dL: (A) fasting glycemic values, (B) fasting GA values, and (C) MGO values. Graphs showing the mean value line and the standard error of the mean (SEM) error bars. Statistical significance (unpaired T-test): *vs. T3 DM, # vs. T3 DM-REC, £ vs. T4 DM. For all symbols reported, $p < 0.05$ (*, #, and £); $p < 0.01$ (**, ##, and ££); $p < 0.001$ (***, ###, and £££).

Notably, at subsequent time points, namely, T4, only two mice maintained a glycemic value over the threshold (481 ± 108 mg/dL, n = 2, T4 DM). The remaining mice displayed a statistically significant decrease in glycemic values (146.42 ± 16.16 mg/dL, n = 12, T4 DM-REC, *p-value* = < 0.001; Figure 6A; Supplementary Table 5).

To verify if the glycemic value assessed at T3 was correlated to GA or MGO, the two above identified groups are plotted in Figures 6B, C. Any statistical difference was recorded for GA among the following: DM mice at T3 (161.79 ± 69.46 pmol/mL), DM-REC animals at T3 (93.96 ± 40.47 pmol/mL), DM mice at T4 (148.67 ± 88.54 pmol/mL), and DM-REC animals at T4 (69.12 ± 14.01 pmol/mL; Figure 6B). It should be noted that GA decreased at both T3 and T4 in DM-REC mice compared to DM mice; however, due to the scattered nature of the data, no statistical significance was observed.

On the contrary, MGO partially mirrored the glycemic effect, becoming significantly lower in DM-REC mice at T4 (1.03 ± 0.14 μg/mL) compared to those measured in DM animals at T3 (2.49 ± 0.34 μg/mL, *p-value* = 0.046) and DM-REC mice at T3 (2.98 ± 0.54 μg/mL, *p-value* = 0.002; Figure 6C).

## 3.5 Histological investigation of pancreatic islets revealed DM insulitis

Coronal pancreatic sections from CTRL, DM, and DM-REC mice were obtained at T4 and further processed for histological evaluation using H&E staining to estimate the potential DM-induced pancreatic alterations. A semiquantitative analysis has been conducted: a scoring system was utilized to evaluate the extent of tissue damage using conventional brightfield microscopy on a semiquantitative scale ranging from undetectable (0) to severe (4), according to Pavlovic et al. (2018).

In detail, the degree of lesions was recorded and graded as follows: score 0, normal islets; score 1, perivascular/periductal infiltration; score 2, peri-insulitis; score 3, mild insulitis (<25% of the islet infiltrated); score 4, severe insulitis (more than 25% of the islets infiltrated).

The examination showed a well-preserved physiological pancreatic cytoarchitecture in CTRL mice characterized by a high percentage (82.82%) of normal islets (score 0); differently, a low percentage (6.94%) of normal islets were assessed in DM mice. Notably, a partial recovery of regular islets (58.53%; Figures 7A, B) was recorded in DM-REC animals.

The occurrence of mild and severe insulitis was revealed in DM mice (22.22% and 30.56% for scores 3 and 4, respectively), while the infiltration decrease led to a percentage decrease in DM-REC animals (2.68% and 4.52% for scores 3 and 4, respectively). Finally, perivascular/periductal infiltration was documented in CTRL mice (13.37%) but enhanced in DM mice (26.96%) before decreasing again in DM-REC animals (20.41%).

Nevertheless, a comparable percentage of peri-insulitis (score 2) was determined in DM mice and DM-REC animals (13.89% and 13.87% for DM and DM-REC, respectively), whereas the percentage was definitely lower in CTRL mice (2.51%). Therefore, in DM mice, the harsh and time-persistent effects of STZ accounted for a high percentage of high-score insulitis in pancreatic sections, which was partially recovered in the histological profile assessed in DM-REC mice (Figures 7A, B).

## 3.6 Recognition memory and metabolic parameters: is there any relationship?

To study the possible relationship between changes in metabolic parameters, diabetes induction, and recognition memory's "knowledge component," specific behavioral tests were performed at different experimental time points (see *Materials and Methods*).

To match the chosen metabolic parameters with recognition performance parameters, the above reported longitudinal approach and experimental time points (i.e., T0, T3, and T4) were maintained.

Concerning behavioral tests in CTRL and DM mice, similarly to the trend obtained for metabolic parameters, any difference was assessed neither in ND nor in HS diet condition (data not shown). Hence, collecting data together regardless of the diet regimen, the two experimental groups, namely, CTRL and DM were compared. Furthermore, considering DM mice and the previously reported difference in fasting glycemic values measured at T3, mice were divided into DM (fasting glycemic value higher than 300 mg/dL) and DM-REC groups (fasting glycemic value lower than 300 mg/dL) (Figure 6A).

The discrimination index (DI) of the parameters obtained from the NOR task (see *Materials and Methods*) was analyzed, and subsequently, a global DI was generated (Figure 8A) together with the corresponding global frailty index (FI) (Figure 8B). Furthermore, Figure 8 presents examples of movement tracking for a single mouse at T3 in CTRL (Figure 8C), DM (Figure 8D), and DM-REC (Figure 8E) groups, and at T4 in CTRL (Figure 8F) and DM-REC (Figure 8G) groups.

During aging, from adulthood (T0) to senescence (T4), the expected physiological decline in recognition memory was recorded in CTRL mice (Ratto et al., 2019), in which the global FI changed from 0.00 ± 0.04 at T0 (n = 35), 0.21 ± 0.11 at T3 (n = 12), and 0.64 ± 0.13 at T4 (n = 12) (Figure 8B).

After 3 months (T3), STZ induction caused a decline in the recognition memory performance of DM mice, influencing both discrimination and the frailty index (Figures 8A, B). In particular, the global frailty index in DM mice at T3 (0.54 ± 0.09, n = 8) was significantly different compared to that measured in CTRL mice at the same time point (*p-value* = 0.04) (Figure 8B; Supplementary Table 6). Concerning DM-REC mice at T3, a recovered global FI (0.21 ± 0.15, n = 10) was determined, which is comparable to that measured in CTRL mice at the same time point.

At T4, most STZ-induced mice exhibited recovery in glycemic (DM-REC mice) values, which was paralleled by recognition memory performance similar to that recorded in CTRL mice at the same time points (Figure 8B). Moreover, the detrimental effect of STZ induction was partially reverted as deductible by examining both the discrimination and global frailty index of the NOR test (0.53 ± 0.09, n = 12) (Figures 8A, B; Supplementary Table 6). The remaining DM mice (n = 3) displayed extremely low locomotor activity, approaching novel and familiar objects for 1–2 times in 5 min for less than 3 s each time. Therefore, the decrease in locomotor activity in DM mice at T4 prevented calculation of the frailty index.

10.3389/fphys.2025.1455434

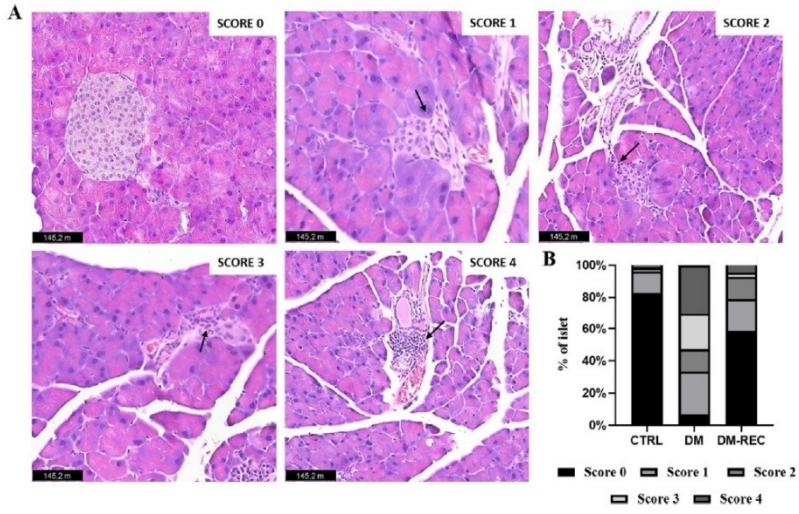


FIGURE 7
Recovering pathophysiology of pancreatic tissue in DM-REC mice after 6 months from STZ injections. Histological characterization via H&E staining. (A) Representative micrographs showing pancreas from different groups. Black arrows for each micrograph indicated the alterations observed for each score. Light microscopy magnification: ×40. Scale bars 145.2 m. (B) Insulitis was reduced in DM-REC mice compared to DM animals. Semiquantitative scale ranging from undetectable (0) to severe (4) tissue damage. In particular, degree of lesions was recorded and graded as follows: 0, normal islet; 1, perivascular/periductal infiltration; 2, peri-insulitis; 3, mild insulitis (<25% of the islet infiltrated); 4, severe insulitis (more than 25% of the islets infiltrated).

### 3.7 Histological investigation of the coronal hippocampus section

Coronal brain sections from CTRL, DM, and DM-REC mice were obtained at T4 and further processed for histological evaluation using H&E staining to estimate the potential alterations in the hippocampus, being crucially involved in recognition and spatial memory, caused by STZ induction. The examinations focused on the dentate gyrus (DG) and the Ammon's horn region, including CA1–CA3 subdivisions. Representative H&E micrographs are illustrated in Figure 9A.

The physiological gross morphology of the whole hippocampus was preserved in both experimental groups. The Ammon's horn region was typically divided into four areas, namely, CA1, CA2, CA3, and CA4, the last of which was included in the V-shaped DG region. High-magnification images of DG from CTRL, DM, and DM-REC mice showed typical three well-defined layers, namely, molecular layer (ML), granule cell layer (GL), and pleomorphic layer (PL). Regarding the CA region, the characteristic three-layer organization was detected, consisting of the outer polymorphic layer (stratum oriens, SO), the middle pyramidal cell layer (stratum pyramidale, SP), and the inner molecular layer (stratum radiatum, SR).

Notably, the quantitative investigation evidenced area-specific alterations, evaluated in terms of both layer thickness and cell density, mainly localized in the CA1 and CA3 regions (Figure 9), while DG and CA2 remained unaffected (data not shown).

In detail, a significant decrease in the thickness of both CA1 ($p$-$value$ < 0.001) and CA3 ($p$-value = 0.0113) of DM mice was revealed compared to CTRL animals. Simultaneously, a significant increase was measured in the thickness of both CA1 ($p$-$value$ < 0.001) and CA3 ($p$-$value$ = 0.0053) in DM-REC mice compared to DM mice (Figures 9B, C).

The calculation of cell density in the CA1 and CA3 regions evidenced a significant cell loss in DM mice compared to CTRL mice in both areas ($p$-$value$ < 0.001 and 0.0011 for CA1 and CA3, respectively). Differently, the cell density increased in DM-REC animals compared to DM mice, both in CA1 ($p$-$value$ = 0.0003) and in CA3 ($p$-$value$ = 0.007) regions (Figure 9D).

## 4 Discussion

The present experimental work addresses the following five main key-points on STZ-induced diabetic mice model:

1. Monitoring fasting glycemia levels over time.

10.3389/fphys.2025.1455434

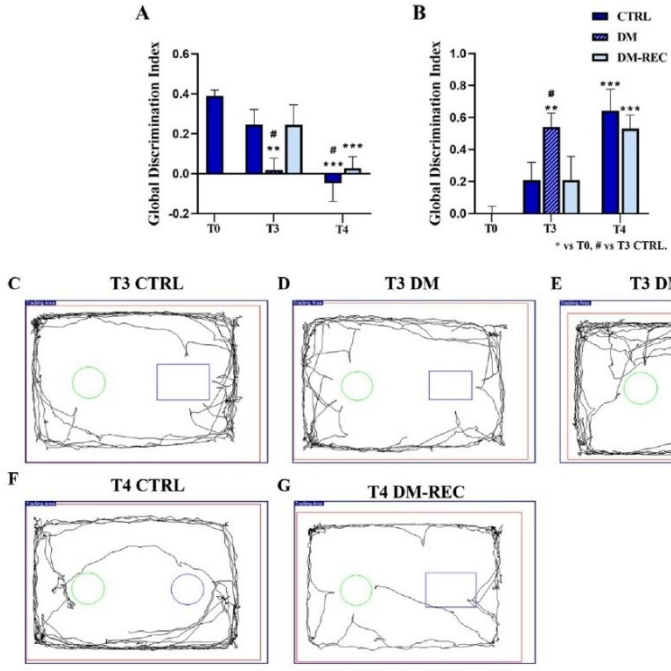


FIGURE 8
Diabetes exacerbates the cognitive decline monitored during aging: novel object recognition test (NOR) data. Panel (A, B): global discrimination index (DI) and global frailty index (FI), respectively. Panel (C–E): representative maps in CTRL (C), DM (D), and DM-REC (E) mice obtained at T3. Panel (F) and (G): representative maps in CTRL (F) and DM-REC (G) mice acquired at T4. Values are presented as the mean ± standard error of the mean (SEM). Statistical significance (one-way ANOVA followed by Bonferroni *post hoc* test): *vs. T0, # vs. T3 CTRL, £ vs. T3 DM, $ vs. T3 DM-REC, § vs. T4 CTRL. For all symbols reported $p < 0.05$ (*, #, £, $, and §); $p < 0.01$ (**, ##, ££, $$, and §§); $p < 0.001$ (***, ###, £££, $$$, and §§§).

2. Investigating the efficacy of new blood biomarkers, such as fasting GA and MGO, in monitoring diabetic conditions and their relationship with fasting glycemia.
3. Exploring the potential detrimental effect of a high sugar water intake on diabetes conditions.
4. Considering the relationship between diabetic conditions and declarative, episodic long-term memory.
5. Examining histological features/alterations of both pancreas and hippocampus in diabetic mice.

A mouse model of type 2 diabetes was reproduced using the low-dose streptozotocin (STZ) induction protocol according to the Animal Models of Diabetic Complications Consortium (AMDCC) (Bolzán and Bianchi, 2002; Burdo et al., 2009). STZ is an antibiotic that causes partial or complete death of pancreatic β-cells and is widely used to induce diabetes in animal models. The high-dose STZ protocol induces a complete destruction of pancreatic β-cells, reproducing T1DM. On the contrary, low-dose STZ administration induces a gradual death of pancreatic β-cells, mimicking the pathogenesis of DM (Cassano et al., 2020; Furman, 2021; Lai et al., 2024). In the literature, several experimental protocols are described, which combine different STZ doses, number of intraperitoneal injections, and dietary regimens (Wu and Huan, 2008; Ventura-Sobrevilla et al., 2011; Cassano et al., 2020; Furman, 2021; Liu et al., 2021; Chen et al., 2022; Bauer et al., 2023b; Lai et al., 2024).

In this animal model, diabetes was induced using low doses of STZ at 13 months of age, corresponding to the late adulthood phase (T1), approximately equivalent to 43 human years (Dutta and Sengupta, 2016). One month later, at 14 months of age (T2) and still in the adulthood phase, comparable to 46 human years, all mice fed with ND (DM-ND) exhibited diabetic fasting glycemic levels

10.3389/fphys.2025.1455434

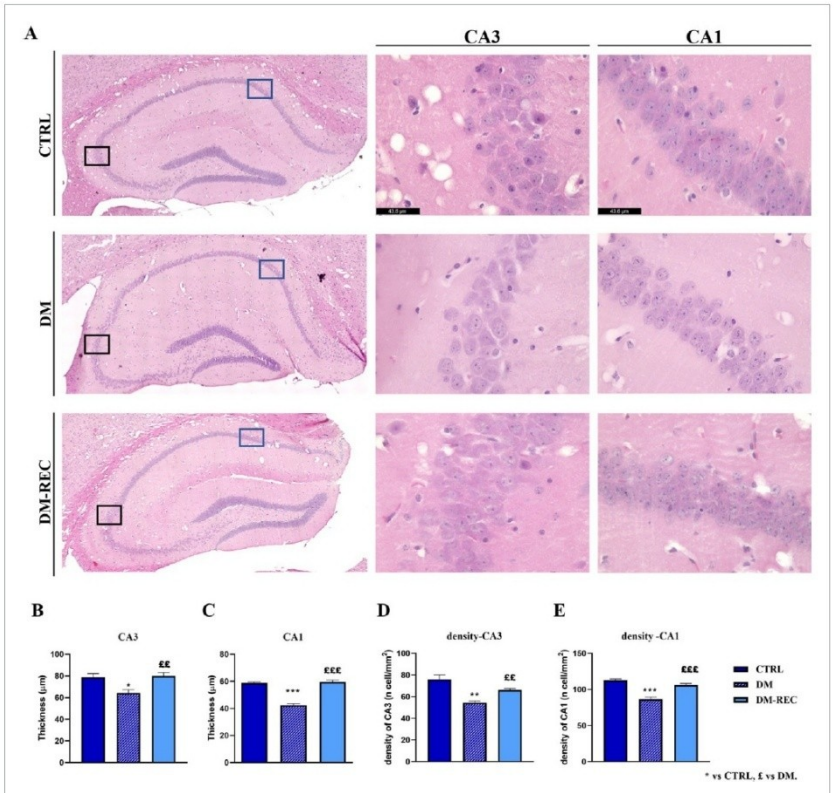


FIGURE 9
Histological characterization of hippocampus via H&E staining. Panel (A): representative brain sections showing the hippocampal cytoarchitecture. *Left column*: the whole hippocampus images were obtained using the LASX Navigator. Black and blue squares indicate the ROI region for CA3 and CA1, respectively. *Center and right column*: high-magnification micrographs of CA3 and CA1, respectively, from CTRL, DM, and DM-REC mice. Light microscopy magnification: ×40. Scale bars 43.6 µm. Panel (B–E): histograms showing the thickness of CA3 (B) and CA1 (C) and the cell density measured in CA3 (D) and CA1 (E) in CTRL, DM, and DM-REC mice. Values are presented as the mean ± standard error of the mean (SEM). Statistical significance (one-way ANOVA followed by Bonferroni *post hoc* test):*vs. CTRL, £ vs. DM. For all symbols reported $p < 0.05$ (*, £), $p < 0.01$ (**and ££); $p < 0.001$ (***and £££).

(four times higher compared to controls). At T3, corresponding to the reproductive senescence phase (16 months of age in mice and equivalent to approximately 53 human years), 55.55% of the mice (n = 10/18) in both experimental groups DM-ND and DM-HS showed partial recovery, achieving fasting glycemic levels below the diabetic threshold (lower than 300 mg/dL). By T4, during the senescence phase (19 months of age in mice and roughly equivalent to 62 human years), 88.9% of the mice in DM-ND and DM-HS groups (n = 16/18) had recovered fasting glycemic levels below the diabetic threshold, which was statistically comparable to the results assessed before induction. These findings indicate that the diabetic mouse model remains stable in fasting glycemic values for 1 month, corresponding to three human years (from 43 to 46 years). During this timeframe, our results show a clear correlation with human data. However, as highlighted in the study, over the subsequent 2 months (equivalent to 7 human years, from 46 to 53 years), approximately 55% of the mice exhibited partial recovery of fasting glycemic levels, resulting in a reduced correlation with human data. Beyond this point, the correlation with human data was completely lost. In conclusion, this longitudinal study demonstrates

that the diabetic mouse model maintains stability for a specific period but later exhibits biological variability, with some mice recovering glycemia by "itself." This unexpected result could pave the way for further investigation into the cellular and molecular mechanisms underlying glycemic recovery, potentially uncovering novel therapeutic strategies for diabetes.

It should be noted that, as measured at T3 and T4, the HS diet did not exert any detrimental effect on the fasting glycemic levels, according to data on previous studies on adult mice (Coirini et al., 2022).

The STZ-induced diabetic mouse model has, therefore, a disease reversible over time, as demonstrated by the diabetic condition which is maintained in a short time window of only 3 months.

In parallel with the glycemia, we monitored the blood levels of GA and MGO. GA is the higher glycated portion of fructosamine and reflects short-term glycemic changes, which occur over a 3-week period (Freitas et al., 2017; Piuri et al., 2020). GA is evaluated in particular clinical conditions such as pregnancy or hemoglobinopathy or chronic kidney disease. In the last decades, based on the easy and fast standardized enzymatic methodology, GA has been suggested as a marker of DM screening and monitoring, as well as a predictor of long-term diabetic outcomes (Freitas et al., 2017). Our data indicate that, despite glycemic values in control animals remaining stable over time regardless of the dietary regimen, GA was statistically higher after 5 months of HS, suggesting that glycated albumin was affected by a long-term effect of HS water intake. In diabetic mice, GA was statistically increased 1 month after STZ i.p. injections and remained stable over time until T4, even though glycemic level decreased and recovered to a normal fasting value in most mice. Hence, GA seems to be a good blood biomarker with the same early onset of glycemia and a long-lasting response compared to fasting glycemia. GA measured in STZ-induced mice was similar in both DM-HS and DM-ND animals, suggesting that diabetes induction had a greater impact on HS water intake. These data suggest that even as glycemia normalized, ongoing metabolic disturbances persisted. GA serves as an important biomarker of short-term glycemic control, and its elevation indicates that chronic hyperglycemic conditions lead to prolonged protein glycation processes.

MGO is a highly reactive dicarbonyl compound, mainly formed as a byproduct of glucose metabolism. MGO is the major precursor of nonenzymatic glycation of proteins and DNA, subsequently leading to the formation of advanced glycation end products (AGEs). MGO is an emerging biomarker of DM due to its strong association with protein glycation and insulin resistance (Ramachandra Bhat et al., 2019). Therefore, monitoring plasma MGO levels could be useful for investigating disease-related complications in diabetic patients. In particular, high MGO levels correlate with chronic kidney disease, macroangiopathy, and cognitive deficits (Ogawa et al., 2010; A; Shamsaldeen et al., 2016).

Surprisingly, in control mice, fasting MGO serum levels tended to decrease during aging in a statistically significant manner, regardless of the dietary regimen followed. Under physiological circumstances, MGO is detoxified by the glyoxalase system consisting of glyoxalase I and II (Glo1 and Glo2). We can speculate that the serum MGO level is inversely correlated to the intracellular MGO level. Few studies have been conducted to explore the effects of aging on MGO serum levels in mice. MGO is highly reactive and can bond with endogenous nucleophilic substances and can be eliminated by the glyoxalase system or form stable AGEs in the cell. In particular conditions, when the glyoxalase system function is compromised, intracellular MGO levels increase and produce intracellular AGEs, leaving little MGO in plasma or serum (Dhar and Desai, 2012; Kold-Christensen and Johannsen, 2020). Furthermore, some investigations reported that patients with type 1 and type 2 diabetes have higher MGO plasma levels compared to healthy individuals (McLellan et al., 1994; Wang et al., 2007). Interestingly, MGO serum levels increased in DM-HS evaluated at T3, correlating the described decrease with aging in CTRL mice. At T4, when glycemic levels recovered to the normal value, MGO decreased, mirroring the fasting glycemic trend.

Concerning histological evaluation, the examination of pancreatic tissue sections confirmed that the STZ-induced diabetic condition was characterized by pathological infiltration leading to insulitis. Interestingly, in DM-REC mice, the recovery inglycemia was mirrored by a partial recovery of normal histological features. This partial recovery could indicate ongoing β-cell regeneration mechanisms, which may include β-cell replication, neogenesis, and inhibition of apoptosis (Trucco, 2005; Levine and Itkin-Ansari, 2008). Studies suggest that the recovery could be caused by different mechanisms, including proliferation via pathways like IRS2/PI3K/Akt (Ji et al., 2022), neogenesisfromprecursorcells(Shahediet al., 2024), andtrans-differentiation of α-cells into β-cells (Dor et al., 2004). Additionally, an antiapoptoticmechanismandimmunomodulation, possiblyinvolving the spleen, could play an indirect role in promoting regeneration (Yin et al., 2006). Our murine model of diabetes appears to be particularly useful for studying and further exploring the mechanisms involved in the recovery from the diabetic condition.

The combination of diabetes and HS has a greater impact on decreasing the survival probability. In fact, the survival probability measured in 18-month-old DM-HS mice was 55.55%. In particular, the survival probability of mice with fasting glycemic value in the range 500–600 mg/dL was 0%. Otherwise, DM-ND mice with a high glycemic value survived, indicating that diabetic animals on the HS dietary regimen have a lower survival likelihood compared to other experimental groups evaluated in the study.

In the novel object recognition task, the recognition memory performance was dramatically impaired in DM mice at T3, underlying the strong relationship between diabetes and cognition. In particular, the global FI at T3 in DM mice was more than doubled compared to that calculated in control animals at the same age, reaching a value comparable to that estimated at T4, which reflects cognitive decline similar to that observed in late senescent non-diabetic mice. Interestingly, at T3, DM-REC mice recovered the memory task performance, obtaining a global FI comparable to that measured in CTRL mice at the same time point. This finding suggests that the STZ-induced decline in recognition memory could be reverted if glycemia is reverted, possibly through enhanced neuroprotective mechanisms or neurogenesis. At T4, DM mice became phenotypically frail with a dramatic decline in the locomotor activity. The hippocampus is a crucial anatomical structure that plays a significant role in learning, memory, and various cognitive functions. Hence, the study of this brain area is crucial for assessing cognitive dysfunction associated with diabetes (Hu et al., 2019; Li et al., 2020).

Based on histological examination, our data in DM mice evidenced STZ-induced cytotoxic injuries, mainly detectable in the hippocampal CA1 and CA3 regions, as demonstrated by both thickness reduction and cell density decrease. Interestingly, the detrimental effect of STZ was reverted in the DM-REC mice, with an increase in both thickness and cell density, in line with the recovery phenomena measured by fasting glycemia and recognition memory performance. Thus, these findings further demonstrated the neural plasticity of these brain areas which regained a physiological feature.

The glycemic level following low-dose STZ induction, whether associated with normal diet regimen or high-sugar intake, reversed over time in 5 months, allowing us to explore the cellular mechanism involved/underlying the recovery phenomena observed both in the pancreas and hippocampus. Potential mechanisms may include enhanced β-cell regeneration and neurogenesis in the pancreas, paralleled by a recovery in hippocampus memory neuronal networks. All these mechanisms require further investigation.

## 5 Conclusion

In conclusion, the currently described STZ induction protocol induces a non-lasting diabetic condition, as evidenced by fasting glycemia and glycated albumin increase. GA should be considered a novel and emerging biomarker for diabetic conditions in mice, with a similar early onset of hyperglycemia but with a longer duration. The survival probability is inversely related to both HS and diabetic conditions. The two hallmarks of the diabetic condition are the presence of pancreatic tissue insulitis and the specific alterations in CA1 and CA3 hippocampal regions. The impairment in recognition memory mirrored hyperglycemia in diabetic mice. The cytoarchitecture of the pancreas and hippocampus and recognition memory showed signs of recovery.

Interestingly, an improvement in recognition memory and a partial regaining of physiological pancreas morphology and hippocampal cytoarchitecture are recorded in mice with recovered fasting glycemia levels,

## Data availability statement

The original contributions presented in the study are included in the article/Supplementary Material; further inquiries can be directed to the corresponding author.

## Ethics statement

The animal study was approved by the Ethics Committee of Pavia University (Ministry of Health, License number 220/2022-PR). The study was conducted in accordance with the local legislation and institutional requirements.

## Author contributions

MV: conceptualization, methodology, writing–original draft, formal analysis, and Writing–review and editing. ER: conceptualization, methodology, writing–original draft, formal analysis, and writing–review and editing. FB: conceptualization, formal analysis, investigation, methodology, writing–original draft, and writing–review and editing. MS: investigation, methodology, writing–original draft, and writing–review and editing, Formal Analysis, Conceptualization. MC: funding acquisition and writing–review and editing. AS: conceptualization, funding acquisition, and writing–review and editing. IS: writing–review and editing. EP: writing–review and editing. FG: writing–review and editing. DR: writing–review and editing. CL: writing–review and editing. PR: conceptualization, funding acquisition, investigation, methodology, supervision, writing–original draft, and writing–review and editing.

## Funding

The author(s) declare that financial support was received for the research, authorship, and/or publication of this article. This research was supported by the Ministry "Ministero dello sviluppo economico" and managed by INVITALIA under "Brevetti +" (protocol: PT205).

## Acknowledgments

The authors would like to thank i) the animal facility "Centro di servizio per la gestione unificata delle attività di stabulazione e di radiobiologi," University of Pavia, for hosting the animals; ii) the OPBA of the University of Pavia for their support in drawing up the animal protocol for the ethical committee; iii) the core facility "Centro Grandi Strumenti" (CGS) at the University of Pavia for providing access to the confocal microscopy laboratory, and iiii) the Ministry "Ministero dello sviluppo economico" for granting and supporting the project.

## Conflict of interest

The authors declare that the research was conducted in the absence of any commercial or financial relationships that could be construed as a potential conflict of interest.

The author(s) declared that they were an editorial board member of Frontiers, at the time of submission. This had no impact on the peer review process and the final decision.

## Generative AI statement

The author(s) declare that no Generative AI was used in the creation of this manuscript.

## Publisher's note

All claims expressed in this article are solely those of the authors and do not necessarily represent those of

their affiliated organizations, or those of the publisher, the editors and the reviewers. Any product that may be evaluated in this article, or claim that may be made by its manufacturer, is not guaranteed or endorsed by the publisher.

## Supplementary material

The Supplementary Material for this article can be found online at: https://www.frontiersin.org/articles/10.3389/fphys.2025.1455434/full#supplementary-material

## References


Aderinto, N., Olatunji, G., Abdulbasit, M., Ashinze, P., Faturoti, O., Ajagbe, A., et al. (2023). The impact of diabetes in cognitive impairment: a review of current evidence and prospects for future investigations. *Med. Baltim.* 102, e35557. doi:10.1097/MD.0000000000035557

Barone, E., Di Domenico, F., Perluigi, M., and Butterfield, D. A. (2021). The interplay among oxidative stress, brain insulin resistance and AMPK dysfunction contribute to neurodegeneration in type 2 diabetes and Alzheimer disease. *Free Radic. Biol. Med.* 176, 16–33. doi:10.1016/j.freeradbiomed.2021.09.006

Bauer, B. M., Bhattacharya, S., Bloom-Saldana, E., Irimia-Dominguez, J. M., and Fueger, P. T. (2023a). Dose-dependent progression of multiple low-dose streptozotocin-induced diabetes in mice. *Physiol. Genomics* 55, 381–391. doi:10.1152/physiolgenomics.00032.2023

Bauer, B. M., Bhattacharya, S., Bloom-Saldana, E., Irimia-Dominguez, J. M., and Fueger, P. T. (2023b). Dose-dependent progression of multiple low-dose streptozotocin-induced diabetes in mice. *Physiol. Genomics* 55, 381–391. doi:10.1152/physiolgenomics.00032.2023

Beilharz, J. E., Maniam, J., and Morris, M. J. (2016). Short-term exposure to a diet high in fat and sugar, or liquid sugar, selectively impairs hippocampal-dependent memory, with differential impacts on inflammation. *Behav. Brain Res.* 306, 1–7. doi:10.1016/j.bbr.2016.03.018

Belinskaia, D. A., Voronina, P. A., and Goncharov, N. V. (2021). Integrative role of albumin: evolutionary, biochemical and pathophysiological aspects. *J. Evol. Biochem. Physiol.* 57, 1419–1448. doi:10.1134/S0022093021060020X

Bettiga, A., Fiorio, F., Di Marco, F., Trevisani, F., Romani, A., Porrini, E., et al. (2019). The modern western diet rich in advanced glycation end-products (AGEs): an overview of its impact on obesity and early progression of renal pathology. *Nutrients* 11, 1748. doi:10.3390/nu11081748

Bhattacharya, R., Alam, M. R., Kamal, M. A., Seo, K. J., and Singh, L. R. (2023). AGE-RAGE axis culminates into multiple pathogenic processes: a central road to neurodegeneration. *Front. Mol. Neurosci.* 16, 1155175. doi:10.3389/fnmol.2023.1155175

Bierhaus, A., Schiekofer, S., Schwaninger, M., Andrassy, M., Humpert, P. M., Chen, J., et al. (2001). Diabetes-associated sustained activation of the transcription factor nuclear factor-kappaB. *Diabetes* 50, 2792–2808. doi:10.2337/diabetes.50.12.2792

Bolzán, A. D., and Bianchi, M. S. (2002). Genotoxicity of streptozotocin. *Mutat. Res. Mutat. Res.* 512, 121–134. doi:10.1016/S1383-5742(02)00044-3

Brandalise, F., Cesaroni, V., Gregori, A., Repetti, M., Romano, C., Orrù, G., et al. (2017). Dietary supplementation of hericium erinaceus increases mossy fiber-CA3 hippocampal neurotransmission and recognition memory in wild-type mice. *Evidence-based Complement. Altern. Med.* 2017, 3864340. doi:10.1155/2017/3864340

Burdo, J. R., Chen, Q., Calcutt, N. A., and Schubert, D. (2009). The pathological interaction between diabetes and presymptomatic Alzheimer's disease. *Neurobiol. Aging* 30, 1910–1917. doi:10.1016/j.neurobiolaging.2008.02.010

Burgeiro, A., Cerqueira, M., Varela-Rodriguez, B., Nunes, S., Neto, P., Pereira, F., et al. (2017). Glucose and lipid dysmetabolism in a rat model of prediabetes induced by a high-sucrose diet. *Nutrients* 9, 638. doi:10.3390/nu9060638

Cai, W., Uribarri, J., Zhu, L., Chen, X., Swamy, S., Zhao, Z., et al. (2014). Oral glycotoxins are a modifiable cause of dementia and the metabolic syndrome in mice and humans. *Proc. Natl. Acad. Sci.* 111, 4940–4945. doi:10.1073/pnas.1316013111

Cao, D., Lu, H., Lewis, T. L., and Li, L. (2007). Intake of sucrose-sweetened water induces insulin resistance and exacerbates memory deficits and amyloidosis in a transgenic mouse model of alzheimer disease. *J. Biol. Chem.* 282, 36275–36282. doi:10.1074/jbc.M703561200

Carrillo-Larco, R. M., Guzman-Vilca, W. C., Xu, X., and Bernabe-Ortiz, A. (2024). Mean age and body mass index at type 2 diabetes diagnosis: pooled analysis of 56 health surveys across income groups and world regions. *Diabet. Med.* 41, e15174. doi:10.1111/dme.15174

Cassano, V., Leo, A., Tallarico, M., Nesci, V., Cimellaro, A., Fiorentino, T. V., et al. (2020). Metabolic and cognitive effects of ranolazine in type 2 diabetes mellitus: data from an *in vivo* model. *Nutrients* 12, 382. doi:10.3390/nu12020382

Castro, M. C., Villagarcia, H. G., Di Sarli Gutiérrez, L., Arbeláez, L. G., Schinella, G., Massa, M. L., et al. (2024). Akt signaling and nitric oxide synthase as possible mediators of the protective effect of N-acetyl-L-cysteine in prediabetes induced by sucrose. *Int. J. Mol. Sci.* 25, 1215. doi:10.3390/ijms25021215

Cheke, L. G., Simons, J. S., and Clayton, N. S. (2016). Higher body mass index is associated with episodic memory deficits in young adults. *Q. J. Exp. Psychol.* 69, 2305–2316. doi:10.1080/17470218.2015.1099163

Chen, Y.-Z., Gu, J., Chuang, W.-T., Du, Y.-F., Zhang, L., Lu, M.-L., et al. (2022). Slowly digestible carbohydrate diet ameliorates hyperglycemia and hyperlipidemia in high-fat diet/streptozocin-induced diabetic mice. *Front. Nutr.* 9, 854725. doi:10.3389/fnut.2022.854725

Coirini, H., Rey, M., Gonzalez Deniselle, M. C., and Kruse, M. S. (2022). Long-term memory function impairments following sucrose exposure in juvenile versus adult rats. *Biomedicines* 10, 2723. doi:10.3390/biomedicines10112723

Dhar, I., and Desai, K. (2012). Aging: drugs to eliminate methylglyoxal, a reactive glucose metabolite, and advanced glycation endproducts. *Pharmacol. (InTech).* doi:10.5772/34337

Ding, X., Yin, L., Zhang, L., Zhang, Y., Zha, T., Zhang, W., et al. (2024). Diabetes accelerates Alzheimer's disease progression in the first year post mild cognitive impairment diagnosis. *Alzheimer's Dement.* 20, 4583–4593. doi:10.1002/alz.13882

Dove, A., Shang, Y., Xu, W., Grande, G., Laukka, E. J., Fratiglioni, L., et al. (2021). The impact of diabetes on cognitive impairment and its progression to dementia. *Alzheimer's Dement.* 17, 1769–1778. doi:10.1002/alz.12482

Dutta, S., and Sengupta, P. (2016). Men and mice: relating their ages. *Life Sci.* 152, 244–248. doi:10.1016/j.lfs.2015.10.025

Farajpour, R., Sadigh-Eteghad, S., Ahmadian, N., Farzipour, M., Mahmoudi, J., and Majdi, A. (2017). Chronic administration of rosa canina hydro-alcoholic extract attenuates depressive-like behavior and recognition memory impairment in diabetic mice: a possible role of oxidative stress. *Med. Princ. Pract.* 26, 245–250. doi:10.1159/000464364

Flister, K. F. T., Pinto, B. A. S., França, L. M., Coêlho, C. F. F., dos Santos, P. C., Vale, C. C., et al. (2018). Long-term exposure to high-sucrose diet down-regulates hepatic endoplasmic reticulum-stress adaptive pathways and potentiates *de novo* lipogenesis in weaned male mice. *J. Nutr. Biochem.* 62, 155–166. doi:10.1016/j.jnutbio.2018.09.007

Freitas, P. A. C., Ehlert, L. R., and Camargo, J. L. (2017). Glycated albumin: a potential biomarker in diabetes. *Arch. Endocrinol. Metab.* 61, 296–304. doi:10.1590/2359-3997000000272

Furman, B. L. (2021). Streptozotocin-induced diabetic models in mice and rats. *Curr. Protoc.* 1, e78. doi:10.1002/cpz1.78

Giacco, F., and Brownlee, M. (2010). Oxidative stress and diabetic complications. *Circ. Res.* 107, 1058–1070. doi:10.1161/CIRCRESAHA.110.223545

Gill, V., Kumar, V., Singh, K., Kumar, A., and Kim, J. J. (2019). Advanced glycation end products (AGEs) may be a striking link between modern diet and health. *Biomolecules* 9, 888–921. doi:10.3390/biom9120888

Graham, M. L., Janecek, J. L., Kittredge, J. A., Hering, B. J., and Schuurman, H.-J. (2011). The streptozotocin-induced diabetic nude mouse model: differences between animals from different sources. *Comp. Med.* 61, 356–360. Available at: http://www.ncbi.nlm.nih.gov/pubmed/22330251.

Guthrie, R. A., and Guthrie, D. W. (2004). Pathophysiology of diabetes mellitus. *Crit. Care Nurs. Q.* 27, 113–125. doi:10.1097/00002727-200404000-00003

Hahn, M., van Krieken, P. P., Nord, C., Alanentalo, T., Morini, F., Xiong, Y., et al. (2020). Topologically selective islet vulnerability and self-sustained downregulation of markers for β-cell maturity in streptozotocin-induced diabetes. *Commun. Biol.* 3, 541. doi:10.1038/s42003-020-01243-2

Holstad, M., and Sandler, S. (1999). Prolactin protects against diabetes induced by multiple low doses of streptozotocin in mice. *J. Endocrinol.* 163, 229–234. doi:10.1677/joe.0.1630229

Hu, B., Yan, L.-F., Sun, Q., Yu, Y., Zhang, J., Dai, Y.-J., et al. (2019). Disturbed neurovascular coupling in type 2 diabetes mellitus patients: evidence from a comprehensive fMRI analysis. *NeuroImage Clin.* 22, 101802. doi:10.1016/j.nicl.2019.101802

Jordan, W. H., Young, J. K., Hyten, M. J., and Hall, D. G. (2011). Preparation and analysis of the central nervous system. *Toxicol. Pathol.* 39, 58–65. doi:10.1177/0192623310391480

Kádár, A., Wittmann, G., Liposits, Z., and Fekete, C. (2009). Improved method for combination of immunocytochemistry and Nissl staining. *J. Neurosci. Methods* 184, 115–118. doi:10.1016/j.jneumeth.2009.07.010

Kalaria, R. N., Maestre, G. E., Arizaga, R., Friedland, R. P., Galasko, D., Hall, K., et al. (2008). Alzheimer's disease and vascular dementia in developing countries: prevalence, management, and risk factors. *Lancet Neurol.* 7, 812–826. doi:10.1016/S1474-4422(08)70169-8

Kanoski, S. E., and Davidson, T. L. (2011). Western diet consumption and cognitive impairment: links to hippocampal dysfunction and obesity. *Physiol. Behav.* 103, 59–68. doi:10.1016/j.physbeh.2010.12.003

Kassab, S., Begley, P., Church, S. J., Rotariu, S. M., Chevalier-Riffard, C., Dowsey, A. W., et al. (2019). Cognitive dysfunction in diabetic rats is prevented by pyridoxamine treatment. A multidisciplinary investigation. *Mol. Metab.* 28, 107–119. doi:10.1016/j.molmet.2019.08.003

Kold-Christensen, R., and Johannsen, M. (2020). Methylglyoxal metabolism and aging-related disease: moving from correlation toward causation. *Trends Endocrinol. Metab.* 31, 81–92. doi:10.1016/j.tem.2019.10.003

Kong, Y., Wang, F., Wang, J., Liu, C., Zhou, Y., Xu, Z., et al. (2020). Pathological mechanisms linking diabetes mellitus and Alzheimer's disease: the receptor for advanced glycation end products (RAGE). *Front. Aging Neurosci.* 12, 217. doi:10.3389/fnagi.2020.00217

Kouzuma, T., Usami, T., Yamakoshi, M., Takahashi, M., and Imamura, S. (2002). An enzymatic method for the measurement of glycated albumin in biological samples. *Clin. Chim. Acta* 324, 61–71. doi:10.1016/S0009-8981(02)00207-3

Krhač, M., and Lovrenčić, M. V. (2019). Update on biomarkers of glycemic control. *World J. Diabetes* 10, 1–15. doi:10.4239/wjd.v10.i1.1

Lai, P., Zhang, L., Qiu, Y., Ren, J., Sun, X., Zhang, T., et al. (2024). Heat stress reduces brown adipose tissue activity by exacerbating mitochondrial damage in type 2 diabetic mice. *J. Therm. Biol.* 119, 103799. doi:10.1016/j.jtherbio.2024.103799

Lattouf, R., Younes, R., Lutomski, D., Naaman, N., Godeau, G., Senni, K., et al. (2014). Picrosirius red staining: a useful tool to appraise collagen networks in normal and pathological tissues. *J. Histochem. Cytochem.* 62, 751–758. doi:10.1369/0022155414545787

Li, C., Zuo, Z., Liu, D., Jiang, R., Li, Y., Li, H., et al. (2020). Type 2 diabetes mellitus may exacerbate gray matter atrophy in patients with early-onset mild cognitive impairment. *Front. Neurosci.* 14, 856. doi:10.3389/fnins.2020.00856

Li, X.-H., Xie, J.-Z., Jiang, X., Lv, B.-L., Cheng, X.-S., Du, L.-L., et al. (2012). Methylglyoxal induces tau hyperphosphorylation via promoting AGEs formation. *NeuroMolecular Med.* 14, 338–348. doi:10.1007/s12017-012-8191-0

Li, Z., Muench, G., Wenhart, C., Goebel, S., and Reimann, A. (2022). Definition of a sectioning plane and place for a section containing hoped-for regions using a spare counterpart specimen. *Sci. Rep.* 12, 13342. doi:10.1038/s41598-022-17380-z

Liu, D., Regenstein, J. M., Diao, Y., Qiu, J., Zhang, H., Li, J., et al. (2019). Antidiabetic effects of water-soluble Korean pine nut protein on type 2 diabetic mice. *Biomed. Pharmacother.* 117, 108989. doi:10.1016/j.biopha.2019.108989

Liu, S., Ma, L., Ren, X., Zhang, W., Shi, D., Huo, Y., et al. (2021). A new mouse model of type 2 diabetes mellitus established through combination of high-fat diet, streptozotocin and glucocorticoid. *Life Sci.* 286, 120062. doi:10.1016/j.lfs.2021.120062

Liu, Y., Zhang, D., Yuan, J., Song, L., Zhang, C., Lin, Q., et al. (2020). Hyperbaric oxygen ameliorates insulin sensitivity by increasing GLUT4 expression in skeletal muscle and stimulating UCP1 in Brown adipose tissue in T2DM mice. *Front. Endocrinol. (Lausanne).* 11, 32. doi:10.3389/fendo.2020.00032

Longnecker, D. S. (2021). Anatomy and histology of the pancreas. *Pancreapedia* 1, 1–24. doi:10.3998/panc.2021.01

Luca, F.De, Roda, E., Ratto, D., Desiderio, A., Venuti, M. T., Ramieri, M., et al. (2023). Fighting secondary triple-negative breast cancer in cerebellum: a powerful aid from a medicinal mushrooms blend. *Biomed. Pharmacother.* 159, 114262. doi:10.1016/j.biopha.2023.114262

McLellan, A. C., Thornalley, P. J., Benn, J., and Sonksen, P. H. (1994). Glyoxalase system in clinical diabetes mellitus and correlation with diabetic complications. *Clin. Sci.* 87, 21–29. doi:10.1042/cs0870021

Meireles, M., Marques, C., Norberto, S., Fernandes, I., Mateus, N., Rendeiro, C., et al. (2015). The impact of chronic blackberry intake on the neuroinflammatory status of rats fed a standard or high-fat diet. *J. Nutr. Biochem.* 26, 1166–1173. doi:10.1016/j.jnutbio.2015.05.008

Melo, B. F., Sacramento, J. F., Ribeiro, M. J., Prego, C. S., Correia, M. C., Coelho, J. C., et al. (2019). Evaluating the impact of different hypercaloric diets on weight gain, insulin resistance, glucose intolerance, and its comorbidities in rats. *Nutrients* 11, 1197. doi:10.3390/nu11061197

Michailidis, M., Moraitou, D., Tata, D. A., Kalinderi, K., Papamitsou, T., and Papaliagkas, V. (2022). Alzheimer's disease as type 3 diabetes: common pathophysiological mechanisms between Alzheimer's disease and type 2 diabetes. *Int. J. Mol. Sci.* 23, 2687. doi:10.3390/ijms23052687

Momeni, Z., Neapetung, J., Pacholko, A., Kiir, T. A. B., Yamamoto, Y., Bekar, L. K., et al. (2021). Hyperglycemia induces RAGE-dependent hippocampal spatial memory impairments. *Physiol. Behav.* 229, 113287. doi:10.1016/j.physbeh.2020.113287

Mori, Y., Terasaki, M., Osaka, N., Fujikawa, T., Yashima, H., Saito, T., et al. (2024). DNA aptamer raised against advanced glycation end products improves sperm concentration, motility, and viability by suppressing receptors for advanced glycation end product-induced oxidative stress and inflammation in the testes of diabetic mice. *Int. J. Mol. Sci.* 25, 5947. doi:10.3390/ijms25115947

Nguyen, T. T., Ta, Q. T. H., Nguyen, T. K. O., Nguyen, T. T. D., and Van Giau, V. (2020). Type 3 diabetes and its role implications in Alzheimer's disease. *Int. J. Mol. Sci.* 21, 3165. doi:10.3390/ijms21093165

Nørgaard, S. A., Søndergaard, H., Sørensen, D. B., Galsgaard, E. D., Hess, C., and Sand, F. W. (2020). Optimising streptozotocin dosing to minimise renal toxicity and impairment of stomach emptying in male 129/Sv mice. *Lab. Anim.* 54, 341–352. doi:10.1177/0023677219872224

Novotny, K., Jung, T., Höhn, A., Weber, D., and Grune, T. (2015). Advanced glycation end products and oxidative stress in type 2 diabetes mellitus. *Biomolecules* 5, 194–222. doi:10.3390/biom5010194

Ogawa, S., Nakayama, K., Nakayama, M., Mori, T., Matsushima, M., Okamura, M., et al. (2010). Methylglyoxal is a predictor in type 2 diabetic patients of intima-media thickening and elevation of blood pressure. *Hypertension* 56, 471–476. doi:10.1161/HYPERTENSIONAHA.110.156786

Oliveira, A. L., de Oliveira, M. G., Mônica, F. Z., and Antunes, E. (2024). Methylglyoxal and advanced glycation end products (AGEs): targets for the prevention and treatment of diabetes-associated bladder dysfunction? *Biomedicines* 12, 939. doi:10.3390/biomedicines12050939

Oliveira, L. S. C., Santos, D. A., Barbosa-da-Silva, S., Mandarim-de-Lacerda, C. A., and Aguila, M. B. (2014). The inflammatory profile and liver damage of a sucrose-rich diet in mice. *J. Nutr. Biochem.* 25, 193–200. doi:10.1016/j.jnutbio.2013.10.006

Orr, M. E., Salinas, A., Buffenstein, R., and Oddo, S. (2014). Mammalian target of rapamycin hyperactivity mediates the detrimental effects of a high sucrose diet on Alzheimer's disease pathology. *Neurobiol. Aging* 35, 1233–1242. doi:10.1016/j.neurobiolaging.2013.12.006

Paradela-Dobarro, B., Bravo, S. B., Rozados-Luis, A., González-Peteiro, M., Varela-Román, A., González-Juanatey, J. R., et al. (2019). Inflammatory effects of *in vivo* glycated albumin from cardiovascular patients. *Biomed. Pharmacother.* 113, 108763. doi:10.1016/j.biopha.2019.108763

Parks, R. J., Fares, E., MacDonald, J. K., Ernst, M. C., Sinal, C. J., Rockwood, K., et al. (2012). A procedure for creating a frailty index based on deficit accumulation in aging mice. *Journals Gerontol. Ser. A* 67A, 217–227. doi:10.1093/gerona/glr193

Patel, S. S., Gupta, S., and Udayabanu, M. (2016). Urtica dioica modulates hippocampal insulin signaling and recognition memory deficit in streptozotocin induced diabetic mice. *Metab. Brain Dis.* 31, 601–611. doi:10.1007/s11011-016-9791-4

Pavlovic, S., Petrovic, I., Jovicic, N., Ljujic, B., Miletic Kovacevic, M., Arsenijevic, N., et al. (2018). IL-33 prevents MLD-STZ induction of diabetes and attenuate insulitis in prediabetic NOD mice. *Front. Immunol.* 9, 2646. doi:10.3389/fimmu.2018.02646

Pejnovic, N. N., Pantic, J. M., Jovanovic, I. P., Radosavljevic, G. D., Milovanovic, M. Z., Nikolic, I. G., et al. (2013). Galectin-3 deficiency accelerates high-fat diet–induced obesity and amplifies inflammation in adipose tissue and pancreatic islets. *Diabetes* 62, 1932–1944. doi:10.2337/db12-0222

Piuri, G., Basello, K., Rossi, G., Soldavini, C. M., Duella, S., Privitera, G., et al. (2020). Methylglyoxal, glycated albumin, PAF, and TNF-α: possible inflammatory and metabolic biomarkers for management of gestational diabetes. *Nutrients* 12, 479. doi:10.3390/nu12020479

Presta, M., Zoratto, F., Mulder, D., Ottomana, A. M., Pisa, E., Arias Vásquez, A., et al. (2024). Hyperglycemia and cognitive impairments anticipate the onset of an overt type 2 diabetes-like phenotype in TALLYHO/JngJ mice. *Psychoneuroendocrinology* 167, 107102. doi:10.1016/j.psyneuen.2024.107102

Ramachandra Bhat, L., Vedartham, S., Krishnan, U. M., and Rayappan, J. B. B. (2019). Methylglyoxal – an emerging biomarker for diabetes mellitus diagnosis and its detection methods. *Biosens. Bioelectron.* 133, 107–124. doi:10.1016/j.bios.2019.03.010

Rao, Y. L., Ganaraja, B., Murlimanju, B. V., Joy, T., Krishnamurthy, A., and Agrawal, A. (2022). Hippocampus and its involvement in Alzheimer's disease: a review. *3 Biotech.* 12, 55. doi:10.1007/s13205-022-03123-4

Ratto, D., Corana, F., Mannucci, B., Priori, E. C., Cobelli, F., Roda, E., et al. (2019). Hericium erinaceus improves recognition memory and induces hippocampal and cerebellar neurogenesis in frail mice during aging. *Nutrients* 11, 715. doi:10.3390/nu11040715

Reed, J., Bain, S., and Kanamarlapudi, V. (2021). A review of current trends with type 2 diabetes epidemiology, aetiology, pathogenesis, treatments and future perspectives. *Diabetes, Metab. Syndr. Obes. Targets Ther.* 14, 3567–3602. doi:10.2147/DMSO.S319895

Roda, E., Barni, S., Milzani, A., Dalle-Donne, I., Colombo, G., and Coccini, T. (2017). Single silver nanoparticle instillation induced early and persisting moderate cortical damage in rat kidneys. *Int. J. Mol. Sci.* 18, 2115. doi:10.3390/ijms18102115

Roda, E., Bottone, M., Biggiogera, M., Milanesi, G., and Coccini, T. (2019). Pulmonary and hepatic effects after low dose exposure to nanosilver: early and long-lasting histological and ultrastructural alterations in rat. *Toxicol. Rep.* 6, 1047–1060. doi:10.1016/j.toxrep.2019.09.008

Roda, E., Ratto, D., De Luca, F., Desiderio, A., Ramieri, M., Goppa, L., et al. (2022). Searching for a longevity food, we bump into hericium erinaceus primordium rich in

ergothioneine: the "longevity vitamin" improves locomotor performances during aging. *Nutrients* 14, 1177. doi:10.3390/nu14061177

Schalkwijk, C. G., and Stehouwer, C. D. A. (2020). Methylglyoxal, a highly reactive dicarbonyl compound, in diabetes, its vascular complications, and other age-related diseases. *Physiol. Rev.* 100, 407–461. doi:10.1152/physrev.00001.2019

Seshadri, S., Rapaka, N., Prajapati, B., Mandaliya, D., Patel, S., Muggalla, C. S., et al. (2019). Statins exacerbate glucose intolerance and hyperglycemia in a high sucrose fed rodent model. *Sci. Rep.* 9, 8825. doi:10.1038/s41598-019-45369-8

Shamsaldeen, A., Mackenzie, L., A, S., Lione, L., and Benham, D. (2016). Methylglyoxal, A metabolite increased in diabetes is associated with insulin resistance, vascular dysfunction and neuropathies. *Curr. Drug Metab.* 17, 359–367. doi:10.2174/1389200217666151222155216

Shieh, J. C. C., Huang, P. T., and Lin, Y. F. (2020). Alzheimer's disease and diabetes: insulin signaling as the bridge linking two pathologies. *Mol. Neurobiol.* 57, 1966–1977. doi:10.1007/s12035-019-01858-5

Silvers, J. M., Harrod, S. B., Mactutus, C. F., and Booze, R. M. (2007). Automation of the novel object recognition task for use in adolescent rats. *J. Neurosci. Methods* 166, 99–103. doi:10.1016/j.jneumeth.2007.06.032

Soares, E., Prediger, R. D., Nunes, S., Castro, A. A., Viana, S. D., Lemos, C., et al. (2013). Spatial memory impairments in a prediabetic rat model. *Neuroscience* 250, 565–577. doi:10.1016/j.neuroscience.2013.07.055

Srikanth, V., Maczurek, A., Phan, T., Steele, M., Westcott, B., Juskiw, D., et al. (2011). Advanced glycation endproducts and their receptor RAGE in Alzheimer's disease. *Neurobiol. Aging* 32, 763–777. doi:10.1016/j.neurobiolaging.2009.04.016

Sutkowska, E., Fecka, I., Marciniak, D., Bednarska, K., Sutkowska, M., and Hap, K. (2023). Analysis of methylglyoxal concentration in a group of patients with newly diagnosed prediabetes. *Biomedicines* 11, 2968. doi:10.3390/biomedicines11112968

Ventura-Sobrevilla, J., Boone-Villa, V. D., Aguilar, C. N., Román-Ramos, R., Vega-Ávila, E., Campos-Sepúlveda, E., et al. (2011). Effect of varying dose and administration of streptozotocin on blood sugar in male CD1 mice. *Proc. West. Pharmacol. Soc.* 54, 5–9.

Wang, H., Meng, Q. H., Gordon, J. R., Khandwala, H., and Wu, L. (2007). Proinflammatory and proapoptotic effects of methylglyoxal on neutrophils from patients with type 2 diabetes mellitus. *Clin. Biochem.* 40, 1232–1239. doi:10.1016/j.clinbiochem.2007.07.016

Wu, K. K., and Huan, Y. (2008). Streptozotocin-induced diabetic models in mice and rats. *Curr. Protoc. Pharmacol.* 40, Unit 5.47. doi:10.1002/0471141755.ph0547s40

Wu, W.-C., Ma, W.-Y., Wei, J.-N., Yu, T.-Y., Lin, M.-S., Shih, S.-R., et al. (2016). Serum glycated albumin to guide the diagnosis of diabetes mellitus. *PLoS One* 11, e0146780. doi:10.1371/journal.pone.0146780

Yazdanpanah, S., Rabiee, M., Tahriri, M., Abdolrahim, M., Rajab, A., Jazayeri, H. E., et al. (2017). Evaluation of glycated albumin (GA) and GA/HbA1c ratio for diagnosis of diabetes and glycemic control: a comprehensive review. *Crit. Rev. Clin. Lab. Sci.* 54, 219–232. doi:10.1080/10408363.2017.1299684

Zhang, J., and Xiong, H. (2014). *Brain tissue preparation, sectioning, and staining*, 3–30. doi:10.1007/978-1-4614-8794-4_1

International Journal of *Molecular Sciences*

MDPI

*Article*

# Role of $Na^+/Ca^{2+}$ Exchanger (NCX) in Glioblastoma Cell Migration (In Vitro)

**Federico Brandalise [1], Martino Ramieri [2], Emanuela Pastorelli [2], Erica Cecilia Priori [2], Daniela Ratto [2], Maria Teresa Venuti [2], Elisa Roda [3], Francesca Talpo [2,*] and Paola Rossi [2,*]**

[1] Department of Biosciences, University of Milan, 20133 Milano, Italy; federico.brandalise@unimi.it
[2] Department of Biology and Biotechnology "L. Spallanzani", University of Pavia, 27100 Pavia, Italy; martino.ramieri01@universitadipavia.it (M.R.); emanuela.pastorelli@unipv.it (E.P.); ericacecilia.priori@unipv.it (E.C.P.); daniela.ratto@unipv.it (D.R.); mariateresa.venuti01@universitadipavia.it (M.T.V.)
[3] Laboratory of Clinical & Experimental Toxicology, Pavia Poison Centre, National Toxicology Information Centre, Toxicology Unit, Istituti Clinici Scientifici Maugeri IRCCS Pavia, 27100 Pavia, Italy; elisa.roda@icsmaugeri.it
* Correspondence: francesca.talpo@unipv.it (F.T.); paola.rossi@unipv.it (P.R.)

**Abstract:** Glioblastoma (GBM) is the most malignant form of primary brain tumor. It is characterized by the presence of highly invasive cancer cells infiltrating the brain by hijacking neuronal mechanisms and interacting with non-neuronal cell types, such as astrocytes and endothelial cells. To enter the interstitial space of the brain parenchyma, GBM cells significantly shrink their volume and extend the invadopodia and lamellipodia by modulating their membrane conductance repertoire. However, the changes in the compartment-specific ionic dynamics involved in this process are still not fully understood. Here, using noninvasive perforated patch-clamp and live imaging approaches on various GBM cell lines during a wound-healing assay, we demonstrate that the sodium-calcium exchanger (NCX) is highly expressed in the lamellipodia compartment, is functionally active during GBM cell migration, and correlates with the overexpression of large conductance K+ channel (BK) potassium channels. Furthermore, a NCX blockade impairs lamellipodia formation and maintenance, as well as GBM cell migration. In conclusion, the functional expression of the NCX in the lamellipodia of GBM cells at the migrating front is a conditio sine qua non for the invasion strategy of these malignant cells and thus represents a potential target for brain tumor treatment.

**Keywords:** glioblastoma; NCX; BK channel; cell migration; brain tumor



**Citation:** Brandalise, F.; Ramieri, M.; Pastorelli, E.; Priori, E.C.; Ratto, D.; Venuti, M.T.; Roda, E.; Talpo, F.; Rossi, P. Role of $Na^+/Ca^{2+}$ Exchanger (NCX) in Glioblastoma Cell Migration (In Vitro). *Int. J. Mol. Sci.* **2023**, *24*, 12673. https://doi.org/10.3390/ijms241612673

Academic Editors: Chiara Bastiancich, Aurélie Tchoghandjian and Alessandra Pagano

Received: 12 July 2023
Revised: 7 August 2023
Accepted: 8 August 2023
Published: 11 August 2023



## 1. Introduction

Glioblastoma (GBM) is the most common and aggressive primary brain tumor [1]. Patients have a median survival rate of 14.6 to 16.7 months and a progression-free survival rate of 6.2 to 7.5 months [2,3]. Only 30% of GBM patients survive longer than one year after diagnosis [2]. GBM represents 30% to 60% of all the central nervous system (CNS) primary tumors [4]. Compared to other CNS cancers, GBM is characterized by a pronounced invasiveness that contributes to a poor prognosis [2]. GBM is resistant to the currently available therapies, including surgical resection accompanied by chemotherapy and radiotherapy [5]. Indeed, the aggressive invasiveness and infiltrative behavior of glioma cells precludes complete surgical resection, with a consequent rapid relapse [6].

Numerous genetic mutations have been found to be associated with GBM, affecting oncogenes and tumor suppressor genes [6]. Interestingly, mutations affecting ion channels and pumps have been found in 90% of GBM cases [7] and seem to be responsible for their highly proliferative rate, as well as for the migratory behavior and invasiveness of these tumoral cells [8,9]. For this reason, the term oncochannels has been coined to define the ion channels most commonly related to tumor development [8–10], which therefore constitute

a potential pharmacological target for future treatment. Members of the $Ca^{2+}$-activated $K^+$ channel family, such as KCa3.1 (intermediate conductance $K^+$ channel or IK) and KCa1.1 (large conductance $K^+$ channel or BK), are especially involved in the development of gliomas by determining their uncontrolled growth, cell volume variation, and tumor cell migration [11]. An overexpression of BK channels has been reported in cell lines of GBM and in biopsies from GBM patients [12]. In addition, the BK channel structure is altered in GBM cells because of the expression of a splice variant producing the so-called gBK channel that displays an increased sensitivity to the intracellular calcium concentration ($[Ca^{2+}]i$) [13].

The fine regulation of the intracellular $Ca^{2+}$ and $Na^+$ concentrations is a key physiological process. Intracellular $Ca^{2+}$ works as a crucial signaling ion in both cytosolic and nuclear compartments, whereas $Na^+$ plays an essential role in regulating cellular osmolarity and cytoskeletal remodeling [14,15]. In parallel with voltage-gated ion channels and ATP-dependent pumps, the $Na^+/Ca^{2+}$ exchanger (NCX) also contributes to maintaining the physiological concentrations of $Na^+$ and $Ca^{2+}$ by mediating their bidirectional flux [16]. NCX has been already subject to investigation in GBM—in particular, related to the activity of the TRPC channel [17] or to $Ca^{2+}$-mediated cell death [18]. However, there is a paucity of reports on its role in GBM cell migration. The generally accepted stoichiometry of the NCX is an influx of three $Na^+$ ions for the extrusion of one $Ca^{2+}$ ion. However, depending on the intracellular concentrations of $Na^+$ and $Ca^{2+}$, it has been demonstrated that the NCX ionic flux ratio can vary from a minimum of 1:1 to a maximum of 4:1 [19,20]. When the intracellular $Ca^{2+}$ concentration rises, the return of the $Ca^{2+}$ concentration to the resting level is promoted by the forward mode of operation of the exchanger, coupling the influx of $Na^+$ to the uphill extrusion of $Ca^{2+}$. If the intracellular $Na^+$ concentration rises or membrane depolarization occurs, the reduced transmembrane electrochemical gradient for $Na^+$ leads the NCX to mediate the extrusion of intracellular $Na^+$ and the influx of $Ca^{2+}$, thus acting in reverse mode.

Three dominant genes comprising the NCX family have been identified in mammals, coding for the NCX1, NCX2, and NCX3 proteins. The NCX1 isoform is expressed in several tissues, including neurons and glial cells [21], whereas the NCX2 and NCX3 proteins have been found exclusively in neuronal and skeletal muscle.

Herein, we investigated the changes in the membrane conductance repertoire adopted by GBM cells during lamellipodia formation and their consequent migration in an in vitro model of invasion by using a battery of complementary assays and methods, e.g., the wound-healing assay, real-time time-lapse microscopy, immunofluorescence, and the non-invasive perforated patch-clamp technique. In particular, we focused on the functional expression of NCX in cells located within the migrating front, employing different GBM cell lines, i.e., U251 and U87, and a primary human glioblastoma culture enriched in stem cells (GSCs). Finally, we speculate about the osmotic and ionic mechanisms involving the NCX in promoting the formation of the migrating front during invasion.

## 2. Results

### 2.1. Cell Migration during a Wound-Healing Assay

We studied the behavior of U251 cells during 2D migration in a wound-healing scratch assay in monolayer confluent cultures, monitoring migration using real-time time-lapse microscopy throughout a 20 h time window. We recognized migrating cells based on their typical "polarized phenotype" characterized by digitiform and lamellipodia-like structures, oriented toward the empty area. We defined these cells as "edge cells", meaning cells at the edge of wound healing (for a comparison of cell morphologies, see the inserts in Figure 1a). Through time-lapse microscopy, we observed that cells at the edge of the scratch migrated longitudinally towards the empty area, causing a significant increase in wound closure from 31.60% after 5 h to 88.47% after 15 h. The wound area produced by the scratch was, on average, 400 µm wide before the start of migration, and complete closure of the wound area was obtained 20 h after the scratch (Figure 1b). Subsequently, we analyzed the movements

of these cells during migration, focusing on their position and trajectory at different time points. Cells at the edge of the scratch initially moved following a straight X-positive direction; then, after covering about 100 µm, they started to move in both the X-positive and Y-positive directions, toward the empty residual scratch area (Figure 1; see multimedia Video S1 in the Supplementary Materials). The dynamic of the migration process suggested that intercellular interactions during cell invasion played a significant role when the cells at the migrating front were at 100–200 µm from each other [22].

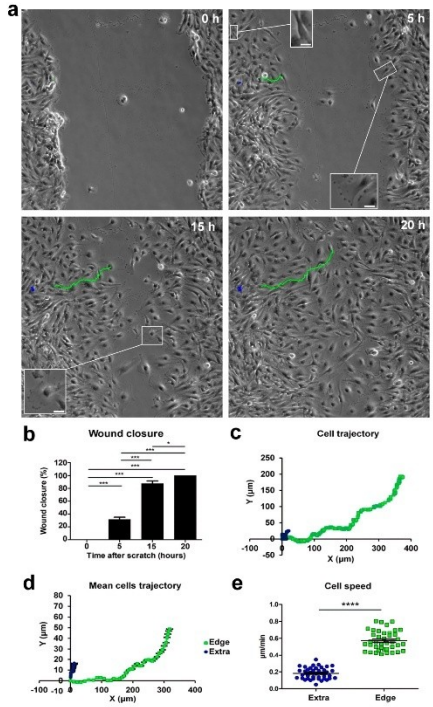


**Figure 1.** Time-lapse microscopy of cell migration in the wound-healing assay on U251 GBM cells. (**a**) Tracking of individual cells located in the extra-scratch (blue) and at the edge of the wounded area (green). Image shots at 0, 5, 15, and 20 h after the wound scratch. Scale bar: 100 µm. Inserts presenting high-magnification images of cells in different positions of the scratch and also showing a lamellipodia as a typical feature of the cells localized at the edge of the scratch. Scale bar: 10 µm (**b**) Wound closure percentages at 0, 5, 15, and 20 h after the wound scratch. (**c**) Plotting of the trajectories of one individual cell located outside (extra, blue) and one individual cell at the edge of the scratch (edge, green). Images were analyzed using the Chemotaxis Tool ImageJ software plugin (Version 2.0). (**d**) Mean trajectories of the cells outside (extra, blue, n = 40 cells) and at the edge of the scratch (edge, green, n = 40 cells). (**e**) Scatter plot of the velocity (µm/min) of single cells outside (extra, blue, n = 40 cells) and at the edge of the scratch (edge, green, n = 40 cells). *p*-values: * $p < 0.05$, *** $p < 0.001$, and **** $p < 0.0001$.

Cells at the edge moved with an average speed of about 0.6 µm/min, whereas cells located outside the wounded area moved slower, at an average speed of about 0.2 µm/min, and followed a random trajectory (Figure 1a,c,d). The speed difference between cells in the two scratch positions was highly statistically significant (extra-scratch: 0.18 ± 0.01 µm/min, n = 40; edge: 0.57 ± 0.02 µm/min, n = 40, *p*-value = $2.93 \times 10^{-30}$; Figure 1e), indicating that cells at the edge of the wounded area were committed to migration, and their direction and speed were directed to fill the empty area. Furthermore, in the light microscopy phase contrast, these cells at the edge of the wounded area displayed a typical "polarized phenotype" with a digitiform structure oriented towards the empty area (insert in Figure 1a, 5 h).

The migrating front can be appreciated in the time-lapse microscopy video (see multimedia Video S1 in the Supplementary Materials).

### *2.2. Noninvasive Perforated Patch-Clamp Recordings Reveal Dramatic Changes in the Physiology of GBM Cells at the Edge of the Migrating Front*

Noninvasive perforated patch-clamp recordings achieved by adding amphotericin in the patch pipette were chosen to avoid intracellular dialysis and changes in the physiological intracellular ions. Whole-cell perforated patch-clamp recordings were performed 1–4 h after the scratch procedure.

#### 2.2.1. Electrophysiological Passive Properties

Perforated patch-clamp recordings were performed on cells located in different positions of the scratch area: outside (extra, n = 25), inside (intra, n = 39), and at the edge of the scratch area (edge, n = 23; Figure 2a). GBM cells were classified as "edge cells" when, in a bright field, they showed a typical phenotype characterized by digitiform and lamellipodia-like structures polarized towards the wound healing but they did not yet enter inside the scratch (see Figure 1a). "Extra" cells were classified as cells that did not enter the scratch and did not have a lamellipodia-like structure (they usually had a typical bipolar morphology). "Intra cells" were classified as the ones that had already entered the wound healing.

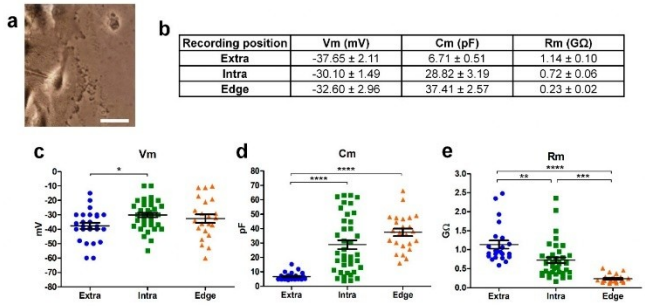


| Recording position | Vm (mV) | Cm (pF) | Rm (GΩ) |
|---|---|---|---|
| Extra | -37.65 ± 2.11 | 6.71 ± 0.51 | 1.14 ± 0.10 |
| Intra | -30.10 ± 1.49 | 28.82 ± 3.19 | 0.72 ± 0.06 |
| Edge | -32.60 ± 2.96 | 37.41 ± 2.57 | 0.23 ± 0.02 |

**Figure 2.** Passive parameters of the cells recorded outside ("Extra"; blue dots), within ("Intra"; green squares), and at the edge (orange triangles) of the wound area. (**a**) Example of a patch pipette approaching a cell at the edge of the scratch. Scale bar: 10 µm. (**b**) Resting membrane potential (Vm), membrane capacitance (Cm), and membrane resistance (Rm) mean values of cells recorded at different positions of the scratch. Scatter plots of the resting membrane potential (Vm; (**c**)), membrane capacitance (Cm; (**d**)), and membrane resistance (Rm; (**e**)). Number of cells: outside (n = 25), inside (n = 39), and at the edge of the scratch area (n = 23). *p*-values: * $p < 0.05$, ** $p < 0.01$, *** $p < 0.001$, and **** $p < 0.0001$.

The passive parameters were measured by analyzing the capacitive transient (see Section 4), and scattered values were reported (Figure 2).

The membrane potential (Vm), membrane capacitance (Cm), and membrane resistance (Rm) of the cells recorded within (intra, n = 39) and outside (extra, n = 25) the wounded area were significantly different ($p$-value = 0.043, $1.24 \times 10^{-7}$, and 0.0012, respectively), in accordance with what has been reported previously [8] (Figure 2). In particular, the Vm was more depolarized, Cm higher, and Rm lower for the cells recorded within the scratch compared to those located outside [8] (Figure 2). As concerns the cells recorded at the edge of the wounded area taking part in the migrating front, the Vm value was not statistically different from those of the other two groups (Figure 2c). The Cm of cells recorded at the edge were similar to the values of cells recorded within the wounded area and about five times higher compared to the cells recorded outside (Figure 2d, $p$-value = $5.17 \times 10^{-10}$). Furthermore, the Rm of the cells recorded at the edge of the wounded area were significantly lower than the Rm of the cells derived both within ($p$-value = 0.0001) and outside the wounded area ($p$-value = $9.04 \times 10^{-10}$, Figure 2e). Therefore, the high Cm and low Rm correlated with a larger cell surface and a bigger membrane conductance in the cells committed to migration.

### 2.2.2. Residual Inward Rectifier Potassium Current

Voltage-dependent currents were investigated in GBM cells recorded at different locations of the scratch area. Firstly, we used a hyperpolarizing voltage steps protocol where we applied consecutive −10 mV steps, from a holding potential of −40 mV down to −120 mV.

The cells inside the scratch displayed a residual inward rectifier current (Figure 3b) that was also present, although reduced in amplitude, in a fraction of the "edge" cells (n = 13/23; Figure 3c and Table 1). No current was recorded outside of the wounded area (Figure 3a and Table 1 [8]).

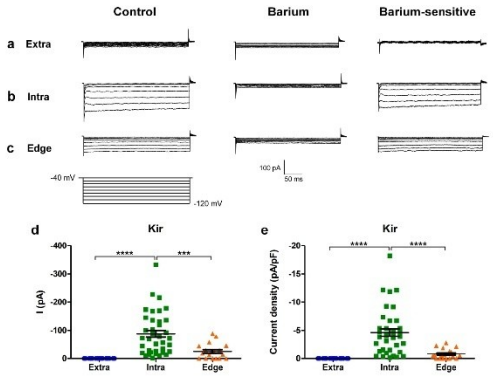


**Figure 3.** Hyperpolarizing protocol for investigating the inward rectifier current. (**a**,**b**) Experimental traces obtained using a hyperpolarizing voltage step protocol (bottom) in the cells recorded extra-scratch (**a**), intra-scratch (**b**), and at the edge (**c**) of the wounded area in the control conditions (left) and after perfusion with barium 1 mM (center). The barium-sensitive current was obtained by digital subtraction (right). (**d**) Scatter plot of the amplitude of the $K_{IR}$ current measured at −120 mV from individual cells at different locations of the scratch area. (**e**) Scatter plot of the current density of the $K_{IR}$ current measured at −120 mV from individual cells at different locations of the scratch area. $p$-values: *** $p < 0.001$, and **** $p < 0.0001$.

**Table 1.** Mean amplitude of the BK and KIR currents, measured at +140 mV and −120 mV, respectively, in cells recorded extra, intra, and at the edge of the wounded area. N.P. = not present.

| Recording Position | BK (pA) | BK (pA/pF) | Kir (pA) | Kir (pA/pF) |
|---|---|---|---|---|
| Extra | 113.84 ± 19.79 (n = 25) | 11.59 ± 1.08 (n = 25) | N.P. | N.P. |
| Intra | 547.41 ± 81.46 (n = 37) | 19.36 ± 1.86 (n = 37) | −87.81 ± 12.41 (n = 37) | −4.62 ± 0.67 (n = 37) |
| Edge | 820.64 ± 92.39 (n = 23) | 27.20 ± 2.21 (n = 23) | −37.94 ± 6.71 (n = 19) | −0.88 ± 0.20 (n = 19) |

The residual inward rectifier current was blocked by 1 mM barium (Figure 3b,c, central panel), and its biophysical properties suggested the involvement of Kir4.1 channels [8].

In particular, the amplitudes of the inward current recorded at −120 mV were significantly higher in the cells inside the scratch compared to the other experimental conditions (Figure 3d; extra n = 25; intra n = 37; edge n = 19; extra vs. intra $p$-value = $3.02 \times 10^{-8}$; extra vs. edge $p$-value = 0.33 (not significant); intra vs. edge $p$-value = 0.00026). In accordance, the inward current density recorded at −120 mV was also significantly higher in the cells inside compared to the other conditions (Figure 3e; extra n = 25; intra n = 37; edge n = 19; extra vs. intra $p$-value = $3.11 \times 10^{-8}$; extra vs. edge $p$-value = 0.99 (not significant); intra vs. edge $p$-value = 0.0000195).

2.2.3. "Edge" GBM Cells Expressed BK Channels and Expressed a Peculiar Inward Current

Voltage-dependent currents elicited by +10 mV depolarizing voltage steps from a holding potential of −60 mV up to +140 mV were subsequently investigated in GBM cells located at different locations of the scratch area.

Cells recorded outside the scratch ("extra") exhibited a small outward current in response to consecutive depolarizing steps (Figure 4a; n = 25), while cells recorded within the wounded area showed a greater outward rectifier current that was TEA- and clotrimazole-sensitive, confirming previously published data [8,9] (Figure 4b,c and Table 1). Notably, cells recorded at the edge of the scratch displayed a larger outward rectifier current compared to the cells recorded both inside ($p$-value = 0.038) and outside ($p$-value = $1.23 \times 10^{-7}$) the wounded area.

Surprisingly, during the depolarizing protocol, a constitutive inward current was recorded in the cells located at the edge of the wounded area (see the arrow in Figure 4c). In cells recorded at the edge, at test potentials more positive than +50 mV, the inward current was followed by an outward rectifier current (n = 18/20, Figure 4c, left traces). Therefore, to isolate the inward current from all the possible outward potassium currents, we locally perfused TEA and clotrimazole (Figure 4c, middle traces), blockers of both the BK and IK potassium channels. The experimental traces for the TEA- and clotrimazole-sensitive current, obtained by digital subtraction (Figure 4c, right traces), were used to quantify the outward currents. The amplitudes of the outward currents recorded at +140 mV were significantly different among the three groups of cells at different locations of the scratch area (Figure 4d; extra n = 25; intra n = 37; edge n = 23; extra vs. intra $p$-value = 0.00025; extra vs. edge $p$-value = 0.00000012; intra vs. edge $p$-value = 0.038). Accordingly, the outward current densities recorded at +140 mV were significantly different among the three groups of cells at different locations of the scratch area (Figure 4e; extra n = 25; intra n = 37; edge n = 23; extra vs. intra $p$-value = 0.00795; extra vs. edge $p$-value = 0.00000042; intra vs. edge $p$-value = 0.00819).

In addition, the averaged current–voltage relationship was computed for the currents recorded in cells at the edge of the scratch, both in the control conditions, and after TEA and clotrimazole local perfusion (Figure 4f). The inward current found in these cells displayed a peculiar current–voltage relationship, increasing proportionally to the depolarized test potentials. We further investigated this inward current to examine its biophysical and pharmacological properties.

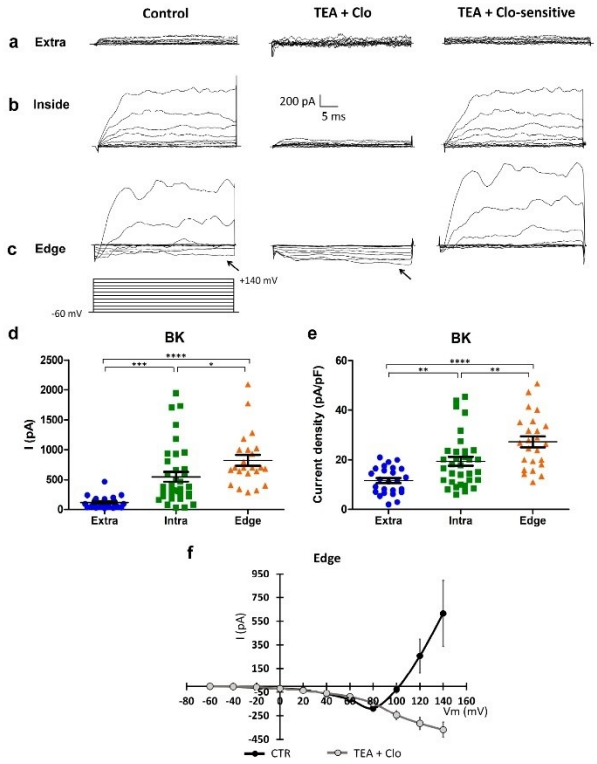


**Figure 4.** Expression of BK channels, and expression of a peculiar inward current elicited by a depolarization protocol in the "edge" GBM cells. (**a**–**c**) Currents elicited by depolarizing steps, from the holding potential of −60 mV, in cells recorded outside (**a**), within (**b**), and at the edge (**c**) of the wounded area in the control condition (left traces) and after clotrimazole 10 µM and TEA 3 mM local perfusion (central traces). Digital subtraction shows TEA- and clotrimazole-sensitive currents (right traces). The depolarizing voltage step protocol is shown at the bottom. Arrows indicate the inward current present in the control condition and after TEA and clotrimazole local perfusion in the cells recorded at the edge. (**d**) Scatter plot of single cell values showing the absolute values of BK currents at +140 mV recorded outside (extra, n = 25, blue dots), within (intra, n = 37, green squares), and at the edge (edge, n = 23, orange triangles) of the wounded area. (**e**) Scatter plot of single cell values showing the BK current density at +140 mV recorded outside (extra, n = 25, blue dots), within (intra, n = 37, green squares), and at the edge (edge, n = 23, orange triangles) of the wounded area. (**f**) Mean I–V relationship in the cells (n = 8) recorded at the edge of the wounded area in the control conditions (CTR) and after the local perfusion of TEA + clotrimazole. *p*-values: * $p < 0.05$, ** $p < 0.01$, *** $p < 0.001$, and **** $p < 0.0001$.

2.2.4. Electrophysiological Characterization of the Depolarization-Mediated Inward Current in "Edge" GBM Cells

To further characterize the unknown inward current recorded from migrating cells at the edge of the wound, we tested different depolarizing step protocols.

It should be noted that, at test potentials where the BK current activates, the total current recorded corresponds to the algebraic sum of the inward and the outward BK rectifier current. To reduce or avoid contamination of the BK current, and to enlarge the interval of potentials to be studied, we elicited the steps from –120 mV.

Furthermore, to verify whether the inward current was present in different cell lines, we repeated the same wound-healing assay on a human glioblastoma primary culture enriched in stem cells (GSCs) and on the U87 cell line. Cells were recorded at the edge of the wound healing and chosen following the above-mentioned criteria: the position at the edge, the "polarized phenotype", and the presence of the digitiform structure, lamellipodia-like. After eliciting the same depolarizing protocol from −120 mV, 1–4 h after the scratch, an inward current was recorded in 87.15% (n = 14/16) of U251 cells, 83.3% of GSCs (n = 10/12), and 83% of U87 cells (n = 8/10) (Figure 5).

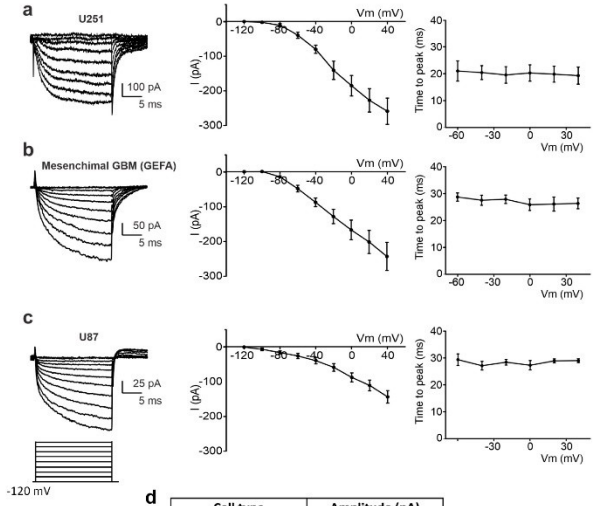


| Cell type | Amplitude (pA) |
|---|---|
| U251 (n=14) | -258.7 ± 37.9 |
| GSCs (n=10) | -239.0 ± 55.9 |
| U87 (n=8) | -147.6 ± 11.6 |

**Figure 5.** Detection of the inward current at the edge of the wounded area in different cell lines. (**a**–**c**) Left: experimental traces elicited by the application of a depolarizing protocol of the voltage steps (shown at the bottom) from a holding potential of −120 mV to + 40 mV in U251 (**a**), mesenchymal GSCs (**b**), and U87 cells (**c**). Center: mean I–V relationship for U251 (n = 14 cells, (**a**)), mesenchymal GSCs (n = 10 cells, (**b**)), and U87 (n = 8 cells, (**c**)). Right: average inward current activation time to peak measured at different test potentials for U251 (n = 14 cells, (**a**)), mesenchymal GSCs (n = 10 cells, (**b**)), and U87 (n = 8 cells, (**c**)). (**d**) Averaged amplitudes of the inward current at +40 mV, measured by means of a depolarizing step from a holding potential of −120 mV, recorded in different cell lines at the edge of the wounded area.

The similarity among the three cell lines, in terms of the current–voltage relationship and time to peak values (Figure 5, central and right panels), revealed that, in edge cells, all the lines expressed this depolarization-mediated inward current, suggesting that this current is a common feature in GBM migrating cells. Figure 5d shows the mean amplitude of the inward current recorded at +40 mV in U251 (n = 14), U87 (n = 8), and mesenchymal GBM (n = 10) edge cells. The amplitudes were not statistically different among the three tested cell lines.

Noteworthy is the consistency of the current–voltage relationship among the three tested cell lines (middle panels in Figure 5a–c), as well as the similarity in the time to peak values and voltage independence of this parameter (right panels in Figure 5a–c).

#### 2.2.5. The Inward Current of the Edge Cells Is Sensitive to a Reduction of Extracellular $Na^+$ Consistent with Activation of the Sodium-Calcium Exchanger (NCX)

The inward current recorded from cells at the edge of the scratch showed a peculiar current–voltage relationship that did not correspond to a voltage-dependent current (Figure 5, middle panels). We hypothesized that this current could arise by the activation of specific pumps or exchangers involved in the complex modulation of the GBM migrating cells. Specifically, we hypothesized a crucial role for the sodium-calcium exchanger (NCX) in the generation of this peculiar current.

We therefore performed a set of experiments aimed at testing this idea by analyzing the effects of blocking the NCX in the inward current.

A "Na-free" extracellular solution was applied to block NCX activity [23]. The inward current amplitude was at first assessed under the control conditions in U251 edge cells; the subsequent perfusion of the "Na-free" solution (see Section 4) robustly inhibited the inward current (Figure 6a). On average, the amplitude recorded at +40 mV decreased from $-368.14 \pm 75.99$ pA to $-109.74 \pm 59.56$ pA (n = 5, *p*-value = 0.022, Figure 6b).

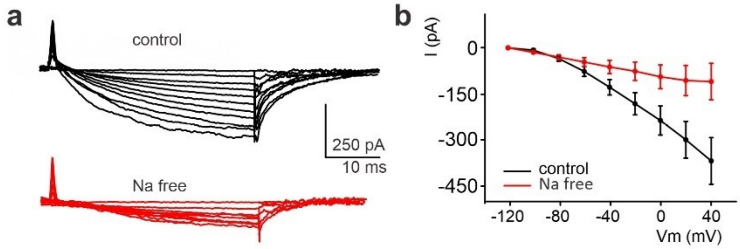


**Figure 6.** Significant reduction of the inward current detected in the U251 edge cells following the perfusion of a Na-free solution. (**a**) Experimental traces elicited by depolarizing the voltage steps from −120 mV to +40 mV before (black traces) and after local perfusion of the extracellular Na-free solution containing lithium chloride (LiCl, red traces) instead of sodium chloride (NaCl). (**b**) Mean I–V relationships before and after LiCl local perfusion (n = 5).

#### 2.2.6. Pharmacological Identification of the Sodium-Calcium Exchanger (NCX) and Its Role in the Migration Process

To confirm the involvement of the NCX, we performed an extensive pharmacological characterization of the inward current, administering drugs that specifically interfered with NCX activity. NCX is inhibited by the external perfusion of nickel [24,25]. To isolate the putative NCX-mediated component of the inward current, we recorded "edge" U251 cells before and after nickel local perfusion (1 mM). In this case, the recordings were performed in the presence of clotrimazole 10 µM and TEA 3 mM to be sure to isolate the sole inward current and then accurately isolate the nickel-sensitive component. The nickel application significantly reduced the inward current, as shown in Figure 7a. At +140 mV, the current

was reduced from −222.39 ± 32.59 pA to −22.01 ± 53.06 pA (n = 5; *p*-value = 0.042; paired *t*-test, Figure 7b). The time constant of the inward current was consistent with the pool recorded in Figure 5 (n = 5; Figure 7c).

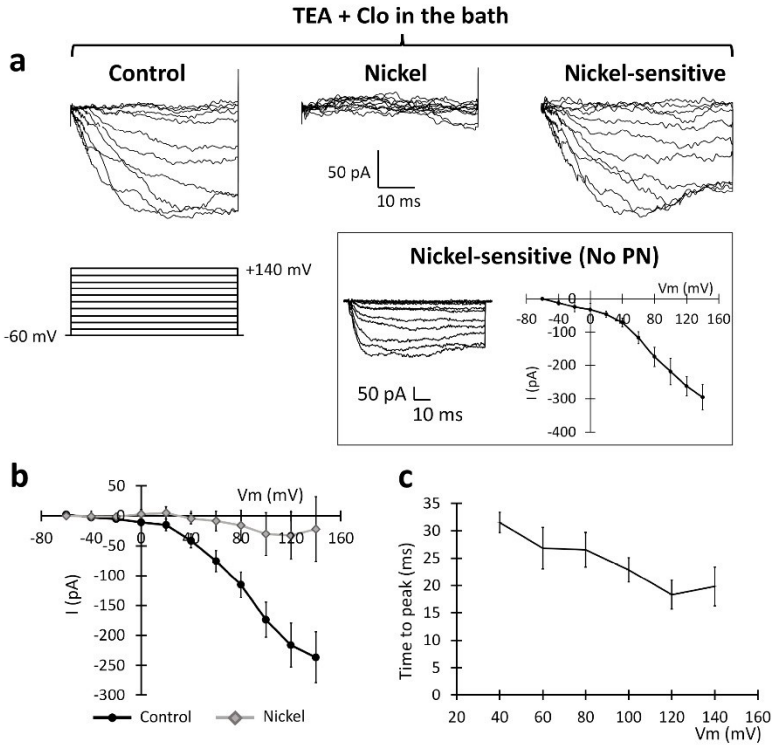


**Figure 7.** Sensitivity of the inward current recorded in the U251 edge cells to 1 mM nickel extracellular perfusion. (**a**) Experimental traces elicited by depolarizing the voltage steps of +10 mV from the holding potential of −60 mV to +140 mV (protocol shown at the bottom) in the control conditions (left traces) and after the local perfusion of 1 mM nickel (central traces). Digital subtraction shows the nickel-sensitive current (right traces). Inset: The PN leak subtraction method (see the Section 4) does not significantly alter the I–V plot of the inward current. (**b**) Mean I–V relationships before (black dots) and after (gray rhombuses) the local perfusion of nickel (n = 5 cells). (**c**) Average inward current activation time to peaks measured at different test potentials.

To further prove the NCX-mediated nature of the recorded inward current, we tested the effect of 5 min of the local perfusion of bepridil (100 μM), an antagonist of the NCX. Figure 8 illustrates experimental traces recorded in the control conditions and after the local perfusion of bepridil (100 μM). In the presence of bepridil, the average amplitude recorded

at +40 mV decreased from −300.09 ± 85.95 pA to +34.19 ± 19.71 pA (n = 6, *p*-value = 0.049). The administration of the NCX antagonist almost abolished the inward current.

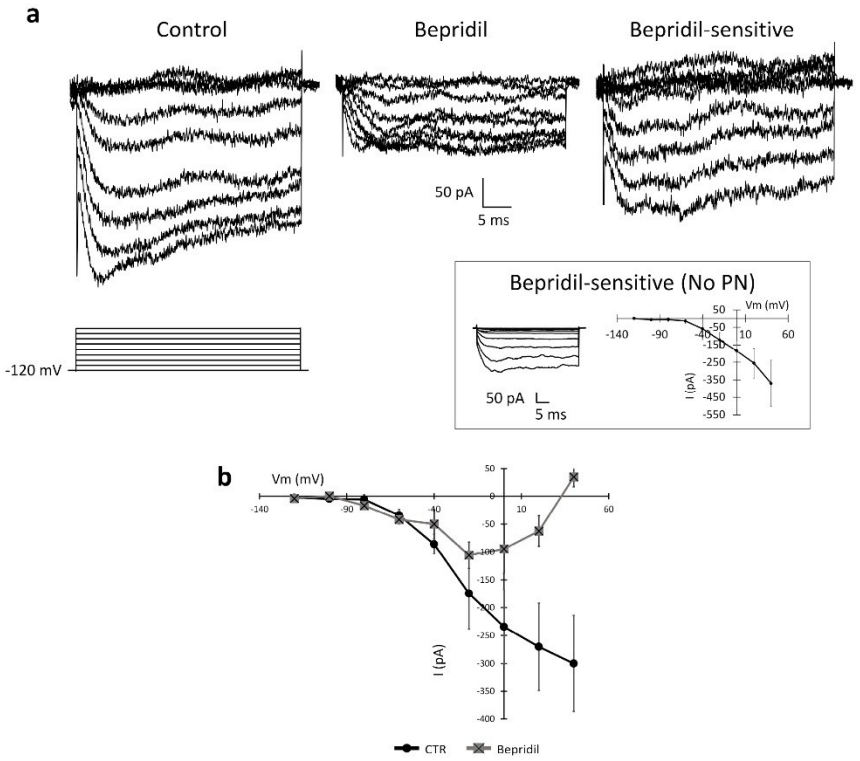


**Figure 8.** Inhibition of the inward current detected in the U251 edge cells by 100 μM bepridil, a competitive antagonist of the NCX. (**a**) Experimental traces elicited by depolarizing the voltage steps from −120 mV to +40 mV before (black traces) and after the local perfusion of bepridil (light grey traces). Inset: The PN leak subtraction method does not significantly alter the I–V plot of the inward current. (**b**) Mean I–V relationship before and after bepridil local perfusion (n = 6 cells).

We also evaluated the effects of bepridil on the passive properties of the investigated cells. The membrane capacitance was significantly reduced when bepridil was added to the medium compared to the control conditions (control: 51.4 ± 4.6 pF, n = 5; bepridil: 40.9 ± 5.2 pF; *p*-value = 0.02), consistent with a reduction in the cell surface area. The membrane resistance was not significantly altered (control: 379.6 ± 14.0 MΩ, n = 5; bepridil: 163.1 ± 11.4 MΩ; *p*-value = 0.18).

2.2.7. Effect of the Block of Na-K ATPase on the NCX Inward Current and the BK Outward Current

The NCX activity is strictly dependent on the intra- and extracellular $Na^+$ and $Ca^{2+}$ concentrations, whereas the BK current is sensitive to the intracellular $Ca^{2+}$ concentration. We tested the effect of the Na-K ATPase blocker ouabain on the currents elicited by depolarization by applying two different protocols: (i) the first protocol started from a holding potential of −120 mV (Figure 9); (ii) the second protocol started from a holding potential of −60 mV (Figure 10). The former depolarizing protocol was chosen to study the NCX current and the latter to evaluate a possible effect of the Na-K ATPase blocker ouabain on the outward BK current [26].

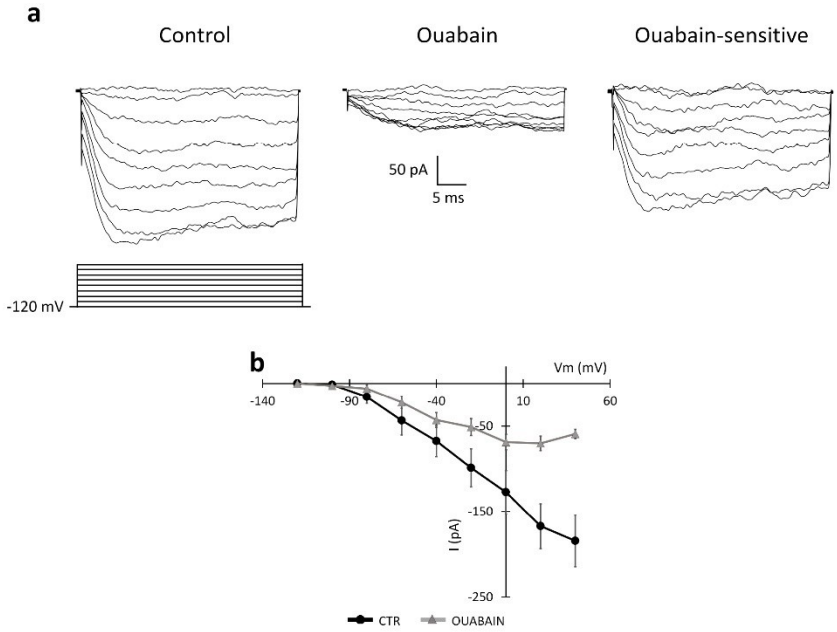


**Figure 9.** Effect of the Na-K ATPase blocker ouabain (perfused for about 10–15 min) on the NCX current in the U251 edge cells. (**a**) Experimental traces elicited by applying a voltage step depolarizing protocol from a holding potential of −120 mV (protocol shown at the bottom) in the control conditions (left traces) and after the local perfusion of ouabain 500 µM (central traces). The ouabain-sensitive current was obtained by digital subtraction (right traces). (**b**) Mean I–V relationships (n = 5 cells) recorded in the control conditions (CTR, black dots) and after the perfusion of ouabain (gray triangles).

Figure 9 shows experimental traces recorded in the control conditions and after the local perfusion of ouabain (500 µM) during the application of the first protocol starting from the −120 mV holding potential. Digital subtraction of the traces for the isolation of the ouabain-sensitive component is also displayed. After the local perfusion of ouabain, the amplitude at +40 mV decreased from −184.45 ± 30.29 pA to −59.31 ± 5.31 pA (n = 5, *p*-value = 0.018).

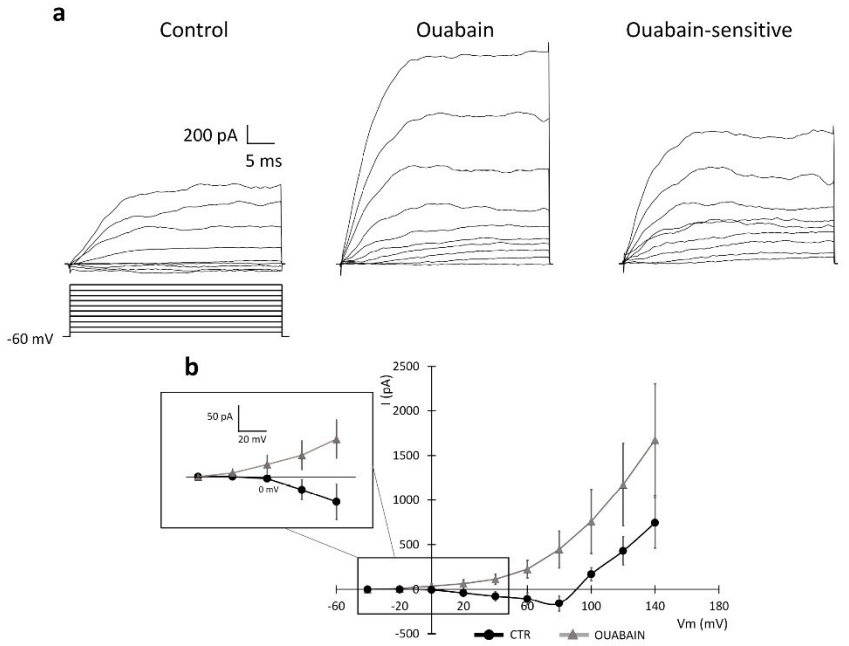


**Figure 10.** Effect of the Na-K ATPase blocker ouabain (perfused for about 10–15 min) on the BK current in U251 edge cells. (**a**) Experimental traces elicited by applying a voltage step depolarizing protocol from a holding potential of −60 mV (protocol shown at the bottom) in the control conditions (left traces) and after the local perfusion of ouabain 500 µM (central traces). The ouabain-sensitive current was obtained by digital subtraction (right traces). (**b**) Mean I–V relationships (n = 5 cells) recorded in the control conditions (CTR, dots) and the ouabain condition (ouabain, triangles). Insert shows the averaged I–V in the interval range between −40 mV and +40 mV at higher magnification to show the I–V shift after the local perfusion of ouabain.

Because the block of the Na-K ATPase is associated with a reversed mode of the exchanger, which normally extrudes calcium from the cell [26], we tested a possible effect of changes in the $Ca^{2+}$ concentration on the BK channels. To this end, we performed experiments using the second protocol, starting from the −60 mV holding potential, as shown in Figure 10. Following the perfusion of 500 µM ouabain, the I–V relationship shifted from inward to outward at the most hyperpolarized steps to +80 mV (see also the insert in Figure 10), and the amplitude of the outward current at +140 mv changed from 846.95 ± 282.79 pA to 1676.6 ± 629.57 pA (n = 5, *p*-value = 0.11, not significant) (Figure 10). The insert in Figure 10 shows the averaged I–V magnified in the interval range between −40 mV and +40 mV to make more visible the I–V shift from inward to outward after the local perfusion of ouabain.

Therefore, these data suggest that a reduction in the forward mode of the NCX and the decrease in the $Ca^{2+}$ extrusion may indeed positively activate the BK and gBK currents.

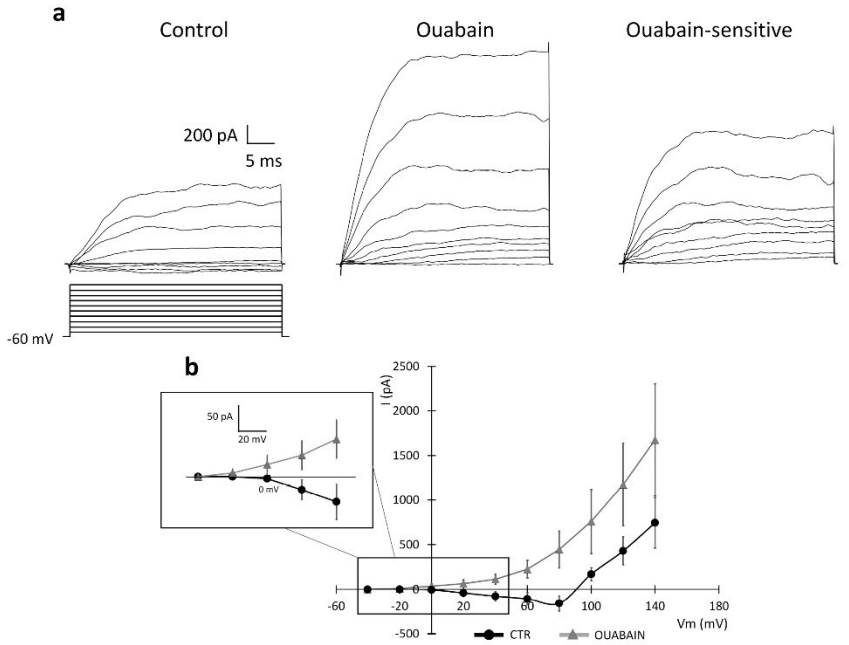


**Figure 10.** Effect of the Na-K ATPase blocker ouabain (perfused for about 10–15 min) on the BK current in U251 edge cells. (**a**) Experimental traces elicited by applying a voltage step depolarizing protocol from a holding potential of −60 mV (protocol shown at the bottom) in the control conditions (left traces) and after the local perfusion of ouabain 500 µM (central traces). The ouabain-sensitive current was obtained by digital subtraction (right traces). (**b**) Mean I–V relationships (n = 5 cells) recorded in the control conditions (CTR, dots) and the ouabain condition (ouabain, triangles). Insert shows the averaged I–V in the interval range between −40 mV and +40 mV at higher magnification to show the I–V shift after the local perfusion of ouabain.

Because the block of the Na-K ATPase is associated with a reversed mode of the exchanger, which normally extrudes calcium from the cell [26], we tested a possible effect of changes in the $Ca^{2+}$ concentration on the BK channels. To this end, we performed experiments using the second protocol, starting from the −60 mV holding potential, as shown in Figure 10. Following the perfusion of 500 µM ouabain, the I–V relationship shifted from inward to outward at the most hyperpolarized steps to +80 mV (see also the insert in Figure 10), and the amplitude of the outward current at +140 mv changed from 846.95 ± 282.79 pA to 1676.6 ± 629.57 pA (n = 5, *p*-value = 0.11, not significant) (Figure 10). The insert in Figure 10 shows the averaged I–V magnified in the interval range between −40 mV and +40 mV to make more visible the I–V shift from inward to outward after the local perfusion of ouabain.

Therefore, these data suggest that a reduction in the forward mode of the NCX and the decrease in the $Ca^{2+}$ extrusion may indeed positively activate the BK and gBK currents.

in bepridil vs. extra control 0.18 ± 0.01 µm/min, n = 40 for both experimental conditions, $p$-value = $2.00 \times 10^{-18}$; edge: 0.25 ± 0.02 µm/min in bepridil vs. edge control 0.57 ± 0.02 µm/min, n = 40 for both experimental conditions, $p$-value = $1.36 \times 10^{-22}$; unpaired $t$-test; Figure 14d). The difference in values between "extra" and "edge" cells in the presence of bepridil was statistically significant ($p$-value = $4.13 \times 10^{-20}$; unpaired $t$-test; Figure 14e).

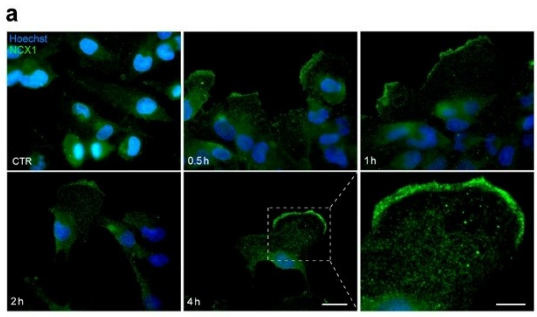


d

| Lamellipodia | | | | | |
|---|---|---|---|---|---|
| Time after scratch (hours) | OD | Statistical significance (p-value) | | | |
| | | 0.5 | 1 | 2 | 4 |
| CTR | 6.77 ± 0.18 | $1.2 \times 10^{-5}$ | $< 1 \times 10^{-14}$ | $< 1 \times 10^{-14}$ | $< 1 \times 10^{-14}$ |
| 0.5 | 8.93 ± 0.29 | | $1.14 \times 10^{-5}$ | $< 1 \times 10^{-14}$ | $< 1 \times 10^{-14}$ |
| 1 | 11.24 ± 0.30 | | | $1.5 \times 10^{-5}$ | $< 1 \times 10^{-14}$ |
| 2 | 13.79 ± 0.38 | | | | $< 1 \times 10^{-14}$ |
| 4 | 21.86 ± 0.40 | | | | |

**Figure 11.** NCX1 expression in U251 cells was specifically upregulated in the lamellipodia after the scratch. (**a**) Representative micrographs showing NCX1 immunopositivity (green signal) in the cytoplasm and lamellipodia of cells located at the edge of the scratch in the control conditions (CTR) and 0.5, 1, 2, and 4 h after the scratch. Nuclear counterstaining with Hoechst 33258 (blue). Scale bar: 20 µm. Lower right panel: high-magnification (180×) micrograph showing the lamellipodia 4 h after the scratch. Scale bar: 10 µm. (**b**,**c**) Optical density (OD) scatter plots illustrating single-cell measurements acquired in the cytoplasm (**b**) and lamellipodia (**c**) in the control conditions (CTR) and at different time points after the scratch. Data are expressed as the mean ± SEM. (**d**) Lamellipodia mean OD values and relative statistical significance in the basal conditions (CTR) and 0.5, 1, 2, and 4 h after the scratch. Data are expressed as the mean ± SEM. $p$-values were calculated using one-way ANOVA, followed by the Bonferroni post hoc test.

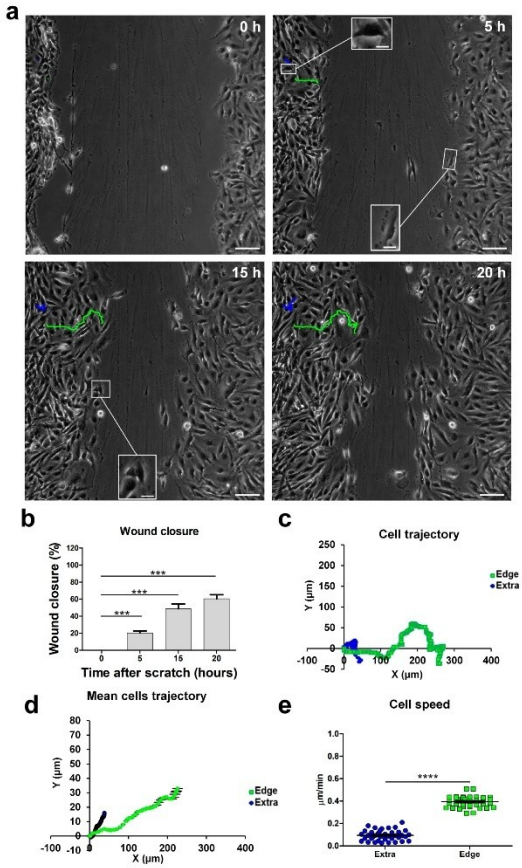


**Figure 12.** Blockade of NCX1 with nickel in U251 cells' impaired migration trajectory and speed in the wound-healing assay. (**a**) Tracking of individual cells located in the extra-scratch (blue) and one at the edge of the wounded area (green) in the presence of nickel 200 µM. Images captured at 0, 5, 15, and 20 h after the wound scratch. Scale bar: 100 µm. Inset: a typical lamellipodia of a cell localized at the edge of the scratch; lamellipodia can be detected 5 h after the scratch, but they are less visible over time. Scale bar: 10 µm. (**b**) Wound closure percentage at 0, 5, 15, and 20 h after the wound scratch in the nickel condition. (**c**) Plotting of the trajectories of one individual cell located outside (extra, blue) and one individual cell at the edge of the scratch (edge, green). Images were analyzed with the Chemotaxis Tool ImageJ software plugin (Version 2.0). (**d**) Mean trajectories of the cells outside (extra, blue, n = 40 cells) and at the edge of the scratch (edge, green, n = 40 cells). (**e**) Scatter plot of the velocity (µm/min) of single cells outside (extra, blue, n = 40 cells) and at the edge of the scratch (edge, green, n = 40 cells). *p*-values: *** $p < 0.001$, and **** $p < 0.0001$.

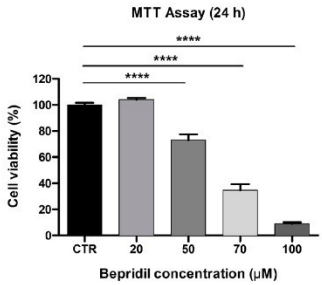


**Figure 13.** Effects of bepridil on cell viability/proliferation of U251 cells. Data obtained with the MTT vitality assay after 24 h exposure to increasing concentrations (20, 50, 70, and 100 μM) of bepridil. The relative cell viability is expressed as a percentage relative to the untreated control cells. Data are expressed as the mean ± SEM. *p*-values: **** $p < 0.0001$ compared to the control (100% cell viability).

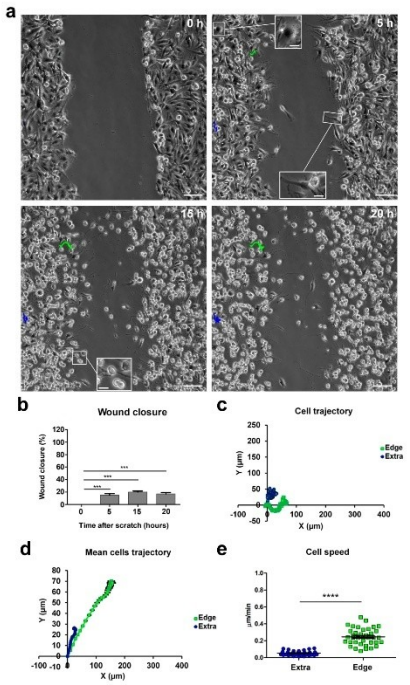


**Figure 14.** Blockade of NCX1 with bepridil in U251 cells' impaired migration trajectory and speed in the wound-healing assay. (**a**) Tracking of individual cells located in the extra-scratch (blue) and at the

edge of the wounded area (green) in the presence of bepridil 50 µM. Images captured at 0, 5, 15, and 20 h after the wound scratch. Scale bar: 100 µm. Inserts (scale bar: 10 µm) depicting lamellipodia as typical features of cells localized at the edge of the scratch; lamellipodia are evident 5 h after the scratch, but they are no longer detectable over time, i.e., 15 and 20 h after the scratch. (**b**) Wound closure percentage at 0, 5, 15, and 20 h after the wound scratch in the bepridil condition. (**c**) Plotting of the trajectories of one individual cell located outside (edge, blue) and one individual cell positioned at the edge of the scratch (edge, green). Images were analyzed by the Chemotaxis Tool ImageJ software plugin (Version 2.0). (**d**) Mean trajectories of cells outside (extra, blue, n = 40 cells) and at the edge of the scratch (edge, green, n = 40 cells). (**e**) Scatter plot of the velocity (µm/min) of single cells outside (extra, blue, n = 40 cells) and at the edge of the scratch (edge, green, n = 40 cells). *p*-values: *** $p < 0.001$, and **** $p < 0.0001$.

## 3. Discussion

Glioblastoma is characterized by its unique ability to grow in a confined space and to infiltrate the cerebral parenchyma. The characterization of ion channels, exchangers, and transporters contributing to the devastating invasiveness of GBM is a crucial task that requires further investigation.

Available data describing ion channels, transporters, and exchangers in GBM hypothesize two main processes to explain their role in cell invasion: (i) the formation of a hyperosmotic intracellular environment that triggers a water influx with a consequent cellular volume increase at the leading edge of the cells; (ii) cell shrinkage of the posterior edge of the cell achieved by an efflux of salt, followed by a reduction in the cytosolic water content [11,14,27,28]. In particular, the current assumptions suggest that, through NKCCl and Na-K ATPase, $Cl^-$ and $K^+$ both accumulated intracellularly, giving rise to the electrochemical driving force needed for triggering these osmotic effects [11,14,27,28]. More recently, other conductance has been described to play a major role in the regulation of the chloride dynamics, such as the volume-regulated anion channel (VRAC/LRRC8) [29,30]. However, the importance of the VRAC/LRRC8 channel in GBM migration is still under debate [31] due to possible variabilities in both the cell line adopted between these works and the migration model used.

One of the strategies adopted by tumor cells to improve proliferation and survival is the up- and downregulation of intracellular $Ca^{2+}$ levels, thus gaining control of intracellular signaling and the metabolism [32]. To this aim, the expression, function, and localization of $Ca^{2+}$ pumps, channels, and exchangers are strongly modulated in cancer cells, although the molecular pathways recruited for these detrimental alterations are still poorly understood, and further research is needed.

HereIn the current study we demonstrated, for the first time, the involvement of the sodium-calcium exchanger (NCX) in GBM-invasive processes, and we tried to elucidate the possible mechanisms responsible for its alteration.

NCX is ubiquitously expressed in mammals, where it exists in three isoforms (NCX1, NCX2, and NCX3), distributed in the plasma membrane. NCX plays a major role in the homeostasis of the intracellular $Ca^{2+}$ concentration, presenting two distinct functional modes: in the so-called forward mode, NCX provides an effective influx of three $Na^+$ ions to the uphill extrusion of one $Ca^{2+}$, whereas, in the reverse mode, it promotes a $Ca^{2+}$ influx against the $Na^+$ efflux. Intriguingly it has also been shown to be involved in the regulation of the migration of the microglia [33]. A large number of effectors can modulate NCX expression and activity, from the pH and hypoxia to intracellular phosphorylation [34,35]. This might explain the unexpected current–voltage relationship of the exchanger at high depolarizing values described here, which we intend to examine further in future investigations.

Several studies have shown the involvement of NCX in cardiac disease, and a therapeutic potential has been proposed for NCX inhibitors to treat heart injuries [36]. However, the experimental evidence for the functional role of NCX in glioblastoma has not been fully clarified [37]. To date, NCX has been reported to play a role mainly in proliferation and

tumor growth [18,38], but little is known about its role in GBM cell migration. In prostate cancer, melanoma, and leukemia, NCX preferentially works in the reverse mode, although the lack of specificity of the KB-R7943 inhibitor used in these investigations complicates the interpretation of the results [35,37].

Our data collected with time-lapse microscopy applied during the wound-healing assay identified, at the edge of the scratch, cells committed to migration. These cells displayed a characteristic feature, the lamellipodia, and were capable of migrating in a specific direction and at high speed to fill in the empty space created by the scratch. We recorded whole-cell currents from these cells by means of amphotericin-perforated patch-clamp so as to avoid intracellular dialysis and alterations of the intracellular calcium and chloride concentrations, as previously described [13].

We found that the cells committed to migration displayed a larger surface and a higher conductance compared to the nonmigrating cells, as demonstrated by the higher Cm and lower Rm, respectively. Upon the depolarizing steps, U251 cells showed a constitutive outward BK current with the same biophysical and pharmacological properties previously described [8,9]. The BK current recorded at the edge was significantly greater compared to the current recorded within the wounded area.

Unexpectedly, 90% of the edge cells displayed, in addition to the BK current, a constitutive inward current never recorded before, neither outside nor inside the wounded area. This peculiar inward current was activated during depolarization, started to appear at a membrane potential of about −20 mV, and displayed an "ohmic" I–V relationship at all tested membrane voltages (up to +140 mV) without presenting a time-dependent inactivation. The same inward current, with a similar amplitude, current–voltage relationship, and time to peak, was also present in GBM cells derived from human glioblastoma cultures enriched in mesenchymal stem cells (GSCs) and in U87 cells when recorded at the edge of the wound-healing assay in a perforated patch-clamp configuration. Therefore, we hypothesized that this inward current is a common feature of GBM.

Based on our pharmacological characterization of this peculiar inward current, we concluded it was mainly mediated by the NCX. Indeed, we demonstrated that this inward current was significantly reduced when recordings were performed in a sodium-free solution. The inward current was also sensitive to bepridil, an antagonist of the NCX. Since the NCX is inhibited by the external perfusion of nickel, we managed to isolate the NCX-mediated component (i.e., the nickel-sensitive component). To avoid potential incomplete blocks of the NCX, future experiments will also replicate our findings using a CRISPR/Cas9 KO model for the same cell lines. A large number of effectors can modulate the NCX expression and activity, from the pH and hypoxia to intracellular phosphorylation [34,35]. This might be one of the reasons why the current–voltage relationship of the exchanger at highly depolarized values has an unexpected trend. Additionally, it is possible that, at higher depolarized holding potentials, other conductance is also activated along with the NCX-mediated current. Further experiments are planned to investigate in greater detail the modulatory mechanisms of the NCX occurring during the invasion by GBM cells. To further confirm the role of NCX in glioblastoma, in vivo experiments should also be considered as in 2D cultures, and by using the scratch assay, we might have a relatively limited predictive value of glioblastoma cell behavior in a more complex and physiological environment.

We then confirmed the presence of NCX by immunofluorescence staining, showing that, during migration, the expression levels of this exchanger increased over time in the lamellipodia of the edge cells but not in the cytoplasm. Finally, a blockade of the forward $Na^+/Ca^{2+}$ exchanger by nickel and bepridil significantly slowed the time for wound closure [18], confirming an active role for the NCX in the GBM invasion process. All features of the migration process in the control conditions were impaired in the presence of nickel or bepridil, and the cells at the edge no longer exhibited the typical lamellipodial structures. Interestingly, in the presence of bepridil, the cells at the edge tended to emit a long "neurite-like structure", and the soma was unable to cover a distance greater than 100 μm while exhibiting a very low speed during the migration process.

Subsequently, we demonstrated that NCX activity depended on a Na-K ATPase for the maintenance of the sodium gradient. The reduction in NCX activity and the subsequent increase in intracellular $Ca^{2+}$ may be responsible for the increase in the BK/gBK currents. GBM cells can adopt other strategies to increase cytosolic calcium during migration, such as the opening of mechanosensitive potassium channels through hypotonicity, as reported in [39] (see also [28]). In conclusion, we propose that the $Na^+/Ca^{2+}$ exchanger could constitute a potential target in antitumor chemotherapy. The inhibition of the forward mode or the stimulation of the reverse mode of the NCX may result in increased intracellular $Ca^{2+}$ concentrations, which could, in turn, trigger intracellular mechanisms of cell death in tumor cells. It is thus interesting to consider the possibility of modulating the aberrant activity of normal or altered NCX isoforms, selectively expressed in cancer cells, to disrupt intracellular $Ca^{2+}$ homeostasis and inhibit GBM progression.

## 4. Materials and Methods

### *4.1. Cell Cultures*

#### 4.1.1. Human U251 GBM Cell Line

Human U251 GBM cells (Sigma-Aldrich, Milan, Italy) were cultured in Eagle's minimal essential medium (EMEM) supplemented with 10% fetal bovine serum (FBS), 1% L-glutamine, 1% non-essential amino acid (NEAA), 1% sodium pyruvate, and 1% penicillin–streptomycin. The cell culture was maintained in 25 or 75 $cm^2$ flasks at 37 °C in a humidified atmosphere (95% air and 5% $CO_2$). All culturing reagents were acquired from Euroclone S.p.a. (Pero, Milan, Italy).

#### 4.1.2. U87 Cell Line

Human U87 GBM cells (Sigma-Aldrich, Milan, Italy) were cultured in Dulbecco's modified Eagle's medium (DMEM) high glucose supplemented with 1% L-glutamine, 10% fetal bovine serum (FBS), and 1% penicillin–streptomycin (pen–strep) (Thermo Fisher Scientific, Monza, Italy). The cell culture was maintained in 25 or 75 $cm^2$ flasks at 37 °C in a humidified atmosphere (95% air and 5% $CO_2$). All culturing reagents were acquired from Euroclone S.p.a. (Pero, Milan, Italy).

#### 4.1.3. Human GBM CSC Cultures

The human glioblastoma culture enriched in stem cells (GSCs) was kindly provided by Professor T. Florio's laboratory at the University of Genova (Genova, Italy). Briefly, the culture was obtained from biopsy specimens from patients who underwent surgical treatment, in the absence of previous therapies, at the Neurosurgery Department IRCCS-AOU San Martino-IST (Genova, Italy) after obtaining informed consent and approval from the Institutional Ethical Committee (IEC). Based on histological and immunohistochemical analyses, the samples were classified as grade IV GBM (referring to the WHO classification) [40].

GSCs were grown in a stem cell-permissive medium, including 1:1 DMEM high glucose and Ham's F-12 Nutrient Mix GlutaMAX™ (Gibco™, Thermo Fisher Scientific, Rodano, MI, Italy) enriched with B27 supplement (Gibco™, Thermo Fisher Scientific, Rodano, MI, Italy), 10 ng/mL human basic fibroblast growth factor (bFGF), and 20 ng/mL human epidermal growth factor (EGF) (Miltenyi Biotec, Bologna, Italy). Cells were cultured as a monolayer on Matrigel (BD Biosciences, Milan, Italy), as previously described [40].

### *4.2. Cell Viability and Bepridil Cytotoxicity Determination Using the MTT Assay*

To determine the optimal concentration of the NCX blocker bepridil (Sigma-Aldrich, Milan, Italy) to be used in the wound-healing assay and time-lapse microscopy, U251 cell viability was determined using the MTT [3-(4,5-dimethylthiazol-2-yl)-2,5-diphenyltetrazolium bromide] assay. Briefly, cells were cultured in a 25 $cm^2$ flask, seeded in a 96-well plate at a density of 10,000 cells/well (0.2 mL per well), and incubated at 37 °C for 24 h in a humidified atmosphere containing 5% of $CO_2$. The day after, the culture medium was replaced with fresh medium added with a range of bepridil concentrations (20, 50, 70, and

100 µM). For the control condition, cells were incubated with the culture medium alone. Twenty-four hours after exposure, the MTT solution (20 µL/well) was added to each well; this operation was performed in darkness, and the plates were subsequently incubated for about three hours at 37 °C. At the end of the incubation time, the quantification was performed by measuring the samples' absorbance at 550 nm with the ELx808TM Absorbance Microplate Reader (Bio-Tek Instruments, Inc., Winooski, VT, USA). Data were expressed as a percentage of the control, and the cell viability percentage was calculated.

*4.3. Wound-Healing Migration Assay and Time-Lapse Microscopy*

U251, U87, and human GBM CSC cells were seeded on glass coverslips (22 mm × 22 mm) and in a 6-well plate for the wound-healing assay and time-lapse microscopy, respectively. Cells were grown in a complete medium and cultured until 90–95% confluence. A disposable pipette tip (1 mL volume) was used to scratch wounds on the midline of the coverslip (mean width: 350 µm), which was carefully washed with the complete medium to remove floating cells and clean the wound area.

Time-lapse imaging experiments were performed on the U251 cell line. The percentage of scratch wound closure was monitored using an Olympus ScanR inverted microscope equipped with a 10× objective taking pictures every 5 min over 24 h. The entire assay was performed using an environmental microscope incubator mimicking the culture conditions (37 °C and 5% $CO_2$). The speed of scratch closure was calculated with LAS X—Leica Microsystems CMS GmbH Software (Version 5.1.0). In addition, individual cell motility and the percentage of area covered by the cells were analyzed in ImageJ using the Chemotaxis Tool ImageJ software plugin (Version 2.0). Experiments were performed at least in triplicate. Only cells that were present in the field of view (FOV) for the whole recording time were included in the analysis of the time lapse for all the conditions applied. Usually, cells located on the bottom left corner of the FOV and with an upward direction during the migration were selected and tracked. For the bepridil and nickel datasets, recording began right after the blocker was applied in the cell medium.

*4.4. Electrophysiological Recording*

Patch-clamp experiments were performed at room temperature as previously described [8]. Briefly, whole-cell perforated patch-clamp recordings were performed using an Axopatch-200B (Molecolar Devices, San Jose, CA, USA) patch-clamp amplifier at the output cut-off frequency of 5 kHz. The extracellular solution contained 140 mM NaCl, 5 mM KCl, 10 mM HEPES, 10 mM glucose, 3 mM $CaCl_2$, and 1.2 mM $MgSO_4$, with a pH of 7.4. For the "Na-free" experiment, the extracellular solution contained 140 mM LiCl, 5 mM KCl, 10 mM HEPES, 10 mM glucose, 3 mM $CaCl_2$, and 1.2 mM $MgSO_4$, with a pH of 7.4. Patch pipettes were filled with an intracellular solution containing 400 µg/mL amphotericin (Sigma-Aldrich, MI, Italy), 140 mM KCl, 4 mM NaCl, 5 mM EGTA, 5 mM HEPES, and 0.5 mM $CaCl_2$, with a pH of 7.3. The series resistance (Rs = 16 ± 1.3 MΩ), input resistance (Rm), and membrane capacitance (Cm, Figure 2) were measured as previously described by eliciting a hyperpolarized step of −10 mV from the holding potential of −60 mV [41,42]. The whole-cell perforated patch-clamp stability was assessed every 5 min by monitoring the Rs. A depolarizing ramp from −120 to +140 mV was stimulated at a rate of 0.077 mV/ms and at a sampling rate of 500 Hz. Other protocols were reported in the figures. The hyperpolarizing protocol from −40 to −120 mV was elicited in steps of 10 mV at a sampling rate of 6.67 kHz, and the depolarizing protocols from –60 to +120 mV or from −120 to +40 mV were elicited in steps of 20 mV at a sampling rate of 20 kHz. For the depolarizing protocols, the PN leak subtraction of the Clampex program was used to eliminate the effects of the leakage current on the whole-cell responses.

The junction potential between the patch pipette and the cytoplasm was +8.8 mV, as calculated according to Horn [43], and the current–voltage (I–V) relationships were shifted to the left by this value.

The following compounds were used in the patch-clamp experiments: clotrimazole 10 µM, TEA 3 mM, barium 1 mM, nickel 1 mM, bepridil 100 µM, and ouabain 500 µM. Clotrimazole (5 mM), bepridil (100 µM), and ouabain (500 µM), as well as amphotericin, were dissolved in DMSO. All reagents were purchased from Sigma-Aldrich (Milan, Italy), except for bepridil, which was bought from Adooq Bioscience (Irvine, CA, USA).

### *4.5. Immunofluorescence Evaluations*

The control and treated U251 cells were grown on coverslips (22 mm × 22 mm) placed in cell culture dishes (35 mm × 10 mm) until 90% confluence, fixed with 4% formalin (20 min), and post-fixed with 70% ethanol at −20 °C for at least 24 h.

The samples were rehydrated for 10 min in PBS and then incubated with 1% BSA to block nonspecific binding sites. Subsequently, the cells were immunolabeled using the anti-NCX1 isoform primary antibody (#MA3-926, mouse monoclonal anti-sodium-calcium exchanger SLC8A1, Thermo Fisher Scientific, Monza, Italy) diluted 1:200 in PBS (Sigma-Aldrich, Milan, Italy) for 1 h at RT in a dark, moist chamber. The specificity of the antibody has been extensively described in different models [44–46]. Then, the cells were washed with PBS and incubated for 45 min with the goat anti-mouse IgG (H + L) highly cross-adsorbed secondary antibody, Alexa Fluor Plus 488, diluted 1:200 in PBS (Thermo Fisher Scientific, Monza, Italy). DNA counterstaining was performed using 0.1 mg/mL of Hoechst 33258 (Sigma-Aldrich, Milan, Italy). Lastly, the cells were mounted with a drop of Mowiol (Calbiochem-Inalco, Italy) for microscopy visualization. Images were recorded using an Olympus BX51 microscope equipped with an Olympus MagniFire camera system and processed with Olympus Cell F and ImageJ software (Version 1.51) to analyze the mean optical density (OD) (ratio of the mean of immunofluorescence intensity on the cell surface). For each condition, 11 quadrants (about 50 cells) were evaluated for random analysis. The channels of each fluorescence were split to obtain single images in grayscale, where the minimum value was 0 (black) and the maximum value was 255 (white). Then, the OD values were normalized to the lamellipodia and cytoplasm areas.

### *4.6. Statistical Analysis*

All data were reported as the mean ± standard error of the mean (SEM). The Bartlett and Shapiro–Wilk tests were performed to determine the normal distribution of the datasets. Statistical significance was determined using the *t*-test when comparing two experimental groups and one-way analysis of variance (ANOVA) with the post hoc Bonferroni test when comparing more than two experimental groups. *p*-values were considered statistically significant at * $p < 0.05$, ** $p < 0.01$, *** $p < 0.001$, and **** $p < 0.0001$. All statistical analyses were performed with GraphPad Prism 8.0 software (GraphPad Software Inc., La Jolla, CA, USA).

**Supplementary Materials:** The following supporting information can be downloaded at https://www.mdpi.com/article/10.3390/ijms241612673/s1.

**Author Contributions:** Conceptualization, P.R. and F.B.; methodology, M.R., E.P., E.C.P., D.R. and M.T.V.; software, F.B., M.R., E.C.P. and D.R.; formal analysis, M.R., E.P., E.C.P. and D.R.; investigation, M.R., E.P., E.C.P., D.R. and M.T.V.; data curation, F.B. and P.R.; writing—original draft preparation, F.B. and P.R.; writing—review and editing, E.R. and F.T.; supervision, F.B., E.R., F.T. and P.R.; and funding acquisition, P.R. All authors have read and agreed to the published version of the manuscript.

**Funding:** This research was funded by (i) the Italian Ministry of Health, Traiettoria 4 del Piano Operativo Salute (POS) linea di Azione 4.1 "Creazione di Hub delle Scienze della Vita" Project IMMUNOHUB,T4-CN-02; (ii) the University of Pavia, Fondi Ricerca Giovani (FRG 2020), Department of Biology and Biotechnology "L. Spallanzani", University of Pavia; and (iii) the Italian Ministry of Education, University and Research (MIUR): Department of Excellence Program (2018–2022), Department of Biology and Biotechnology "L. Spallanzani", University of Pavia.

**Institutional Review Board Statement:** Not applicable.

**Informed Consent Statement:** Not applicable.

**Data Availability Statement:** The datasets generated during and/or analyzed during the current study are not publicly available.

**Acknowledgments:** We thank Tullio Florio for providing the primary GBM cell line and U87 cells. We thank the 3Brain-The Massimo Grattarola Award for supporting the research of Brandalise's Lab. We thank Maria Grazia Bottone for providing the U251 cell line. We thank Urs Gerber for revising the English form of the manuscript. The graphical abstract was created with BioRender.com (agreement number: TY25F9O1GL).

**Conflicts of Interest:** The authors declare no conflict of interest.

## References

1. Thakkar, J.P.; Dolecek, T.A.; Horbinski, C.; Ostrom, Q.T.; Lightner, D.D.; Barnholtz-Sloan, J.S.; Villano, J.L. Epidemiologic and Molecular Prognostic Review of Glioblastoma. *Cancer Epidemiol. Biomark. Prev.* **2014**, *23*, 1985–1996. [CrossRef]
2. Stupp, R.; Hegi, M.E.; Mason, W.P.; van den Bent, M.J.; Taphoorn, M.J.B.; Janzer, R.C.; Ludwin, S.K.; Allgeier, A.; Fisher, B.; Belanger, K.; et al. Effects of Radiotherapy with Concomitant and Adjuvant Temozolomide versus Radiotherapy Alone on Survival in Glioblastoma in a Randomised Phase III Study: 5-Year Analysis of the EORTC-NCIC Trial. *Lancet Oncol.* **2009**, *10*, 459–466. [CrossRef]
3. Ohka, F.; Natsume, A.; Wakabayashi, T. Current Trends in Targeted Therapies for Glioblastoma Multiforme. *Neurol. Res. Int.* **2012**, *2012*, 878425. [CrossRef] [PubMed]
4. Berntsson, S.G.; Merrell, R.T.; Amirian, E.S.; Armstrong, G.N.; Lachance, D.; Smits, A.; Zhou, R.; Jacobs, D.I.; Wrensch, M.R.; Olson, S.H.; et al. Glioma-Related Seizures in Relation to Histopathological Subtypes: A Report from the Glioma International Case-Control Study. *J. Neurol.* **2018**, *265*, 1432–1442. [CrossRef] [PubMed]
5. Sanai, N.; Polley, M.-Y.; McDermott, M.W.; Parsa, A.T.; Berger, M.S. An Extent of Resection Threshold for Newly Diagnosed Glioblastomas. *J. Neurosurg.* **2011**, *115*, 3–8. [CrossRef]
6. Maher, E.A.; Furnari, F.B.; Bachoo, R.M.; Rowitch, D.H.; Louis, D.N.; Cavenee, W.K.; DePinho, R.A. Malignant Glioma: Genetics and Biology of a Grave Matter. *Genes. Dev.* **2001**, *15*, 1311–1333. [CrossRef] [PubMed]
7. Molenaar, R.J. Ion Channels in Glioblastoma. *ISRN Neurol.* **2011**, *2011*, 590249. [CrossRef]
8. Ratto, D.; Ferrari, B.; Roda, E.; Brandalise, F.; Siciliani, S.; De Luca, F.; Priori, E.C.; Di Iorio, C.; Cobelli, F.; Veneroni, P.; et al. Squaring the Circle: A New Study of Inward and Outward-Rectifying Potassium Currents in U251 GBM Cells. *Cell Mol. Neurobiol.* **2020**, *40*, 813–828. [CrossRef] [PubMed]
9. Brandalise, F.; Ratto, D.; Leone, R.; Olivero, E.; Roda, E.; Locatelli, C.A.; Grazia Bottone, M.; Rossi, P. Deeper and Deeper on the Role of BK and Kir4.1 Channels in Glioblastoma Invasiveness: A Novel Summative Mechanism? *Front. Neurosci.* **2020**, *14*, 595664. [CrossRef]
10. Huber, S.M. Oncochannels. *Cell Calcium.* **2013**, *53*, 241–255. [CrossRef]
11. Turner, K.L.; Sontheimer, H. $Cl^-$ and $K^+$ Channels and Their Role in Primary Brain Tumour Biology. *Philos. Trans. R. Soc. Lond. B Biol. Sci.* **2014**, *369*, 20130095. [CrossRef] [PubMed]
12. Catacuzzeno, L.; Caramia, M.; Sforna, L.; Belia, S.; Guglielmi, L.; D'Adamo, M.C.; Pessia, M.; Franciolini, F. Reconciling the Discrepancies on the Involvement of Large-Conductance $Ca^{(2+)}$-Activated K Channels in Glioblastoma Cell Migration. *Front. Cell Neurosci.* **2015**, *9*, 152. [CrossRef] [PubMed]
13. Ransom, C.B.; O'Neal, J.T.; Sontheimer, H. Volume-Activated Chloride Currents Contribute to the Resting Conductance and Invasive Migration of Human Glioma Cells. *J. Neurosci.* **2001**, *21*, 7674–7683. [CrossRef] [PubMed]
14. Annunziato, L.; Pignataro, G.; Di Renzo, G.F. Pharmacology of Brain $Na^+/Ca^{2+}$ Exchanger: From Molecular Biology to Therapeutic Perspectives. *Pharmacol. Rev.* **2004**, *56*, 633–654. [CrossRef] [PubMed]
15. Roger, S.; Gillet, L.; Le Guennec, J.-Y.; Besson, P. Voltage-Gated Sodium Channels and Cancer: Is Excitability Their Primary Role? *Front. Pharmacol.* **2015**, *6*, 152. [CrossRef]
16. Ottolia, M.; Philipson, K.D. NCX1: Mechanism of Transport. *Adv. Exp. Med. Biol.* **2013**, *961*, 49–54. [CrossRef]
17. Song, M.; Chen, D.; Yu, S.P. The TRPC Channel Blocker SKF 96365 Inhibits Glioblastoma Cell Growth by Enhancing Reverse Mode of the $Na^+/Ca^{2+}$ Exchanger and Increasing Intracellular $Ca^{2+}$. *Br. J. Pharmacol.* **2014**, *171*, 3432–3447. [CrossRef]
18. Hu, H.-J.; Wang, S.-S.; Wang, Y.-X.; Liu, Y.; Feng, X.-M.; Shen, Y.; Zhu, L.; Chen, H.-Z.; Song, M. Blockade of the Forward $Na^+/Ca^{2+}$ Exchanger Suppresses the Growth of Glioblastoma Cells through $Ca^{2+}$ -Mediated Cell Death. *Br. J. Pharmacol.* **2019**, *176*, 2691–2707. [CrossRef]
19. Fujioka, Y.; Hiroe, K.; Matsuoka, S. Regulation Kinetics of Na+-$Ca^{2+}$ Exchange Current in Guinea-Pig Ventricular Myocytes. *J. Physiol.* **2000**, *529 Pt 3*, 611–623. [CrossRef]
20. Kang, T.M.; Hilgemann, D.W. Multiple Transport Modes of the Cardiac $Na^+/Ca^{2+}$ Exchanger. *Nature* **2004**, *427*, 544–548. [CrossRef]
21. Shono, Y.; Kamouchi, M.; Kitazono, T.; Kuroda, J.; Nakamura, K.; Hagiwara, N.; Ooboshi, H.; Ibayashi, S.; Iida, M. Change in Intracellular PH Causes the Toxic $Ca^{2+}$ Entry via NCX1 in Neuron- and Glia-Derived Cells. *Cell Mol. Neurobiol.* **2010**, *30*, 453–460. [CrossRef] [PubMed]

22. Brückner, D.B.; Arlt, N.; Fink, A.; Ronceray, P.; Rädler, J.O.; Broedersz, C.P. Learning the Dynamics of Cell-Cell Interactions in Confined Cell Migration. *Proc. Natl. Acad. Sci. USA* **2021**, *118*, e2016602118. [CrossRef] [PubMed]
23. Scheff, N.N.; Yilmaz, E.; Gold, M.S. The Properties, Distribution and Function of $Na^+$–$Ca^{2+}$ Exchanger Isoforms in Rat Cutaneous Sensory Neurons. *J. Physiol.* **2014**, *592*, 4969–4993. [CrossRef] [PubMed]
24. Hinde, A.K.; Perchenet, L.; Hobai, I.A.; Levi, A.J.; Hancox, J.C. Inhibition of Na/Ca Exchange by External Ni in Guinea-Pig Ventricular Myocytes at 37 Degrees C, Dialysed Internally with CAMP-Free and CAMP-Containing Solutions. *Cell Calcium.* **1999**, *25*, 321–331. [CrossRef] [PubMed]
25. Liu, T.; O'Rourke, B. Regulation of the Na+/Ca2+ Exchanger by Pyridine Nucleotide Redox Potential in Ventricular Myocytes*. *J. Biol. Chem.* **2013**, *288*, 31984–31992. [CrossRef]
26. Skogestad, J.; Aronsen, J.M. Regulation of Cardiac Contractility by the Alpha 2 Subunit of the $Na^+/K^+$-ATPase. *Front. Physiol.* **2022**, *13*, 827334. [CrossRef]
27. Sontheimer, H. An Unexpected Role for Ion Channels in Brain Tumor Metastasis. *Exp. Biol. Med.* **2008**, *233*, 779–791. [CrossRef]
28. Caramia, M.; Sforna, L.; Franciolini, F.; Catacuzzeno, L. The Volume-Regulated Anion Channel in Glioblastoma. *Cancers* **2019**, *11*, 307. [CrossRef]
29. Zhang, Y.; Li, Y.; Thompson, K.N.; Stoletov, K.; Yuan, Q.; Bera, K.; Lee, S.J.; Zhao, R.; Kiepas, A.; Wang, Y.; et al. Polarized NHE1 and SWELL1 Regulate Migration Direction, Efficiency and Metastasis. *Nat. Commun.* **2022**, *13*, 6128. [CrossRef]
30. Wong, R.; Chen, W.; Zhong, X.; Rutka, J.T.; Feng, Z.-P.; Sun, H.-S. Swelling-Induced Chloride Current in Glioblastoma Proliferation, Migration, and Invasion. *J. Cell Physiol.* **2018**, *233*, 363–370. [CrossRef]
31. Liu, T.; Stauber, T. The Volume-Regulated Anion Channel LRRC8/VRAC Is Dispensable for Cell Proliferation and Migration. *Int. J. Mol. Sci.* **2019**, *20*, 2663. [CrossRef] [PubMed]
32. Hanahan, D.; Weinberg, R.A. Hallmarks of Cancer: The next Generation. *Cell* **2011**, *144*, 646–674. [CrossRef] [PubMed]
33. Noda, M.; Ifuku, M.; Mori, Y.; Verkhratsky, A. Calcium Influx through Reversed NCX Controls Migration of Microglia. *Adv. Exp. Med. Biol.* **2013**, *961*, 289–294. [CrossRef] [PubMed]
34. Chovancova, B.; Liskova, V.; Babula, P.; Krizanova, O. Role of Sodium/Calcium Exchangers in Tumors. *Biomolecules* **2020**, *10*, 1257. [CrossRef] [PubMed]
35. Loeck, T.; Schwab, A. The Role of the $Na^+/Ca^{2+}$-Exchanger (NCX) in Cancer-Associated Fibroblasts. *Biol. Chem.* **2023**, *404*, 325–337. [CrossRef]
36. Hobai, I.A.; O'Rourke, B. The Potential of $Na^+/Ca^{2+}$ Exchange Blockers in the Treatment of Cardiac Disease. *Expert. Opin. Investig. Drugs* **2004**, *13*, 653–664. [CrossRef] [PubMed]
37. Rodrigues, T.; Estevez, G.N.N.; Tersariol, I.L.D.S. $Na^+/Ca^{2+}$ Exchangers: Unexploited Opportunities for Cancer Therapy? *Biochem. Pharmacol.* **2019**, *163*, 357–361. [CrossRef]
38. Esteves, G.N.N.; Ferraz, L.S.; Alvarez, M.M.P.; da Costa, C.A.; de Mello Lopes, R.; Tersariol, I.L.D.S.; Rodrigues, T. BRAF and NRAS Mutated Melanoma: Different $Ca^{2+}$ Responses, $Na^+/Ca^{2+}$ Exchanger Expression, and Sensitivity to Inhibitors. *Cell Calcium* **2020**, *90*, 102241. [CrossRef]
39. Michelucci, A.; Sforna, L.; Di Battista, A.; Franciolini, F.; Catacuzzeno, L. $Ca^{2+}$-Activated $K^+$ Channels Regulate Cell Volume in Human Glioblastoma Cells. *J. Cell Physiol.* **2023**, *2023*, 1–15. [CrossRef]
40. Corsaro, A.; Bajetto, A.; Thellung, S.; Begani, G.; Villa, V.; Nizzari, M.; Pattarozzi, A.; Solari, A.; Gatti, M.; Pagano, A.; et al. Cellular Prion Protein Controls Stem Cell-like Properties of Human Glioblastoma Tumor-Initiating Cells. *Oncotarget* **2016**, *7*, 38638–38657. [CrossRef]
41. Rossi, P.; D'Angelo, E.; Taglietti, V. Differential Long-Lasting Potentiation of the NMDA and Non-NMDA Synaptic Currents Induced by Metabotropic and NMDA Receptor Coactivation in Cerebellar Granule Cells. *Eur. J. Neurosci.* **1996**, *8*, 1182–1189. [CrossRef] [PubMed]
42. D'Angelo, E.; Rossi, P.; Taglietti, V. Voltage-Dependent Kinetics of N-Methyl-D-Aspartate Synaptic Currents in Rat Cerebellar Granule Cells. *Eur. J. Neurosci.* **1994**, *6*, 640–645. [CrossRef] [PubMed]
43. Horn, R.; Marty, A. Muscarinic Activation of Ionic Currents Measured by a New Whole-Cell Recording Method. *J. Gen. Physiol.* **1988**, *92*, 145–159. [CrossRef] [PubMed]
44. Wan, H.; Gao, N.; Lu, W.; Lu, C.; Chen, J.; Wang, Y.; Dong, H. NCX1 Coupled with TRPC1 to Promote Gastric Cancer via $Ca^{2+}$/AKT/β-Catenin Pathway. *Oncogene* **2022**, *41*, 4169–4182. [CrossRef]
45. Stern, M.D.; Maltseva, L.A.; Juhaszova, M.; Sollott, S.J.; Lakatta, E.G.; Maltsev, V.A. Hierarchical Clustering of Ryanodine Receptors Enables Emergence of a Calcium Clock in Sinoatrial Node Cells. *J. Gen. Physiol.* **2014**, *143*, 577–604. [CrossRef]
46. Dan, P.; Lin, E.; Huang, J.; Biln, P.; Tibbits, G.F. Three-Dimensional Distribution of Cardiac $Na^+$-$Ca^{2+}$ Exchanger and Ryanodine Receptor during Development. *Biophys. J.* **2007**, *93*, 2504–2518. [CrossRef]

Journal of *Fungi*

MDPI

*Review*

# *Hericium erinaceus* in Neurodegenerative Diseases: From Bench to Bedside and Beyond, How Far from the Shoreline?

**Federico Brandalise [1], Elisa Roda [2], Daniela Ratto [3], Lorenzo Goppa [4], Maria Letizia Gargano [5], Fortunato Cirlincione [6], Erica Cecilia Priori [3], Maria Teresa Venuti [3], Emanuela Pastorelli [3], Elena Savino [4] and Paola Rossi [3,*]**

1 Department of Biosciences, University of Milan, 20133 Milano, Italy; federico.brandalise@unimi.it
2 Laboratory of Clinical & Experimental Toxicology, Pavia Poison Centre, National Toxicology Information Centre, Toxicology Unit, Istituti Clinici Scientifici Maugeri IRCCS, 27100 Pavia, Italy; elisa.roda@icsmaugeri.it
3 Department of Biology and Biotechnology, University of Pavia, 27100 Pavia, Italy; daniela.ratto@unipv.it (D.R.); ericacecilia.priori@unipv.it (E.C.P.); mariateresa.venuti01@universitadipavia.it (M.T.V.); empas97@icloud.com (E.P.)
4 Department of Earth and Environmental Science, University of Pavia, 27100 Pavia, Italy; lorenzo.goppa01@universitadipavia.it (L.G.); elena.savino@unipv.it (E.S.)
5 Department of Soil, Plant, and Food Sciences, Via G. Amendola, 165/A, 70126 Bari, Italy; marialetizia.gargano@uniba.it
6 Department of Agricultural, Food and Forest Sciences, University of Palermo, Viale delle Scienze, Bldg. 5, 90128 Palermo, Italy; fortunato.cirlincione@unipa.it
* Correspondence: paola.rossi@unipv.it; Tel.: +39-0382-986076

**Abstract:** A growing number of studies is focusing on the pharmacology and feasibility of bioactive compounds as a novel valuable approach to target a variety of human diseases related to neurological degeneration. Among the group of the so-called medicinal mushrooms (MMs), *Hericium erinaceus* has become one of the most promising candidates. In fact, some of the bioactive compounds extracted from *H. erinaceus* have been shown to recover, or at least ameliorate, a wide range of pathological brain conditions such as Alzheimer's disease, depression, Parkinson's disease, and spinal cord injury. In a large body of in vitro and in vivo preclinical studies on the central nervous system (CNS), the effects of erinacines have been correlated with a significant increase in the production of neurotrophic factors. Despite the promising outcome of preclinical investigations, only a limited number of clinical trials have been carried out so far in different neurological conditions. In this survey, we summarized the current state of knowledge on *H. erinaceus* dietary supplementation and its therapeutic potential in clinical settings. The bulk collected evidence underlies the urgent need to carry out further/wider clinical trials to prove the safety and efficacy of *H. erinaceus* supplementation, offering significant neuroprotective applications in brain pathologies.

**Keywords:** *Hericium erinaceus*; erinacines; hericenones; ergothioneine; NGF; BDNF; depression; aging; Alzheimer; mild cognitive impairment

check for updates

**Citation:** Brandalise, F.; Roda, E.; Ratto, D.; Goppa, L.; Gargano, M.L.; Cirlincione, F.; Priori, E.C.; Venuti, M.T.; Pastorelli, E.; Savino, E.; et al. *Hericium erinaceus* in Neurodegenerative Diseases: From Bench to Bedside and Beyond, How Far from the Shoreline? *J. Fungi* **2023**, *9*, 551. https://doi.org/10.3390/jof9050551

Academic Editor: Mingwen Zhao

Received: 7 April 2023
Revised: 5 May 2023
Accepted: 9 May 2023
Published: 10 May 2023



## 1. Introduction

Among all the modifiable risk factors for age-induced cognitive impairment, diet composition plays a crucial role [1] due to its capability to induce structural and functional changes in brain connectivity [2], modulate the developmental programming of the brain and behavior [3], as well as affect cognition and emotion [4]. The well-known nutritional and culinary properties of mushrooms go hand in hand with their nature-based nutraceutical value, specifically known to mitigate age-related cognitive disturbances typical of neurodegenerative disorders, such as Alzheimer's disease (AD).

The relationship between mushroom intake and mild cognitive impairment (MCI) has been investigated in cross-sectional and longitudinal studies carried out on well characterized cohorts at the Diet and Healthy Aging (DaHA) Research Centre, at the National University of Singapore (NUS). Interestingly, community-living elderly subjects who consumed more than two weekly portions of mushrooms (a portion being defined as 150 g) displayed up to 50 per cent reduced odds of developing MCI compared with aged participants who consumed mushrooms less than once per week. These research findings supports the likely role of mushrooms and their bioactive substances in promoting cognitive wellbeing, also delaying neurodegeneration [5,6].

Among all culinary medicinal mushrooms (MMs), *Hericium erinaceus* is a well-established candidate in promoting a "healthy brain" [7].

Despite the evidence obtained both in vitro and in preclinical studies describing the neuro-health properties of *H. erinaceus*, only few pilot clinical trials are available, although the scientific community feels the urgency and need to translate basic and preclinical research findings to clinical practices. This shift remains difficult for all MMs, possibly due to the different regulatory systems adopted by the Western and Eastern medicines regarding mushroom preparation. In China, a number of fungal glycan-based drugs were approved by the Chinese Food and Drug Administration (SFDA). Glycan-based drugs approved by the SFDA are extracted with hot water, either from cultured mycelium and/or sporophore, and have been used clinically in China since the 1980s [8].

Among them, glycans were extracted from the sporophores of *Lentinula edodes*, *Polyporus umbellatus*, *Tremella fuciformis*, and the cultured mycelium of *Trametes versicolor*, *Poria cocos*, and *Grifola frondosa*. For example, Krestine (PSK) and PSP, two extracts from *T. versicolor*, the lentinan extracted from *L. edodes*, and the schizophyllan from *Schizophyllum commune* were recognized as drugs in the antitumor field since 1970 [9–12].

As far as we known, no drugs based on *H. erinaceus* components are still available for clinical use in China or Japan. In China, the traditional use of *H. erinaceus* is mainly based on its gastrointestinal properties, as a preventive or curative supplement in chronic gastrointestinal disease, such as Crohn's disease. In Japan, the traditional use of *H. erinaceus* is more related to its known neuroprotective properties of the central nervous system [13].

MM extracts are defined as dietary supplements (DSs) in most Western countries following the directions of the World Health Organization (WHO) and the Dietary Supplement Health Education Act (DSHEA). Hence, clinical studies are not required for DSs to enter the market, and the consumer can take DSs without any medical prescription. DSs are consumed for their health benefits and their use has become part of complementary alternative medicine (CAM) or, even better, complementary integrative medicine (CIM). Paradoxically, this unregulated and large use of MMs as DSs has held back and delayed the development of proper clinical trials. Otherwise, in China and other Asian countries, the use of MMs, the so-called mycotherapy, has traditional and deep-seated heritages, and MM extracts are considered drugs. Concerning *H. erinaceus*, since ancient times, it has been widely employed as a neuroprotector in treating dementia in diverse Asian regions; nevertheless, clinical studies are still needed.

Since 2014, Professor Wasser, one of the leading experts for MMs, hoped and urged the scientific community to bridge the gap between Western and Eastern medicine, since "it is to our advantage" [14,15].

Despite existing data revealing the nootropic effects of *H. erinaceus*, only a limited number of intervention studies have been conducted so far, while others are currently ongoing [16].

This review focuses on available and updated evidence disclosing the neuroprotective and nootropic effects of *H. erinaceus* dietary supplementation, trying to fill the gap between preclinical studies and clinical trials.

**2. *Hericium erinaceus***

According to the main international databases, *Hericium erinaceus* (Bull.) Pers. belongs to the kingdom of fungi, Dikarya, Basidiomycota, Agaricomycetes, Russulales, and *Hericiaceae*, *Hericium* (http://www.indexfungorum.org accessed on 6 April 2023; http://www.mycobank.org accessed on 6 April 2023).

Taxonomy and phylogeny of the genus *Hericium* Pers. have been intensely debated in the last decades regarding its collocation within Agaricomycetes and the intra-genus discrimination of a single species. Thus, the *Hericium* genus is currently located in Russulales on the basis of both synapomorphic characters and molecular data [17]. Phylogenetically, the *Hericium* species are classified in the *Hericiaceae* family within the russuloid linage, very closely to *Laxitextum*, with steroid sporophores [18]. *Hericium* sporophores are clavariod or pileate, fleshy, and with a typical hydnoid hymenophore (this explains the genus name, which means hedgehog in Latin). The *Hericium* species have been classified taking into account different aspects, such as macro- and micro-morphological characters, host trees, geographical areas, and molecular data [19]. For species delimitation, phylogenetic analysis was carried out by comparing the rDNA internal transcribed tracer, ITS1 and ITS2 sequences. The comparison of ITS regions in nuclear ribosomal DNA is generally assumed to be the most appropriate approach for the molecular discrimination of fungal species, although it is regarded as not completely satisfactory, since a phylogenetic inference and molecular clades cannot be fully resolved by employing the ITS sequence only [20]. The 28S nuclear ribosomal large subunit rRNA gene (LSU) region (GeneBank), that has contiguity with the ITS region, is also used for identification, even though less frequently [21].

The monophyletic group *Hericium* was separated in two subtrees, showing that one includes *H. erinaceus*, *H. americanum*, *H. alpestre*, and *H. abietis* with a strong bootstrap support, whereas a separate tree resulted for the species *H. coralloides*, which is therefore phylogenetically more distant from *H. erinaceus* [21,22].

Most *Hericium* species have been reported from Europe, North and South America, and Asia, but new species are being described from different geographical areas [23–26].

*H. erinaceus* is also known by different common names, such as lion's mane, monkey head mushroom, bearded tooth, bearded hedgehog or Yamabushitake. This species is mainly distributed in Asia, Europe, and North America, but new finds in different geographical areas have been recently reported [27]. In Europe, its spreading has reached Poland, Hungary, Belgium, Czech Republic, Netherlands, Slovakia, Romania, Bulgaria, Portugal, Turkey, Italy, Sweden, Denmark, Spain, and Ukraine [28]. In Italy, it is widely distributed and known in the Mediterranean area, which mainly includes central and southern Italy, besides the Sardinian and Sicilian islands [28].

*H. erinaceus* is widespread and abundant in a few areas, but very rare in others. The loss of habitat is the main threat for this species that is decreasing, above all, where it is rare. For this reason, it is included on the Red Lists of a few countries, and according to Kałucka and Olariaga (2019), it is classified as LC (least concern) [29].

Concerning its habitat, *H. erinaceus* preferentially grows on living, dying or dead broadleaved trees, mainly oak, walnut, beech, and others. It is generally found in knotholes and wounds. Figure 1 shows a sporophore of *H. erinaceus* found in Bedonia (province of Parma, Emilia Romagna, Italy) in October 2022, on a dying *Quercus cerris* (personal communication by Lorenzo Goppa).

*H. erinaceus* is morphologically characterized by a pileate, globose, hedgehog-like sporophore, with non-forking aculei 1–4 cm long [30]. The sporophore is more or less hirsute to tomentose, characterized by a hymenophore hydnoid, as well as an obtrusive odor. The external portion is whitish and fibrous. In particular, the color is white in the early stages of growth, then becomes cream, and at the end turns yellow–brown or brown when aged. *H. erinaceus* has a monomitic hyphal system: hyphae have clamps, thick and amyloid walls, and they are frequently ampullate and variable in size [28].

**Figure 1.** *H. erinaceus* grown on *Q. cerris*: the collected sporophore lies on the ground (photo by L. Goppa).

### 3. Untargeted Metabolomics as a New Approach for *Hericium erinaceus* Metabolite Detection

Untargeted metabolomics comprises methods and techniques used to analyze all small-molecules metabolites present in a biological sample in a particular physiological state, and it is currently one of the most rapidly evolving research fields. Metabolomics studies are characterized by high resolution, good quality and precision, both at qualitative and quantitative levels. The strength of this new approach is the possibility of investigating the entire set of metabolites of a biological sample. This new approach is very different from the traditional chemical characterization techniques, as it is typically targeted, therefore able to characterize only a single class of compounds or a single metabolite, defined a priori. With untargeted metabolomics, it is possible to take a "snapshot" of the sample, identifying and quantifying all the metabolites with a weight lower than 1000 Da [31]. The classes of investigated metabolites can include amino acids, flavonoids, nucleotides, organic acids, phenolic acids, phenylpropanoids, steroids, terpenoids, and unsaturated fatty acids [32]. This entire set of metabolites, defined as the metabolome, is extremely sensitive to the external environmental variations and/or growth conditions, so many recent works have aimed to clarify how the different sample preparation parameters can influence, and therefore improve, the metabolomic profile enhancement, for example, the synthesis of biocompounds of interest. Among the -omics approaches, which are genomics, transcriptomics, proteomics, and metabolomics, the last provides the closest representation of the metabolic phenotype.

Nowadays, several investigations apply untargeted metabolomics to vegetal samples [33], but only few of them performed it with mushrooms [34]. The analysis of the metabolome, i.e., the complete set of metabolites in the sample, could have multiple applications, such as the comparison of the metabolome profile among different strains, and/or under different growth condition, and/or at different developmental stages [35].

Therefore, metabolomics studies may be useful to investigate the presence and abundance of nootropic molecules in mushroom samples, but could also be useful to define the better experimental condition to boost them.

Furthermore, the implementation of metabolomics investigations with those of chemotaxonomy may allow for the dissection of metabolite/metabolites patterns, which can help clarify the phylogenetic relationships of a genus with a multidisciplinary approach [35].

Species of the genus *Hericium* are known to produce a lot of secondary metabolites, many of which are responsible for the beneficial properties for humans and animals.

In particular, *H. erinaceus* is well-known for its content in neuroprotective metabolites such as the terpenoids hericenones and erinacines [36], antioxidant and immunomodulating metabolites such as polysaccharides [37], and anti-aging metabolites such as the "longevity vitamin" L-ergothioneine (ERGO) [38].

Data about *H. erinaceus* compounds are continuously published, many of which were obtained by comparing with standard molecules, but research remains to be carried out. Untargeted metabolomics can be useful for comparing the bioactivity of different *Hericium* species, different *H. erinaceus* strains, and strains grown on different substrates or under different conditions [32].

## 4. *Hericium erinaceus* Bioactive Metabolites

Many mushrooms contain bioactive compounds in sporophores, cultured mycelium, cultured broth, and the primordium [39–42].

*H. erinaceus* mycelia and sporophore contain an exceptionally large amount of structurally different and potentially bioactive molecules, including about 70 different secondary metabolites [43]. These bioactive compounds can be subdivided in major classes of organic substances: polysaccharides, cyathan-type diterpenoids, and geranyl-resorcilate derivatives, alkaloids, lactones, and steroids (to depict the chemical structures, see [43,44]). Among these, erinacines, cyathin diterpenoids, and hericenones (C-H), benzyl alcohol derivatives extracted from the mycelium and sporophore have attracted scientists for their nootropic effects [45,46].

With the aim to provide a further step toward the standardization of procedures required in the accurate development process of a dietary supplements, the mycelium, primordium, and sporophore (wild type and cultivated) of an *H. erinaceus* strain (He2 MicUNIPV) from Italy were analyzed using a HPLC-UV-ESI/MS in our lab [42]. Erinacine A in the mycelium, and hericenones C and D in the sporophore were quantified through comparison with their standard molecules. For the first time, *H. erinaceus* primordium was also investigated to assess the presence of these molecules. Hericenes, structurally similar to hericenones at the molecular level, were detected in all analyzed samples. Compared to the wild type, a higher content of hericenones C and D was measured in cultivated sporophore. The comparison of these results, with those obtained studying another Italian *H. erinaceus* strain (He1 MicUNIPV), was then described. These findings led us to punctually select particular *H. erinaceus* strains being more suitable for mycelium production or sporophore cultivation, aimed at obtaining extracts which contain an elevated content of bioactive compounds (see Table 1).

**Table 1.** Erinacine A, hericenone C, hericenone D, ergothioneine in the sporophore, mycelium, and primordium of Italian strains, He1 and He2 (data from [39–42,47]).

| | He1 | | He2 | | |
|---|---|---|---|---|---|
| | **Sporophore** | **Mycelium** | **Sporophore** | **Mycelium** | **Primordium** |
| Erinacine A (μg/g) | - | 150 | - | 105 | - |
| Hericenone C (μg/g) | 500 | - | 1560 | - | - |
| Hericenone D (μg/g) | <20 | - | 188 | - | - |
| L-Ergothioneine (μg/g) | 340 | 580 | 2400 (unpublished data) | 940 (unpublished data) | 1300 |

The content of erinacine A, measured in the two *H. erinaceus* Italian strains maintained at the MicUNIPV (Fungal Research Culture Collection, DSTA, University of Pavia, Italy), is between 105 and 150 μg/g, respectively, in lyophilized mycelium [42,47]. This value is comparable to that reported by Kryczkowski in improved submerged cultivation [48]. The differences in the content of hericenones C and hericenones D in the two dried sporophores, and erinacine A in the mycelium assessed in the two Italian *Hericium* species were also described (see Table 1). It has to be mentioned that gauged values were comparable with those reported in a previous work [49].

Ergothioneine (ERGO) is another "essential" nutrient, a diet-derived thiolated derivative of histidine, avidly taken up by some tissues owing to a specific high-affinity transporter, namely OCNT1, also called the ERGO transporter (ETT), or based on the encoding gene name, SLC22A4 [40,50–52]. The de novo synthesis of ERGO has been depicted in various fungi, including Basidiomycota [51,52]. ERGO is a powerful antioxidant in vitro and in vivo, acting as free radical scavenger and cytoprotective able to attenuate oxidative stress and nitrosamine damage induced by neurotoxic peptide, and reducing the beta-amyloid-induced apoptotic death in PC12 cells [53]. The intracellular antioxidant pathway involving the p38 MAPK cascade is activated by ERGO in rescuing cells to escape stress-induced apoptosis [53]. ERGO was demonstrated to mitigate cisplatin-induced nephrotoxicity targeting the apoptotic phenomena through p53 [54].

Dietary ERGO is efficiently and rapidly absorbed by OCTN1 from the small intestine and distributed to many body tissues, including the mouse brain [55], and it is highly retained after oral administration in humans [56]. In particular, increased ERGO, mediated by OCTN1 overexpression, was shown to have a cytoprotective effect in injured tissues (such as liver, heart, joints, and intestine), characterized by high oxidative stress and inflammation [57,58]. Therefore, the accumulation of the antioxidant ERGO in vivo could be an adaptive useful mechanism put into effect to minimize oxidative damage through an exogenous natural compound, also regulating its uptake and concentration.

A bulk of literature data has also demonstrated the in vivo beneficial effects of ERGO on cognition and memory. Some papers revealed that ERGO treatment was able to prevent the cognitive deficits in murine models of AD, reducing amyloid plaques, oxidative stress, and rescued glucose metabolism [59,60]. Furthermore, other in vivo investigations showed that 88-day-lasting ERGO supplementation protected against memory and learning deficits in a model of accelerated senescence, reducing the oxidative stress. It was also reported that the combined treatment of ERGO and melatonin displayed higher beneficial effects compared to each single treatment [61]. Moreover, ERGO treatment reverted the learning and memory deficits induced by cisplatin in mice, probably through the inhibition of oxidative stress and lipid peroxidation in brain [62]. Additionally, it was demonstrated that the two-week-lasting ERGO treatment was sufficient to improve the response to behavioral tests in mice, increasing the expression of synapse formation markers in hippocampal neurons [63].

Concerning our investigations, the presence of ERGO was recently assessed in Italian *H. erinaceus* strains using HPLC-UV-ESI/MS. ERGO was measured in comparable amounts both in the mycelium and sporophore, with the *H. erinaceus* primordium showing the highest concentration (Tables 1 and 2).

Earlier studies demonstrated that a *H. erinaceus* blend, composed of mycelium and sporophore, partially rescued cognitive and locomotor frailty in a mouse model of physiological aging [39,42,47,64]. Recently, we studied the preventive effect during physiological aging on cognitive [40] and locomotor frailty [41] of the *H. erinaceus* primordium characterized by a high content of ERGO and the lack of erinacines and hericenones [42]. Notably, the ERGO amount was higher in *H. erinaceus* primordium compared to the mycelium and sporophore, as previously described. A similar quantity of ERGO was described by other groups in different *H. erinaceus* samples (Table 2).

**Table 2.** ERGO content in different *H. erinaceus* dried samples (from published papers).

| Growth Stage | ERGO Content (mg/g) | Reference |
|---|---|---|
| Sporophore | 0.96 | [65] |
| Sporophore | 1.12 | [66] |
| Sporophore | 1.6–3.7 | [67] |
| Sporophore | 1.31 | [38] |
| Mycelium | 0.38 | [68] |

### 5. *H. erinaceus In Vitro* Preclinical Studies and Molecular Mechanism Underlying the Nootropic Effects

In the last decade, an increasing body of evidence has shown that *H. erinaceus* administration can improve neuronal conditions in animal models of neurodegenerative diseases such as AD, depression, Parkinson's disease, and spinal cord injury. Indeed, preclinical trials have successfully demonstrated that *H. erinaceus* bioactive compounds significantly improve cognitive function and rescue behavioral deficits [16]. Several in vitro and in vivo studies provided evidence demonstrating the nootropic and neuroprotective effects displayed by erinacines. In particular, in vivo investigation in mouse models revealed that erinacine A in the mycelia confers nootropic effects and reduces oxidative stress against stroke [46], AD [69], depression [70], and aging [71]. On the other hand, the neuroprotective role played in vivo by hericenones from the *H. erinaceus* sporophores is still controversial, even though oral sporophore supplementation exerted a nootropic action in pilot clinical trials, as reported in the Section 8 [72–74]. Nonetheless, few studies have been conducted thus far on the bioavailability and tissue distribution of these relatively hydrophobic metabolites with a low molecular weight. Erinacine A and S distribution in the CNS has been analyzed after oral administration in rats, revealing the presence of the bioactive compound in the brain already one hour after ingestion, suggesting a passive diffusion of erinacines A and S through the blood-brain barrier as the dominant transport method [75,76]. Concerning the mechanisms of action involved in the nootropic effect, erinacine A from *H. erinaceus* mycelium stimulates the nerve growth factor (NGF) synthesis and promotes the NGF-induced neurite outgrowth stimulation, but also protects neuronally differentiated PC12 pheochromocytoma cells against NGF deprivation [77]. In vivo, erinacine A successfully upregulated the NGF level in the hippocampus and locus coeruleus of rats [78]. Furthermore, erinacine A displayed a protective role in vitro, preventing glutamate-insulted apoptosis in PC12 cells [79]. Moreover, an in vivo study conducted using a rat model of global ischemic stroke further revealed the *H. erinaceus* defensive function, showing the inhibition of inducible NO synthase (iNOS), phosphorylation of p38 MAPK and CHOP, and the reduction of acute inflammatory cytokine levels [46]. Lately, the beneficial regenerative effect of *H. erinaceus* has been described in a mouse peripheral nerve injury model, demonstrating that, compared to NGF, *H. erinaceus* possesses higher neuroprotective and neurotogenic action, improving axonal regeneration ability [80]. Additionally, an aqueous extract of *H. erinaceus* was demonstrated to stimulate neurite outgrowth in NG108-15, a neuroblastoma–glioma cell line, with a synergistic interaction with exogenous NGF [81].

In 1321N1 human astrocytoma cells, hericenones C, D and E from the *H. erinaceus* sporophore, failed to promote NGF gene expression [82], while only isolated hericenone E, among all the present hericenones, was able to stimulate NGF-mediated neurite outgrowth via the MEK/ERK and PI3K-Akt signaling pathways in PC12 cells [83]. The involvement of the MEK/ERK intracellular signaling pathway has also been described for isolated erinacine A [84].

Within the elderly population (over 65 years old), the functional deficiency of NGF is related to progressive neurodegeneration and dementia-like diseases. Natural compounds able to induce the NGF biosynthesis are considered potentially effective against cognitive disturbances, e.g., dementia [45]. In this context, the neuroprotective role of *H. erinaceus*

extracts is crucial and typically embraces five major aspects, one related to each other: aging, memory, dementia, depression, and AD [39–41,47,73,85–87].

During the last years, we focused our research on this key topic, firstly addressing whether the *H. erinaceus* nootropic effect could be discernible in wild-type animals also, and during their physiological aging [39–41,47,64,88].

In hippocampal brain slices obtained from wild-type middle-aged mice supplemented for two months with a *H. erinaceus* blend made of mycelium and sporophore ethanol extracts, an increase in glutamatergic neurotransmission was recorded in the synapses between mossy fiber and granule cells, both in spontaneous and evoked post-synaptic currents [88]. The increased efficiency of neurotransmission fitted with the increase in recognition memory, a declarative explicit form of long-term memory fundamental for human personality and behavior. Interestingly, another *H. erinaceus* blend made of mycelium and sporophore, containing defined amount of erinacine A, hericenones C and D, was able to partially revert the cognitive and locomotor frailty index during physiological aging [47]. Additionally, an increase in proliferating cell nuclear antigen (PCNA) and doublecortin (DCX) measured in the hippocampus and cerebellum of *H. erinaceus*-supplemented mice supported the occurrence of neurogenesis in elderly frail mice [47]. Accordingly, one-month-long administration of *H. erinaceus* extracts in adult wild-type mice significantly increased the expression of PCNA and Ki67 in hippocampal progenitor cells, suggesting an increase in their proliferation, and hence, an increase in neurogenesis [89].

In the cerebellar cortex, lobules VI–VIII are particularly sensitive to aging-induced locomotor and cognitive decline [90]. Our recent in vivo study on the cerebellum demonstrated that a two-month oral supplementation was able to ameliorate age-induced cerebellar alterations (e.g., volume reduction, molecular layer thickness decrease, and shrunken neurons), also decreasing inflammation, oxidative stress, and reactive gliosis. These findings supported the neuroprotective action played by *H. erinaceus*, which parallelly increased a key longevity regulator [39].

Further, we studied the preventive effect of *H. erinaceus* primordium (He2 strain) extract containing a high amount of ERGO, on cognitive and locomotor decline during physiological aging in wild-type animals. Eight-month dietary supplementation with the He2 primordium extract (starting at the adulthood phase of the mouse lifespan and lasting until senescence) was able to reduce both the locomotor decline, as well as oxidative stress in the cerebellum. Therefore, we demonstrated that ERGO-rich He2 primordium exerted a neuroprotective and preventive action, ameliorating/mitigating/reverting age-dependent impairments [41].

Additionally, the same extract was demonstrated to decrease oxidative stress and inflammation in the hippocampus, also preventing recognition memory decline and increasing the expression of specific receptors crucially involved in glutamatergic neurotransmission [40].

Concerning the evaluation of the neuroprotective effects in preclinical studies using animal models, erinacine A-enriched *H. erinaceus* mycelium (EAHEM) was tested in AD APP/PS1 mice. A recovery in cognitive disability was described in diverse behavioral tests, i.e., passive avoidance and active shuttle avoidance tasks. Additionally, a *H. erinaceus*-induced lowering of oxidative stress and inflammation levels was reported, paralleled by the decrease in amyloid plaque aggregation [36].

Moreover, an investigation in transgenic APP/PS1 mice revealed that a 30-day short-term EAHEM feeding induced (i) a decrease in Aβ plaque burden, and (ii) the prevention of recruitment and activation of plaque-associated astrocytes and microglia. Additionally, the increased NGF/proNGF ratio was paralleled by (i) an enhanced proliferation of neurons progenitors and (ii) an increased neuronal proliferation in the dentate gyrus [87]. Several studies proved that the *H. erinaceus* mycelium ameliorates AD-related pathologies. In particular, isolated erinacine A and S displayed beneficial effects in the cerebrum of APPswe/PS1dE9 transgenic mice. In fact, a 30-day-long administration of erinacine A and S attenuated cerebral plaque loading by inhibiting plaque growth, diminishing glial cell activation and promoting hippocampal neurogenesis [69].

In another AD animal model induced by an aluminum ($AlCl_3$) intraperitoneal injection, *H. erinaceus* administration reduced neuronal degeneration in the rat hippocampus, also lessening oxidative and inflammatory alterations. Additionally, at a molecular level, *H. erinaceus* reduced the β-amyloid accumulation, aberrant APP overexpression, phosphorylated Tau, and the activation of the NLRP3 inflammasome components. Finally, *H. erinaceus* had protective effects on behavioral changes, increasing the discrimination ratio in novel object recognition tasks and animal permanence in target quadrants [91].

The effects of *H. erinaceus* on amyloid β(25-35)-peptide, intracerebroventricularly injected, were assessed in peptide-induced learning and memory deficits in mice. *H. erinaceus* prevented impairments of spatial and visual recognition memory induced by amyloid β(25-35)-peptide, tested by the Y-maze novel-object recognition behavioral tests [92].

The neuroprotective effects of the *H. erinaceus* mycelium polysaccharide-enriched aqueous extract was tested in an AD mouse model ($AlCl_3$ combined with d-galactose-induced). *H. erinaceus* aqueous extract administration ameliorated the endurance time in the rotarod test, enhanced the horizontal and vertical movements in the activity test, and decreased the escape latency time in the water maze test. The mechanism involved was an *H. erinaceus*-induced improvement in the central cholinergic system function, also responsible for the dose-dependent enhancement of acetylcholine (Ach) and choline acetyltransferase (ChAT) concentrations, both in the serum and hypothalamus [93].

In the SAMP8 (senescence accelerated mouse prone 8) model of accelerated senescence and APP/PS1 model of AD, *H. erinaceus* ameliorated learning and memory abilities. These behavioral changes were paralleled by a significant reduction in brain tissue swelling, neuronal apoptosis, and the down-regulation of Tau and Aβ1-42 [94].

The mechanism by which EAHEM delays the brain cognitive decline during aging was assessed using the SAMP8 mouse model. iNOS, Thiobarbituric acid reactive substances (TBARS), and 8-Hydroxy-2′-deoxyguanosine (8-OHdG) brain levels significantly decreased in mice supplemented with EAHEM, with a dose-dependent recovery of cognitive skills, such as learning and memory. Moreover, in an animal model of ischemic stroke, EAHEM reduced the ratio of cerebral infarction [46].

Table 3 summarizes the cited effects of the *H. erinaceus* metabolites in terms of targets and pathways, and Figure 2 resumes the principal effects of bioactive molecules (ERGO, erinacine A, and hericenone E) contained within *H. erinaceus*.

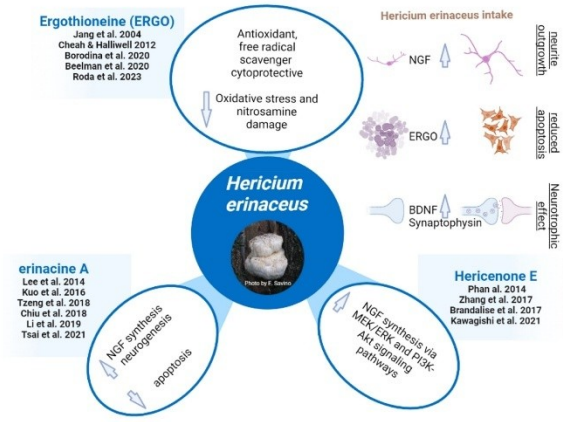


**Figure 2.** *H. erinaceus* potentials (photo by E. Savino) [40,45,46,50–53,69–71,77,83,88].

**Table 3.** Summary of the main in vitro and preclinical studies on *H. erinaceus* in the CNS. In the table the up arrows indicate an increase, and the down arrows indicate a decrease.

| *H. erinaceus* Bioactive Compound | Target | Pathway/Intracellular Mechanism | Effect | Reference |
|---|---|---|---|---|
| **Erinacine A/ erinacine A-enriched *H. erinaceus* mycelium (EAHEM)** | NGF [1], ↑ NGF/proNGF ratio | TrkA/Erk1/2 pathway<br>Others? | Neuroprotection and nootropic in vitro.<br>↑ Neurite outgrowth.<br>↑ Neuronal proliferation.<br>↓ Cognitive decline during aging in a SAMP8 mouse model. | [46,77–79,84] |
| | ↓ iNOS [2] | Phosphorylation of p38 MAPK [3] and CHOP [4]. | Protection against stroke in rats.<br>↓ Inflammation. | [46] |
| | ↑ IDE [5] | ? | ↓ Cerebral β-amyloid plaque loading in AD [6] APPswe/PS1dE9 transgenic mice. | [69] |
| | ↓ 8-OHdG [7], iNOS, and TBARS [8] levels in mice brain | ? | ↑ Cognitive performances in AD APP/PS1 mice.<br>↓ Oxidative stress, inflammation, brain Aβ plaque number. | [36] |
| **Erinacine S** | ↑ IDE | ? | ↓ Cerebral β-amyloid plaque loading in AD APPswe/PS1dE9 transgenic mice. | [69] |
| **Hericenone E** | ↑ NGF | MEK/ERK and PI3K-Akt pathways | ↑ Neurite outgrowth in vitro. | [83] |
| **Mix of Erinacine A and Hericenone C and D (sporophore and mycelium *H. erinaceus* extract)** | ↑ Hippocampal and cerebellar PCNA [9] and DCX [10] expression | ? | ↑ Neurogenesis and cognitive performances in aged frail mice. | [47] |
| | ↓ Cerebellar expression of IL-6 [11], iNOS, COX-2 [12], and SOD-1 [13] | ? | Inflammation and ↓ Oxidative stress in the cerebellum.<br>↑ Locomotor functions in aged frail mice. | [39] |
| **Ergothioneine-enriched primordium** | ↓ Cerebellar expression of iNOS and COX-2 | ? | ↓ Oxidative stress in the cerebellum and hippocampus, and of locomotor aging-related decline in frail mice. | [41] |
| | ↓ Hippocampal expression of IL-6, Nrf2 [14], SOD-1, COX-2, and iNOS.<br>↓ Hippocampal NMDAR1 [15] and mGlutR2 [16] receptors expression | TGF-beta1 [17] | ↓ Hippocampal inflammation and oxidative stress.<br>↑ Glutamatergic neurotransmission.<br>↓ Cognitive aging-related decline in frail mice. | [40] |

Abbreviations: [1] nerve growth factor (NGF), [2] inducible nitric oxide synthase (iNOS), [3] mitogen-activated protein kinase (MAPK), [4] homologous protein (CHOP), [5] insulin-degrading enzyme (IDE), [6] Alzheimer's disease (AD), [7] 8-hydroxy-2′-deoxyguanosine (8-OHdG), [8] thiobarbituric acid reactive (TBARS), [9] proliferating cell nuclear antigen (PCNA), [10] doublecortin (DCX), [11] interleukin 6 (IL-6), [12] cyclooxygenase-2 (COX-2), [13] superoxide dismutase 1 (SOD-1), [14] nuclear factor erythroid 2–related factor 2 (Nrf2), [15] N-methyl-D-aspartate receptor 1 (NMDAR1), [16] metabotropic glutamate receptor 2 (mGlutR2), [17] transforming growth factor beta 1 (TGF-beta1).

### 6. *H. Erinaceus* and Its Potential within the Gut-Microbiome–Brain Axis

The gut microbiota and the brain communicate with each other through several mechanisms, and this bidirectional communication is named the gut-microbiome–brain axis. Today, even if the processes leading to the communication between the gut microbiota and the brain are not yet clear, it is known that this communication can be direct, through the intestinal nervous system and the vagal nerve, or indirect through the stimulation of the release of several molecules such as short-chain fatty acids, amino acids, vitamins, hormones, and neurotransmitters that affect metabolism and the immune system, which in turn affects the integrity of the blood-brain barrier and brain function. On the other

hand, it was demonstrated that variations in the central nervous system neurotransmitter concentrations influence the proliferative activity of several gut bacteria [95–98].

The gut-microbiome–brain axis lies at the intersection between microbiology and neuroscience, looking for the correlation between the ecological fitness of our microbial communities and neurological/neurodegenerative diseases, e.g., schizophrenia, autism spectrum disorder, depression, anxiety, AD, and multiple sclerosis [99]. The gut-microbiome–brain research gives us new and intriguing challenges/opportunities to implement currently existing therapeutic approaches for the treatment of brain diseases. The cause–effect relationship and the bidirectional interaction between the gut and complex human diseases related to brain development, mood, and neurodegeneration is still an open and fascinating debate in science [100]. Several recent papers demonstrated that treatment with prebiotics or probiotics could alter neuroplasticity and behavior, influencing the gut microbiota composition [98,101–106]. Beta-glucan polysaccharides, as fibers, could elicit a direct prebiotic effect and/or an immune-modulating effect. Both mechanisms could be involved in changing the gut microbiome composition [107,108]. *H. erinaceus* is known to ameliorate gastrointestinal diseases, and a widespread interest concerns the possible effects of *H. erinaceus* polysaccharides (HEPs) in modulating the gut microbiota (GM) (for a review see [109]), and Table 4 summarizes the ones discussed in this review.

The digestibility and fermentation of HEPs and their influence on the GM composition was investigated in vitro on human fecal microbiota fermentation. The SCFA content, as well as the relative abundance of SCFA-producing bacteria (for detail see Table 4), were significantly enhanced. Furthermore, HEPs reduced several opportunistic pathogenic bacteria (Table 4) [110].

The role of two *H. erinaceus*-extracted polysaccharides in maintaining the integrity of the intestinal barrier was investigated both in vitro and in vivo (using murine models). One of the two polysaccharides significantly increased TEER and paracellular permeability. Both polysaccharides were able to significantly (i) increase the expression of occludin, ZO-1, ZO-2, claudin-3, claudin-4, and MUC2, (ii) decrease claudin-2, and (iii) alter the composition of the gut microbiota, boosting *Bacteriodetes*, *Firmicutes* and lessening *Klebsiella* and *Shigella* [111].

In a pilot clinical study on 13 healthy adults, seven days of *H. erinaceus* dry powder in submerged culture displayed beneficial health effects on the GM detected as 16S ribosomal RNA. In particular, *H. erinaceus* upregulated the relative abundance of some short-chain fatty acid (SCFA)-producing bacteria and downregulated some pathobionts (Table 4) [112].

Prebiotics may restore the gut microbial imbalance during the aging process, as evidenced by three different studies. Briefly, (i) by using an in vitro batch culture fermentations and fecal inocula from elderly donors, *H. erinaceus* increased the production of SCFA [113]; (ii) in aged dogs, the GM community improved immunity and anti-obesity [114]; (iii) in middle- and old-aged mice, the relative abundances of *Akkermansiaceae* and *Lachnospiraceae* significantly enhanced, while the relative abundance of *Bacteroidaceae* and *Rikenellaceae* declined [115].

Further, in cyclophosphamide (CTX)-immunodeficient mice, HEP improved the GM structure and inhibited the CTX-induced GM dysregulation [110].

In two different animal models of induced Ulcerative colitis (UC), *H. erinaceus* mycelium beneficial action was reported. EP-1, a purified unique polysaccharide, remarkably changed the GM, increasing SCFA production, also showing antioxidant/anti-inflammatory effect, and enhancing immune activities [116]. A novel low-weight polysaccharide altered the GM composition, and promoted functional shifts and structure by increasing *Akkermansia muciniphila*. Moreover, HEP10 treatment significantly suppressed the activation of the NLRP3 inflammasome, NF-κB, AKT and MAPK pathways [117].

Again, HEP was administrated for 2 weeks in rats suffering from induced inflammatory bowel disease (IBD). Tissue damage scoring in colonic mucosa was ameliorated, and the GM composition significantly changed compared to that determined in the untreated group [118]. A single-band protein (HEP3) isolated from *H. erinaceus* played a prebiotic role in the case of disproportionate use of antibiotics in IBD [119].

*H. erinaceus* (HEP) was administered in a xenografted mouse model of cancer with the chemotherapy drug 5-Fluorouracil (5-Fu), with the purpose of identifying new potential prebiotic bacteria for complementary and integrative antitumor treatment. HEP bettered the dysbiosis induced by 5-Fu, as it inhibited certain aerobic and micro aerobic bacteria, also increasing some probiotic bacteria (Table 4) [120].

Despite (i) all the reported *H. erinaceus* prebiotic effects on the GM, described during aging in diverse diseases, e.g., ulcerative colitis, IBD, and in integrative cancer therapy, and (ii) the *H. erinaceus* effects on the CNS, it has to be underlined that, until now, no data were available about the possible *H. erinaceus*-induced outcomes on the gut-microbiota–brain axis.

**Table 4.** Summary of the effects of *H. erinaceus* treatment on the GM in different models.

| Model/Condition/Disease | Treatment (Doses and Duration) | Increased Bacteria | Decreased Bacteria | Other Effects | Reference |
|---|---|---|---|---|---|
| In vitro (after simulated gastrointestinal digestion and 24-h-fermentation) on fermentation broth of human feces | HEPs [1] (HEP-30, HEP-50, and HEP-70) | SCFA [2]-producing bacteria: *Lactobacillus*, *Faecalibacterium*, *Bifidobacterium*, *Blautia*, *Butyricicoccus* | Pathogenic bacteria: *Klebsiella*, *Escherichia-Shigella*, *Enterobacter* | - | [110] |
| In vitro (static batch culture 24 h fermentations and fecal inocula from elderly donors) | HEBS [3] and HEOLRP [4] | - | - | Increasing propionate and butyrate levels. | [113] |
| Healthy adults (30.0 ± 4.9 years old) | 1 g of *H. erinaceus* powder three times a day (7 days of washout) | SCFA-producing bacteria: *Eubacterium rectale*, *Faecalibacterium prausnitzii*, *Kineothrix alysoides*, *Gemmiger formicilis*, *Fusicatenibacter saccharivorans* | Pathobionts: *Bacteroides caccae*, *Streptococcus thermophilus*, *Romboutsia timonensis* | Increasing in GM [5] alpha diversity. GM changes related to blood ALP [6], LDL [7], UA [8], and CREA [9]. | [112] |
| Aged dogs | *H. erinaceus* 0.8 g per bw [10] with daily diets for 16 weeks | *Bacteroidetes* (order *Bacteroidales*) | *Firmicutes: Streptococcus*, *Tyzzerella*, *Campylobacteraceae* (genus *Campylobacter*) | - | [114] |
| Middle (8-week-old) and old (6-month-old)-aged mice | HEPs from the *H. erinaceus* sporophore 0.5 or 1 g/bw/day by gavage for 28 days | *Lachnospiraceae*, *Akkermansiaceae* | *Rikenellaceae*, *Bacteroidaceae* | Anti-inflammatory activity and immunomodulatory activity. | [115] |
| Acetic-acid-induced UC [11] adult rats | EP-1 [12] 0.6 and 1.2 g/kg by gavage for 11 days | SCFA producers | - | Antioxidant, anti-inflammatory, and immunoregulatory activities. Restoring a normal GM. | [116] |
| DSS [13]-induced UC C57BL/6 adult male mice | HEP10 [14] 50, 100, or 200 mg/kg by gavage for 7 days | *Akkermansia muciniphila*. | *Proteobacteria* | Restoring GM-alpha and -beta diversities. Anti-inflammatory activity in colons. | [117] |
| IBD [15] adult rats and mice | HE/HEP3 100 mg/(kg * day) by gavage for 14 days | Anti-inflammatory bacteria, *Corynebacterium*, *Bacteroides*, *Enterobacter*, *Acinetobacter*, *Desulfovibrio*, *Lactobacillus* | Pro-inflammatory bacteria | Anti-inflammatory activity. Improving the GM composition. | [118,119] |
| CTX [16]-immunodeficient adult mice | HEP and FHEP 300 mg/kg/day by gavage for 21 days | *Bacteriodetes*, *Firmicutes* | *Klebsiella* and *Shigella* | Anti-inflammatory activity. Improving TJ [17] and MUC [18] expression. | [111] |
| CTX-immunodeficient adult mice | HEPs 75, 150, and 300 mg/kg by gavage for 4 weeks | SCFA-producing bacteria, *Alistipse*, *Muribaculaceae*, *Lachnospiraceae_NK4A136_group*, *Lachnospiracea*, *Ruminococcaceae*, *Ruminococcaceae_UCG-014* | *Lactobacillus*, *Bacteroides*, *Alloprevotella* | Improving the body weight and immune organ index. Increasing OTUs and adjusting GM-alpha and -beta diversities. | [121] |

**Table 4.** *Cont.*

| Model/Condition/Disease | Treatment (Doses and Duration) | Increased Bacteria | Decreased Bacteria | Other Effects | Reference |
|---|---|---|---|---|---|
| Xenograft adult male Balb/C mice, implanting with 100,000 CT-26 wt cancer cells | HEP 100 mg/kg/day per os for 21 days | Probiotic bacteria: *Bifidobacterium*, *Gemellales*, *Blautia*, *Sutterella*, *Anaerostipes*, *Roseburia*, *Lachnobacterium*, *Lactobacillus*, and *Desulfovibrio* | *Parabacteroides*, *Christensenellaceae*, *Anoxybacillus*, *Staphylococcus*, *Aggregatibacter*, *Comamonadaceae*, *Desulfovibrionaceae*, *Sporosarcina*, *Planococcaceae*, *Aerococcaceae*, *Flavobacteriaceae*, and *Bilophila* | Reducing the 5-Fu-induced GM dysbiosis, suppressing tumor growth, and inhibiting inflammatory markers. | [120] |

Abbreviations: [1] *H. erinaceus* polysaccharides (HEPs), [2] shorty-chain fatty acid (SCFA), [3] *H. erinaceus* LGAM 4514 in 100% beech sawdust (HEBS), [4] *H. erinaceus* LGAM 4514 in olive pruning residues (HEOLRP), [5] gut microbiota (GM), [6] alkaline phosphatase (ALP), [7] low-density lipoprotein (LDL), [8] uric acid (UA), [9] creatinine (CREA), [10] body weight (Bw), [11] ulcerative colitis (UC), [12] purified unique polysaccharide isolated from *H. erinaceus* mycelium (EP-1), [13] dextran sulfate sodium (DSS), [14] low-weight polysaccharide from *H. erinaceus* with Mw: 9.9 kDa (HEP10), [15] intestinal bowel disease (IBD), [16] cyclophosphamide (CTX), [17] tight junctions (TJ), [18] mucin (MUC).

### 7. *H. Erinaceus* Pilot Clinical Trials on Antidepressants

One of the foremost causes of global disease burdens is depression, a severe neuropsychiatric disorder. Currently, a number of antidepressants are available, but their efficacy is only just adequate and the side effects are very common. Four pilot clinical studies investigating the potential antidepressant action played by *H. erinaceus* were conducted so far on a small number of patients (for a review, see [122]).

Nagano and colleagues (2010) examined the clinical effects of *H. erinaceus* on menopause, depression, and sleep quality in 30 females (average age of 41.3 years) over a period of 4 weeks [72]. The consumption of cookies containing 0.5 g of sporophore powder alleviated the symptoms of depression, frustration, anxiety, and palpitation. However, this study was gender-specific by design, related to menopause, and a small population was used, making the conclusions only partially relevant [72].

In 2014, Inanaga and collaborators described a case-report of an 86-year-old male patients affected by recurrent depressive disorder which presented an improvement in neurocognition after treatment with a standardized extract of amycenone and hericenones, Amyloban® 3399. However, mirtazapine, an antidepressant drug, was also administered together with Amyloban® 3399, making it difficult to assess whether the alleviation of depression symptoms was a result of mirtazapine or Amyloban® 3399, or both [123].

Additionally, a pilot study on eight female undergraduate students with sleep disorder demonstrated that a 4-week administration of Amyloban® 3399 was associated with an improvement in anxiety and sleep quality, measured by the increase in the salivary level of free 3-methoxy-4-hydroxyphenylglycol, a biological index of anxiety disorders [124].

Lastly, epidemiological data indicated that obese subjects have an increased risk of developing mood disorders and vice versa, giving a bidirectional relationship between obesity and depression. In a first clinical study, patients affected by overweight or obesity were evaluated through self-assessment questionnaires, and then recruited only when positive for one or more administered tests, including Symptom Checklist-90, Zung's Anxiety and Zung's Depression Self-Assessment Scales, and the binge eating scale. This study was conducted at the Department of Preventive Medicine, Luigi Devoto Clinic of Work, Obesity Centre, at the IRCCS Foundation Policlinico Hospital of Milan (Italy). The 4-week oral supplementation using a *H. erinaceus* blend made of 80% mycelia and 20% sporophore, water, and ethanolic extract alleviated symptoms of depression, anxiety, and sleep disorders in patients [85]. This observation was linked to an increase in the serum level of proBDNF, the precursor form of BDNF, and in the proBDNF/BDNF ratio, without any significant change in the BDNF circulating level [85].

### 8. *H. Erinaceus* Pilot Clinical Trials on Cognitive Functions

Few clinical studies have been conducted on *H. erinaceus* nootropic effects [125].

A pilot interventional study was conducted on 31 subjects over 50 years old that were healthy, and with normal cognitive functions after *H. erinaceus* oral administration. The dry powder of *H. erinaceus* sporophore (0.8 g four times a day, for 12 weeks) was tested in this randomized, double-blind placebo-controlled parallel-group comparative study [74]. Three different tests were used to assess the effects of *H. erinaceus* on cognitive functions: Mini Mental State Examination (MMSE), standard verbal-paired-associate learning test, and Benton visual retention. The first is an assessment of associative and episodic memory. *H. erinaceus* oral intake significantly improved cognitive functions and prevented deterioration. The authors concluded that *H. erinaceus* oral consumption is safe and seems a convenient method for preventing dementia so far. In a college-age cohort ($n$ = 24), the 4-week-long ingestion of 10 g *H. erinaceus*/day did not elicit any statistically significant changes of either cognition nor metabolic flexibility markers [86].

Mild cognitive impairment (MCI) is typically considered the initial stage between the cognitive decline of normal aging and the more serious decline of dementia [126].

The efficacy of *H. erinaceus* oral administration for improving cognitive impairment was tested in a double-blind placebo-controlled parallel-group clinical trial of thirty Japanese patients diagnosed with MCI [73]. MCI was tested with the cognitive function scale, based on the Revised Hasegawa Dementia Scale (HDS-R). *H. erinaceus* was administrated for 16 weeks as four 250 mg tablets containing 96% of sporophore dry powder, three times a day. After 4 weeks of intake, cognitive functions were monitored. Compared with the placebo group, the *H. erinaceus* group showed significantly increased scores of the cognitive function scale (score value 22–25 vs. 30); meanwhile, after intake termination, the scores decreased significantly. The safety of *H. erinaceus* intake was tested through laboratory analysis and confirmed by the absence of adverse outcomes. Nonetheless, the bioactive compounds contained within *H. erinaceus* tablets used for this study have not been extensively addressed [73].

Patients with mild AD ($n$ = 49) were investigated for their cognitive functions in a double-blind placebo-controlled parallel-group study. The oral administration consisted of 15 mg erinacine A per day as dried erinacine-A-enriched *H. erinaceus* mycelia (EAHE) [127]. Cognitive assessments, ophthalmologic examinations, biomarker collection, neuroimaging, and laboratory test analyses to check for safety were followed throughout. In the EAHE group, after 49 weeks of EAHE intervention, a significant improvement in the MMSE score was observed, and a significant Instrumental Activities of Daily Living score difference was found between the two groups [127].

In relation to blood markers, only the placebo group displayed a significantly lower amount of calcium, albumin, apolipoprotein E4, hemoglobin, and BDNF, and parallelly showed a significant increase in alpha1-antichymotrypsin and amyloid-beta peptide 1–40. Furthermore, in neuroimaging of the dominant hemisphere, the mean apparent diffusion coefficient values obtained from the arcuate fasciculus region was significantly enhanced in the placebo group. Any significant difference was determined in the EAHE group after intervention compared to the baseline level. Moreover, ADC values from the parahippocampal cingulum region were significantly diminished in the EAHE group [127].

Figure 3 shows the timeline of the principal published papers related to the effects of *H. erinaceus* on patients with mood disorders or some cognitive impairments.

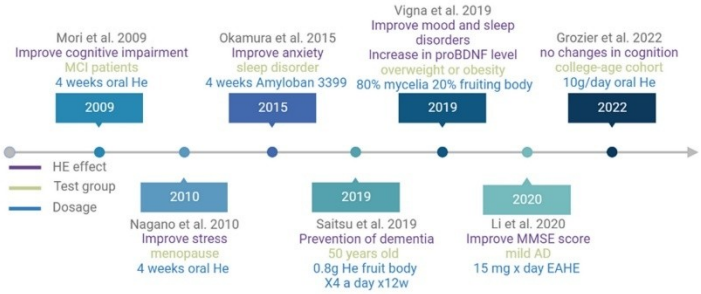


**Figure 3.** Timeline of the published papers relating the effects of *H. erinaceus* in clinical studies [72–74,85,86,124,127].

## 9. Conclusions

To sum up, the mass of scientific data reported leaves no doubt about the nootropic properties of *H. erinaceus*. It also clearly appears that different nootropic substances are present in both the *H. erinaceus* mycelium and sporophore. The efforts of our laboratory aimed to obtain standardized extracts by performing chemical analysis and/or through a metabolomics approach on specific bioactive compounds. We suggest that this could be a general practice to follow. In our in-depth thinking, among the bioactive compounds, ERGO is one of the most promising. This research activity is needed to obtain dietary supplements, functional foods, or drugs to promote a healthy brain. Furthermore, the pharmacologically active ingredients, as well as the mode of action, require further in-depth clinical investigation.

Erinacine A contained within the mycelium is one of the key components responsible for the *H. erinaceus* nootropic effects, as confirmed both in vitro, as well as in preclinical investigations in vivo. Moreover, sporophore extracts were proven to possess nootropic or neuroprotective power, too. In the above-reported pilot clinical studies, sporophore oral consumption was checked as a beneficial food, revealing an improvement of specific cognitive functions. To increase the array of nootropic substances even more, the free radical scavenger and cytoprotective powerful antioxidant ERGO, contained in both the mycelium and sporophore, attenuates oxidative stress and nitrosamine damage in an injured or aging brain.

More intriguingly, we want to underline that following *H. erinaceus* intervention, on top of the improved pathological phenotype consistently evidenced in clinical trials, the downstream molecular pathway responsible for the phenotypic rescue involves, as evidenced in vitro and in preclinical studies, the NGF and BDNF. However, we highlight the urgent need for additional in-depth clinical studies to clarify the mode of action by which *H. erinaceus* compounds are able to promote functional neurophysiological recovery in human, and assess the link between *H. erinaceus*, microbiota, and cognition in more detail.

**Author Contributions:** Conceptualization, P.R. and E.S.; software, F.B., L.G. and D.R.; resources, E.C.P., M.T.V. and E.P.; writing—original draft preparation, F.B., L.G., D.R. and P.R.; writing—review and editing, E.R., M.L.G., F.C. and E.S.; supervision, P.R. All authors have read and agreed to the published version of the manuscript.

**Funding:** This research was funded by the University of Pavia: Fondi Ricerca Giovani (FRG 2018). This research was also supported by Italian Ministry of Education, University and Research (MIUR): Dipartimenti di Eccellenza Program (2018–2022) Dept. of Biology and Biotechnology "L. Spallanzani", University of Pavia.

**Institutional Review Board Statement:** Not applicable.

**Informed Consent Statement:** Not applicable.

**Data Availability Statement:** Not applicable.

**Acknowledgments:** The authors wish to thank (i) Valentina Cesaroni and Carolina Elena Girometta (DSTA, University of Pavia, Italy); (ii) the staff of Centro Grandi Strumenti, University of Pavia, and (iii) the Animal Facility "Centro di servizio per la gestione unificata delle attività di stabulazione e di radiobiologia", University of Pavia, for the valuable technical assistance given to the development of the research projects on *Hericium erinaceus.* Figures 2 and 3 have been created with BioRender.com.

**Conflicts of Interest:** The authors declare no conflict of interest.

## References

1. Sindi, S.; Kåreholt, I.; Eskelinen, M.; Hooshmand, B.; Lehtisalo, J.; Soininen, H.; Ngandu, T.; Kivipelto, M. Healthy Dietary Changes in Midlife Are Associated with Reduced Dementia Risk Later in Life. *Nutrients* **2018**, *10*, 1649. [CrossRef]
2. Park, B.-Y.; Lee, M.J.; Kim, M.; Kim, S.-H.; Park, H. Structural and Functional Brain Connectivity Changes between People with Abdominal and Non-abdominal Obesity and Their Association With Behaviors of Eating Disorders. *Front. Neurosci.* **2018**, *12*, 741. [CrossRef]
3. Bolton, J.L.; Bilbo, S.D. Developmental programming of brain and behavior by perinatal diet: Focus on inflammatory mechanisms. *Dialogues Clin. Neurosci.* **2014**, *16*, 307–320. [CrossRef] [PubMed]
4. Spencer, S.J.; Korosi, A.; Layé, S.; Shukitt-Hale, B.; Barrientos, R.M. Food for thought: How nutrition impacts cognition and emotion. *NPJ Sci. Food* **2017**, *1*, 7. [CrossRef]
5. Feng, L.; Cheah, I.K.-M.; Ng, M.M.-X.; Li, J.; Chan, S.M.; Lim, S.L.; Mahendran, R.; Kua, E.-H.; Halliwell, B. The Association between Mushroom Consumption and Mild Cognitive Impairment: A Community-Based Cross-Sectional Study in Singapore. *J. Alzheimers Dis.* **2019**, *68*, 197–203. [CrossRef]
6. Yu, R.; Sun, Y.; Ye, K.X.; Feng, Q.; Lim, S.L.; Mahendran, R.; Cheah, I.K.-M.; Foo, R.S.Y.; Chua, R.Y.; Gwee, X.; et al. Cohort profile: The Diet and Healthy Aging (DaHA) study in Singapore. *Aging* **2020**, *12*, 23889–23899. [CrossRef] [PubMed]
7. Gargano, M.L.; Venturella, G.; Bosco, F.; Fabrini, M.G.; Gao, W.; Pecoraro, L. The Role of Medicinal Mushrooms in Brain Cancer Therapies: Review. *Int. J. Med. Mushrooms* **2021**, *23*, 13–20. [CrossRef] [PubMed]
8. Yang, D.; Zhou, Z.; Zhang, L. An overview of fungal glycan-based therapeutics. *Prog. Mol. Biol. Transl. Sci.* **2019**, *163*, 135–163. [CrossRef]
9. Tsukagoshi, S.; Hashimoto, Y.; Fujii, G.; Kobayashi, H.; Nomoto, K.; Orita, K. Krestin (PSK). *Cancer Treat. Rev.* **1984**, *11*, 131–155. [CrossRef]
10. Tabata, K.; Ito, W.; Kojima, T.; Kawabata, S.; Misaki, A. Ultrasonic degradation of schizophyllan, an antitumor polysaccharide produced by *Schizophyllum commune* Fries. *Carbohydr. Res.* **1981**, *89*, 121–135. [CrossRef]
11. Wasser, S.P. Medicinal mushrooms as a source of antitumor and immunomodulating polysaccharides. *Appl. Microbiol. Biotechnol.* **2002**, *60*, 258–274. [CrossRef]
12. Blagodatski, A.; Yatsunskaya, M.; Mikhailova, V.; Tiasto, V.; Kagansky, A.; Katanaev, V.L. Medicinal mushrooms as an attractive new source of natural compounds for future cancer therapy. *Oncotarget* **2018**, *9*, 29259–29274. [CrossRef]
13. Hericium erinaceus—An Overview | ScienceDirect Topics. Available online: https://www.sciencedirect.com/topics/pharmacology-toxicology-and-pharmaceutical-science/Hericium-erinaceus (accessed on 6 April 2023).
14. Wasser, S.P. Current findings, future trends, and unsolved problems in studies of medicinal mushrooms. *Appl. Microbiol. Biotechnol.* **2011**, *89*, 1323–1332. [CrossRef]
15. Wasser, S.P. Medicinal mushroom science: Current perspectives, advances, evidences, and challenges. *Biomed. J.* **2014**, *37*, 345–356. [CrossRef]
16. Li, I.-C.; Lee, L.-Y.; Tzeng, T.-T.; Chen, W.-P.; Chen, Y.-P.; Shiao, Y.-J.; Chen, C.-C. Neurohealth Properties of *Hericium erinaceus* Mycelia Enriched with Erinacines. *Behav. Neurol.* **2018**, *2018*, 5802634. [CrossRef]
17. Larsson, E.; Larsson, K.-H. Phylogenetic relationships of russuloid basidiomycetes with emphasis on aphyllophoralean taxa. *Mycologia* **2003**, *95*, 1037–1065. [CrossRef]
18. Larsson, K.-H. Re-thinking the classification of corticioid fungi. *Mycol. Res.* **2007**, *111*, 1040–1063. [CrossRef]
19. Hallenberg, N.; Nilsson, R.H.; Robledo, G. Species complexes in *Hericium* (Russulales, Agaricomycota) and a new species-*Hericium* rajchenbergii-from southern South America. *Mycol. Prog.* **2013**, *12*, 413–420. [CrossRef]
20. Das, K.; Stalpers, J.A.; Stielow, J.B. Two new species of hydnoid-fungi from India. *IMA Fungus* **2013**, *4*, 359–369. [CrossRef]
21. Park, H.G.; Kim, S.H.; Ko, H.G.; Park, W.M. Molecular Identification of Asian Isolates of Medicinal Mushroom *Hericium* erinaceum by Phylogenetic Analysis of Nuclear ITS rDNA. *J. Microbiol. Biotechnol.* **2004**, *14*, 816–821.
22. Cesaroni, V.; Brusoni, M.; Cusaro, C.M.; Girometta, C.; Perini, C.; Picco, A.M.; Rossi, P.; Salerni, E.; Savino, E. Phylogenetic Comparison between Italian and Worldwide *Hericium* Species (Agaricomycetes). *Int. J. Med. Mushrooms* **2019**, *21*, 943–954. [CrossRef] [PubMed]

23. Chen, Z.; Bishop, K.S.; Tanambell, H.; Buchanan, P.; Quek, S.Y. Assessment of In Vitro Bioactivities of Polysaccharides Isolated from *Hericium* Novae-Zealandiae. *Antioxidants* **2019**, *8*, 211. [CrossRef] [PubMed]
24. Jumbam, B.; Haelewaters, D.; Koch, R.A.; Dentinger, B.T.M.; Henkel, T.W.; Aime, M.C. A new and unusual species of *Hericium* (Basidiomycota: Russulales, Hericiaceae) from the Dja Biosphere Reserve, Cameroon. *Mycol. Prog.* **2019**, *18*, 1253–1262. [CrossRef]
25. Singh, U.; Das, K. *Hericium rajendrae* sp. nov. (Hericiaceae, Russulales): An edible mushroom from Indian Himalaya. *Nova Hedwig.* **2019**, *108*, 505–515. [CrossRef]
26. Sugawara, R.; Maekawa, N.; Sotome, K.; Nakagiri, A.; Endo, N. Systematic revision of *Hydnum* species in Japan. *Mycologia* **2022**, *114*, 413–452. [CrossRef]
27. Ouali, Z.; Sbissi, I.; Boudagga, S.; Rhaiem, A.; Hamdi, C.; Venturella, G.; Saporita, P.; Jaouani, A.; Gargano, M.L. First report of the rare tooth fungus *Hericium erinaceus* in North African temperate forests. *Plant Biosyst.* **2020**, *154*, 24–28. [CrossRef]
28. Bernicchia, A.; Gorjón, S.P. *Corticiaceae s.l.*; Candusso, Ed.; Libreria «l'Antro di Ulisse»: Alassio (SV), Italy, 2010.
29. Kałucka, I.L.; Olariaga Ibarguren, I. IUCN Hericium erinaceus: The IUCN Red List of Threatened Species 2019: E.T70401627A70401637. Available online: https://redlist.info/iucn/species_view/356812/ (accessed on 6 April 2023).
30. Stamets, P. *Growing Gourmet and Medicinal Mushrooms*, 3rd ed.; Ten Speed Press: Berkeley, CA, USA, 2000.
31. Pelle, J.; Castelli, F.A.; Rudler, M.; Alioua, I.; Colsch, B.; Fenaille, F.; Junot, C.; Thabut, D.; Weiss, N. Metabolomics in the understanding and management of hepatic encephalopathy. *Anal. Biochem.* **2022**, *636*, 114477. [CrossRef]
32. Yang, F.; Wang, H.; Feng, G.; Zhang, S.; Wang, J.; Cui, L. Rapid Identification of Chemical Constituents in *Hericium erinaceus* Based on LC-MS/MS Metabolomics. *J. Food Qual.* **2021**, *2021*, e5560626. [CrossRef]
33. Commisso, M.; Negri, S.; Bianconi, M.; Gambini, S.; Avesani, S.; Ceoldo, S.; Avesani, L.; Guzzo, F. Untargeted and Targeted Metabolomics and Tryptophan Decarboxylase In Vivo Characterization Provide Novel Insight on the Development of Kiwifruits (*Actinidia deliciosa*). *Int. J. Mol. Sci.* **2019**, *20*, 897. [CrossRef]
34. Satria, D.; Tamrakar, S.; Suhara, H.; Kaneko, S.; Shimizu, K. Mass Spectrometry-Based Untargeted Metabolomics and α-Glucosidase Inhibitory Activity of Lingzhi (*Ganoderma lingzhi*) During the Developmental Stages. *Molecules* **2019**, *24*, 2044. [CrossRef]
35. Flores, G.A.; Girometta, C.E.; Cusumano, G.; Angelini, P.; Tirillini, B.; Ianni, F.; Blasi, F.; Cossignani, L.; Pellegrino, R.M.; Emiliani, C.; et al. Untargeted Metabolomics Used to Describe the Chemical Composition, Antioxidant and Antimicrobial Effects of Extracts from *Pleurotus* spp. Mycelium Grown in Different Culture Media. *Antibiotics* **2022**, *11*, 1468. [CrossRef]
36. Lee, L.-Y.; Chou, W.; Chen, W.-P.; Wang, M.-F.; Chen, Y.-J.; Chen, C.-C.; Tung, K.-C. Erinacine A-Enriched *Hericium erinaceus* Mycelium Delays Progression of Age-Related Cognitive Decline in Senescence Accelerated Mouse Prone 8 (SAMP8) Mice. *Nutrients* **2021**, *13*, 3659. [CrossRef]
37. Wang, X.-Y.; Zhang, D.-D.; Yin, J.-Y.; Nie, S.-P.; Xie, M.-Y. Recent developments in *Hericium erinaceus* polysaccharides: Extraction, purification, structural characteristics and biological activities. *Crit. Rev. Food Sci. Nutr.* **2019**, *59*, S96–S115. [CrossRef]
38. Tripodi, F.; Falletta, E.; Leri, M.; Angeloni, C.; Beghelli, D.; Giusti, L.; Milanesi, R.; Sampaio-Marques, B.; Ludovico, P.; Goppa, L.; et al. Anti-Aging and Neuroprotective Properties of Grifola frondosa and *Hericium erinaceus* Extracts. *Nutrients* **2022**, *14*, 4368. [CrossRef]
39. Roda, E.; Priori, E.C.; Ratto, D.; De Luca, F.; Di Iorio, C.; Angelone, P.; Locatelli, C.A.; Desiderio, A.; Goppa, L.; Savino, E.; et al. Neuroprotective Metabolites of *Hericium erinaceus* Promote Neuro-Healthy Aging. *Int. J. Mol. Sci.* **2021**, *22*, 6379. [CrossRef]
40. Roda, E.; De Luca, F.; Ratto, D.; Priori, E.C.; Savino, E.; Bottone, M.G.; Rossi, P. Cognitive Healthy Aging in Mice: Boosting Memory by an Ergothioneine-Rich *Hericium erinaceus* Primordium Extract. *Biology* **2023**, *12*, 196. [CrossRef]
41. Roda, E.; Ratto, D.; De Luca, F.; Desiderio, A.; Ramieri, M.; Goppa, L.; Savino, E.; Bottone, M.G.; Locatelli, C.A.; Rossi, P. Searching for a Longevity Food, We Bump into *Hericium erinaceus* Primordium Rich in Ergothioneine: The "Longevity Vitamin" Improves Locomotor Performances during Aging. *Nutrients* **2022**, *14*, 1177. [CrossRef]
42. Corana, F.; Cesaroni, V.; Mannucci, B.; Baiguera, R.M.; Picco, A.M.; Savino, E.; Ratto, D.; Perini, C.; Kawagishi, H.; Girometta, C.E.; et al. Array of Metabolites in Italian *Hericium erinaceus* Mycelium, Primordium, and Sporophore. *Molecules* **2019**, *24*, 3511. [CrossRef]
43. Friedman, M. Chemistry, Nutrition, and Health-Promoting Properties of *Hericium erinaceus* (Lion's Mane) Mushroom Fruiting Bodies and Mycelia and Their Bioactive Compounds. *J. Agric. Food Chem.* **2015**, *63*, 7108–7123. [CrossRef]
44. Venturella, G.; Ferraro, V.; Cirlincione, F.; Gargano, M.L. Medicinal Mushrooms: Bioactive Compounds, Use, and Clinical Trials. *Int. J. Mol. Sci.* **2021**, *22*, 634. [CrossRef]
45. Kawagishi, H. Chemical studies on bioactive compounds related to higher fungi. *Biosci. Biotechnol. Biochem.* **2021**, *85*, 1–7. [CrossRef] [PubMed]
46. Lee, K.-F.; Chen, J.-H.; Teng, C.-C.; Shen, C.-H.; Hsieh, M.-C.; Lu, C.-C.; Lee, K.-C.; Lee, L.-Y.; Chen, W.-P.; Chen, C.-C.; et al. Protective effects of *Hericium erinaceus* mycelium and its isolated erinacine A against ischemia-injury-induced neuronal cell death via the inhibition of iNOS/p38 MAPK and nitrotyrosine. *Int. J. Mol. Sci.* **2014**, *15*, 15073–15089. [CrossRef] [PubMed]
47. Ratto, D.; Corana, F.; Mannucci, B.; Priori, E.C.; Cobelli, F.; Roda, E.; Ferrari, B.; Occhinegro, A.; Di Iorio, C.; De Luca, F.; et al. *Hericium erinaceus* Improves Recognition Memory and Induces Hippocampal and Cerebellar Neurogenesis in Frail Mice during Aging. *Nutrients* **2019**, *11*, 715. [CrossRef] [PubMed]
48. Krzyczkowski, W.; Malinowska, E.; Herold, F. Erinacine A biosynthesis in submerged cultivation of *Hericium* erinaceum: Quantification and improved cultivation. *Eng. Life Sci.* **2010**, *10*, 446–457. [CrossRef]

49. Lee, D.G.; Kang, H.-W.; Park, C.-G.; Ahn, Y.-S.; Shin, Y. Isolation and identification of phytochemicals and biological activities of *Hericium* ernaceus and their contents in *Hericium* strains using HPLC/UV analysis. *J. Ethnopharmacol.* **2016**, *184*, 219–225. [CrossRef]
50. Beelman, R.B.; Kalaras, M.D.; Phillips, A.T.; Richie, J.P. Is ergothioneine a "longevity vitamin" limited in the American diet? *J. Nutr. Sci.* **2020**, *9*, e52. [CrossRef]
51. Borodina, I.; Kenny, L.C.; McCarthy, C.M.; Paramasivan, K.; Pretorius, E.; Roberts, T.J.; van der Hoek, S.A.; Kell, D.B. The biology of ergothioneine, an antioxidant nutraceutical. *Nutr. Res. Rev.* **2020**, *33*, 190–217. [CrossRef]
52. Cheah, I.K.; Halliwell, B. Ergothioneine; antioxidant potential, physiological function and role in disease. *Biochim. Biophys. Acta* **2012**, *1822*, 784–793. [CrossRef]
53. Jang, J.-H.; Aruoma, O.I.; Jen, L.-S.; Chung, H.Y.; Surh, Y.-J. Ergothioneine rescues PC12 cells from beta-amyloid-induced apoptotic death. *Free Radic. Biol. Med.* **2004**, *36*, 288–299. [CrossRef]
54. Salama, S.A.; Abd-Allah, G.M.; Mohamadin, A.M.; Elshafey, M.M.; Gad, H.S. Ergothioneine mitigates cisplatin-evoked nephrotoxicity via targeting Nrf2, NF-κB, and apoptotic signaling and inhibiting γ-glutamyl transpeptidase. *Life Sci.* **2021**, *278*, 119572. [CrossRef]
55. Tang, R.M.Y.; Cheah, I.K.-M.; Yew, T.S.K.; Halliwell, B. Distribution and accumulation of dietary ergothioneine and its metabolites in mouse tissues. *Sci. Rep.* **2018**, *8*, 1601. [CrossRef]
56. Cheah, I.K.; Tang, R.M.Y.; Yew, T.S.Z.; Lim, K.H.C.; Halliwell, B. Administration of Pure Ergothioneine to Healthy Human Subjects: Uptake, Metabolism, and Effects on Biomarkers of Oxidative Damage and Inflammation. *Antioxid. Redox Signal.* **2017**, *26*, 193–206. [CrossRef]
57. Halliwell, B.; Cheah, I.K.; Drum, C.L. Ergothioneine, an adaptive antioxidant for the protection of injured tissues? A hypothesis. *Biochem. Biophys. Res. Commun.* **2016**, *470*, 245–250. [CrossRef]
58. Halliwell, B.; Cheah, I.K.; Tang, R.M.Y. Ergothioneine—A diet-derived antioxidant with therapeutic potential. *FEBS Lett.* **2018**, *592*, 3357–3366. [CrossRef]
59. Yang, N.-C.; Lin, H.-C.; Wu, J.-H.; Ou, H.-C.; Chai, Y.-C.; Tseng, C.-Y.; Liao, J.-W.; Song, T.-Y. Ergothioneine protects against neuronal injury induced by β-amyloid in mice. *Food Chem. Toxicol.* **2012**, *50*, 3902–3911. [CrossRef]
60. Whitmore, C.A.; Haynes, J.R.; Behof, W.J.; Rosenberg, A.J.; Tantawy, M.N.; Hachey, B.C.; Wadzinski, B.E.; Spiller, B.W.; Peterson, T.E.; Paffenroth, K.C.; et al. Longitudinal Consumption of Ergothioneine Reduces Oxidative Stress and Amyloid Plaques and Restores Glucose Metabolism in the 5XFAD Mouse Model of Alzheimer's Disease. *Pharmaceuticals* **2022**, *15*, 742. [CrossRef]
61. Song, T.-Y.; Lin, H.-C.; Chen, C.-L.; Wu, J.-H.; Liao, J.-W.; Hu, M.-L. Ergothioneine and melatonin attenuate oxidative stress and protect against learning and memory deficits in C57BL/6J mice treated with D-galactose. *Free Radic. Res.* **2014**, *48*, 1049–1060. [CrossRef]
62. Song, T.-Y.; Chen, C.-L.; Liao, J.-W.; Ou, H.-C.; Tsai, M.-S. Ergothioneine protects against neuronal injury induced by cisplatin both in vitro and in vivo. *Food Chem. Toxicol.* **2010**, *48*, 3492–3499. [CrossRef]
63. Nakamichi, N.; Nakao, S.; Nishiyama, M.; Takeda, Y.; Ishimoto, T.; Masuo, Y.; Matsumoto, S.; Suzuki, M.; Kato, Y. Oral Administration of the Food-Derived Hydrophilic Antioxidant Ergothioneine Enhances Object Recognition Memory in Mice. *Curr. Mol. Pharmacol.* **2021**, *14*, 220–233. [CrossRef]
64. Rossi, P.; Cesaroni, V.; Brandalise, F.; Occhinegro, A.; Ratto, D.; Perrucci, F.; Lanaia, V.; Girometta, C.; Orrù, G.; Savino, E. Dietary Supplementation of Lion's Mane Medicinal Mushroom, *Hericium erinaceus* (Agaricomycetes), and Spatial Memory in Wild-Type Mice. *Int. J. Med. Mushrooms* **2018**, *20*, 485–494. [CrossRef]
65. Dubost, N.J.; Beelman, R.B.; Royse, D.J. Influence of selected cultural factors and postharvest storage on ergothioneine content of common button mushroom Agaricus bisporus (J. Lge) Imbach (Agaricomycetes). *Int. J. Med. Mushrooms* **2007**, *9*, 163–176. [CrossRef]
66. Kalaras, M.D.; Richie, J.P.; Calcagnotto, A.; Beelman, R.B. Mushrooms: A rich source of the antioxidants ergothioneine and glutathione. *Food Chem.* **2017**, *233*, 429–433. [CrossRef] [PubMed]
67. Ryu, S.R.; Lee, W.Y.; Ka, K.H. Comparative Study on the Sawdust Cultivation and the Antioxidants of *Hericium* spp. *Korean J. Mycol.* **2009**, *37*, 80–85. [CrossRef]
68. Chen, S.-Y.; Ho, K.-J.; Hsieh, Y.-J.; Wang, L.-T.; Mau, J.-L. Contents of lovastatin, γ-aminobutyric acid and ergothioneine in mushroom fruiting bodies and mycelia. *LWT-Food Sci. Technol.* **2012**, *47*, 274–278. [CrossRef]
69. Tzeng, T.-T.; Chen, C.-C.; Chen, C.-C.; Tsay, H.-J.; Lee, L.-Y.; Chen, W.-P.; Shen, C.-C.; Shiao, Y.-J. The Cyanthin Diterpenoid and Sesterterpene Constituents of *Hericium erinaceus* Mycelium Ameliorate Alzheimer's Disease-Related Pathologies in APP/PS1 Transgenic Mice. *Int. J. Mol. Sci.* **2018**, *19*, 598. [CrossRef]
70. Chiu, C.-H.; Chyau, C.-C.; Chen, C.-C.; Lee, L.-Y.; Chen, W.-P.; Liu, J.-L.; Lin, W.-H.; Mong, M.-C. Erinacine A-Enriched *Hericium erinaceus* Mycelium Produces Antidepressant-Like Effects through Modulating BDNF/PI3K/Akt/GSK-3β Signaling in Mice. *Int. J. Mol. Sci.* **2018**, *19*, 341. [CrossRef]
71. Li, I.-C.; Lee, L.-Y.; Chen, Y.-J.; Chou, M.-Y.; Wang, M.-F.; Chen, W.-P.; Chen, Y.-P.; Chen, C.-C. Erinacine A-enriched *Hericium erinaceus* mycelia promotes longevity in *Drosophila melanogaster* and aged mice. *PLoS ONE* **2019**, *14*, e0217226. [CrossRef]
72. Nagano, M.; Shimizu, K.; Kondo, R.; Hayashi, C.; Sato, D.; Kitagawa, K.; Ohnuki, K. Reduction of depression and anxiety by 4 weeks *Hericium erinaceus* intake. *Biomed. Res. Tokyo Jpn.* **2010**, *31*, 231–237. [CrossRef]

73. Mori, K.; Inatomi, S.; Ouchi, K.; Azumi, Y.; Tuchida, T. Improving effects of the mushroom Yamabushitake (*Hericium erinaceus*) on mild cognitive impairment: A double-blind placebo-controlled clinical trial. *Phytother. Res.* **2009**, *23*, 367–372. [CrossRef]
74. Saitsu, Y.; Nishide, A.; Kikushima, K.; Shimizu, K.; Ohnuki, K. Improvement of cognitive functions by oral intake of *Hericium erinaceus*. *Biomed. Res. Tokyo Jpn.* **2019**, *40*, 125–131. [CrossRef]
75. Tsai, P.-C.; Wu, Y.-K.; Hu, J.-H.; Li, I.-C.; Lin, T.-W.; Chen, C.-C.; Kuo, C.-F. Preclinical Bioavailability, Tissue Distribution, and Protein Binding Studies of Erinacine A, a Bioactive Compound from *Hericium erinaceus* Mycelia Using Validated LC-MS/MS Method. *Molecules* **2021**, *26*, 4510. [CrossRef]
76. Hu, J.-H.; Li, I.-C.; Lin, T.-W.; Chen, W.-P.; Lee, L.-Y.; Chen, C.-C.; Kuo, C.-F. Absolute Bioavailability, Tissue Distribution, and Excretion of Erinacine S in *Hericium erinaceus* Mycelia. *Molecules* **2019**, *24*, 1624. [CrossRef]
77. Zhang, C.-C.; Cao, C.-Y.; Kubo, M.; Harada, K.; Yan, X.-T.; Fukuyama, Y.; Gao, J.-M. Chemical Constituents from *Hericium erinaceus* Promote Neuronal Survival and Potentiate Neurite Outgrowth via the TrkA/Erk1/2 Pathway. *Int. J. Mol. Sci.* **2017**, *18*, 1659. [CrossRef]
78. Shimbo, M.; Kawagishi, H.; Yokogoshi, H. Erinacine A increases catecholamine and nerve growth factor content in the central nervous system of rats. *Nutr. Res.* **2005**, *25*, 617–623. [CrossRef]
79. Chang, C.-H.; Chen, Y.; Yew, X.-X.; Chen, H.-X.; Kim, J.-X.; Chang, C.-C.; Peng, C.-C.; Peng, R.Y. Improvement of erinacine A productivity in *Hericium erinaceus* mycelia and its neuroprotective bioactivity against the glutamate-insulted apoptosis. *LWT-Food Sci. Technol.* **2016**, *65*, 1100–1108. [CrossRef]
80. Üstün, R.; Ayhan, P. Regenerative activity of *Hericium erinaceus* on axonal injury model using in vitro laser microdissection technique. *Neurol. Res.* **2019**, *41*, 265–274. [CrossRef]
81. Lai, P.-L.; Naidu, M.; Sabaratnam, V.; Wong, K.-H.; David, R.P.; Kuppusamy, U.R.; Abdullah, N.; Malek, S.N.A. Neurotrophic properties of the Lion's mane medicinal mushroom, *Hericium erinaceus* (Higher Basidiomycetes) from Malaysia. *Int. J. Med. Mushrooms* **2013**, *15*, 539–554. [CrossRef]
82. Mori, K.; Obara, Y.; Hirota, M.; Azumi, Y.; Kinugasa, S.; Inatomi, S.; Nakahata, N. Nerve growth factor-inducing activity of *Hericium erinaceus* in 1321N1 human astrocytoma cells. *Biol. Pharm. Bull.* **2008**, *31*, 1727–1732. [CrossRef]
83. Phan, C.-W.; Lee, G.-S.; Hong, S.-L.; Wong, Y.-T.; Brkljača, R.; Urban, S.; Abd Malek, S.N.; Sabaratnam, V. *Hericium erinaceus* (Bull.: Fr) Pers. cultivated under tropical conditions: Isolation of hericenones and demonstration of NGF-mediated neurite outgrowth in PC12 cells via MEK/ERK and PI3K-Akt signaling pathways. *Food Funct.* **2014**, *5*, 3160–3169. [CrossRef]
84. Zhang, C.-C.; Yin, X.; Cao, C.-Y.; Wei, J.; Zhang, Q.; Gao, J.-M. Chemical constituents from *Hericium erinaceus* and their ability to stimulate NGF-mediated neurite outgrowth on PC12 cells. *Bioorganic Med. Chem. Lett.* **2015**, *25*, 5078–5082. [CrossRef]
85. Vigna, L.; Morelli, F.; Agnelli, G.M.; Napolitano, F.; Ratto, D.; Occhinegro, A.; Di Iorio, C.; Savino, E.; Girometta, C.; Brandalise, F.; et al. *Hericium erinaceus* Improves Mood and Sleep Disorders in Patients Affected by Overweight or Obesity: Could Circulating Pro-BDNF and BDNF Be Potential Biomarkers? *Evid.-Based Complement. Altern. Med.* **2019**, *2019*, 7861297. [CrossRef] [PubMed]
86. Grozier, C.D.; Alves, V.A.; Killen, L.G.; Simpson, J.D.; O'Neal, E.K.; Waldman, H.S. Four Weeks of *Hericium erinaceus* Supplementation Does Not Impact Markers of Metabolic Flexibility or Cognition. *Int. J. Exerc. Sci.* **2022**, *15*, 1366–1380. [PubMed]
87. Tsai-Teng, T.; Chin-Chu, C.; Li-Ya, L.; Wan-Ping, C.; Chung-Kuang, L.; Chien-Chang, S.; Chi-Ying, H.F.; Chien-Chih, C.; Shiao, Y.J. Erinacine A-Enriched *Hericium erinaceus* Mycelium Ameliorates Alzheimer's Disease-Related Pathologies in APPswe/PS1dE9 Transgenic Mice. *J. Biomed. Sci.* **2016**, *23*, 49. [CrossRef] [PubMed]
88. Brandalise, F.; Cesaroni, V.; Gregori, A.; Repetti, M.; Romano, C.; Orrù, G.; Botta, L.; Girometta, C.; Guglielminetti, M.L.; Savino, E.; et al. Dietary Supplementation of *Hericium erinaceus* Increases Mossy Fiber-CA3 Hippocampal Neurotransmission and Recognition Memory in Wild-Type Mice. *Evid.-Based Complement. Altern. Med.* **2017**, *2017*, 3864340. [CrossRef]
89. Ryu, S.; Kim, H.G.; Kim, J.Y.; Kim, S.Y.; Cho, K.-O. *Hericium erinaceus* Extract Reduces Anxiety and Depressive Behaviors by Promoting Hippocampal Neurogenesis in the Adult Mouse Brain. *J. Med. Food* **2018**, *21*, 174–180. [CrossRef]
90. Bernard, J.A.; Seidler, R.D. Moving forward: Age effects on the cerebellum underlie cognitive and motor declines. *Neurosci. Biobehav. Rev.* **2014**, *42*, 193–207. [CrossRef]
91. Cordaro, M.; Salinaro, A.T.; Siracusa, R.; D'Amico, R.; Impellizzeri, D.; Scuto, M.; Ontario, M.L.; Cuzzocrea, S.; Di Paola, R.; Fusco, R.; et al. Key Mechanisms and Potential Implications of *Hericium erinaceus* in NLRP3 Inflammasome Activation by Reactive Oxygen Species during Alzheimer's Disease. *Antioxidants* **2021**, *10*, 1664. [CrossRef]
92. Mori, K.; Obara, Y.; Moriya, T.; Inatomi, S.; Nakahata, N. Effects of *Hericium erinaceus* on amyloid β(25-35) peptide-induced learning and memory deficits in mice. *Biomed. Res. Tokyo Jpn.* **2011**, *32*, 67–72. [CrossRef]
93. Zhang, J.; An, S.; Hu, W.; Teng, M.; Wang, X.; Qu, Y.; Liu, Y.; Yuan, Y.; Wang, D. The Neuroprotective Properties of *Hericium erinaceus* in Glutamate-Damaged Differentiated PC12 Cells and an Alzheimer's Disease Mouse Model. *Int. J. Mol. Sci.* **2016**, *17*, 1810. [CrossRef]
94. Zhu, X.; Zhang, Z.; Yang, X.; Qi, L.; Guo, Y.; Tang, X.; Xie, Y.; Chen, D. Improvement of extraction from *Hericium erinaceus* on the gut-brain axis in AD-like mice. *Brain Res.* **2022**, *1793*, 148038. [CrossRef]
95. Forsythe, P.; Kunze, W.A.; Bienenstock, J. On communication between gut microbes and the brain. *Curr. Opin. Gastroenterol.* **2012**, *28*, 557–562. [CrossRef]
96. Mayer, E.A.; Tillisch, K.; Gupta, A. Gut/brain axis and the microbiota. *J. Clin. Investig.* **2015**, *125*, 926–938. [CrossRef]
97. Foster, J.A.; McVey Neufeld, K.-A. Gut-brain axis: How the microbiome influences anxiety and depression. *Trends Neurosci.* **2013**, *36*, 305–312. [CrossRef]

98. Cryan, J.F.; O'Riordan, K.J.; Cowan, C.S.M.; Sandhu, K.V.; Bastiaanssen, T.F.S.; Boehme, M.; Codagnone, M.G.; Cussotto, S.; Fulling, C.; Golubeva, A.V.; et al. The Microbiota-Gut-Brain Axis. *Physiol. Rev.* **2019**, *99*, 1877–2013. [CrossRef]
99. Leccioli, V.; Oliveri, M.; Romeo, M.; Berretta, M.; Rossi, P. A New Proposal for the Pathogenic Mechanism of Non-Coeliac/Non-Allergic Gluten/Wheat Sensitivity: Piecing Together the Puzzle of Recent Scientific Evidence. *Nutrients* **2017**, *9*, 1203. [CrossRef]
100. Zhu, X.; Li, B.; Lou, P.; Dai, T.; Chen, Y.; Zhuge, A.; Yuan, Y.; Li, L. The Relationship Between the Gut Microbiome and Neurodegenerative Diseases. *Neurosci. Bull.* **2021**, *37*, 1510–1522. [CrossRef]
101. Vázquez, E.; Barranco, A.; Ramírez, M.; Gruart, A.; Delgado-García, J.M.; Martínez-Lara, E.; Blanco, S.; Martín, M.J.; Castanys, E.; Buck, R.; et al. Effects of a human milk oligosaccharide, 2′-fucosyllactose, on hippocampal long-term potentiation and learning capabilities in rodents. *J. Nutr. Biochem.* **2015**, *26*, 455–465. [CrossRef]
102. Allen, A.P.; Hutch, W.; Borre, Y.E.; Kennedy, P.J.; Temko, A.; Boylan, G.; Murphy, E.; Cryan, J.F.; Dinan, T.G.; Clarke, G. Bifidobacterium longum 1714 as a translational psychobiotic: Modulation of stress, electrophysiology and neurocognition in healthy volunteers. *Transl. Psychiatry* **2016**, *6*, e939. [CrossRef]
103. Burokas, A.; Arboleya, S.; Moloney, R.D.; Peterson, V.L.; Murphy, K.; Clarke, G.; Stanton, C.; Dinan, T.G.; Cryan, J.F. Targeting the Microbiota-Gut-Brain Axis: Prebiotics Have Anxiolytic and Antidepressant-like Effects and Reverse the Impact of Chronic Stress in Mice. *Biol. Psychiatry* **2017**, *82*, 472–487. [CrossRef]
104. Yang, X.-D.; Wang, L.-K.; Wu, H.-Y.; Jiao, L. Effects of prebiotic galacto-oligosaccharide on postoperative cognitive dysfunction and neuroinflammation through targeting of the gut-brain axis. *BMC Anesthesiol.* **2018**, *18*, 177. [CrossRef]
105. Gronier, B.; Savignac, H.M.; Di Miceli, M.; Idriss, S.M.; Tzortzis, G.; Anthony, D.; Burnet, P.W.J. Increased cortical neuronal responses to NMDA and improved attentional set-shifting performance in rats following prebiotic (B-GOS®) ingestion. *Eur. Neuropsychopharmacol.* **2018**, *28*, 211–224. [CrossRef] [PubMed]
106. Osadchiy, V.; Martin, C.R.; Mayer, E.A. The Gut-Brain Axis and the Microbiome: Mechanisms and Clinical Implications. *Clin. Gastroenterol. Hepatol.* **2019**, *17*, 322–332. [CrossRef] [PubMed]
107. Murphy, E.J.; Rezoagli, E.; Major, I.; Rowan, N.J.; Laffey, J.G. β-Glucan Metabolic and Immunomodulatory Properties and Potential for Clinical Application. *J. Fungi* **2020**, *6*, 356. [CrossRef] [PubMed]
108. Singdevsachan, S.K.; Auroshree, P.; Mishra, J.; Baliyarsingh, B.; Tayung, K.; Thatoi, H. Mushroom polysaccharides as potential prebiotics with their antitumor and immunomodulating properties: A review. *Bioact. Carbohydr. Diet. Fibre* **2016**, *7*, 1–14. [CrossRef]
109. Fernandes, A.; Nair, A.; Kulkarni, N.; Todewale, N.; Jobby, R. Exploring Mushroom Polysaccharides for the Development of Novel Prebiotics: A Review. *Int. J. Med. Mushrooms* **2023**, *25*, 1–10. [CrossRef] [PubMed]
110. Tian, B.; Geng, Y.; Xu, T.; Zou, X.; Mao, R.; Pi, X.; Wu, X.; Huang, L.; Yang, K.; Zeng, X.; et al. Digestive Characteristics of *Hericium erinaceus* Polysaccharides and Their Positive Effects on Fecal Microbiota of Male and Female Volunteers during In Vitro Fermentation. *Front. Nutr.* **2022**, *9*, 858585. [CrossRef]
111. Su, Y.; Cheng, S.; Ding, Y.; Wang, L.; Sun, M.; Man, C.; Zhang, Y.; Jiang, Y. A comparison of study on intestinal barrier protection of polysaccharides from *Hericium erinaceus* before and after fermentation. *Int. J. Biol. Macromol.* **2023**, *233*, 123558. [CrossRef]
112. Xie, X.Q.; Geng, Y.; Guan, O.; Ren, Y.; Guo, L.; Lv, Q.; Lu, Z.M.; Shi, J.S.; Xu, Z.H. Influence of Short-Term Consumption of *Hericium erinaceus* on Serum Biochemical Markers and the Changes of the Gut Microbiota: A Pilot Study. *Nutrients* **2021**, *13*, 1008. [CrossRef]
113. Mitsou, E.K.; Saxami, G.; Stamoulou, E.; Kerezoudi, E.; Terzi, E.; Koutrotsios, G.; Bekiaris, G.; Zervakis, G.I.; Mountzouris, K.C.; Pletsa, V.; et al. Effects of Rich in B-Glucans Edible Mushrooms on Aging Gut Microbiota Characteristics: An In Vitro Study. *Molecules* **2020**, *25*, 2806. [CrossRef]
114. Cho, H.-W.; Choi, S.; Seo, K.; Kim, K.H.; Jeon, J.-H.; Kim, C.H.; Lim, S.; Jeong, S.; Chun, J.L. Gut microbiota profiling in aged dogs after feeding pet food contained *Hericium erinaceus*. *J. Anim. Sci. Technol.* **2022**, *64*, 937–949. [CrossRef]
115. Yang, Y.; Ye, H.; Zhao, C.; Ren, L.; Wang, C.; Georgiev, M.I.; Xiao, J.; Zhang, T. Value added immunoregulatory polysaccharides of *Hericium erinaceus* and their effect on the gut microbiota. *Carbohydr. Polym.* **2021**, *262*, 117668. [CrossRef]
116. Shao, S.; Wang, D.; Zheng, W.; Li, X.; Zhang, H.; Zhao, D.; Wang, M. A unique polysaccharide from *Hericium erinaceus* mycelium ameliorates acetic acid-induced ulcerative colitis rats by modulating the composition of the gut microbiota, short chain fatty acids levels and GPR41/43 respectors. *Int. Immunopharmacol.* **2019**, *71*, 411–422. [CrossRef]
117. Ren, Y.; Sun, Q.; Gao, R.; Sheng, Y.; Guan, T.; Li, W.; Zhou, L.; Liu, C.; Li, H.; Lu, Z.; et al. Low Weight Polysaccharide of *Hericium erinaceus* Ameliorates Colitis via Inhibiting the NLRP3 Inflammasome Activation in Association with Gut Microbiota Modulation. *Nutrients* **2023**, *15*, 739. [CrossRef]
118. Chen, D.; Zheng, C.; Yang, J.; Li, J.; Su, J.; Xie, Y.; Lai, G. Immunomodulatory Activities of a Fungal Protein Extracted from *Hericium erinaceus* through Regulating the Gut Microbiota. *Front. Immunol.* **2017**, *8*, 666. [CrossRef]
119. Chen, D.; Yang, X.; Zheng, C.; Yang, J.; Tang, X.; Chen, J.; Shuai, O.; Xie, Y. Extracts from *Hericium erinaceus* Relieve In-flammatory Bowel Disease by Regulating Immunity and Gut Microbiota. *Oncotarget* **2017**, *8*, 85838–85857. [CrossRef]
120. Wang, D.; Zhu, X.; Tang, X.; Li, H.; Xie, Y.; Chen, D. Auxiliary antitumor effects of fungal proteins from *Hericium erinaceus* by target on the gut microbiota. *J. Food Sci.* **2020**, *85*, 1872–1890. [CrossRef]
121. Tian, B.; Liu, R.; Xu, T.; Cai, M.; Mao, R.; Huang, L.; Yang, K.; Zeng, X.; Peilong, S. Modulating effects of *Hericium erinaceus* polysaccharides on the immune response by regulating gut microbiota in cyclophosphamide-treated mice. *J. Sci. Food Agric.* **2023**, *103*, 3050–3064. [CrossRef]

Biomedicine & Pharmacotherapy 159 (2023) 114262

Contents lists available at ScienceDirect

Biomedicine & Pharmacotherapy

journal homepage: www.elsevier.com/locate/biopha

# Fighting secondary triple-negative breast cancer in cerebellum: A powerful aid from a medicinal mushrooms blend

Fabrizio De Luca [a,1], Elisa Roda [b,1], Daniela Ratto [a], Anthea Desiderio [c], Maria Teresa Venuti [a], Martino Ramieri [a], Maria Grazia Bottone [a], Elena Savino [c], Paola Rossi [a,*]

[a] Department of Biology and Biotechnology "L. Spallanzani", University of Pavia, 27100 Pavia, Italy
[b] Laboratory of Clinical & Experimental Toxicology, Pavia Poison Centre, National Toxicology Information Centre, Toxicology Unit, Istituti Clinici Scientifici Maugeri IRCCS, 27100 Pavia, Italy
[c] Department of Earth and Environmental Science, University of Pavia, 27100 Pavia, Italy

ARTICLE INFO

*Keywords:*
TNBC
Cerebellum
Medicinal mushrooms
Metastases
Locomotor activity
Cancer proliferation
Apoptosis
Integrative medicine

ABSTRACT

Breast cancer (BC) is the second most common cause of brain metastasis onset in patients, with the cerebellum accounting for the 33% of cases. In the current study, using a 4T1 triple-negative mouse BC model, we revealed that an orally administered medicinal mushrooms (MM) blend, rich in β-glucans, played a direct and specific anti-cancer action on cerebellar metastases, also bettering locomotor performances. The neuroprotective effect of the MM blend plays through (i) a direct and specific inhibition of cerebellar metastatization pattern typical of TNBC (with an induced reduction of about 50% of metastases density) and (ii) the regulation of apoptosis and proliferation-related genes, as suggested by expression changes of specific molecular markers, i.e. PCNA, p53, Bcl2, BAX, CASP9, CASP3, Hsp70 and AIF. Therefore, inhibiting the metastatization process, triggering a significant apoptosis increase, and lessening cell proliferation, this MM supplement, employed as adjuvant treatment in association with conventional therapy, could represent a promising approach, in the field of Integrative Oncology, for patients' management in both prevention and treatment of brain metastases from BC.

## 1. Introduction

Female breast cancer (BC) is the most commonly diagnosed cancer worldwide, with an incidence of 2,261,419 cases and mortality of 684,996 individuals in 2020 [1]. BC is a heterogeneous disease, showing a tumour phenotype characterized by peculiar histological and metastatic features, as well as different therapeutic response and clinical outcome [2,3]. Nowadays, 5 clinical subtypes of BC have been identified, based on their gene expression profile or biomarkers expression [4]. Among these tumours, approximately 10–20% are triple-negative breast cancer (TNBC), testing negative for estrogenic and progesterone receptors, and for the epidermal growth factor receptor 2 (HER2). TNBC is the most aggressive BC, with either high proliferation or metastatic phenomena, high rate of recurrence, often associated with poor prognosis, and unresponsiveness to current targeted therapies [5–7].

Metastatic colonization in TBNC involves cellular and molecular processes, which act to stimulate angiogenesis and tumour-stroma interactions, as well as intravasation through the basement membrane with subsequent extravasation into the distant target organs [8]. Actually, BC is the second most common cause of brain metastasis onset. In particular, Central nervous system (CNS) is the first metastatic target in 12% of BC patients, being also detected in 30% of autopsy series [9–11].

*Abbreviations:* BC, Breast Cancer; TNBC, Triple-Negative Breast Cancer; HER2, Human Epidermal growth factor Receptor 2; CNS, Central Nervous System; BMBC, Brain Metastases from BC; BBB, Blood Brain Barrier; MM, medicinal mushrooms; BRMs, Biological response modifiers; MU-care, Micotherapy U-care; TME, Tumor Microenvironment; PCNA, Proliferating Cell Nuclear Antigen; Bcl-2, B-cell lymphoma 2; BAX, Bcl2 Associated X; CASP9, Caspase 9; CASP3, Caspase 3; Hsp70, 70 kDa Heat shock protein; PBS, Phosphate-Buffer Saline; QoL, Quality of Life; H&E, Hematoxylin and Eosin; PSR, Picrosirius Red; OD, Optical Density; IGL, Internal Granular Layer; PCs, Purkinje cells; WM, White matter; ML, Molecular layer; AIF, Apoptosis-inducing factor.

* Corresponding author.
*E-mail addresses:* fabrizio.deluca01@universitadipavia.it (F. De Luca), elisa.roda@icsmaugeri.it (E. Roda), daniela.ratto01@universitadipavia.it (D. Ratto), anthea.desiderio01@universitadipavia.it (A. Desiderio), mariateresa.venuti01@universitadipavia.it (M.T. Venuti), martino.ramieri01@universitadipavia.it (M. Ramieri), mariagrazia.bottone@unipv.it (M.G. Bottone), elena.savino@unipv.it (E. Savino), paola.rossi@unipv.it (P. Rossi).
[1] These authors have contributed equally to this work and share first authorship.

https://doi.org/10.1016/j.biopha.2023.114262
Received 14 November 2022; Received in revised form 5 January 2023; Accepted 14 January 2023
Available online 17 January 2023

During the last 40 years an increase in the onset of brain metastases from BC (BMBC) has been perceived, possibly due to the discovery and use of novel therapies, which result in longer patient survival, as well as to advances in neuroimaging allowing a punctual detection of early metastases [12,13]. Notably, among the different regions of CNS, cerebellum is the main site of metastases occurrence accounting for the 33% of cases, together with basal ganglia, [14–16]. This preferential location is probably ascribable to the high blood supply of this area [17] and to a "leaky" blood brain barrier (BBB) that allows the passage of metastatic cells into the CNS [17,18], a process characterized by a close cross-talk between the microenvironment and the tumour cells [19].

Currently, the standard of care consists of chemotherapy in case of BMBC, although with reduced efficacy due to the presence BBB, which limits the efficacy of chemotherapic drugs to reach the CNS. Alternative conventional therapeutic approaches, resulting in longer patients' survival, include surgery, whole-brain radiation and stereotactic radiosurgery. Nevertheless, the lack of an effective targeted therapy and the TNBC heterogeneity emphasized the urgent need to identify new therapeutic targets and develop novel effective medicines capable to overcome drug resistance.

One of the most promising sources of "drug discovery" in cancer adjuvant therapy are medicinal mushrooms (MM), which possess a long story of use in traditional oriental medicine mainly in China and Asia, also employed as nutritionally functional foods. A bulk of literature clearly evidenced that MM own peculiar anticancer, onco-immunological, and immunomodulatory properties, also improving quality of life during conventional oncological treatment protocols in humans [20,21].

Indeed, in the last years, the use of several MM has been approved as adjuvant supplements in antitumor therapy in different countries. Different MM produce hundreds of bioactive compounds which are able to influence, often in a synergistic way, numerous cancer-related pathways, modulating cellular targets typically involved in cell proliferation, survival, and angiogenesis [21,22]. In particular, anticarcinogenic, antimutagenic, onco-immunological and immunomodulatory effects in BC are closely linked to the type and amount of β1–3 and β1–6 glucans and to their modulation of the innate and cell-mediated immune response [7,23]. Such compounds act as biological response modifiers (BRMs), stimulating the immune system and consequently helping on cancer fighting. In fact, β-glucans are recognized by dectin-1 receptors by antigen presenting cells, thus "training innate immunity", which results in enhanced host reaction. This trained immunity holds great potential for boosting immune responses in frail subjects, i.e. oncological patients, and even some of these fungal β-glucans are already under evaluation on clinical trials [24–27].

Numerous literature data evidenced that the use of MM extracts or their compounds is secure and helpful when employed alone or even combined with conventional anticancer treatments [21,22].

One of the cellular mechanism that is involved in cancer is the evasion of apoptosis which results in therapy resistance [28]. Furthermore, inefficient apoptotic pathway activation and proliferation are two combined mechanisms leading to further cancer progression and metastatization. New apoptosis-targeted agents developed in breast cancer, such as Bcl2-inhibitors, are in front line and are undergoing clinical trials and other are needed as a new way to treat cancer [28].

Our previous studies employing a syngeneic mouse of 4T1 triple-negative BC demonstrated the striking beneficial effects of an oral supplementation with "Micotherapy U-care" (MU-care), a MM blend, containing a combination of extracts of mycelia and sporophores. In particular, we proved that three month-lasting MU-Care supplementation ameliorated murine quality of life and contextually led to a remarkable decrease of metastases density and nodules number in pulmonary district, paralleled by a substantial decrease of inflammation and oxidative stress in metastases [7,29]. Moreover, we revealed that MU-Care was efficacious to influence cell death/proliferation balance, being these mechanisms strictly joined and inversely associated. Hence, our findings highlighted that MM blend owns a direct effect on tumour cells compelling cancer cells to apoptosis.

Recently, the same MM blend was employed for cancer patients' management after the failure of conventional treatment; specifically, MU-care has been administered in four subjects suffering from different tumour types, including breast cancer, with an improvement of survival and quality of life [30].

Herein, we evaluated the effect of MU-care in the before reported experimental conditions, using the 4T1 triple-negative mouse BC model, focusing on cerebellum. In particular, we addressed distinctive endpoints relative to cell death pathway also exploring pathological outcomes of the murine cerebellar tissue, comparing metastatic areas and neighbouring Purkinje cells. Specifically, cerebellar histopathology was investigated, together with the immunohistochemical assessment of key molecules, i.e., PCNA, p53, Bcl2, BAX, CASP9, CASP3, Hsp70 and AIF. Parallelly, locomotor performances were examined in vivo, being the cerebellum critically implicated in the control of motor behavior over cortical regions via cerebello-thalamic-cortical loops, also playing a pivotal role in balance and locomotion. In particular, we intended to evaluate possible functional changes due to damages in the cerebellar circuits [29–32].

Using a comparative approach, overall results were evaluated with the final goal to assess whether MU-care could exert beneficial effects also on CNS secondary breast cancer.

## 2. Results

As previously described [7] using the same preclinical model, i.e. the 4T1 triple-negative mouse BC, we demonstrated that MU-Care supplementation was accompanied by a betterment of QoL. Among selected parameters, we analyzed locomotor performances, demonstrating an astonishingly improvement of locomotor capabilities of treated mice, paralleled by a striking beneficial effect in pulmonary tissue [7].

In current investigation, we focused on the MU-care supplementation effect on the cerebellum, the main metastatic target area in BMBC patients. Therefore, functional measures of locomotor performances were complemented by histopathological characterization and immunohistochemical data about the expression of specific biomarkers representative of proliferation/cell death pathway in treated and not treated syngeneic mice compared to healthy control animals.

### 2.1. MU-care supplementation increased locomotor activities

We monitored locomotor parameters of mice before and after 4T1 cells injections in treated and not treated mice. In a variant of the open-field test, mice were left to explore freely an open and safety environment for eight minutes. We measured three locomotor parameters, i.e. the total distance, the mean speed, and the resting time. Specifically, open arena test was performed in treated mice (i) before starting MU-care treatment and prior to the tumor injection, namely "pre" condition (experimental time T1), and (ii) 20 days after 4T1 cells inoculation (T2). In untreated mice open arena test were performed (i) prior to the tumor injection, namely "pre" condition, and (ii) 20 days after 4T1 cells inoculation, namely "post" condition, in which pre and post represent T1 and T2, respectively.

Notably, concerning untreated mice only, all the examined parameters were similar pre- and post-4T1 injection, while the MU-care supplementation significantly improved locomotor performances (Fig. 1 A, B, C and Table 1). In particular, in untreated mice the total distance Fig. 1A), the mean speed Fig. 1B), and the resting time Fig. 1C) recorded "pre" and "post" were comparable. Any statistically significant difference was measured between "pre" and "post" condition in untreated mice and "pre" condition in the treated experimental group.

MU-care supplementation significantly enhanced murine locomotor activities despite 4T1 cells injection, as evidenced by a 57.2% increase in total distance Fig. 1A), a 22.2% increment in mean speed Fig. 1B) and a

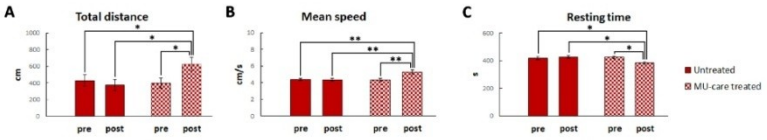


**Fig. 1.** Locomotor activity measured before (pre) and after (post) 4T1 cell injections in Untreated (red) and MU-care treated (blue) mice. A: Total distance (cm). B: Mean speed (cm/s). C: Resting time (s). $p < 0.05$ (*) and $p < 0.01$ (**) was calculated by One-way Anova followed by Bonferroni's post hoc test.

**Table 1**
Quantitative measurement of selected parameters, i.e. total distance (cm), mean speed (cm/s) and resting time (s), for studying locomotor performances before (pre) and after (post) 4T1 cell injections in Untreated and MU-care treated mice.

| | Total distance (cm) | | Mean Speed (cm/s) | | Resting time (s) | |
|---|---|---|---|---|---|---|
| | *pre* | *post* | *pre* | *post* | *pre* | *post* |
| Untreated | 425.07 ± 70.35 | 373.15 ± 66.66 | 4.36 ± 0.13 | 4.33 ± 0.15 | 417.14 ± 10.96 | 427.14 ± 9.57 |
| MU-care treated | 397.42 ± 59.67 | 624.82 ± 83.41 | 4.32 ± 0.17 | 5.28 ± 0.27 | 424.74 ± 9.07 | 384.19 ± 9.24 |

9.5% decrease in resting time Fig. 1C).

### 2.2. Cerebellar metastases density reduction in syngeneic mice by MU-care blend

Cerebellar vermes (sagittal sections) were processed to evaluate injury extent in cerebellar cortex comparing healthy controls, untreated, and MU-care treated mice by H&E, Nissl and PSR staining. All evaluations were performed focusing the attention on both cortical and bottom areas of cerebellar lobules.

Morphological picture obtained by H&E and Nissl staining in healthy controls (**a**), MU-care treated (**b-c**) and Untreated (**d-f**) mice are illustrated in Fig. 2. Healthy controls displayed a physiological cerebellar cytoarchitecture. Diversely, both Untreated and MU-care treated mice displayed the presence of a similar amount of micrometastases, localized in the entire thickness of cerebellar cortex, (Fig. 2, Panel H and Table 2).

Furthermore, in the same experimental groups, metastases were identified, mainly located within the internal granular layer (IGL) thickness and in the white matter (WM). These pathological formations were frequently surrounded by hemorrhagic foci scattered in the deep portions of the cerebellar lobules. Strikingly, the successive quantitative analyses revealed a statistically significant reduction (about 50%) in the number of deep WM cerebellar metastases after MU-care supplementation (Fig. 2, Panel I and Table 2). Focusing on the different cell types of cerebellar cortex layers, any morphological change was perceived in the three experimental groups.

Therefore, based on the significant metastases' density difference between Untreated and MU-care treated mice, we focused our attention on metastases.

### 2.3. Effect of MU-care on collagen staining in syngeneic mice

Results acquired after PSR cerebellum staining in healthy controls (a, d), and MU-care treated (b, c) and Untreated (e, f) mice are depicted in Fig. 3. This staining allows the study of collagen networks in normal and pathological paraffin-embedded tissues. The PSR labeling was mainly evident both at meningeal level as well as in the IGL cells in all experimental groups. In particular, a statistically extremely significant increase of PSR OD was measured in the meninges of Untreated mice compared to healthy controls. Remarkably, in MU-care treated animals the measured OD fell between the two aforementioned values, being therefore significantly different compared to that determined both in Untreated mice and healthy controls, (Fig. 3, Panel H and Table 2). Otherwise, concerning the PSR OD assessed at IGL cells level, any significant difference was established among the three experimental groups (Fig. 3, Panel I and Table 2). Concerning metastatic areas, although no quantifiable collagen-positivity was detectable in the cerebellar metastases, PSR staining enabled an easier identification of metastatic tissue, evidencing the occurrence of surrounding hemorrhaging foci engulfed by yellow-labeled erythrocytes.

### 2.4. MU-care neuroprotection affecting proliferation/cell death imbalance in cerebellar metastases of syngeneic mice

The persistence of inflammation and oxidative state can lead to extensive cell and tissue damage over time. As adaptive response to injury, cells can trigger several defense mechanisms such as increasing antioxidant enzyme levels or activating programmed cell death pathways. The following sections report the data obtained investigating precise molecules, as specific markers of cell death pathways with the goal to explore the occurrence of such hypothesized adaptive mechanism.

The maintenance of a balance between proliferation and cell death is crucial for physiological cells and tissues homeostasis. **PCNA** is one of the key molecules involved in DNA replication, as a nuclear proliferation marker typically overexpressed in cancer cells. PCNA immunopositivity was detected at metastatic level (Fig. 4). The quantitative analysis revealed an extremely statistically significant increase in the number of immunoreactive metastatic cells OD (Fig. 4, **Panel I** and Table 3) and, with a similar trend, an extremely statistically significant enhancement of immunopositive cell density was detected in the metastatic areas of Untreated animals compared to MU-care treated mice (Fig. 4, **Panel H** and Table 3).

**p53** is one of the most studied transcription regulators molecules and a tumor suppressor factor which regulates a wide range of genes involved in countless cellular functions, ranging from the DNA repair mechanisms to cell cycle regulation as well as to cell death mechanisms, i.e. apoptosis and autophagy, being these latter two critical points in cancer [33]. Our current data demonstrated that p53 immunoreactivity was mainly localized in the IGL both in MU-care treated and Untreated animals (Fig. 5). The presence of some p53-immunopositive micrometastases was also observed in the IGL of MU-care treated mice. Concerning metastases, a scarce number of p53-immunopositive cells were present, while an extremely significant increase of p53 immunopositive cells OD was detected comparing MU-care treated and Untreated mice (Fig. 5, **Panel H** and Table 3).

**Bcl2** protein is a well-known anti-apoptotic factor. In the present study, Bcl2 immunoreactivity was mainly localized at PCs level in all experimental groups and also in metastatic areas (Fig. 6). Notably, focusing on metastases, a slight decrease was measured in metastatic cell density comparing MU-care treated and Untreated animals (Fig. 6, **Panel H** and Table 4). Interestingly, concerning metastases OD, a very significant immunopositivity decrease was perceived in MU-care treated mice compared to Untreated animals () (Fig. 6, **Panel I** and Table 4).

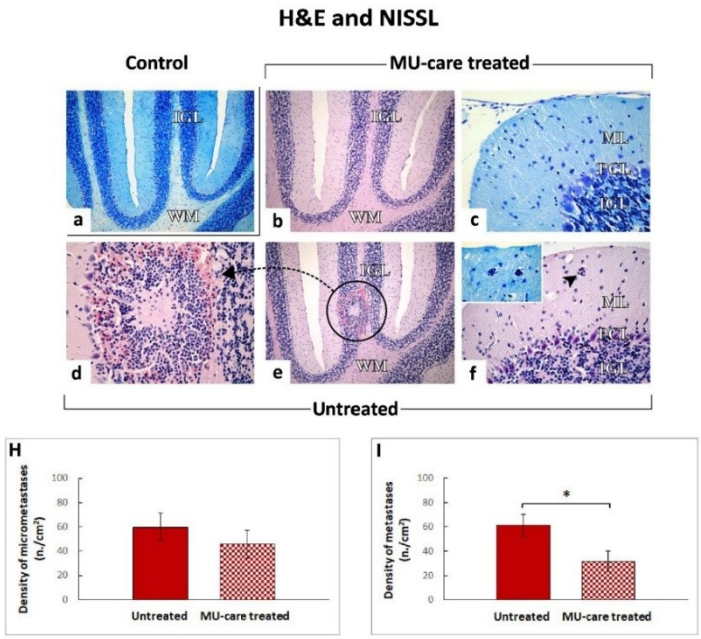


**Fig. 2.** Histological characterization by H&E and Nissl staining. Representative serial cerebellar vermis sections, showing parenchyma and metastatic areas (both macro- and micro-metastases), from healthy control (**a**), MU-care treated (**b, c**), and Untreated (**d-f**) mice. The physiological cerebellar structure appeared well preserved in healthy controls (**a**). Peculiar structural alterations evident in cerebellar parenchyma are presented, together with different metastatic features, in both MU-care treated and Untreated mice. ML: Molecular layer; PCL: Purkinje cells layer; IGL: Internal granular layer; WM: White matter. Circle and dotted arrow: deep metastasis identified in WM. Arrowhead: micro-metastasis localized in ML. Light microscopy magnification: 10x (**a, b** and **c**); 40 × (**c, d** and **f**); 60 × (insert in **f**). **Panels H** and **I**: Histograms showing quantification of micrometastases and metastases density, respectively. *p* value calculated by unpaired Student's t-test: (*) < 0.05.

**Table 2**
Quantitative assessment of (i) metastases and micrometastases density by H&E and NISSL staining and (ii) Meninges and IGL cells OD by PSR staining. —: *not present.*

| | H&E and NISSL | | Picrosirius Red | |
|---|---|---|---|---|
| | *Density of micrometastases* | *Density of metastases* | *Meninges OD* | *IGL cells OD* |
| Control | — | — | 75.80 ± 2.80 | 55.80 ± 0.93 |
| Untreated MU-care treated | 59.52 ± 11.64 | 61.22 ± 9.24 | 101.06 ± 3.09 | 57.05 ± 1.15 |
| | 45.63 ± 11.52 | 31.74 ± 8.46 | 90.62 ± 3.11 | 58.72 ± 1.04 |

Concerning the pro-apoptotic molecule **BAX**, its expression was particularly manifest at metastatic level in all synergic tumor-bearing mice, both Untreated and MU-care treated (Fig. 7). In detail, an extremely statistically significant enhancement of both immunopositive cells OD and density were measured in MU-care treated mice compared to those determined in Untreated animals (Fig. 7, **Panel H and I,** and Table 4). Notably, in the same experimental groups, at parenchyma level the immunoreactivity was not measurable, similarly to the situation observed in healthy controls.

**CASP9** is the most well-studied initiator caspase, playing a key role in the mitochondrial or intrinsic pathway. In particular, CASP9 immunolabeling was primarily detected at PCs soma level as well as in the metastases (Fig. 8). In particular, as regards to metastases, an extremely significant increase of immunopositive cell density was assessed in MU-care treated mice compared to Untreated (Fig. 8, **Panel H** and Table 5). Similarly, an extremely significant augment of immunopositive cells OD was measured in MU-care treated mice compared to Untreated animals (Fig. 8, **Panel I** and Table 5).

**CASP3** is one of the effector molecules triggering apoptosis (Fig. 9). A slight augment was determined evaluating metastases cell density in MU-care treated compared to Untreated animals). (Fig. 9, **Panel I** and Table 5). Likewise, a slight increase of CASP3 immunopositive cells OD was measured in MU-care treated mice compared to Untreated animals (). (Fig. 9, **Panel J** and Table 5).

As a chaperone protein, **Hsp70** is chiefly involved in inhibiting apoptosis. Hsp70 immunostaining was mainly observed at PCs level (both soma and main dendrites) in all experimental groups, and also in

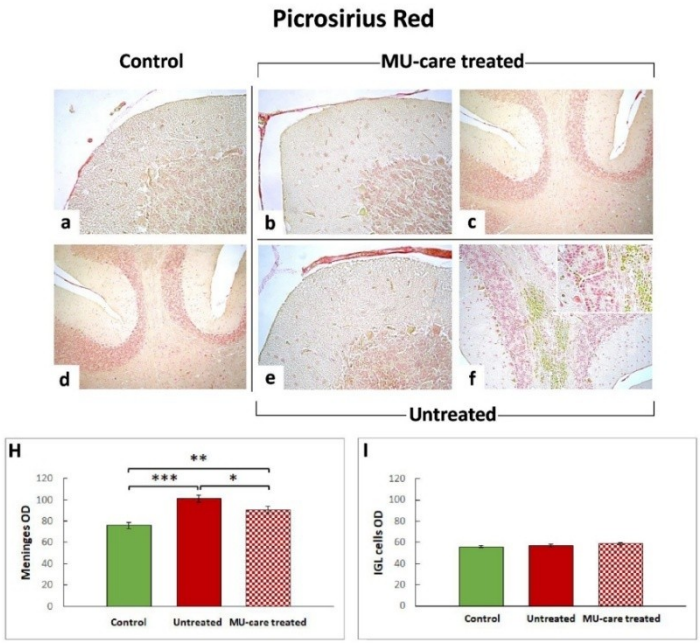


**Fig. 3.** Bright-field PSR staining. Representative cerebellar specimens, showing parenchyma and metastasis, from healthy control (a, d), MU-care treated (b, c), and Untreated (e, f) mice. Intensely labeled meninges were observable in Untreated mice (e). A weaker PSR OD positivity was detected in the IGL of healthy controls (a, d), MU-care treated (b, c), and Untreated (e, f) mice. The presence of a hemorrhagic core, engulfed with PSR yellow-labeled erythrocytes, surrounding unstained metastatic cells, was also evident (f). Light microscopy magnification: 10x (c and d); 20x (f); 40 × (a, b and e; insert in f). Panel H and I: Quantification of meninges and IGL cells OD, respectively. *p* values calculated by one-way ANOVA followed by Bonferroni's post-hoc test: (*) < 0.05; (**) < 0.01; (***) < 0.001.

metastatic areas in 4T1 injected mice (Fig. 10). (Fig. 10**, Panel H and I,** and Table 6). Notably, Hsp70 immunopositive cell density was generally extremely elevated in cerebellar metastatic tissues. In particular, Untreated mice displayed a significantly higher Hsp70 immunopositive cell density compared to MU-care treated animals (Fig. 10**, Panel H and I** and Table 6) Parallelly, concerning Hsp70 immunopositive cells OD, a significant lessening was measured comparing MU-care treated and untreated mice (Fig. 10**, Panel H** and **I and** Table 6).

### *2.5. MU-care parthanatos induction in cerebellar metastases of syngeneic mice*

Parthanatos is a cell death mechanism which differs from all other known types of cell death, e.g. apoptosis or necrosis. This multistep cell death pathway plays a key role in tumorigenesis and includes several critical molecules involved in tumor progression, invasion and metastatization. **AIF** is one of the main molecules involved in parthanatos and the translocation of this factor from the cytoplasm to the nucleus is a critical event in this cell death [34]. Results obtained after AIF immunohistochemistry in healthy controls (**a**), MU-care treated (**b - d**) and Untreated (**e – i**) mice are reported in Fig. 11 **and** Table 6. The AIF labeling was mainly evident in ML and metastatic tissue of both MU-care treated (**c, d**) and Untreated (**g, i**) mice, as well as in the IGL of Untreated animals only (**e**). Focusing on metastatic regions, a slight increase of AIF immunopositive cell density was observed comparing MU-care treated and Untreated animals (Fig. 11**, Panel J** and Table 6). Showing a similar trend, a significant increase of AIF immunopositive cell OD was measured in metastases of MU-care treated mice compared to the Untreated animals (Fig. 11**, Panel K** and Table 6).

## 3. Discussion

MU-care is a MM blend rich in β-glucans. In the current study, using a syngeneic tumour-bearing mouse of TNBC, we explored the MU-care effects on secondary breast cancer in cerebellum. We previously described, in the same animal model, MU-care beneficial action on lung metastases and in mice QoL. MM and their main active constituents β-glucans are known for their anticancer, anti-inflammatory and immunomodulatory properties both in vitro and in vivo [35–37] Few available papers focused on MM-derived β-glucans effects on brain cancer in vivo [26]. In the present study, we describe, for the first time, the in vivo effect of a MM blend rich in β-glucans on cerebellar secondary breast cancer in a triple negative syngeneic mouse. Notably, any other therapy was associated with MU-care during experimental time,

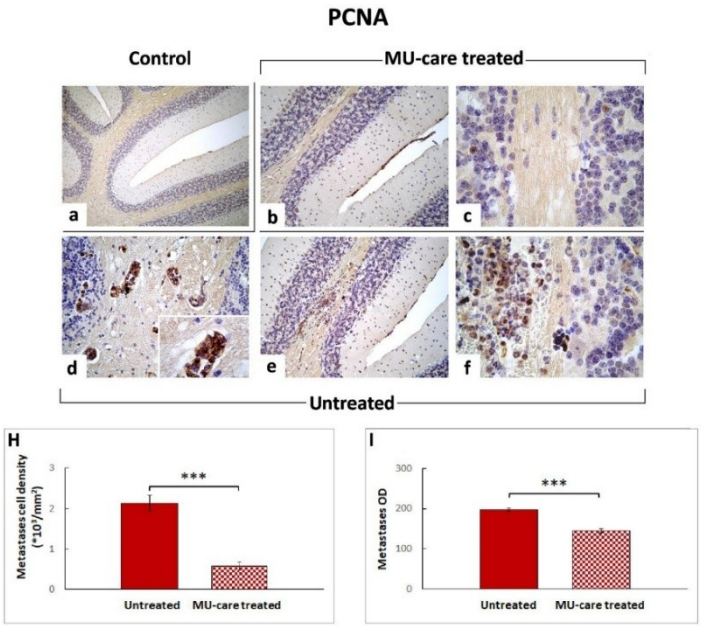


**Fig. 4.** Immunohistochemical labelling for PCNA in healthy control (a), MU-care treated (b, c), and Untreated (d–f) mice. A marked PCNA immunopositivity was evident mainly at metastatic level, more intense in Untreated (f) mice compared to MU-care treated (c). A strong immunolabeling was also visible in the deep WM of Untreated mice only (d). Light microscopy magnification: 10 × (a); 20 × (b, e); 40 × (d); 60 × (c, f, insert in d). Panels H and I: Histograms illustrating the quantitative assessment of immunoreactive metastases cell density and OD, respectively. *p* value calculated by unpaired Student's t-test: (***) < 0.001.

**Table 3**
Quantitative measurement of key proliferation/suppression molecules, namely PCNA and p53, in metastases. n.c.: not comparable.

| | PCNA | | P53 | |
|---|---|---|---|---|
| | Cell density | OD | Cell density | *OD* |
| Untreated | 2.13 ± 0.20 | 196.90 ± 4.14 | n.c. | 112.27 ± 1.99 |
| MU-care treated | 0.58 ± 0.10 | 144.49 ± 4.52 | n.c. | 139.21 ± 1.67 |

therefore we assumed that all described effects could be ascribable to the preventive and therapeutic (namely, effective during supplementation) effect of the MM blend.

In our experimental design, the syngeneic tumour-bearing mice were supplemented starting two months before 4T1 injection and lasting for an additional 35 days during tumour development, employing the MU-care drink, consisting of a mixture of five MM species, and characterized by a high 1,3–1,6 β-glucans content [7].

Through behavioural test experiments to assess locomotor activity, we revealed that supplemented mice, after 4T1 injection, were more active compared to untreated animals. Cerebellum is known to mediate sensorimotor adaptation, fine movement and coordination control, as well as instrumental conditioning [38–40]; hence, different behavioural tests could be conducted in lab animals. Nonetheless, it has to be highlighted that only a spontaneous behavioural test, namely open arena test, was chosen in our study, due to physiological BALB/c mice characteristics, e.g. high anxiety-like behaviour and limited exploratory performance [41,42]. All the tested locomotor parameters, i.e., the mean speed, the total distance, and the resting time, demonstrated a significant improvement in locomotor performances in MU-care mice. For fairness, it has to be mentioned that we cannot completely ruled out that the improvement of the locomotor activity could be attributable to MM beneficial effect on other brain regions and/or on muscular system, but the cerebellar metastatic areas observed in untreated mice tends to suggest a possible decline in their cerebellar network function. Remarkable, MU-care supplementation significantly increased the murine mean speed, a parameter analogous to the gait speed in humans. Gait speed is an important measure of functional status and health, since the ability to walk is one of the basic everyday activities [43–45], but it is a complex task that requires higher cognitive processes [46]. In particular, gait is related to and supported by cerebellar functions [47] and cerebellar volume loss was recorded in patients with decline in memory and gait speed [48,49]. Indeed, it is known that the cerebellum plays a fundamental role in gait and motor functioning, as demonstrated by poor gait in patients with cerebellar ataxia [48,50] and also by neuroimaging studies confirming the cerebellar involvement in

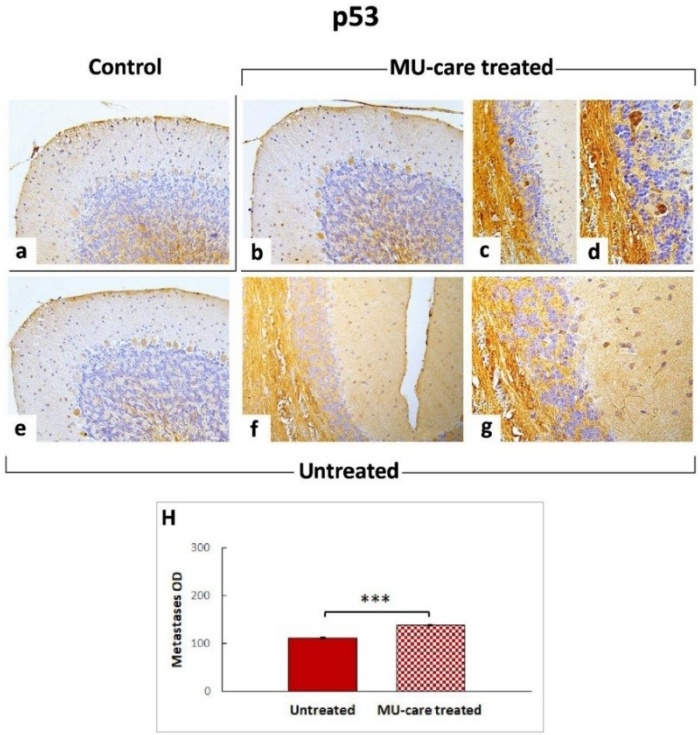


**Fig. 5.** Representative micrographs showing p53 immunohistochemical reaction in healthy control (**a**), MU-care treated (**b-d**), and Untreated (**e-g**) mice. An intensely marked p53 immunopositivity was observable particularly in micrometastases of MU-care treated mice (**c, d**); in these animals, metastases were also evidently immunoreactive (**c, d**). In Untreated mice, immunoposivity was clearly detected in metastatic areas (**f, g**). Light microscopy magnification: 40 × (**a, b, c, e, f**); 60 × (**d, g**). **Panel H**: histogram illustrating the quantitative analysis of immunopositive metastases OD. *p* values calculated by unpaired Student's t-test: (*) $< 0.05$, (**) $< 0.01$, (***) $< 0.001$.

sensorimotor coordination [51,52].

Histological, histochemical and immunohistochemical analyses in cerebellum were devoted to examine potential pathological features, in terms of cytoarchitectural alterations (with attention to different cerebellar cortex layers and cell types) and occurrence/number/extension of metastases.

H&E, having stood the test of time as the standard stain for histologic examination of tissues, enabling the recognition of different cells types and morphological changes, still remains the basis of contemporary cancer diagnosis [53,54].

In the current study, data obtained by means of H&E and Nissl techniques let us to highlight strong alterations in cerebellum of 4T1 tumour-bearing mice. In particular, the occurrence of several micrometastases and deep metastases was revealed, both in Untreated and in MU-care treated animals. This outcome fully matched with previous literature demonstrating that cerebellum is a typical metastatic site in BC patients [55]. These cerebellar neoformations were scattered both in WM as well as in ML of 4T1-injected mice. Notably, focusing on WM deep metastases, it has to be underlined that MU-care supplementation triggered a strikingly significant reduction in their number (about 50%). This data suggests that MU-care directly and specifically inhibit cerebellar metastasis of TNBC. Metastases were typically surrounded by haemorrhagic foci, appearing engulfed by yellow-labelled erythrocytes. It has also to be reported that, concerning the other different cell types of cerebellar cortex, any significant morphological alteration was observed neither in Untreated nor in MU-care treated animals.

Regarding collagen detection, PSR staining represents one of the most selective technique to identify and quantitatively estimate collagen deposition in histological sections. Fibrosis, resulting from chronic inflammatory process, is caused by an imbalance between collagen deposition and reabsorption. Tissue collagen quantification represents an important tool in the clinical diagnosis as well as for patients' outcome prediction and therapy individualization [56]. In the present investigation, PSR staining revealed a significant increase in collagen

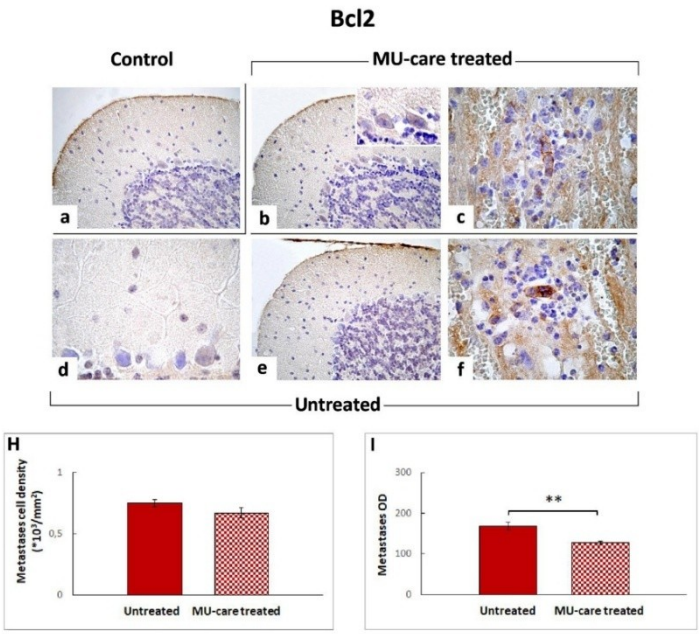


**Fig. 6.** Representative micrographs showing Bcl2 immunohistochemical reaction in healthy control (**a**), MU-care treated (**b, c**), and Untreated (**d–f**) mice. An intensely marked Bcl2 immunopositivity was observable particularly in PCs soma of MU-care treated mice (**b**); in these animals, metastases were also evidently immunoreactive (**c**). In Untreated mice, immunopositivity was detected in metastatic areas (**f**). Light microscopy magnification: 40 × (**a, b, e**); 60 × (**c, d, f**). **Panel H** and **I**: histograms illustrating the quantitative analysis of immunopositive metastases cell density and OD, respectively. *p* value calculated by unpaired Student's t-test: (**) < 0.01.

**Table 4**
Quantitative appraisal of crucial pro- and anti-apoptotic factors, namely Bcl2 and BAX, in cerebellar metastases.

| | Bcl2 | | BAX | |
|---|---|---|---|---|
| | *Cell density* | *OD* | *Cell density* | *OD* |
| Untreated | 0.75 | 168.01 | 0.39 | 120.99 |
| MU-care | ± 0.03 | ± 9.84 | ± 0.04 | ± 6.75 |
| treated | 0.67 | 127.23 | 0.74 | 168.37 |
| | ± 0.04 | ± 4.14 | ± 0.05 | ± 5.04 |

expression level in the meninges of 4T1-injected animals, with the Untreated mice resulting the most affected. In fact, cerebellar fibrosis tended to be reduced after MU-care supplementation. It has to be mentioned that, even though no quantifiable collagen-positivity was perceived in cerebellar metastases, Picric Acid itself enabled an easier recognition of deep metastases, highlighting the presence of yellow-labelled erythrocytes constituting haemorrhaging foci.

Based on our previous findings [7,29,57], we putatively assumed that MM blend could determine an imbalance between proliferation and cell death, driving to a significant increase in apoptotic event in metastatic tissue.

To test our hypothesis, we firstly assessed PCNA expression pattern after MM blend supplementation. In detail, a selective effect on the reduction of proliferation in cerebellar metastatic areas was evidenced in MU-care treated mice compared to untreated mice. Consequently, we postulated a protective role played by MM extract in DNA replication mechanism, and a direct and specific inhibitory effect on cancer cell proliferation.

Subsequently, we investigated the effect of MU-care on different apoptotic pathways. Initially, we examined Bcl2 immunohistochemical expression pattern [58–60]. Based on our data, we supposed that the lower Bcl-2 OD levels measured in cerebellar metastases of MU-care treated mice could be related to an imbalance between proliferation and apoptosis. Concerning cerebellar parenchyma (namely, PCs), Bcl-2 expression levels were comparable both in Untreated as well as in MU-care treated mice, thus suggesting a selective and specific apoptotic effect triggered by MM blend on metastases only.

Our aforementioned postulate was further reinforced by results obtained investigating BAX and p53. In particular, BAX, predominantly detected at metastatic level, displayed the highest expression levels in MU-care treated mice. This significant increase appeared to be in line with the well-known role of BAX, which acts as a proapoptotic protein. Thus, we could assume that an enhancement in BAX levels after MM supplementation could trigger tumour suppression. In accordance with our results, literature data demonstrated that, conversely, a decreased

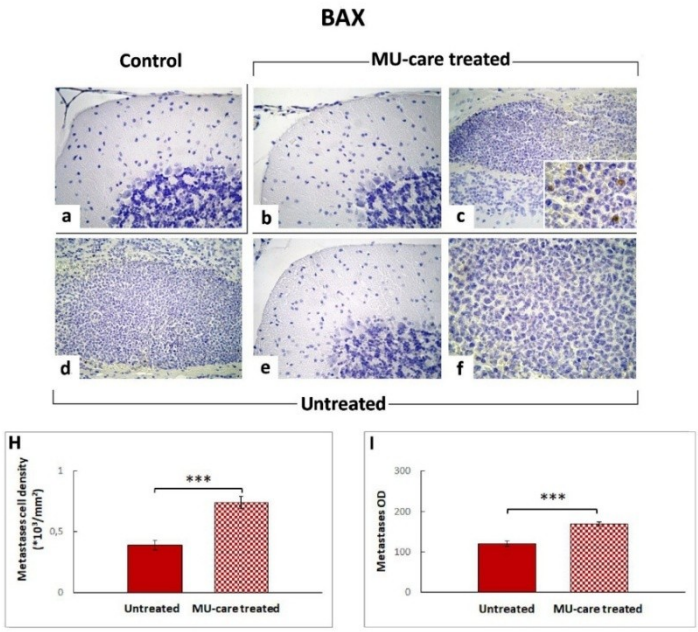


**Fig. 7.** Immunohistochemical labelling for BAX in healthy control (**a**), MU-care treated (**b, c**), and Untreated (**d–f**) mice. An intensely marked BAX immunoreactivity was clearly evident in metastatic areas of MU-care treated mice (**c**). Light microscopy magnification: 40 × (**a, b, c, d, e**); 60 × (**f**, insert in **c**). **Panels H** and **I**: Histograms showing the quantitative analysis of immunopositive metastases OD and cell density, respectively. *p* value calculated by unpaired Student's t-test: (***) < 0.001.

BAX expression would provide tumour cells with a selective survival advantage, contributing to their expansion and invasion [58]. Showing a similar trend, p53 exhibited the most marked increase in metastatic regions of MU-care treated mice. This enhanced immunopositivity for the wild type p53 isoform (wtp53), playing a crucial role deciding whether DNA would be repaired or the damaged cell would self-destruct, could indicate a possible attempt to cell cycle arrest, in order to inhibit proliferation of damaged cells. In fact, wtp53, a key regulator of cellular homeostasis, frequently referred to as the "guardian of the genome", fosters apoptosis and also inhibits VEGF-dependent angiogenesis, thereby opposing tumor growth and metastatization [61]. Concerning apoptosis, the selectivity of MM blend-mediated regulatory effect on this programmed cell death pathway was further confirmed analysing CASP9 and CASP3 expression patterns.

Specifically, the modulatory action of the MM blend on apoptotic pathway observed in cerebellar metastatic tissue was highlighted by the presence of enhanced CASP9 levels reported in MU-care treated mice only, thus evidencing increased cell death events in the metastases after supplementation. Our findings are in agreement with previous literature data revealing that a reduction in CASP9 expression levels can represent a tumour escape mechanism of apoptosis [62]. Furthermore, caspase-9 inhibition was related to increased resistance of cancer cells to chemotherapeutics treatment [63].

Then, following the known molecular apoptotic cascade, with the aim to explore the occurrence of a specific apoptotic pathway, we addressed the effect of MU-care supplement on CASP3. Caspase-3 is a key regulator of the apoptotic response, chiefly involved in tumorigenesis. Several studies demonstrated that increased CASP3 expression levels are closely associated with adverse breast cancer-specific patients' survival [64]. Notably, showing a different expression trend compared to other aforementioned markers, a lack of a direct CASP3 apoptotic effect on metastases was revealed.Concerning Hsp70, evidence that it is overexpressed in cancer, and that its high expression correlates with increased tumour grade and poor prognosis, is extensive also in patients affected by breast cancer [65]. In particular, this chaperon acts endowing malignant cells selective advantage by suppressing multiple apoptotic pathways (including autophagy), regulating necrosis, evading cellular senescence program, also promoting angiogenesis and thus supporting metastatization [66,67] Based on its clinical significance, assessment of several Hsp70-based immunotherapy protocols is still ongoing in clinical trials, together with the experimental use of Hsp70 inhibitors as promising chemotherapeutics. In accordance with these literature evidences, our current results in cerebellum revealed a strikingly high Hsp70-immunopositive cell density in metastases, with a value 50–100-fold higher compared to all other evaluated markers in the same metastatic regions. Notably, a significant reduction of Hsp70 levels (in terms of both cell density and OD) was assessed equally in metastases and parenchyma (namely, PCs) of MU-care treated mice compared to

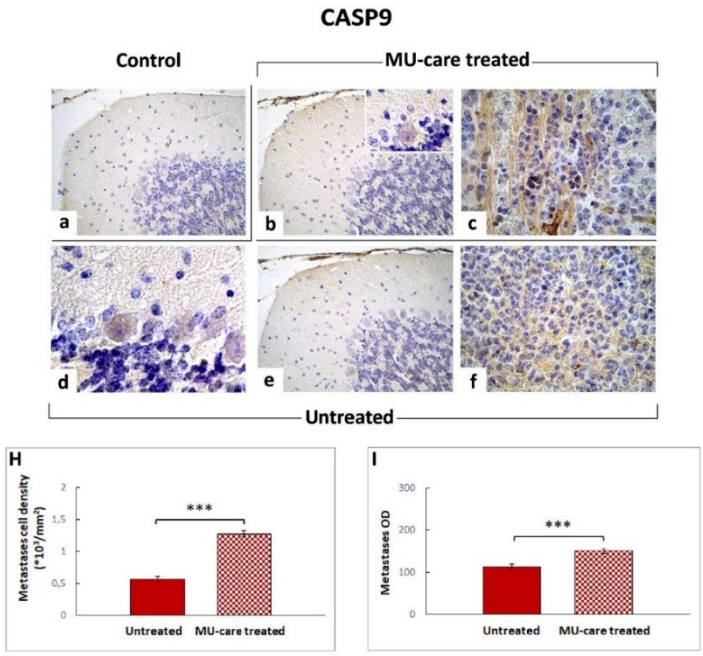


**Fig. 8.** Immunohistochemical labelling for CASP9 in healthy control (**a**), MU-care treated (***b, c***), and Untreated (**d–f**) mice. CASP9 immunopositivity was perceivable in the PCs soma of MU-care treated (**b**) and Untreated animals (**d, e**). An intensely marked immunolabeling was also evident in metastatic areas of MU-care treated mice (**c**). Immunopositivity was also noticeable in Untreated animals' metastases (**f**). Light microscopy magnification: 40 × (**a, b, e**); 60 × (**c, d, f,** insert in **b**). **Panels H** and **I**: Histograms illustrating quantitative evaluation of immunopositive metastases cell density and OD, respectively. *p* value calculated by unpaired Student's t-test: (***) < 0.001.

**Table 5**
Quantitative evaluation of initiator and effector caspases, i.e. CASP9 and CASP3, in cerebellar metastatic area.

| | CASP9 | | CASP3 | |
|---|---|---|---|---|
| | *Cell density* | *OD* | *Cell density* | *OD* |
| Untreated | 0.57 | 113.40 | 0.49 | 187.35 |
| MU-care | ± 0.04 | ± 6.49 | ± 0.04 | ± 5.16 |
| treated | 1.28 | 150.31 | 0.50 | 193.65 |
| | ± 0.05 | ± 5.98 | ± 0.04 | ± 5.39 |

Untreated animals. This extremely significant decrease was accompanied by the above-mentioned lessening in PCNA expression. This concurrent trend appeared in line with previous clinical findings reporting a conversely positive correlation between elevated PCNA and Hsp70 expression levels measured in human breast cancer patients [65].

The significant increase of CASP9 expression levels in metastatic areas of MU-care animals, was not succeeded by the expected increase of CASP3 in the same tissue, opening the hypothesis that other caspase effectors could be involved in the proapoptotic effects. Furthermore, the significant reduction of apoptosis-inducing factor (AIF) in metastases of syngeneic tumour-bearing mice suggests that metastatic BC cells would be able to escape cellular mechanisms which lead to both caspase-dependent and -independent apoptotic pathways, nonetheless leaving the hypothesis standing that an involvement of other cell death mechanisms would occurred in metastatic cells after MM supplementation.

Whether this beneficial action is to be ascribable to a direct β-glucans or other MM blend active metabolites effect, carried out crossing the BBB, or rather to a systemic anti-tumoral, immunomodulatory MM extract effect still needs to be clarified. We could even hypothesize that both mechanisms may contribute to the observed CNS outcomes. To elucidate this hypothesis, our recent in vitro data investigated the possible contribution of micotherapy in the fight against GBM and its synergic effect with a newly synthesized platinum-based compound, using human GBM U251 cells [68]. Interestingly, in line with the present in vivo results, we demonstrated that MU-care was able to regulate cell cycle, control cellular redox state, and to induce regulated form of necrosis, such as ferroptosis in U251 cells, thereby supporting the efficacy of this new combined therapy.

In conclusion, these data demonstrated that MU-care inhibit breast cancer cerebellar metastasis both by (i) a direct and specific inhibition of cerebellar metastatization pattern typical of TNBC, as well as by (ii) regulating apoptosis and proliferation-related genes. Therefore, this

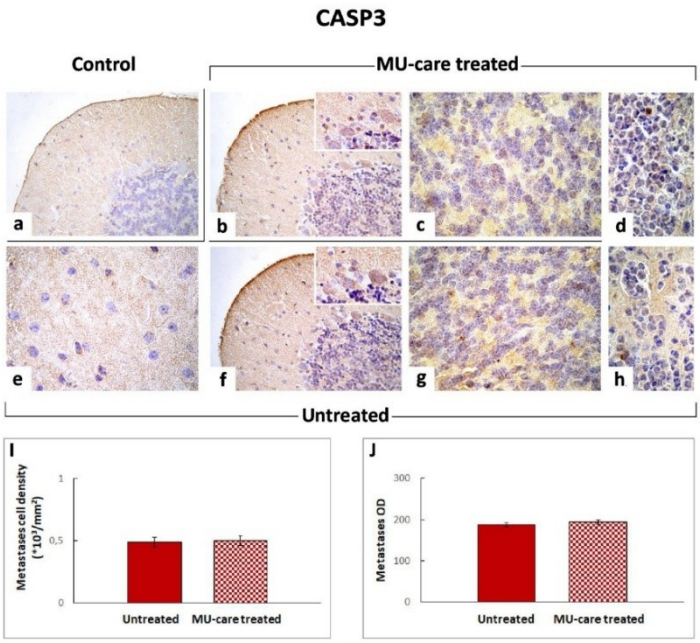


**Fig. 9.** Representative micrographs showing CASP3 immunohistochemical expression in healthy control (**a**), MU-care treated (**b-d**) and Untreated (**e–h**) mice. An intensely marked CASP3 immunopositivity was observed in ML of Untreated mice (**e, f**) as well as in IGL of both MU-care treated (**c**) and Untreated animals (**g**). Few immunolabeled cells were spotted in metastases, both in Untreated (**h**) and MU-care treated (**d**) mice. Light microscopy magnification: 40 × (**a, b, f**); 60 × (**c, d, e, g, h,** insert in **b** and **f**). **Panels I** and **J**: Histograms demonstrating quantitative data concerning metastases cell density and OD, respectively. *p* value calculated by unpaired Student's t-test: $> 0.05$.

MU-care-induced pleiotropic action make this MM blend a powerful, non-pharmacological therapeutic tool to be employed in integrative oncology, aiding the fight against TNBC-derived BM occurrence. Fig. 12.

## 4. Materials and methods

### 4.1. MU-care blend: raw materials from medicinal mushrooms, extraction procedure, beta-glucan title

The MU-care blend consisted of a mixture of five fungal species, produced and supplied by A.V.D. Reform s.r.l. (Noceto, Parma, Italy), and registered by the Italian Ministry of Health as a dietary supplement (registration number 627 I.5.i.h.2/2020/627). The detailed MU-care supplement (batch n. XMBLEND25032020) composition is reported here following (Table 7).

By sequencing Internal Transcribed Spacer (ITS) regions of nuclear DNA and confirming the ID code, specific MM species strains were established (for primers selection, see [29]). The PCR products were purified and sequenced by Eurofins Genomics (Konstanz, Germany). The identification was performed by using NCBI Nucleotide Blast software, version 2.9.0 (Table 7, ID code).

Subsequently, the sporophores and mycelia were cultivated for two to four months at 23 °C in a 1000 ± 100 ppm $CO_2$ atmosphere. After harvesting, the fresh material was extracted for 3 h at 95 °C in distilled water plus ethanol 10% (1 kg of raw material in 15 L of water/ethanol solution). After extraction, the fluid component was dehydrated until it reached less than 7% of humidity. Dry extracts were grounded and blended to obtain the 20% of each selected mushroom in the MU-care (Table 7).

All raw materials and final products were regularly verified following GMP, accordingly to the Hazard Analysis and Critical Control Points (HACCP) system, also to ensure traceability, even in accordance to Regulation (EC) No. 178/2002.

Finally, using a β-Glucan Assay Kit (Megazyme, LTD., Wicklow, Ireland), the MU-care blend was checked to measure the polysaccharide content, expressed as total (α plus β) glucan content and 1,3–1,6 β-glucans. This analysis revealed a polysaccharide content more than 30%. Out of this percentage (30%), > 15% were identified as 1,3–1,6 β-glucans, the main key active ingredients in MU-care.

### 4.2. Animals and experimental design

Wild-type (strain BALB/c) female (n = 34) mice (Charles River Italia, Calco, Italy) entered the Animal Care Facility of the University of Pavia

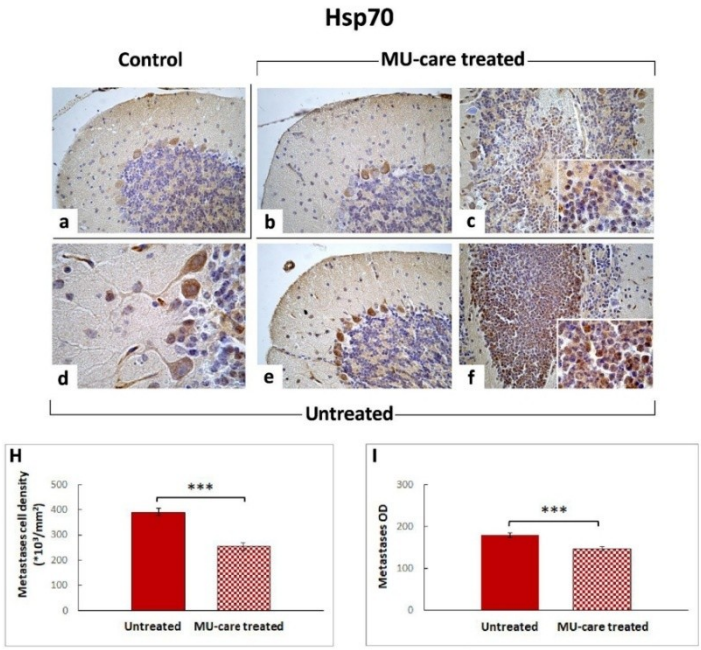


**Fig. 10.** Representative serial cerebellar sections immunostained for Hsp70 in healthy control (**a**), MU-care treated (**b, c**), and Untreated (**d–f**) mice. A marked Hsp70 immunopositivity was detectable in the PCs (soma and main dendrites) of healthy controls (**a**), MU-care treated (**b, c**) and Untreated (**d, e**) animals. An extremely intense immunolabeling was also evident in the metastases of Untreated mice (**f**). Immunopositivity was also strong in metastases of MU-care treated animals (**c**). Light microscopy magnification: 40 × (**a, b, c, e, f**); 60 × (**d,** insert in **c**, insert in **f**). **Panels H** and **I**: Quantification of immunopositive metastases cell density and OD, respectively. *p* value calculated by unpaired Student's t-test: (***) < 0.001.

**Table 6**
Quantitative measurement of essential markers of apoptosis and parthanatos, i.e. Hsp70 and AIF, respectively, in metastases.

| | HSP70 | | AIF | |
|---|---|---|---|---|
| | *Cell density* | *OD* | *Cell density* | *OD* |
| Untreated | 390.63 ± 15.32 | 179.92 ± 5.90 | 0.60 ± 0.05 | 124.67 ± 5.70 |
| MU-care treated | 254.16 ± 15.82 | 146.81 ± 4.26 | 0.66 ± 0.04 | 146.67 ± 4.43 |

at ~8 weeks of age. The pathogen-free mice were acclimatized for three weeks before experiments, housed in temperature and humidity-controlled (21 ± 2 °C with humidity at 50 ± 10%) vivaria (two animals/cage) under a 12:12 h light/dark cycle throughout the experiments. 12:12 h light: dark cycles. Mice had ad libitum access to food and water. Experimental procedures were performed in agreement with the European Council Directive 2010/63/EU on the care and use of laboratory animals, also following the guidelines established by the institution's animal welfare committee, the Ethics Committee of Pavia University (Ministry of Health, License number 364/2018-PR, approval date:17 May 2018). All animals employed have been treated humanely, with due concern for distress and discomfort alleviation.

To prevent any bias in study results, researchers were blinded to the group assignment for all experimental procedures.

For a three month-period, after acclimatization and until sacrifice, 16 (MU-care treated) out of 34 mice were provided with a Micotherapy U-care drink, consisting of a mixture of mycelium plus sporophores extracts of five MM species, including (20%) *Agaricus blazei* Murrill, *Agaricaceae*, (20%) *Ganoderma lucidum* (Curtis) P. Karst., *Polyporaceae*, (20%) *Grifola frondosa* (Dicks.) Gray, *Grifolaceae*, (20%) *Lentinula edodes* (Berk.) Pegler, *Omphalotaceae*, and (20%) *Ophiocordyceps sinensis* (Berk.) G.H. Sung, J.M. Sung, Hywel-Jones & Spatafora, *Ophiocordycipitaceae*. The fungal scientific names are currently accepted according to Index fungorum (http://www.indexfungorum.org/). The blend was solubilized in water and the dose of 4 mg supplement/day/mouse (corresponding to 0.16 g/kg/day) was selected to simulate human oral supplementation. The residual n = 14 not-treated mice (namely Untreated) and n = 4 healthy controls were fed without any supplementation. The syngeneic tumour-bearing mice were generated by injecting 4T1 cells ($10^6$) into the nape of the neck of the BALB/c female animals. The healthy controls were inoculated with the vehicle (i.e. phosphate-buffer saline, PBS). The quality of life (QoL), measured in terms of body weight gain and water consumption, and locomotor activity were

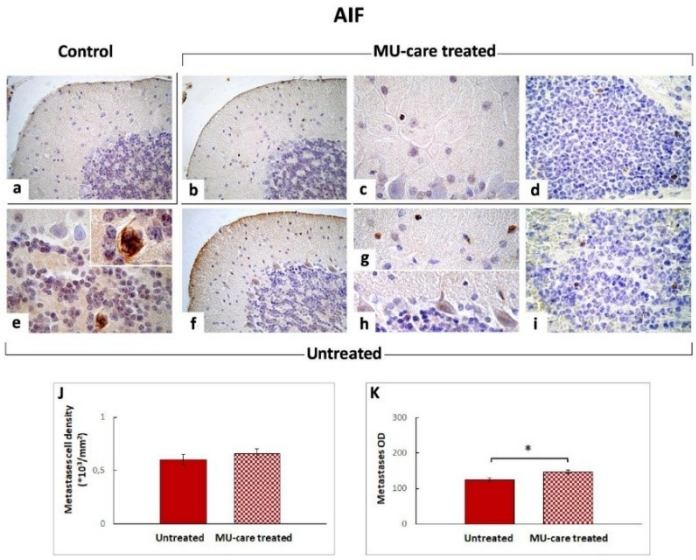


**Fig. 11.** Representative cerebellar sections immunostained for AIF in healthy control (**a**), MU-care treated (**b-d**), and Untreated (**e-i**) mice. An intensely marked AIF immunopositivity was observed in IGL of Untreated mice (**e**) as well as in ML of both MU-care treated (**c**) and Untreated (**g**) animals. Several immunolabeled cells were spotted in metastases, both in Untreated (**i**) and MU-care treated (**d**) mice. Light microscopy magnification: 40 × (**a, b, f**); 60 × (**c, d, e, g, h, i**); 100x (insert in **e**). **Panels J** and **K**: Histograms demonstrating quantitative data concerning metastases cell density and OD, respectively. *p* value calculated by unpaired Student's t-test: (*) < 0.05.

checked every day. Experimental time plan comprised: T0, animals' randomization; T1, Micotherapy U-care oral supplementation initiation (for MU-care treated mice, only); T2 (about 2 months later), 4T1 cells inoculation in both Untreated and MU-care treated mice; T3 (about 20 days later): monitoring and evaluations beginning; T4 (about 15 days later): monitoring and evaluations ongoing. At T1 and T3, the locomotor activity was examined by using a behavioural test. Twenty-four hours after T4, mice were euthanized and cerebella were removed and processed for histopathological and immunohistochemical investigations.

### 4.3. Emergence test

At chosen timepoints, i.e. T1 and T3, all mice performed the emergence task, a spontaneous behavioural test being a variant of the open-field test, properly designed to reduce anxiety by providing a safe enclosure within the open field. The emergence task was used to assess exploratory behaviour and locomotor activities. The free exploration test consisted of housing mice in a compartment prior to giving the animal a free choice between a familiar compartment and a novel one. During the test, each animal was located in a familiar environment (cage measures: 13 cm x 15 cm x 33 cm, length x width x height) with a hole in one side (4 cm wide and 5 cm long) through which it could emerge in a larger arena (60 cm x 90 cm, width x length) without walls but with a laminated floor. The observation lasted 8 min/mouse, during the free exploring of the arena. Three locomotor parameters were assessed: total distance (cm), mean speed (cm/s), and resting time (s). The animals' movement was tracked and quantified using a SMART video automated tracking system (2 Biological Instruments, Besozzo, Varese, Italy) with 40 ms/point sampling time and a Sony CCD colour video camera (PAL; Sony Europe B.V.- Italian headquarters, Milan, Italy) [69]. Emergence test results were expressed as a score index, calculated as reported below.

### 4.4. Histology and immunohistochemistry

#### 4.4.1. Cerebellar tissue

Thirty-five days after 4T1 injection, mice were deeply anesthetized before decapitation by using isoflurane inhalation (Aldrich, Milwaukee, WI, USA). Cerebella were immediately excised as previously described [57], washed in 0.9% NaCl, and post-fixed by immersion for 7 h in 4% paraformaldehyde in 0.1 M phosphate buffer (pH 7.4), dehydrated through a graded series of ethanol and finally embedded in Paraplast X-TRA. Using a manual rotatory microtome, sagittal Section (8 μm thick) of cerebellar vermis, were cut serially and collected on silane-coated slides.

#### 4.4.2. Morphological and histochemical evaluations

To reveal cerebellar cortex cytoarchitecture and estimate potential structural alterations by light microscopy, Haematoxylin and Eosin (H&E), Nissl and Picrosirius Red (PSR) staining were executed as previously described [70–73]. Briefly, serial tissue sections were processed as follows: (i) *H&E*: 10 min staining with Carazzi's Haematoxylin (Bio-Optica Milano S.p.A., Milano, Italy), followed by 20 min wash in running tap water and counterstaining with 1% eosin solution

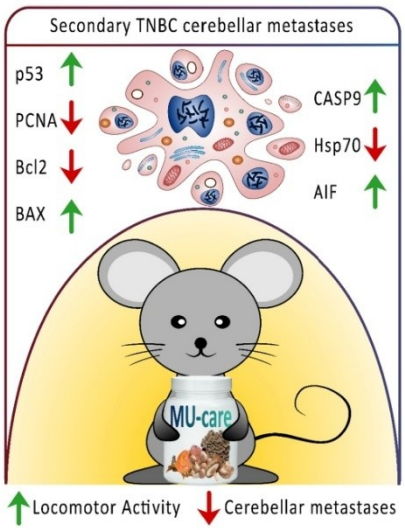


**Fig. 12.** Illustrative picture summarizing main findings and take-home message.

**Table 7**
MU-care blend: MM composition.

| Medicinal mushroom | Fungal part | % | ID code |
|---|---|---|---|
| *Agaricus blazei* | Fruiting body | 20 | 7700 |
| *Ganoderma lucidum* | Fruiting body | 20 | Gac |
| *Grifola frondosa* | Fruiting body | 20 | Gf3 |
| *Lentinula edodes* | Fruiting body | 20 | Le.ed.1 |
| *Ophiocordyceps sinensis* | Fruiting body + mycelium | 20 | Cm2 |

(Bio-Optica Milano S.p.A., Milano, Italy); the nucleic acids stain violet to dark blue while the proteins stain pink to red; (ii) *Nissl*: 1% cresyl violet (Sigma, St. Louis, MO, USA) solution for 3 min followed by differentiation in acetic acid in 100% ethanol (at 1:50,000 dilution) for 5 s; (iii) *PSR*: 1 h staining with Picrosirius Red solution (0.1% of Sirius Red in saturated aqueous picric acid), followed by a wash in 5% acidified water [71–73]. Lastly, all differently stained cerebellar sections were dehydrated in ethanol, cleared in xylene, and mounted in Eukitt (Kindler, Freiburg, Germany).

#### 4.4.3. Immunohistochemistry

With the aim at preventing potential staining discrepancies due to minor changes in the protocol, immunocytochemical reactions were performed simultaneously on slides from different experimental groups. Immunohistochemistry was carried out using commercial antibodies on murine cerebellar specimens, to localize presence and distribution of different cell death markers: (i) Proliferating Cell Nuclear Antigen (PCNA), (ii) B-cell lymphoma 2 (Bcl-2), (iii) Bcl2 Associated X (BAX), (iv) Caspase 9 (CASP9), (v) Caspase 3 (CASP3), and (vi) 70 kDa Heat shock protein (Hsp70).

After being de-paraffinized in xylene and rehydrated, cerebellar sections of healthy controls, Untreated, and MU-care treated mice underwent antigen retrieval and were then incubated overnight at room temperature in a dark moist chamber with selected monoclonal and polyclonal primary antibodies (Table 8) diluted in PBS.

Subsequently, proper biotinylated secondary antibodies (Table 8) and an avidin biotinylated horseradish peroxidase complex (Vector Laboratories, Burlingame, CA, USA) were employed to uncover the antigen/antibody interaction sites. The 3,3'-diaminobenzidine tetrahydrochloride peroxidase substrate (Sigma, St. Louis, MO, USA) was utilized as the chromogen, while the nuclear counterstaining was done using Carazzi's Haematoxylin.

Next, sections were dehydrated in ethanol, cleared in xylene, and mounted in Eukitt (Kindler, Freiburg, Germany). As negative untreated, some tissues were incubated with PBS in absence of primary antibodies: no immunoreactivity was detected in this condition.

#### 4.4.4. Microscopes, imaging systems and histochemical/immunohistochemical measurements

After morphological and histochemical reactions, slides were observed and scored using a bright-field Zeiss Axioscop Plus 612 microscope (Carl Zeiss S.p.A., Milan, Italy). Five slides (about 18–20 randomized sections) per animal were analysed; 5 microscopic fields were examined in each section for each mouse per time/condition. The images were recorded with an Olympus Camedia C-5050 digital camera and stored on a PC running Olympus software (Olympus Italia, Segrate, MI, Italy). Following immunohistochemical procedures, slides were examined using an Olympus BX51 optical microscope (model BX51TF). The images were acquired with an Olympus CAMEDIA C4040ZOOM camera (Olympus Italia, Segrate, MI, Italy). For each marker, six slides (about 30 sections) per animal were analysed. Cerebellar specimens from all experimental group displayed different immunolabelling extent and the figures show the most representative changes for each immunohistochemical reaction. The diverse labelling extents were evaluated on acquired digitized section images under exposure time avoiding any pixel saturation effect. The labelling intensity was measured exploiting densitometric analysis (Image-J 1.46p; NIH, Bethesda, MA, USA). The mask shape was adjusted depending on the spatial distribution of the cell type and/or tissue specimens under measurement; the labelling was measured as the mean intensity value over the area. The immunocytochemical intensity, specified as optical density (OD), was assessed in 3 randomized images/section (making at least 10 measurements/image) per 5 slides/animal from each experimental group, with the operator blinded to the experimental condition. Results were recorded on Microsoft Office Excel Software spreadsheets and the analysis was achieved using the ImageJ software. The following additional measurements were carried out: immunopositive metastases and micrometastases density count (number of metastases and micrometastases/area in $cm^2$); immunopositive cells density count ($*10^3$) (number of immunopositive cells/area in $mm^2$).

### 4.5. Statistics

Data were expressed as means ± standard error of the mean (SEM). The Bartlett and Shapiro Wilk Tests was used to establish and confirm the normality of parameters. Then, data were analysed to verify statistically significant differences. One-way ANOVA and Bonferroni post-hoc tests were performed to compare the different groups as regards to the behavioural test analysis. The statistical analysis for histology (namely H&E) was performed using unpaired Student's t-test. Concerning Picrosirius Red staining, one-way ANOVA followed by Bonferroni's post-hoc test was carried out. Regarding immunohistochemistry, unpaired Student's t-test was employed for metastatic areas to measure significant changes between MU-care treated and Untreated mice. The differences were considered statistically significant for $p < 0.05$ (*), $p < 0.01$ (**), and $p < 0.001$ (***). Statistical analyses were performed by using GraphPad Prism 7.0 (GraphPad Software Inc., La Jolla, CA, USA) and R software.

**Table 8**
Primary/secondary antibodies employed for light microscopy experimental procedures.

| | Antigen | Immunogen | Manufacturer, Species, Mono-Polyclonal, Cat./Lot. No., RRID | Dilution |
|---|---|---|---|---|
| Primary antibodies | Anti-B-Cell Leukemia/ Lymphoma 2 protein (N-19) | Purified antibody raised against a peptide mapping at the N-terminus of Bcl-2 of human origin | Santa Cruz Biotechnology (Santa Cruz, CA, USA), Rabbit polyclonal IgG, Cat# sc-492, RRID: AB_2064290 | 1:100 |
| | Anti-Bcl-2-associated X protein (P-19) | Purified antibody raised against a peptide mapping at the amino terminus of BAX of mouse origin | Santa Cruz Biotechnology (Santa Cruz, CA, USA), Rabbit polyclonal IgG, Cat# sc-526, RRID: AB_2064668 | 1:100 |
| | Anti- caspase-3 (31A1067) | Purified antibody raised against an epitope mapping between amino acids 50–86 of caspase-3 p17 of human origin | Santa Cruz Biotechnology (Santa Cruz, CA, USA), Mouse monoclonal IgG, Cat# sc-56053, RRID: AB_781826 | 1:100 |
| | Anti-Caspase 9 p35 (A-9) | Purified antibody raised against amino acids 100–270 of caspase-9 p35 of human origin. | Santa Cruz Biotechnology (Santa Cruz, CA, USA), Mouse monoclonal IgG, Cat# sc-133109, RRID: AB_2073466 | 1:100 |
| | Anti-HSP 70/HSC 70 (5A5) | Purified antibody raised against recombinant HSP 70/HSC 70 of human origin | Santa Cruz Biotechnology (Santa Cruz, CA, USA), Mouse monoclonal IgG, Cat# sc-32239, RRID: AB_627759 | 1:100 |
| | Anti-apoptosis-inducing factor (E-1) | Purified antibody raised against amino acids 1–300 of AIF of human origin | Santa Cruz Biotechnology (Santa Cruz, CA, USA), Mouse monoclonal IgG, Cat# sc-13116, RRID: AB_626654 | 1:100 |
| | Anti-p53 (Ab-5) | Purified antibody raised against the ~53 kDa wild type p53 protein of mouse origin | Sigma-Aldrich (St. Louis, MO, USA), Mouse monoclonal IgG2a, Cat# OP33–100UG, RRID: AB_564977 | 1:100 |
| | Anti-Proliferating Cell Nuclear Antigen (Ab-1) | Purified antibody raised against the ~37 kDa PCNA protein of mouse origin | Sigma-Aldrich (St. Louis, MO, USA), Mouse monoclonal IgG2a, Cat# NA03–200UG, RRID: AB_213111 | 1:500 |
| Secondary antibodies | Biotinylated goat anti-rabbit IgG | Gamma immunoglobulin | Vector Laboratories (Burlingame, CA, USA), Goat, lot# PK-6101, RRID: AB_2336820 | 1:200 |
| | Biotinylated horse anti-mouse IgG | Gamma immunoglobulin | Vector Laboratories (Burlingame, CA, USA), Horse, Cat# PK-6102, RRID: AB_2336821 | 1:200 |

## 5. Conclusions

Overall, our current findings revealed that MU-care display a selective anti-cancer effect addressed on cerebellar metastases, accompanied by a beneficial action on locomotor performances, thus supporting the efficacy of the MM blend on CNS secondary breast cancer. This MU-care played mechanism, inhibiting the metastatization pattern, triggering an imbalance between proliferation and cell death, hence driving to a significant apoptosis increase, could therefore representing a promising approach for patients' management as adjuvant therapy in the prevention and treatment of secondary breast cancer in brain. In fact, being the TNBC the most aggressive malignant BC, characterized by unresponsiveness to current clinical treatments, high relapse rate and typical metastatization pattern targeting CNS, the synergistic effect of MU-care supplement joint with conventional therapies targeting crucial cancer signalling pathways, i.e., proliferation and apoptosis, may hamper cellular and molecular processes feeding TNBC growth, thus delaying or even impeding the TNBC metastatic pattern, often associated with poor prognosis. Therefore, taken as a whole, the reported data support the use of MU-care oral supplementation as a new promising adjuvant strategy, in the field of integrative oncology, which could help to fight the occurrence of TNBC-derived BM.

## Funding

This research was supported by the University of Pavia: Fondi Ricerca Giovani (FRG 2018). This research was also supported by Italian Ministry of Education, University and Research (MIUR): Dipartimenti di Eccellenza Program (2018–2022) Dept. of Biology and Biotechnology "L. Spallanzani", University of Pavia.

## CRediT authorship contribution statement

**Paola Rossi**: Conceptualization, Methodology, Formal analysis, Writing – original draft, Writing – review & editing, Supervision, Project administration. **Elisa Roda**: Conceptualization, Methodology, Investigation, Formal analysis, Writing – original draft, Writing – review & editing, Supervision. **Fabrizio De Luca**: Methodology, Investigation, Formal analysis, Writing – original draft. **Daniela Ratto**: Software, Investigation, Formal analysis. **Anthea Desiderio**: Software, Validation. **Maria Teresa Venuti**: Software, Data curation. **Martino Ramieri**: Software, Validation. **Maria Grazia Bottone**: Resources. **Elena Savino**: Resources.

## Conflict of interest statement

The authors declare that the research was conducted in the absence of any commercial or financial relationships that could be construed as a potential conflict of interest.

## Acknowledgments

We thank Dr Carmine Di Iorio (Heallo S.r.l) for his technical assistance.

*Author Contributions*

E.R., P.R. conceived and designed the experiments. F.D.L., E.R., D.R., and P.R. performed the experiments and analysed the data. M.G.B. and E.S. contributed reagents, materials and analysis tools. A.D., M.T.V. and M.R. searched and reviewed the literatures. F.D.L., E.R. and P.R. drafted the paper. E.R. and P.R. critically revised the article. All authors provided critical feedback, helping shape the research and analysis. All

authors read and agreed to the published version of the manuscript.

## References


[1] H. Sung, J. Ferlay, R.L. Siegel, M. Laversanne, I. Soerjomataram, A. Jemal, F. Bray, Global cancer statistics 2020: GLOBOCAN estimates of incidence and mortality worldwide for 36 cancers in 185 countries, CA Cancer J. Clin. 71 (2021) 209–249, https://doi.org/10.3322/caac.21660.

[2] I. Cetin, M. Topcul, Triple negative breast cancer, Asian Pac. J. Cancer Prev. 15 (2014) 2427–2431, https://doi.org/10.7314/APJCP.2014.15.6.2427.

[3] V. Ossovskaya, Y. Wang, A. Budoff, Q. Xu, A. Lituev, O. Potapova, G. Vansant, J. Monforte, N. Darasella, Exploring molecular pathways of triple-negative breast cancer, Genes Cancer 2 (2011) 870–879, https://doi.org/10.1177/1947601911432496.

[4] P. Boyle, Triple-negative breast cancer: epidemiological considerations and recommendations, Ann. Oncol. 23 (6) (2012) vi7–vi12, https://doi.org/10.1093/annonc/mds187.

[5] F. Podo, L.M.C. Buydens, H. Degani, R. Hilhorst, E. Klipp, I.S. Gribbestad, S. V. Huffel, H.W.M. van Laarhoven, J. Luts, D. Monleon, et al., Triple-negative breast cancer: present challenges and new perspectives, Mol. Oncol. 4 (2010) 209–229, https://doi.org/10.1016/j.molonc.2010.04.006.

[6] D.C. Brady-West, D.A. McGrowder, Triple negative breast cancer: therapeutic and prognostic implications, Asian Pac. J. Cancer Prev. 12 (2011) 2139–2143.

[7] E. Roda, F. De Luca, C. Di Iorio, D. Ratto, S. Siciliani, B. Ferrari, F. Cobelli, G. Borsci, E.C. Priori, S. Chinosi, et al., Novel medicinal mushroom blend as a promising supplement in integrative oncology: a multi-tiered study using 4t1 triple-negative mouse breast cancer model, Int. J. Mol. Sci. 21 (2020) 3479, https://doi.org/10.3390/ijms21103479.

[8] C. Neophytou, P. Boutsikos, P. Papageorgis, Molecular mechanisms and emerging therapeutic targets of triple-negative breast cancer metastasis, Front. Oncol. 8 (2018) 31, https://doi.org/10.3389/fonc.2018.00031.

[9] K. Altundag, M.L. Bondy, N.Q. Mirza, S.-W. Kau, K. Broglio, G.N. Hortobagyi, E. Rivera, Clinicopathologic characteristics and prognostic factors in 420 metastatic breast cancer patients with central nervous system metastasis, Cancer 110 (2007) 2640–2647, https://doi.org/10.1002/cncr.23088.

[10] U.Y. Arslan, Breast cancer subtypes and outcomes of central nervous system metastases, Breast (2011) 6.

[11] R.-H. Yeh, J.-C. Yu, C.-H. Chu, C.-L. Ho, H.-W. Kao, G.-S. Liao, H.-W. Chen, W.-Y. Kao, C.-P. Yu, T.-Y. Chao, et al., Distinct MR imaging features of triple-negative breast cancer with brain metastasis, J. Neuroimaging 25 (2015) 474–481, https://doi.org/10.1111/jon.12149.

[12] N. Niikura, J. Liu, N. Hayashi, E.A. Mittendorf, Y. Gong, S.L. Palla, Y. Tokuda, A. M. Gonzalez-Angulo, G.N. Hortobagyi, N.T. Ueno, Loss of human epidermal growth factor receptor 2 (HER2) expression in metastatic sites of HER2-overexpressing primary breast tumors, J. Clin. Oncol. 30 (2012) 593–599, https://doi.org/10.1200/JCO.2010.33.8889.

[13] S.Y. Jung, M. Rosenzweig, S.M. Sereika, F. Linkov, A. Brufsky, J.L. Weissfeld, Factors associated with mortality after breast cancer metastasis, Cancer Causes Control 23 (2012) 103–112, https://doi.org/10.1007/s10552-011-9859-8.

[14] S. Paknesha, D. Safarpour, F. Tavassoli, B. Jabbari, Brain metastasis from ovarian cancer: a systematic review, J. Neurooncol. 119 (2014) 1–6, https://doi.org/10.1007/s11060-014-1447-9.

[15] A.H. Graf, W. Buchberger, H. Langmayr, K.W. Schmid, Site preference of metastatic tumours of the brain, Virchows Arch. A Pathol. Anat. Histopathol. 412 (1988) 493–498, https://doi.org/10.1007/BF00750584.

[16] C. Bailleux, L. Eberst, T. Bachelot, Treatment strategies for breast cancer brain metastases, Br. J. Cancer 124 (2021) 142–155, https://doi.org/10.1038/s41416-020-01175-y.

[17] R. Rostami, S. Mittal, P. Rostami, F. Tavassoli, B. Jabbari, Brain metastasis in breast cancer: a comprehensive literature review, J. Neurooncol. 127 (2016) 407–414, https://doi.org/10.1007/s11060-016-2075-3.

[18] P.D. Bos, X.H.-F. Zhang, C. Nadal, W. Shu, R.R. Gomis, D.X. Nguyen, A.J. Minn, M. J. van de Vijver, W.L. Gerald, J.A. Foekens, et al., Genes that mediate breast cancer metastasis to the brain, Nature 459 (2009) 1005–1009, https://doi.org/10.1038/nature08021.

[19] D.P. Fitzgerald, D. Palmieri, E. Hua, E. Hargrave, J.M. Herring, Y. Qian, E. Vega-Valle, R.J. Weil, A.M. Stark, A.O. Vortmeyer, et al., Reactive glia are recruited by highly proliferative brain metastases of breast cancer and promote tumor cell colonization, Clin. Exp. Metastasis 25 (2008) 799–810, https://doi.org/10.1007/s10585-008-9193-z.

[20] S.P. Wasser, Medicinal mushrooms in human clinical studies. Part I. Anticancer, oncoimmunological, and immunomodulatory activities: a review, Int. J. Med. Mushrooms 19 (2017) 279–317, https://doi.org/10.1615/IntJMedMushrooms.v19.i4.10.

[21] P. Rossi, R. Difrancia, V. Quagliariello, E. Savino, P. Tralongo, C.L. Randazzo, M. Berretta, B-glucans from grifola frondosa and ganoderma lucidum in breast cancer: an example of complementary and integrative medicine, Oncotarget 9 (2018) 24837–24856, https://doi.org/10.18632/oncotarget.24984.

[22] K. Tanaka, Y. Matsui, S. Ishikawa, T. Kawanishi, M. Harada, Oral ingestion of lentinula edodes mycelia extract can restore the antitumor T cell response of mice inoculated with colon-26 cells into the subserosal space of the cecum, Oncol. Rep. 27 (2012) 325–332, https://doi.org/10.3892/or.2011.1549.

[23] J. Jiang, D. Sliva, Novel medicinal mushroom blend suppresses growth and invasiveness of human breast cancer cells, Int. J. Oncol. 37 (2010) 1529–1536, https://doi.org/10.3892/ijo_00000806.

[24] B.G.J. Moerings, P. de Graaff, M. Furber, R.F. Witkamp, R. Debets, J.J. Mes, J. van Bergenhenegouwen, C. Govers, Continuous exposure to non-soluble β-glucans induces trained immunity in M-CSF-differentiated macrophages, Front. Immunol. 12 (2021), 672796, https://doi.org/10.3389/fimmu.2021.672796.

[25] L. Steimbach, A.V. Borgmann, G.G. Gomar, L.V. Hoffmann, R. Rutckeviski, D.P. de Andrade, F.R. Smiderle, Fungal beta-glucans as adjuvants for treating cancer patients - a systematic review of clinical trials, Clin. Nutr. 40 (2021) 3104–3113, https://doi.org/10.1016/j.clnu.2020.11.029.

[26] N. Kodama, K. Komuta, H. Nanba, Effect of maitake (Grifola Frondosa) D-fraction on the activation of NK cells in cancer patients, J. Med. Food 6 (2003) 371–377, https://doi.org/10.1089/109662003772519949.

[27] G. Deng, H. Lin, A. Seidman, M. Fornier, G. D'Andrea, K. Wesa, S. Yeung, S. Cunningham-Rundles, A.J. Vickers, B. Cassileth, A phase I/II trial of a polysaccharide extract from grifola frondosa (maitake mushroom) in breast cancer patients: immunological effects, J. Cancer Res. Clin. Oncol. 135 (2009) 1215–1221, https://doi.org/10.1007/s00432-009-0562-z.

[28] P. Singh, B. Lim, Targeting apoptosis in cancer, Curr. Oncol. Rep. 24 (2022) 273–284, https://doi.org/10.1007/s11912-022-01199-y.

[29] E. Roda, F. De Luca, C.A. Locatelli, D. Ratto, C. Di Iorio, E. Savino, M.G. Bottone, P. Rossi, From a medicinal mushroom blend a direct anticancer effect on triple-negative breast cancer: a preclinical study on lung metastases, Molecules (2020) 25, https://doi.org/10.3390/molecules25225400.

[30] M. Berretta, A. Morra, R. Taibi, F. Monari, N. Maurea, M. Ippolito, U. Tirelli, F. Fiorica, L. Montella, G. Facchini, et al., Improved survival and quality of life through an integrative, multidisciplinary oncological approach: pathophysiological analysis of four clinical cancer cases and review of the literature, Front. Pharmacol. 13 (2022), 867907, https://doi.org/10.3389/fphar.2022.867907.

[31] E. D'Angelo, P. Rossi, G. De Filippi, J. Magistretti, V. Taglietti, The relationship between synaptogenesis and expression of voltage-dependent currents in cerebellar granule cells in situ, J. Physiol. Paris 88 (1994) 197–207, https://doi.org/10.1016/0928-4257(94)90006-x.

[32] P. rossi, E. D'Angelo, V. Taglietti, Differential long-lasting potentiation of the NMDA and Non-NMDA synaptic currents induced by metabotropic and NMDA receptor coactivation in cerebellar granule cells, Eur. J. Neurosci. 8 (1996) 1182–1189, https://doi.org/10.1111/j.1460-9568.1996.tb01286.x.

[33] Y. Xiong, Y. Zhang, S. Xiong, A.E. Williams-Villalobo, A glance of P53 functions in brain development, neural stem cells, and brain cancer, Biology 9 (2020) 285, https://doi.org/10.3390/biology9090285.

[34] Y. Zhou, L. Liu, S. Tao, Y. Yao, Y. Wang, Q. Wei, A. Shao, Y. Deng, Parthanatos and its associated components: promising therapeutic targets for cancer, Pharmacol. Res. 163 (2021), 105299, https://doi.org/10.1016/j.phrs.2020.105299.

[35] M. Jeitler, A. Michalsen, D. Frings, M. Hübner, M. Fischer, D.A. Koppold-Liebscher, V. Murthy, C.S. Kessler, Significance of medicinal mushrooms in integrative oncology: a narrative review, Front. Pharmacol. 11 (2020) 1758, https://doi.org/10.3389/fphar.2020.580656.

[36] P. Nowakowski, R. Markiewicz-Żukowska, K. Gromkowska-Kępka, S.K. Naliwajko, J. Moskwa, J. Bielecka, M. Grabia, M. Borawska, K. Socha, Mushrooms as potential therapeutic agents in the treatment of cancer: evaluation of anti-glioma effects of coprinus comatus, cantharellus cibarius, lycoperdon perlatum and lactarius deliciosus extracts, Biomed. Pharmacother. 133 (2021), 111090, https://doi.org/10.1016/j.biopha.2020.111090.

[37] S.K. Panda, G. Saheo, S.S. Swain, W. Luyten, Anticancer activities of mushrooms: a neglected source for drug discovery, Pharmaceuticals 15 (2022) 176, https://doi.org/10.3390/ph15020176.

[38] A. Sathyanesan, V. Gallo, Cerebellar contribution to locomotor behavior: a neurodevelopmental perspective, Neurobiol. Learn. Mem. 165 (2019), 106861, https://doi.org/10.1016/j.nlm.2018.04.016.

[39] S.M. Morton, A.J. Bastian, Cerebellar control of balance and locomotion, Neuroscientist 10 (2004) 247–259, https://doi.org/10.1177/1073858404263517.

[40] J.-B. Passot, D. Sheynikhovich, É. Duvelle, A. Arleo, Contribution of cerebellar sensorimotor adaptation to hippocampal spatial memory, PLoS One 7 (2012), e32560, https://doi.org/10.1371/journal.pone.0032560.

[41] J.N. Crawley, J.K. Belknap, A. Collins, J.C. Crabbe, W. Frankel, N. Henderson, R. J. Hitzemann, S.C. Maxson, L.L. Miner, A.J. Silva, et al., Behavioral phenotypes of inbred mouse strains: implications and recommendations for molecular studies, Psychopharmacology 132 (1997) 107–124, https://doi.org/10.1007/s002130050327.

[42] R.M. Saré, A. Lemons, C.B. Smith, Behavior testing in rodents: highlighting potential confounds affecting variability and reproducibility, Brain Sci. 11 (2021) 522, https://doi.org/10.3390/brainsci11040522.

[43] M. Chang, J.S. Saczynski, J. Snaedal, S. Bjornsson, B. Einarsson, M. Garcia, T. Aspelund, K. Siggeirsdottir, V. Gudnason, L.J. Launer, et al., Midlife physical activity preserves lower extremity function in older adults: age gene/environment susceptibility-reykjavik study, J. Am. Geriatr. Soc. 61 (2013) 237–242, https://doi.org/10.1111/jgs.12077.

[44] A. Middleton, S.L. Fritz, M. Lusardi, Walking speed: the functional vital sign, J. Aging Phys. Act. 23 (2015) 314–322, https://doi.org/10.1123/japa.2013-0236.

[45] H. Mehmet, S.R. Robinson, A.W.H. Yang, Assessment of gait speed in older adults, J. Geriatr. Phys. Ther. 43 (2020) 42–52, https://doi.org/10.1519/JPT.0000000000000224.

[46] P. Mahlknecht, S. Kiechl, J. Willeit, W. Poewe, K. Seppi, Motoric cognitive risk syndrome: multicenter incidence study, Neurology 85 (2015) 388–389, https://doi.org/10.1212/01.wnl.0000470376.04336.ea.

[47] E. Buckley, C. Mazzà, A. McNeill, A systematic review of the gait characteristics associated with cerebellar ataxia, Gait Posture 60 (2018) 154–163, https://doi.org/10.1016/j.gaitpost.2017.11.024.

[48] A. Droby, M.M. El Mendili, N. Giladi, J.M. Hausdorff, I. Maidan, A. Mirelman, Gait and cognitive abnormalities are associated with regional cerebellar atrophy in elderly fallers - a pilot study, Gait Posture 90 (2021) 99–105, https://doi.org/10.1016/j.gaitpost.2021.08.012.
[49] Q. Tian, S.A. Studenski, M. Montero-Odasso, C. Davatzikos, S.M. Resnick, L. Ferrucci, Cognitive and neuroimaging profiles of older adults with dual decline in memory and gait speed, Neurobiol. Aging 97 (2021) 49–55, https://doi.org/10.1016/j.neurobiolaging.2020.10.002.
[50] L.F. Koziol, D. Budding, N. Andreasen, S. D'Arrigo, S. Bulgheroni, H. Imamizu, M. Ito, M. Manto, C. Marvel, K. Parker, et al., Consensus paper: the cerebellum's role in movement and cognition, Cerebellum 13 (2014) 151–177, https://doi.org/10.1007/s12311-013-0511-x.
[51] C.J. Stoodley, J.D. Schmahmann, Functional topography in the human cerebellum: a meta-analysis of neuroimaging studies, Neuroimage 44 (2009) 489–501, https://doi.org/10.1016/j.neuroimage.2008.08.039.
[52] K. Kansal, Z. Yang, A.M. Fishman, H.I. Sair, S.H. Ying, B.M. Jedynak, J.L. Prince, C. U. Onyike, Structural cerebellar correlates of cognitive and motor dysfunctions in cerebellar degeneration, Brain 140 (2017) 707–720, https://doi.org/10.1093/brain/aww327.
[53] A.H. Fischer, K.A. Jacobson, J. Rose, R. Zeller, Hematoxylin and eosin staining of tissue and cell sections, pdb.prot4986, CSH Protoc. 2008 (2008), https://doi.org/10.1101/pdb.prot4986.
[54] D. Komura, A. Kawabe, K. Fukuta, K. Sano, T. Umezaki, H. Koda, R. Suzuki, K. Tominaga, M. Ochi, H. Konishi, et al., Universal encoding of pan-cancer histology by deep texture representations, Cell Rep. 38 (2022), 110424, https://doi.org/10.1016/j.celrep.2022.110424.
[55] S.M. Yamada, Y. Tomita, S. Shibui, T. Kurokawa, Y. Baba, A case of breast cancer brain metastasis with a 16-year time interval without evidence of cancer recurrence, J. Breast Cancer 20 (2017) 212–216, https://doi.org/10.4048/jbc.2017.20.2.212.
[56] C. Segnani, C. Ippolito, L. Antonioli, C. Pellegrini, C. Blandizzi, A. Dolfi, N. Bernardini, Histochemical detection of collagen fibers by sirius red/fast green is more sensitive than van gieson or sirius red alone in normal and inflamed rat colon, PLoS One 10 (2015), e0144630, https://doi.org/10.1371/journal.pone.0144630.
[57] E. Roda, E.C. Priori, D. Ratto, F. De Luca, C. Di Iorio, P. Angelone, C.A. Locatelli, A. Desiderio, L. Goppa, E. Savino, et al., Neuroprotective metabolites of hericium erinaceus promote neuro-healthy aging, Int. J. Mol. Sci. 22 (2021) 6379, https://doi.org/10.3390/ijms22126379.
[58] S. Krajewski, A.D. Thor, S.M. Edgerton, D.H. Moore, M. Krajewska, J.C. Reed, Analysis of bax and Bcl-2 expression in P53-immunopositive breast cancers, Clin. Cancer Res. 3 (1997) 199–208.
[59] S.E. Bodrug, C. Aimé-Sempé, T. Sato, S. Krajewski, M. Hanada, J.C. Reed, Biochemical and functional comparisons of Mcl-1 and Bcl-2 proteins: evidence for a novel mechanism of regulating Bcl-2 family protein function, Cell Death Differ. 2 (1995) 173–182.
[60] Z.N. Oltvai, C.L. Milliman, S.J. Korsmeyer, Bcl-2 heterodimerizes in vivo with a conserved homolog, bax, that accelerates programed cell death, Cell 74 (1993) 609–619, https://doi.org/10.1016/0092-8674(93)90509-O.
[61] T.P. Berke, S.H. Slight, S.M. Hyder, Role of reactivating mutant P53 protein in suppressing growth and metastasis of triple-negative breast cancer, Onco Targets Ther. 15 (2022) 23–30, https://doi.org/10.2147/OTT.S342292.
[62] P. Li, L. Zhou, T. Zhao, X. Liu, P. Zhang, Y. Liu, X. Zheng, Q. Li, Caspase-9: structure, mechanisms and clinical application, Oncotarget 8 (2017) 23996–24008, https://doi.org/10.18632/oncotarget.15098.
[63] J.L.Y. Chee, S. Saidin, D.P. Lane, S.M. Leong, J.E. Noll, P.M. Neilsen, Y.T. Phua, H. Gabra, T.M. Lim, Wild-type and mutant P53 mediate cisplatin resistance through interaction and inhibition of active caspase-9, Cell Cycle 12 (2013) 278–288, https://doi.org/10.4161/cc.23054.
[64] X. Pu, S.J. Storr, Y. Zhang, E.A. Rakha, A.R. Green, I.O. Ellis, S.G. Martin, Caspase-3 and caspase-8 expression in breast cancer: caspase-3 is associated with survival, Apoptosis 22 (2017) 357–368, https://doi.org/10.1007/s10495-016-1323-5.
[65] L.M. Vargas-Roig, M.A. Fanelli, L.A. López, F.E. Gago, O. Tello, J.C. Aznar, D. R. Ciocca, Heat shock proteins and cell proliferation in human breast cancer biopsy samples, Cancer Detect. Prev. 21 (1997) 441–451.
[66] J.M. Murphy, P.E. Czabotar, J.M. Hildebrand, I.S. Lucet, J.-G. Zhang, S. Alvarez-Diaz, R. Lewis, N. Lalaoui, D. Metcalf, A.I. Webb, et al., The pseudokinase MLKL mediates necroptosis via a molecular switch mechanism, Immunity 39 (2013) 443–453, https://doi.org/10.1016/j.immuni.2013.06.018.
[67] Z. Albakova, G.A. Armeev, L.M. Kanevskiy, E.I. Kovalenko, A.M. Sapozhnikov, HSP70 multi-functionality in cancer, Cells 9 (2020), E587, https://doi.org/10.3390/cells9030587.
[68] L. Gaianschi, E. Roda, C. Favaron, F. Gola, E. Gabano, M. Ravera, P. Rossi, M. G. Bottone, The power of a novel combined anticancer therapy: challenge and opportunity of micotherapy in the treatment of glioblastoma multiforme, Biomed. Pharmacother. 155 (2022), 113729, https://doi.org/10.1016/j.biopha.2022.113729.
[69] D. Ratto, F. Corana, B. Mannucci, E.C. Priori, F. Cobelli, E. Roda, B. Ferrari, A. Occhinegro, C. Di Iorio, F. De Luca, et al., Hericium erinaceus improves recognition memory and induces hippocampal and cerebellar neurogenesis in frail mice during aging, Nutrients 11 (2019), E715, https://doi.org/10.3390/nu11040715.
[70] Godwin Avwioro Histochemical Uses of Haematoxylin. Journal of Physics; Conference Series 2011, 1, 24–34.
[71] A. Kidár, G. Wittmann, Z. Liposits, C. Fekete, Improved method for combination of immunocytochemistry and nissl staining, J. Neurosci. Methods 184 (2009) 115–118, https://doi.org/10.1016/j.jneumeth.2009.07.010.
[72] E. Roda, S. Barni, A. Milzani, I. Dalle-Donne, G. Colombo, T. Coccini, Single silver nanoparticle instillation induced early and persisting moderate cortical damage in rat kidneys, Int. J. Mol. Sci. 18 (2017), E2115, https://doi.org/10.3390/ijms18102115.
[73] R. Lattouf, R. Younes, D. Lutomski, N. Naaman, G. Godeau, K. Senni, S. Changotade, Picrosirius red staining, J. Histochem. Cytochem. 62 (2014) 751–758, https://doi.org/10.1369/0022155414545787.